Transactions of the ASME®

Technical Editor
G. K. SEROVY
Associate Technical Editors
Advanced Energy Systems
M. J. MORAN
Environmental Control
H. E. HESKETH
Fuels and Combustion Technologies
D. W. PACER
Gas Turbine
S. A. MOSIER
Internal Combustion Engine
J. A. CATON
Nuclear Engineering
S. M. CHO
Power
R. W. PORTER

BOARD ON COMMUNICATIONS
Chairman and Vice-President
R. NICKELL

Members-at-Large
W. BEGELL
T. F. CONRY
M. FRANKE
R. L. KASTOR
M. KUTZ
R. MATES
T. C. MIN
E. M. PATTON
R. E. REDER
R. D. ROCKE
F. W. SCHMIDT
W. O. WINER
A. J. WENNERSTROM
B. ZIELS

President, C. O. VELZY
Executive Director,
D. L. BELDEN
Treasurer, ROBERT A. BENNETT

PUBLISHING STAFF
Mng. Dir., Publ.,
CHARLES W. BEARDSLEY
Managing Editor,
CORNELIA MONAHAN
Sr. Production Editor,
VALERIE WINTERS
Editorial Prod. Asst.,
MARISOL ANDINO

Transactions of the ASME, Journal of Turbomachinery (ISSN 0889-504X) is published quarterly (Jan., Apr., July, Oct.) for $100 per year by The American Society of Mechanical Engineers, 345 East 47th Street, New York, NY 10017. Second-class postage paid at New York, NY and additional mailing offices. POSTMASTER: Send address change to Transactions of the ASME, Journal of Turbomachinery, c/o The AMERICAN SOCIETY OF MECHANICAL ENGINEERS, 22 Law Drive, Box 2300, Fairfield, NJ 07007-2300."

CHANGES OF ADDRESS must be received at Society headquarters seven weeks before they are to be effective. Please send old label and new address.

PRICES: To members, $29.00, annually: to nonmembers, $100.00. Add $15.00 for postage to countries outside the United States and Canada.

INDEXED by Applied Mechanics Reviews and Engineering Information, Inc.

Journal of Turbomachinery

Published Quarterly by The American Society of Mechanical Engineers

VOLUME 111 • NUMBER 4 • OCTOBER 1989

TECHNICAL PAPERS

ANNOUNCEMENTS

Low Aspect Ratio Axial Flow Compressors: Why and What It Means

A. J. Wennerstrom
Aero Propulsion and Power Laboratory,
Wright Research and Development Center
(AFSC),
Wright-Patterson Air Force Base, OH
45433-6563

One of the more visible changes that has occurred in fans and compressors for aircraft turbine engines that have entered development since about 1970 has been a significant reduction in the aspect ratio of the blading. This has brought with it a greatly reduced engine parts count and improved ruggedness and aeroelastic stability. This paper traces the evolution of thinking concerning appropriate aspect ratios for axial flow compressors since the early years of the aircraft turbine engine. In the 1950's, moderate aspect ratios were favored for reasons of mechanical design. As mechanical design capability became more sophisticated, several attempts were made, primarily in the 1960s, to employ very high aspect ratios to reduce engine size and weight. Four of these programs are described that were largely unsuccessful for both mechanical and aerodynamic reasons. After 1970, the pendulum swung strongly in the other direction and designs of very low aspect ratio began to emerge. This has had a significant impact on compressor design systems, and a number of the ways in which design systems have been affected are discussed. Some concluding remarks are made concerning the author's opinion of trends in the near future in aerodynamic design technology.

By about 1970, the aerodynamic design of axial-flow compressors as practiced by U.S. aero engine manufacturers appeared to be reaching a plateau of development. Axisymmetric through-flow computations of the streamline curvature type, such as described by Novak (1967) and others, were and still are the workhorse of the industry. Coupled with a large empirical data base, these provided reasonable, reliable, and consistent designs within the envelope of past design experience. Most designs of that era were accomplished using computing stations only at blade row edges and in unbladed spaces. Airfoils employed were usually of specific geometric families such as the NACA 65-series, double circular arc, etc. A few designers were even then including computing stations within bladed regions and producing designs incorporating airfoils having camber lines of arbitrary configuration, defined by other criteria such as a blade loading distribution. The first example of this, coupled with a streamline curvature computing procedure, was presented by Wright and Novak (1960).

Most of these designs had many features in common. Deviation angles were typically defined by some form of Carter's rule, adjusted by company experience. Endwall boundary layers were usually treated as blockages and were as often prescribed based upon past experience as by computations such as Jansen (1967) or Stratford (1967). Losses were most often defined by the sum of diffusion losses plus shock losses, with the former defined empirically as a function of Lieblein's diffusion factor (Lielein et al., 1953) and the latter by the Miller, Lewis, and Hartmann normal shock model (Miller et al., 1961). The effects that violate the assumption of flow following axisymmetric stream surfaces across which no mass, momentum, or energy is exchanged were usually neglected as small, second or third-order influences. The whole concept of design in this period revolved around the application of two-dimensional cascade-plane information, both experimental as well as analytical, to an axisymmetric design framework. Virtually all concepts defining loading limits and losses were derived from two-dimensional cascade-plane results.

These techniques were successfully applied to the design of many fine highly efficient compressors of the past, many of which are still providing outstanding service in aviation today. These techniques are still representative of the state-of-the-art in most companies designing industrial compressors. In aircraft engines, one of the results of this approach was to drive the designer toward relatively high aspect ratio blading. It stands to reason that, if you can only get so much loading out of a given stage turning at a particular speed, if the aspect ratio of all stages is increased, the overall compressor can be made shorter and lighter. Of course, making engines more compact and lighter weight to do the same job has always been a major goal of the aircraft engine designer, so this was the obvious way to go given the design philosophy of the time. How high one could go in aspect ratio was felt by many in the early 1960s to be primarily a structural consideration rather than an aerodynamic one. Aspect ratio did not enter directly into any aerodynamic predictions, and with high aspect ratios, the majority of the assumptions made for aerodynamic design purposes were reasonably valid. Three-dimensional effects tended to be small and could be safely ignored. By the late 1960s,

Contributed by the International Gas Turbine Institute and presented as the Cliff Garrett Turbomachinery Award Lecture at the Aerospace Technology Conference of the Society of Automotive Engineers in Long Beach, California, October 14, 1986; Paper No. SAE SP-636. Manuscript received at ASME Headquarters March 1989.

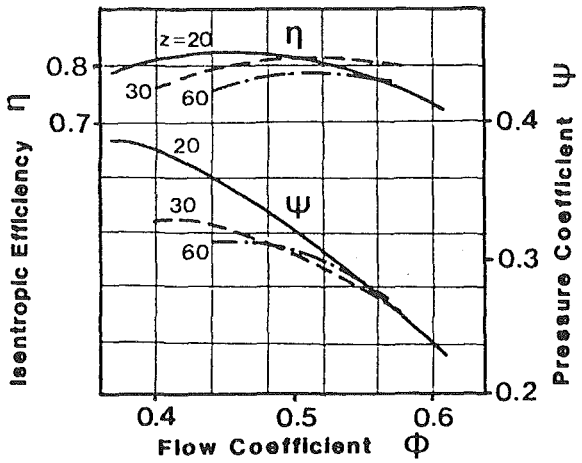

Fig. 1 Influence of aspect ratio at constant solidity of the impeller of an air blower

because of a series of bad experiences, most designers had converged on intermediate aspect ratios. For purposes of this paper, low aspect ratio is considered to be less than 2.0 and high as greater than 4.0.

The trend that had developed toward high aspect ratio designs is somewhat paradoxical. On the one hand, computational methods available to the designer up to 1970, and considerably beyond, could not deal with three-dimensional flow phenomena in any meaningful way. Thus high aspect ratios that minimized these effects seemed a safe way to go. It gave the designer more confidence in getting what he expected. On the other hand, there was some early experimental evidence that aspect ratio could play a very significant role in axial compressor performance. However, it appears to have been largely ignored. The earliest reference I have found to the influence of aspect ratio is contained in a book by A. N. Sherstyuk (1955), which was based on lectures given at the Moscow V. M. Molotov Order of Lenin Power Engineering Institute. The original work cited in this book was performed by V. A. Stefanovskiy at the N. Ye. Zhukovskiy Central Institute of Aerohydrodynamics in 1946. The results are reproduced in Fig. 1. These results present the characteristics of three stages of an air blower with identically shaped profiles and an identical cascade solidity, but with a differing number of blades, i.e., different chord lengths and thus aspect ratio. It is obvious from the figure that as aspect ratio (blade number) is decreased, there is a dramatic increase in stalling pressure rise and range as well as a modest increase in peak efficiency.

Rolls-Royce is also known to have developed a good appreciation of the effects of aspect ratio on range and performance by the mid-1950's as a result of a large number of unpublished in-house test data.

A few early examples can be found in U.S. literature. One of the best is the NACA eight-stage compressor. This compressor contained two transonic inlet stages. One of the tests involved a configuration for which the chord lengths of the two transonic inlet stages were doubled while solidity was held constant. The long-chord version had a larger stable operating range from 60 percent to design speed. These results are described by Standahar and Geye (1955) and Sievers et al. (1958). Similar results were observed by Kussoy and Bachkin (1958) in NACA tests of two single-stage rotors in which the chord length varied by a ratio of 2.5. Both of the foregoing results were published in 1958. However, in 1955, an opposite conclusion had been reached from results published by Lewis et al. (1954) and Tysl et al. (1955). In that instance, it was concluded that, through proper design, aspect ratio could be increased without adversely affecting aerodynamic performance, although an observation of the data does show greater range for the low aspect ratio design. The foregoing NACA results are conveniently summarized by Lieblein and Johnson (1961).

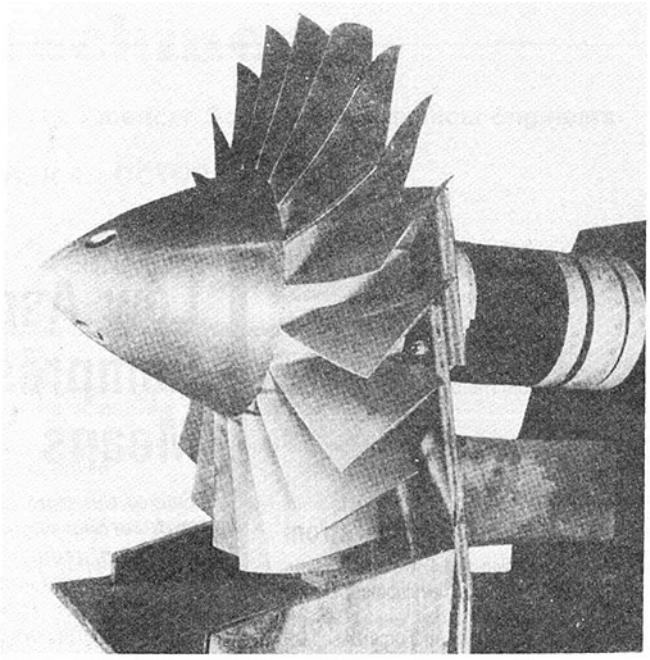

Fig. 2 Rotor of Propulsion Research Corporation research compressor stage

Another interesting set of data, which seems to have gone largely unnoticed, was presented by Page (1956) and Young (1957), respectively, of the Propulsion Research Corporation, Santa Monica, CA. This was a single stage designed for a stage total pressure ratio of 2.0 at a tip speed of 1346 ft/s (411.5 m/s). Design flow per unit frontal area was 34.6 lb/s/ft^2 (168.8 kg/s/m^2) and, at its inlet hub/tip radius ratio of 0.45, design flow per unit annulus area was 43.3 lb/s/ft^2 (211.7 kg/s/m^2). The rotor is pictured in Fig. 2. The stage slightly exceeded its design flow rate and came close to achieving design pressure ratio although it could not be throttled to stall above 90 percent speed because of mechanical difficulties with the throttle. Also, stator losses were not accurately measured. In spite of that, it achieved a rotor total pressure ratio of 2.01 with an isentropic efficiency of 0.88 at design speed. This substantially exceeded the pressure ratio of the NACA rotors of the mid-1950s at comparable levels of flow rate, tip speed, and efficiency. Conspicuous features of the design were a rotor aspect ratio of only 1.11, a cylindrical outer casing, and a hub ramp angle of 25 deg. These characteristics are much more typical of the modern high-through-flow designs than of designs subsequently developed in the 1960s. Also, the flow per unit annulus area appeared to be the highest pumped to that date and rivals the highest used in the most modern designs.

Yet another early observation of the effect of aspect ratio was reported by Swan (1958). Swan deduced from an analytical study that aspect ratio might play an important role in controlling flow range. He postulated that if stall in any blade row occurs as a result of excessive losses arising from increased loading at increased angle of attack, then the magnitude of the losses, for the same blade loading near stall, may possibly be reduced by lowering the aspect ratio, and stall itself may be deferred by this mechanism. This led to an experiment reported by Capiaux and Swan (1958) in which an inlet stage having a rotor of aspect ratio 2.5 was experimentally compared with an aerodynamically similar rotor of aspect

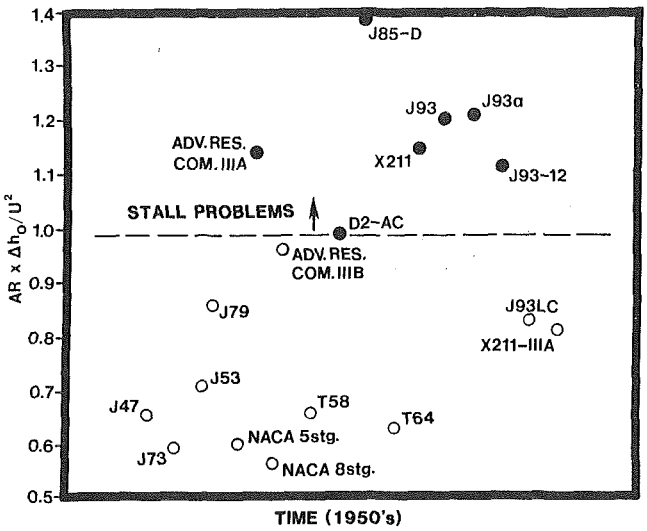

Fig. 3 Average product of aspect ratio × work coefficient of various compressors

ratio 1.33. The experiment was not as clean as it might have been, however, because the tip solidity of the low aspect ratio rotor was increased to 1.2 from a value of 1.02 for the higher aspect ratio design. The range of the low aspect ratio design was increased, as expected, but it was not possible to conclude how much aspect ratio contributed relative to solidity. This work was later summarized by Swan (1964) and was related to the development of the Fairchild J-83 engine compressor.

Some Unsuccessful Development Attempts of the 1960s

Four Air Force sponsored development efforts of the late 1950s and 1960s are described in this section in chronological order. A common characteristic of these efforts was that they all attempted to exploit high aspect ratio to reduce compressor size and weight, and they did so unsuccessfully. Few, if any, of these efforts have been previously reported in open literature as they were all at one time classified.

The first of these involved original versions of the General Electric X211 and J93 compressors. The X211 compressor was designed for the Aircraft Nuclear Propulsion Program in the late 1950s. The first version of the J93 compressor was a smaller scale near relative of the X211 compressor, destined for the XB-70 aircraft. The original versions of these designs had short chords with aspect ratios between 4.0 and 5.0 near the front of the compressor. Serious stall problems became evident in the late 1950s. In Jan. 1959, a decision was reached to launch a two-pronged program to find a solution. One path consisted of modifications to the original design; the other was a new design having lower aspect ratios. A great variety of tests were conducted aimed at salvaging the short-chord design. None led to a satisfactory compressor. The long-chord design proved highly successful and was the path ultimately followed by both programs. The long-chord design achieved an isentropic efficiency of 87 percent at a nominal design speed operating point and about 88 percent at the best point of the map. Comparable figures for the short-chord machine were 81 percent and 84 percent, respectively. Also, the long-chord design had ample stall margin, which the short chord design consistently lacked. Figure 3 shows an interesting plot extracted from anon. (1960), which illustrates some General Electric experience up to 1960, and which was precipitated by this experience.

The second example was a Pratt and Whitney effort to develop a lightweight gas generator, initiated in July 1959. This was aimed at a lightweight turbojet engine for the Mach 3+ flight regime. The compressor design concept attempted to achieve this end through high aspect ratio. Rotor aspect ratios varied from 4.65 at the inlet to 2.51 at the discharge. Stator aspect ratios varied from 9.0 in stage 1 down to 3.42 in stage 6 according to dimensions presented in anon. (1961). The final design was a seven-stage compressor with a design pressure ratio of 6.5 (surge pressure ratio 7.1), at a tip speed averaging about 1125 ft/sec (381 m/s). The best compressor performance achieved after eighteen compressor builds and four engine builds is illustrated in Table 1 presented by Stibich (1967).

Table 1 Best LWGG Performance

	Design	Compressor rig	Engine
Surge pressure ratio	7.1	6.8	6.23
Airflow, lb/s (kg/s)	115 (52.2)	117 (53.1)	116.5 (52.9)
Isentropic efficiency, percent	81.0	79.0	78.0
Peak efficiency, percent	86.0	82.5	84.0

The results in Table 1 were achieved only with a high compressor discharge Mach number, which resulted in an excessive burner pressure drop as well as a poor pattern factor. In this effort, the designers adhered to the initial design concept to the bitter end, voicing optimism that the original development goals could be met with (an implied modest) additional development effort and stating words to the effect that the short chord (high aspect ratio) design concept had been vindicated by the results. Comparing this program with other results of that period, and with the benefit of hindsight, that hardly seems to have been the case.

The third effort was the XJ-95 Lift Engine Demonstrator program initiated in July 1962 at Continential Aviation and Engineering Corporation (now Teledyne CAE). This program included demonstrations of both turbojet and turbofan versions of the engine, and long-chord and short-chord versions were built of both fan and compressor. The short-chord fan was the initial engine design and had a rotor aspect ratio based upon root chord of 6.35. It was designed for a pressure ratio of 1.38 at a tip speed of 1560 ft/s (475 m/s). A rig version of this fan was also designed with a rotor aspect ratio of approximately 3.7 (estimated by comparing cross sections of both versions). Mechanical difficulties limited the speed of the short-chord fan to 90 percent of design. However, at that speed it was at least 7 percent low in flow, and pressure ratio barely exceeded 1.2 relative to a design projection on the order of 1.3. The long-chord design was much more successful, achieving design pressure ratio and about 96 percent of design flow. The efficiency was not impressive, being on the order of 75 percent, but that is hardly surprising considering the tip speed and pressure ratio and the state-of-the-art at that time.

The turbojet compressor, which was also the core compressor of the turbofan engine when stripped of its first stage, was first designed in a long-chord version. Its design objective was a pressure ratio of 6.0 at a tip speed of 1301 ft/s (396 m/s) in five stages. Aspect ratios of this design varied from 2.35 in the first rotor to 1.56 in the fifth rotor. An aerodynamically similar short-chord version was also designed with the usual objective of reduced size and weight. Its aspect ratios ranged from 3.64 in the first rotor to 2.11 in the fifth. The long chord design achieved design pressure ratio at design speed with about 8 percent stall margin and passing about 103 percent of design flow. Isentropic efficiency at this point was about 81.5 percent and peaked at 83 percent just below 90 percent speed. Ten configurations of the short-chord version were tested. Most were aimed at solving mechanical problems. However, three were successfully run at design speed. At its best, the short-chord compressor barely exceeded a pressure ratio of 5.0 at design speed, and peak efficiency, occurring at the stall line, was about 75 percent. The foregoing information was derived from Carl (1967).

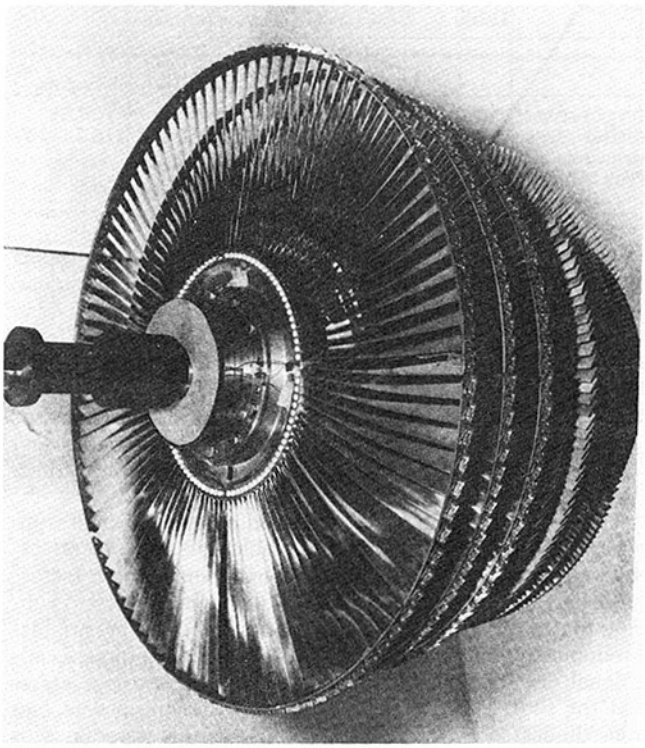

Fig. 4 Curtiss-Wright TJ60 compressor rotor assembly

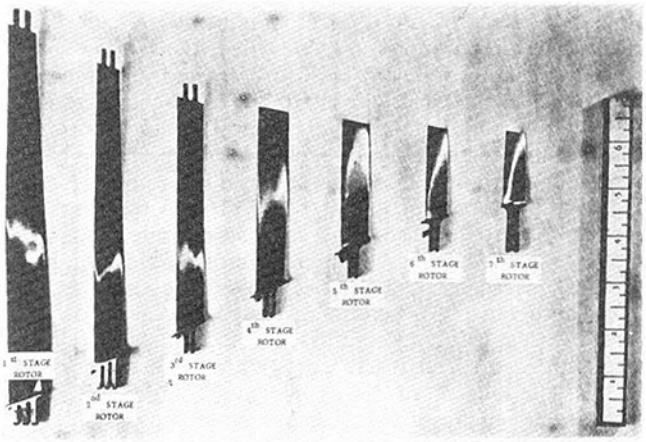

Fig. 5 Curtiss-Wright TJ60 compressor rotor blades

The fourth effort cited was initiated in Aug. 1963 at the Curtiss-Wright Corporation for development of the TJ60 gas generator for a V/STOL application. The objectives of this program were quite similar to those of the two programs previously mentioned corresponding to anon. (1961) and Carl (1967). Curtiss-Wright's approach for the compressor design to achieve design goals was a lightweight, seven-stage compressor using high aspect ratio, short-chord blading to achieve a pressure ratio of 9.0 at an inlet corrected tip speed of 1313 ft/s (400 m/s). Rotor aspect ratios declined from 8.02 in the first stage to 3.0 in the seventh. The rotor blading is illustrated in Figs. 4 and 5. Stator aspect ratios were comparable. The best performance achieved in compressor rig testing, within the life of the program, was approximately 5.2 pressure ratio at 90 percent corrected design speed. Curtiss-Wright's estimate of the performance extrapolated to design speed, according to Rawley (1967), was a pressure ratio of about 6.5 and 90 percent of design airflow. This compressor incorporated the highest aspect ratios yet attempted, and was also the least successful with respect to the compressor's development. The highest efficiencies recorded were approximately 67 percent at about 80 percent corrected design speed. Every one of these four development programs experienced serious mechanical problems with the high aspect ratio configurations during development. However, even if the mechanical problems had been solved, and they appeared to be close in some cases, the aerodynamic performance prognosis appeared to be limited to efficiencies in the low 80 percent bracket, and poor surge margin or overall loading capability.

Research Efforts

The development efforts that unsuccessfully attempted to exploit very high aspect ratios, and isolated bits of evidence indicating improved range at low aspect ratios, led to several research efforts aimed at a quantitative assessment. One of the first of these was published by Fligg (1966). Fligg tested a low-speed three-stage axial flow compressor with aspect ratios of 1, 2, and 4 in various combinations at a constant Reynolds number, end-wall clearance, and solidity. He found that as aspect ratio increased, the end-wall boundary layers increased, leading to earlier stalling of rotors and stators near the walls, particularly at the root. Very little difference in efficiency was noted between aspect ratios. He speculated that this effect should be less pronounced at low hub/tip radius ratios.

A purely theoretical investigation was reported by Horlock and Fahmi (1967). They examined the influence of aspect ratio in single, double, and multi-stage compressors using actuator disk theory. They drew some conclusions concerning where stall originates under various circumstances and indicated that the results suggest severe stator stall and early rotor tip stall in high aspect ratio designs. This appears reasonably consistent with Fligg's results.

Smith (1970) reported on results obtained with a four-stage low-speed compressor at several different aspect ratios. Aspect ratios were nominally 2, 2.8, and 5. Over this range, he found that peak pressure rise could be correlated against two variables: tip-clearance-to-staggered-spacing ratio and axial-gap-to-spacing ratio. Blade span was not found to be a significant variable for normalizing end-wall clearance. He further concluded that since high aspect ratio stages have a smaller fraction of the total flow influenced by end-wall effects, end-wall boundary layer growth, as stall is approached, does not cause the stage characteristic curve to roll back as much as with lower aspect ratio stages. Thus, the range reduction together with a reduced pressure rise due to clearance effects was felt to be the reason that high-aspect-ratio stages have reduced stall capability. At first glance, this appears contrary to Fligg's results. On the other hand, since end-wall clearance was held constant in Fligg's experiments, clearance-to-staggered-spacing ratio increased with increasing aspect ratio. This could have caused the greater end-wall boundary layer growth observed, making the results consistent with Smith's.

Foreign Developments

An interesting development that occurred quite isolated from the foregoing Western technology was the work of Sergei Tumansky in the Soviet Union. According to Janes (anon., 1984), the Tumansky R-11 engine probably first ran in 1953 and entered service in 1956. Considering these dates, its development had to occur concurrently and quite independently of the early NACA work and much in advance of most other references cited. The distinctive feature of this engine, from the point of view of the compressor, was that it employed low aspect ratios averaging about 1.5 for the rotors and achieved a pressure ratio of about 8.9 in six stages. Although the efficiency of this engine, and in fact most Soviet engines, remains relatively unimpressive with respect to fuel consumption, this engine does represent something of a land-

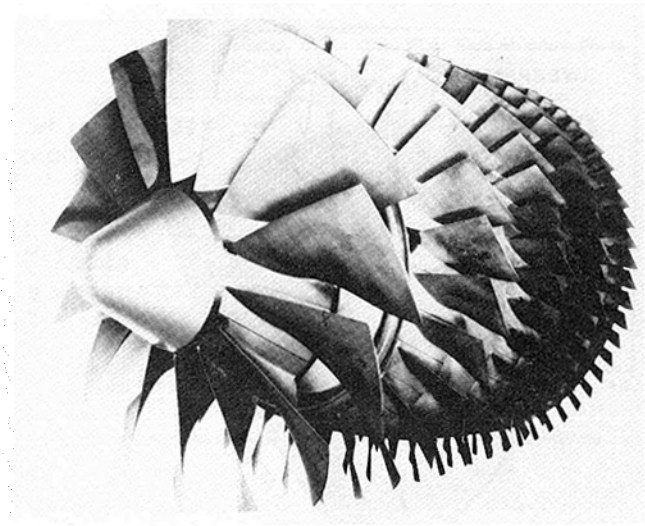

Fig. 6 Allison high flow compressor rotating assembly

mark relative to average stage pressure ratio for production engines of that era. This engine and its descendants remained unique even within the Soviet Union. Most other Soviet engine design bureaus followed the same path as Western technology of the 1950s and 1960s. Tumansky was unique in choosing a design direction in the 1950s that has become the path of choice for designers of military engines of the 1970s and later. It is interesting to note that the total production of Tumansky engines exceeds that of any other family of aircraft gas turbines in the post-1955 era, according to Janes (anon., 1984).

The Winds of Change

During the course of the 1960s, all of the foregoing information jelled in the minds of a number of people in Government and industry responsible for compressor design. In individual cases, this may have occurred much earlier. In any case, by about 1970, a number of programs germinated that led to the birth of the current generation of low aspect ratio, high-throughflow fan and compressor designs. The most important change that seems to have occurred is that most of the early work that was done with varying aspect ratios never departed from the notion that blade row design points should be defined by cascade data, most of which was taken at high aspect ratios in order to be two-dimensional. The new idea that emerged was essentially to take advantage of the greater range of low aspect ratio stages by setting their design points at much higher loading levels. Thus, the number of stages required to achieve a given pressure ratio could be reduced, shortening the machine and making its weight and size more competitive with its higher aspect ratio ancestors. One of the first of these was a program to develop a Turbine Engine High Flow Compressor, which was awarded to the Detroit Diesel Allison Division (now Allison Gas Turbine Division) of General Motors Corporation in June 1972. This led to the development of an axial flow compressor that achieved a pressure ratio of 12.1 in five stages with an isentropic efficiency of 81.9 percent and 11 percent surge margin. Tip speed was 1500 ft/s (457 m/s) and the flow rate achieved per unit frontal area was 39.5 lb/s/ft^2 (192.5 kg/s/m^2). Mean rotor aspect ratios ranged from a high of 1.204 in the first stage to less than 1.0 in the last three stages.

While the efficiency achieved may not appear too impressive, it should be noted that this was achieved with the original set of hardware and only minor stator vane stagger angle adjustments. The examples cited in a previous section showed the best results achieved after major engine development efforts, which included many design and test iterations and some relatively major changes. A comparable effort applied to this compresssor would have been likely to achieve several additional points of efficiency. Individual stages did achieve significantly higher values. A photograph of the rotor system of this compressor is shown in Fig. 6. The above results were extracted from Bettner and Alverson (1977).

A related Air Force program was pursued in-house starting in early 1971. An alternative inlet stage was designed aimed at the same application as the Allison program just described. This work and its results are summarized by Wennerstrom (1984). This was designed for the same flow per unit frontal area and the same tip speed, but for a slightly higher pressure ratio than the Allison first stage. The mean rotor aspect ratio was 1.32. At design speed and the design pressure ratio of 1.912, this stage overflowed 0.8 percent, passing 40 lb/s/ft^2 (195 kg/s/m^2) per unit frontal area, at an isentropic efficiency of 85.4 percent with 11 percent stall margin. Design speed efficiency peaked at 88.2 percent, and maximum efficiency was 90.9 percent with a pressure ratio of 1.804 at 90 percent corrected speed.

Both of the foregoing efforts confirmed the high loading capability, high efficiency, and good range attainable with blades of significantly lower aspect ratio. A number of development efforts since that time have moved in that direction.

Impact of Low Aspect Ratio on Design Systems

Streamsurface Assumption. The biggest aerodynamic design problem introduced by a move to lower aspect ratios was the increasing three-dimensionality of the flow. The fact that the early low aspect ratio multistage designs worked as well as they did was probably partly due to the wide range of these stages, rendering them less sensitive to incidence mismatches, as well as to improvements achieved through trial and error in the course of development programs. As aspect ratio declined, secondary flows increased in significance and the assumption that the flow could be described by a concentric series of stream tubes across which no mass or momentum was transferred became progressively less valid. There is a large body of literature on secondary flows dating back into the 1950s, if not before. However, generally speaking, little of this had been applied to practical designs and the concept of strip theory was still the predominant approach throughout the 1960s.

One of the first attempts to develop a hybrid flow analysis was presented by Tipton (1968). By hybrid analysis, I am referring to a scheme whereby an axisymmetric solution is corrected during a series of iterations to adjust the solution so that energy and momentum are transferred across stream surfaces rather than being preserved. In this way, a computation that is constructed along axisymmetric, two-dimensional lines can be corrected for three-dimensional effects. Tipton's model attempted to correct the spanwise loss distribution by taking into account radial transport of boundary layers. His correlation with experimental data appeared reasonably impressive.

Hearsey attempted to apply Tipton's work to an axisymmetric streamline curvature code in about 1973. In rederiving Tipton's equations, Hearsey discovered some small terms left out of a force balance. When these were included, the equations degenerated to an identity and the solution evaporated. He then went off in a different direction and created two secondary flow models (Hearsey, 1975). One model concerned radial transport of blade wakes. The other concerned turbulent mixing of the axisymmetric flow field. Although it was apparent from Hearsey's results that his models exhibited the right trends, their use consumed large amounts of computer time and the data base used to generate the empirical coefficients was small enough that one did not have great confidence

in their wide applicability. At least one engine company did have the courage to use these models in the design of a multistage compressor in the late 1970s and was quite successful. However, these models have rarely been exercised.

The first really comprehensive and practical approach to this problem, coupled with a fairly extensive data base, was published by Adkins and Smith (1982). The model they presented included five effects: (1) mainstream, non-free-vortex flow; (2) end-wall boundary layers; (3) blade end clearance; (4) blade end shrouding; and (5) blade boundary layer and wake centrifugation. The method was efficient enough to be reasonably convenient to use from the standpoint of computer time and the results correlated with a good cross section of data. One of the important contributions of this effort was that in addition to adjusting spanwise loss distributions, spanwise deviation angle and total temperature distributions were also corrected. This model was a reasonably successful attempt at capturing nearly all of the most important effects necessary to ensure good matching of a low aspect ratio, multistage compressor. The model was of necessity semi-empirical and included many coefficients subject to revision or future theoretical prediction. However, it represented by far the most successful attempt along these lines to that date.

The newest model to come along is based upon experiments by Gallimore and Cumpsty (1986) and a mathematical model of Gallimore (1986). They conclude that the dominant mechanism is that of turbulent type diffusion and not the radial convection of flow properties. Their correlation with data is also impressive. It is interesting to note that all of the models for spanwise mixing that have been published, Tipton's, Hearsey's, Adkins and Smith's and Gallimore's, have shown relatively good correlation with whatever data were available even though they were constructed quite differently and, to some degree, did not even attempt to model the same physical mechanism. One conclusion one might reach is that the introduction of any spanwise mixing model is better than none at all in attempting to predict multistage compressor performance. Since all have been semi-empirical, coefficients were available to permit a reasonable match of some quantity of data. However, it is clear that only the model or models that come closest to the true physics will demonstrate reliability when making a significant departure from their existing data base.

Shock Losses. Another effect of decreasing aspect ratio is that, as aspect ratio decreases, shock geometry becomes more three-dimensional. This three-dimensionality has nothing to do with violation of the streamsurface assumption. It stems from the fact that significant spanwise sweep is introduced into the shock surface. It was observed by Prince (1980) that near peak efficiency operation, the principal passage shock wave was usually approximately normal to the flow direction in the cascade plane. This explains the significant degree of success enjoyed by the Miller, Lewis, and Hartmann shock loss model (Miller et al., 1961) in its application to a wide variety of past designs with aspect ratios in excess of 2.0. However, as aspect ratio declines further, significant spanwise sweep of the shock surface can occur even if the leading edge remains radial and the shock remains normal in the cascade plane of each section. This results because of blade twist and solidity variations and is therefore much more pronounced in blade rows of low hub/tip ratio. This is illustrated in Fig. 7. Since the shock impinges on the suction surface of each blade close to the leading edge near the hub and close to the trailing edge near the tip, substantial spanwise sweep can occur near the suction surface even if it is negligible at the leading edge. This was pointed out by Prince (1980) and inspired the shock loss model of Wennerstrom and Puterbaugh (1984). If the shock is then viewed as an oblique shock in the radial direction, a substantial reduction in shock loss can occur given sufficient obliquity, relative to that loss which would be predicted if this spanwise sweep were ignored. This is one fact that has undoubtedly contributed to the high efficiency of some low aspect ratio stages operating at relatively high Mach numbers, such as that of Page (1956) and Wennerstrom (1984).

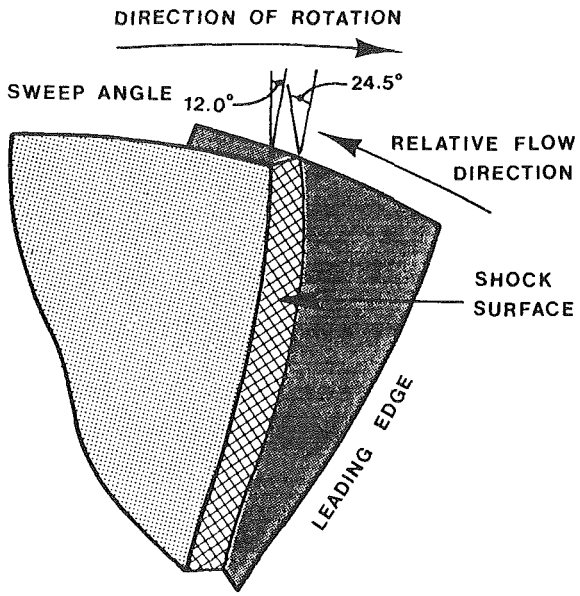

Fig. 7 Three-dimensional rotor passage shock

Nonsteady Effects. There is recent evidence to support the conclusion that a compressor cascade operating supersonically may pass a higher mass flow when subjected to a periodically varying inlet condition than when subjected to a steady flow having the same mass-averaged thermodynamic properties. This situation could occur, for example, in a multi-stage compressor operating at a sufficiently high speed that Mach numbers relative to the second rotor were still supersonic over some portion of the span. This has the potential of introducing serious matching problems in high-speed multistage compressors since the current state of the art is to set the unique incidence of a supersonic section based upon information calculated or measured under steady-flow circumstances.

Coincident with decreasing aspect ratios, Mach numbers have been steadily rising because of our improving ability to design aerodynamically efficient sections for higher Mach numbers as well as because improved metallurgical and manufacturing technology has permitted higher tip speeds. As aspect ratios have decreased, the ratio of the spacing between blade rows to the average chord length has also substantially decreased in the interest of keeping the compressor as short as possible. The reduced deflections experienced by stiffer low aspect ratio blading have aided in this objective. As a result, the wakes of one blade row have had much less opportunity to mix out before entering the following blade row relative to a high aspect ratio design since the scale of a blade wake is related directly to chord length for a given level of diffusion. There have been several interesting experimental cases where it is believed this effect may have been at least partially responsible for a mismatch.

One of these was the Allison compressor of Bettner and Alverson (1977), pictured in Fig. 6. All five rotors had relative inlet Mach numbers equaling or exceeding 1.0 at the tip and stages two and three had supersonic relative Mach numbers across the entire leading-edge span. At design blade setting angles, stage two appeared to be approximately 6 percent high in flow capacity. It was necessary to close down the first-stage stator several degrees in order to reduce the flow capacity of

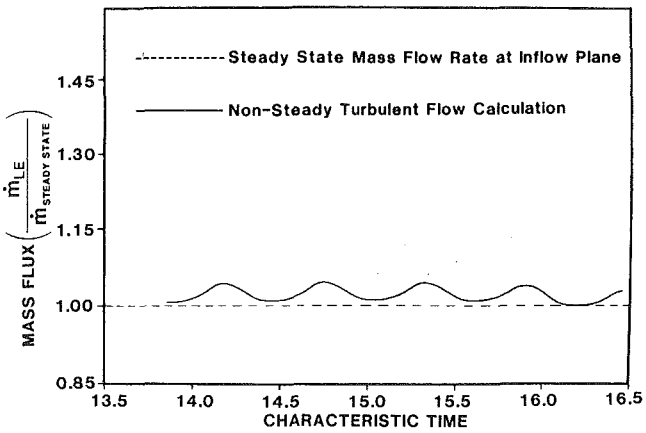

Fig. 8 Mass flow comparison at cascade leading edge plane

stage two and force the first stage up to its design pressure ratio and a higher efficiency.

A second example involved a Pratt and Whitney design. This was a very highly loaded, close-coupled, three-stage compressor having an average aspect ratio of only 0.58 and Mach numbers in the transonic range. The situation here is less clear. However, the data available imply an improbably high flow rate entering the second and third stators. Large, relatively unmixed wakes would have been entering these stators, which, because of high camber, were transonic. It is at least plausible that the same phenomenon may have played a role in this situation.

Some computational evidence supporting this hypothesis was presented by Scott and Hankey (1986). Using a viscous nonsteady Navier–Stokes code including a turbulence model, they compared the flow passed by a supersonic cascade under periodic non-steady conditions with the flow passed by the same cascade under uniform inlet conditions having the same mass-averaged thermodynamic properties. The nonuniform inlet conditions corresponded to the experimentally measured wake profile of a stator row immediately upstream of the rotor from which the cascade section was taken. Their results, reproduced in Fig. 8, show that the cascade does pass a higher flow under nonsteady conditions than under thermodynamically equivalent steady flow conditions. The difference in this instance was approximately 3.0 percent. The significance of this is that all contemporary methods of defining the unique incidence of a supersonic cascade rely upon the assumption of uniform steady inlet conditions. If the blade row follows another, the uniform inlet conditions are assumed to correspond to the circumferential mass average of the true conditions, consistent with the usual design presumption of axial symmetry. However, if the wakes are pronounced and the blade rows close coupled, there is reason to expect that the downstream row may pass more flow than the designer anticipated, leading to a mismatch. Knowing how much more and what parameters it is sensitive to is one of the designer's current unsolved problems.

Another feature of nonsteady flow is likely to be increased losses at supersonic Mach numbers. Ng and Epstein (1985) have shown how unsteadiness caused by vortex shedding can produce on the order of 1.0 percent of rotor loss due to shock oscillation even under clean uniform inlet conditions and very limited shock motion. They suggest, and it is highly plausible, that unsteadiness present in succeeding stages operating supersonically may incur much larger losses because the magnitude of the nonuniformities is likely to be substantially greater. This is another question of unknown magnitude that the designer of high Mach number, close-coupled stages must face.

Maximum Loading Capability. The influence of aspect ratio on maximum loading capability of a compressor stage had been noted on many occasions since the 1940s as cited in earlier sections of this paper. Koch (1981) developed a diffuser analogy to predict stalling pressure rise capability. However, he referenced Smith (1970) to conclude that the aspect ratio effect was primarily a result of differences in Reynolds number and clearance-to-staggered-spacing ratio. Aspect ratio was felt to be implicitly accounted for through its effect on Reynolds number, normalized clearances, and wall boundary layer blockage. Smith had also noted the influence of axial gap/spacing ratio on peak pressure rise, and most lower aspect ratio designs do have lower axial gap/spacing ratios as a natural result of the motive to keep the machine as short as possible. Schweizer and Garberoglio (1984) followed a diffuser analogy approach similar to Koch but also introduced the concept of the equivalent cone angle. This takes blade aspect ratio (span/chord) directly into account in defining a maximum static pressure rise coefficient. Passage aspect ratio (span/staggered spacing) is considered separately with respect to its effect on loss coefficient. Kholschevnikov (1970) also referred to the equivalent cone angle and mentioned that, with increasing aspect ratio, the divergence angle of the equivalent circular diffuser will increase leading to earlier separation. However, he did not reference any other work or go on to elaborate in any quantitative fashion.

Distortion tolerance tends to go hand in hand with a compressor's loading capability and stability margin. Hence, the low aspect ratio designs have tended to be more tolerant of distorted inlet flows than designs of higher aspect ratio. What is less obvious is the greatly improved distortion transfer characteristics exhibited by low aspect ratio stages. Distortion transfer refers to the level of distortion coming out of a stage relative to that which entered it. It has been found that low aspect ratio stages tend to attenuate distortion much more than high aspect ratio designs. However, no data of this type have yet been found in the open literature.

Structural Analysis. All of the comments so far have dealt with aerodynamic phenomena. Low aspect ratio designs also imposed important new requirements in the area of structural analysis. The first of these is that the use of beam theory to predict stresses and deflections gave way to finite element modeling. This was partly due to the inadequacy of beam theory to cope with low aspect ratio shapes and partly due to its inability to deal with boundary conditions such as a steep ramp angle covering a significant span of the blade. A second change was that corrections for blade deflection could no longer be confined to a simple restaggering of the airfoil. Low aspect ratio fans and inlet stages were now experiencing significant changes in camber line shape as well as untwist. This has required shape corrections to the entire surface of a low aspect ratio airfoil to insure that the hot running configuration corresponds to the design intent. Finally, although low aspect ratio airfoils are much less prone to flutter than high aspect ratio airfoils, flutter has been experienced. Flutter prediction is still a highly empirical and imperfect science and much work remains to put this on a more reliable basis.

Future Prognosis

Several compressors and fans of conspicuously low aspect ratio have entered service in the late 1970s and early 1980s as a result of the earlier efforts and observations described. One of these is the axial portion of the General Electric T700 engine compressor, which entered service in about 1979. The Garrett TFE 731-5, certified in Nov. 1983, employs a relatively wide chord fan. Another is the Rolls-Royce 535E4 fan, which has been in service since Oct. 1984 and is sometimes known as the RB211 wide-chord fan. The latter has two offspring under development: the International Aero Engines V2500 fan and

the new Rolls-Royce Tay fan. A number of other fans and compressors exhibiting this characteristic are known to be under development by a variety of manufacturers for both military and commercial applications. The appeal of this technology is strong because the newest designs are offering superior efficiency and range at weights that are often equal to or less than their higher aspect ratio predecessors. In addition, they offer cost advantages through a greatly reduced parts count, and ruggedness by virture of the larger size of the remaining parts, as pointed out by Pickering (1985) in this lecture one year ago.

The most useful aerodynamic design tool for most of the next decade is likely to be the hybrid semi-axisymmetric throughflow computation of the sort described by Adkins and Smith (1982) or Gallimore (1986). This is an approach that is practical and economical and has the potential of capturing most of the three-dimensional effects that become important in low aspect ratio turbomachinery, particularly multistage turbomachinery. We still have much to learn with respect to the importance of nonsteady effects in close-coupled, highly loaded, high Mach number blade rows and how to deal with them. Computational and experimental efforts within the next several years will undoubtedly shed some light on this.

One area about which I have deliberately said relatively little is the contribution of three-dimensional computational fluid dynamics (CFD). Intensive work has been going on within the engine community on the development of Euler (inviscid) and Navier–Stokes (viscous) three-dimensional flow analysis codes. The first practical results of their use were achieved with turbines and they have since been applied to critical compressor blade rows such as fan rotors. The Garret Company was among the first to emphasize CFD and the Garrett 731 fan was an early example of its practical application to compressors (Clemmons et al., 1983). The useful application of these codes to multistage compressors is much further in the future, however. Most of these codes, to date, can only deal with an isolated blade row. Consequently, it can be extremely difficult to model the inlet and discharge boundary conditions correctly. It is entirely possible that a three-dimensional CFD analysis of an isolated blade row might lead a designer down the wrong path when inlet and discharge conditions cannot be modeled adequately. Denton (1985) was the first to create a three-dimensional (Euler) CFD code in which adjacent blade rows are modeled in a circumferentially averaged sense and his approach shows much promise of permitting accurate analyses of buried blade rows.

Two major limitations currently inhibit the use of CFD, particularly for multi-stage turbomachines. The first is a hardware limitation. Even the biggest of the current generation of supercomputers is not large enough or fast enough to deal with a three-dimensional, multistage, nonsteady analysis. Even considering the rapid growth we have seen in computer technology, computers of the size and speed necessary may still be as much as five to ten years in the future. The second limitation is strategic. Three-dimensional CFD codes remain analysis codes. The geometry that is analyzed must still be created by some more pedestrian method. No one has yet conceived of a strategy for dealing with the inverse solution in three-dimensions and creating a design in this manner. However, it may eventually happen.

Acknowledgments

The author would like to express his appreciation in particular to Richard A. Novak, Marvin A. Schmidt, Prof. George K. Serovy, and Dr. Leroy H. Smith, Jr., for their advice and valuable insights on historical developments in which they played roles.

References

Adkins, G. G., Jr., and Smith, L. H., Jr., 1982, "Spanwise Mixing in Axial-Flow Turbomachines," ASME *Journal of Engineering for Power*, Vol. 104, No. 1, pp. 104–110.

Anon., 1960, "J-93 Compressor Review ," General Electric Company.

Anon., 1961, "Compressor Development for a Lightweight Turbojet Engine," Report PWA-1971, Pratt and Whitney Aircraft.

Anon., 1984, "Jane's All the World's Aircraft 1984-85," Jane's Publishing Company Ltd., London, United Kingdom, pp. 844–845.

Bettner, J. L., and Alverson, R. F., 1977, "Turbine Engine High Flow Compressor," AFAPL-TR-77-23, Air Force Aero Propulsion Laboratory, Wright-Patterson Air Force Base, OH.

Capiauz, R., and Swan, W. C., 1958, "An Experiment Concerning the Extension of the Unstalled Range of a Transonic Axial Flow Compressor Inlet Stage," Technical Report 58-337, Wright Air Development Center, Air Research and Development Command, Wright-Patterson Air Force Base, OH.

Carl, J., 1967, "Design and Component Evaluation of Lift Engine Demonstrators," AFAPL-TR-66-124, Vols. I, II, and III, Air Force Aero Propulsion Laboratory, Wright-Patterson Air Force Base, OH.

Clemmons, D. R., Dodge, P. R., and Blackmore, W. L., 1983, "The Impact of Three-Dimensional Analysis on Fan Design," ASME Paper No. 83-GT-136.

Denton, J. D., 1985, "The Calculation of Fully Three-Dimensional Flow Through Any Type of Turbomachine Blade Row," AGARD Lecture Series No. 140, *3-D Computation Techniques Applied to Internal Flows in Propulsion Systems*.

Fligg, J., 1966, "Test of a Low Speed, Three Stage Axial Flow Compressor With Aspect Ratios of 1, 2, and 4," AIAA Paper No. 66-613.

Gallimore, S. J., and Cumpsty, N. A., 1986, "Spanwise Mixing in Multistage Axial Flow Compressors: Part I—Experimental Investigation," ASME JOURNAL OF TURBOMACHINERY, Vol. 108, No. 1, pp. 2–9.

Gallimore, S. J., 1986, "Spanwise Mixing in Multistage Axial Flow Compressors: Part II—Throughflow Calculations Including Mixing," ASME JOURNAL OF TURBOMACHINERY, Vol. 108, No. 1, pp. 10–16.

Hearsey, R. M., 1975, "A Revised Computer Program for Axial Compressor Design, Vol I," ARL TR 75-0001, Vol. 1, Aerospace Research Laboratories, Wright-Patterson Air Force Base, OH.

Horlock, J. H., and Fahmi, G. J., 1967, "A Theoretical Investigation of the Effect of Aspect Ratio on Axial Flow Compressor Performance," Current Paper No. 943, Aeronautical Research Council.

Jansen, W., 1967, "The Application of End-Wall Boundary Layer Effects in the Performance Analysis of Axial Compressors," ASME Paper No. 67-WA/GT-11.

Kholschevnikov, K. V., 1970, "Theory and Design of Aircraft Turbomachines," translation of *Teoriya i Raschet Aviatsionnukh Lopatocknykh Mashin*, Foreign Technology Division, Wright-Patterson Air Force Base, OH, FTD-HC-23-754-71, 1972, p. 281.

Koch, C. C., 1981, "Stalling Pressure Rise Capability of Axial Flow Compressor Stages," ASME *Journal of Engineering for Power*, Vol. 103, No. 4.

Kussoy, M. I., and Bachkin, D., 1958, "Comparison of Performance of Two Aerodynamically Similar 14-Inch-Diameter Single Stage Compressor Rotors of Different Chord Length," NACA RM E57I03.

Lewis, G. W., Jr., Schwenk, F. C., and Serovy, G. K., 1954, "Experimental Investigation of a Transonic Axial-Flow-Compressor Rotor With Double-Circular-Arc Airfoil Blade Sections, I-Design, Over-All Performance, and Stall Characteristics," NACA RM E53L21a.

Lieblein, S., Schwenk, F. C., and Broderick, R. L., 1953, "Diffusion Factor for Estimating Losses and Limiting Blade Loadings in Axial-Flow-Compressor Blade Elements," NACA RM E53D01.

Lieblein, S., and Johnson, I. A., 1961, "Resume of Transonic-Compressor Research at NACA Lewis Laboratory," ASME *Journal of Engineering for Power*, Vol. 83, pp. 219–234.

Miller, G. R., Lewis, G. W., Jr., and Hartmann, M. J., 1961, "Shock Losses in Transonic Compressor Blade Rows, ASME *Journal of Engineering for Power*, Vol. 83, pp. 235–242.

Ng, W. F., and Epstein, A. H., 1985, "Unsteady Losses in Transonic Compressors,' ASME *Journal of Engineering for Gas Turbines and Power*, Vol. 107, No. 2, pp. 345–353.

Novak, R. A., 1967, "Streamline Curvature Computing Procedures for Fluid-Flow Problems," ASME *Journal of Engineering for Power*, Vol. 89, pp. 478–490.

Page, R. J., 1956, "The Study and Design of a Research Inlet Stage Transonic Compressor With an Average Pressure Ratio of 2.0 and a Mass Flow per Frontal Area of 70% of the Theoretical Maximum," Technical Report 55-8, Wright Air Development Center, Air Research and Development Command, Wright-Patterson Air Force Base, OH.

Pickering, F. E., 1985, "A Decade of Progress in Turbomachinery Design and Development," SAE Paper No. SP-637.

Prince, D. C., Jr., 1980, "Three-Dimensional Shock Structures for Transonic/Supersonic Compressor Rotors," *Journal of Aircraft*, Vol. 17, No. 1.

Rawley, W. N., 1967, "Demonstration of a Gas Generator for V/STOL Application," AFAPL-TR-67-65, Vols. I and II, Air Force Aero Propulsion Laboratory, Wright-Patterson Air Force Base, OH.

Schweitzer, J. K., and Garberoglio, J. E., 1984, "Maximum Loading Capability of Axial Flow Compressors," *Journal of Aircraft*, Vol. 21, No. 8, pp. 593–600.

Scott, J. N., and Hankey, W. L., 1986, "Navier-Stokes Solutions of Unsteady Flow in a Compressor Rotor," ASME JOURNAL OF TURBOMACHINERY, Vol. 108, No. 2, pp. 206-215.

Sherstyuk, A. N., 1955, "Design of Compressors, Aerodynamic Calculations," translation of *Osevyye Kompressory. Aerodinamicheskiy Raschet*, Foreign Technology Division, Wright-Patterson Air Force Base OH, FTD-HC-23-781-70, 1971 (AD 727191), pp. 231-232.

Sievers, G. K., Geye, R. P., and Lucas, J. G., 1958, "Preliminary Analysis of Over-All Performance of an Eight-Stage Axial-Flow Research Compressor With Two-Long-Chord Transonic Inlet Stages," NACA RM E57H14.

Smith, L. H., Jr., 1970, "Casing Boundary Layers in Multistage Axial-Flow Compressors," in: *Flow Research on Blading*, L. S. Dzung, ed., Elsevier Publishing Co., Amsterdam, pp. 275-296.

Standahar, R. M., and Geye, R. P., 1955, "Investigation of a High-Pressure-Ratio Eight-Stage Axial Flow-Research Compressor With Two Transonic Inlet Stages, V—Preliminary Analysis of Over-All Performance of Modified Compressor," NACA RM E55A03.

Stibich, M. A., 1967, "History of Two Demonstrator Engine Programs," Technical Memorandum APTC-TM-67-17, Air Force Aero Propulsion Laboratory, Wright-Patterson Air Force Base, OH.

Stratford, B. S., 1967, "The Use of Boundary Layer Techniques to Calculate the Blockage From the Annulus Boundary Layers in a Compressor," ASME Paper No. 67-WA/GT-7.

Swan, W. C., 1958, "A Practical Engineering Solution to the Three-Dimensional Flow in Transonic Type Axial Flow Compressors," Technical Report 58-57, Wright Air Development Center, Air Research and Development Command, Wright-Patterson Air Force Base, OH.

Tipton, D. L., 1968, "Improved Techniques for Compressor Loss Calculation," AGARD Conference Proceeding No. 34, *Advanced Components for Turbojet Engines*, Part I.

Tysl, E. R., Schwenk, F. C., and Watkins, T. B., 1955, "Experimental Investigation of a Transonic Compressor Rotor With a 1.5-Inch Chord Length and an Aspect Ratio of 3.0, I-Design, Over-All Performance, and Rotating Stall Characteristics," NACA RM E54L31.

Wennerstrom, A. J., and Puterbaugh, S. L., 1984, "A Three-Dimensional Model for the Prediction of Shock Losses in Compressor Blade Rows," ASME *Journal of Engineering for Gas Turbines and Power*, Vol. 106, No. 2, pp. 295-299.

Wennerstrom, A. J., 1984, "Experimental Study of a High-Throughflow Transonic Axial Compressor Stage," ASME *Journal of Engineering for Gas Turbines and Power*, Vol. 106, No. 3, pp. 552-560.

Wright, L. C., and Novak, R. A., 1960, "Aerodynamic Design and Development of the General Electric CJ805-23 Aft Fan Component," ASME Paper No. 60-WA-270.

Young, W. H., 1957, "The Experimental Investigation of a Research Transonic Inlet Stage Compressor," Technical Report 57-207, Wright Air Development Center, Air Research and Development Command, Wright-Patterson Air Force Base, OH (AD 118172).

Investigations of Boundary Layer Transition in an Adverse Pressure Gradient

J. P. Gostelow
Dean of Engineering.

A. R. Blunden
Research Engineer.

University of Technology, Sydney,
Sydney, Australia

Boundary layer transition was measured on a flat plate for four different turbulence levels. A range of adverse pressure gradients was imposed for one of these. The zero pressure gradient results were in agreement with accepted data for transition inception, length, and turbulent spot formation rate. They were also well represented by Narasimha's universal intermittency distribution. A surprisingly strong similarity was also exhibited by intermittency distributions under adverse pressure gradients. Dimensionless velocity profiles were reasonable for the zero pressure gradient cases but difficulties with skin-friction prediction were experienced under adverse pressure gradient conditions. For this moderate turbulence level the transition inception Reynolds number remained reasonably constant with pressure gradient. Transition lengths, however, were greatly reduced by the imposition of even a weak adverse pressure gradient. This was associated with a strong increase in turbulent spot formation rate.

Introduction

A principal constraint in the application of computer-aided design procedures to the design of high-performance turbomachines is the paucity of information on boundary layer transition. Information is required on the inception and completion of transition for a wide range of pressure gradients and under the conditions of high free-stream turbulence encountered in turbomachinery. Accurate calculations of displacement thickness are needed in the throat region, for setting flow-passing capacity, and at the trailing edge, to enable the pressure distribution to be calculated. Similarly, blade loss predictions require computation of the momentum thickness. In this introduction previous work is briefly reviewed, indicating serious conflicts between existing data and regions of experimental data coverage still unavailable to the designer.

Criteria in use for transition and laminar separation are based on the use of a plot of the Crabtree (1958) type extended to account for variations in free-stream turbulence level. Crabtree proposed a correlation of available low-turbulence-level data for transition inception in the form of Re_θ against λ_θ defined by

$$\lambda_\theta = (\theta^2/\nu)\cdot(dU/dx) \quad (1)$$

To use correlations of the Crabtree type one plots the locus of the developing laminar boundary layer (either measured or calculated) in the form of Re_θ as a function of λ_θ. Laminar separation would be indicated by reaching the Thwaites (1949) limit of -0.082 or the Curle and Skan (1955) limit of -0.09. Assuming laminar separation is not encountered first then transition is predicted where the locus crosses the Crabtree curve. The approach works well for low turbulence levels; the difficulties occur in extending it to the high turbulence levels encountered in turbomachines. Turbulence levels vary between 2 and 14 percent in axial flow compressors and can be even higher in turbines, thus constituting an important independent variable.

Confidence in most results at zero pressure gradient is high because of the considerable research on flat plates. Further supporting evidence for zero pressure gradients will be presented in this paper. In the context of the present investigation the zero pressure gradient situation is seen as a vehicle for the development of techniques and as a check on the quality of the measurements.

Discrepancies exist in the favorable pressure gradient region. These are of concern to turbine designers. The tentative extrapolation of Hall (1968) is now considered to have too steep a slope. The measurements of Blair (1982) and Abu-Ghannam and Shaw (1980) appear to be reliable and are in reasonable accord with calculations of Van Driest and Blumer (1963). The data of Abu-Ghannam and Shaw are the most comprehensive and fitted curves for these are presented in Fig. 1.

The aim of the present investigation is the resolution of the serious discrepancies in the adverse pressure gradient region. An important facet of the Seyb (1965) correlation is the projection of transition curves of constant $Re_{\theta t}$ for a range of turbulence levels under adverse pressure gradient conditions. Rather than the absolute inception of transition, the Seyb data represent a more developed stage in the transition process. The Seyb projection was based on nozzle test data and the heuristic argument that at high turbulence levels transition is more dependent on the inability of damping mechanisms to cope with introduced disturbances than upon the amplification of

Contributed by the International Gas Turbine Institute and presented at the 33rd International Gas Turbine and Aeroengine Congress and Exhibition, Amsterdam, The Netherlands, June 5–9, 1988. Manuscript received by the International Gas Turbine Institute September 18, 1987. Paper No. 88-GT-298.

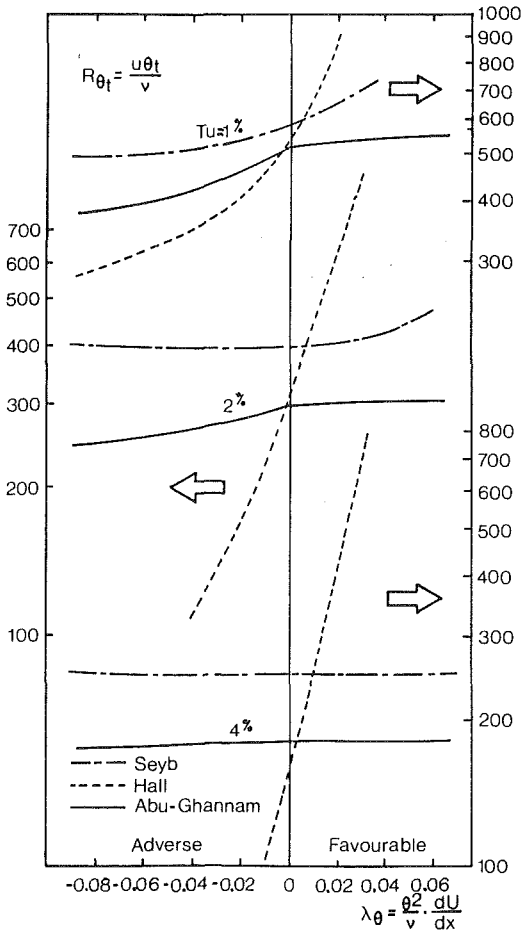

Fig. 1 Transition inception Reynolds number as a function of turbulence level and pressure gradient parameter

small perturbations. High turbulence levels would bring about transition regardless of the value of adverse pressure gradient. Hall used the Pretsch stability limit as a basis for his projections. His curves were reasonably compatible with available test data up to turbulence levels of 1.2 percent. Although their data were comprehensive at lower turbulence levels Abu-Ghannam and Shaw have given little useful information on turbulence levels above 2 percent under adverse pressure gradients. For these conditions there are still major uncertainties that require clarification.

The constant $Re_{\theta t}$ proposal has not been confirmed for high turbulence levels. The results of Schlichting and Das (1970) and unpublished measurements by the author and co-workers suggest that for turbulence levels above a critical level, between 2.5 and 3.0 percent, the free-stream turbulence causes nonlinear bypass effects. This results in the occurrence of transition independent of the linear amplification of Tollmien–Schlichting waves.

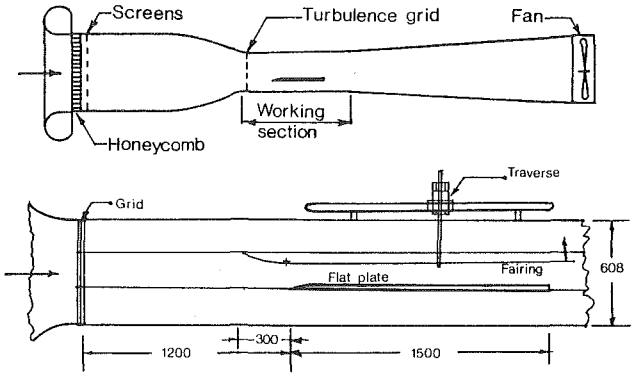

Fig. 2 Low-speed wind tunnel showing flat plate in working section

Following useful preliminary work at Cambridge University a program was established at the University of Technology, Sydney (formerly NSWIT) to provide information on transition under conditions of high turbulence level and adverse pressure gradient.

The initial experiments were confined to zero pressure gradient conditions with the objective of validating the measurement techniques for transition inception and development, investigating similarity of the intermittency distribution, and obtaining information on transition length. The transition investigations were to result in the measurement of intermittency distribution, velocity profile, and integral boundary layer parameters through the transition region. Emphasis was to be placed on readings of high quality at the beginning and end of the transition process, expressed in terms of appropriate Reynolds numbers.

Subsequent experiments have addressed the effect of the imposition of an adverse pressure gradient in the developing boundary layer for various levels of free-stream turbulence. One such series of results will be presented in this paper.

In a parallel investigation data have been analyzed to determine the stochastic nature of flows in the transition zone. Some recent results have been reported by Gostelow et al. (1988).

Equipment

The investigations were conducted in the octagonal section open circuit tunnel shown in Fig. 2. The working section has width and height dimensions of 608 mm. Air enters through a bellmouth to the settling chamber, which contains a

Nomenclature

c_f = skin-friction coefficient
H = form factor
N = nondimensional spot formation rate $= n\,\sigma\,\theta_t^3/\nu$
n = spot formation rate
Re_x = length Reynolds number
Re_θ = momentum thickness Reynolds number
T = turbulence level
U = free-stream velocity
u = local velocity
u^+ = dimensionless velocity $= u/v^*$
v^* = friction velocity $= \sqrt{\tau_w/\rho}$
x = streamwise distance from leading edge
y = normal distance from wall
y^+ = dimensionless distance from wall $= yv^*/\nu$
γ = intermittency factor
δ = absolute thickness
η = dimensionless distance $= (x-x_S)/(x_E-x_S)$
θ = momentum thickness
λ = distance between 0.25 and 0.75 intermittency
λ_θ = pressure gradient parameter
ν = kinematic viscosity
ξ = dimensionless distance $= (x-x_t)/\lambda$
ρ = density
σ = dependence area factor
τ_w = wall shear stress

Subscripts

E = end of transition (γ = 0.99)
S = start of transition (γ = 0.01)
t = start of transition (by Narasimha method)

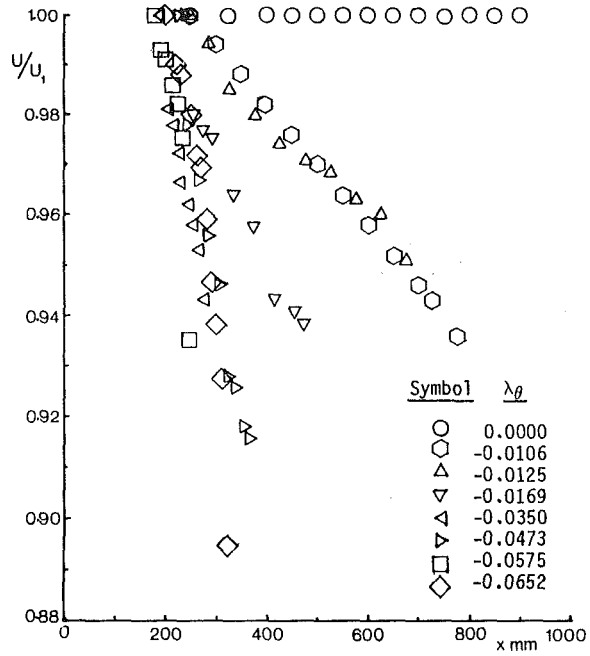

Fig. 3 Streamwise velocity distribution for different fairing settings

honeycomb for reduction of swirl and a set of screens for turbulence reduction. A contraction of area ratio 3.88 precedes the working section, which has a maximum velocity of 40 m/s. The free-stream turbulence level is around 0.3 percent.

Boundary layer measurements were made on the top surface of a flat aluminum plate 1500 × 608 × 25 mm mounted in the working section. Particular attention was paid to surface finish giving excellent flatness and smoothness. The leading edge had an elliptical arc form to avoid leading edge separation and was located 1200 mm from the test section entrance. Static pressures were measured using centerline taps of 0.5 mm diameter at 75 mm intervals. It was found necessary to impart a negative incidence of 1/4 deg to the plate to avoid laminar separation bubbles; this had an imperceptible effect on the pressure distribution.

For the series of measurements involving variable pressure gradients a fairing having a variable-angle straight flap was mounted above the flat plate. This fairing was rotatable about an axis upstream of the flat plate leading edge.

The velocity distributions in a streamwise direction were measured using static pressures from the centerline taps and are presented in Fig. 3. It is difficult to impose a diffusion of constant gradient using a simple linear fairing but the velocity distributions showed that departures from the desired pattern were not serious. Some separations are undoubtedly present on the variable flap that will result in some scatter in the results on the flat plate.

The turbulence grid is mounted at a fixed distance of 1200 mm upstream of the plate leading edge (the origin of the x axis in the plots). The grid is also 900 mm upstream of the fairing. Higher turbulence levels required for this study were generated by inserting square array biplanar grids, constructed from cylindrical steel bars, at the entrance to the test section. Four grids were designed, using a relation given by Frenkiel (1948), to produce homogeneous, well-mixed turbulence over the plate. There is a minor effect of fairing interference (the normal throat dimension is 130 mm) but this is not considered to be a first-order problem. Turbulence levels at the plate leading edge for grids 1–4 are 1.3, 2.1, 3.2, and 6.3 percent, respectively, when the fairing is not installed.

A traverse carried the probe longitudinally over 1 m from the leading edge and a lead-screw system were mounted on the carriage for vertical traverse. A dial gage having a least count of 0.01 mm was used for close-interval measurements of vertical movement. A concentrated beam of light was focused on the probe tip, the reflection of which on the polished aluminum plate was used for accurate positioning close to the wall.

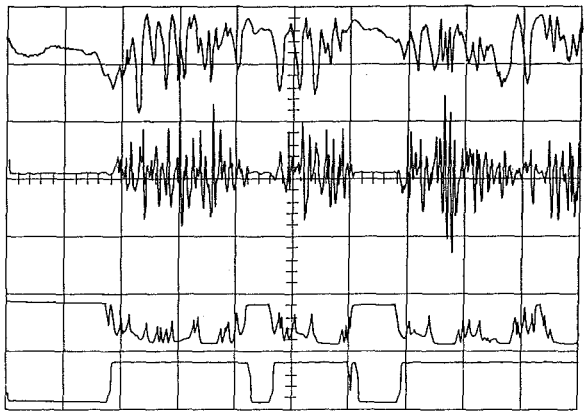

Fig. 4 Sample hot-wire traces in the transition zone

The reference velocity was set using a pitot tube. Boundary layer traverses were performed using a 1.2 × 0.72 mm flat end pitot tube in conjunction with plate static pressures. Transition measurements were performed using a DISA hot-wire probe having a 1.2 mm platinum-coated wire of 5 μm diameter and a DISA 55M10 anemometer. The probe was located at a distance from the plate where the mean local velocity was 80 percent of the free-stream velocity.

Examples of typical hot-wire traces from a transitional boundary layer are given in Fig. 4. The top trace is the raw signal trace, directly from the anemometer. High-pass filtering has been applied at an appropriate frequency for elimination of low-frequency interference and Tollmien–Schlichting instability waves and the effects of this are shown in the second trace. The bottom trace is the final on-off pulse, which triggers a counter-timer to produce an on-line intermittency reading. A comparator stage and two series stages of monostable amplification precede the final signal.

Many previous investigators of boundary layer transition have been hampered by the lack of on-line instrumentation capable of sampling intermittency over a suitable time period. In the previous experiments on this flat plate intermittency was established by manual investigation of ultraviolet traces. This was time consuming and sampling time was limited to a maximum of 4 s. With the on-line intermittency meter (Alt, 1987) there is no practical upper limit to sampling time and 100 s is in routine use.

Variation of Turbulence Level at Zero Pressure Gradient

The results for the zero pressure gradient case at four different turbulence levels are presented in this section. A typical "raw" intermittency distribution is given in Fig. 5, which was taken for grid 2 under zero pressure gradient conditions. The start of transition has been arbitrarily defined as the 1 percent intermittency location and the end of transition as that for 99 percent intermittency. The results are compared with those of Dhawan and Narasimha (1958) and of Abu-Ghannam and Shaw (1980) for reference purposes. It can be seen that the present data are mostly intermediate between the two established results. The present results are within the band of accepted data and are consistent with the previous data from this facility (Gostelow and Ramachandran, 1983).

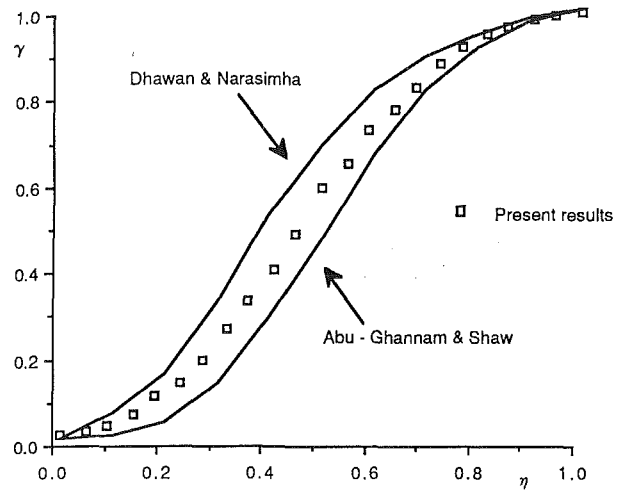

Fig. 5 Intermittency distribution for grid 2 at zero pressure gradient

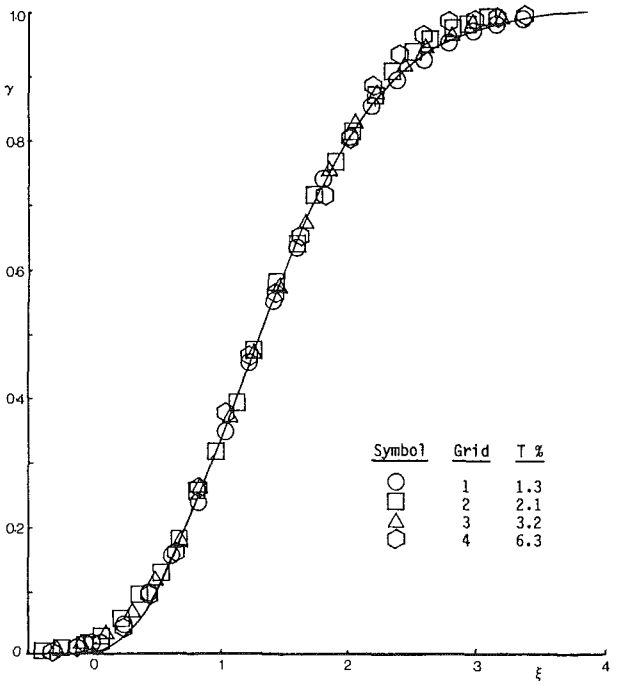

Fig. 6 Intermittency data for the four different turbulence levels compared with Narasimha's universal intermittency distribution

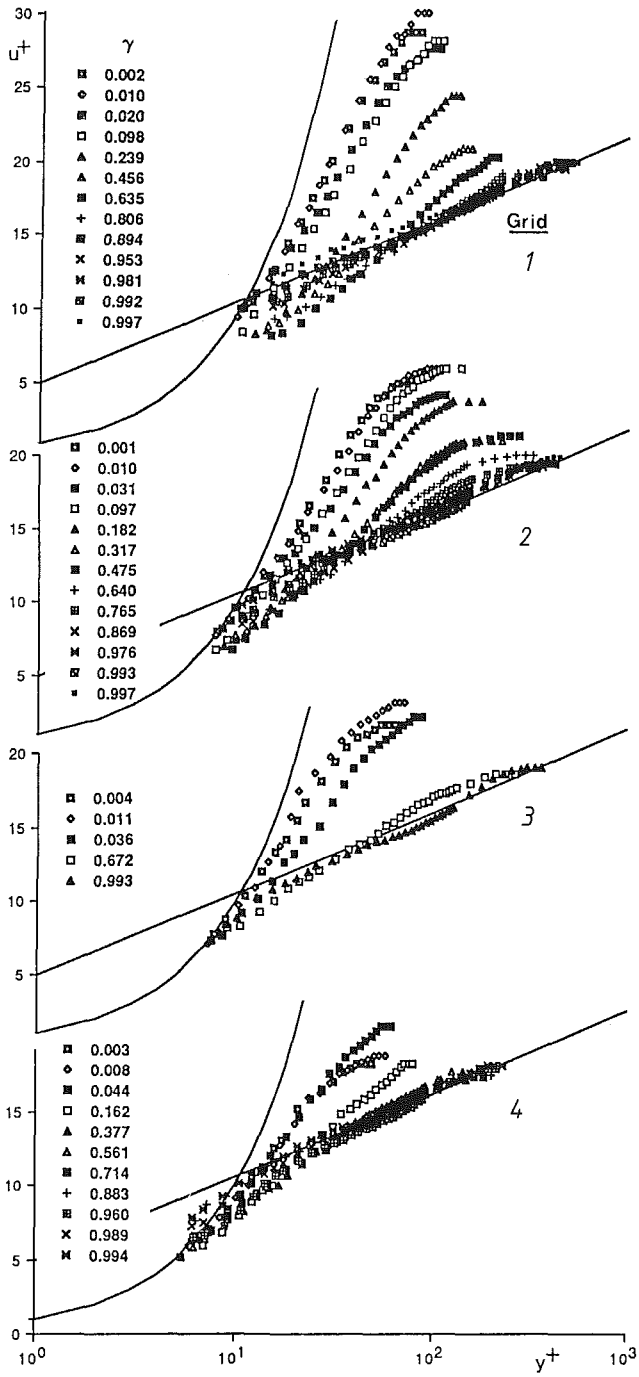

Fig. 7 Dimensionless velocity profiles for the four different turbulence levels

Intermittency data from each of the four grids were reduced in the form

$$F(\gamma) = [-\ln(1-\gamma)]^{1/2} \tag{2}$$

used by Narasimha and from the resulting plots, which tended to be linear for intermittencies above 0.1, the effective transition inception x_t and effective transition length λ were determined. These were used to replot the intermittency distributions in comparison with Narasimha's universal intermittency function

$$\gamma = 1 - \exp(-0.412\,\xi^2) \tag{3}$$

The results are presented in Fig. 6 and, over most of the distribution, the agreement with the universal distribution is good. There is a region of less satisfactory agreement at low intermittency where the intermittency measurements depend somewhat on the discrimination threshold. Since all measurements fall above the predicted distribution, for intermittencies less than 0.1, this could be taken as evidence for a weak "subtransition" of the type reported by Narasimha for various flow configurations.

The only other significant departure from the similarity curve is for higher intermittencies at the higher turbulence level of grid 4. In this case the measured results gave a slightly higher intermittency than the predicted value. The authors have experienced inconsistencies in measurements of the completion of transition under high free-stream turbulence levels and this is an area that requires further detailed attention.

In Fig. 7, velocity profiles are presented in the form of dimensionless velocity u^+, as a function of height y^+. The traverses were performed with the pitot tube and it has not been possible to extend the results significantly into the laminar sublayer.

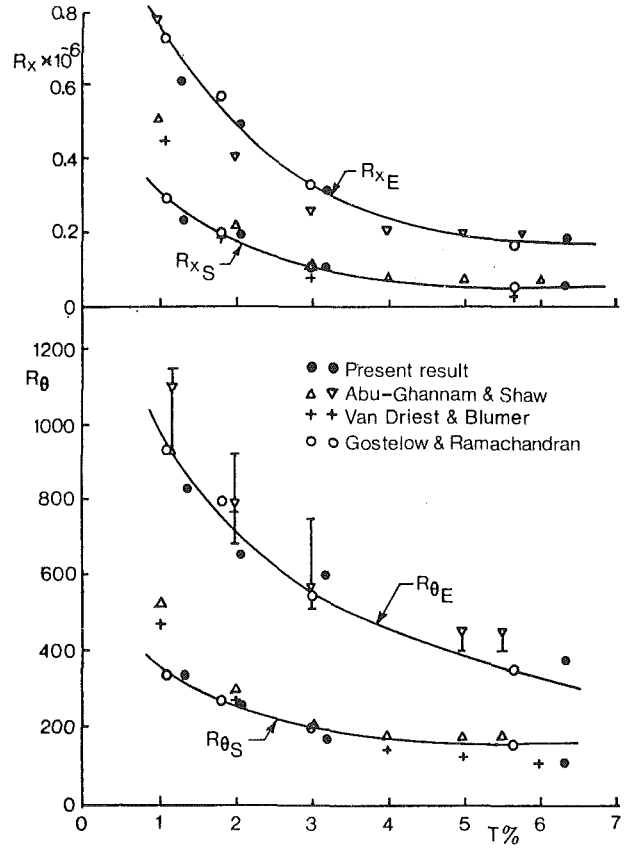

Fig. 8 Effect of turbulence levels on Reynolds numbers at start and end of transition for zero pressure gradient

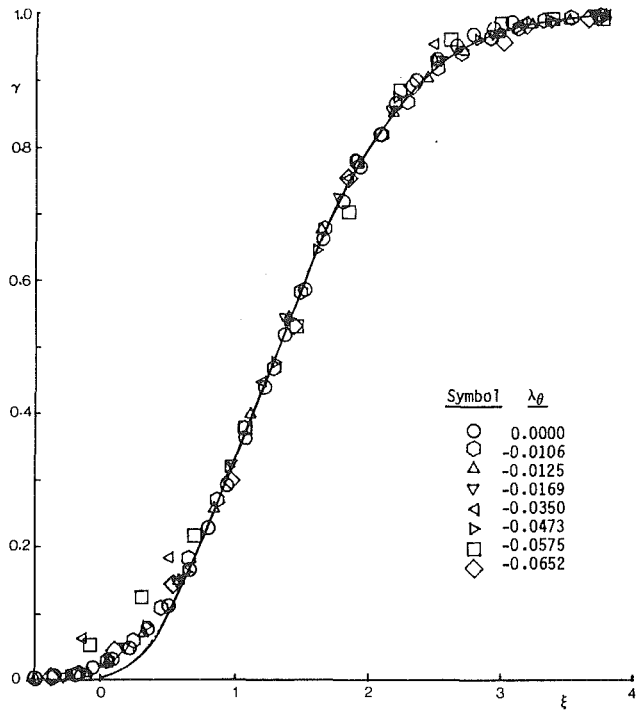

Fig. 9 Intermittency data for eight values of pressure gradient parameter compared with Narasimha's universal intermittency distribution

Different methods were adopted for deriving the laminar and turbulent values of skin-friction coefficient. For the laminar layer the measured values of u^+ and y^+ nearest the wall were extrapolated to give a wall value on a linear $u^+ = y^+$ basis. For the turbulent value the power law formulation

$$\tau_w/\rho = 0.0464\ (\nu/U\delta)^{1/4}\ U^2/2 \tag{4}$$

was used.

Obviously in plotting the velocity profiles through the intermittency region neither the laminar nor the turbulent derived values of wall stress are entirely appropriate. For intermediate values of intermittency the superposition relationship of Emmons (1951) was most useful

$$c_f = (1-\gamma)c_{f\text{lam}} + \gamma\ c_{f\text{turb}} \tag{5}$$

This results in

$$v^{*2} = (1-\gamma)v^{*2}_{\text{lam}} + \gamma\ v^{*2}_{\text{turb}} \tag{6}$$

For a given set of traverses v^*_{lam} and v^*_{turb} have therefore been evaluated. These have then been combined in the above equation to give a local value of v^*, which was used to produce the plots of Fig. 7.

Outboard of the laminar sublayer the low intermittency plots falls below the linear sublayer curve $u^+ = y^+$ as is appropriate outside the sublayer. The behavior through the transition region follows the pattern that would be expected with rising intermittency. In the outer region of the boundary layer the "end of transition" plots collapse onto the "law of the wall" curve

$$u^+ = 2.439 \ln y^+ + 5.0 \tag{7}$$

Values of Re_x and Re_θ at the start and end of transition have been plotted as a function of turbulence level in Fig. 8. The data follow the established results quite well, particularly those of Gostelow and Ramachandran (1983). In common with those latter results transition is predicted to start and end a little earlier than the results of other workers for the 1 percent turbulence level results of grid 1. However the discrepancies are not large and the results are relatively consistent. There is no large scatter or uncertainty band in identifying the completion of transition for these results.

Variation of Pressure Gradient for Moderate Turbulence

The variable diffusion fairing was in place for all readings in this series. The fairing was firstly set to give a zero static pressure gradient in a streamwise direction. The angle was subsequently adjusted to give various levels of adverse pressure gradient. All readings in this series were taken with grid 2 in place. At zero pressure gradient, with the fairing in place, grid 2 gave a turbulence level of 1.7 percent at the leading edge. The corresponding average value over the range of pressure gradients tested was 1.6 percent.

Comparison of the zero pressure gradient data with the equivalent data from the previous series gives an indication of any anomalies that may have been introduced with the insertion of the fairing. When raw intermittency plots for the zero pressure gradient grid 2 data with and without the fairing present were compared little discernible difference was observed.

The level of adverse pressure gradient was adjusted incrementally toward the limiting value imposed by equipment geometry. A series of eight sets of readings was taken including the zero pressure gradient case. The raw intermittency plots for these sets of readings were of the general form given in Fig. 5 although some steepening of the curve was present for the more adverse pressure gradients.

These plots were also reduced using the intermediate plot of equation (2) and compared with the universal distribution of equation (3). The resulting distributions are presented in Fig. 9 for the eight values of pressure gradient parameter. Although it has not been claimed that equation (3) gives a similarity representation for high adverse pressure gradients, in this case

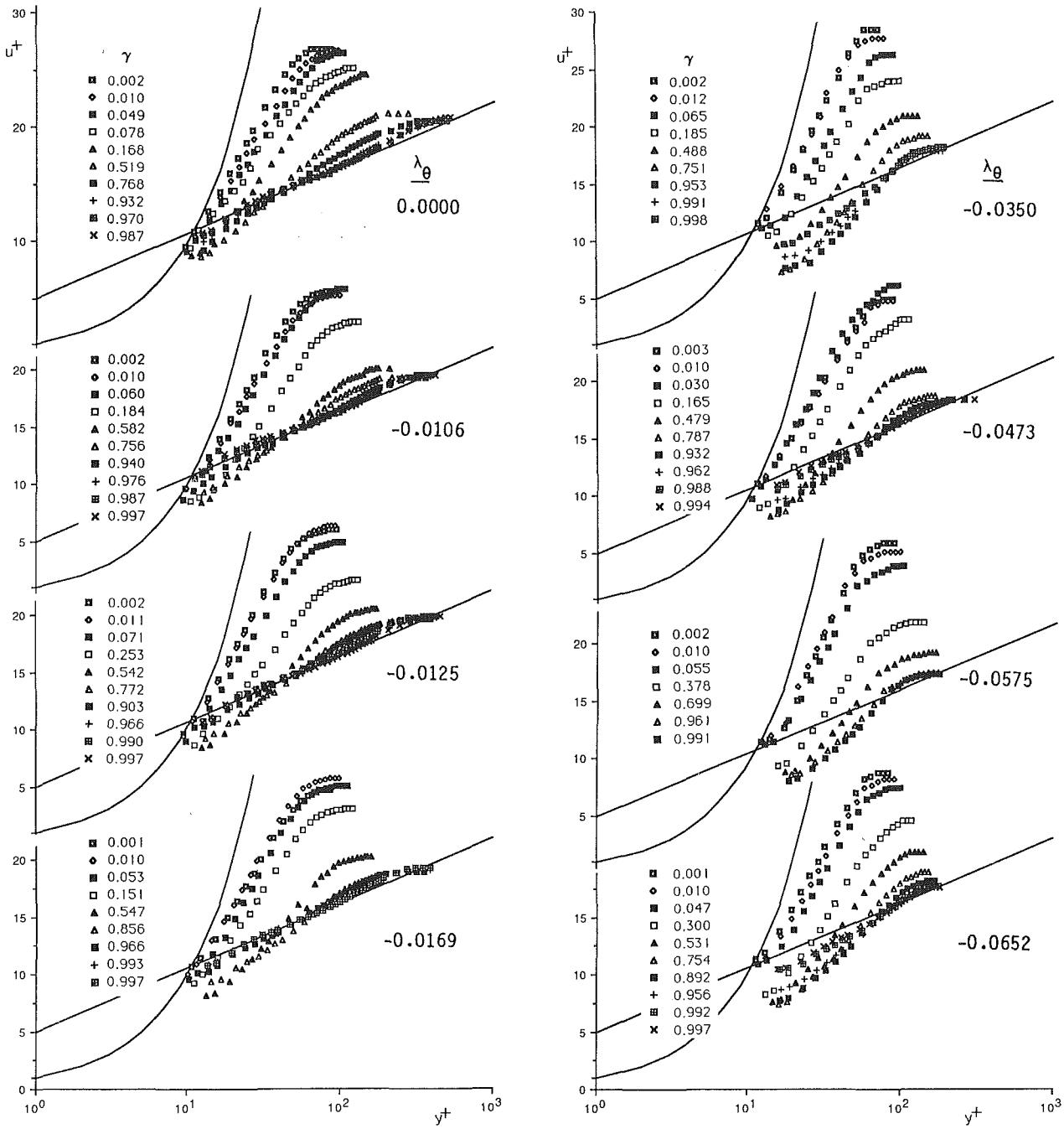

Fig. 10 Dimensionless velocity profiles for the eight pressure gradients

agreement remains good for some moderately strong adverse pressure gradients. For intermittencies below 0.2 some of the results for the more adverse pressure gradients are above the theoretical distribution, again indicating the possibility of a subtransition.

It should be pointed out that the values of c_f assigned are quite sensitive to local perturbations in velocity gradients; the velocity distributions have some significant deviations from linear (Fig. 3). In these results the value of λ_θ at an intermittency of 0.01 has been used to characterize each set of readings. Although this was based on the local momentum thickness at the 0.01 intermittency station the velocity gradient taken was the average for the entire transition region. In general this gives a more extreme value of λ_θ than would the use of a local velocity gradient and, for the two most severe adverse pressure gradients, this sensitivity to the method of determining velocity gradient was quite strong. There is a case for assigning a more conservative value to the readings labeled $\lambda_\theta = -0.0575$ and $\lambda_\theta = -0.0652$.

Having said this the consistency of readings in Fig. 9, and their agreement with the universal intermittency distribution over a range of moderately strong adverse pressure gradients, are surprisingly good.

Following boundary layer traverses throughout the transition region velocity profiles were obtained and presented in the form of plots of u^+ against y^+ in Fig. 10. The conditions were identical to those of the intermittency data of Fig. 9. The procedures for determining skin-friction coefficient, for the results show in Fig. 10, were identical to those adopted for the previous series of readings without the fairing present.

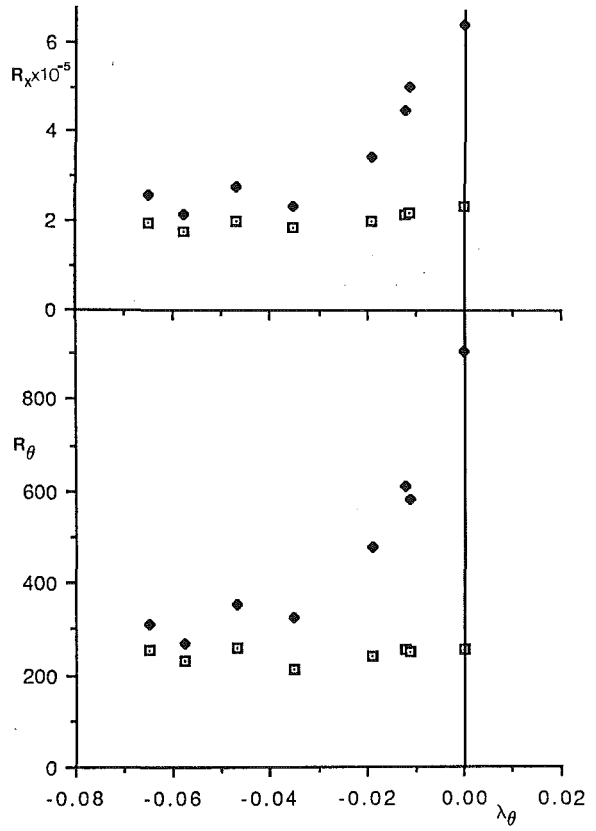

Fig. 11 Variation of Re_x and Re_θ with pressure gradient parameter for transition inception (□) and completion (◇) at an average turbulence level of 1.6 percent

Again it is instructive and reassuring to compare the plots for the grid 2 zero pressure gradient results with and without the fairing present (Figs. 7*b* and 10*a*). The velocity profiles are essentially similar, thus confirming the consistency of the results.

It is of concern that, for the more adverse pressure gradients, the velocity profiles fall below the law of the wall line in the intermediate region, for which there should be a good fit. This reflects the sensitivity of the adverse pressure gradient data to the method of determination of turbulent skin-friction coefficient. In this case the power law representation of equation (4) was used. An alternative determination, using the Coles relation

$$c_{f\text{turb}} \approx 0.3e^{-1.33H}/(\log \mathrm{Re}_\theta)^{1.74+0.31H} \qquad (8)$$

gave velocity profiles above the law of the wall line, suggesting too low a value of $c_{f\text{turb}}$. Although not affecting the other results, these difficulties do lend support to the view of Walker (1987a) that further work is needed on determination of skin-friction coefficients for conditions of moderately high free-stream turbulence level and adverse pressure gradient.

Traverse profiles were integrated to give the variation of integral parameters through the transition zone. The values of pressure gradient parameter, λ_θ, corresponding to each reading were also evaluated. As a result it was possible to summarize the results in the form of plots of Re_x and Re_θ, as a function of λ_θ, for the start and end of transition. These results are presented for the grid 2 data in Fig. 11.

As indicated previously the value of λ_θ chosen to characterize the results is that corresponding to the start of transition. The values of Re_x and Re_θ for the end of transition therefore appear vertically above the inception value on the plots.

The zero pressure gradient grid 2 results for transition inception agree well with the previous zero pressure gradient grid 2 results. For the completion of transition the new results, taken with the fairing mounted in the working section, do not agree as well with the earlier results from this flat plate, giving a higher value of Re_θ for transition completion, although still within the accepted band of previous data. This is an unexplained discrepancy.

Nevertheless the plots of Fig. 11 have significant implications for the design process. While agreeing well with accepted results for transition inception at zero pressure gradient, the results do indicate a fairly constant Re_θ for transition inception at all adverse pressure gradients. This is in accordance with the prediction of Seyb (1965).

The data for the end of transition show a very different trend. At zero pressure gradient the value of Re_θ reaches the high value of 900 before transition is completed. As the adverse pressure gradient is increased a fully turbulent state is attained for much lower values of Re_θ. This tendency for the transition zone to become shorter is a strong and consistent one. The change is most rapid when a zero pressure gradient is replaced by even a weak adverse pressure gradient.

These results were quite surprising. Although little of the previous published work has shown any indication of this trend that of Evans (1971) did contain some such indications. Evans observed that the transition length on the suction surface of a compressor blade was much shorter than the laminar region, whereas in flat plate experiments the opposite was the case. With hindsight the resulting inference should have been that transition length is strongly dependent on the level of adverse pressure gradient. It probably has theoretical implications for consideration of both the effect of disturbance amplification rates on the extent of transition and also for the effect of these parameters on the formation and closure of laminar separation bubbles.

Discussion

The measurements of intermittency distribution, velocity profile, and integral parameters for the zero pressure gradient cases are in reasonable agreement with previous results. This establishes confidence in the techniques presently in use. An important means of quality improvement was the development of an on-line intermittency meter, which enabled very long sampling times to be used.

Each set of readings was analyzed using the approach of Narasimha (1975) to facilitate comparisons with the earlier predictions. The data obtained for zero pressure gradient conditions provided a further useful check on the Narasimha data. As with the previous data the results were in good agreement with Narasimha's transition length prediction. When plotted on a similarity rule basis good agreement was obtained with the universal intermittency distribution of equation (3), even for adverse pressure gradient conditions.

Significant progress for transition prediction had been made by Narasimha in assuming that the turbulent spot formation could be represented as a concentrated or local breakdown by a Dirac delta function located at transition inception. Such a representation was acknowledged to be a simplification and warrants close scrutiny. Experience shows, for example, that a hot-wire probe near the plate leading edge will occasionally detect spot inception. It is also unrealistic to postulate a sudden termination of spot formation. This useful model for spot formation is in need of further refinement.

Narasimha (1985) has subsequently made progress in defining and confirming a nondimensional spot formation parameter N. Narasimha demonstrated that the zero pressure gradient data of Gostelow and Ramachandran (1983) were consistent with a value of 0.7×10^{-3} for N. It was therefore expected that the new zero pressure gradient data would be compatible with that criterion. In fact values of $N \times 10^3$ of 1.13, 0.85, 0.49, and 0.36 were obtained for grids 1–4, respec-

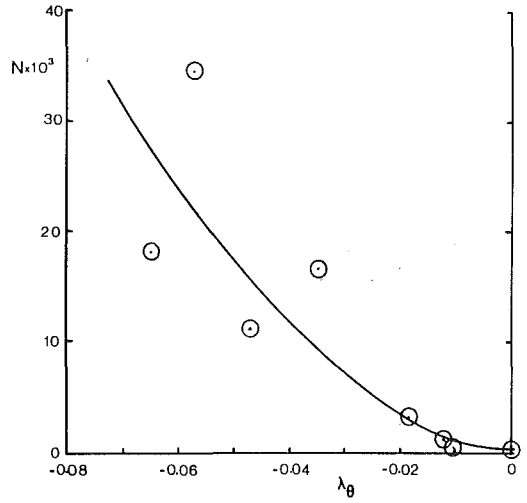

Fig. 12 Variation of nondimensional spot formation rate parameter *N* with pressure gradient parameter

tively. On average these data are in excellent agreement with Narasimha's value, but they do seem to indicate a consistent trend of decreasing spot formation parameter as turbulence level increases. In view of the sensitivity of these measurements and the paucity of other confirming data, this level of agreement is considered to be reasonable.

The data for the various adverse pressure gradient conditions have also been analyzed to obtain the variation of spot formation rate with pressure gradient. The results for grid 2 are presented in Fig. 12. Application of the procedures, used by Narasimha for zero pressure gradient flows, to adverse pressure gradient cases depends upon a number of assumptions and is best regarded as an estimate. However, as Fig. 9 shows, the departures from similarity are not sufficiently strong to invalidate the analysis. Although the results presented are scattered, the trend is consistent with that of other data and is considered to be reliable. The spot formation rates under adverse pressure gradient conditions do, however, vary markedly with turbulence level, Fig. 12 corresponds only to a leading edge turbulence level of 1.7 percent and should not be taken to be a universal representation.

It is clear from Fig. 12 that any significant departure from zero pressure gradient conditions causes a rapid increase in nondimensional spot formation rate. As the laminar separation limit is approached the spot formation rate parameter may increase by a factor of 50. Clearly there is a direct connection (an inverse square law relationship) between the increased spot formation rate and the strong reduction in transition length indicated in Fig. 11.

Flows over compressor blading have high turbulence levels and are subject to severe pressure gradients. The transition length for adverse pressure gradients has been shown to be much shorter than that for the well-researched zero pressure gradient case. Although no attempt has been made to extract from the data an explanation for this behavior, some clues are readily forthcoming. The high spot formation rates, for example, and the correspondingly reduced transition lengths, are entirely consistent with the model advanced by Walker (1987b).

Walker showed that transition length correlations developed for constant pressure flows could seriously overestimate the transition length in an adverse pressure gradient situation. He attributed this discrepancy to the tendency for natural transition in the absence of a pressure gradient to evolve from the breakdown of laminar instability waves in "sets" interspersed by regions of stable laminar flow. Walker argued that under adverse pressure gradients transition tended to be a forced process with a continuous breakdown of instability waves into turbulence and hence a much shorter transition zone.

This explanation is a fundamental one for axial flow compressors. Were the transition length not considerably shorter than indicated by the flat plate correlations the boundary layer would be transitional over most of the blade surface. The blade would be quite incapable of sustaining the required aerodynamic loadings.

The strong increases in spot formation rate as laminar separation is approached are also thought to be a strong determinant of the bubble mode of separation. If these increases in spot formation rate did not occur any laminar separation would result in the more severe mode of complete breakaway from the surface.

Conclusions

An intermittency meter has been developed that permits the on-line monitoring of intermittency with sampling periods of up to 100 s. The meter was an essential feature of the reported program in which extensive intermittency and velocity profile data were generated.

Results for four different turbulence levels were obtained under zero pressure gradient conditions. These were useful in confirming previous results for transition inception and length and the validity of the experimental techniques in use.

The results are represented well by Narasimha's universal intermittency distribution. Surprisingly strong similarity was also exhibited by intermittency distributions under adverse pressure gradient conditions.

Dimensionless velocity profiles are reasonable under zero pressure gradient conditions and the turbulent profiles are represented closely by the law of the wall. This is not the case for moderate adverse pressure gradients where difficulties were experienced with both the power law and Coles relationships for determination of skin-friction coefficient.

It has been shown that serious discrepancies exist in the adverse pressure gradient region between the various predictions of transition inception available to designers of turbomachinery. The results obtained in the current investigation tend to support the use of a constant momentum thickness Reynolds number for transition inception at moderate turbulence levels up to about 2 percent.

The completion of transition (and hence the transition length), however, has a very different behavior. In the absence of an imposed pressure gradient the transition region is long, in keeping with other established results from flat plate testing. Any departure from a zero pressure gradient into the adverse region results in a strong reduction in transition length. For even quite a modest adverse pressure gradient the completion of transition occurs much earlier and the transition length has become reduced to a much lower, and roughly constant, level.

Associated with this shortening of transition is a dramatic increase in turbulent spot formation rate. This is consistent with Walker's model, in which transition in the absence of a streamwise pressure gradient occurs in sets of instability waves interspersed with period of stable laminar flow. In contrast transition under an adverse pressure gradient is a forced transition with a continuous breakdown of individual intermittency waves into turbulence.

The observed strong reduction in transition length under adverse pressure gradients, with the associated rapid increase in turbulence spot formation rate, is seen to be fundamental for the loading capability of an axial flow compressor and also an important prerequisite for laminar separation bubble formation.

Acknowledgments

The research was performed under contract from Rolls-Royce plc., and the authors would particularly like to acknowledge the interest and suggestions of Dr. P. Stow and Mr. N. T. Birch.

References

Abu-Ghannam, B. J., and Shaw, R., 1980, "Natural Transition of Boundary Layers – the Effects of Turbulence, Pressure Gradient and Flow History," *J. Mech. Eng. Sci.*, Vol. 22, No. 5, p. 213.

Alt, P., 1987, "An Intermittency Meter for Investigating Boundary Layer Transition," NSWIT/ME 17.

Blair, M. F., 1982, "Influence of Free-Stream Turbulence on Boundary Layer Transition in Favorable Pressure Gradients," ASME *Journal of Engineering for Power*, Vol. 104, pp. 743–750.

Crabtree, L. F., 1958, "Prediction of Transition in the Boundary Layer on an Aerofoil," *J. Roy. Aer. Soc.* Vol. 62.

Curle, N., and Skan, S. W., 1955, "Approximate Method for Predicting Separation of Laminar Boundary Layers," *Aero Quart.*, Vol. 8.

Dhawan, S., and Narasimha, R., 1958, "Some Properties of Boundary Layer Flow During the Transition from Laminar to Turbulent Motion," *J. Fluid Mech.*, Vol. 3, p. 418.

Emmons, H. W., 1951, "The Laminar-Turbulent Transition in a Boundary Layer – Part I", *Journal of Aero. Sci.*, Vol. 8.

Evans, B. J., 1971, "Effects of Free-Stream Turbulence on Blade Performance in a Compressor Cascade," Ph.D. Thesis, Cambridge University, Cambridge, United Kingdom.

Frenkiel, F. N., 1948, "The Decay of Isotropic Turbulence," *Trans. ASME*, Vol. 70, p. 311.

Gostelow, J. P., Blunden, A. R., and Blunden, W. R., 1988, "Measurements and Stochastic Analysis of Boundary Layer Transition for a Range of Free-Stream Turbulence Levels," *Proc. 2nd Int. Symp. on Transport Phenomena, Dynamics and Design of Rotating Machinery*, Honolulu, HI.

Gostelow, J. P., and Ramachandran, R. M., 1983, "Some Effects of Free Stream Turbulence on Boundary Layer Transition," *Proc. 8th Australasian Fluid Mech. Conf.*

Hall, D. J., 1968, "Boundary Layer Transition," Ph.D. Thesis, Liverpool University, London, United Kingdom.

Narasimha, R., 1957, "On the Distribution of Intermittency in the Transition Region of the Boundary Layer," *J. Aero Sci.*, Vol. 24, pp. 711–712.

Narasimha, R., 1985, "The Laminar-Turbulent Transition Zone in the Boundary Layer," *Progress in Aerospace Sci.*, Vol. 22, pp. 29–80.

Schlichting, H., and Das, A., 1970, "On the Influence of Turbulence Level on the Aerodynamic Losses of Axial Turbomachines," in: *Flow Research on Blading*, L. S. Dzung, ed., Elsevier, New York.

Seyb, N. J., 1965, "Determination of Cascade Performance With Particular Reference to the Prediction of the Boundary Layer Parameters," A.R.C. Rept. 27, 214.

Thwaites, B., 1949, "Approximate Calculation of the Laminar Boundary Layer," *Aero. Quart.*, Vol. 1, p. 245.

Van Driest, E. R., and Blumer, C. B., 1963, "Boundary Layer Transition: Free Stream Turbulence and Pressure Gradient Effects," *AIAA Journal*, Vol. 1, p. 1303.

Walker, G. J., 1987a, "Turbulent Skin Friction on Axial Compressor Blading," *Proc. 8th ISABE*, Cincinnati, OH.

Walker, G. J., 1987b, "Transitional Flow on Axial Turbomachine Blading, Paper No. AIAA-87-0010.

Acknowledgments

The research was performed under contract from Rolls-Royce plc., and the authors would particularly like to acknowledge the interest and suggestions of Dr. P. Stow and Mr. N. T. Birch.

References

Abu-Ghannam, B. J., and Shaw, R., 1980, "Natural Transition of Boundary Layers – the Effects of Turbulence, Pressure Gradient and Flow History," *J. Mech. Eng. Sci.*, Vol. 22, No. 5, p. 213.

Alt, P., 1987, "An Intermittency Meter for Investigating Boundary Layer Transition," NSWIT/ME 17.

Blair, M. F., 1982, "Influence of Free-Stream Turbulence on Boundary Layer Transition in Favorable Pressure Gradients," ASME *Journal of Engineering for Power*, Vol. 104, pp. 743–750.

Crabtree, L. F., 1958, "Prediction of Transition in the Boundary Layer on an Aerofoil," *J. Roy. Aer. Soc.* Vol. 62.

Curle, N., and Skan, S. W., 1955, "Approximate Method for Predicting Separation of Laminar Boundary Layers," *Aero Quart.*, Vol. 8.

Dhawan, S., and Narasimha, R., 1958, "Some Properties of Boundary Layer Flow During the Transition from Laminar to Turbulent Motion," *J. Fluid Mech.*, Vol. 3, p. 418.

Emmons, H. W., 1951, "The Laminar-Turbulent Transition in a Boundary Layer – Part I", *Journal of Aero. Sci.*, Vol. 8.

Evans, B. J., 1971, "Effects of Free-Stream Turbulence on Blade Performance in a Compressor Cascade," Ph.D. Thesis, Cambridge University, Cambridge, United Kingdom.

Frenkiel, F. N., 1948, "The Decay of Isotropic Turbulence," *Trans. ASME*, Vol. 70, p. 311.

Gostelow, J. P., Blunden, A. R., and Blunden, W. R., 1988, "Measurements and Stochastic Analysis of Boundary Layer Transition for a Range of Free-Stream Turbulence Levels," *Proc. 2nd Int. Symp. on Transport Phenomena, Dynamics and Design of Rotating Machinery*, Honolulu, HI.

Gostelow, J. P., and Ramachandran, R. M., 1983, "Some Effects of Free Stream Turbulence on Boundary Layer Transition," *Proc. 8th Australasian Fluid Mech. Conf.*

Hall, D. J., 1968, "Boundary Layer Transition," Ph.D. Thesis, Liverpool University, London, United Kingdom.

Narasimha, R., 1957, "On the Distribution of Intermittency in the Transition Region of the Boundary Layer," *J. Aero Sci.*, Vol. 24, pp. 711–712.

Narasimha, R., 1985, "The Laminar-Turbulent Transition Zone in the Boundary Layer," *Progress in Aerospace Sci.*, Vol. 22, pp. 29–80.

Schlichting, H., and Das, A., 1970, "On the Influence of Turbulence Level on the Aerodynamic Losses of Axial Turbomachines," in: *Flow Research on Blading*, L. S. Dzung, ed., Elsevier, New York.

Seyb, N. J., 1965, "Determination of Cascade Performance With Particular Reference to the Prediction of the Boundary Layer Parameters," A.R.C. Rept. 27, 214.

Thwaites, B., 1949, "Approximate Calculation of the Laminar Boundary Layer," *Aero. Quart.*, Vol. 1, p. 245.

Van Driest, E. R., and Blumer, C. B., 1963, "Boundary Layer Transition: Free Stream Turbulence and Pressure Gradient Effects," *AIAA Journal*, Vol. 1, p. 1303.

Walker, G. J., 1987a, "Turbulent Skin Friction on Axial Compressor Blading," *Proc. 8th ISABE*, Cincinnati, OH.

Walker, G. J., 1987b, "Transitional Flow on Axial Turbomachine Blading, Paper No. AIAA-87-0010.

DISCUSSION

M. W. Johnson[1]

Gostelow and Blunden have obtained some valuable transition data for adverse pressure gradients. However, the method used for determining intermittency may give differing results from other published work. Figure 13 shows the variation of intermittency through the boundary layer as obtained by Acharya (1985). Similar data taken at the University of Liverpool are also shown in Fig. 14. These results demonstrate how turbulent spots originate close to the wall and then diffuse out toward the free stream. Clearly a hot-wire probe placed close to the wall will detect start of transition earlier than one placed further out. In Acharya's work, and at Liverpool, the hot-wire probe is placed in the constant intermittency region very close to the wall ($y/\delta \simeq 0.05$) in order to detect the first turbulent spots. In contrast, in the current paper, it is stated that intermittency is measured at a point where the velocity is 80 percent of the free-stream velocity, which corresponds to a y/δ of between 0.49 and 0.58 (depending on the pressure gradient) and so lower intermittencies will be measured. The current results will therefore predict start of transition later than results made elsewhere where the probe is closer to the wall. This will lead to a discrepancy between these new data and previously published results.

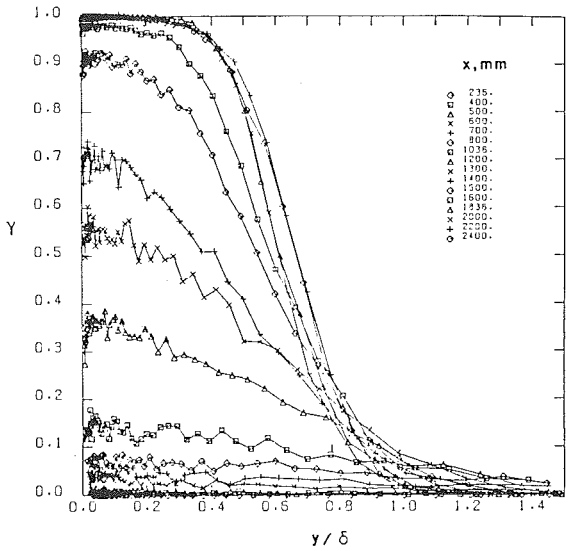

Fig. 13 Acharya's intermittency data

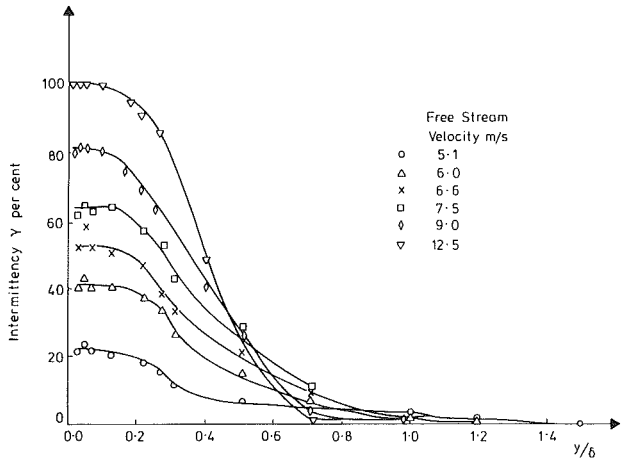

Fig. 14 Liverpool intermittency data

References

Acharya, M., 1985, *Pressure Gradient and Free Stream Turbulence Effects on Boundary Layer Transition*, Brown Boveri KLR 85-127C, Switzerland.

Authors' Closure

Although Dr. Johnson is right to emphasize the potential significance of the variation of intermittency with traverse distance, this variable has not exerted a major influence on the present investigations.

[1]Department of Mechanical Engineering, The University of Liverpool, Liverpool L69 3BX, United Kingdom.

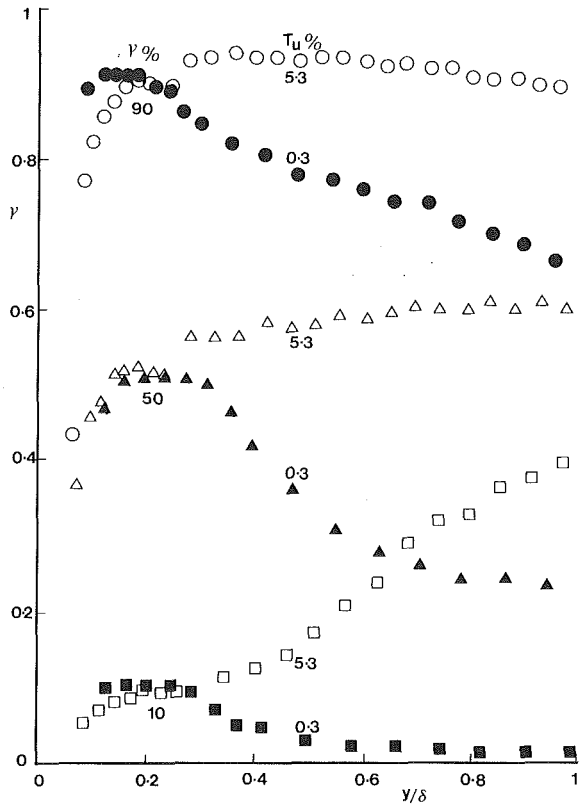

Fig. 15 Variation of measured intermittency with dimensionless traverse distance under moderate adverse pressure gradient conditions; nominal intermittency values of 10, 50, and 90 percent for inlet turbulence levels of 0.3 and 5.3 percent

Dr. Johnson's principal claim is that the current results will predict transition inception later than other results taken with the probe closer to the wall, leading to a discrepancy between the new data and previous results. It was in order to monitor how closely the results matched others that the first series of experiments was undertaken under zero pressure gradient conditions. The range of turbulence levels was between 1.3 and 6.3 percent and the techniques were identical to those used for the subsequent adverse pressure gradient work. Figure 8 of the paper demonstrates that transition inception was not found to occur later than in the measurements of other investigators. Dimensionless velocity profiles provide an important means of quality control in transition measurements and Fig. 7 gives an indication of the appropriateness of the velocity profiles for a given quoted intermittency.

Dr. Johnson refers to his own work and to that of Acharya. While those results showed a strong variation of intermittency with traverse distance, this tendency is by no means universal. Reference is made, for example, to the work of Abu-Ghannam, which showed no variation of intermittency with traverse distance for values of U/U_0 up to 0.65 for a turbulent layer and 0.8 for a laminar layer.

The authors' results were part of a comprehensive investigation covering more severe adverse pressure gradients and higher turbulence levels than previous tests. The variation of intermittency with traverse distance was observed for turbulence levels of 0.3 and 5.3 percent and is plotted in Fig. 15. Traverses are presented for three different intermittency levels for each turbulence level. At the lower turbulence level of 0.3 percent the behavior tends toward that described by Dr. Johnson. It is appropriate in this case for intermittency to be measured relatively close to the wall, where the intermittency plateau associated with the turbulent spots predominates.

For higher turbulence levels, on the other hand, intermittency continues to rise with distance from the wall. The inlet turbulence level of 1.6 percent for the second series of published results is intermediate between the extremes of turbulence level chosen, resulting in a minimization of errors. The range of y/δ corresponding to $U/U_0 = 0.8$ in these tests was quite wide, varying between 0.1 and 0.6 (the corresponding range for the Acharya results was 0.12 to 0.5). The authors' preferred location when the objective is to take representative intermittency measurements at higher turbulence levels, rather than to focus on the local behavior of turbulent spots, therefore tends to be further out than that favored by Dr. Johnson. While intermittency will neither be as high as the values at the edge of the boundary layer, nor necessarily coincide with the plateau value that is attained under lower free-stream turbulence levels, this does tend to give a reasonable average across the boundary layer.

Stability of a Laminar Boundary Layer Flowing Along a Concave Surface

M. V. Finnis

A. Brown

School of Mechanical, Materials, and Civil Engineering, Royal Military College of Science, Shrivenham, Swindon, Wilts, SN6 8LA, United Kingdom

Görtler instability for incompressible laminar boundary-layer flows over constant curvature concave surfaces is considered. The full linearized disturbance equations are solved by the Galerkin method using Chebyshev polynomials to represent the disturbance functions. Stability curves relating Görtler number, wave number, and vortex amplification for a Blasius mean flow are presented. The effect of streamwise pressure variation is investigated using the Falkner–Skan boundary-layer solutions for the mean flow. The importance of including the normal velocity terms for these flows is shown by their effect on the stability curves. The streamwise velocity distribution in the boundary layer on a 3-m radius of curvature plate was investigated experimentally. The results are compared with the stability curves and predicted disturbance functions.

Introduction

A boundary layer on a concave surface is subject to an instability due to the presence of centrifugal forces. The instability results in a secondary flow in the form of counter-rotating vortices with axes parallel to the direction of the mean flow, as sketched in Fig. 1 (taken from Crane and Sabzvari, 1982). These vortices first predicted by Görtler are known to be a modulator of transition to turbulence. Interest in the vortex structure and its effects on transition is prompted partly by the generally poor performance of two-dimensional methods in predicting skin friction and heat transfer on turbine blade pressure surfaces (Brown and Martin, 1982). Görtler vortices have been observed in cascade flows (Han and Cox, 1983) and it has been suggested that their presence could account for the increased heat transfer experienced on blade pressure surfaces.

Many experimental and analytical efforts have been made in determining the form of the instability and the conditions under which it occurs. Since the work of Görtler (1940) there have been many attempts at modeling the instability. The different assumptions and simplifications made by authors have resulted in many different neutral stability curves. Until recently there was little or no agreement between the different neutral curves. Herbert (1976) reviewed the theoretical work to 1976. Figure 2 shows the neutral curves of a few authors. The analysis of Görtler (1940) was the simplest, neglecting all normal flow terms. He assumed the vortices to be confined to the boundary layer and time dependent and solved the resulting equations using Green's functions to transform the resulting eigenvalue problem to an integral equation. Smith (1953) made no assumptions as to the normal extent of the vortices and included some of the normal velocity terms. He assumed that the vortices grow in space rather then time (an assumption made in almost all subsequent analyses). Smith solved the resulting equations using the Galerkin method. It has been suggested by Chang and Sartory (1964) that the Galerkin method used by Smith (1953) may not provide sufficient accuracy for low wave numbers. Kahawita and Meroney (1977) used essentially the same equations as Smith (1953) (though their published equations are in error) and produced their neutral curve shown in Fig. 2. This curve is markedly different from almost all other neutral curves produced in having a limiting wave number for small or zero Görtler number. Their method of solution differed from that of Smith (1953) in that they used a differential equation solver with orthonormalization. Yeo et al. (1984) followed the analysis of Smith (1953) though they retained all the terms in the governing equations. They used the same solution method and obtained

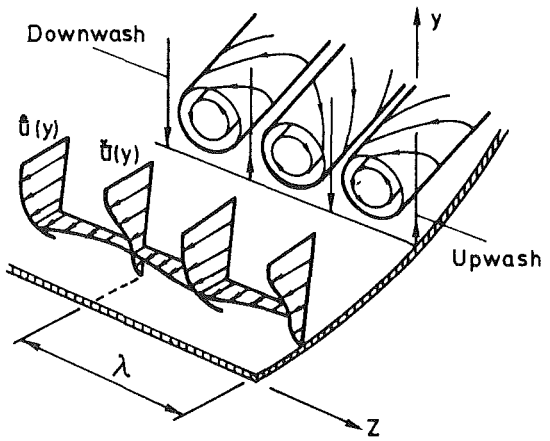

Fig. 1 Görtler vortices showing idealized velocity distribution

Contributed by the International Gas Turbine Institute and presented at the 33rd International Gas Turbine and Aeroengine Congress and Exhibition, Amsterdam, The Netherlands, June 5–9, 1988. Manuscript received by the International Gas Turbine Institute September 15, 1987. Paper No 88-GT-40.

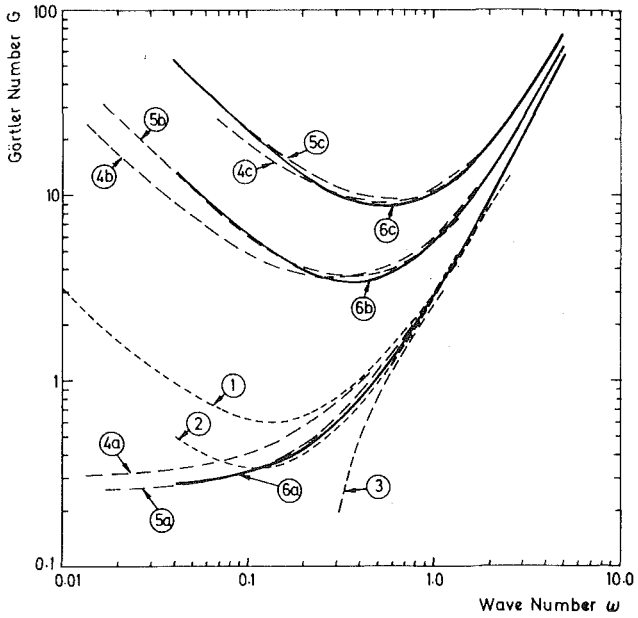

Fig. 2 Neutral curves from different models of Görtler instability: (1) Görtler (1940); (2) Smith (1953); (3) Kahawita and Meroney (1977); (4a-c) Herbert (1979); (5a) Floryan and Saric (1982); (5b, c) Floryan (1983); (6a-c) present authors

more or less the same neutral curve as Kahawita and Meroney (1977). However, the modeling of the mean flow was in error. This raises questions as to the accuracy of the neutral curve of Kahawita and Meroney (1977).

More recently Ragab and Neyfeh (1981) and Floryan and Saric (1982) have looked more closely at the inviscid streamline flow and produced neutral curves that agree. The method of solution used by both in integrating the governing equations was the superposition coupled with orthonormalization scheme developed by Scott and Watts (1977). Ragab and Neyfeh (1981) also looked at the effect of free-stream pressure gradient using the Falkner-Skan profiles and flow over a prescribed concave surface with variable curvature.

The above theoretical treatments all used the Blasius solution or an approximation to it for the mean flow. Other analyses using different mean flows or including heat transfer have been published. Kahawita and Meroney (1977) included the energy equation and investigated the effect of heating on the stability. Earlier DiPrima and Dunn (1956) had considered heating, neglecting viscous dissipation and density variation. With these restrictions they concluded that heating and cooling have only a slight influence on the neutral curve. Floryan and Saric (1983) have looked at the effects of suction, concluding that the flow is stabilized by suction. Floryan (1985) has also investigated the effects of blowing. El-Hady and Verma (1983) have formed the complete compressible equations, again using the method of Scott and Watts (1977) to solve the eigenvalue problem. Their paper considers the effect of Mach number on the neutral curve, as well as the effect on the disturbance velocities and growth rates.

There have also been many experimental investigations into the stability of flows on concave surfaces. Before Görtler's theoretical work, Clauser and Clauser (1937) had recognized that laminar flows on a concave surface become turbulent at lower Reynolds numbers than on flat or convex surfaces. Liepman (1943, 1945) in two publications investigated the stability and transition on concave surfaces. He suggested the Görtler number as a criterion for the onset of transition, though the critical values varied with free-stream turbulence intensity. Tani (1962) measured velocities in the boundary layers on two different concave surfaces mounted in separate wind tunnels. He measured spanwise variation in streamwise velocity, which revealed wavelengths that remained almost constant in the streamwise direction. Wortwann (1964) investigated the neutral curve by generating vortices of a specific wavelength on a 20-m radius of curvature surface in a water channel. Later Wortmann (1969) visualized a steady second-order instability prior to transition. McCormack et al. (1970) investigated vortices on a 5-in. radius of curvature plate and their effect on heat transfer. Their results showed a 100–150 percent increase in Nusselt number over that on a flat surface. There has been surprisingly little interest in following up this finding. Bippes (1972) visualized Görtler vortices in water using hydrogen bubbles. Naturally occurring vortices as well as artificially generated vortices were investigated and their effect on transition. Winoto and Crane (1980) used hydrogen bubble visualization and laser-Doppler anemometry in investigating naturally occurring vortices in water channels with 90 deg bends. Görtler numbers ranged from 4 to 15 and amplification was found to cease at a Görtler number of about 9 followed by increasing distortion of the vortex pattern. Crane and Sabzvari (1982) using laser-Doppler anemometry in water channels investigated the disturbance source concluding that the final screen in their settling chamber determined the vortex pattern observed on the concave surface. They also determined that the amplitude (κu_{max}) reached a value between 0.3 and 0.4 before the distortion of the vortex pattern. This review, by no

Nomenclature

a = constant in coordinate transformation
A = dimensionless wave number $= \alpha\delta$
B = dimensionless amplification rate $= \beta\delta$
C_p = pressure coefficient $= (p - p_\infty)/\frac{1}{2}\rho\bar{u}^2$
$C_r'(\eta')$, $C_r''(\eta')$ = functions of Chebyshev polynomials
D = shorthand for $\dfrac{\delta}{u_\infty}\dfrac{\partial(\hat{v}_0 u_\infty)}{\partial x}$
$f(\eta)$ = dimensionless stream function in the Blasius and Falkner-Skan equations
G = Görtler number $= \mathrm{Re}_\theta(\theta/r)^{1/2}$
H = shape parameter $= \delta^*/\theta$
K = dimensionless curvature $= \delta/r$
p = dimensional pressure
p_1 = dimensional disturbance pressure component with x and z dependence separated out
p' = dimensional disturbance pressure
$\hat{p}_1$ = dimensionless pressure, normalized with respect to free-stream dynamic pressure
p_∞ = atmospheric pressure
r = radius of curvature
Re = Reynolds number based on δ
Re_θ = Reynolds number based on θ
$R(\eta')$ = equation residual
$T_r(\eta')$ = Chebyshev polynomial of order r defined on $[-1, 1]$
u, v, w = dimensional velocity components
$\hat{u}_1'$, $\hat{v}_1'$, $\hat{w}_1'$ = transformed dimensionless velocity components

means complete, illustrates the range of publications on the stability of flows on a concave surface.

Theoretical Analysis

The stability of a laminar boundary layer on a concave surface of constant curvature is considered with respect to three-dimensional disturbances in the form of counterrotating streamwise vortices known as Görtler vortices. The flow is assumed steady and incompressible and is expressed as a mean flow with the disturbances superimposed. Thus

$$\left.\begin{aligned} u &= u_0(x, y) + u'(x, y, z) \\ v &= v_0(x, y) + v'(x, y, z) \\ w &= \qquad\quad w'(x, y, z) \\ p &= p_0(x, y) + p'(x, y, z) \end{aligned}\right\} \tag{1}$$

where the zero subscript refers to the mean flow; the disturbance terms are primed. The spanwise (z) dependence is separated out by assuming a periodic spanwise variation. The streamwise (x) dependence is also separated out by introducing a growth term, the analysis having a local significance. Thus the disturbed flow is assumed to be described by

$$\left.\begin{aligned} u &= u_0(x, y) + u_1(y) \cdot \cos\,\alpha z \cdot e^{\beta x} \\ v &= v_0(x, y) + v_1(y) \cdot \cos\,\alpha z \cdot e^{\beta x} \\ w &= \qquad\quad w_1(y) \cdot \sin\,\alpha z \cdot e^{\beta x} \\ p &= p_0(x, y) + p_1(y) \cdot \cos\,\alpha z \cdot e^{\beta x} \end{aligned}\right\} \tag{2}$$

Following Smith (1953) the momentum and continuity equations are transformed to a body orientated, orthogonal curvilinear coordinate system and equations (2) substituted into the resulting equations. Neglecting products of the disturbance velocities, extracting the mean flow terms that independently satisfy the momentum and continuity equations, and normalizing with the following substitutions:

$$\left.\begin{aligned} u_0 &= \hat{u}_0 u_\infty & v_0 &= \hat{v}_0 u_\infty & & \\ u_1 &= \hat{u}_1 u_\infty & v_1 &= \hat{v}_1 u_\infty & w_1 &= \hat{w}_1 v_\infty \\ y &= \eta\delta & p_1 &= \hat{p}_1 \tfrac{1}{2}\rho u_\infty^2 & \mathrm{Re} &= u_\infty \delta/\nu \\ \alpha &= A/\delta & \beta &= B/\delta & K &= \delta/r \end{aligned}\right\} \tag{3}$$

where δ is a boundary layer reference length and r the radius of curvature, gives

$$\frac{B\hat{u}_1}{(1+K\eta)} + \frac{d\hat{v}_1}{d\eta} + A\hat{w}_1 + \frac{K\hat{v}_1}{(1+K\eta)} = 0 \tag{4}$$

$$\begin{aligned} &\frac{d^2\hat{u}_1}{d\eta^2} + \left\{\frac{K}{(1+K\eta)} - \hat{v}_0\mathrm{Re}\right\}\frac{d\hat{u}_1}{d\eta} \\ &\quad + \left\{\frac{B^2}{(1+K\eta)^2} - A^2 - \frac{K^2}{(1+K\eta)^2} - \frac{B\mathrm{Re}\hat{u}_0}{(1+K\eta)} + \mathrm{Re}\,\frac{\partial\hat{v}_0}{\partial\eta}\right\}\hat{u}_1 \\ &\quad + \left\{\frac{2KB}{(1+K\eta)^2} - \frac{K\hat{u}_0\mathrm{Re}}{(1+K\eta)} - \frac{\partial\hat{u}_0}{\partial\eta}R\right\}\hat{v}_1 \\ &\quad - \frac{B\mathrm{Re}}{2(1+K\eta)}\hat{p}_1 = 0 \end{aligned} \tag{5}$$

$$\begin{aligned} &\frac{d^2\hat{v}_1}{d\eta^2} + \left\{\frac{K}{(1+K\eta)} - \hat{v}_0 R\right\}\frac{d\hat{v}_1}{d\eta} \\ &\quad + \left\{\frac{B^2}{(1+K\eta)^2} - A^2 - \frac{K^2}{(1+K\eta)^2} - \frac{B\mathrm{Re}\hat{u}_0}{(1+K\eta)} - \mathrm{Re}\,\frac{\partial\hat{v}_0}{\partial\eta}\right\}\hat{v}_1 \\ &\quad + \left\{-\frac{2KB}{(1+K\eta)^2} - \frac{D\mathrm{Re}}{(1+K\eta)} + \frac{2K\hat{u}_0\mathrm{Re}}{(1+K\eta)}\right\}\hat{u}_1 \\ &\quad - \frac{\mathrm{Re}}{2}\frac{d\hat{p}_1}{d\eta} = 0 \end{aligned} \tag{6}$$

$$\begin{aligned} &\frac{d^2\hat{w}_1}{d\eta^2} + \left\{\frac{K}{(1+K\eta)} - \hat{v}_0\mathrm{Re}\right\}\frac{d\hat{w}_1}{d\eta} \\ &\quad + \left\{\frac{B^2}{(1+K\eta)^2} - A^2 - \frac{B\mathrm{Re}\hat{u}_0}{(1+K\eta)}\right\}\hat{w}_1 \\ &\quad + \frac{A\mathrm{Re}2\hat{p}_1}{2} = 0 \end{aligned} \tag{7}$$

where

$$D = \frac{\delta}{u_\infty}\frac{\partial(\hat{v}_0 u_\infty)}{\partial x}.$$

The boundary conditions are obtained from no slip and no penetration at the wall and the decay of the disturbances away from the wall. The continuity equation (4) also provides a further boundary condition giving

Nomenclature (cont.)

u_0, v_0 = dimensional mean flow velocities
$\hat{u}_0$, $\hat{v}_0$, $\hat{u}_1$, $\hat{v}_1$, $\hat{w}_1$ = dimensionless velocity components, normalized with respect to free-stream velocity $u_\infty(x)$
u_1, v_1, w_1 = dimensional disturbance velocity components with x and z dependence separated out
u', v', w' = dimensional disturbance velocity components
u_∞ = free-stream velocity
u_{up}, u_{down} = dimensional streamwise velocities at upwash and downwash
x, y, z = streamwise, normal, and spanwise coordinates
α = dimensional wave number $= 2\pi/\lambda$
β = dimensional amplification rate
β_0, m, A = constants in Falkner-Skan free-stream velocity
δ = boundary layer reference length or boundary layer thickness depending on context
δ^* = displacement thickness
δ_{av} = boundary layer thickness of average profile (99 percent)
η = dimensionless coordinate normal to surface $= y/\delta$
η' = transformed dimensionless coordinate normal to surface $= 1 - 2e^{-a\eta}$
θ = momentum thickness
$\kappa u(\eta)$ = vortex amplitude $= (u_{down} - u_{up})/2u_\infty$
λ = dimensional wavelength
ν = kinematic viscosity
ρ = density
ω = dimensionless wave number $= \alpha\theta$

$$\left.\begin{aligned} &\hat{u}_1 = \hat{v}_1 = \hat{w}_1 = d\hat{v}_1/d\eta = 0 \quad \text{at} \quad \eta = 0 \\ &\hat{u}_1 = \hat{v}_1 = \hat{w}_1 = \hat{p}_1 \to 0 \qquad \text{as} \quad \eta \to \infty \end{aligned}\right\} \tag{8}$$

The above system of equations forms an eigenvalue problem for the parameters (A, B, K) for a given mean flow and Re.

Computational Procedure. Equations (4) to (8) are solved using the Galerkin method. The equations are first transformed to the range $[-1, 1]$ using the transformation $\eta' = 1 - 2e^{-a\eta}$, where a is an arbitrary constant analogous to the "decay factor" of Smith (1953). It is assumed that the transformed disturbance functions can be approximated by finite Chebyshev series. Thus

$$\left.\begin{aligned} \hat{u}_1' &= \sum_{r=0}^{n}{}' a_r T_r(\eta') \\ \hat{v}_1' &= \sum_{r=0}^{n}{}' b_r T_r(\eta') \\ \hat{w}_1' &= \sum_{r=0}^{n}{}' c_r T_r(\eta') \\ \hat{p}_1' &= \sum_{r=0}^{n}{}' d_r T_r(\eta') \end{aligned}\right\} \tag{9}$$

The differentials of the transformed disturbance functions can be written in terms of the coefficients a_r, b_r, c_r, and d_r, for example

$$\left.\begin{aligned} \frac{d\hat{u}_1'}{d\eta'} &= \sum_{r=1}^{n} a_r C_r'(\eta') \\ \frac{d^2\hat{u}_1'}{d\eta'^2} &= \sum_{r=2}^{n} a_r C_r''(\eta') \end{aligned}\right\} \tag{10}$$

where $C_r'(\eta')$ and $C_r''(\eta')$ are functions of Chebyshev polynomials. The coefficients a_r, b_r, c_r, and d_r are obtained using Galerkin conditions and applying the boundary conditions of equation (8) at $\eta' = -1$ and $\eta' = 1$.

To solve equations (4) to (7) inclusive for A or B as the eigenvalue it is necessary to multiply through by $(1+K\eta)^2$ and solve the resulting quadratic eigenvalue problem. To solve for K as the eigenvalue it is necessary to expand terms like $(1+K\eta)^{-n} = 1 - nK\eta + n(n+1)/2\ K^2\eta^2 + O(K^3)$ neglecting terms $O(K^3)$ or neglecting terms $O(K^2)$ and solve the resulting quadratic or linear eigenvalue problem.

To illustrate the solution procedure the linear eigenvalue problem in K is solved (essentially the same problem solved by Smith, 1953, and Kahawita and Meroney, 1977). Substituting $(1+K\eta)^{-n} = 1 - nK\eta$ into equations (4) to (7) and collecting terms gives

$$B\hat{u}_1 + \frac{d\hat{v}_1}{d\eta} + A\hat{w}_1 + K\{(-B\eta)\hat{u}_1 + \hat{v}_1\} = 0 \tag{11}$$

$$\left(B^2 - A^2 - \mathrm{Re}B\hat{u}_0 + \mathrm{Re}\frac{\partial \hat{v}_0}{\partial \eta}\right)\hat{u}_1 + (-\mathrm{Re}\hat{v}_0)\frac{d\hat{u}_1}{d\eta} + \frac{d^2\hat{u}_1}{d\eta^2} + \left(-\mathrm{Re}\frac{\partial \hat{u}_0}{\partial \eta}\right)\hat{v}_1 + \left(\frac{-\mathrm{Re}B}{2}\right)\hat{p}_1 + K\left\{(\mathrm{Re}B\hat{u}_0\eta - 2B^2\eta)\hat{u}_1 + \frac{d\hat{u}_1}{d\eta} + (2B - \mathrm{Re}\hat{u}_0)\hat{v}_1 + \frac{\mathrm{Re}B\eta}{2}\hat{p}_1\right\} = 0 \tag{12}$$

$$(-\mathrm{Re}D)\hat{u}_1 + \left(B^2 - A^2 - \mathrm{Re}B\hat{u}_0 - \mathrm{Re}\frac{\partial \hat{v}_0}{\partial \eta}\right)\hat{v}_1 + (-\mathrm{Re}\hat{v}_0)\frac{d\hat{v}_1}{d\eta} + \frac{d^2\hat{v}_1}{d\eta^2} + \left(\frac{-\mathrm{Re}}{2}\right)\frac{d\hat{p}_1}{d\eta} + K\left\{(2\hat{u}_0\mathrm{Re} - 2B + \mathrm{Re}D\eta)\hat{u}_1 + (\mathrm{Re}B\hat{u}_0\eta - 2B^2\eta)\hat{v}_1 + \frac{d\hat{v}_1}{d\eta}\right\} = 0 \tag{13}$$

$$(B^2 - A^2 - \mathrm{Re}B\hat{u}_0)\hat{w}_1 + (-\mathrm{Re}\hat{v}_0)\frac{d\hat{w}_1}{d\eta} + \frac{d^2\hat{w}_1}{d\eta^2} + \frac{A\mathrm{Re}}{2}\hat{p}_1 + K\left\{(\mathrm{Re}B\hat{u}_0\eta - 2B^2\eta)\hat{w}_1 + \frac{d\hat{w}_1}{d\eta}\right\} = 0 \tag{14}$$

Making the transformation to η' and substituting equations (9) and equations such as equations (10) gives

$$\left[\left\{\sum_{i=1}^{4n+4}\Phi_{c_i}(\eta')\right\} + K\left\{\sum_{i=1}^{4n+4}X_{c_i}(\eta')\right\}\right]\begin{bmatrix} a_0 & \cdots & a_n \\ b_0 & \cdots & b_n \\ c_0 & \cdots & c_n \\ d_0 & \cdots & d_n \end{bmatrix} = R_c(\eta') \tag{15}$$

$$\left[\left\{\sum_{i=1}^{4n+4}\Phi_{x_i}(\eta')\right\} + K\left\{\sum_{i=1}^{4n+4}X_{x_i}(\eta')\right\}\right]\begin{bmatrix} a_0 & \cdots & a_n \\ b_0 & \cdots & b_n \\ c_0 & \cdots & c_n \\ d_0 & \cdots & d_n \end{bmatrix} = R_x(\eta') \tag{16}$$

$$\left[\left\{\sum_{i=1}^{4n+4}\Phi_{y_i}(\eta')\right\} + K\left\{\sum_{i=1}^{4n+4}X_{y_i}(\eta')\right\}\right]\begin{bmatrix} a_0 & \cdots & a_n \\ b_0 & \cdots & b_n \\ c_0 & \cdots & c_n \\ d_0 & \cdots & d_n \end{bmatrix} = R_y(\eta') \tag{17}$$

$$\left[\left\{\sum_{i=1}^{4n+4}\Phi_{z_i}(\eta')\right\} + K\left\{\sum_{i=1}^{4n+4}X_{z_i}(\eta')\right\}\right]\begin{bmatrix} a_0 & \cdots & a_n \\ b_0 & \cdots & b_n \\ c_0 & \cdots & c_n \\ d_0 & \cdots & d_n \end{bmatrix} = R_z(\eta') \tag{18}$$

where the $\Phi(\eta')$ and $X(\eta')$ are functions of the mean flow, A, B, Re, and a, the right-hand sides being the residues due to the series approximation to the disturbance functions. Using $4n-4$ Galerkin conditions and the eight boundary conditions (equations (8)) gives

Table 1 Variation of Görtler number G with decay factor a; $Re_\theta = 1E5$, 19th-order polynomial, 32 integration points

ω	$\beta\theta Re_\theta$	G_{min}	G_{max}	% error in mean
0.04	0.0	0.2697	0.2804	± 1.9
0.04	0.5	5.6671	5.6845	± 0.2
0.04	5.0	40.9688	41.1074	± 0.2
0.06	0.0	0.2874	0.2904	± 0.5
0.1	0.0	0.3219	0.3222	± 0.05
1.0	0.0	2.8713	2.8713	-

$$\left.\begin{aligned} &\{[F]+K[G]\}\underline{C}=[0] \\ &\underline{C}=(a_0 \ldots a_n, b_0 \ldots b_n, c_0 \ldots c_n, d_0 \ldots d_n)^T \end{aligned}\right\} \quad (19)$$

an eigenvalue problem with K as the eigenvalue and the coefficients of the disturbance functions series as the eigenfunction. Equation (19) is solved using the implementation of the QZ algorithm in the NAG library.

Zero Pressure Gradient. The mean flow terms required to solve equations (4) to (8) are

$$\hat{u}_0(\eta), \quad \frac{\partial \hat{u}_0}{\partial \eta}, \quad \hat{v}_0(\eta), \quad \frac{\partial \hat{v}_0}{\partial \eta}, \quad D=\frac{\delta}{u_\infty}\frac{\partial(\hat{v}_0 u_\infty)}{\partial x}$$

(Note: all normal flow terms, those containing $\hat{v}_0$ and its derivatives, are retained in the governing equations.) The stability of any mean flow for which the above terms can be provided can be established by using equations (4) to (8). It can be shown that for zero free-stream pressure gradient, provided the radius of curvature $r>>\delta$, the flat plate Blasius mean flow is appropriate (Herbert, 1976). The solution of the Blasius equation

$$\left.\begin{aligned} &f\cdot f''+2f'''=0 \\ &f=f'=0 \text{ at } \eta=0 \quad f'\to\eta \text{ as } \to\infty \end{aligned}\right\} \quad (20)$$

where $\hat{u}_0(\eta)=f'(\eta)$, was obtained using a fourth-order Runge–Kutta integration coupled with a shooting method with a step size in η of 0.025. The normal flow terms were obtained by integration of the stream function.

The integrations required for the Galerkin conditions were performed using 32-point Gaussian integration. This was required for convergence on the eigenvalue in the low wave number/low Görtler number regime (there was no improvement in convergence on increasing the number of integration points). The choice of the arbitrary constant a in the coordinate transformation was found to affect the eigenvalue obtained in solving the equations particularly for low Görtler numbers and wave numbers. The effect was reduced by increasing the order of polynomial used. In general 19th-order Chebyshev polynomials were used, again to improve convergence on the eigenvalue in the low wave number/low Görtler number regime and for convergence on nonoscillating eigenfunctions in the high wave number/high Görtler number regime. Table 1 shows the variation in Görtler number with decay factor. For most of the results presented in this paper the value of a used was chosen to put the edge of the boundary layer in the center of the transformed range giving an equal number of integration points inside and outside the boundary layer.

The range of wave numbers investigated was limited to 0.04 to 5. Wave numbers below 0.04 were considered as being of little practical importance and as can be seen from Table 1 the solution for the neutral curve increasingly deteriorates for low wave numbers. This deterioration is due in part to the orthogonal transformation used. The streamline curvature does not decay in the free stream, there being a singularity at the center of curvature. This is of little consequence for disturbances confined close to the wall though the solution for disturbances extending far into the free stream becomes unstable.

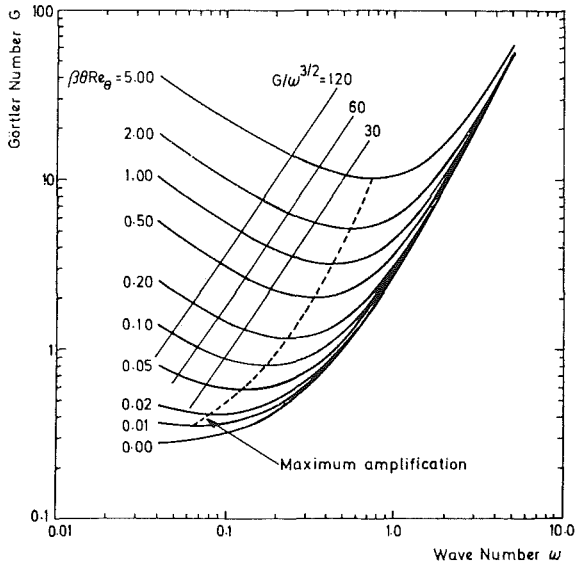

Fig. 3 Curves of constant $\beta\theta Re_\theta$ for Blasius mean flow

Figure 2 shows the neutral stability curves for the first three eigenvalues compared with some previous authors. Herbert (1979) has shown that the higher order neutral curves may be important in describing the onset of higher modes of Görtler instability. By phase shifting and combining the disturbance velocities for the first and second-order eigenvalues Herbert modeled the second-order instability described by Wortmann (1969). The first-order neutral curve of Floryan and Saric (1982) is essentially the same as those of Ragab and Neyfeh (1981) for zero pressure gradient and El-Hady and Verma (1983) for zero Mach number as they all have a similar analysis and use the same solution technique for integrating the governing equations, the superposition coupled with orthonormalization scheme developed by Scott and Watts (1977).

The neutral curves are in good agreement with those of the more recent authors, who have included all the normal terms in their analyses. The stability chart for the first-order eigenvalue is shown in Fig. 3 together with the curve of maximum amplification and lines of constant wavelength. The chart is calculated for large Re_θ (1.0×10^5), which implies large r/small K, though as the Blasius flow is a similar solution of the boundary layer equations the chart is valid for moderate to infinite Re_θ. The neutral curve shows negligible difference for Re_θ as low as 50 at a wave number $\omega=0.16$. Thus for given mean flow conditions—free-stream velocity u_∞ and kinematic viscosity ν—and radius of curvature, the Görtler number G represents streamwise position ($G\propto x^{3/4}$).

Nonzero Pressure Gradient. For the case of nonzero streamwise pressure gradient the Falkner–Skan flows were used. The free-stream velocity is given by

$$u_\infty(x)=Ax^m \quad (21)$$

where A and m are constants. An often-quoted pressure gradient factor β_0 is related to m by

$$\beta_0=2m/(m+1) \quad (22)$$

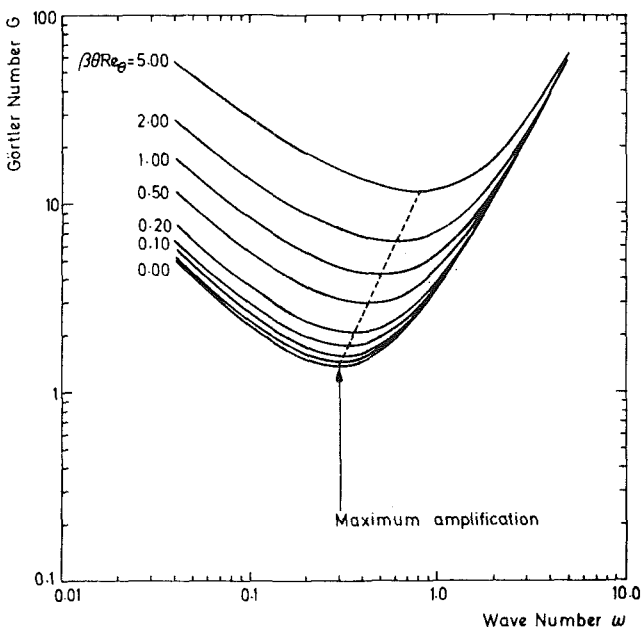

Fig. 4 Curves of constant $\beta\theta Re_\theta$ for Falkner-Skan mean flow; $m = 4$

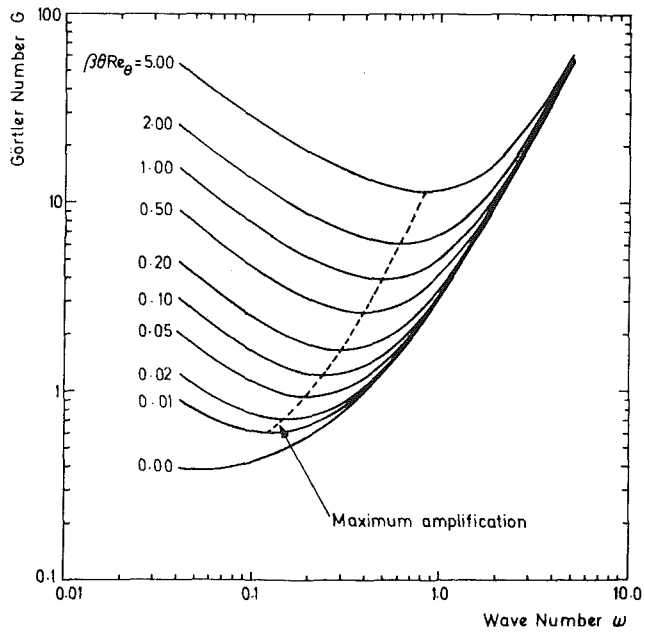

Fig. 6 Curves of constant $\beta\theta Re_\theta$ for Falkner-Skan mean flow; $m = 4$; normal flow terms ignored

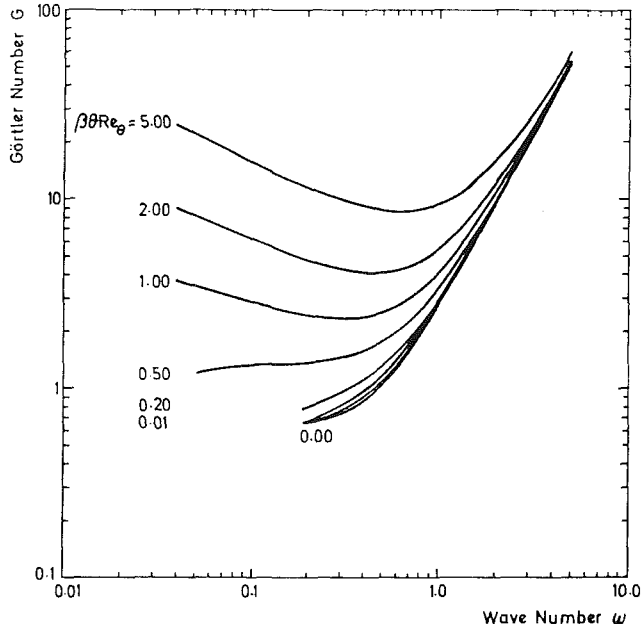

Fig. 5 Curves of constant $\beta\theta Re_\theta$ for Falkner-Skan mean flow; $m = -0.09$

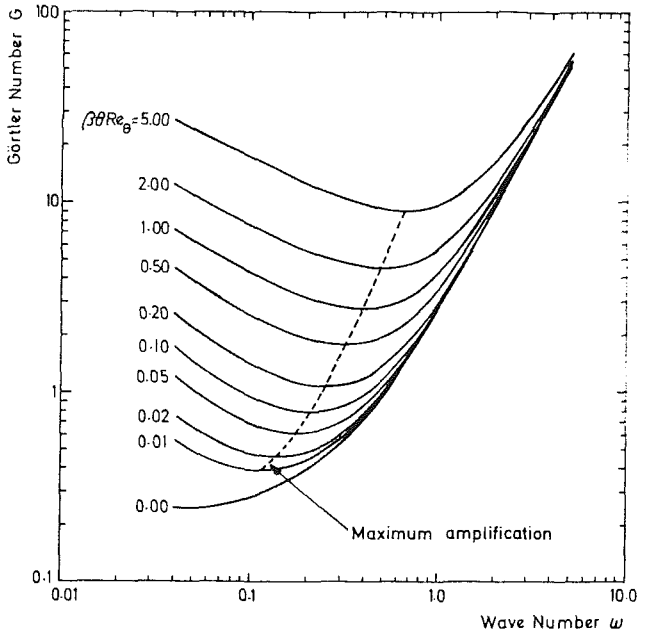

Fig. 7 Curves of constant $\beta\theta Re_\theta$ for Falkner-Skan mean flow; $m = -0.09$; normal flow terms ignored

The solution of the Falkner-Skan equation

$$\left.\begin{aligned} &f''' + f \cdot f'' + \beta_0(1 - f'^2) = 0 \\ &f = f' = 0 \text{ at } \eta = 0 \qquad f' \to 1 \text{ as } \eta \to \infty \end{aligned}\right\} \quad (23)$$

where $\hat{u}_0(\eta) = f'(\eta)$ was obtained in the same manner as for the Blasius flow though for a step size in η of 0.01. The free-stream velocity is that of potential flow near the stagnation point of a wedge of included angle $\beta_0 \pi$ radians. As such the Falkner-Skan flows do not represent real flows. Two velocity profiles were used to assess the effect of pressure gradient on Görtler stability: a profile given by $m = 4$ representing a considerable favorable gradient and the separation profile, given by $m = -0.09$, representing an adverse gradient. Figures 4 and 5 show the stability charts for these profiles. Again, as the Falkner-Skan flows give similar solutions to the boundary layer equations the charts are valid for a wide range of Re_θ. Figure 4, corresponding to $m = 4$, shows a marked increase in stability. The neutral curve has shifted upward, the curves of constant $\beta\theta Re_\theta$ becoming compressed, and a minimum occurs at $\omega = 0.28$, $G = 1.38$. Figure 5, corresponding to the separation profile, shows the curves of constant $\beta\theta Re_\theta$ spread out. The trend is apparent although the stability of the solution has deteriorated at low values of wave number and $\beta\theta Re_\theta$. Curves of lower $\beta\theta Re_\theta$ and the neutral curve appear to have a limiting wave number signifying Görtler instabilty at zero Görtler number, thus indicating a marked decrease in the boundary layer stability. The trends described agree with the work of

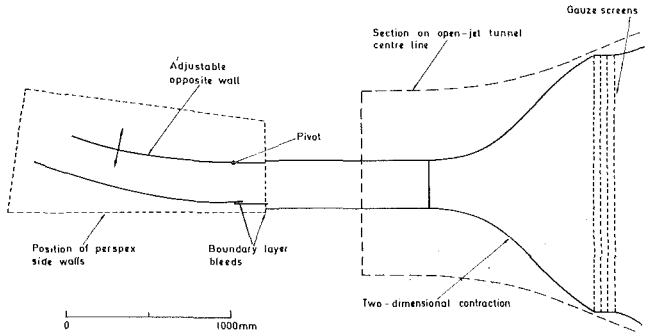

Fig. 8 Scheme of experimental rig

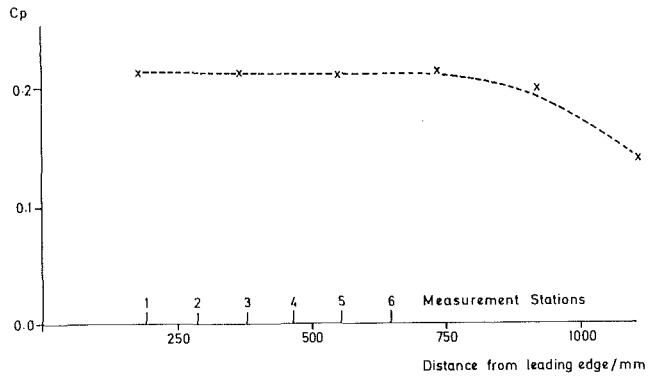

Fig. 9 Streamwise variation of pressure coefficient

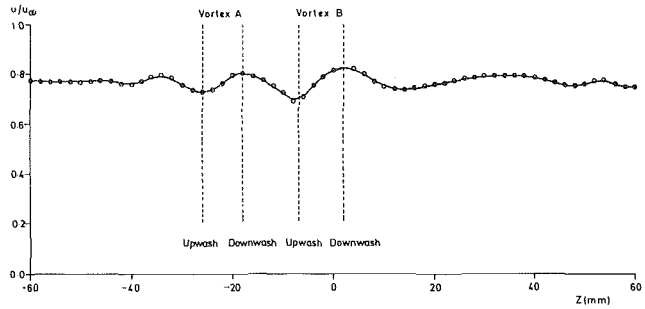

Fig. 10 Spanwise variation of streamwise velocity component within the boundary layer; vortex *B* at sixth location

Ragab and Neyfeh (1981), who calculated the neutral stability curves for a number of Falkner–Skan flows.

Figures 6 and 7 show the stability charts for the above profiles with the normal velocity terms omitted in the governing equations. As can be seen the differences between the stability curves with and without the inclusion of the normal velocity terms are great. The curves of Figs. 6 and 7 are essentially the same exhibiting none of the characteristics of Figs. 4 and 5. This illustrates the importance of the inclusion of the normal velocity terms in the governing equations.

The Falkner–Skan flows should be used with care in estimating the stability of real flows. The use of the Falkner–Skan mean flow is in general an approximation. By fitting a Falkner–Skan profile to an actual profile an estimate of the stability at a single streamwise position may be obtained, although this amounts to neglecting the history of the boundary layer up to the position under consideration and ignoring the change in pressure gradient. Also, the growth rate of the boundary layer will be in error. This will affect the normal velocity terms, which, as shown, will distort the stability curves. Thus for a stability analysis of a general streamwise velocity variation the mean flow must be calculated up to the point under consideration. Stability curves produced in this way will, in general, be valid at a single streamwise position.

Experimental Rig and Experimentation

The concave surface of radius of curvature 3 m and length 1.3 m formed one wall of a channel of width 0.8 m and depth 0.3 m. The upstream boundary layer was bled passively at the start of curvature at a splitter leading edge. The channel itself was mounted in the working section of an open jet wind tunnel. It was found that naturally occurring amplifying vortices could only be obtained for free-stream turbulence intensity below about 0.3 percent. This was obtained by placing a two-dimensional contraction and four gauze screens (32 mpi, 63 percent open area) in the settling chamber of the open jet wind tunnel. Figure 8 shows the layout of the rig. The opposite wall of the channel could be adjusted (albeit crudely) to give nearly zero pressure gradient over the streamwise region of interest. Static pressure tappings on the concave surface and a pitot tube that could be traversed within the flow were used to determine the flow structure. The pitot tube was rectangular in section with external dimensions 2.79 mm by 0.82 mm and a hole area of 9.69×10^{-5} mm^2. A pitot-static tube, used for setting the free-stream velocity, was mounted 175 mm from one of the side walls and 850 mm from the leading edge on the channel center line (no correction for streamline curvature was made).

The inability to achieve a detectable vortex structure easily must raise some doubts over the extent to which laboratory-generated Görtler vortices are relevant to real flows. However, no difficulties of this nature have been reported by previous authors who have obtained naturally developing Görtler vortex flows in free streams of turbulence intensity ranging from 0.025 percent (Dagenhart and Mangalam, 1986) to 7.2 percent (Shigemi et al., 1987). Kottke (1986) has demonstrated that a vortex structure can be prevented from forming by varying the size and position of turbulence generating grids.

Pitot-tube measurements were made at six streamwise locations between 192 mm and 645 mm from the leading edge of the curved surface for a nominal free-stream velocity of 5 m/s. The existence of a vortex structure was established by making total-pressure measurements across the span within the boundary layer and observing the variation with spanwise position. All pressure readings were obtained by averaging 3000 readings taken at approximately 38 readings per second. The experimental rig was required to be dismantled between test programs to allow other users of the wind tunnel access. It was found that a different vortex structure was apparent for each set of tests run. This, it was presumed, was due to the "edge effects" of the rig, for example the positioning of the wire gauzes, being slightly altered each time the rig was assembled. It should be noted, however, that day-to-day repeatability for a given configuration was excellent.

Figure 9 shows the streamwise variation of pressure coefficient $Cp = (p - p_\infty)/\frac{1}{2}\rho\bar{u}^2$ where p is local static pressure, p_∞ is atmospheric pressure, ρ is local density, and $\bar{u}$ is the nominal free-stream velocity. Figure 10 shows the spanwise variation of streamwise velocity component within the boundary layer at the sixth location ($x = 645$ mm). This variation was observable at all six locations developing progressively from the first to the sixth. Two vortices, denoted A and B, were chosen to be studied. Figure 11 shows the shear-corrected boundary layer profiles at the upwash and downwash locations associated with vortex B at the sixth location. Also shown is the mean profile—obtained by averaging the upwash and downwash profiles—compared with the Blasius profile. For the two vortices the mean profile shape factor $H = \delta^*/\theta$ for the six streamwise locations ranged between 2.48 and 2.57 compared with a value for the Blasius profile of 2.59. Figure 12 shows the streamwise variation of Re_θ for the two vortices compared with the Blasius values. In view of the good agree-

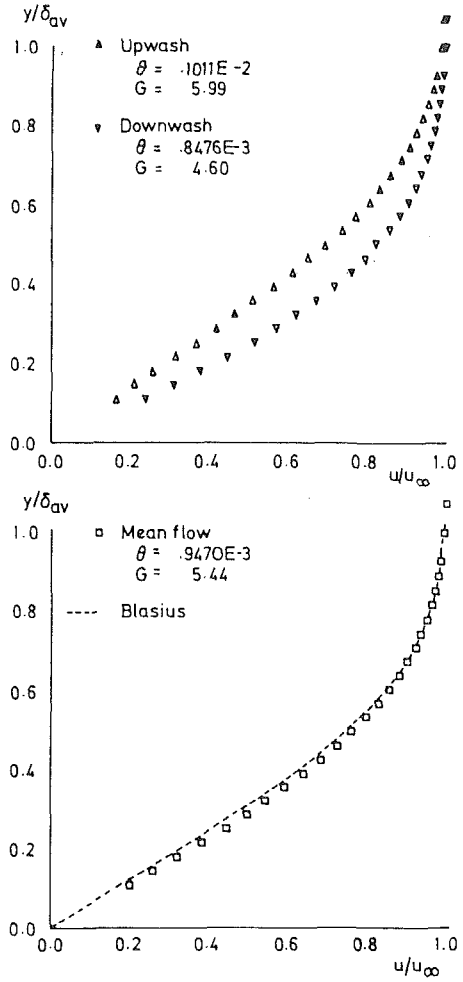

Fig. 11 Boundary layer velocity profiles; vortex *B* at sixth location

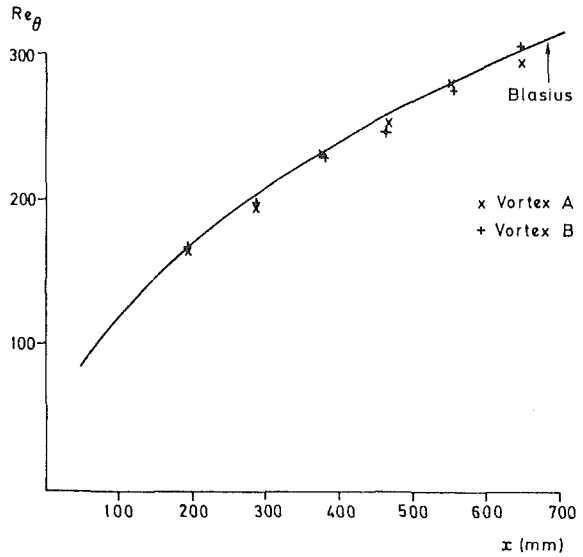

Fig. 12 Streamwise variation of Re_θ

ment between the measured mean flow boundary layer parameters and the Blasius values, the Blasius mean flow was used in the comparison between the experimental results and theoretical prediction.

From the spanwise variation of streamwise velocity shown in Fig. 10, a representative wavelength for each vortex can be estimated and from the measured values of θ and Re_θ a Görtler number obtained. This information fixes a position on the stability chart. Figure 13 shows the experimental points for vortices *A* and *B* at the six locations on the theoretical stability chart. The points fall in the unstable region as expected and are clustered around a line of constant wavelength, indicating that the wavelength is conserved in the streamline direction.

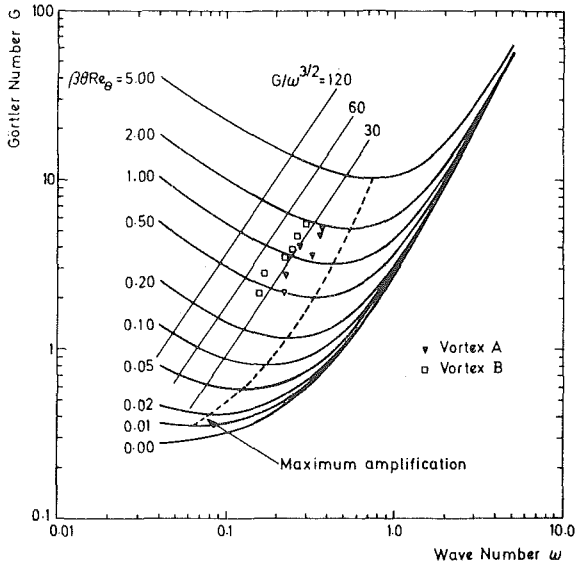

Fig. 13 Comparison of experimental points with theoretical prediction

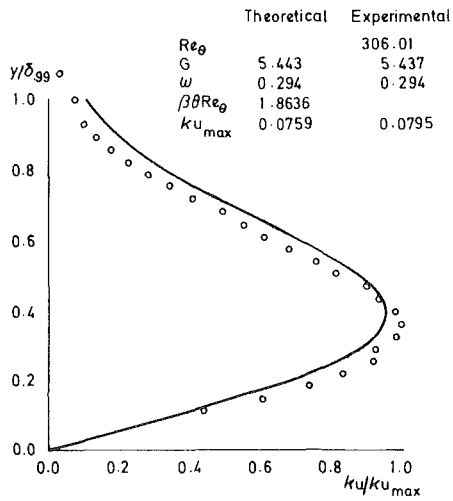

Fig. 14 Experimental and predicted κu curves; vortex *B* at sixth location

As a measure of the growth of the vortices a parameter κu can be defiend as

$$\kappa u(\eta) = (u_{\text{down}}(\eta) - u_{\text{up}}(\eta))/2u_\infty \tag{24}$$

where u_{up} is the velocity at upwash and u_{down} the velocity at downwash. Figure 14 shows the experimental κu profile for vortex *B* at the sixth location compared with the predicted theoretical profile.

The theoretical profile was obtained by solving equations (4) to (8) for the values of Görtler number and wave number determined for the experimental point. As the theoretical profile is derived from an eigenfunction its absolute magnitude cannot be predicted. The scaling of the theoretical profile in Fig. 14 is obtained by "fitting" to the experimental data.

Substituting from equation (2) into equation (13) we have

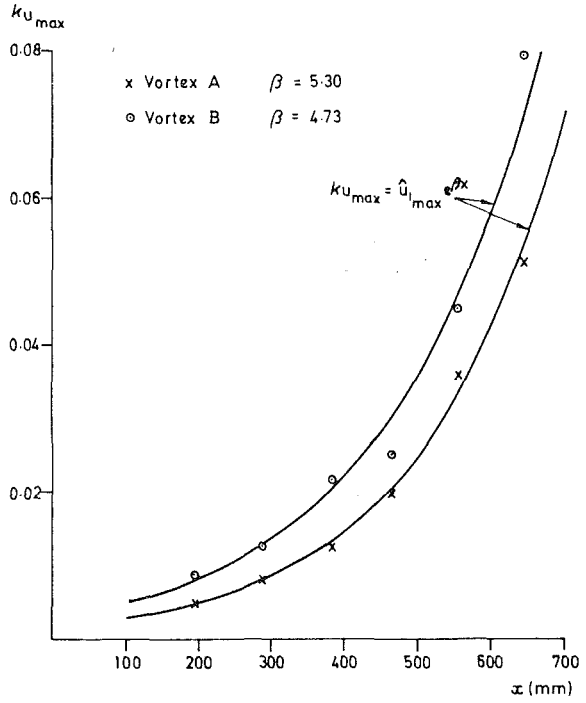

Fig. 15 Streamwise variation of κu_{max}

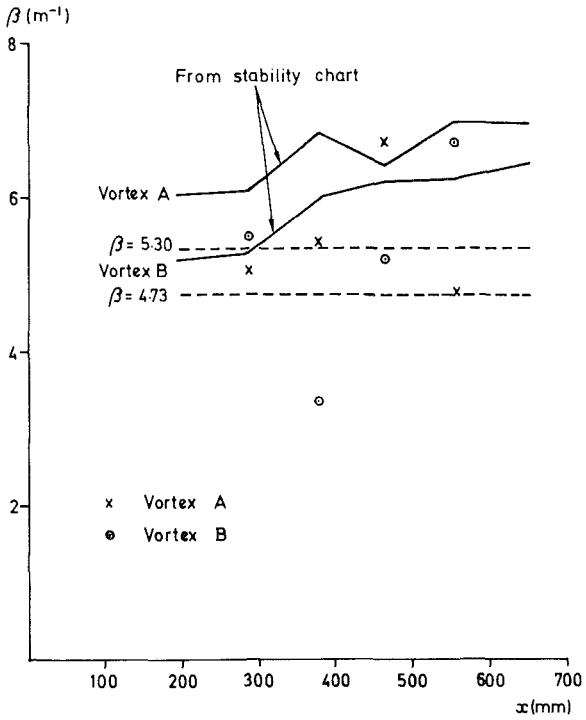

Fig. 16 Streamwise variation of β

$$\kappa u = \{(u_0 + u_1 e^{\beta x}) - (u_0 - u_1 e^{\beta x})\}/2u_\infty$$
$$= \hat{u}_1 e^{\beta x} \tag{25}$$

For each pair of upwash and downwash profiles there will be a maximum value of κu, denoted κu_{max}, corresponding to the maximum value of $\hat{u}_1(\eta)$, which represents the amplitude of the vortex. Assuming that the change in $\hat{u}_1(\eta)$ with x is small over the region of interest, then equation (26) can be written for κu_{max}, thus

$$\kappa u_{max}(x) = \hat{u}_{1_{max}} e^{\beta x} \tag{26}$$

By fitting a curve of the form of equation (26) to the experimental values of κu_{max} a value of β for a vortex can be obtained. Figure 15 shows the variation of κu_{max} with x for the two vortices and the fitted curves giving values of β.

There are two alternative methods of obtaining values of β for the vortices. Firstly, on differentiating equation (26) with respect to x we have

$$\frac{d(\kappa u_{max})}{dx} = \hat{u}_{1_{max}} \beta e^{\beta x} = \beta \kappa u_{max}$$

Thus

$$\beta = \frac{1}{\kappa u_{max}} \frac{d(\kappa u_{max})}{dx} \tag{27}$$

Again, the assumption is that variations in $\hat{u}_{1_{max}}$ and β with x are small over the range of interest. Using the experimental values we have for equally spaced x

$$\beta_i \simeq \frac{1}{\kappa u_{max_i}} \frac{(\kappa u_{max_{i+1}} - \kappa u_{max_{i-1}})}{(x_{i+1} - x_{i-1})} \tag{28}$$

Secondly, values of $\beta\theta \mathrm{Re}_\theta$ can be obtained from the position of the experimental points on the stability chart and local values of β extracted by dividing by $\theta \mathrm{Re}_\theta$. Figure 16 shows the values of β obtained by the three methods for the two vortices A and B.

Discussion

The theoretical analysis makes no prediction for vortex wavelength or amplitude. Indeed, it makes no prediction for the existence of vortices at all, only that if vortices of a given wavelength occur for a given mean flow then their growth or damping may be predicted. The theoretical analysis considers an infinite number of counterrotating vortex pairs of equal strength and amplitude, or conversely a single vortex pair with identical vortex pairs on either side. Experimentally it is observed that naturally occurring Görtler vortex flows contain vortices of various wavelengths and strengths. In comparing experimental data with the theoretical analysis either an average wavelength with representative upwash and downwash profiles may be used giving a global description of the flow or a single vortex can be considered by using neighboring upwash and downwash profiles and a representative wavelength. In the comparisons made here the latter choice is made, the representative wavelength being twice the distance between the upwash and downwash locations of the vortex for a given streamwise location.

For the experimental configuration under consideration the Görtler number has a value of zero at the leading edge. On moving downstream the Görtler number increases with streamwise position ($G \propto x^{3/4}$). While the Görtler number is less than the critical value (i.e., lies below the neutral curve of Fig. 13) all disturbances will be damped. Damping will be high for large wave numbers—small disturbances—light for moderate wavenumbers and almost nonexistent for small wave numbers. On increasing the Görtler number through the neutral curve the disturbances will begin to be amplified. The theoretical analysis does not allow for the prediction of which wavelength will be amplified and emerge as the characteristic wavelength of the flow. Previous experimental results (Tani and Sakagami, 1962) have indicated that the "edge effects" of the experimental apparatus may be important in determining the characteristic wavelength. This suggestion has been strengthened by the variety of growth paths through the stability chart of naturally occurring Görtler vortex flows reported in the literature. Floryan and Saric (1984) have shown that a free stream containing vorticity of a characteristic wavelength causes double-exponential growth of vortices having twice that wavelength, forcing a preferred wavelength on the flow. Consequently the wavelength selection mechanism must be heavily influenced by the turbulence characteristics of the oncoming free stream at the start of cur-

vature. A number of authors (Crane and Sabzvari, 1982; Swearingen and Blackwelder, 1986; etc.) have found that the final screen prior to the test section influences the characteristics of the developing vortex flow.

In order to predict the characteristic wavelength of a vortex flow it may be postulated that for a free stream of low isotropic turbulence the vortices grow along the curve of maximum amplification on the stability chart. For a given Görtler number the maximum value of $\beta\theta \mathrm{Re}_\theta$ lies on this line and is a minimum on a line of constant $\beta\theta \mathrm{Re}_\theta$. A vortex growing along the line of maximum amplification will have a wavelength that changes with streamwise position; lines of constant wavelength appear as straight lines of slope 3/2 on the stability chart. This is contrary to the findings of the majority of previous authors, namely that wavelength is conserved in the streamwise direction. However, recent measurements by Dagenhart and Mangalam (1986) in a free stream of turbulence intensity of 0.025 percent indicate vortex growth close to the curve of maximum amplification. It should be noted that vortex growth in this way implies a uniform vortex structure: vortices having equal wavelengths, amplitudes, and growth rates for a given streamwise position. The high quality of the oncoming flow required to achieve wavelength selection in this way raises the question of the relevance to real flows.

Figure 13 showing the experimental points for the two vortices A and B clustered around lines of constant wavelength is consistent with the findings of the majority of previous authors. It is presumed that the differing wavelengths are determined by the characteristics of the oncoming flow and are essentially conserved in the streamwise direction. Streamwise variation in the wavelength for a given vortex is due to the developing flow structure as discussed below.

The theoretical disturbance components u', v', w', and p' are derived from eigenfunctions in the governing equations and as such can only be calculated to within a multiplicative constant. However, some estimate of their magnitude can be made from their influence on the flow field when combined with the mean flow terms. The streamwise component u' represents the defect in the mean flow that is indirectly produced by the instability. As such the sum of the mean flow component u_0 and the disturbance u' cannot exceed the free-stream velocity. Hence, an upper limit to the magnitude of u', and $\kappa u_{\max} = u_{\max}/u_\infty$, can be estimated using this criterion. However, as noted by Hall (1983), the linear analysis presented here does not adequately model the decay of the vortices at the edge of the boundary layer. Because the modeled disturbance does not decay rapidly enough, any value of $\kappa u_{\max}$ other than zero results in the sum of u_0 and u' exceeding the free-stream velocity at some point in the flow, though by arbitrarily applying the condition at the boundary layer edge an estimate of $\kappa u_{\max}$ can be obtained. A second limit on the maximum value of $\kappa u_{\max}$ can be obtained by ensuring that the upwash profile remains positive. Presumably the votrex structure breaks down before this condition is met, especially as the first condition is inevitably exceeded in applying the second. Consequently the limit of $\kappa u_{\max}$ based on this condition is overestimated. A limit on the minimum value of $\kappa u_{\max}$ can be obtained from the normal flow components. For a vortex structure to be maintained the normal disturbance component v' must be greater than the mean flow component v_0 at downwash (for a growing mean flow boundary layer). As an example the limits based on the above three conditions for vortex B at the sixth location corresponding to the κu profile of Fig. 14 are:

Condition	Limit in $\kappa u_{\max}$
$u_{\text{down}} < u_\infty$	0.0913 (upper limit)
$u_{\text{up}} > 0$	0.422 (upper limit)
$v_{\text{down}} > v_0$	0.0109 (lower limit)

The experimental value of 0.0795 is contained within this range.

The measured vortices appear to be weak in comparison with the results of some other authors. For example, Crane and Sabzvari (1982) have measured values of $\kappa u_{\max}$ between 0.3 and 0.4 before a meandering secondary instability sets in. Meandering itself would tend to decrease the measured values of $\kappa u_{\max}$ due to a reduction in time-averaged difference between fixed spanwise positions. However, there was no evidence of meandering of the vortices for the results shown here. As discussed above, the characteristics of the flow are influenced by the rig "edge effects" and the differences in $\kappa u_{\max}$ measured on different rigs are not inconsistent with the theory.

From Fig. 10 it can be seen that vortex pairs of different wavelength exist across the span. Indeed, distances between upwash and downwash locations vary within wavelengths. Figure 16 shows that the two vortices A and B have different growth rates. This is to be expected if a distribution of random disturbances in the free stream is to produce the vortex pattern. However, there is a restriction to the wavelengths that can occur for small disturbances. From the stability chart there is an upper limit to the wave number of which the vortices will be amplified (a lower limit on wavelength) for moderate Görtler numbers. Thus very small vortices, i.e., small disturbances, are damped out. The upper limit on wavelength, in the extreme, is the width of the surface. For small disturbances it is experimentally observed (Swearingen and Blackwelder, 1986; Tani and Sakagami, 1962; etc.) that the vortex structure is contained within the boundary layer. For moderate Görtler numbers this limits the wavelength to an order similar to that of the boundary layer thickness. This was the case for all measurements made in the present rig; for example, the ratio of wavelength to boundary layer thickness for vortex A ranged from 2.34 to 3.83 and for vortex B from 2.87 to 5.49. Thus there is a practical upper limit to the wavelength, albeit vague.

Most authors have found they have little variation of wavelength in the streamwise direction for a given vortex. However, the range of different vortices occurring will affect the development of a vortex structure. Vortices of different wavelengths coexisting in the same flow will have different growth rates. This is different from differences in $\kappa u_{\max}$ or amplitude, which will be determined by variations in the initial disturbances that determine the vortex pattern, though different growth rates will either increase or reduce differences in amplitude. Assuming that the stability chart is valid, then for a given streamwise location the mean flow momentum thickness will be essentially constant across the span; for small disturbances the average profiles between different upwashes and downwashes will be similar. Thus the Görtler number will be constant across the span. For different wavelengths the wave numbers and hence, from the stability chart, the values of β will be different. As the vortices grow at different rates they may interfere with neighboring vortices, altering their wavelengths and spanwise positions. Thus a "well-ordered" flow in which the range of wavelengths coexisting is small will tend to develop with little streamwise variation in vortex position.

Conclusions

(*i*) A linear analysis of Görtler instability and a solution technique have been developed that give predictions agreeing with various recent authors using the Blasius mean flow for zero free-stream pressure gradient. Predictions for the effect of free-stream pressure gradient on Görtler instability made using the Falkner–Skan mean flows indicate an increased stability for favorable pressure gradient and decreased stability for adverse pressure gradient.

(*ii*) The importance of including the normal velocity terms in deriving the theoretical model is critical in determining the

stability curves, particularly for mean flows with streamwise pressure gradient,

(*iii*) Results of measurements made on a concave surface in a flow with essentially zero streamwise pressure gradient have been compared with the theoretical predictions. In view of the difficulties experienced in obtaining a Görtler vortex structure on the experimental surface it must be said that wall concave curvature is no guarantee of the existence of Görtler vortices. Predictions of streamwise velocity profiles and ranges of vortex amplitude agreed well with the experimental results for the linear growth regime of the vortex flow. The vortex wavelength and spanwise structure was found to be conserved in the streamwise direction.

Acknowledgments

The authors are indebted to the Science and Engineering Research Council for their financial support. The authors also wish to thank Mrs. C. A. Smith, Mrs. J. Mosley, and Mrs. P. Jenkins for their help in preparing the paper.

References

Bippes, H., 1972, "Experimentelle untersuchung des laminar turbulenten umschlags an einer parallel angeströmten konkaven wand," Heidleberger Akademie der Wissenschaften, Matematischnaturwissenschaftliche klasse, Sitzungsberichte, Vol. 3, pp. 103–180; translated as "Experimental Study of the Laminar-Turbulent Transition of a Concave Wall in Parallel Flow," NASA-TM-75243.

Brown, A., and Martin, B. W., 1982, "Flow Transition Phenomena and Heat Transfer Over the Pressure Surfaces of Gas Turbine Blades," ASME *Journal of Engineering for Power*, Vol. 104, pp. 360–367.

Chang, T. S., and Sartory, W. K., 1964, "Hydromagnetic Görtler Instability in a Boundary Layer on a Concave Wall," *Developments in Theoretical and Applied Mechanics*, Vol. 4, Academic Press, New York, pp. 489–499.

Clauser, M., and Clauser, F., 1937, "The Effect of Curvature on Transition From Laminar to Turbulent Boundary Layer," NACA TN 613.

Crane, R. I., and Sabzvari, J., 1982, "Laser-Doppler Measurements of Görtler Vortices in Laminar and Low-Reynolds-Number Turbulent Boundary Layers," *1st Int. Symp. on Applications of Laser-Doppler Anemometry to Fluid Mechanics*, Lisbon; also in *Laser Anemometry in Fluid Mechanics*, R. J. Adrian et al., eds., Ladoan-Inst. Sup. Tec., Lisbon, 1984.

Dagenhart, J. R., and Mangalam, S. M., 1986, "Disturbance Functions of the Görtler Instability on an Aerofoil," ICAS-86-1.8.1.

DiPrima, R. C., and Dunn, D. W., 1956, "The Effect of Heating and Cooling on the Stability of the Boundary-Layer Flow of a Liquid Over a Curved Surface," *J. Aeronaut. Sci.*, Vol. 23, pp. 913–916.

El-Hady, N. M., and Verma, A. K., 1983, "Growth of Görtler Vortices in Compressible Boundary Layers Along Curved Surfaces," *J. Eng. Appl. Sci.*, Vol. 2, pp. 213–238.

Floryan, J. M., 1983, "The Second Mode of the Görtler Instability of Boundary Layers," *AIAA Journal*, Vol. 23, No. 11, pp. 1828–1830.

Floryan, J. M., 1985, "Effects of Blowing on the Görtler Instability of Boundary Layers," *AIAA Journal*, Vol. 23, No. 8, pp. 1287–1288.

Floryan, J. M., and Saric, W. S., 1982, "Stability of Görtler Vortices in Boundary Layers," *AIAA Journal*, Vol. 20, No. 3, pp. 316–324.

Floryan, J. M., and Saric, W. S., 1983, "Effects of Suction on the Görtler Instability of Boundary Layers," *AIAA Journal*, Vol. 21, No. 12, pp. 1635–1639.

Floryan, J. M., and Saric, W. S., 1984, "Wavelength Selection and Growth of Görtler Vortices," *AIAA Journal*, Vol. 22, No. 11, pp. 1529–1538.

Görtler, H., 1940, "Über eine dreidimensionale instabilität laminarer grenzschichten an konckaven wänden," Ges. d. Wiss. Gottingen, Nachr. a.d., Math., Vol. 2(1); translated as "On the Three-Dimensional Instability of Laminar Boundary Layers on Concave Walls," NACA-TM-1375, 1954.

Hall, P., 1983, "The Linear Development of Görtler Vortices in Growing Boundary Layers," *J. Fluid Mech.*, Vol. 130, pp. 41–58.

Han, L. S., and Cox, W. R., 1983, "A Visual Study of Turbine Blade Pressure-Side of Boundary Layers," ASME *Journal of Engineering for Power*, Vol. 105, pp. 47–52.

Herbert, T. H., 1976, "On the Stability of the Boundary Layer Along a Concave Wall," *Archives of Mechanics*, Vol. 28, Nos. 5–6, pp. 1039–1055.

Herbert, T. H., 1979, "Higher Eigenstates of Görtler Vortices," *Recent Developments in Theoretical and Experimental Fluid Mechanics*, U. Muller, K. G. Roesner, and B. Schmidt, eds., Springer-Verlag, New York, pp. 331–338.

Kahawita, R., and Meroney, R., 1977, "The Influence of Heating on the Stability of Laminar Boundary Layers Along Concave Curved Walls," ASME *Journal of Applied Mechanics*, Vol. 44, pp. 11–17.

Kottke, V., 1986, "Taylor–Görtler Vortices and Their Effect on Heat and Mass Transfer," *Proc. Eighth Int. Heat Transfer Conf.*, San Francisco, CA, Vol. 3, pp. 1139–1144.

Liepman, H. W., 1943, "Investigation of Laminar Boundary-Layer Stability and Transition on Curved Boundaries," NACA Wartime Report, ACR 3H30.

Liepman, H. W., 1945, "Investigation of Boundary Layer Transition on Concave Walls," NACA Wartime Report, ACR 4J28.

McCormack, P. D., Welker, H., and Kelleher, M., 1970, "Taylor–Görtler Vortices and Their Effect on Heat Transfer," ASME *Journal of Heat Transfer*, Vol. 92, pp. 101–112.

Ragab, S. A., and Nayfeh, 1981, A. H., "Görtler Instability," *Phys. Fluids*, Vol. 24, No. 8, pp. 1405–1417.

Scott, M. R., and Watts, H. A., 1977, "Computational Solution of Linear Two-Point Boundary Value Problems via Orthonormalization," SIAM *J. Numer. Anal.*, Vol. 14, No. 1, pp. 40–70.

Shigemi, M., Johnson, M. W., and Gibbings, J. C., 1987, "Boundary Layer Transition on a Concave Surface," *I.Mech.E. Int. Turbomachinery Conf.*, C262/87.

Smith, A. M. O., 1953, "On the Growth of Taylor–Görtler Vortices Along Highly Concave Walls," Douglas Aircraft Company Inc. E.S. 17110.

Swearingen, J. D., and Blackwelder, R. F., 1986, "The Growth and Breakdown of Streamwise Vortices in the Presence of a Wall," *J. Fluid Mech.*, Vol. 182, pp. 255–290.

Tani, I., 1962, "Production of Longitudinal Vortices in the Boundary Layer Along a Concave Wall," *J. Geophys. Res.*, Vol. 67, No. 8, pp. 3075–3080.

Tani, I., and Sakagami, J., 1962, "Boundary-Layer Instability at Subsonic Speeds," *Proceedings of Third Congress of International Council of Aerospace Sciences*, Stockholm, Spartan, Washington, DC, 1964, pp. 391–403.

Winoto, S. H., and Crane, R. I., 1980, "Vortex Structure in Laminar Boundary Layers on a Concave Wall," *Int. J. Heat and Fluid Flow*, Vol. 2, No. 4, pp. 221–231.

Wortmann, F. X., 1964, "Experimental Investigations of Vortex Occurrence at Transition in Unstable Laminar Boundary Layers," AFOSR Report 64-1280, AF 61(052)-220.

Wortmann, F. X., 1969, "Visualization of Transition," *J. Fluid Mech.*, Vol. 38, No. 3, pp. 473–480.

Yeo, K. H., Brown, A., and Martin, B. W., 1984, "Stability of a Laminar Boundary Layer Flowing Along a Concave Surface With Uniform Mainstream Velocity," *Int. J. Heat and Fluid Flow*, Vol. 5, No. 2, pp. 67–79.

Numerical Prediction of Turbine Vane-Blade Aerodynamic Interaction

J. P. Lewis
Senior Project Engineer.

R. A. Delaney
Supervisor, Computational Fluid Mechanics.

E. J. Hall
Project Engineer.

Allison Gas Turbine Division,
General Motors Corporation,
Indianapolis, IN 46206

A time-accurate analysis for turbine vane-blade interaction is presented. The analysis simultaneously solves the unsteady isentropic Euler equations in the vane and blade rows on a blade-to-blade surface of revolution. The equations are integrated on overlapped O-type grids using a rapid and robust explicit hopscotch algorithm. Vane and blade rows with unequal numbers of airfoils in each row are treated using a single passage model with phase-lagged periodic boundary conditions. Boundary conditions between the rows are set by a combination of bilinear interpolation and a reference plane method of characteristics. Nonreflective inflow and outflow boundary point calculation procedures are incorporated to ensure that outward-radiating planar waves pass out of the solution domain without reflection. Presented results for a turbine stage show significant effects of the interaction on the time-mean airfoil surface pressure distributions.

1 Introduction

Computational fluid dynamics is used extensively in the design of modern turbines. Engineers carefully choose the number and shape of airfoils to minimize losses while providing the desired work from each stage. However, much of the design is based upon models that assume steady relative flow through each blade row. This is done by assuming that the inlet and outlet conditions for each blade row are steady and uniform in the circumferential direction.

In reality, these assumptions are not valid. Rotating blade rows sweep through circumferentially nonuniform flow fields, which causes the flow to be unsteady in the rotor frame of reference. This unsteadiness affects the inlet and outlet conditions of the adjacent stator rows. Since adjacent rows rarely have equal numbers of airfoils, the inlet conditions to each row are not only nonuniform, but the spatial period in the circumferential direction is not equal to one blade or vane pitch. Thus, the actual inlet and outlet conditions to a blade row are unsteady and nonuniform in the circumferential direction. Including the unsteady flow effects in the design process may provide further improvements in stage performance.

Experimental studies of turbine stages have shown the complexity of the unsteady flow field. The unsteady effects are generally divided into potential effects that propagate upstream and downstream, and wake effects that convect downstream. For large axial gaps between rows (approximately 60 percent axial chord), the wake effects dominate (Dring et al., 1982). However, for small axial gaps (approximately 15 percent axial chord), the potential effects of the downstream row on the upstream row can also be important. In modern turbomachines, an axial gap of 15 percent axial chord is not uncommon. Therefore, both potential and wake effects should be considered.

The wakes from upstream rows have a very pronounced effect on the downstream rows (Gallus et al., 1982; Hodson, 1985). The relative movement of adjacent cascade rows causes the downstream airfoils to cut through the wakes of the upstream airfoils in an unsteady manner. As the wakes are cut, there is increased turbulence energy, which can cause a laminar boundary layer temporarily to become locally turbulent (Ashworth et al., 1985; Binder et al., 1987). These wake-induced turbulent patches greatly affect the heat transfer. Since the boundary layer is sometimes turbulent, sometimes laminar, and sometimes in transition, heat transfer predictions based on steady-state methods do not generally correlate with experimental measurements (Dunn et al., 1986).

Over the past decade significant effort has been devoted to the development of interactive stage analyses for turbines and compressors. A summary of the truly interactive unsteady analyses reported in the literature is given in Table 1. The earliest work was performed ten years ago by Erdos et al. (1977). They pioneered the development of nonreflective inflow and outflow boundary point calculations. They also devised a procedure to calculate the interactive flow field in a stage with unequal numbers of airfoils in each row using a single passage flow model. Koya and Kotake (1985) were the first to calculate the three-dimensional unsteady flow in a turbine stage using an Euler solver. In that same year, Rai (1985) performed two-dimensional thin-layer Navier–Stokes calculations for a turbine stage with equal numbers of airfoils in each row. Rai used a novel flux-conserving patched grid scheme to couple the vane and blade row solutions. Fourmaux (1986) published the first conclusive two-dimensional inviscid Euler predictions for a compressor stage with unequal numbers of rotor and stator airfoils.

Upon reviewing the individual strengths of the numerical

Contributed by the International Gas Turbine Institute and presented at the AIAA/SAE/ASME/ASEE 23rd Joint Propulsion Conference, San Diego, California, June 29–July 2, 1987. Manuscript received by the International Gas Turbine Institute October 1987.

Table 1 Comparison of fully interactive turbine stage analyses

Author(s) or affiliation	Year	No. of dimensions	Application	System of equations	Numerical scheme	Grid type	Grid interface treatment	Inflow and outflow boundary conditions	Periodic boundary treatment
Erdos, Alzner and McNally[7]	77	2	Comp.	Euler	Explicit MacCormack	H	Patched-MOC*	Nonreflective MOC	Phase-lagged
Koya and Kotake[8]	85	3	Turb.	Euler	Explicit Denton	H	Overlapped interpolation	MOC	Phase-lagged
Rai[9]	85	2	Turb.	Thin-layer Navier-Stokes	Implicit Osher	H/O	Patched-conservative F-D	Nonreflective MOC	Spatially periodic
Fourmaux[10]	86	2	Comp.	Euler	Explicit MacCormack	H	Patched-conservative F-D	MOC	Spatially periodic over multiple passages
Present study	87	2	Turb.	Euler	Explicit Hopscotch	O	Overlapped interpolation/MOC	Nonreflective MOC	Phase-lagged

*MOC — Method of Characteristics

studies presented in Table 1, it is apparent that the following characteristics of a predictive computer code are desirable:

1 The code must incorporate time-accurate interior and boundary point calculations. The boundary conditions must not artificially reflect the unsteady waves back into the flow field.

2 The code must accurately model both the potential and the wake effects.

3 It must be easily adaptable to different geometries.

4 It should not require excessive computer resources. Only then will the code be used as a design tool.

This paper presents the first phase of the development of a vane-blade interaction computer code that will eventually have all of the characteristics listed above. The first phase is based on a two-dimensional isentropic Euler equation model. In the second phase of the development, the Euler solver will be extended to a viscous Navier–Stokes solver. An efficient and accurate explicit hopscotch time-marching algorithm is used to solve the governing partial differential equations at the interior points. The stage inlet and outlet boundary conditions are specified using a nonreflective method of characteristics to allow outward-traveling waves to pass out of the flow domain. The equations are discretized on capped O-grids. The vane and blade O-grids are overlapped and information is passed back and forth between solutions to predict the flow field in both rows simultaneously. Overlapping the grids allows easy modification of the axial spacing between the two rows without the need to generate new grids. Phase-lagged periodic relations are used to enforce boundary conditions at the periodic boundaries and on portions of the overlap boundaries. With this phase-lagged periodic boundary point treatment, the computational domain consists of only one blade passage and one vane passage. This procedure is more adaptable to different turbine geometries than the method of stacking multiple passages to span one circumferential period. Although a code using the stacking method may be more efficient for a few special blade count ratios, many airfoils would have to be stacked to reproduce the exact airfoil count found in most turbine stages. For this reason, the phase-lagged method was used exclusively in this study.

2 Aerodynamic Equations

The unsteady Euler equations for flow on a blade-to-blade surface of revolution, shown in Fig. 1, are

$$\frac{\partial E}{\partial t}+\frac{\partial F}{\partial m}+\frac{\partial G}{\partial \theta}=H \tag{1}$$

where

$$E=rb\begin{bmatrix}\rho\\ \rho u\\ \rho v\\ \rho e_0\end{bmatrix},\quad F=rb\begin{bmatrix}\rho u\\ \rho u^2+p\\ \rho uv\\ \rho uh_0\end{bmatrix},\quad G=b\begin{bmatrix}\rho v\\ \rho uv\\ \rho v^2+p\\ \rho vh_0\end{bmatrix}$$

$$H=rb\begin{bmatrix}0\\ (\rho v^2+p)\dfrac{1}{r}\dfrac{dr}{dm}+p\dfrac{1}{b}\dfrac{db}{dm}\\ -\rho uv\dfrac{1}{r}\dfrac{dr}{dm}\\ 0\end{bmatrix}$$

where m and θ are the meridional and polar coordinates, respectively; r is the radius; b, the stream tube thickness; u and v, the velocity components in the m and θ directions, respectively; p, the pressure; ρ, the density; e_0, the total internal energy; and h_0, the total enthalpy.

For a perfect gas, the total energy per unit mass e_0 and the total enthalpy per unit mass h_0 can be expressed in terms of the other variables as

$$e_0=\frac{p}{\rho(\gamma-1)}+\frac{1}{2}(u^2+v^2),\quad h_0=e_0+p/\rho$$

In this initial study, the isentropic expression

$$p/p_0=(\rho/\rho_0)^\gamma \tag{2}$$

was invoked in lieu of the full energy equation to simplify the calculations. This substitution is valid for the inviscid flow of a perfect gas without strong shocks.

In order to apply a discretized form of equation (1) to an O-type grid on a stream surface, equation (1) was first transformed to an arbitrary curvilinear coordinate system, defined as follows:

$$\xi=\xi(m,\theta,t)$$
$$\eta=\xi(m,\theta,t)$$

After transformation, equation (1) becomes

$$\frac{\partial E'}{\partial t}+\frac{\partial F'}{\partial \xi}+\frac{\partial G'}{\partial \eta}=H' \tag{3}$$

where

$$E'=\frac{rb}{J}\begin{bmatrix}\rho\\ \rho u\\ \rho v\end{bmatrix},\quad F'=\frac{rb}{J}\begin{bmatrix}\rho U\\ \rho uU+\xi_m p\\ \rho vU+\xi_\theta p/r\end{bmatrix},$$

$$G'=\frac{rb}{J}\begin{bmatrix}\rho V\\ \rho uV+\eta_m p\\ \rho vV+\eta_\theta p/r\end{bmatrix}$$

$$H'=\frac{H}{J}$$

with

$$U=\xi_m u+\xi_\theta/r(v-r\omega),\quad V=\eta_m u+\eta_\theta/r(v-r\omega)$$
$$J=\xi_m\eta_\theta-\xi_\theta\eta_m=1/(m_\xi\theta_\eta-m_\eta\theta_\xi)$$

and where U and V are the contravariant velocities, J is the

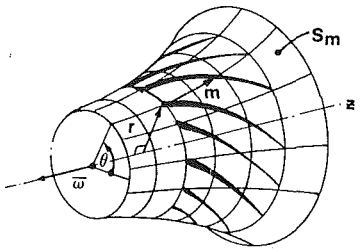

Fig. 1 Quasi-three-dimensional stream surface coordinate system

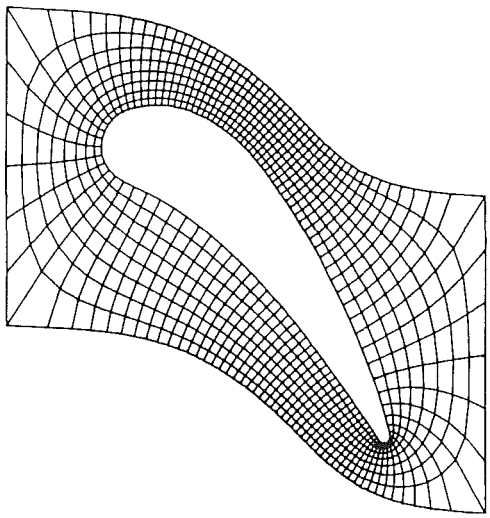

Fig. 2 Overlapped capped O-grid

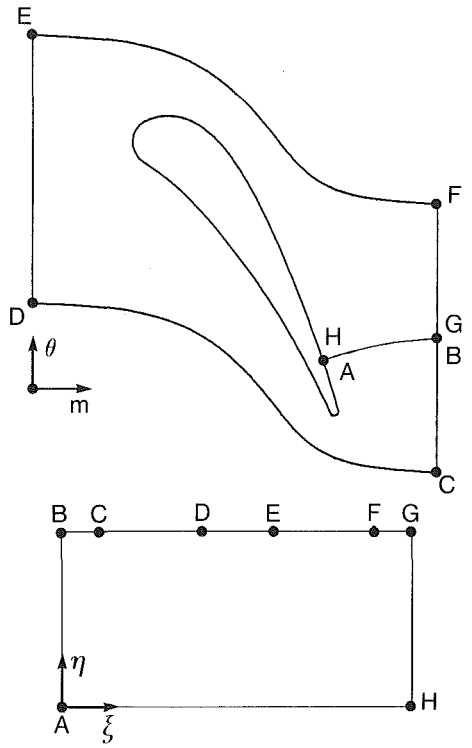

Fig. 3 Schematic of mapping from physical plane to computational plane for capped O-type grid

Jacobian of the transformation, ω is the angular velocity of the transformed coordinate system, and ξ_m, ξ_θ, etc., are the metrics of the transformation. The metrics are calculated from the relations

$$\xi_m = J\theta_\eta, \quad \xi_\theta = -Jm_\eta, \quad \eta_m = -J\theta_\xi, \quad \eta_\theta = Jm_\xi$$

where the inverse metrics m_ξ, m_θ, etc., are computed in the transformed rectangular computational space.

3 Grid System

The governing equations were discretized on a grid system consisting of two body-conforming capped O-grids (Fig. 2). This type of grid has the desirable characteristic that it affords accurate resolution of the flow near the leading and trailing edges of airfoils. Unsteady measurements of the flow through a turbine stage indicate that for close axial spacing, the downstream rotor significantly affects the surface pressure at the vane trailing edge (Dring et al., 1982). This effect may not be well predicted if the grid does not represent the actual airfoil geometry in that region.

The grids are initially generated using an elliptic grid generation procedure (Adamcyzk, 1980) and are subsequently modified using a variational scheme (Brackbill and Saltzman, 1982). The elliptic generator establishes the location of the airfoil surface grid points, $m = m(\xi, \eta)$ and $\theta = \theta(\xi, \eta)$, from a singular line integral that represents the potential due to an electrostatic charge distribution on the airfoil surface. A finite-difference solution of Laplace's equation then gives the location of the remaining grid points in the physical domain. This preliminary grid is then modified using the variational scheme, which allows control of the grid orthogonality, density, and smoothness by minimizing the functional

$$I = I_s + \lambda_0 I_0 + \lambda_w I_w \tag{4}$$

where

$$I_s = \iint [(\nabla\xi)^2 + (\nabla\eta)^2]\, dm\, d\theta$$

$$I_0 = \iint [(\nabla\xi)\cdot(\nabla\eta)]^2 dm\, d\theta$$

$$I_w = \iint w(m, \theta) J\, dm\, d\theta$$

The grid smoothness is represented by I_s, the orthogonality by I_0, and the density by I_w. The constants λ_0 and λ_w may be used to control the relative importance of the orthogonality and point density, respectively. The function $w(m, \theta)$ controls the location of any grid refinement.

The computational ξ–η grid, shown in Fig. 3, is rectangular with equal spacing between grid points. Lines of constant ξ radiate outward from the airfoil; lines of constant η enclose the airfoil. On the surface of the airfoil, $\eta = 0$. The distances between the airfoil and the inlet and outlet boundary, planes are specified. An arbitrary number of grid points can be placed on the outlet and inlet caps of the grids, which provides for the control of grid density in the region between the two rows. A reasonably fine grid is required to resolve effectively the unsteady waves that travel to and from the inflow and outflow boundaries. The metrics at each grid point are calculated using finite differences that satisfy the grid conservation law.

4 Interior Point Solution Scheme

Equation (3) is solved using the hopscotch finite-difference algorithm (Gourlay and Morris, 1972). Past experience has shown this algorithm to be a robust and accurate procedure for solving the Euler (Delaney, 1983) and the Navier–Stokes equations (Kwon and Delaney, 1985). The hopscotch algorithm incorporates central differences for the spatial derivatives and two-point, one-sided differences for the time derivatives. It follows that the algorithm is second-order accurate in space and first-order accurate in time. Two separate sweeps are used to advance the solution between time levels with half the grid points calculated during each sweep. Specifically, equation (3) is discretized as

(first sweep, $i+j+n$ even)

$$E^{n+1}_{i,j} = E^n_{i,j} - \frac{\Delta t}{2\Delta\xi}(F^n_{i+1,j} - F^n_{i-1,j}) - \frac{\Delta t}{2\Delta\eta}(G^n_{i,j+1} - G^n_{i,j-1}) - \Delta t H^n_{i,j} + \alpha_\xi(E^n_{i+1,j} - 2E^n_{i,j} + E^n_{i-1,j}) + \alpha_\eta(E^n_{i,j+1} - 2E^n_{i,j} + E^n_{i,j-1}) \quad (5)$$

(second sweep, $i+j+n$ odd)

$$E^{n+1}_{i,j} = E^n_{i,j} - \frac{\Delta t}{2\Delta\xi}(F^{n+1}_{i+1,j} - F^{n+1}_{i-1,j}) - \frac{\Delta t}{2\Delta\eta}(G^{n+1}_{i,j+1} - G^{n+1}_{i,j-1}) - \Delta t H^n_{i,j} + \alpha_\xi(E^{n+1}_{i+1,j} - 2E^{n+1}_{i,j} + E^{n+1}_{i-1,j}) + \alpha_\eta(E^{n+1}_{i,j+1} - 2E^{n+1}_{i,j} + E^{n+1}_{i,j-1}) \quad (6)$$

where $\xi = i\Delta\xi$, $\eta = j\Delta\eta$, and $t = n\Delta t$. The last two terms of equations (5) and (6) are added damping terms needed to stabilize the solution in regions of large gradients.

If the coefficients in the damping terms, α_ξ and α_η, are not functions of $E^{n+1}_{i,j}$, equation (5) can be replaced with a simple extrapolation in time given by

$$E^{n+1}_{i,j} \approx 2E^n_{i,j} - E^{n-1}_{i,j} \quad (7)$$

The simplification results in a significant increase in computational speed. Equation (7) is derived by repeatedly applying the full two-sweep scheme, equations. (5) and (6).

The damping scheme incorporates a combination of second-order and product fourth-order terms. The damping coefficients, α_ξ and α_η, are of the form

$$\alpha_\xi = [\alpha_2 + \alpha_4 \left| \rho^{n+1}_{i+1,j} - 2\rho^n_{i,j} + \rho^{n+1}_{i-1,j} \right| / \rho^n_{i,j}] \mathrm{CFL}_{\mathrm{local}} \quad (8)$$

$$\alpha_\eta = [\alpha_2 + \alpha_4 \left| \rho^{n+1}_{i,j+1} - 2\rho^n_{i,j} + \rho^{n+1}_{i,j-1} \right| / \rho^n_{i,j}] \mathrm{CFL}_{\mathrm{local}} \quad (9)$$

The optimum values for α_2 and α_4 were found to be 0.025 and 0.5, respectively. Numerical experimentation has shown that the solution is relatively insensitive to slight changes in these coefficients. The fourth-order damping terms are significant only in areas having high gradients such as near shocks or at the trailing edges of the airfoils. The damping is made proportional to the CFL number so that it decreases as the time step is reduced.

The maximum allowable time step is limited by the CFL stability criterion. For explicit finite-difference algorithms, the method of characteristics can be used to derive the expression for the maximum allowable time step. The resulting expression is

$$\Delta t \le [\frac{1}{\Delta\xi}(|U| + J\sqrt{(m_\eta/r)^2 + \theta^2_\eta}\, a) + \frac{1}{\Delta\eta}(|V| + J\sqrt{(m_\xi/r)^2 + \theta^2_\xi}\, a)]^{-1} \quad (10)$$

Because of the limit on the time increment, the first-order time accuracy of the scheme is not a major concern. Typically on the order of 1000 time steps are required to march through one blade passage period.

It is convenient to choose a time increment Δt that satisfies the geometric constraint that there be an integral number of time steps for the rotor to advance one vane and one blade pitch. This simplifies the application of the phase-lagged boundary conditions. To obtain Δt, equation (10) is used to find the most restrictive time step from steady solutions for the isolated rotor and stator blade rows. This Δt is then multiplied by a safety factor between 0.9 and 0.95, and then further relaxed to satisfy the geometric constraint. This procedure ensures that equation (10) is satisfied during the unsteady calculation.

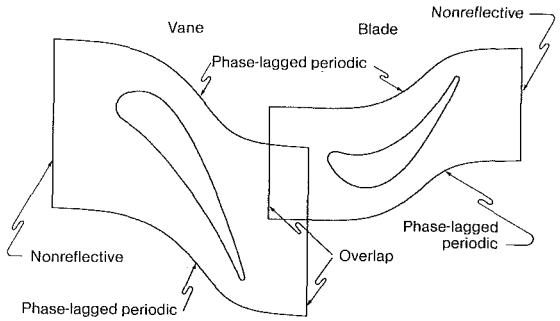

Fig. 4 Location of different types of boundary points

5 Boundary Point Calculations

Figure 4 shows the five different types of boundary points involved in the interactive analysis. They are: (1) airfoil surface boundary points, (2) stage inlet and exit boundary points, (3) boundary points along the periodic grid boundary, (4) vane exit overlap boundary points, and (5) blade inlet overlap boundary points. Incorporation of accurate boundary point calculation procedures is extremely important for unsteady internal flows. If unsteady waves reflect unnaturally off the boundaries, the solution may not converge and the time accuracy of the solution will be destroyed.

Airfoil Surface Boundary Points. The surface boundary condition is set by imposing the tangent flow condition, $V = 0$, on the airfoil surface. This is done with an adaption of the full two-sweep version of the interior point algorithm. Central differences in equations (5) and (6) are replaced with three-point one-sided differences. Also, the damping term in the η direction is removed. Following the solution of the difference equations, the tangent flow condition is enforced by projecting the calculated velocity onto the airfoil surface. This is accomplished by solving for u and v from the definition of the contravariant velocity components, U and V, with V (normal to the surface) set equal to zero.

Inlet and Exit Boundary Points. The inlet and exit boundary point calculations are similar to those proposed by Erdos et al. (1977) for rotor-stator calculations. These calculations are totally nonreflective for planar waves. Wave components inclined to the inlet and exit boundaries will be reflected, but this is viewed as a higher order effect.

The scheme is based on a reference plane method of characteristics in a plane of constant ξ. The derivatives in the η direction are lagged one time step and treated as source terms. By using this approach, the number of spatial dimensions is reduced from two to one. The characteristic directions and corresponding compatibility relations then become

$$\eta_\theta / r du - \eta_m dv = dt(\eta_\theta r \psi_1 + \eta_m \psi_2) \quad (11)$$

on

$$\frac{d\eta}{dt} = V \qquad \text{(particle path)} \quad (12)$$

and

$$\pm \rho a \eta_m du \pm \rho a \eta_\theta (r dv + \Gamma dp = dt(\pm \rho a \eta_m \psi_1 \mp \rho a \eta_\theta \psi_2 - \Gamma \psi_3) \quad (13)$$

on

$$\frac{d\eta}{dt} = V \pm a\Gamma \qquad \text{(wave paths)} \quad (14)$$

where

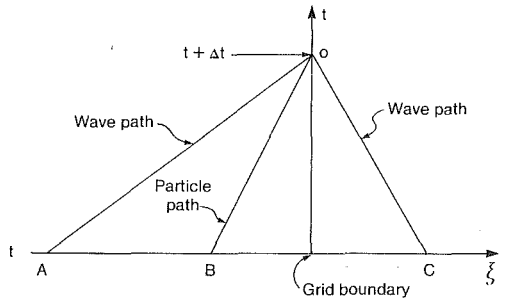

Fig. 5 Reference plane method of characteristics network

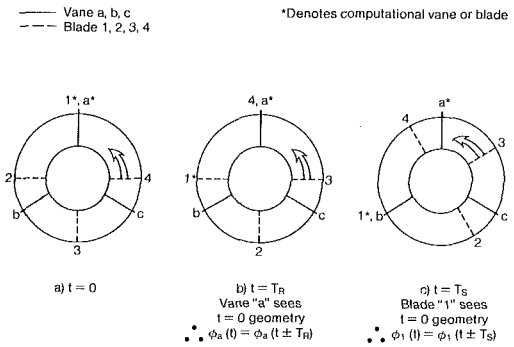

Fig. 6 Simplified turbine frontal view showing relative positions at different times

$$\psi_1 = -U\frac{\partial u}{\partial \xi} + \xi_m \frac{\partial p}{\partial \xi} + \frac{v^2}{r}\frac{dr}{dm}$$

$$\psi_2 = U\frac{\partial v}{\partial \xi} + \xi_\theta / r \frac{\partial p}{\partial \xi} + \frac{uv}{r}\frac{dr}{dm}$$

$$\psi_3 = U\frac{\partial p}{\partial \xi} + \gamma p\left[\xi_m \frac{\partial u}{\partial \xi} + \xi_\theta / r \frac{\partial v}{\partial \xi} + \frac{u}{rb}\frac{drb}{dm}\right]$$

$$\Gamma = \sqrt{\eta_m^2 + (\eta_\theta / r)^2}$$

Equation (12) defines the particle path line B–O of Fig. 5, and equation (14) defines the wave path lines A–O and C–O.

If it is assumed that the flow upstream and downstream of the stage is uniform in the circumferential direction, the stream surface is cylindrical ($dr/dm = 0$), and the isentropic relation applies, then the wave path compatibility relation, equation (13) reduces to the Riemann invariant form

$$da \pm \frac{\gamma - 1}{2} du = 0 \tag{15}$$

By using equation (15), known values of the acoustic and axial velocities can be specified as far field boundary conditions. The values of the dependent variables at the boundaries are thus allowed to "float" and are fixed only at $m = \pm\infty$, thus greatly suppressing the reflection of outward traveling waves.

The particular equations and near-field boundary conditions used in the nonreflective boundary calculations are as follows. At the inlet plane, equations (13) and (15) are solved along C–O and A–O, respectively, in combination with the isentropic relation, equation (2). The only near field boundary condition is specification of the relative flow angle, $\tan^{-1}[(v - r\omega)/u]$. At the outlet plane, equation (13) is solved along A–O, equation (15) along C–O, and equation (11) along B–O. Equation (2) is also used at the exit plane.

Periodic Boundary Points. With the phase-lagged periodic boundary point treatment, the solution domain spans only one vane and one blade pitch. Because the circumferential period is not the same in vane and blade rows with unequal numbers of airfoils in each row, special treatment of points along the grid periodic boundaries and at the overlap boundaries is required. Prior to discussing the phase-lagged periodic boundary point calculations, it is necessary to establish the temporal period of the flow field and to relate the flow fields in adjacent passages. For this purpose, it is assumed that the only unsteadiness is caused by the relative motion of the two airfoil rows and that the inlet and outlet flow to the stage is steady at infinity and uniform in the θ direction outside the computational grid.

Under the above conditions, the temporal period of the solution can be established by a simple geometric proof, as was first related by Erdos et al. (1977). Figure 6 shows a simplified frontal view of a turbine stage having three vanes and four blades. At $t = 0$, vane a and blade 1 are aligned. The blade 1 flow field is represented by ϕ_1, the vane a flow field by ϕ_a. At $t = T_r$, the rotor has advanced one blade pitch, aligning blade 4 with vane a. Since vane a sees the same geometry at $t = T_r$ as it did at $t = 0$, $\phi_a(0) = \phi_a(T_r)$, which indicates the vane flow is periodic with a period of T_r. At $t = T_s$, blade 1 is aligned with vane b. Since blade 1 sees the same geometry as it did at $t = 0$, the flow at 1 repeats every T_s. This geometric proof is valid for any ratio of vanes to blades. It establishes the temporal period in the vane row as T_r, and the temporal period of the blade row as T_s.

The relationship of the solution in adjacent passages within the same row is also shown by Fig. 6. Since blade 1 leads blade 4 by T_r and lags blade 2 by T_r,

$$\phi_4(t, m, \theta) = \phi_1(t - T_r, m, \theta) \tag{16}$$

$$\phi_2(t, m, \theta) = \phi_1(t + T_r, m, \theta) = \phi_1(t + T_r - T_s, m, \theta) \tag{17}$$

where m and θ are referenced to each of the particular blades. Similarly, by noting the relative movement of the vane row

$$\phi_c(t, m, \theta) = \phi_a(t + T_s, m, \theta) = \phi_a(t + T_s - 2T_r, m, \theta) \tag{18}$$

$$\phi_b(t, m, \theta) = \phi_a(t - T_s, m, \theta) = \phi_a(t - T_s + T_r, m, \theta) \tag{19}$$

In equations (17) and (18), multiples of the temporal periods, T_r and T_s, have been subtracted from the original phase lags to ensure that they are less than 0. In equation (19), T_r has been added to the original phase lag so that its magnitude is as small as possible.

Equations (16) through (19) are used to calculate the conditions along the grid periodic boundaries. The dependent variables at a point just outside the computational domain are equal to those of a corresponding point one pitch away within the domain at an earlier time. In order for these values to be available, the variables at points adjacent to the grid periodic boundaries are averaged over two temporal periods and stored at each time step. The averaging provides underrelaxation at the boundaries. Only the data for the last temporal period need to be retained.

Overlap Boundary Points. The vane and blade flow fields are coupled at the vane exit plane. The two grids are overlapped as shown in Fig. 7. Originally, all dependent variables along the vane exit and blade inlet boundaries were obtained by bilinear interpolation (Mastin and McConnaughey, 1984) from the other row's solution. This scheme did not converge because it did not allow spurious waves to pass out of the overlap region. This same procedure is currently used at the blade inlet boundary. However, at the vane exit, only the static pressure is interpolated and the remaining variables are obtained using a reference plane method of characteristics. The velocity components are given by equations (11) and (13), and the density by equation (2).

When interpolating at a point, if the point happens to be in the computational grid of the opposite row, the dependent variables are interpolated directly. If the point is not in the opposite row's computational grid, the phase lag relations given by equations (16) through (19) are used to access previously

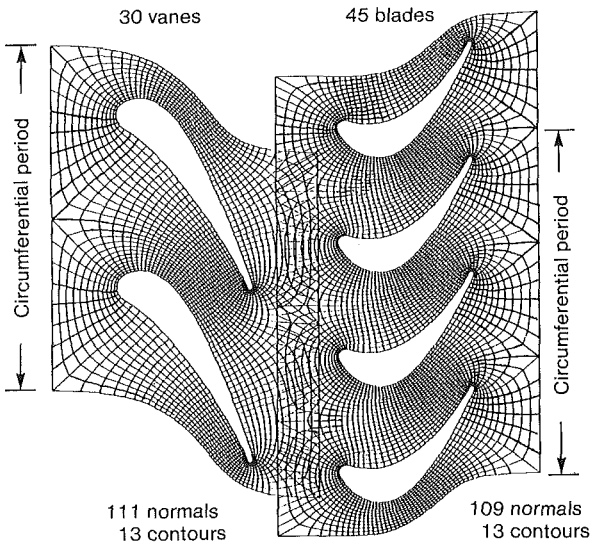

Fig. 7 Overlapped capped O-grid system

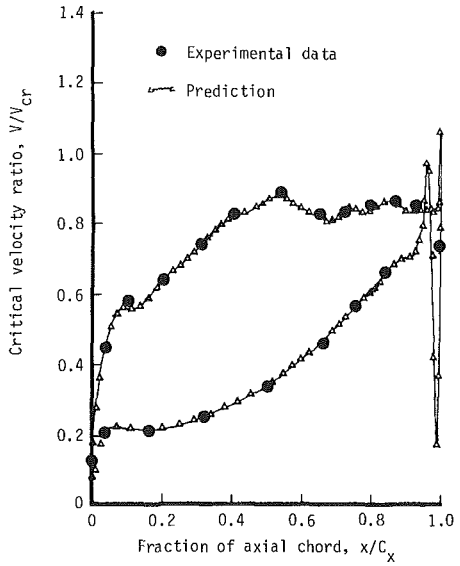

Fig. 8 Comparison of predicted and experimental airfoil surface critical velocity ratio distribution for the Goldman and Seasholtz (1982) annular vane cascade (M = 0.749)

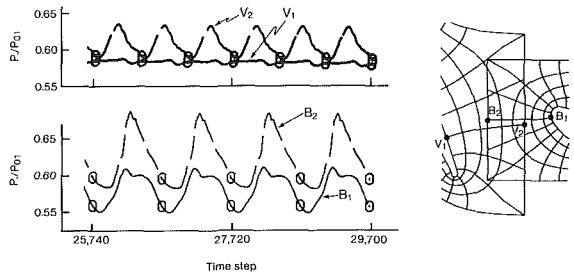

Fig. 9 Pressure histories of two points in each domain that show the convergence to the desired temporal period

stored information. Equations (16) through (19) relate the points outside the computational domain in the opposite grid at time = t to those inside at an earlier time. This allows the specification of boundary conditions on the overlap boundaries at all locations. The information stored for retrieval is a weighted average of the dependent variables necessary for interpolation for the last two temporal periods. The averaging provides an underrelaxation to accelerate convergence to the correct temporal period.

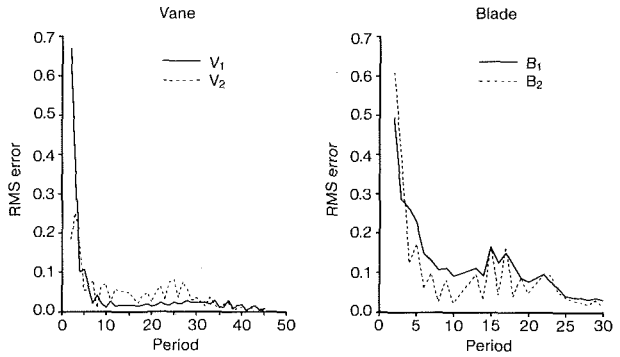

Fig. 10 The error between two successive periods that show convergence to the desired temporal period

6 Results

Both steady isolated vane row and the fully interactive unsteady vane-blade solutions are presented. The steady-state solution is compared with experimental data to demonstrate the accuracy of the analysis method. The steady vane row solution is for an annular vane cascade tested by Goldman and Seasholtz (1982) and shown in Fig. 2. Figure 8 shows that the predicted airfoil surface critical velocity ratio distributions for an exit Mach number $M_2 = 0.75$ agree very well with the measured data. The high degree of resolution around the airfoil leading edge is attributed to the use of the O-type grid system.

The unsteady results are for the turbine stage shown in Fig. 7. This particular stage was analyzed because of a concurrent parallel effort, funded by the Air Force, the determine experimentally the unsteady surface pressures for this stage. These data will likely be the first transonic, compressible, unsteady pressure data available to compare with the computer predictions. The stage has 30 vanes and 45 blades, so there are two vanes and three blades per circumferential period. For the computations the inlet Mach number was 0.197, the outlet Mach number was 0.437, and the inlet total to exit static pressure ratio was 2.55. The axial spacing between the two rows was 63 percent of the vane axial chord. Figure 7 shows the vane and blade grids used in the calculation. The vane grid had 111 grid lines normal to the surface and 13 grid contours, whereas the blade had 109 grid normals and 13 grid contours. Initial conditions were obtained from the flow fields for isolated vane and blade rows. The unsteady calculations required 16 min of CRAY X-MP cpu time to converge to the periodic solution.

When converged, the solution must be periodic in time and have the known temporal period. The static pressure histories at two points in each domain were used to determine when the solution had converged. Figure 9 shows the pressure history and the location of the four points. The markers on the pressure traces designate the required temporal period. The vane temporal period and blade temporal periods consisted of 660 and 990 time steps, respectively. The predicted solution is periodic and has the correct temporal period after 29,700 time steps, corresponding to one complete revolution of the rotor.

Convergence to a periodic solution is shown quantitatively in Fig. 10. In this figure, the root-mean-square of the difference between the current and previous period's pressure traces are presented. The error plotted is defined as

$$(\text{RMS error})_{i,j} = \left[\sum_{n=1}^{ntspp} (P_{i,j}^{n+ntspp} - P_{i,j}^{n})^2 \right]^{1/2} \tag{20}$$

where *ntspp* is the number of time steps per temporal period.

Figure 11 shows the instantaneous pressure field at four different times as the rotor advances one rotor pitch. The coupling of the solution in the two rows is apparent. Collectively, these figures show the unsteadiness of the flow and that the

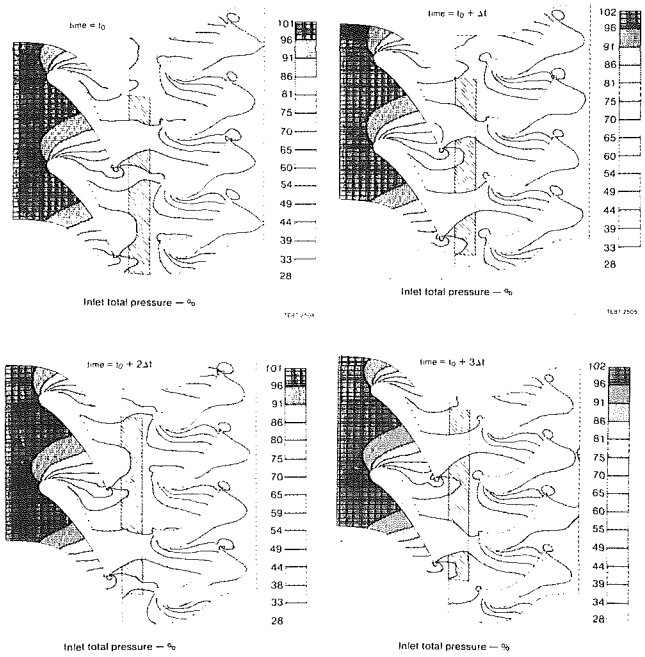

Fig. 11 Sequence of static pressure contour plots as the rotor advances one blade pitch

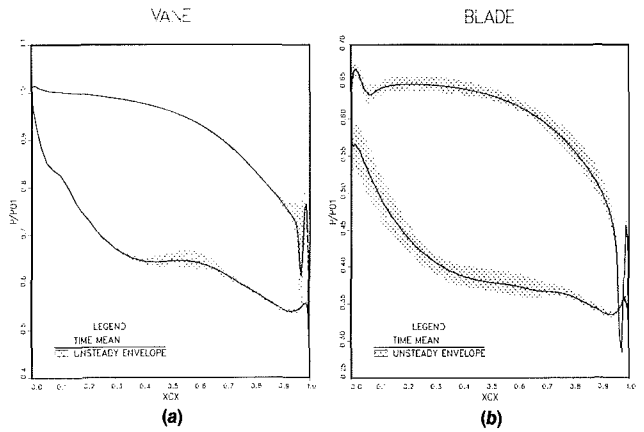

Fig. 12 Unsteady airfoil surface pressure distributions for the vane (*a*) and the blade (*b*)

flow is not periodic over one airfoil pitch. The fact that the solutions match at the phase-lagged periodic boundaries indicates a converged solution was predicted.

The magnitude of the flow unsteadiness is shown in Fig. 12. The time mean unsteady surface pressure shown is an average over one temporal period after the converged periodic solution has been reached. The unsteady envelope defines the maximum deviation of the unsteady surface pressures from the time mean. Comparing Figs. 12(*a*) and 12(*b*) shows that the blade surface pressure is more unsteady than the vane surface pressure, as expected. However, Fig. 12(*a*) shows there is still a significant amount of unsteadiness at the vane trailing edge and on the vane suction surface near the throat across from the trailing edge. The static pressure prediction on the vane pressure surface at the leading edge is greater than the inlet total pressure because the flow has readjusted slightly due to the nonreflective boundary point treatment at the inlet.

7 Summary

Results from the first phase of a computational study on the effects of turbine vane-blade interaction have been presented. Under this study, a fully interactive unsteady vane-blade analysis based on the isentropic Euler equations was developed. The analysis incorporates nonreflecting inflow and outflow boundary point calculations, an overlapping grid procedure to couple the vane and blade row solutions, and a phase-lagged periodic boundary point treatment to allow for unequal numbers of vanes and blades. The cost of each computer run is reasonable considering the complexity of the problem and the code's potential impact on the turbine aerodynamic design process.

Predictions indicate a significant effect of the unsteadiness on the surface pressure over the entire blade surface, at the vane trailing edge, and at the throat on the vane suction surface.

Future plans include the modeling of the viscous terms in the Navier–Stokes equations to account for the effects of the wake on the downstream row. The predictions will be compared with experimental measurements to be taken in a short duration shock tube facility at Calspan Advanced Technology Center, Buffalo, New York.

Acknowledgments

This work was supported by the Aero Propulsion Laboratory, Air Force Wright Aeronautical Laboratories, Air Force Systems Command, Wright-Patterson AFB, Ohio, contract number F33615-83-C-2339 under the direction of Dr. C. MacArthur and Capt. M. J. Stanek.

References

Adamczyk, J. J., 1980, "An Electrostatic Analog for Generating Cascade Grids," NASA Conference Publication 2166, *Numerical Grid Generation Techniques*, pp. 129–142.

Ashworth, D. A., LaGraff, J. E., Schultz, D. L., and Grindrod, K. J., 1985, "Unsteady Aerodynamic and Heat Transfer Processes in a Transonic Turbine Stage," ASME *Journal of Engineering for Gas Turbines and Power*, Vol. 107, pp. 1022–1030.

Binder, A., Forster, W., Mach, K., and Rogge, H., 1987, "Unsteady Flow Interaction Caused by Stator Secondary Vortices in a Turbine Rotor," ASME JOURNAL OF TURBOMACHINERY, Vol. 109, pp. 251–257.

Brackbill, J. V., and Saltzman, J. S., 1982, "Adaptive Zoning for Singular Problems in Two Dimensions," *Journal of Computational Physics*, Vol. 46, pp. 342–368.

Delaney, R. A., 1983, "Time-Marching Analysis of Steady Transonic Flow in Turbomachinery Cascades Using the Hopscotch Method," ASME *Journal of Engineering for Power*, Vol. 105, pp. 272–279.

Dunn, M. G., George, W. K., Rae, W. J., Woodward, S. H., Moller, J. C., and Seymour, P. J., 1986, "Heat-Flux Measurements for the Rotor of a Full-Stage Turbine: Part II—Description of Analysis Technique and Typical Time-Resolved Measurements," ASME JOURNAL OF TURBOMACHINERY, Vol. 108, pp. 98–107.

Dring, R. P., Joslyn, H. D., Hardin, L. W., and Wagner, J. H., 1982, "Turbine Rotor-Stator Interaction," ASME *Journal of Engineering for Power*, Vol. 104, pp. 729–742.

Erdos, J. I., Alzner, E., and McNally, W., 1977, "Numerical Solution of Periodic Transonic Flow Through a Fan Stage," *AIAA Journal*, Vol. 15, No. 11, pp. 1559–1568.

Fourmaux, A., 1986, "Unsteady Flow Calculation in Cascades," ASME Paper No. 86-GT-178.

Gallus, H. E., Grollius, H., and Lambertz, J., 1982, "The Influence of Blade Number Ratio and Blade Row Spacing on Axial-Flow Compressor Stator Blade Dynamic Load and Stage Sound Pressure Level," *ASME Journal of Engineering for Power*, Vol. 104, pp. 633–641.

Goldman, L. J., and Seasholtz, R. G., 1982, "Comparison of Laser Anemometer Measurements and Theory in an Annular Turbine Cascade With Experimental Accuracy Determined by Parameter Investigation," NASA TM 82860.

Gourlay, A. R., and Morris, J. L., 1972, "Hopscotch Difference Methods for Nonlinear Hyperbolic Systems," *IBM Journal Research and Development*, Vol. 16, No. 4, pp. 349–353.

Hodson, H. P., 1985, "Measurements of Wake-Generated Unsteadiness in the Rotor Passages of Axial Flow Turbines," ASME *Journal of Engineering for Gas Turbines and Power*, Vol. 107, pp. 467–476.

Mastin, C. W., and McConnaughey, H. V., 1984, "Computational Problems on Composite Grids," AIAA Paper No. 84-1611.

Koya, M., and Kotake, S., 1985, "Numerical Analysis of Fully Three-Dimensional Periodic Flows Through a Turbine Stage," ASME *Journal of Engineering for Gas Turbines and Power*, Vol. 107, pp. 945–952.

Kwon, O. K., and Delaney, R. A., "A Navier-Stokes Solution Procedure for Analysis of Steady Two-Dimensional Transonic Nozzle Flows," AIAA Paper No. 86-1597.

Rai, M. M., 1985, "Navier-Stokes Simulations of Rotor-Stator Interaction Using Patched and Overlaid Grids," AIAA Paper No. 85-1519.

A Study of Unsteady Rotor-Stator Interactions

Reda R. Mankbadi
Cairo University,
Cairo, Egypt

This work is concerned with simulations of rotor-generated unsteady response of the turbulent flow in a stator. The rotor's effect is represented by moving cylinders of equivalent drag coefficient that produce passing wakes at the entrance of the stator. The unsteady incompressible Navier–Stokes equations are solved on a staggered grid and eddy viscosities are obtained using a k–ϵ *model. The rotor-generated wakes were found to produce a pressure field at the stator's entrance that increases in the direction of the wake traverse. At a streamwise distance equal to the distance between the stator blades, the pressure becomes uniform across the channel and the oscillations in the pressure field decay. Because of the initial asymmetry of the pressure field, the time-averaged mean velocity is no longer symmetric. This asymmetry of the mean flow continues along the passage even after the pressure has regained its symmetry. As a result of the passing of the rotor-generated wakes, large periodic oscillations are introduced into the mean velocity and turbulence energy. The time-averaged turbulence energy and the wall shear stress increases in the direction of the rotor traverse.*

Introduction

Unsteady aerodynamic forces on a cascade of blades play an important role in noise generation, heat transfer, and aerodynamic loading. In a stage of an axial flow machine, the most common aerodynamic excitation sources are the wakes shed by upstream blades. Thus, considering the stator blades in a single-stage axial flow machine, the exit flow field from the upstream rotor defines the unsteady aerodynamic forcing function to the downstream rotor blades. Walker (1974), Kerrebrock and Mikolojczak (1970), Dring et al. (1982), and Dooly et al. (1985) have examined experimentally the unsteady effects of the rotor on the stator. Their investigations have indicated that the rotor-generated wakes alter the development of the boundary layer on the stator blades. This influences the aerodynamic forces and the heat transfer. Thus, the nature of the unsteady boundary layer, which develops in response to the upstream unsteadiness, is of fundamental importance in altering the scale of heat transfer and the aerodynamic forces. Although these investigations have contributed to the understanding of unsteady flows in turbomachines, little information on the detailed process of the boundary layer development caused by the rotor-generated unsteadiness was obtained. This is unavoidable in view of the limitations on the measurement techniques that could successfuly be applied to a rotating rig, and the flow complexity.

Several attempts have been made to simulate numerically the rotor-stator unsteady flow. Hodson (1984) described an inviscid time-marching calculation of the unsteady flow generated by the interaction of upstream wakes with a moving blade row. Henderson (1978) reported some results of theoretical predictions of the unsteady lift on a cascade of airfoils. Rai (1987) presented a Navier-Stokes simulations of rotor–stator interaction using patched and overlaid grids. The purpose of the present work is to consider the real unsteady and turbulent flow in the stator passages.

Because of the complexity of the flow in turbomachines, a better understanding of the rotor's unsteady effects on the stator can be obtained by considering a simplified situation. In the present work the flow between two parallel plates of length-to-width ratio 2:1 is taken to represent the flow between the stator blades. The upstream rotor is replaced by a train of cylinders that move in the transverse direction at the channel inlet, as shown in Fig. 1. The effect of the rotor on the stator is thus replaced by the effect of the cylinder-generated wakes on the channel flow. The amplitude and shape of the rotor wakes are determined by the viscous forces on the rotor

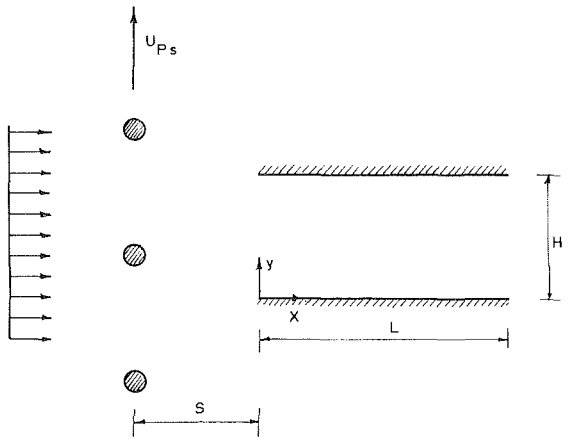

Fig. 1 Nomenclature

Contributed by the International Gas Turbine Institute for publication in the JOURNAL OF TURBOMACHINERY. Manuscript received at ASME Headquarters June 14, 1988.

blades. The speed at which a wake crosses the channel entrance is determined by the rotor's rotational speed. Thus, the equivalent drag coefficient of the cylinders, diameter of the cylinder, and their traverse speed are chosen such that the cylinder-generated wakes simulate the rotor-generated wakes.

Governing Equations

The present work considers the unsteady incompressible turbulent flow between two parallel plates of infinite aspect ratio. The mass conservation and the Reynolds-averaged momentum equations are written in Cartesian tensor form as

$$\frac{\partial(\rho U_i)}{\partial x_i} = 0 \tag{1}$$

$$\frac{\partial(\rho U_i)}{\partial t} + \frac{\partial(\rho U_i\, U_j)}{\partial x_j} = -\frac{\partial P}{\partial x_i} + \frac{\partial}{\partial x_j}\left(\mu \frac{\partial U_i}{\partial x_j} - \rho\overline{u_i' u_j'}\right) \tag{2}$$

where U_i, $i=1, 2$ are the mean velocity components in the x and y directions, respectively. x is the streamwise direction parallel to the plate and measured from the entrance. y is the perpendicular direction measured from the bottom plate. u_i', $i=1, 2, 3$ are the turbulent velocity components in the x, y, and z directions, respectively. All velocities are normalized by the incoming free-stream velocity. ρ and μ are the fluid density and molecular viscosity, respectively. The Reynolds stress closure problem is handled through the use of Boussinesq's turbulent velocity concept. The turbulent viscosity μ_t is obtained from the k–ϵ model of Jones and Launder (1972) where k is the turbulence kinetic energy per unit mass and ϵ is its rate of dissipation. In Jones and Launder (1972) model k and ϵ are obtained by solving the following transport equations simultaneously with the mean flow equations:

$$\rho \frac{Dk}{Dt} = \frac{\partial}{\partial x_j}\left(\frac{\mu_{\text{eff}}}{\sigma_k}\frac{\partial k}{\partial x_j}\right) + G - \rho\epsilon C_d \tag{3}$$

$$\frac{D\epsilon}{Dt} = \frac{\partial}{\partial x_j}\left(\frac{\mu_{\text{eff}}}{\sigma_\epsilon}\frac{\partial \epsilon}{\partial x_j}\right) + C_1\epsilon G/k - C_2\rho\epsilon^2/k \tag{4}$$

G is the production of turbulent energy by working of the mean flow on the turbluent Reynolds stresses and μ_{eff} is the effective viscosity given by

$$\mu_{\text{eff}} = \mu + \mu_t \tag{5}$$

The constants appearing in the above equations are

$C_1 = 1.44$, $C_2 = 1.92$, $\sigma_k = 1$, $\sigma_\epsilon = 1.3$, $C_\mu = 0.09$, and $C_d = 1$

Numerical Solution

Following Patankar (1980), the finite-difference equations are formulated by integrating the above differential equations over rectangular control volumes to obtain the discretized equations in the general form

$$a_p\,\phi_p = \Sigma_j\, a_j\,\phi_j + S_c,$$
$$a_p = \Sigma_j\, a_j - S_p - \rho\,\phi^o\,\delta v/\delta t \tag{6}$$

ϕ is u, v, k, or ϵ; δt is the time-step; δv is the volume of the control volume considered. The source terms S_ϕ are linearized and split into two parts S_c and S_p such that $S_p \le 0$.

Various integrations in the above equations are approximated by interpolating values at the nodal points of the computational grid. For the integration of the convection terms, the hybrid approximation scheme of Gosman and Pon (1974) is used. Several other approximation schemes, such as the polynomial approximation and Patankar's (1980) hybrid scheme, were tested but no significant difference was found either in the accuracy or the computation speed.

Computational Grid. A fully staggered system is employed for the velocities and pressure to avoid the decoupling effects between the velocity and the pressure that are frequently observed with nonstaggered arrangements. On the computational domain two velocity components are stored between the pressure nodes along the gridlines. Values of k and ϵ are stored at the pressure nodes. In the y direction the grid is symmetric around the midline of the channel. More points are concentrated in the vicinity of the walls. A stretching factor for y of 1.1 is used. The grid is designed such that the v node lies on the solid boundary and the u node closest to the surface should be within the inertial sublayer ($20 < y^+ < 400$). In the x direction more nodes are concentrated near the inlet and an expansion factor for the x direction of 1.05 is used. The number of mesh points is 48×48 and the cycle of the wake passing is divided into 36 time steps. Coarser grids were tested and the results showed that the numerical solution is not grid-size dependent.

Boundary Conditions. At the channel inlet the velocity distribution and the turbulence kinetic energy are specified at the inlet. The energy dissipation at the inlet is given by

$$\epsilon = C_\mu\, k^{1.5}/L_c \tag{7}$$

where L_c is a characteristic length scale taken as $0.01\,H$, where H is the channel height. At the exit plane, the flow is assumed parabolic, i.e., independent of the unknown downstream values. Thus, zero-gradient conditions are given at the outlet. The overall mass conservation through the passage is strictly imposed by correcting the outlet velocity components with the calculated velocity profile on the plane next to the inlet and the inlet flow mass during each iteration.

The existence of wall similarity in a constant-stress layer enabled the use of the wall function for the velocity vector to reduce the number of grid points near the wall. At the nodes nearest to the wall, the velocity vector lies on the plane parallel

Nomenclature

C_d = equivalent drag coefficient of the cylinder
H = channel height
k = turbulence kinetic energy
L = channel length
p = pressure
Re = Reynolds number $= \rho U_i\, H/\mu$
t = time
T = passing period $= H/U_{ps}$
U = mean velocity component in the axial direction
u' = turbulent velocity component in the axial direction
U_{ps} = passing speed in the transverse direction
U_* = shear velocity
V = mean velocity component in the transverse direction
v' = turbulent velocity component in the transverse direction
x = longitudinal direction
y = transverse direction
γ_w = wall shear stress
ϵ = turbulence dissipation
μ = molecular viscosity
μ_t = turbulent viscosity
ρ = fluid density

Superscripts

$\bar{}$ = time-averaged over a passing cycle
$*$ = root-mean-square
$'$ = turbulence

Subscripts

c = centerline value

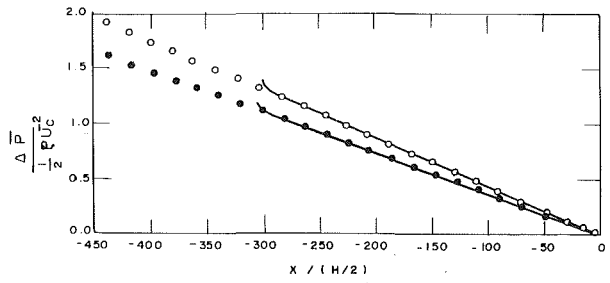

Fig. 2 Calculated pressure distribution along the channel for fully developed flow in comparison with Hussain and Reynolds (1975) data: ——— theory; o o o o experiment at Re = 24; 300; ● ● ● ● experiment at Re = 57,800

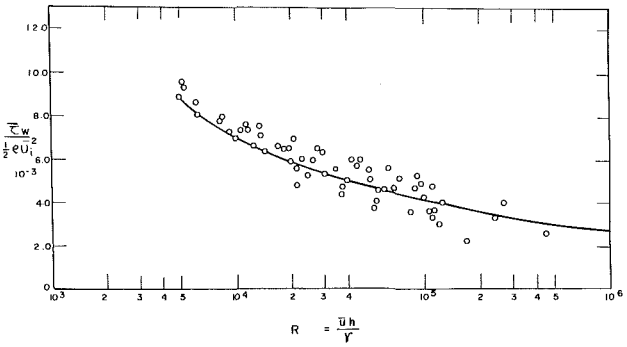

Fig. 3 Dependency of the wall shear stress on Reynolds number for undisturbed flow: ——— theory; o o o o data collected by Dean (1978)

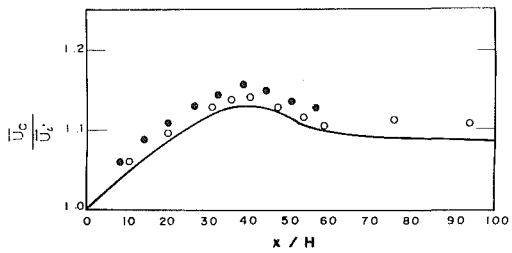

Fig. 4 Calculated centerline velocity along the channel in comparison with experimental data for the undisturbed developing flow: ——— theory; o o o o Dean (1974); ● ● ● ● Comte-Bellot (1963)

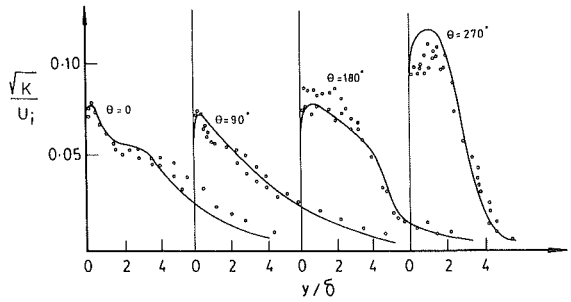

Fig. 5 The turbulence kinetic energy at different parts of the passing cycle in comparison with the data of Cousteix et al. (1977): ——— theory; ● ● ● ● experiment

to the wall and the logarithmic wall function is applied for the velocity. With the assumption of local equilibrium and the logarithmic law, the wall shear stress and the dissipation at the nodes next to the wall are related to the turbulence energy through the logarithmic law as proposed by Gosman and Pon (1974).

Solution Procedure. At each time step the two momentum equations are first solved to get the two velocity components with the assumed pressure field. As the new velocity field obtained with the intermediate pressure field does not satisfy the mass conservation, the pressure field is adjusted toward the solution of the continuity equation as in Patankar (1980). After solving the momentum equations, the turbulence equations are solved with the updated values. Three residuals are calculated: the residual of the continuity equation normalized by the incoming flow rate, the residual of the x-momentum equation normalized by the incoming x momentum, and the residual of the y-momentum equation normalized by the incoming x momentum. When the largest of these quantities is less than the prescribed value, the solution is considered to have converged for this time step. The procedure is then repeated for the following time step. The computation is continued for several cycles until the cycle-to-cycle variations are negligible. Results presented here pertain to the last computed cycle.

Test Cases. In order to verify the model and the calculation procedure, several test cases were considered. First, the undisturbed steady turbulent flow in a channel was considered. The length-to-height ratio was taken as 150 to achieve fully developed flow by the end of the channel. For this test case the flow is taken as uniform at the inlet. The calculated pressure drop along the channel is shown in Fig. 2 in comparison with Hussain and Reynolds' (1975) data for two-dimensional fully developed flow. The figure shows excellent agreement between the theory and the experiment. The pressure variation becomes linear after a short distance from the entrance indicating that tahe pressure reaches an asymptotic state much faster than the mean velocity as observed by Hussain and Reynolds (1975). For the undisturbed fully developed flow the calculated velocity profiles at Re = 20,000 and 40,000 were also found to be in good agreement with the data of Hussain and Reynolds (1975). The velocity defect $(U_c - U)/U_*$ was also compared with Comte-Bellot's (1963) data at the same Reynolds number of 240,000 and was found to be in good agreement. The calculated wall shear stress as a function of the Reynolds number is shown in Fig. 3 in comparison with the data collected by Dean (1978). The figure shows good agreement between theory and experiment. This indicates that the k–ϵ model predicts the wall shear stress quite accurately.

For the developing flow in the entrance of the channel, the calculated variation in the centerline mean velocity is shown in Fig. 4 in comparison with Comte-Bellot's (1963) data. The figure shows that the centerline velocity is slightly underestimated. This can be attributed to the difference between the specified uniform velocity distribution at the inlet and the actual one of the experiment. However, the figure shows that the agreement is generally satisfactory.

To test the code for an unsteady flow case, the flow was computed for a pulsating turbulent flow at the inlet. The numerical results are compared in Fig. 5 with the experimental data of Cousteix et al. (1977) for a turbulent boundary layer with oscillating external flow. The amplitude of oscillation is 37 percent of the time-averaged velocity and Reynolds number is 200,000. Figure 5 shows the turbulence kinetic energy at different parts of the cycle. The figure shows satisfactory agreement between theory and experiment.

Reprsentation of the Rotor Outflow. As discussed before, the rotor-stator configuration is simulated here with the cylinder-channel geometry shown in Fig. 1. This is based on the assumption of equivalent drag, which means that the wake flow behind the cylinder is the same as that behind a rotor blade. The diameter of the cylinder is thus chosen to match the

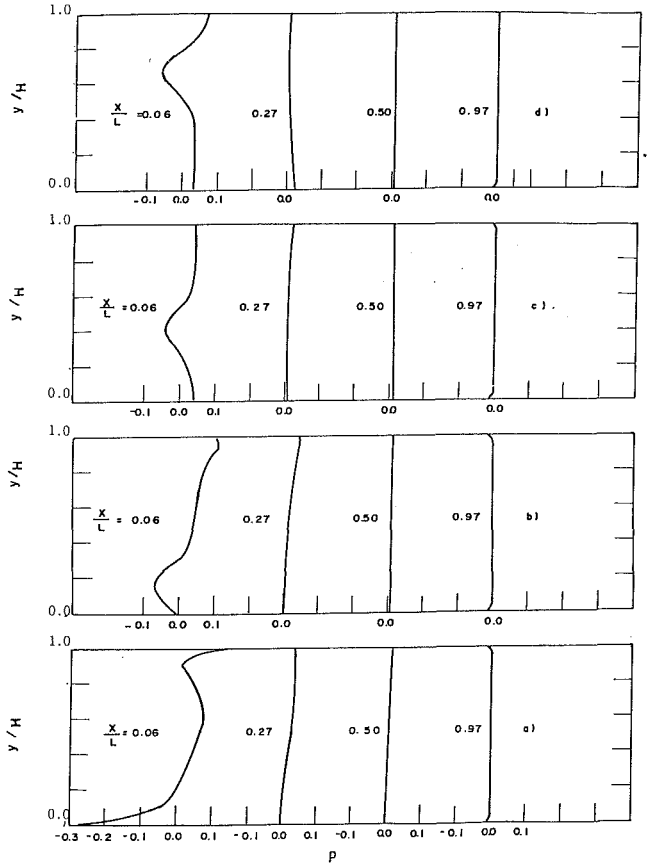

Fig. 6 The instantaneous mean pressure field at different parts of the passing cycle: $U_{ps} = 1.0$, $C_d = 0.001$

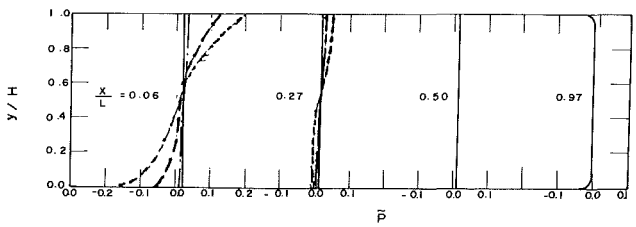

Fig. 7 The time-averaged profile of the pressure along the channel: ——— undisturbed flow; — · — · — · — · — $U_{ps} = 0.5$, $C_d = 0.001$; ——— $U_{ps} = 1.0$, $C_d = 0.001$; · · · · · · · · · · $U_{ps} = 1.0$, $C_d = 0.002$

drag of the rotor blades. At the inlet plane of the channel, time-dependent profiles are prescribed that simulate the wake flow and account for the influence of the spacing, chord length of the rotor, and the drag of the rotor blade. The prescription of the velocity profile at the stator inlet is based on the decay law for the wake flow behind a stationary cylinder, which is given by Reichardt (1950) as

$$u_w/u_{cw} = \exp\{-\ln 2(y_w^2/b^2)\}$$
$$u_{cw}/U_{ow} = 0.939\sqrt{C_d}\sqrt{(x_w/d)}$$
$$b/d = 0.25\sqrt{C_d}\sqrt{(x_w/d)}$$

where the subscript w denotes the coordinate system of a stationary wake. C_d is the drag coefficient; d is the diameter of the cylinder; b is the wake half-width; u_{cw} is the velocity defect; and U_{ow} is the incoming velocity for a stationary cylinder. As the cylinders are moving with respect to the channel with a velocity U_{ps}, the decay laws are transformed into the stationary stator-(x, y) coordinate system. In the results presented here, the spacing between the cylinders is taken equal to the channel height. The wakes are located at a

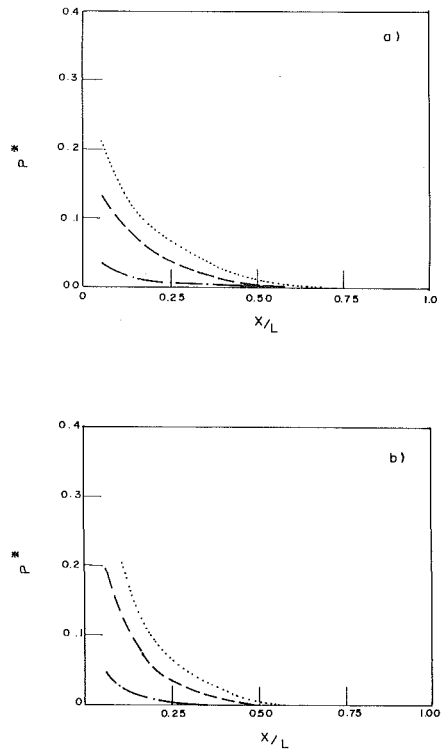

Fig. 8 Root-mean-square values of the pressure oscillations at the walls: (*a*) upper wall, (*b*) lower wall: — · — · — · — · — $U_{ps} = 0.5$, $C_d = 0.001$; ——— $U_{ps} = 1.0$, $C_d = 0.001$; · · · · · · · · · · $U_{ps} = 1.0$, $C_d = 0.002$

distance away from the channel S equal to the channel height, and the diameter of each cylinder is taken as 0.04 H to produce drag coefficients within that of the rotor blades.

Results and Discussion

The effects of wake passing at the entrance of the channel on the pressure field, mean velocity, turbulence, and the wall shear stress will be presented here. The length-to-height ratio of the channel is taken to be 2 for a realistic representation of the stator passage.

Pressure Field. For the wake-passing flow, the instantaneous mean (phase-averaged) pressure field at different parts of the passing cycle is shown in Fig. 6. The figure shows that large pressure variations in the y direction are introduced due to the wake passing. These variations decay rapidly along the channel. By $x/H = 1$ the transverse variation in the pressure becomes negligible.

The time-averaged profile of the pressure distribution along the channel is shown in Fig. 7 for several wake parameters. The figure shows that wake passing increases the pressure at the channel inlet in the direction of the wake traverse. The wake passing produces a transverse velocity component that alters the pressure field through the momentum equations. This asymmetry in the pressure distribution decays rapidly along the channel. At $x > H$, the pressure distribution becomes uniform for the rest of the channel as in the no-wake case.

The root-mean-square values of the periodic oscillations in the pressure field at the lower and upper walls are shown in Fig. 8. The figure shows that the oscillations in the pressure field increase with increasing the passing speed or the wake equivalent drag coefficient. Again the figure shows that by $x = H$ all oscillations in the pressure field are negligible.

The time-averaged pressure distribution along the lower and the upper walls is shown in Fig. 9 for several wake-passing conditions. The figure shows that a large pressure difference

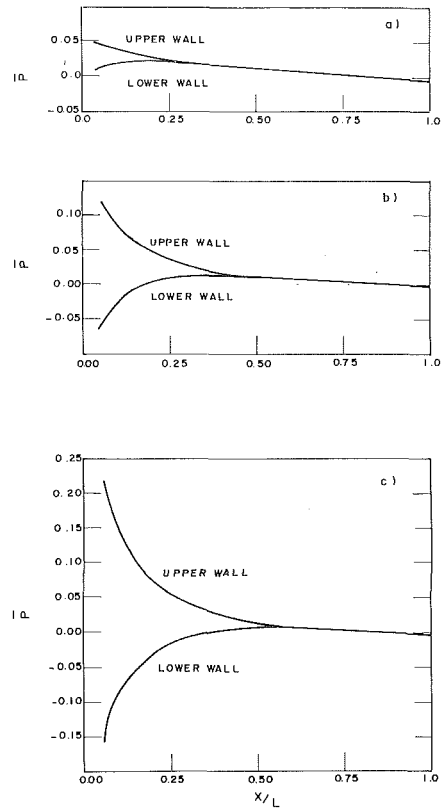

Fig. 9 Time-averaged pressure distribution at the upper and lower walls: (*a*) $U_{ps} = 0.5$, $C_d = 0.001$; (*b*) $U_{ps} = 1.0$, $C_d = 0.001$; (*c*) $U_{ps} = 1.0$, $C_d = 0.002$

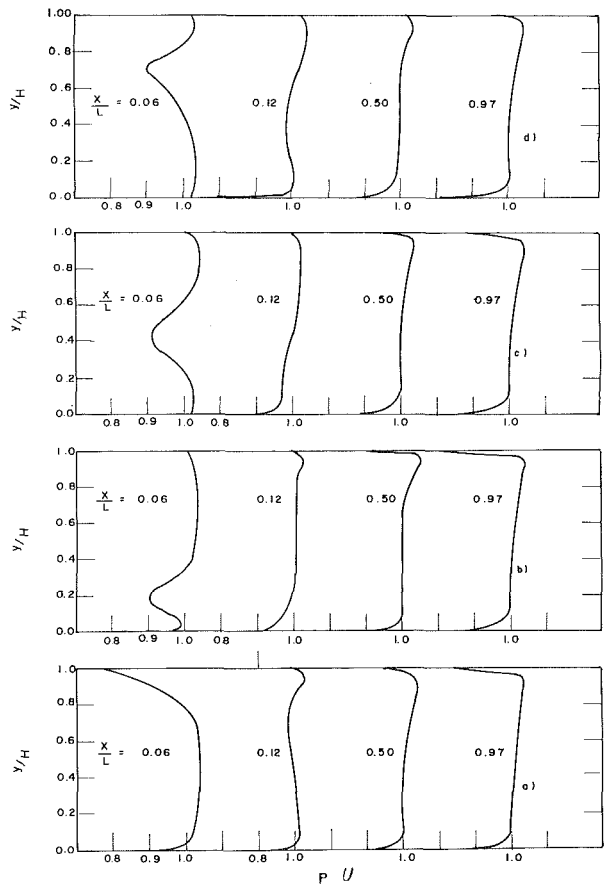

Fig. 10 Mean velocity distribution at different parts of the cycle: $U_{ps} = 1.0$, $C_d = 0.001$: (*a*) $t/T = 0.0$, (*b*) $t/T = 0.25$, (*c*) $t/T = 0.50$, (*d*) $t/T = 0.75$

between the upper and the lower walls is created due to the wake passing. The pressure decreases at the lower wall and increases at tahe upper wall. By $x = H$, the pressure field is restored to its undisturbed case. Taking the pressure distribution shown in the figure as the pressure distribution over a flat plate cascade, the figure shows that the wake-passing can produce an upward lift. For a passing speed of 1.0 and an equivalent drag coefficient of 0.002, the wake passing causes a lift coefficient of approximately 0.06.

Mean Velocity. The mean (phase-averaged) velocity profile at several intervals of the passing cycle is shown in Fig. 10 for several axial locations. Figure 10(*a*) is at $t/T = 0$, which corresponds to the wake located at $y = 0$ (and 1) at the entrance. Figures 10 (*a*, *b*, *c*) are at $t/T = 0.25$, 0.50, and 0.75, which corresponds to wake locations at the inlet of $y = 0.25$, 0.50, and 0.75, respectively. Figure 10 shows that the wake-produced deficit in the mean flow decreases along the channel due to the viscous dissipation effects. At a given time, comparing the locations of the maximum deficit in the mean velocity at different axial locations indicates that there is a time lag in the response of the mean flow to the passing wake. Thus, the location of tahe mean flow deficit at a certain downstream station at a given time is given by the location of the passing wake at a previous time.

Doorly et al.'s (1985) analysis of the convection and spreading of boundary layers on the surface of turbine blades subjected to wake passing has shown that there is a marked delay between the time at which the wake segment traveling in the free stream has cleared a given position on the surface, and the instance when the boundary layer responds. This delay is a consequence of the slow rate at which events propagate in the boundary layer, as Fig. 10 has indicated. The figure also shows that the mean velocity profile is no longer symmetric with respect to the channel centerline. The wake-passing flow

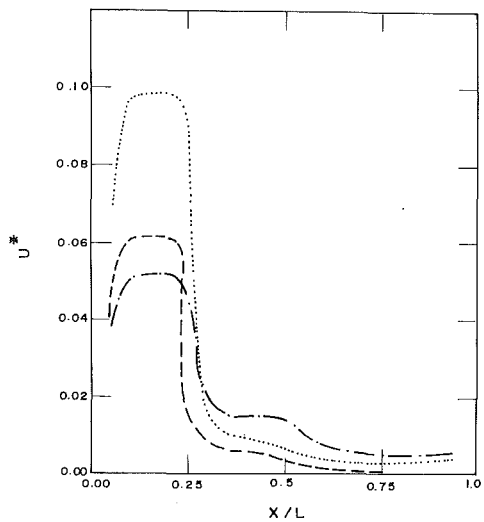

Fig. 11 Root-mean-square values of oscillations in the centerline velocity: — · — · — · — $U_{ps} = 0.5$, $C_d = 0.001$; — — — — $U_{ps} = 1.0$, $C_d = 0.001$; · · · · · · · · · $U_{ps} = 1.0$, $C_d = 0.002$

produces a transverse velocity and a pressure field that distorts the symmetry of the axial velocity distribution.

The root-mean-square values of the oscillations in the centerline mean velocity is shown in Fig. 11 for different wake-passing conditions. The figure shows that the oscillations peak along the channel before they decay. The oscillations continue for larger distances through the channel as compared to the decay of the pressure oscillations. For steady

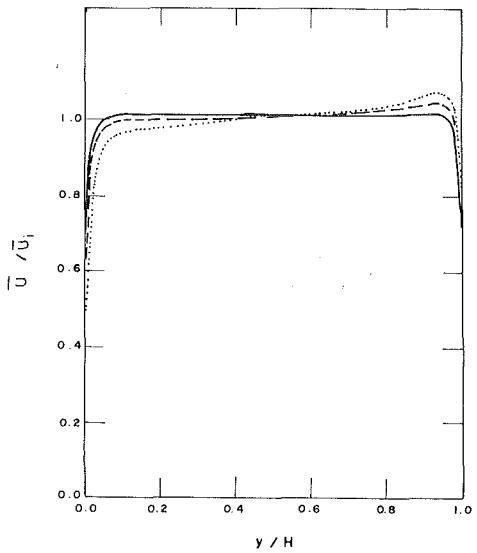

Fig. 12 Time-averaged mean velocity profile at $x/L = 0.097$: ——— undisturbed flow; — — — — — $U_{ps} = 1.0$, $C_d = 0.001$; ····· $U_{ps} = 1.0$, $C_d = 0.002$

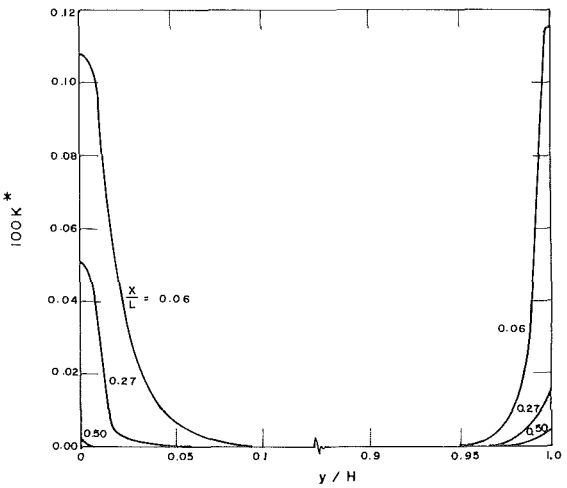

Fig. 13 Root-mean-square of the oscillations in the turbulence energy: $U_{ps} = 1.0$, $C_d = 0.001$

flow in a two-dimensional channel Hussain and Reynolds (1975) have also noticed that the pressure reaches its asymptotic state before the velocity does. The initial oscillations in the mean velocity increase with increasing passing speed; however they decay faster along the channel.

The time-averaged mean velocity profile is shown in Fig. 12 for several wake-passing conditions. The figure shows that the symmetry of the time-averaged mean velocity is distorted due to wake passing. In the present problem, the wake passes from bottom to top. As a result, the time-averaged mean velocity tend to be reduced near the bottom wall and is increased near the top wall.

Turbulence Energy. Figure 13 shows the root-mean-square values of the oscillations in the turbulence energy. The figure shows that the oscillations are restricted to a small layer next to the wall and diminish outside the boundary layer. The time-averaged turbulence energy at $x/L = 0.97$ is shown in Fig. 14. Because of the asymmetry of the mean velocity profile, the mean velocity gradient at the bottom wall is reduced due to wake passing. Therefore, the turbulence energy at the bottom wall is reduced while that at upper wall is increased due to wake passing.

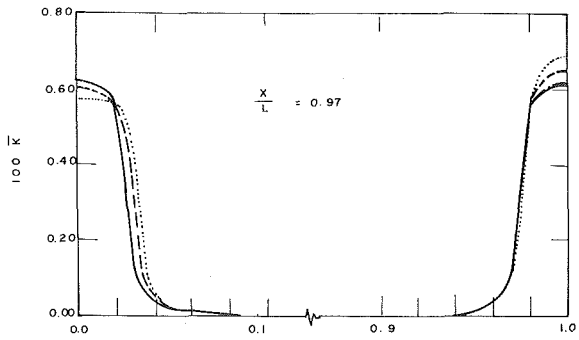

Fig. 14 The time-averaged turbulence kinetic energy at $x/L = 0.97$: ——— undisturbed flow; — · — · — · — · — $U_{ps} = 0.5$, $C_d = 0.001$; — — — — — $U_{ps} = 1.0$, $C_d = 0.001$; ····· $U_{ps} = 1.0$, $C_d = 0.002$

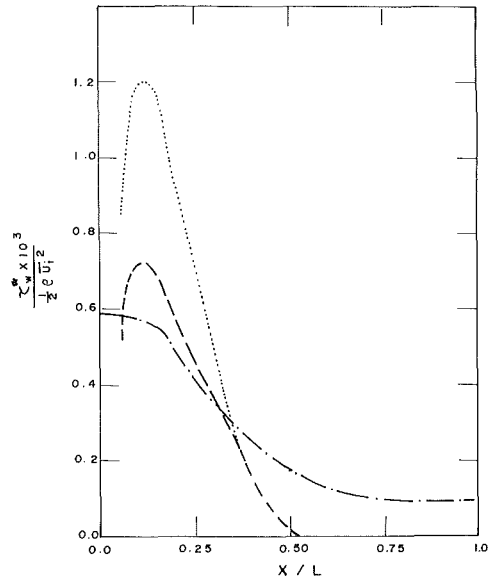

Fig. 15 Root-mean-square values of the oscillations in the wall shear stress at the lower wall: — · — · — · — · — $U_{ps} = 0.5$, $C_d = 0.001$; — — — — — $U_{ps} = 1.0$, $C_d = 0.001$; ····· $U_{ps} = 1.0$, $C_d = 0.002$

Wall Shear Stress Figure 15 shows the distribution of the oscillations in the lower wall shear stress along the channel under several wake conditions. The figure shows that the oscillations initially increase at the channel entrance with increasing passing speed but rapidly decrease along the channel as compared to slower passing wakes.

The time-averaged wall shear stress is shown in Fig. 16 for both the lower and upper walls. The figure shows that the wake passing tends to increase the wall shear stress at the upper wall and to decrease it at the lower wall. The change in the time-averaged wall shear stress due to wake passing can be as much as 12 percent at the end of the channel. The amount of enhancement in the wall shear stress for the upper wall is almost the same as the amount of its reduction at the lower wall. Therefore, it appears that wake passing does not alter the net viscous drag of the blade.

Summary and Conclusions

The purpose of this study was to simulate numerically the unsteady response of stator blades to the wakes of an upstream rotor. The rotor effect is simulated by a train of cylinders of equivalent drag coefficient. The stator flow is replaced by that of a two-dimensional passage. Although the geometry is very simple, the trends predicted by this study can

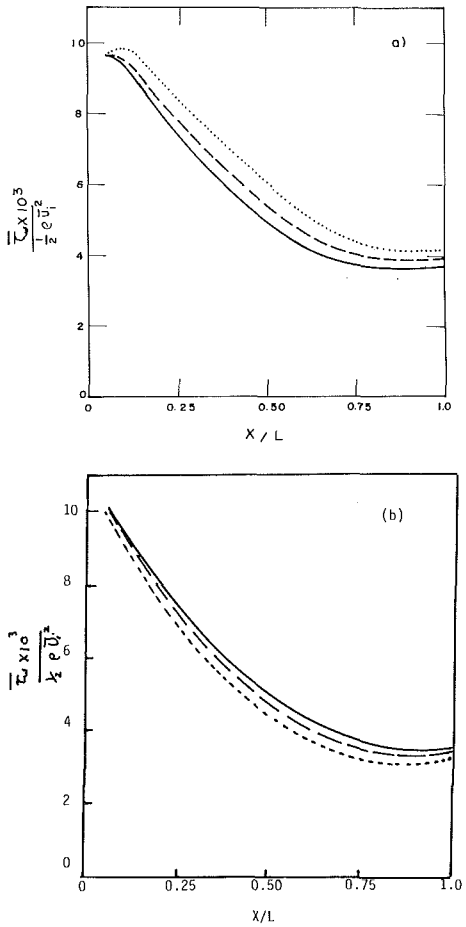

Fig. 16 Effect of wake passing on the time-averaged wall shear stress: (*a*) upper wall, (*b*) lower wall: ———— undisturbed flow; —·—·—·— $U_{ps} = 0.5$, $C_d = 0.001$; — — — — $U_{ps} = 1.0$, $C_d = 0.001$; ····· $U_{ps} = 1.0$, $C_d = 0.002$

be used to interpret results obtained for more complicated geometries. The effects of the rotor-generated wakes that pass at the entrance of the stator can be summarized as follows:

1 The wake passing produces an increase in the time-averaged pressure field in the direction of the rotor traverse. This results in a rotor-induced lift on the stator blades.

2 Within a distance along the stator equal to its height, the rotor's effect on the pressure field of the stator diminishes.

3 Large oscillations in the mean velocities are introduced due to wake passing. These oscillations peak along the channel before they decay. The mean velocity takes larger distances along the channel, as compared with the pressure, to reach its asymptotic state.

4 The rotor-generated wakes increase the wall shear stress on the upper wall (lower surface of the stator blade) and decrease the wall shear stress at the lower wall (upper surface of the stator's blade) by the same amount. Thus, wake passing has a negligible effect on the stator's viscous drag.

5 As the equivalent drag coefficient of the cylinders increases, the oscillations in the velocity, pressure, and turbulence energy increase.

6 Increasing the rotor speed increases the initial oscillations in the flow field but causes its rapid decay along the channel.

References

Comte-Bellot, G., 1963, "Turbulent Flow Between Two Parallel Walls," Ph.D. Thesis (in French), University of Grenoble; English translation ARC 31609, FM4102.

Cousteix, J., Desopper, A., and Houdeville, R., 1977, "Structure and Development of a Turbulent Boundary Layer in Oscillating External Flow," *Turbulent Shear Flow I*, Springer-Verlag, New York, pp. 154–170.

Dean, R. B., 1974, "An Investigation of Shear Layer Interaction in Ducts and Diffusers," Ph.D. Thesis, Imperial College, London University, United Kingdom.

Dean, R. B., 1978, "Reynolds Number Dependence of Skin Friction and Other Bulk Flow Variables in Two-Dimensional and Rectangular Duct Flow," ASME *Journal of Fluids Engineering*, Vol. 109, pp. 215–223.

Doorly, D. J., Oldfield, L. G., and Scrivener, C. T. J., 1985, "Wake-Passing in a Turbine Rotor Cascade," *Heat Transfer and Cooling in Gas Turbines*, AGARD Conference Preprint No. B10, Beljen, Norway, May 6-10.

Dring, R. P., Joslyn, H. D., Hardin, L. W., and Wagner, J. H., 1982, "Turbine Rotor-Stator Interaction," ASME *Journal of Engineering for Power*, Vol. 104, pp. 729–742.

Gosman, A. D., and Pun, W. M., 1974, Lecture Notes on "Computation of Recirculating Flows," Imperial College, London, United Kingdom.

Henderson, R. E., 1978, "The Unsteady Design of Axial-Flow Turbomachines," *Proceedings of the ASME/ASCE Symposium on Fluid Machinery*, Fort Collins, CO, Vol. 2, pp. 91–108.

Hodson, H. P., 1984, "Boundary Layer and Loss Measurements on the Rotor of an Axial-Flow Turbine," ASME *Journal of Engineering for Gas Turbines and Power*, Vol. 106, pp. 391–399.

Hussain, A.K.M.F., and Reynolds, W. C., 1975, "Measurements in Fully Developed Turbulent Channel Flow," ASME *Journal of Fluids Engineering*, Vol. 97, pp. 568–580.

Jones, W. P., and Launder, B. E., 1972, "The Prediction of Laminarization With Two-Equation Model of Turbulence," *Int. J. Heat Mass Transfer*, Vol. 15, pp. 301–314.

Kerrebrock, J. L., and Mikolajczak, A. A., 1970, "Influence of Unsteadiness of the Flow on the Efficiency of Turbine Stages," *Teploenergetika*, Vol. 17, No. 10, pp. 21–23.

Patankar, V. S., 1980, *Numerical Methods in Heat Transfer and Fluid Flow*, McGraw-Hill, New York.

Rai, M. M., 1987, "Navier-Stokes Simulations of Rotor-Stator Interactions Using Patched and Overlaid Grids," *AIAA Journal of Propulsion and Power*, Vol. 3, No. 5, pp. 387–396.

Reichardt, H., 1950, "Gesetzmabigkeiten der freien Turbulenz," *VDI-Forschungsheft*, Vol. 44, VDI-Verlag, Dusseldorf, Federal Republic of Germany.

Walker, G. J., 1974, "The Unsteady Nature of Boundary Layer Transition in Axial-Flow Compressor Blades," ASME Paper No. 74-GT-135.

G. Cerri[1]
Professor,
Department of Mechanics and Aeronautics,
University of Rome,
Rome, Italy

W. F. O'Brien
J. Bernard Jones Professor of Mechanical Engineering,
Virginia Polytechnic Institute and State University,
Blacksburg, VA

Sensitivity Analysis and Optimum Design Method for Reduced Rotor-Stator-Strut Flow Interaction

A potential flow model based on the Douglas–Neumann formulation that can handle interaction problems has been used to analyze the pressure distribution produced by a stator-strut system at the rotor trailing edge. A pressure disturbance sensitivity analysis of some stator and strut parameters was performed and results are discussed in both space and frequency domains. A method for pressure distribution optimization is presented and the outcome analyzed. The optimum stator-strut configuration brings about reduced potential flow disturbances. The pressure wave amplitude produced by the strut is lowered to the same order of magnitude as that induced by the stator alone.

Introduction

In aircraft gas turbine engines flow unsteadiness occurs because of interaction between moving and stationary blade rows as well as struts in the flow field.

Thick struts are often necessary because they not only act as structural elements, but can also allow the passage of oil lines to the main bearings, cabling, and shafts driving the auxiliaries. Struts may be cambered or noncambered according to their lifting or nonlifting potentialities.

For analysis, separating viscous flow effects from potential effects is advisable, since the former are confined to the wake regions.

Viscous effect unsteadiness is connected with rotor blades cutting the wakes coming from the upstream stator vanes and rotor blade wakes cut by the following downstream stator vanes. The wake region moves more slowly than the free stream and is pushed against the blade pressure side, resulting in blade surface pressure fluctuations.

Potential flow effects are related to the inertia of the fluids moving around the bodies, causing flow field perturbations. Such perturbations emanate from the bodies immersed in the flow field and propagate in all directions, particularly downstream and upstream. They may result in large blade surface pressure fluctuations. As the blade rows move through the nonuniformities the unsteady forces due to the above fluctuations excite vibrations, thus noise and fatigue problems must be seriously considered.

Various experiments have shown that potential flow effects are primary sources of unsteady forces acting on the rotor blades. Preisser et al. (1981) and McArdle et al. (1980) tested a JT15D turbofan engine manufactured by Pratt and Whitney Aircraft of Canada Limited. In analyzing the engine noise they recognized that the interaction of the rotor with a six-per-revolution circumferentially varying pressure field (produced by downstream thick struts internal to the engine) appeared to be the dominant blade passage frequency source mechanism at simulated forward speed for high subsonic fan speed. Ho (1981) and Nakamura et al. (1986) have performed related experiments.

The first systematic experiment related to this observation was performed by O'Brien et al. (1983) at the Virginia Polytechnic Institute and State University, from 1982 to 1983. Experiments were run on a research compressor with a 37-vane stator row. A removable five-strut cascade simulating a strut row could be installed at various axial positions downstream of the stator blade trailing edge.

During the experiments, dynamic pressures at various points on the rotor blade surfaces were measured. These experiments clearly pointed out the importance of the potential flow interaction between rotor, stator, and struts in the production of rotor blade pressure fluctuations. Further experiments made by Woodward and Balombin (1984) confirmed the previous results.

There have been only a few investigations dealing with design of a stator-strut system able to produce small rotor pressure fluctuations.

Rubbert et al. (1972) analyzed a rotor-stator-strut system by considering a model of potential flow around a thick strut. The stator was considered to be made up of thin blades with an assumed vorticity distribution shape along the camber line. Stator blade camber angles were considered as variable to shield the rotor from the thick strut pressure disturbance. This approach, however, does not always appear practical from the manufacturing point of view since it involves building stator cascades having blade groups with various camber angles. Moreover, since the stator contour design is based on inviscid flow analysis, it may not be physically possible to turn the flow through the angles resulting from the analysis because flow separation could occur.

[1] Visiting Professor at the Mechanical Engineering Department, Virginia Polytechnic Institute and State University, Blacksburg, VA.

Contributed by the International Gas Turbine Institute and presented at the 33rd International Gas Turbine and Aeroengine Congress and Exhibition, Amsterdam, The Netherlands, June 5–9, 1988. Manuscript received by the International Gas Turbine Institute September 15, 1987. Paper No. 88-GT-310.

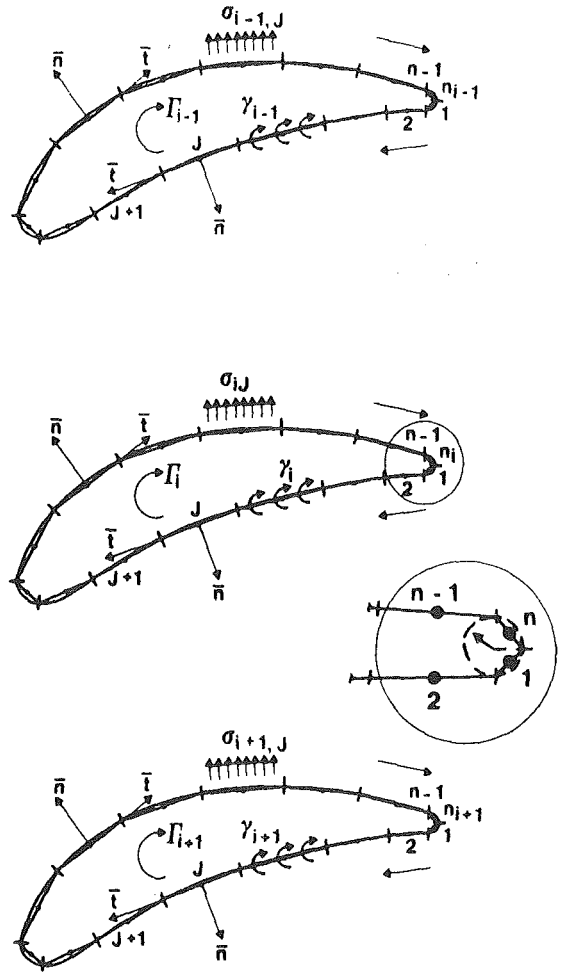

Fig. 1 Airfoil infinite cascade model

Yokoi et al. (1981) analyzed the stator-strut system as made up of thick bodies (the struts) and straight one-dimensional diffusers (the stator vanes). These diffusers broadcast strut pressure disturbances upstream. The stator setting angles in the neighborhood of the struts were considered as relevant parameters. Ordered angle changes from zero (far from the strut) to about 5 deg (close to the strut) were taken into consideration.

In all of the above references, no special criterion was adopted for selecting the final parameter (camber or stagger angle) set.

The aim of the present study has been to perform a sensitivity analysis on the effect of some stator blade and strut parameters on the circumferential pressure distribution as well as to find an automatic procedure to determine the optimum setting for such parameters to minimize the pressure fluctuation at the rotor trailing edge axial location. The method described assumes incompressible flow and considers the flow downstream of the rotor trailing edge plane.

The compressor under analysis is that used by O'Brien et al. (1983).

Computational Model

The two-dimensional flow model adopted for the present analysis is based on the classical Douglas–Neumann singularity superposition method (Giesing, 1964; Barber and Weingold, 1978).

The flow field described in terms of velocity potential is defined as a solution of the Laplace equation

$$\nabla^2\phi = 0 \tag{1}$$

The solution for equation (1), for a general stator-strut system, is constructed by using the distributed singularity method. This method utilizes the linearity of the governing equation to get a solution by superimposing elementary solutions, each satisfying equation (1), and all the solutions together satisfying the boundary conditions. As shown in Fig. 1, the contour of each body (I) immersed in the flow field is broken into n_I panels. On each panel (J), constant density sources of strength σ_{IJ} are distributed together with a constant vorticity density γ_I.

An infinite body cascade (whose periodic length is SP) is considered and the velocity induced at a Jth panel midpoint by unitary strength sources of constant density distributed on the kth panel is:

$$W_{Jk} = \frac{e^{-i\beta_k}}{2\pi} \ln \frac{\sinh\left[\frac{\pi}{SP}(z_J - C_{1k})\right]}{\sinh\left[\frac{\pi}{SP}(z_J - C_{2k})\right]} \tag{2}$$

with

$$z = x + iy \tag{3}$$

being the complex vector of the Jth panel midpoint (x is the axial direction and y is the circumferential direction), C_{1k} and C_{2k} being the complex vectors of the two endpoints of the kth panel and β_k being the slope of the panel with respect to the x axis.

The complex velocity component normal to the panel at its midpoint is

$$A_{Jk} = W_{Jk} \cdot n_J \tag{4}$$

and the normal velocity component due to the source distribution is

$$A^S_{Jk} = IM(A_{Jk}) \tag{5}$$

while that due to the unitary density strength vortex distribution is

$$A^V_{Jk} = RE(A_{Jk}) \tag{6}$$

Three onset flows are considered:

1. A uniform flow orthogonal to the cascade (angle of attack $\alpha = 0$ deg with respect to the axial direction), which has a normal velocity component at the Jth panel midpoint

$$W_\infty \cdot n_J = -\sin\beta_J \tag{7}$$

2. A uniform flow parallel to the cascade ($\alpha = 90$ deg) causing a normal velocity component at the Jth panel midpoint

$$W_\infty \cdot n_J = \cos\beta_J \tag{8}$$

3. A nonuniform flow due to the circulation Γ_n around the nth airfoil whose perimeter is P_n produces a normal velocity component at the Jth panel midpoint

$$W_\infty \cdot n_J = \frac{\Gamma_n}{P_n} \sum_{k=1}^{N_n} A^v_{Jk} \tag{9}$$

The overall solution is constructed by superimposing the solutions from the distribution on each airfoil and from the three above onset flows; then boundary conditions are imposed.

The boundary conditions stipulate that the body surface be impermeable (so the velocity component normal to each panel midpoint must be zero) and that the Kutta condition be applied. The above leads to the following equation set:

$$|A^S_{Jk}|\ \{s_k\} = \{-W_\infty \cdot n_J\} \tag{10}$$

By substituting for the second member array with equations (7), (8), and (9), the final equation set is obtained.

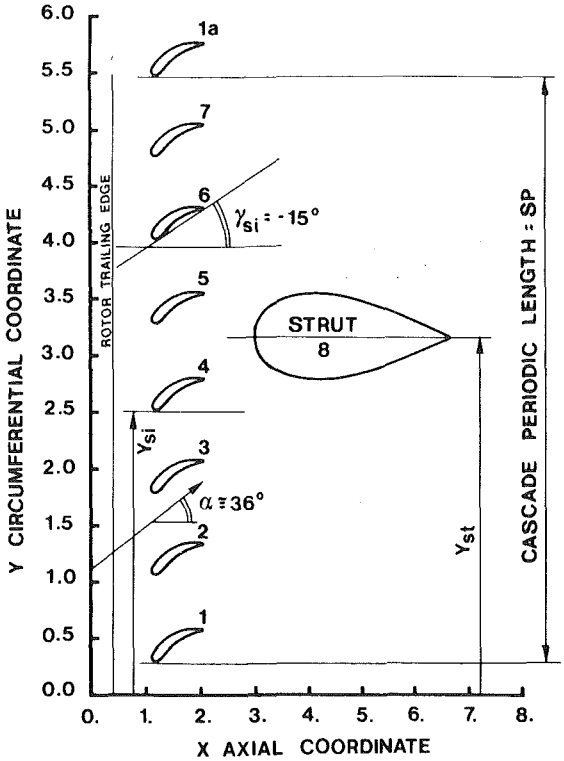

Fig. 2 Periodic segment of stator and strut cascade system (coordinates are nondimensionalized with respect to the stator blade chord)

σ_k and Γ_n are unknown. The base solution is obtained putting $\Gamma_n = 1$ and the actual Γ_n magnitude is found by the Kutta condition, i.e., the tangential velocity component at the body trailing edge must be zero. The Kutta condition, for the assumed round trailing edges, is imposed by constructing two segments bisecting the angle from the trailing edge circle tangency points on both upper and lower surfaces, as shown in Fig. 1.

The solution is obtained by evaluating the violation of the Kutta condition by the difference of the first and last panel midpoint velocity

$$W_t(1) - W_t(N) = \Delta V \tag{11}$$

For the cascade m, the Kutta condition violation is

ΔV_m^0 due to the the $\alpha = 0$ deg onset flow

ΔV_m^{90} due to the $\alpha = 90$ deg onset flow

ΔV_m^n due to the circulation on cascade n

So for each airfoil cascade and for the average flow

$$\Delta V_m^0 U \cos\alpha + \Delta_m^{90} U \sin\alpha + \sum_{n=1}^{Nc} \Delta V_m^n \Gamma_n = 0 \tag{12}$$

Nc is the number of infinite body cascades, U is the average of upstream and downstream velocity, and α is the angle of the average velocity vector with respect to the axial (x) direction.

The Kutta condition equation set is

$$|\Delta V_m^n| \{\Gamma_n\} = U\{\Delta V_m^0 \cos\alpha + \Delta V_m^{90} \sin\alpha\} \tag{13}$$

If α and U are input, the solution of the above equation set is performed directly. If α is not given, iterations are needed depending on the input. The input can be the angle of attack α_i, the lift coefficient Cl, or the turning angle

$$\Delta\alpha = \alpha_i - \alpha_0 \tag{14}$$

This model allows multiple cascade analysis. Each cascade can have any arbitrary blade geometry (profile, camber line, stagger angle), can be located at any position, and can be lifting or nonlifting.

Restrictions are that the cascades must have the same spacing, and may not move relative to each other. This means that a proper periodicity has to be recognized in the stator-strut system and the rotor cannot be taken into account.

The solution is expressed as a static pressure coefficient

$$C_p = \frac{p_{si} - p_{s\infty}}{\frac{1}{2}\rho U^2} = 1 - \left(\frac{W_1}{U}\right)^2 \tag{15}$$

and is calculated using the velocity distribution at any set of off-body points. The model allows the calculation of circumferential static pressure at the rotor trailing edge axial location. Thus, the fluctuating pressure forces acting on the rotor blades are not defined, but if the circumferential pressure disturbance produced by the stator-strut system is reduced the fluctuating forces should be also.

For an observer on the rotor the circumferential static pressure variation at the trailing edge appears as a periodic disturbance with fundamental wavelength equal to the cascade spacing. In general, this periodic signal will contain energy over a range of frequencies. If the peak disturbance frequencies in the stator-strut pressure disturbance spectrum were far from any resonance, there would probably not be any dangerous conditions. However, the potential for generation of acoustic modes would still exist.

Model Application on a Compressor Stator-Strut System

The model discussed in the previous section can handle interaction problems of two or more cascades, so it has been used to analyze the disturbances produced at the rotor trailing edge axial location by a stator-strut cascade system whose geometric arrangement (i.e., camber line, blade chord, and thickness) is the same as in O'Brien's experimental compressor (O'Brien et al., 1983). Since the stator was made up of 37 blades and there were five struts, the system periodicity has been reduced to seven stator blades and one strut (Fig. 2) to get an acceptable computer memory occupancy.

The reference stator-strut system was characterized by:

- Seven stator blades. Each stator blade is the first blade of an infinite cascade whose spacing is SP. The blade chord is Cs, the stagger angle $\gamma_{si} = -15$ deg, and the stator blade leading edges are located 0.75 Cs downstream of the rotor trailing edge line;
- One strut (the eighth cascade) located 3 Cs downstream of the rotor trailing edges. The strut stagger angle $\gamma_{st} = 0$ deg;
- The incoming flow angle $\alpha \sim 36$ deg (about zero incidence for the stator camber present).

The study has been performed to recognize how the geometric parameters (i.e., six circumferential coordinates of the stator blades $\{y_{si}\}_{i=2,\ldots,7}$; seven stator blade stagger angles $\{\gamma_{si}\}_{i=1,2,\ldots,7}$; one circumferential strut position y_{st}) influence the pressure distribution given by the pressure coefficient at the rotor trailing edge line. Analysis of the pressure coefficient in the frequency domain has also been performed.

Cp(y) Distribution Sensitivity Analysis

A first investigation involved the strut circumferential coordinate variation from the third to the fourth stator trailing edge positions (y_{st3} to y_{st4}). Figure 3 shows the Cp distribution. Curve #0 is for the stator alone set at the reference stagger and with the strut removed; Fig. 4 shows the corresponding power spectrum; only mode $k = 35$ (related to the stator blades) exists.

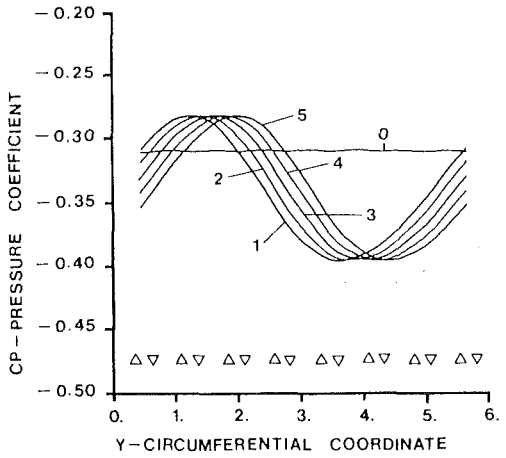

Fig. 3 Strut position (y_{st}) influence on pressure distribution

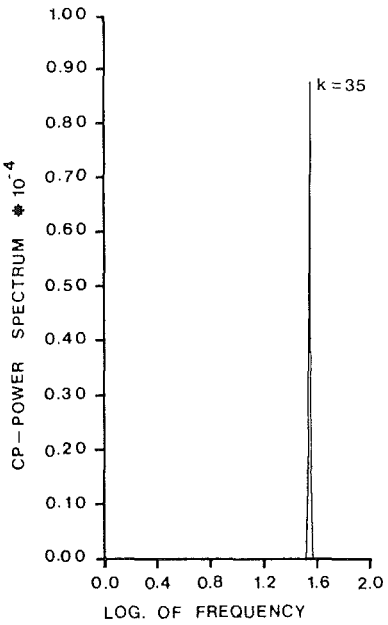

Fig. 4 Pressure coefficient power spectrum due to the stator blades set at reference condition, $\gamma_{si} = -15$ deg, when the strut is removed

Curves # 1–5 of Fig. 3 include the effect of the strut for equally spaced strut positions from y_{st3} to y_{st4}. The spatial Cp amplitude disturbance introduced by the strut is three orders of magnitude higher than than that introduced by the stator alone. The strut circumferential position (y_{st}) does not substantially alter the pressure wave amplitude but does influence the phase. This is very important when dealing with optimization problems as interference among the components of the $Cp(y)$ wave occurs.

Figure 5 shows the power spectrum of such a $Cp(y)$ distribution; peaks of modes $k=5$ and 10 are seen related to the strut. The power spectrum peak of mode $k = 5$ (due to the strut) is about 7×10^3 times that due to the stator alone (strut removed), mode $k=35$ of Fig. 4. The circumferential positions of the stator blades have almost no influence in the $Cp(y)$ distribution; thus, these parameters $\{y_{si}\}_{i=2,\ldots,7}$ have not been taken into consideration in the optimization study.

To investigate the influence on the $Cp(y)$ distribution of the stator blade stagger angles $\{\gamma_{si}\}$, the strut has been located at the middle spacing between the fourth and fifth stator blade trailing edges (see Fig. 2).

Figure 6(*a*) shows the influence of changing the fourth

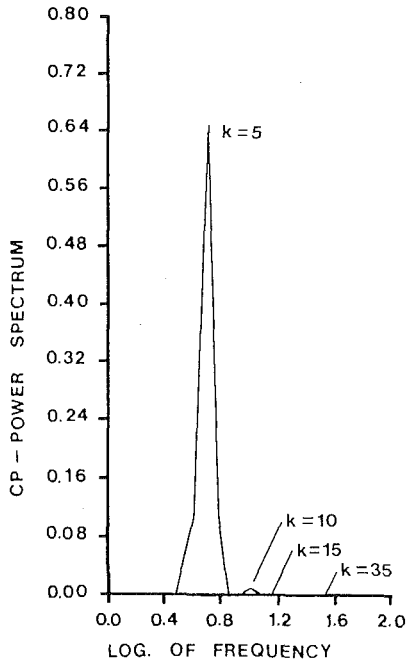

Fig. 5 *Cp* power spectrum due to the stator-strut system. Stator blades set at the reference condition $\gamma_{si} = -15$ deg.

stator blade stagger angle with a $\Delta\gamma = 2$ deg, both clockwise and conterclockwise. Figure 6(*b*) illustrates the $Cp(y)$ distribution with the third stator blade set at different stagger angles.

Figure 6(*c*) shows the effect on $Cp(y)$ of setting the second and third blades at different angles. Finally, Fig. 6(*d*) gives two $Cp(y)$ distributions connected with two different arrays ($\{\gamma_{si}\}_{i=1,2,\ldots,7}$) of the stator blade stagger angles.

Looking at the phenomena analyzed in the frequency domain, the power spectrum given in Fig. 7 is for the stator row alone when the fourth stator blade angle is set at $\gamma_{s4} = -12$ deg. Mode $k = 5$ is amplified at values comparable to those introduced by the strut as seen in Fig. 5.

Optimization

The above results show the possibility of finding a stator-strut configuration with minimum $Cp(y)$ disturbance. This can be achieved by an optimization technique, which is an attempt to arrive at the best solution of a given problem as judged by a testing criterion-objective function, whose values are minimized or maximized by the technique while also satisfying the constraints on the system.

The mathematical expression is

$$\text{minimize } TG = F(P) \tag{16}$$

$$\text{subject to } h_i(P) < 0 \text{ for } 1 = 1,2,\ldots m \tag{17}$$

The vector P contains the variables to be optimized to minimize the objective function $F(P)$ while satisfying constraints $h_i(P)$. $F(P)$ can be a linear or nonlinear function of the variables.

For the problem under analysis, the seven stator blade stagger angles $\{\gamma_{si}\}_{i=1,2,\ldots,7}$ and the strut position y_{st} have been chosen as optimizing variables according to the previous $Cp(y)$ sensitivity study. Constraints have been selected for the stagger angles $\gamma_{max} = -11$ deg and $\gamma_{min} = -19$ deg in order to avoid excessive lowering of the cascade aerodynamic performance. In fact, stagger angle changes of more than 4 deg should require the redesigning of the blade camber lines and blade profiles (i.e., thickness along the camber line), which is quite costly.

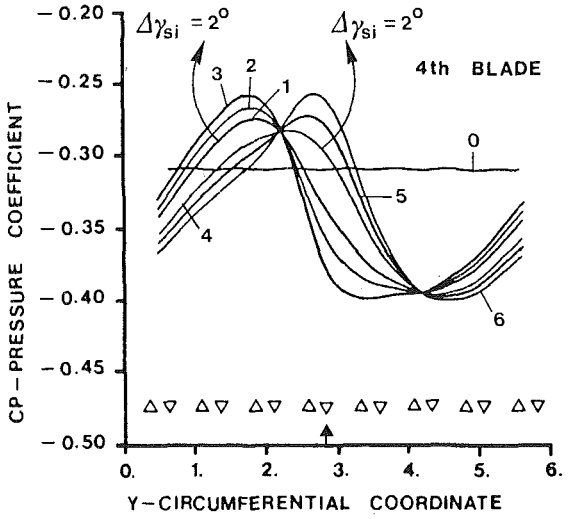

a) 4th blade stagger angle influence

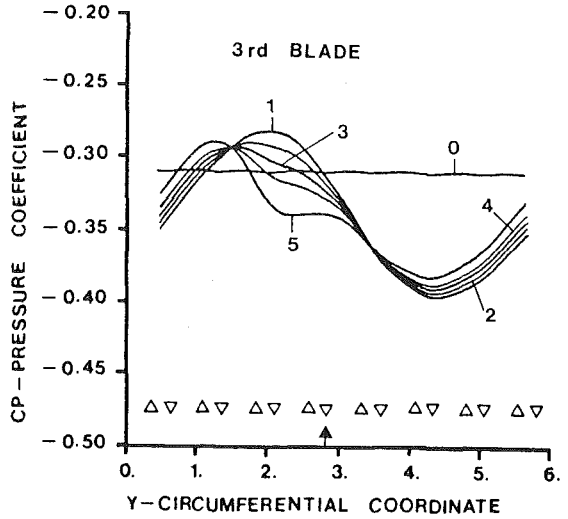

CURVE	no	1	2	3	4	5
3rd SBA	dgs	-15	-14	-13	-12	-10

b) 3rd blade stagger angle influence

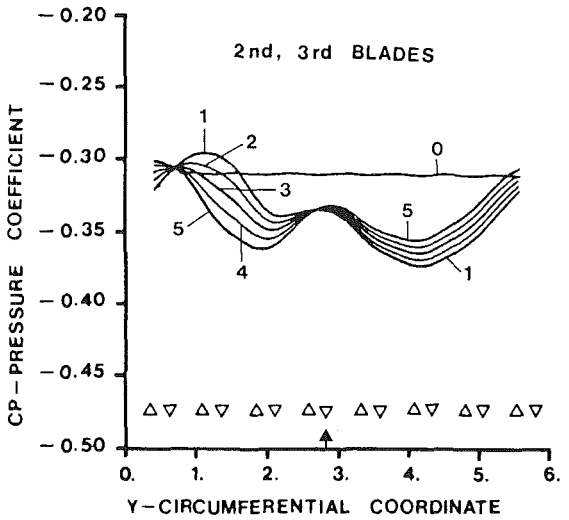

CURVE	1	2	3	4	5
2nd SBA degs	-14	-13	-12	-11	-10
3rd SBA	-10	-10	-10	-10	-10

c) 2nd and 3rd blade stagger angle influence

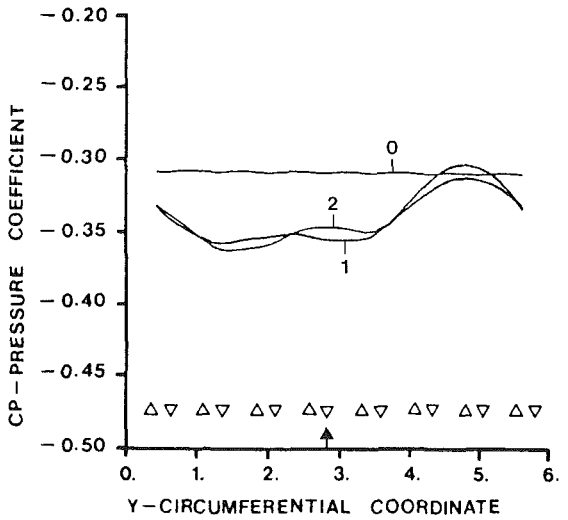

Stator blade no.	1	2	3	4	5	6	7
Curve 1	-13	-12	-13	-15	-17	-19	-17
Curve 2	-13	-11	-12	-15	-16	-18	-16

d) Stator blade angle setting influence

Fig. 6 Pressure distribution due to the stator-strut system when the stator blades are set at different stagger angles. ↑ strut circumferential position. Curve No. 0 - stator set at γ_{si}.

The circumferential strut position constants are the fourth and fifth stator blade trailing edge coordinates

$$y_{s4} < y_{st} < y_{s5} \tag{18}$$

Two different objective functions have been used:

(*a*) an objective function related to amplitude of the $Cp(y)$ wave

$$TG1 = Cp_{\max} - Cp_{\min} \tag{19}$$

has been named *amplitude function*.

(*b*) an objective function related to the area of the Cp wave

$$TG2 = \int_0^{SP} (Cp - Cp_{\min})\, dy \tag{20}$$

which has been named *area function*.

This second objective function also accounts for the time during which the pressure disturbance acts on the rotor. In this way, high-amplitude and short-time duration peaks have a reduced weight.

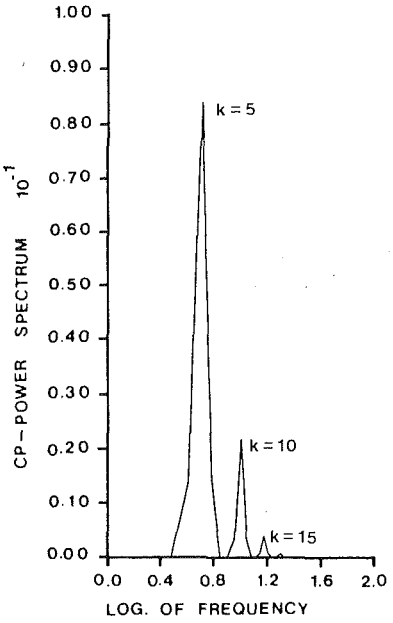

Fig. 7 Pressure coefficient power spectrum due to the stator alone (strut removed) when the fourth blade is set at $\gamma_{s4} = -12$ deg stagger angle

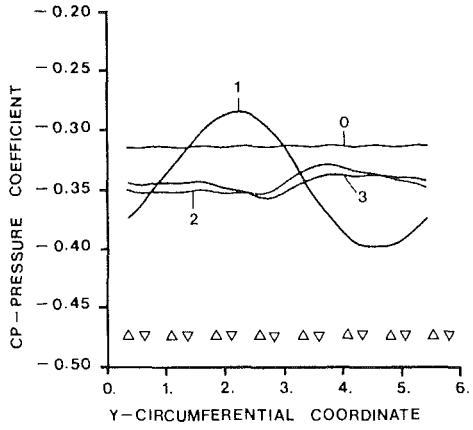

Fig. 8 Pressure distributions due to: (0) stator alone (strut removed), $\gamma_{si} = -15$ deg; (1) stator-strut system at reference conditions; (2) optimum *TG*1; (3) optimum *TG*2

Optimization calculations have been performed by using a computer code based on a quasi-Newton method. The method is based on the idea of performing iterations by using gradient vector (g) and Hessian matrix (which contains second-order partial derivatives). The parameter set for the $(k+1)$th iteration is defined according to the following equation:

$$p_{k+1} = p_k - a_k H_k g_k \tag{21}$$

where H_k is the kth approximation to the inverse H of the Hessian matrix, a_k is a positive scalar, and g_k is the gradient vector.

The matrix H_k is an operator that turns the location direction of the steepest descent $(-g_k)$ at p_k into the true direction from p_k to the center of the ellipsoids, which approximates the objective function.

According to the Fletcher-Powell technique (Daniels, 1978; Gill et al., 1981) the strategy of the method is that a sequence of positive symmetric matrices H_k is generated and used to define the search direction $(-H_k g_k)$. At the first iteration the H_k matrix is initialized as identity matrix ($H_k = I$). In this way, the first step direction coincides with the steepest descent.

For the following iterations H_k is updated using the Davidson-Fletcher-Powell formula, which approximates the objective function with a quadratic one.

To prevent numerical inaccuracies in H_k from accumulating, H_k is reinitialized and set equal to the identity matrix every five iterations by the numerical code.

The steplength parameter a_k is established according to Fletcher's original suggestion.

Since the above method is for the unconstrained parameter optimization problem, to solve the present constrained parameter optimization problem the following parameter transformation is adopted:

$$p_i = l_i + (u_i - l_i) \sin^2 t_i \tag{22}$$

where l_i and u_i are the lower and upper constraints for p_i. In this way the new parameter t_i is unconstrained while $l_i < p_i < u_i$.

In the numerical code it is not necessary to furnish the first derivative function; it is evaluated numerically.

In order to increase the probability that the minimum reached is not a local minimum, but really the global one, a certain number of initial search points are randomly scattered in the domain of definition of the objective function.

Optimization Results

An initial analysis was carried out to find the stator blade stagger angle optimum set $\{\bar{\gamma}_{si}\}$ and the circumferential strut location $\bar{y}_{st}$ using both *TG*1 and *TG*2. The two optimum parameter sets differ only in the optimum value for $\bar{y}_{st}$.

Optimum *TG*1 and *TG*2 angles are

Blade i	1	2	3	4	5	6	7
Angle $\bar{\gamma}_{si}$	−14	−13	−12	−12,5	−17	−17	−16

Optimum *TG*1 $y_{st} = 3.22Cs$
Optimum *TG*2 $y_{st} = 3.35Cs$

where Cs is the chord of the stator row airfoils used as a reference quantity.

The two resulting $Cp(y)$ distributions are shown in Fig. 8, together with that for the stator alone (without strut) and with the reference geometry $Cp(y)$ distribution.

The function

$$Cp(y) = F(\{\gamma_{si}\}, y_{st}) \tag{23}$$

has been investigated in order better to understand the role of y_{st}.

If we locate the strut at different coordinates between the fourth and fifth stator blade trailing edges *TG*1 and *TG*2 assume the values shown in Fig. 9. It is shown that *TG*1 and *TG*2 touch the minimum for two different strut locations (i.e., $\bar{y}_{st} = 3.22\ Cs$ for optimum *TG*1 and $\bar{y}_{st} = 3.35\ Cs$ for optimum *TG*2). Strut position plays an important role by shifting the phase of the harmonics.

In Fig. 10, the $Cp(y)$ harmonic amplitude and phase are given for the reference geometry $\{\gamma_{si}\} = -15$ deg and $y_{st} = 3.18\ Cs$ (midway between the fourth and fifth stator blade trailing edges). In Fig. 11 the $Cp(y)$ harmonic amplitude and phase are given for the optimum angle set $\{\gamma_{st}\}$ when the strut is removed. It should be pointed out that the amplitude of the mode $k = 5$ is on the same order for (interfering) $Cp(y)$ distributions caused by the optimum stagger angle set. The two modes are almost opposite in phase and the disturbance reduction mechanism is seen to be primarily wave interference. Shifting the strut position changes the disturbance by this same mechanism.

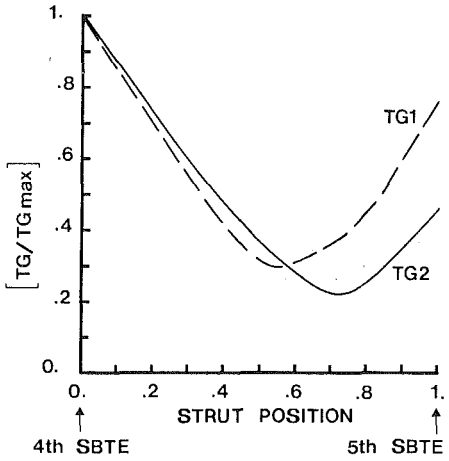

Fig. 9 Influence of strut circumferential position on *TG1* and *TG2* objective functions

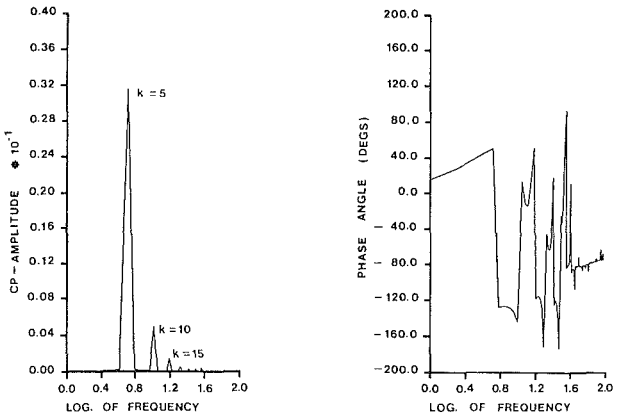

Fig. 10 Pressure coefficient harmonic amplitude and phase angle for stator blades set at design stagger angle ($\gamma_{Si} = -15$ deg) and strut circumferential position at midway between fourth and fifth trailing edges

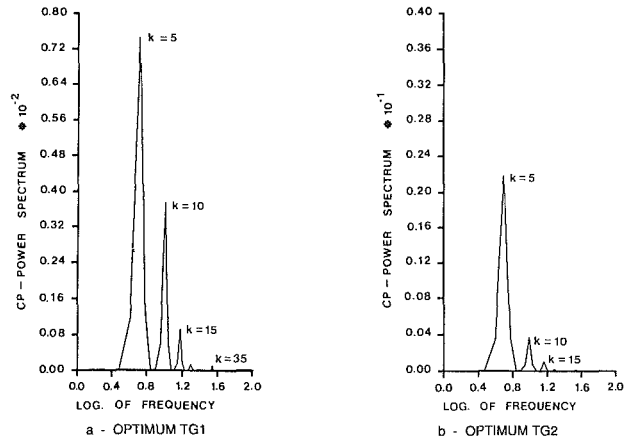

Fig. 11 Pressure coefficient harmonic amplitude and phase angle for the stator alone (strut removed) when blades are set at the optimum objective function angle array

Figure 12 gives the power spectrum for the optimum *TG1* (Fig. 12*a*) and *TG2* (Fig. 12*b*) $Cp(y)$ distributions. Noteworthy results are that the amplitude of the mode $k = 5$ is reduced to 3.4 percent of the reference geometry by adopting the optimum *TG2* strut position ($\bar{y}_{st} = 3.22$ *Cs*). Figure 12 also shows that the amplitude of the $Cp(y)$ disturbance is reduced to the same order as that produced by the stator with the strut removed ($k = 35$).

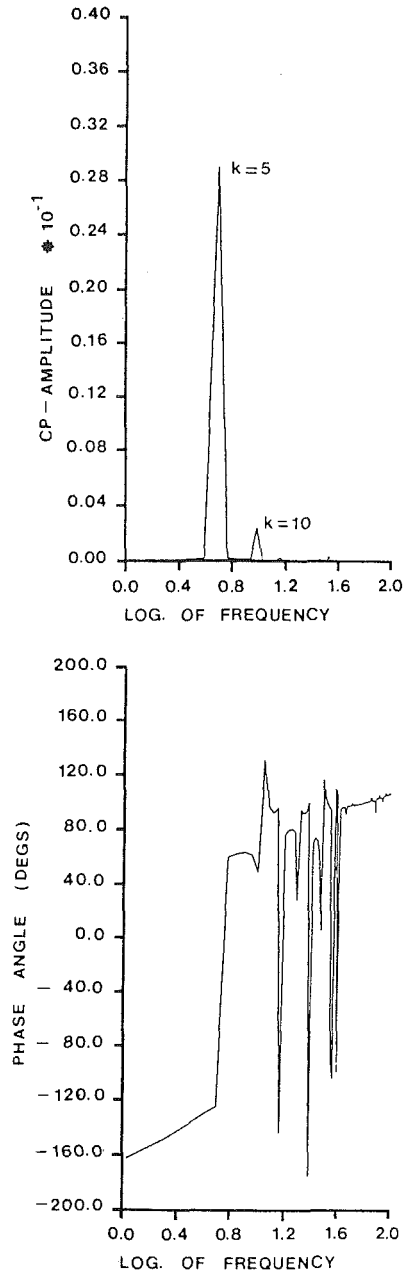

Fig. 12 Pressure distribution power spectra due to the stator-strut system at the optimum *TG1* and *TG2* geometric configurations

Conclusion

The pressure distribution analysis at the rotor trailing edge axial location has demonstrated how it is possible to produce interference phenomena among *Cp* harmonics by setting some stator strut geometric parameters.

The sensitivity $Cp(y)$ study has pointed out relevant parameters for $Cp(y)$ optimization.

The main results can be summarized in the following statements:

1. It is possible to achieve a quite flat $Cp(y)$ distribution of nearly the same disturbance level as that produced by a stator row alone using appropriate stator blade stagger angle settings;

2. optimized $Cp(y)$ distributions can be achieved by changing the original constant stagger angles of stator blades having all the same camber line and profile by 2–3 deg. Aerodynamic blade performance would be only slightly affected;

3. it appears that an optimum stagger angle $\{\gamma_{si}\}$ distribution is not subject to any particular rule. Probably there are many satisfactory solutions;

4. the analysis in the frequency domain suggests that an optimization criterion based on depressing dangerous frequencies can be adopted.

Acknowledgments

This work has been supported by the MPI (Ministry of Education) and CNR (National Research Committee), Italy, under NATO Senior Fellowships scheme and carried out at the Mechanical Engineering Department of Virginia Polytechnic Institute and State University, Blacksburg, VA, Dr. R. A. Comparin, Head.

References

Barber, T. J., and Weingold, H. D., 1978, "Vibration Forcing Functions Produced by Nonuniform Cascades," ASME *Journal of Engineering for Power*, Vol. 100, No. 1, pp. 82–88.

Daniels, R. W., 1978, *An Introduction to Numerical Methods and Optimization Techniques*, Elsevier North-Holland, New York.

Giesing, J. P., 1964, "Extension of the Douglas–Neumann Program to Problems of Lifting Infinite Cascades," Douglas Aircraft Report, LB 31653.

Gill, P. E., Murray, W., and Wright, M. H., 1981, *Practical Optimization*, Academic Press, London.

Ho, P. Y., 1981, "The Effect of Vane-Frame Design on Rotor-Stator Interaction Noise," AIAA, Paper No. 81–2034.

McArdle, J. B., Jones, W. L., Heidelberg, L. J., and Homyak, L., 1980, "Comparison of Several Inflow Control Devices for Flight Simulation of Fan Tone Noise Using a JT15D-1 Engine," AIAA Paper No. 80-1025.

Nakamura, Y., Isomura, K., and Kodama, H., 1986, "Rotor-Strut Interaction Noise of a Model Fan," AIAA Paper No. 86–1971.

O'Brien, W. F., Jr., Reimers, S. L., and Richardson, S. W., 1983, "Interaction of Fan Rotor Flow With Downstream Struts," AIAA Paper No. 83–0682.

Preisser, J. S., Schoenster, J. A., Golub, R. A., and Horne, C., 1981, "Unsteady Fan Blade Pressure and Acoustic Radiation From a JT15D-1 Turbofan Engine at Simulated Forward Speed," AIAA Paper No. 81–0096.

Rubbert, P. E., Boctor, M. L., Cowan, S. J., and LaPrete, R. D., 1972, "Concept and Design of Stators Tailored to Shield a Fan From Pressure Disturbances Arising in the Downstream Fan Ducts," AIAA Paper No. 72–84.

Woodward, R. P., and Balombin, J. R., 1984, "Tone Generation by Rotor-Downstream Strut Interaction," *AIAA Journal of Aircraft*, Vol. 21, pp. 135–142.

Yokoi, S., Nagano, S., and Kakehi, T., 1981, "Reduction of Strut Induced Rotor Blade Vibration With the Modified Stator Setting Angles," *International Symposium on Airbreathing Engines*, Bangalore, India, Feb. 16–21, pp. 61–1 to 61–7.

Experimental Investigation of Multistage Interaction Gust Aerodynamics

V. R. Capece[1]

S. Fleeter

Thermal Sciences and Propulsion Center,
School of Mechanical Engineering,
Purdue University,
West Lafayette, IN 47907

The fundamental flow physics of multistage blade row interactions are experimentally investigated at realistic reduced frequency values. Unique data are obtained that describe the fundamental unsteady aerodynamic interaction phenomena on the stator vanes of a three-stage axial flow research compressor. In these experiments, the effect on vane row unsteady aerodynamics of the following are investigated and quantified: (1) steady vane aerodynamic loading; (2) aerodynamic forcing function waveform, including both the chordwise and transverse gust components; (3) solidity; (4) potential interactions; and (5) isolated airfoil steady flow separation.

Introduction

Airfoil rows of advanced gas turbine engines are susceptible to destructive aerodynamically induced vibrational responses, with upstream blade and vane wakes the most common excitation source. For example, in the single-stage compressor flow field schematically depicted in Fig. 1, the rotor wake velocity deficits appear as a temporally varying excitation source to a coordinate system fixed to the downstream stator vanes, i.e., the rotor blade wakes are the forcing function to the downstream stator vanes. Also as shown, the reduction of the rotor relative velocity causes a decrease in the absolute velocity and increases the incidence to the stator vanes. This produces a fluctuating aerodynamic lift and moment on the vanes, which can result in high vibratory stress and high cycle fatigue failure.

First-principle forced response predictive techniques require a definition of the unsteady forcing function in terms of harmonics. The total response of the airfoil to each harmonic is then assumed to be comprised of two parts. One is due to the disturbance being swept past nonresponding airfoils. The second arises when the airfoils respond to the forcing function. A gust analysis predicts the unsteady aerodynamics of the nonresponding airfoils, with a harmonically oscillating airfoil analysis used to predict the additional motion-induced unsteady aerodynamics.

Both gust and harmonically oscillating unsteady aerodynamic models are being developed (e.g., Fleeter, 1973; Verdon and Caspar, 1981; Englert, 1982; Atassi, 1984; Chiang and Fleeter, 1988). Within these models are many numerical, analytical, and physical assumptions. Unfortunately, there is only a limited quantity of high reduced frequency data appropriate for model verification and direction.

Carta and St. Hilaire (1979) and Carta (1982) measured the surface chordwise unsteady pressure distribution on an harmonically oscillating cascade in a linear wind tunnel. This work was extended by Hardin et al. (1987) to an isolated rotor with oscillating blades. In addition, inlet distortion generated gust response unsteady aerodynamics were also studied. Although the interblade phase angles in these experiments were within the range found in turbomachines, the reduced frequencies, less than 0.4, were low for forced response unsteady aerodyanmics found in the mid and aft stages of multistage turbomachines where the reduced frequency is typically greater than 2.0. Fleeter et al. (1978, 1980, 1981) investigated the effects of airfoil profile and rotor–stator axial

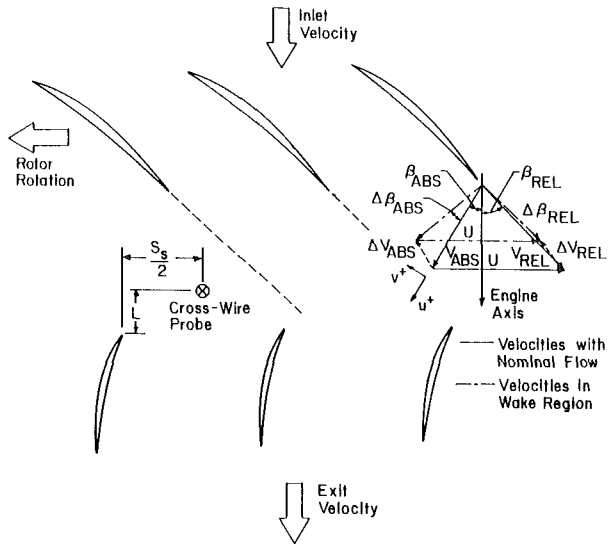

Fig. 1 Single-stage compressor flow field

[1]Currently at Pratt & Whitney Engineering Division South.

Contributed by the International Gas Turbine Institute and presented at the 33rd International Gas Turbine and Aeroengine Congress and Exhibition, Amsterdam, The Netherlands, June 5–9, 1988. Manuscript received at ASME Headquarters February 11, 1988. Paper No. 88-GT-56.

Table 1 Overall compressor and airfoil characteristics

	ROTOR	STATOR
Airfoil Type	C4	C4
Number of Airfoils	43	41
Chord, C (mm)	30	30
Solidity, C/S	1.14	1.09
Camber, θ	27.95	27.70
Stagger Angle, λ	36	-36.1
Aspect Ratio	2.0	2.0
Thickness/Chord (%)	10	10
Axial Gap (cm)	1.27	
Flow Rate (kg/s)	2.66	
Design Axial Velocity (m/s)	32.0	
Rotational Speed (RPM)	3000	
Number of Stages	3	
Stage Pressure Ratio	1.003	
Inlet Tip Diameter (mm)	420	
Hub/Tip Radius Ratio	0.714	
Stage Efficiency (%)	85	

spacing on the transverse gust unsteady aerodynamic response in a single-stage, low-speed research compressor at realistic values of the reduced frequency, with these data also showing the influence of the forcing function waveform.

These previous experimental investigations were performed in linear cascades, isolated rotor rows, and single-stage compressors. They did not consider the multistage and potential interaction effects that exist in the mid and aft stages of turbomachines. For multistage compressors, the unsteady aerodynamics on the first two vane rows of a three-stage low-speed research compressor were studied for the first time by Capece et al. (1986). The transverse gust forcing function and the chordwise distributions of the harmonic pressure difference coefficients on the first two vane rows were determined for a variety of geometric and compressor operating conditions. These results indicated that the unsteady aerodynamic loading of an airfoil row was related to the aerodynamic forcing function, which itself is significantly influenced by the multistage blade row interactions. This work was extended by Capece and Fleeter (1987) to include all three vane rows, with the effects of both the transverse and chordwise gust components quantified.

In this paper, the fundamental flow physics of multistage blade row interactions are experimentally investigated at realistic reduced frequency values, with unique data obtained to describe the fundamental unsteady aerodynamic phenomena on the stator vanes of a three-stage research compressor. In particular, a series of experiments are performed to investigate and quantify the effect of the following on vane row unsteady aerodynamics: (1) steady loading; (2) forcing function waveform, including both the chordwise and transverse gust components; (3) solidity; (4) potential interactions, and (5) steady flow separation.

Research Compressor and Instrumentation

The Purdue University Three-Stage Axial Flow Research Compressor is driven by a 15 hp d-c electric motor over a speed range of 300 to 3000 rpm. The three identical compressor stages consist of 43 rotor blades and 41 stator vanes, with the first-stage rotor inlet flow field controlled by variable setting angle inlet guide vanes. The free-vortex design airfoils have a British C4 section profile, a chord of 30 mm, an aspect ratio of 2, and a maximum thickness-to-chord ratio of 0.10. The overall airfoil and compressor characteristics are presented in Table 1.

The aerodynamic forcing functions to the stator rows are the upstream airfoil wakes. The first-stage vane row forcing function is varied by changing the setting angle of the inlet guide vanes, thereby altering the inlet flow to the first stage rotor (Fig. 2). This results in a change in the rotor blade exit flow field, in particular, the chordwise and transverse gust components. The second and third-stage vane row forcing function variations are accomplished by independently circumferentially indexing the upstream vane rows relative to one another, as also depicted.

The stator vane forcing function is quantified by measuring the stator inlet time-variant velocity and flow angle with a cross-wire probe located midway between rotor and stator at midstator circumferential spacing (Fig. 1). The rotor mean absolute exit flow angle is determined by rotating the probe until a zero voltage difference is obtained between the two hot-wire channels. This mean angle is then used as a reference for calculating the instantaneous absolute and relative flow angles and defines the vane steady incidence angle. From the instantaneous velocity triangles, the individual fluctuating velocity components parallel and normal to the mean flow, the aerodynamic gust components, are calculated. The accuracy of the velocity magnitude and angle are ± 4 percent and ± 2 deg, respectively.

The steady and unsteady aerodynamic loading on the vane surfaces are measured with chordwise distributions of midspan surface pressure taps and tranducers. Flow visualization along this streamline shows the flow to be two dimensional for the operating conditions of this investigation. A

Nomenclature

C = vane chord

$\bar{C}_l$ = steady lift coefficient $= \int_0^C (\bar{p}_p - \bar{p}_s)dx \Big/ \frac{1}{2}\rho U_t^2 C$

C_p = first harmonic dynamic pressure coefficient $= \Delta\hat{p}/\rho V_x \hat{v}^+$

$\bar{C}_p$ = static pressure coefficient $= (\bar{p} - \bar{p}_{exit}) \Big/ \frac{1}{2}\rho U_t^2$

i = incidence angle

k = reduced frequency $= \omega C/2V_x$

$\bar{p}$ = stator surface static pressure

$\bar{p}_{exit}$ = stator exit static pressure

$\Delta\hat{p}$ = first harmonic dynamic pressure difference

u^+ = instantaneous chordwise gust component

$\hat{u}^+$ = first harmonic chordwise gust

U_t = blade tip speed

v^+ = instantaneous transverse gust component

$\hat{v}^+$ = first harmonic transverse gust

V_x = absolute axial velocity

$\bar{\sigma}$ = solidity

ω = blade passing frequency

reverse transducer mounting technique is utilized to minimize disturbances, with the transducer connected to the measurement surface by a pressure tap. Static and dynamic calibrations of the embedded transducers demonstrate no hysteresis, with the mounting method not affecting the frequency response. The accuracy of the unsteady pressure measurements is ±3.5 percent.

Data Acquisition and Analysis

The steady-state data define the steady aerodynamic loading on the vane surfaces and the compressor operating point. A root-mean-square error analysis is performed, with the steady data defined as the mean of 30 samples and their 95 percent confidence intervals determined. The detailed steady loading on the vanes is defined by the chordwise distribution of the vane surface steady static pressure coefficient $\bar{C}_p$, with the overall loading level specified by the incidence angle i and the steady lift coefficient $\bar{C}_l$.

The time-variant data quantify the aerodynamic forcing function and the resulting unsteady pressure difference on the stator vanes, and are analyzed by means of a data-averaging or signal enhancement concept, as proposed by Gostelow (1977). The key to this technique is the sampling of data at a preset time, which is accomplished with a shaft-mounted optical encoder. At a steady-state operating point, an averaged time-variant data set consisting of the two hot-wire and the vane-mounted transducer signals, digitized at a rate of 200 kHz and averaged over 200 rotor revolutions, is obtained. Each is Fourier decomposed into harmonics by means of a Fast Fourier Transform algorithm, with the magnitude and phase angle of the first harmonic referenced to the data initiation pulse determined. Analyzing the data in this form was found to be equivalent to averaging the Fourier transforms for each rotor revolution. Also, ensemble averaging and then Fourier decomposing of the signal is used because it significantly reduces the data storage requirements.

The rotor and stator spacing, the axial spacing between the vane leading edge plane and the probe, and the absolute and relative flow angles are known. To time relate the hot wire and vane surface unsteady pressure signals, the rotor exit velocity triangles are examined and the following asumptions made: (1) The wakes are identical at the hot wire and stator leading edge planes, and (2) the wakes are fixed in the relative frame. The wakes are located relative to the hot wires and the leading edges of the instrumented vanes and the times at which the wakes are present at various locations determined. The incremented times between occurrences at the hot wire and the vane leading edge planes are then related to phase differences between unsteady velocities and the vane surfaces. These assumptions are necessary in order to correlate the data with a gust analysis, which fixes the gust at the airfoil leading edge. The hot wire was located approximately midway between the rotor and stator and was less than 25 percent of the stator chord upstream of its leading edge.

In final form, the detailed waveform of the aerodynamic forcing function is specified by the first harmonics of the chordwise and transverse gust components, $\hat{u}^+$ and $\hat{v}^+$, respectively. The unsteady pressure data describe the chordwise variation of the first harmonic pressure difference across a stator vane, presented as a dynamic pressure difference coefficient magnitude and phase. As a reference, these data are correlated with predictions from Fleeter (1973). This gust analysis assumes the flow to be inviscid, irrotational, two dimensional, and compressible. Small unsteady transverse velocity perturbations, v^+, are assumed to be convected with the uniform flow past a cascade of flat plate airfoils. The parameters modeled include the cascade solidity, stagger angle, inlet Mach number, reduced frequency, and the interblade phase angle. The analysis does not consider flow separation or chordwise gust perturbations u^+.

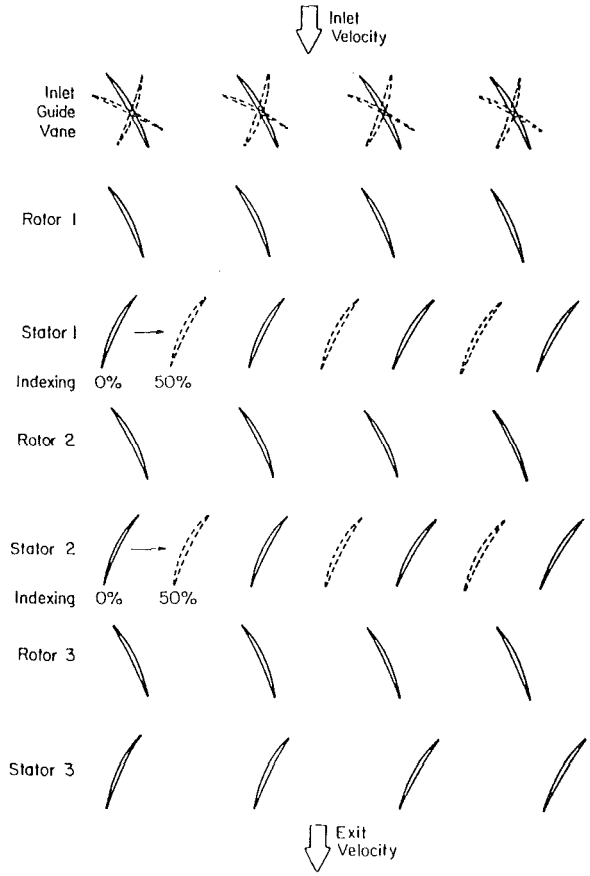

Fig. 2 Compressor geometry variations to alter forcing function

Results

Three stator vane solidities are investigated: the design value of 1.09; a reduced value of 0.545; and 0.10, which results in a spacing between vanes large enough so that the influence of neighboring vanes is negligible; i.e., each vane is an isolated airfoil. The results are presented for each solidity for variations in one of the key parameters. All design solidity data, except for the potential interaction effects, are presented for the first stator vane row. The data sets for the other solidities are presented for the third stator vane row. Since there are no airfoil rows downstream of the third stage vane row, there are no potential interaction effects on the trailing edge region of these vanes. Data from Capece and Fleeter (1987) have been added for the design solidity in order to have a complete presentation of the results and to indicate the significant effects that solidity has on the unsteady aerodynamic response of the stator vanes. Also, the error in the static pressure coefficient data is represented by the symbol size.

Vane Steady Loading

Steady aerodynamic loading effects are considered for the design and reduced solidities of 1.09 and 0.545. The first harmonics of the forcing function are maintained nearly constant (Fig. 3). Note that relative to the absolute velocity, the instantaneous gust components are not small. For example, the instantaneous transverse and chordwise gust components are approximately 40 and 25 percent of the absolute velocity at −5.9 deg of incidence. However, in terms of the first harmonics these gust components are approximately 11 and 6 percent of the absolute velocity.

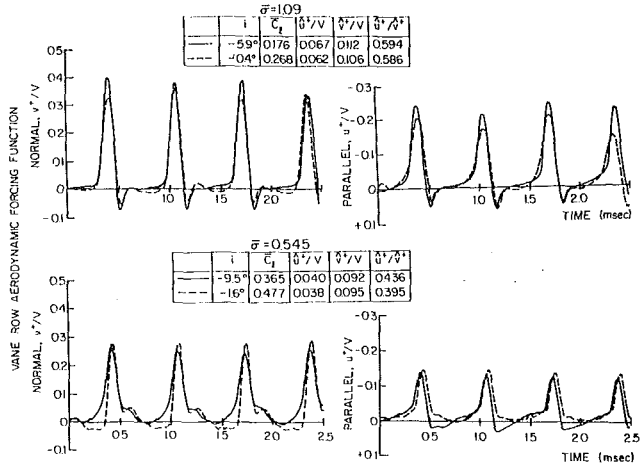

Fig. 3 Aerodynamic forcing functions for steady loading study

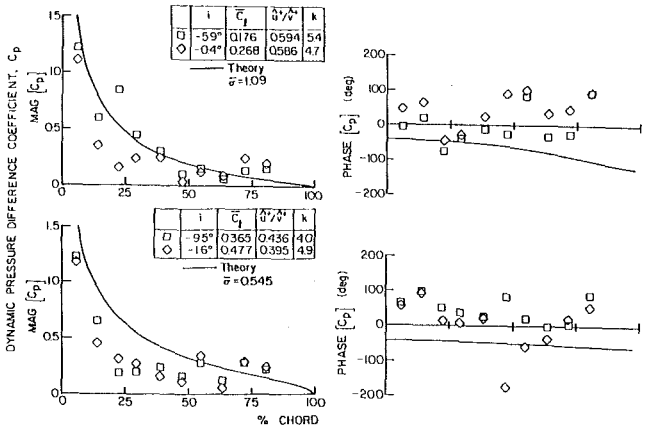

Fig. 5 Effect of steady loading on the complex unsteady pressure coefficient

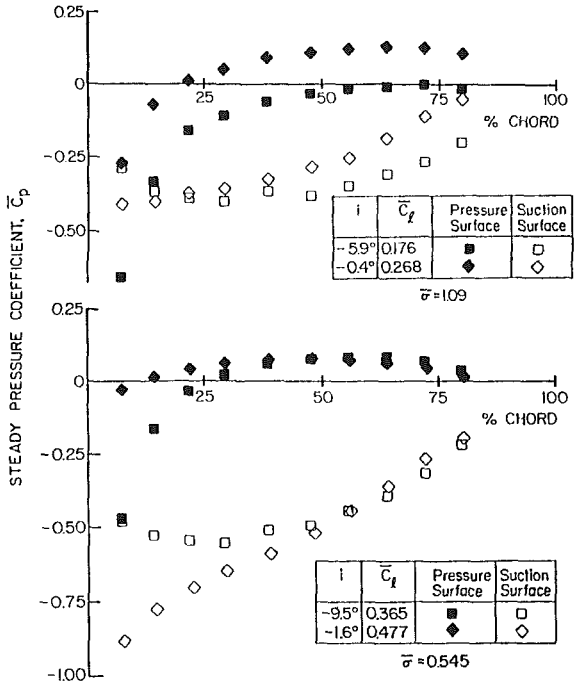

Fig. 4 Vane static pressure distributions for steady loading study

For each solidity, the vane surface steady pressure distributions are smooth and show no indication of flow separation (Fig. 4). At the design solidity, the surface static pressures for the lift coefficient of 0.268 are greater than those for the lift coefficient of 0.176, a result of the inlet guide vane indexing altering the compressor operating point. Also, the reduced solidity has much higher pressure differences and steady lift coefficients due to the decreased number of vanes.

The resulting chordwise distributions of the dynamic pressure difference coefficient and the predictions are shown in Fig. 5. At the design solidity, good correlation exists between the magnitude data and the prediction for the lift coefficient of 0.176, with an increase in lift to 0.268 resulting in poorer correlation. The higher loading data are decreased in amplitude relative to both the prediction and the lower loading data over the front 25 percent of the vane. Aft of 25 percent chord, the data correlate well with each other and the prediction until 63 percent chord, with both data sets then increasing to a larger value than the prediction.

The phase data exhibit a somewhat different chordwise distribution than the prediction. In particular, the phase data are increased relative to the prediction over the first 14 percent of vane chord. The data then decrease to the level of the prediction and then increase to values greater than the prediction with increasing chordwise position. The phase data for both loading levels exhibit the same trends, with the higher loading data increased relative to both the prediction and the lower loading data over most of the chord. The differences between the phase data and the prediction are attributed to the vane camber and the detailed steady loading distributions on the vane surfaces.

The magnitude data for the reduced solidity are also decreased relative to the prediction over the front 50 percent of the vane, with the higher loading data having, in general, a decreased amplitude relative to the lower loading data. The decrease in amplitude relative to the prediction is due to the high levels of steady aerodynamic loading. Aft of 50 percent chord, the magnitude data increase to the level of the prediction and show better correlation. The phase data increase to a level larger than the prediction over the front 14 percent of the vane, then decrease toward the prediction, and from approximately 25 to 50 percent chord, the phase data are almost constant. Aft of 50 percent chord this trend changes, with the higher loading data decreased relative to both the lower loading data and the prediction, and then increasing as the chordwise position increases. Thus, from these results it is evident that steady loading primarily affects the magnitude of the dynamic pressure difference coefficient.

The best correlation of the dynamic pressure difference coefficient data and the prediction is obtained at the low level of steady loading at the design solidity, as expected, since this most closely approximates the unloaded flat plate cascade model. Also, the steady loading level and distribution have a significant effect on the unsteady aerodynamics of the vane row. In general, different airfoil designs will produce different steady surface pressure distributions and steady lift for the same incidence angle. Therefore, the level of steady aerodynamic loading, not the incidence angle, is the key parameter in obtaining good correlation with mathematical models.

Aerodynamic Forcing Function

The influence of each gust component on the complex dynamic pressure coefficient, with the steady aerodynamic loading held constant, is considered.

Transverse Gust. The surface static pressure distributions for each solidity are smooth, with no evidence of separation and only small variations apparent near the leading edge, which result in the slight variations in the steady lift coeffi-

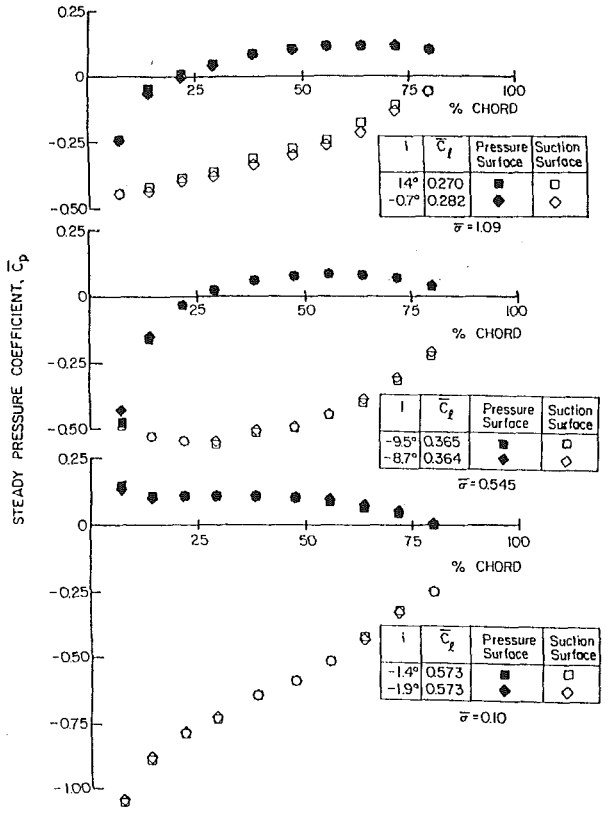

Fig. 6 Surface static pressure distributions for transverse gust study

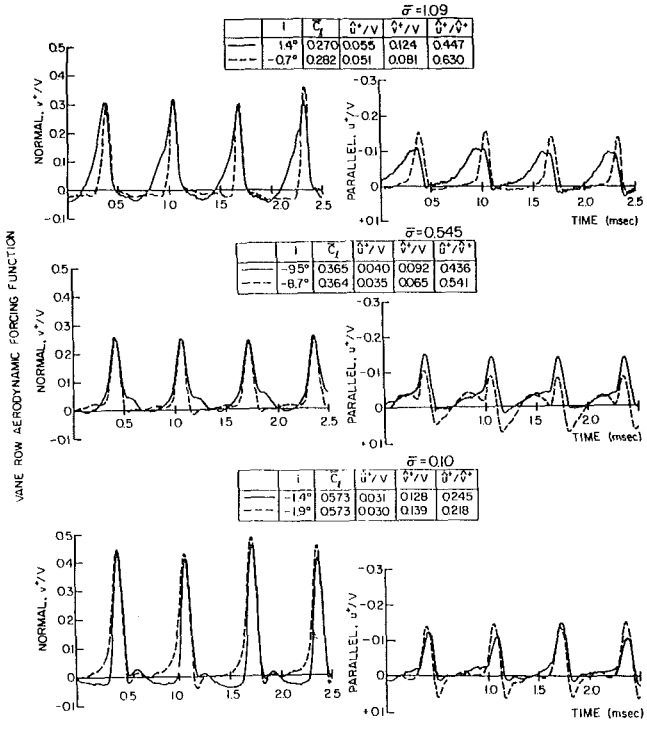

Fig. 7 Aerodynamic forcing functions for transverse gust study

cients (Fig. 6). As the solidity is decreased, there is an increase in the level of steady surface pressures and a corresponding increase in the steady lift coefficient. The chordwise gust $\hat{u}^+$ is held approximately constant while the transverse gust $\hat{v}^+$ is varied (Fig. 7), with the difference between the configurations specified by the first harmonic gust ratio $\hat{u}^+/\hat{v}^+$.

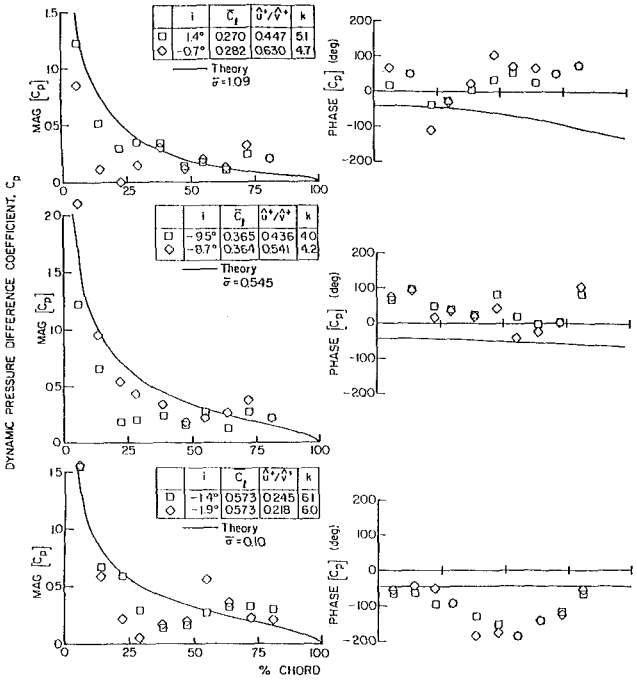

Fig. 8 Effect of transverse gust on the complex unsteady pressure coefficient

The effect of the transverse gust on the chordwise distributions of the dynamic pressure difference coefficient data is presented in Fig. 8. At the design solidity, both configurations show the magnitude data to be decreased relative to the prediction over the leading 30 percent of the vane, with the $(\hat{u}^+/\hat{v}^+)$ data of 0.630 having a decreased amplitude relative to the 0.447 data. However, in the midchord region, the data for these two configurations correlate well with each other and with the prediction. As in the previous cases, aft of 70 percent chord the data increase relative to the prediction. This is a result of both the potential interaction from the downstream second-stage rotor row and the parallel gust component $\hat{u}^+$, as the design solidity data are acquired on the first stage. This phenomenon will be discussed in greater detail in the section on Potential Flow Interactions.

The reduced solidity and the isolated airfoil data show a different trend with the ratio of $(\hat{u}^+/\hat{v}^+)$ than that of the design solidity, with the data for the larger values of $(\hat{u}^+/\hat{v}^+)$ increased in value relative to the lower values. This is opposite to the trend noted at the design solidity. However, examination of the magnitudes of the first harmonics of the chordwise gust component $\hat{u}^+$ indicates that the magnitudes of the chordwise gust are lower in value than the design case. This indicates that the chordwise pressure distributions are not governed simply by the ratio of the two gust components but also by their magnitudes.

For each of the reduced solidity values, 0.545 and 0.10, the magnitude data are generally decreased relative to the prediction over the leading 50 percent of the vane, with the lower $(\hat{u}^+/\hat{v}^+)$ data having a decreased amplitude relative to the higher $(\hat{u}^+/\hat{v}^+)$ data. In the trailing edge portion of the vane, the magnitude data correlate well with each other but are increased in level relative to the prediction. This is a result of the chordwise gust, which is not considered by the model.

The design solidity phase data are increased relative to the prediction over the front 14 percent of the vane, decrease to the level of the prediction at 22 percent chord, and then increase to values greater than the prediction with increasing chordwise position, becoming nearly constant aft of 40 percent chord. At the reduced solidity, the phase data are in-

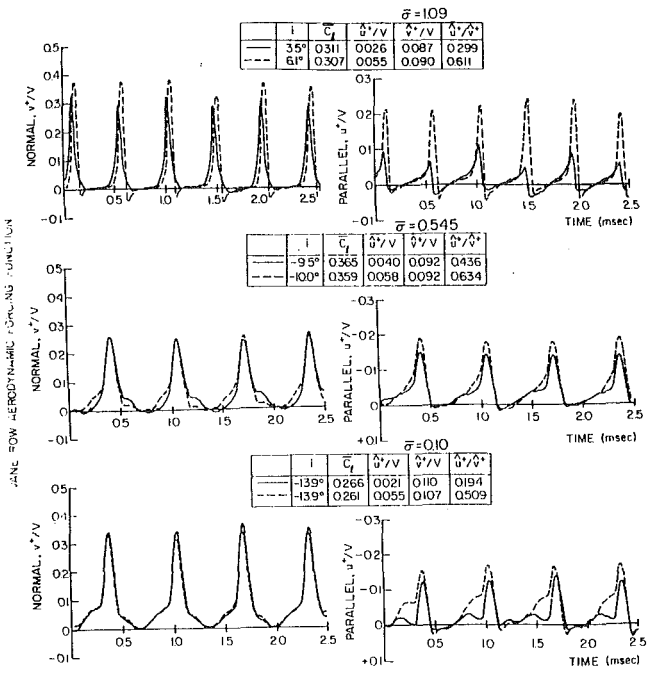

Fig. 9 Aerodynamic forcing function for chordwise gust study

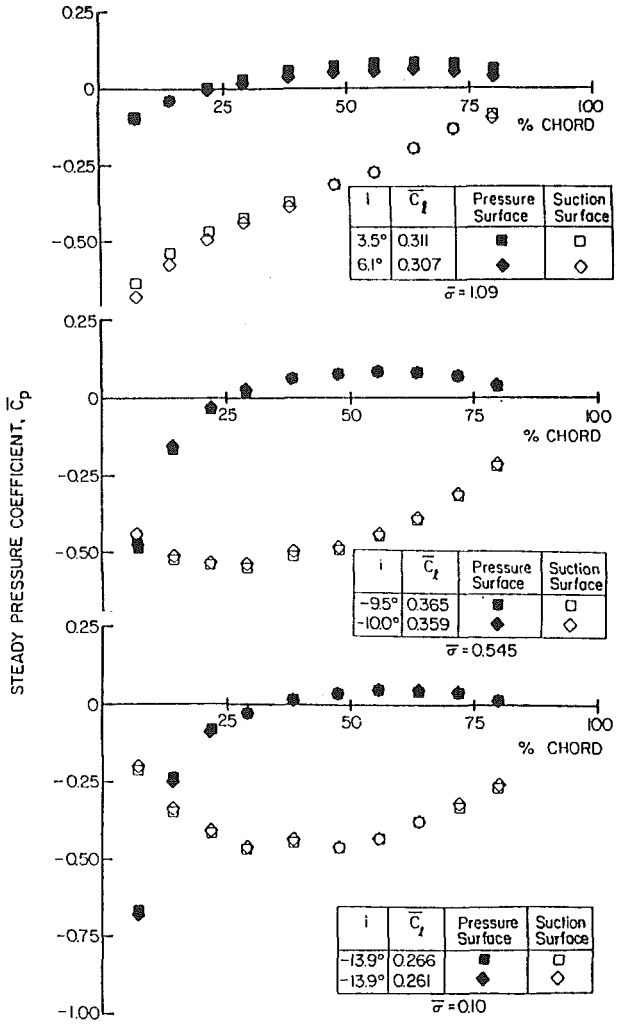

Fig. 10 Steady vane loading distributions for chordwise gust study

creased relative to the prediction over the entire vane chord, being nearly constant in the 22 to 38 percent chord region. For the isolated airfoil, the phase data show good trendwise correlation with the prediction over the leading 29 percent of the vane, with the $(\hat{u}^+/\hat{v}^+)$ data of 0.245 decreasing relative to both the prediction and the $(\hat{u}^+/\hat{v}^+)$ 0.218 data. Aft of 29 percent chord, where the vane does most of its turning, the phase data decrease until 54 percent chord and then increase with increasing chordwise position.

These results show that the transverse gust primarily influences the magnitude of the dynamic pressure difference coefficient. Also, the unsteady data variations with forcing function waveform cannot be predicted by harmonic gust models. This is because the forcing function waveforms and the resulting unsteady pressure distributions have been Fourier decomposed, with the first harmonic of the unsteady data presented. Thus, all of these first harmonic data are correlated with the same prediction curve; i.e., the predictions from these harmonic gust models are identical for all of the forcing function waveforms.

Chordwise Gust. The effect of the forcing function chordwise gust component $\hat{u}^+$ on the vane row unsteady aerodynamics for each solidity is considered. This is accomplished by establishing compressor configurations such that the transverse gust and the steady aerodynamic loading are nearly identical; see Figs. 9 and 10, respectively.

The resulting chordwise distributions of the dynamic pressure coefficient data and the predictions are presented in Fig. 11. In general, the magnitude data exhibit analogous trends for each solidity, decreasing over the front of the vane and increasing over the aft part. The magnitude data increase over the prediction at the design solidity, whereas they increase up to the prediction for the other two solidity values. This is again the result of the design solidity data being acquired on the first stage, with the data for the other solidities being acquired on the third stage. Also, the higher $(\hat{u}^+/\hat{v}^+)$ data are decreased relative to both the prediction and the lower $(\hat{u}^+/\hat{v})$ data for each solidity. This is particularly apparent at the design and reduced solidity.

The design solidity phase data at a $(\hat{u}^+/\hat{v}^+)$ of 0.611 show good trendwise correlation with the prediction over the aft 50

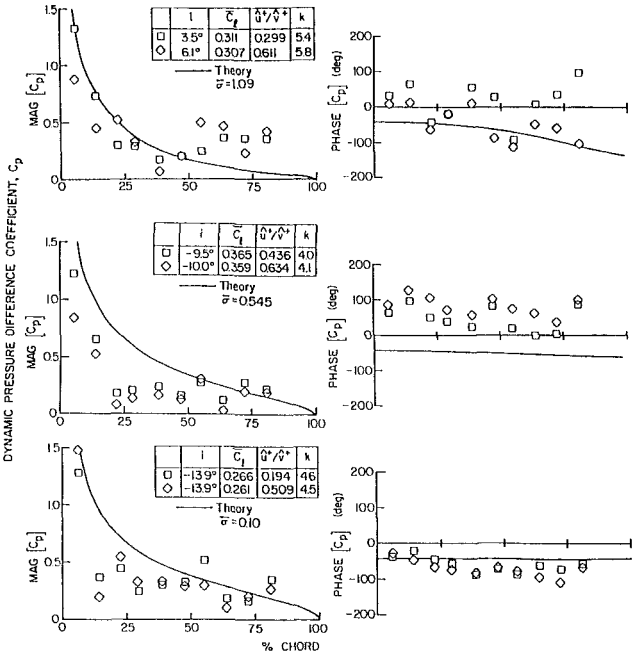

Fig. 11 Effect of chordwise gust on the complex unsteady pressure coefficient

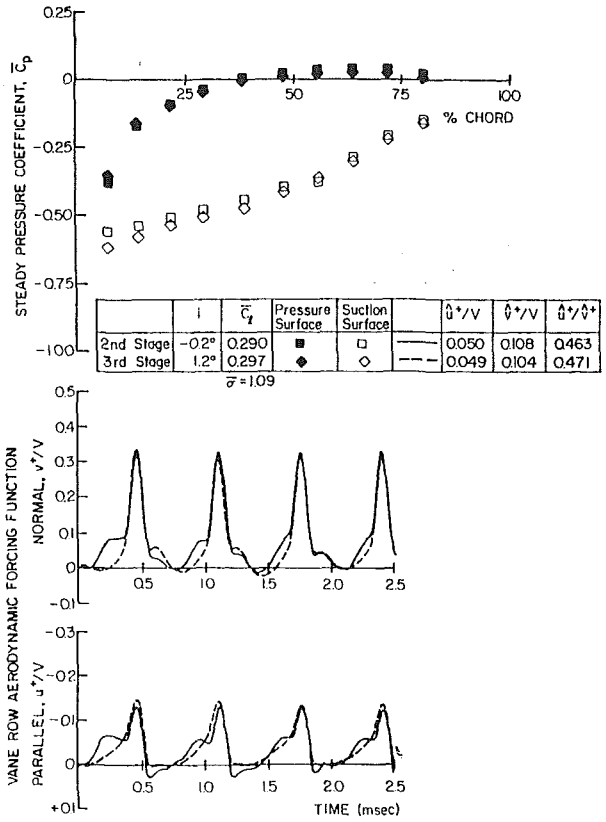

	i	$\bar{C}_l$	Pressure Surface	Suction Surface		$\hat{u}^+/V$	$\hat{v}^+/V$	$\hat{u}^+/\hat{v}^+$
2nd Stage	-0.2°	0.290	■	□	——	0.050	0.108	0.463
3rd Stage	1.2°	0.297	◆	◇	- - -	0.049	0.104	0.471

Fig. 12 Steady loading and forcing functions for potential flow interaction study

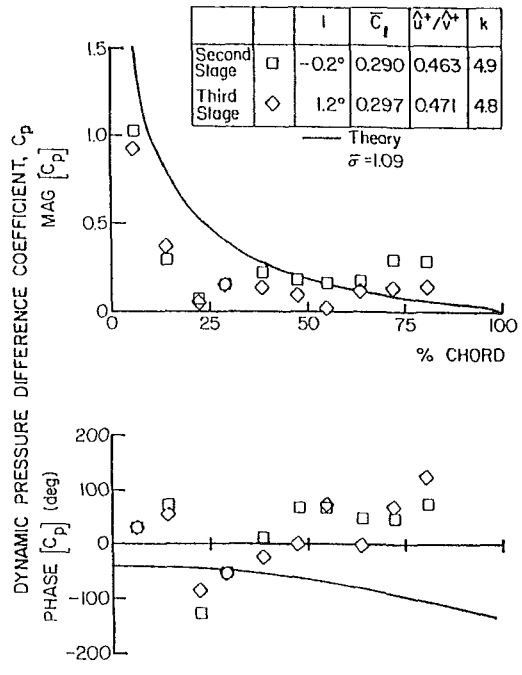

		i	$\bar{C}_l$	$\hat{u}^+/\hat{v}^+$	k
Second Stage	□	-0.2°	0.290	0.463	4.9
Third Stage	◇	1.2°	0.297	0.471	4.8

Fig. 13 Potential flow interaction effect on the complex unsteady pressure coefficient

percent of the vane while the lower $(\hat{u}^+/\hat{v}^+)$ data are increased relative to the prediction, as seen in previous cases. Over the front 50 percent of the vane, the data correlate trendwise with each other but are increased compared to the prediction. The reduced solidity phase data are increased relative to the prediction and remain relatively constant over the entire vane chord, with the $(\hat{u}^+/\hat{v}^+)$ phase data of 0.634 consistently increased over the $(\hat{u}^+/\hat{v}^+)$ 0.436 data.

A somewhat different trend is evident in the phase data for the isolated airfoil than previous isolated airfoil cases and the other solidity values. In this case, the data are seen to correlate trendwise with the prediction over the front of the vane, then decrease slightly lower than the prediction and remain almost constant for the remainder of the vane. In addition, the phase data for these two configurations correlate quite well with one another over almost the entire vane. Comparing these results to the phase data of Fig. 8 for a $(\hat{u}^+/\hat{v}^+)$ of 0.218 indicates that loading has a dramatic effect on the phase as well as the magnitude data: Both the phase and the magnitude data show the maximum deviations from the analysis in the 25 to 50 percent chord locations. Aft of this point the magnitude and phase increase to the prediction.

The differences apparent in the dynamic pressure difference coefficient phase data for the three different solidity values are a result of the details of the steady static pressure distributions and the spacing between the airfoils. As the airfoil spacing increases for low levels of aerodynamic loading, the correlation of the phase data with the predictions gets increasingly better. This indicates that the influence of adjacent airfoils is much greater than predicted by the zero incidence flat plate analysis.

Thus, both the transverse and chordwise gust components affect the magnitude data, with the chordwise gust having a larger influence on the phase, particularly at the design solidity. In addition, the magnitude of the chordwise gust is not small as compared to either the absolute velocity or the transverse gust.

Potential Flow Interactions

Data in the vane trailing edge region are consistently increased relative to the prediction. Part of this increase is attributable to the chordwise gust that is not modeled by the prediction. However, first-stage magnitude data exhibit larger deviations in the trailing edge region than third-stage data with similar steady lift coefficients. To investigate this phenomenon, unsteady data are acquired on the second and third stages at the design solidity for operating conditions where the steady loading and the forcing function are nearly identical (Fig. 12). Thus the only difference between these two configurations is the presence of the third stage downstream of the second-stage stator row.

The resulting dynamic pressure difference coefficient data and corresponding prediction are presented in Fig. 13. The magnitude data are decreased relative to the prediction over the leading 30 percent of the vane due to the steady loading level, with the deviations in the amplitude attributed to the differences in the steady surface pressure distributions in the leading edge region. Aft of 30 percent chord, the data increase to the level of the prediction, with the second-stage data higher in amplitude than the third-stage data, particularly in the trailing edge region. Since the steady pressure distributions and the forcing function are nearly identical, this deviation of the second-stage data is attributed to a potential interaction effect caused by the downstream third stage. The increase of the third-stage data above the prediction in this region is a result of the chordwise gust since there are no downstream airfoil rows, with the further increase in the second-stage data due to the potential interaction.

The phase data also show different trends in the trailing edge region due to potential interactions. Over the front part of the vane, the data are increased with respect to the prediction, but then decrease in relation to the prediction at 22 percent chord. The data then increase until 50 percent chord, with the data up to this point exhibiting good trendwise correlation. Aft of 50 percent chord the second-stage data are nearly constant with increasing chordwise position, whereas the third-

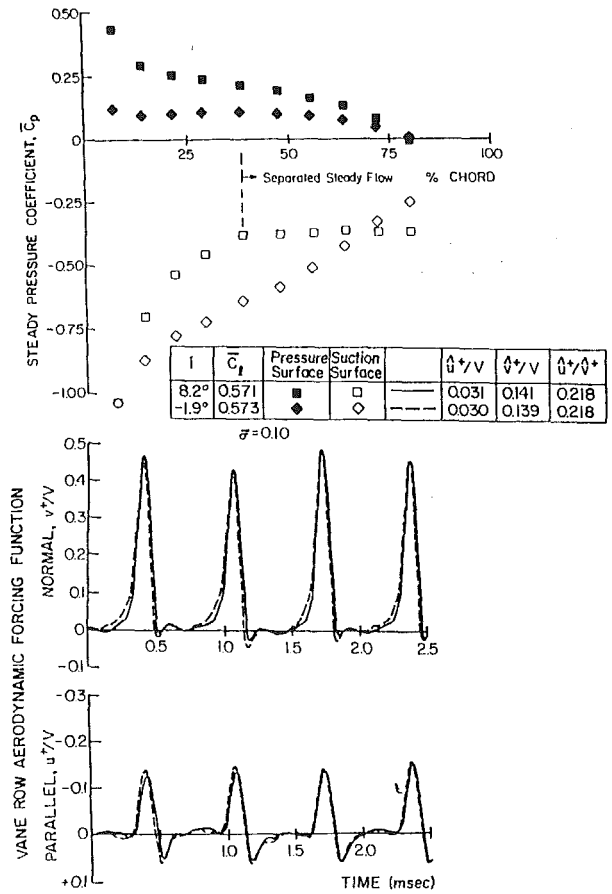

Fig. 14 Steady loading and forcing functions for isolated airfoil separated flow investigation

stage data show another decrease in phase and then increase with increasing chordwise position.

Thus, potential interaction effects influence both the magnitude and phase, with the larger effect being upon the magnitude of the dynamic pressure difference coefficient. Hence, the downstream airfoil row is another aerodynamic excitation source to the upstream blade or vane row and would act on the trailing edge region.

Isolated Airfoil Separation

The effect of separated flow on the stator vane unsteady aerodynamics for a solidity of 0.10, i.e., an isolated airfoil, is now investigated. The separated flow is generated by restaggering the stator vanes such that a mean flow incidence angle of 8.2 deg is established. At this incidence angle, the flow separates from the vane suction surface as indicated by the region of constant static pressure, which originates at 38 percent chord (Fig. 14). The separated flow data are compared with data for a configuration where the steady lift coefficient and both the chordwise and transverse gust componets are nearly identical, but the flow is not separated.

The resulting dynamic pressure difference coefficient data and the attached flow flat plate prediction are shown in Fig. 15. The attached and separated flow data show somewhat different trends in the leading and trailing edge regions. The separated flow magnitude data are nearly constant over the front 14 percent of the vane, whereas the attached flow data and prediction indicate a decrease in amplitude with increasing chordwise position. Aft of 14 percent chord the data show analogous trends, with both separated and attached flow data decreasing with increasing chordwise position and attaining a minimum amplitude value at 20 percent chord, similar to previous isolated airfoil results. The magnitude data for both

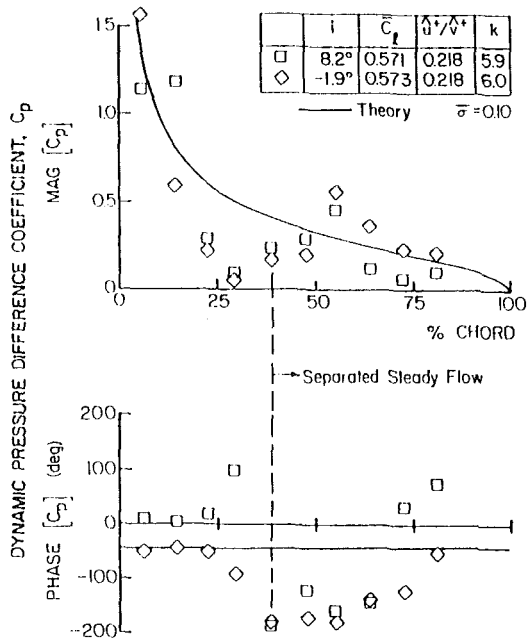

Fig. 15 Steady suction surface separation effect on the complex unsteady pressure coefficient

cases then gradually increase to values that are greater than the prediction at 54 percent chord, with the attached flow data being lower in magnitude up to this point. Both data sets then decrease with further chordwise position, with the separated data decreased in amplitude relative to both the prediction and the attached flow data. This is a result of the increased steady loading in this region of the airfoil due to the separation zone.

The attached and separated flow phase data have different trends near the separation point and in the trailing edge region. Over the front 22 percent of the vane, the data and the prediction show analogous trends, being nearly constant. The separated data are increased relative to the prediction, with the attached flow data exhibiting excellent correlation with the prediction. Aft of 22 percent chord the separated data increase, whereas the attached flow data decrease relative to the prediction. In the separated flow region, both the separated and attached flow data exhibit similar trends. However, at 70 percent chord the separated data indicate a jump to values larger than the prediction and increase with further chordwise position. On the other hand, the attached flow phase data show a gradual increase. Thus, separation affects both the magnitude and phase of the dynamic pressure difference coefficient.

Summary and Conclusions

A series of experiments were performed to investigate the wake-generated gust aerodynamics on each vane row of a three-stage axial flow research compressor at high reduced frequency values, including multistage interactions. In these experiments, the effects, on vane row unsteady aerodynamics of the following were investigated and quantified: (1) steady vane aerodynamic loading; (2) aerodynamic forcing function waveform, including both the chordwise and transverse gust components; (3) solidity; (4) potential interactions; and (5) isolated airfoil steady flow separation. The analysis of these unique vane row unsteady aerodynamic data determined the following.

- The steady aerodynamic loading level, not the incidence angle, is the key parameter to obtain good correlation with flat plate cascade gust models.
- The steady loading level and chordwise loading distribution have a significant effect on vane row unsteady

aerodynamics, having a larger influence on the magnitude than on the phase.

- The aerodynamic forcing function chordwise gust affects both the dynamic pressure coefficient magnitude and phase, whereas the transverse gust primarily affects the magnitude. These effects cannot be predicted with harmonic gust models because these data have been Fourier decomposed, with the predictions thus identical for all forcing function waveforms.
- The chordwise gust is not small compared to either the absolute velocity or the transverse gust. Thus, to provide accurate predictions, unsteady aerodynamic models must consider this gust component.
- For closely spaced stages (the compressor rotor–stator axial spacing herein is 0.432 chord), downstream airfoil rows are potential aerodynamic excitation sources, which affect the unsteady loading in the trailing edge region of the upstream airfoils. Since the trailing edge is thin, it would be highly susceptible to fatigue failure.
- Flow separation of the low solidity vane row affects the unsteady surface pressures upstream of the separation point, with the phase affected in the trailing edge region.

Acknowledgments

Support of this research program by the Air Force Office of Scientific Research, Dr. James Wilson, program manager, is most gratefully acknowledged.

References

Atassi, H. M., 1984, "The Sears Problem for a Lifting Airfoil Revisited—New Results," *Journal of Fluid Mechanics*, Vol. 141, pp. 109–122.

Capece, V. R., Manwaring, S. R., and Fleeter, S., 1986, "Unsteady Blade Row Interactions in a Multi-stage Compressor," *AIAA Journal of Propulsion*, Vol. 2, No. 2, pp. 168–174.

Capece, V. R., and Fleeter, S., 1987, "Unsteady Aerodynamic Interactions in a Multi-stage Compressor," ASME JOURNAL OF TURBOMACHINERY, Vol. 109, No. 3, pp. 420–428.

Carta, F. O., and St. Hilaire, A. O., 1979, "Effect of Interblade Phase Angle and Incidence Angle on Cascade Pitching Stability," ASME Paper No. 79-GT-153.

Carta, F. O., 1982, "An Experimental Investigation of Gapwise Periodicity and Unsteady Aerodynamic Response in an Oscillating Cascade, Part I: Experimental and Theoretical Results," NASA CR 3513.

Chiang, H. D., and Fleeter, S., 1988, "Prediction of Loaded Airfoil Unsteady Aerodynamic Gust Response by a Locally Analytical Method," *International Journal of Mathematical Modeling*, in press.

Englert, G. W., 1982, "Interaction of Upstream Flow Distortions With High Mach Number Cascades," ASME Paper No. 82-GT-137.

Fleeter, S., 1973, "Fluctuating Lift and Moment Coefficients for Cascaded Airfoils in Nonuniform Compressible Flow," *AIAA Journal of Aircraft*, Vol. 10, pp. 93–98.

Fleeter, S., Jay, R. L., and Bennett, W. A., 1978, "Rotor Wake Generated Unsteady Aerodynamic Response of a Compressor Stator," ASME *Journal of Engineering for Power*, Vol. 100, pp. 664–675.

Fleeter, S., Bennett, W. A., and Jay, R. L., 1980, "The Time Variant Aerodynamic Response of a Stator Row Including the Effects of Airfoil Camber," ASME *Journal of Engineering for Power*, Vol. 102, pp. 334–343.

Fleeter, S., Jay, R. L., and Bennett, W. A., 1981, "Wake Induced Time Variant Aerodynamics Including Rotor–Stator Axial Spacing Effects," ASME *Journal of Fluids Engineering*, Vol. 103, No. 1, pp. 59–66.

Gostelow, J. P., 1977, "A New Approach to the Experimental Study of Turbomachinery Flow Phenomena," ASME *Journal of Engineering for Power*, Vol. 99, pp. 97–105.

Hardin, L. W., Carta, F. O., and Verdon, J. M., 1987, "Unsteady Aerodynamic Measurements on a Rotating Compressor Blade Row at Low Mach Number," ASME JOURNAL OF TURBOMACHINERY, Vol. 109, No. 4, pp. 499–507.

Verdon, J. M., and Caspar, J. R., 1981, "Development of an Unsteady Aerodynamic Analysis for Finite Deflection Subsonic Cascades," NASA CR 3455.

Experimental Investigation of Rotating Stall in a Mismatched Three-Stage Axial Flow Compressor

G. L. Giannissis

A. B. McKenzie

R. L. Elder

Turbomachinery Research Group,
School of Mechanical Engineering,
Cranfield Institute of Technology,
Cranfield, Bedford, MK43 OAL,
United Kingdom

This paper reports on an examination of rotating stall in a low-speed three-stage axial flow compressor operating with various degrees of stage mismatch. The objective of this study was to simulate the mismatching that occurs in high-speed multistage compressors when operating near surge. The study of the stall zones involved the use of fast response measurement techniques. The study clearly shows how stages can operate in an axisymmetric fashion even when heavily stalled, since rotating stall inception requires the stall of more than one stage. The study also compares conditions required for full-span and part-span stall and suggests that the part-span stall structure is more relevant to high-speed multistage compressors.

Introduction

Multistage compressors need to be capable of operating over a wide range of conditions and inevitably incur stall at low flow rates, which eventually provides a limit to the operating range. It is well known that when a multistage compressor operates at low speeds (and low flow rates) the front stages will tend to stall first. The reason for this is that at low speeds the operating density ratio is lower than the design value, causing the axial flow coefficients in the rear stages to increase above the design value, eventually causing high negative incidence losses. These losses restrict the axial velocity in the inlet stages, eventually causing stall.

At high speeds, surge usually occurs due to the rear stages stalling. This is because, at high speed and low flow rates, the front stages operate at a density ratio above the design value causing a reduction in axial velocity in the rear stages. This reduced axial velocity will eventually cause an increase of positive incidence and stage stall in the rear stages.

The objective of this study has been to investigate the stall process of multistage compressors operating with mismatched stages. In this case the stage mismatch has been simulated by varying (from design) the blade stagger in a three-stage, low-speed (parallel annulus) compressor. It is clear that conventional compressor mismatch occurs due to the occurrence of different flow coefficients in adjacent (usually similar) stages, whereas in the present study the same flow coefficient is imposed on all stages and the stages are arranged to have different stall points. It is also clear that the present tests involved an exaggeration of the actual mismatch conditions prevailing in a three-stage compressor operating at off-design conditions.

Contributed by the International Gas Turbine Institute and presented at the 33rd International Gas Turbine and Aeroengine Congress and Exhibition, Amsterdam, The Netherlands, June 5-9, 1988. Manuscript received by the International Gas Turbine Institute October 10, 1987. Paper No. 88-GT-205.

Test Rig and Instrumentation

Compressor. The compressor used for the present investigation was a low-speed constant annulus three-stage machine, which could be configured in a variety of different builds. The design speed was 3000 rpm with a mean blade speed of 50 m/s.

The blades were of free vortex design with the degree of reaction varying from 0.66 at the tip to 0.31 at the hub and with 0.5 at the midheight. The blades could be set to any stagger angle desired. In order that the blade rows in the compressor should be fully interchangeable, the width of each rotor and stator ring (in which the blades were mounted) was identical. This simply means that the axial distance between the center lines of each blade row was fixed. When the blades were set at design stagger, the axial gap between blade rows could be either 40 or 70 percent of axial chord length (depending on the spacers used). When the stagger was altered, however, the spacing between the trailing edges of adjacent blade rows was clearly a function of the stagger setting.

The flow rate was controlled by a manually operated throttle. The mass flow through the compressor was measured by a venturi flow meter some distance downstream. Details of the compressor geometry are given in Fig. 1 and Table 1. Details of the builds tested are given in Table 2 where the variation

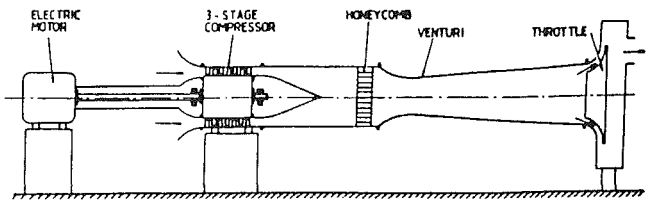

Fig. 1 Layout of compressor rig

Table 1

Compressor geometry	
Blade tip diameter	406 mm
Hub–tip ratio	0.7
No. of blades on each rotor	38
No. of blades on each stator	37
Blade chord	30.5 mm
Aspect ratio	2
Blade camber at midheight	27 deg
Blade stagger at midheight	38 deg
Blade cross-sectional profile	C4
Design speed	350 rev/s
Bell mouth length	160 mm
Compressor length	310 mm
Downstream duct length	1000 mm
Downstream duct diameter	406 mm
Exit duct length	1800 mm
Venturi throat diameter	254 mm

Details of compressor builds tested

Blade row	Build A	Build B	Build C
IGV	0	−12	12
R1	0	−8	8
S1	0	−4	4
R2	0	0	0
S2	0	4	−4
R3	0	8	−8
S3	0	12	−12

from the design stagger of 36 deg is shown (0 deg indicates the design stagger).

Slow Response Instrumentation. The rig was equipped with conventional (time average) wall static tappings at the inlet, the interrow gaps, and the outlet of the compressor. At each measuring station there are four static tappings at 90-deg intervals connected to a common manometer tube.

The data acquired from the wall static tappings were used to obtain the steady-state overall and individual stage characteristics of the compressor as well as the time unsteady average rotating stall characteristics.

The mass flow rate through the machine was measured using the calibrated downstream venturi. The flow through the venturi was straightened using an upstream honeycomb mesh. The venturi had four static tappings at 90-deg intervals at both the 406 mm diameter inlet and at the 256 mm throat.

Instantaneous (Real Time) Instrumentation for the Unsteady Measurements. The instantaneous or real time instrumentation is shown schematically in Fig. 2, consisting of cylindrical yaw probes with closely coupled fast response pressure transducers, a bank of amplifiers, low pass filters, a sample and hold unit with a trigger circuit, an oscilloscope, an analog-to-digital converter, and a BBC computer with a floppy disk drive.

The flow measurements in the rotating stall regime were performed using the cylindrical three-hole-type yaw probe, which was 4 mm in diameter, and a wall static probe (to be described later). The three-hole probe had been used earlier for the rotating stall investigation by Das and Jiang (1984) and

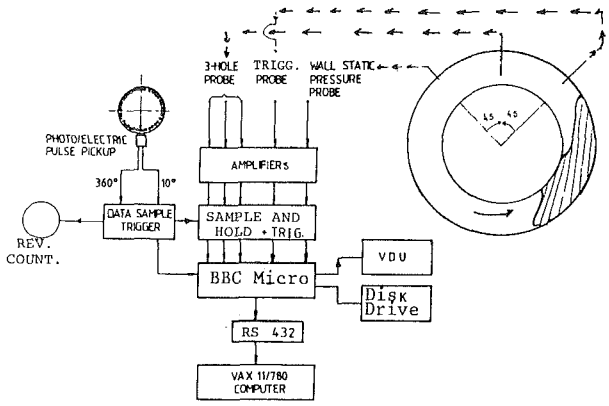

Fig. 2 Layout of data acquisition system

was found to be suitable for the present investigation. Each of the three tappings of the yawmeter was separately connected to a Kulite solid state transducer (XCQ-080-1G), the measuring range of which was 7.0 KPa. The natural frequency of the transducer was 100 kHz but because of the interconnecting tube length (maximum 33 mm between the transducers and the pressure tappings), the overall system natural frequency response was a lot lower, but adequate to define stall cells, which rotate at up to 60 percent of the rotor rotational frequency. The calibration procedure and the analysis of the data was performed as described by Das and Jiang (1984).

A static probe (incorporating a fourth fast response transducer) was also used in order to verify dynamic static pressure measurements near the tip. The wall static probe was always placed 45 deg after the measuring probe and was also used to measure the speed of propagation of the stall cell.

The accuracy of the results was influenced by voltage drifts in the transducer outputs caused by small temperature drifts. Observations showed that measurement of yaw gave the largest error especially in regions where the airflow velocity was small. These errors were of the order of ±1 deg, which would not influence the conclusions of this study.

An ensemble-averaging technique was employed to overcome the randomness in the signal and for this purpose a trigger probe was positioned at a fixed station to phase lock the measuring process to the rotating stall cell.

Time Average Results. The time average measurements were taken using the conventional instrumentation. The overall total-to-static characteristics for the three builds are shown in Fig. 3(*a*), the individual static-to-static stage characteristics for the first build in Fig. 3(*b*), for the second build in Fig. 3(*c*), and for the third build in Fig. 3(*d*).

General Observations

Build 1 (All Stages Geometrically Repeating). From Fig. 3(*b*), it can be seen that all stages stalled simultaneously at the same throttle position (as would be expected).

The compressor noise increased as the stall point was ap-

Nomenclature

U = mean rotor speed
V_a = axial velocity
V = absolute velocity
Vw = whirl velocity
Va/U = flow coefficient

$DPtt/1/2\rho U^2$, ψtt = nondimensional total-to-total pressure rise coefficient
$DPts/1/2\rho U^2$, ψts = nondimensional inlet total-to-exit static pressure rise coefficient
$DPss/1/2\rho U^2$, ψss = nondimensional static-to-static pressure rise coefficient

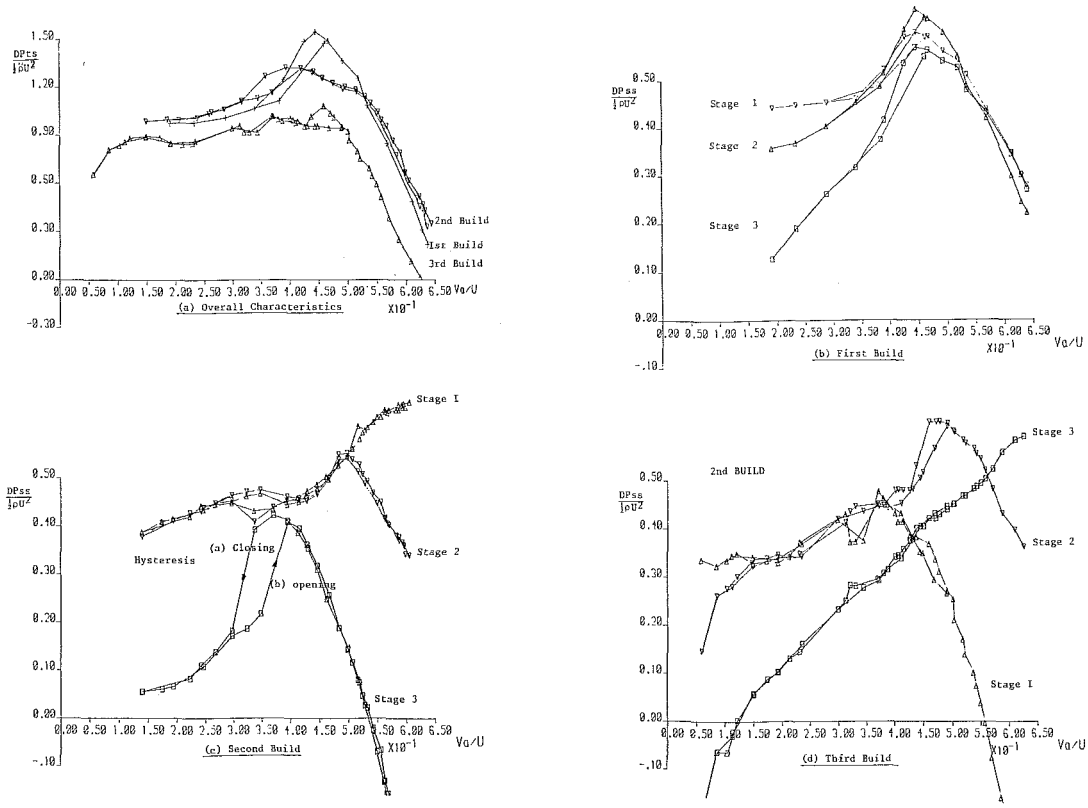

Fig. 3 Pressure rise characteristics for the three builds

proached. Immediately prior to stall the compressor noise had a distinct high frequency, but when it stalled the dominant frequency component was that of the rotating stall. The stall inception occurred at $Va/U = 0.45$, and the first stable flow condition established after stall was at $Va/U = 0.43$. At this flow coefficient, the compressor exhibited single-cell part-span rotating stall at the tip, with a speed of propagation of 55 percent of the rotor speed. Closing the throttle further to $Va/U = 0.394$, part-span stall was still present but with a smaller speed of propagation and a larger circumferential extent. At $Va/U = 0.343$ the compressor stalled more severely and exhibited full-span single-cell rotating stall. Opening the throttle from this operating point, the usual hysteresis occurred before the compressor moved from the stalled stable operating point of $Va/U = 0.391$, into the axisymmetric part of the compressor's performance curve.

Build 2 (Increased Stagger Toward the Rear Stages). In Fig. 3(*c*) the static-to-static characteristics are shown for the first, second, and third stages, for both accelerating and retarding flow rates. As we can see the first stage was stalled (i.e., had a pressure characteristic with positive slope) at the fully open throttle position. As the flow was reduced from this flow condition, the next stage to stall was the second, and as the flow was reduced even further, at the point where the third stage reached its maximum pressure ($Va/U = 0.36$) and the slope of the compressor performance curve became positive, small flow perturbations appeared, which involved the annulus averaged flow. As the flow was slowly reduced, part-span rotating stall appeared progressively at the tip with its circumferential extent eventually covering 80 percent of the circumference. This part-span stall changed abruptly to a single-cell full-span stall with a further small reduction of flow. The stable point following the full span onset was at $Va/U = 0.33$. At flow rates above those where rotating stall was established, the first and second stages were operating stalled (i.e., on pressure characteristics with positive slopes) although there was no apparent rotating stall. This leads us to the conclusion that the two inlet stages (up to $Va/U = 0.36$) were operating in axisymmetric stalled flow.

Reducing the flow further from $Va/U = 0.33$, the basic single-cell full-span rotating stalled flow properties were again observed, with the stall cell increasing in size circumferentially and reducing the speed.

Opening the throttle resulted in a hysteresis in the overall total-to-static characteristics before rotating stall recovery. The first and second stage characteristics (Fig. 3*c*) showed only a small degree of hysteresis (with a small pressure change and a small discontinuity) whereas the third stage suffered a significant influence. Opening the throttle further (Fig. 3*c*), there was no further evidence of any hysteresis.

Build 3 (Decreasing Stagger Toward the Rear Stages). From Fig. 3(*d*) we can see that the third stage stalled even at the maximum flow (when the throttle was fully open). As for Build 2, however, no rotating flow disturbances were observed. As the compressor was throttled further, the second stage stalled at about $Va/U = 0.47$, which was accompanied by an abrupt drop in pressure and flow (Fig. 3*d*). This was the first flow condition at which rotating flow disturbances were observed for this build. The discontinuity associated with this abrupt stall affected all the blade rows and the overall compressor characteristics. The first stage, however, continued to operate unstalled (with a pressure characteristic with negative slope). After the second stage stalled the first stable flow was at $Va/U = 0.42$. The rotating cells were of part-span and multiple type (stable at the hub), which are more common on low hub-type ratio machines, where the stalling process is usually progressive.

Reducing the flow further, as we can see from the overall total-to-static characteristics, the outlet pressure started to rise again. At $Va/U = 0.37$ the first rotor reached its maximum pressure rise and the compressor again stalled abruptly, but in this case, quite severely, with a sharp pressure discontinuity.

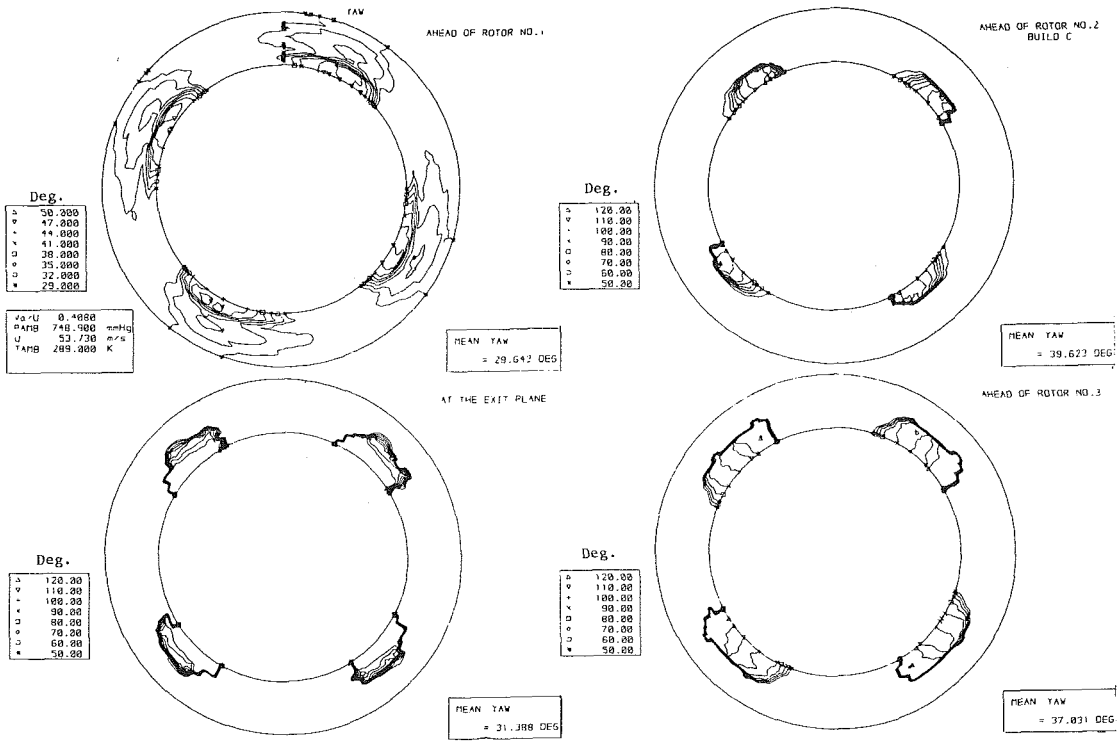

Fig. 4 Yaw ahead of rotors and exit plane

With this event the behavior of the whole compressor changed and it started exhibiting full-span rotating stall throughout the axial extent of the machine although at the station ahead of the first rotor, the stall cell did not initially cover the whole blade.

At flow coefficients between 0.280 and 0.150 there was an irregular nonperiodic type of intermittent rotating stall. This intermittent rotating stall changed pattern at such a frequency and also affected the annulus average flow in such a manner that made it very difficult to record the wall static pressures.

Reducing the flow below $Va/U = 0.150$ the intermittent type of stall changed and the normal periodic full-span rotating stall resumed. Increasing the flow, a very small hysteresis occurred (Fig. 3*d*) before the single-cell rotating stall recovery. The more noticeable hysteresis, however, occurred at the point of multicell stall recovery on the first and second stages.

Instantaneous Measurements (Phase Locked, Unsteady Measurements). Instantaneous measurements using the fast response instrumentation were performed for all three builds at various flow rates. In this paper, however, instantaneous measurements will only be presented for the third build (with the high stagger in the inlet and the low stagger at the rear stages), for $Va/U = 0.408$. This was the operating point where the multicell structure consisted of four rotating cells. The basic reason for not presenting the unsteady flow results for the other two builds was the bulk of the results obtained and the limited space available and also because the results obtained for the third build are considered to be more relevant to multistage high-speed operation. It is interesting to note, however, that the full-span rotating stall encountered (eventually) in all the builds tested had general properties that were similar to those reported by Das and Jiang (1984), and Day (1976), when studying rotating stall in low-speed multistage compressors with repeating stages, the most significant differences being in the actual shape of the cell.

When the compressor first stalled at $Va/U = 0.46$ the first rotating stall pattern to appear was a single cell, which randomly gave way to a two-cell structure. This flow situation, however, was not stable enough for flow measurements. The first stable flow was at $Va/U = 0.420$ and detailed measurements were obtained at $Va/U = 0.408$.

The rotating stall cells (initially three) were symmetrically spaced. Their speed of propagation was 36 percent of the rotor speed. As the flow was reduced further (prior to full-span stall) their number increased to seven.

This type of multiple-cell part-span rotating stall is usually encountered with low hub-to-tip ratio machines and also, probably, at the front and middle stages of multistage high-speed compressors. According to Benser and Hupert (1953) part-span rotating stall could originate at the hub in free vortex blading machines. In this particular case, the stall cells not only originated at the hub, but, as the results show, they were stably established in this position.

As we can see from the axial extent of the flow (Fig. 4), the biggest variation in flow angle took place ahead of rotors two and three, at the exit, and always at the hub. In the same axial positions, negative axial velocities (which indicate reverse flow), can also be seen (Fig. 5). Between midheight and tip, however, the positive axial velocity took its maximum value (being some 60 percent larger than the axial velocity in the part of the annulus where the flow was completely unstalled). Ahead of rotor one the flow seemed to be almost undisturbed (by the downstream stall) where even at the hub the flow disturbance had been considerably attenuated, diminishing even further at the inlet plane ahead of the IGVs.

The amplitude of the flow variations and the circumferential and radial extent of the stall cell suggest that it was the third stage that caused the flow instability; the fact that the third rotor has the lowest stagger supports this suggestion. However, the third rotor only exhibited rotating stall after the second stage stalled (resulting in the sudden pressure drop in the static-to-static pressure characteristic, and the reduction of flow coefficient from $Va/U = 0.46$ to $Va/U = 0.42$, Fig. 3*d*).

Since this multicell stall structure had the unusual feature of being stable at the hub, a more detailed investigation was initiated during which detailed measurements were performed at

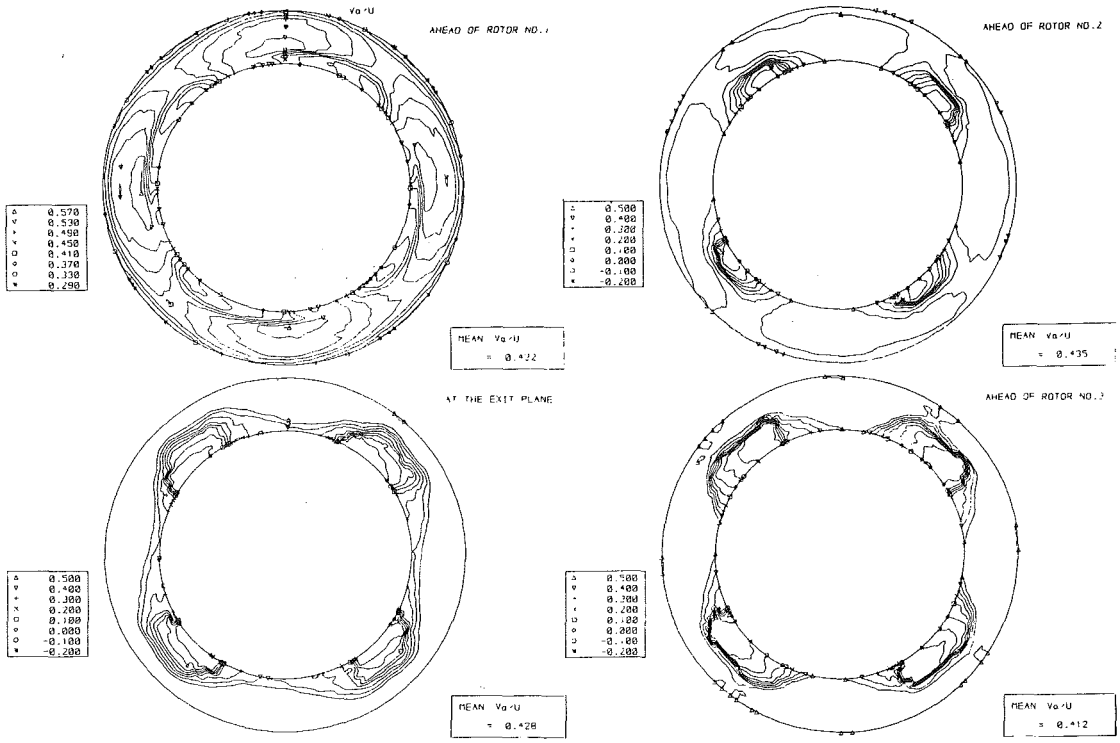

Fig. 5 *Va/U* ahead of rotors and exit

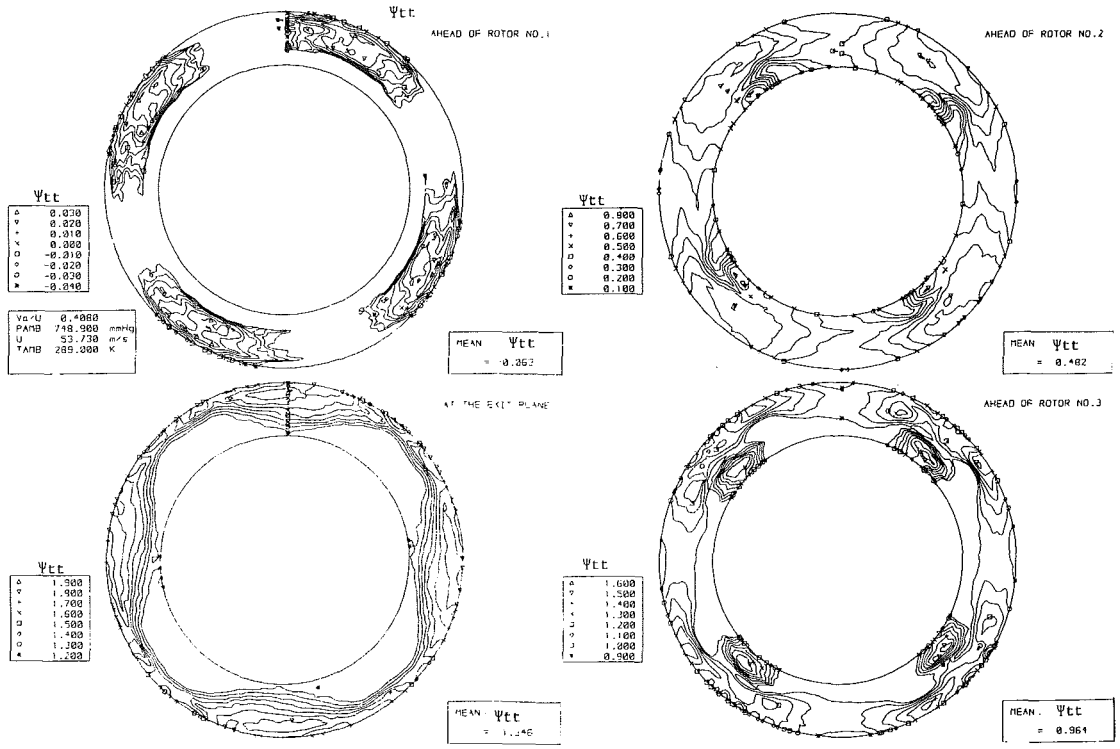

Fig. 6 PTOTAL ahead of rotors and exit plane

twelve radial positions ahead of each rotor, ahead of the last stator, and at the exit plane. The results are presented as annular contour plots (Figs. 4–8). The individual stall cells can very easily be distinguished, and the flow properties are further discussed below.

(*a*) *Yaw Angle* (*Fig. 4*). Figure 4 shows the radial and circumferential extent of the flow angle variation. The axial nature of the cells can very easily be seen. Radially they extend halfway between hub and tip, each occupying several blade passages. The biggest circumferential and radial extent was

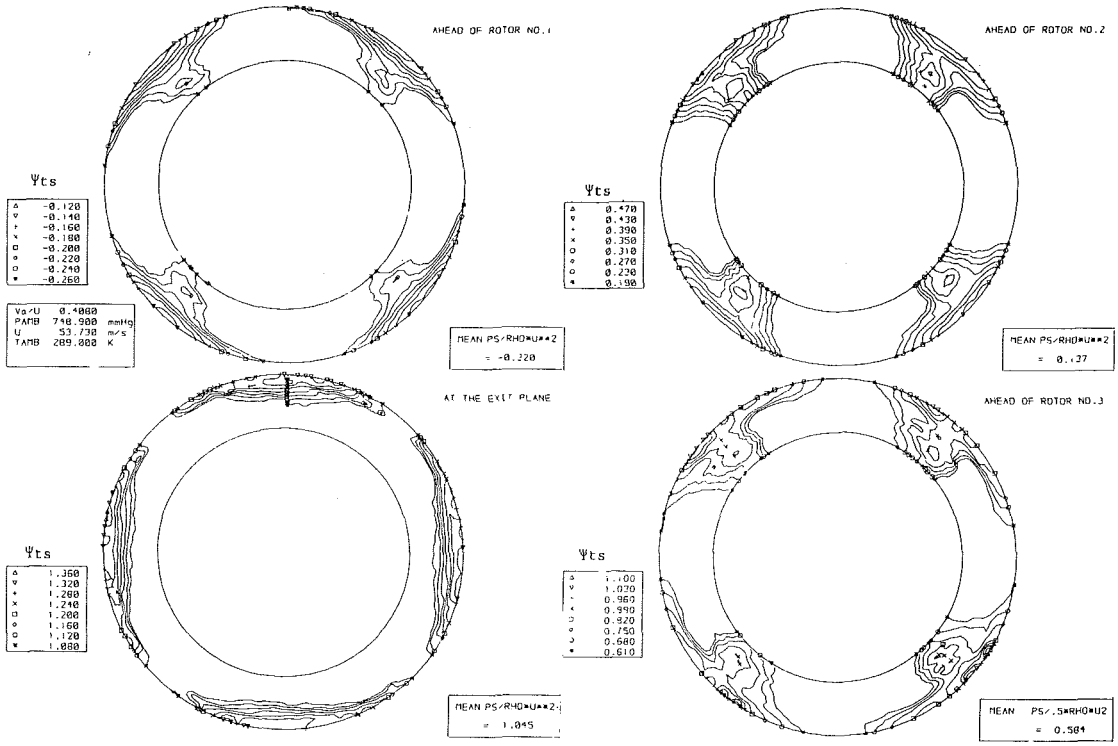

Fig. 7 PSTATIC ahead of rotors and exit

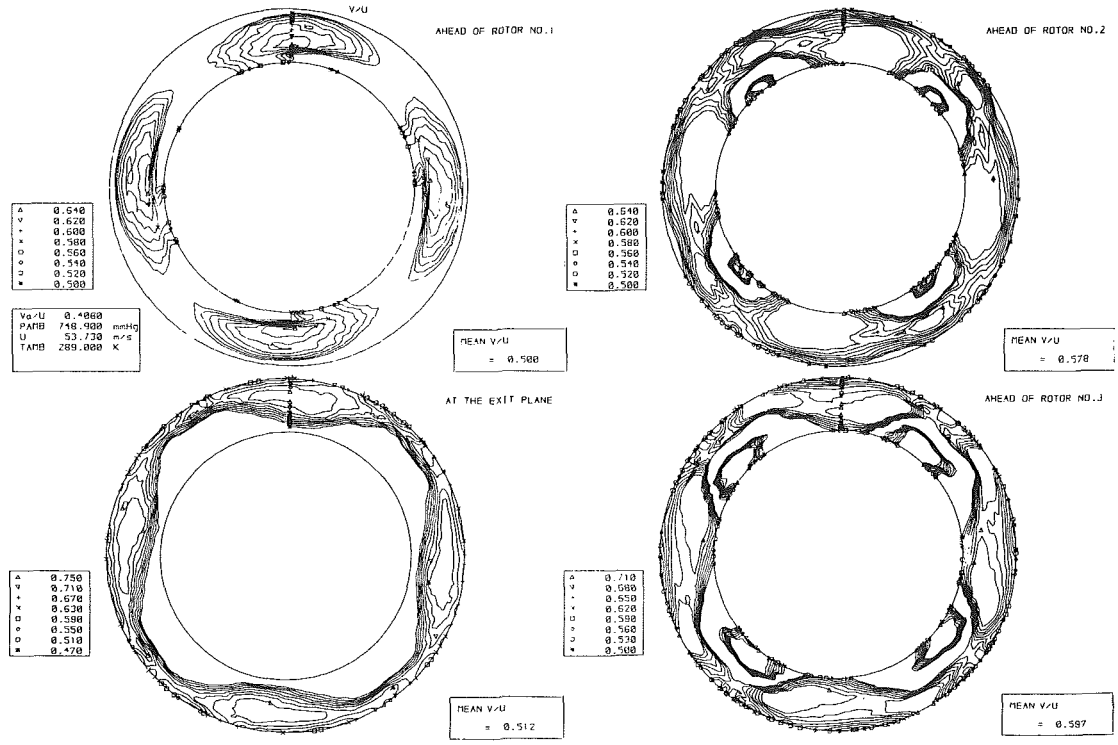

Fig. 8 *V/U* velocity ahead of rotors and exit plane

found ahead of the third rotor. The third rotor, as already mentioned, had the lowest stagger of the three and was the first stage to stall.

In the three measuring planes ahead of rotor two, rotor three, and at the exit, the flow angle reached a maximum value of 120 deg (0 deg being axial and forward) indicating a strong tangential and reversed flow. Behind rotors two and three, however, the maximum angle was 100 deg and the above 90-deg regions were extremely small compared with the size of the cell.

Ahead of rotor two the radial and circumferential extents had been considerably reduced with the maximum angle again of 120 deg, but with a smaller circumferential extent.

Ahead of rotor one the maximum angle was 50 deg, which indicated that there was no reversed flow. The flow areas of high angle simply show the influence that the stalled flow (of the rear stages) had on the unstalled flow ahead of rotor one where the stalled flow was seen as a rotating distortion.

(*b*) *Nondimensional Total Pressure* (*Fig. 6*). The total pressure in the exit plane and behind rotor three was lower in the stall cell regions. Ahead of rotor three, however, the total pressure distribution had its maximum in the center of the cell with a lower total pressure at the hub of the unstalled flow. Ahead of rotor two, the maximum total pressure was again in the cell with the minimum at the trailing edge near the hub. The cause of high total pressure in the stall cell was due to the high circumferential (whirl) component of the flow in the stall region.

Ahead of rotor one, where there was no stalled flow, the high total pressure areas had shifted toward the tip of the annulus rather than the hub, and as we can see, the variation between regions of high and low total pressure are quite small.

(*c*) *Nondimensional Static Pressure* (*Fig. 7*). The static pressure rise at the exit plane appears to show its highest value in the unstalled flow areas (similar to the distribution of total pressure) and the tip regions. Similarly, high static pressure occurred at the tip ahead of the third stator, but in this case the high static pressure variation extended through the annulus to the hub with the highest static pressure at the tip.

Ahead of the third, second, and first rotors, the high static pressure regions were at the stall cell's trailing edge with the maximum at the tip region of the annulus.

(*d*) *Absolute Velocity* (*Fig. 8*). At the exit plane the highest absolute velocity was at the centers of the unstalled flow in the midspan region. Ahead of the third stator the low absolute velocity areas were those in the stall cell.

Ahead of rotors two and three, the magnitude of the absolute velocity had its maximum in the centers of the stalled and unstalled flow, although the flow direction was different in the two regions. The lowest values of absolute velocity were at the boundaries between stalled and unstalled flow with almost zero flow at the trailing edge.

Ahead of rotor one the highest velocity was at the center of the unstalled flow; however, the difference between the two regions was very small.

(*e*) *Axial Velocity* (*Fig. 5*). Ahead of rotors two, three, and at the exit, the axial velocity was negative indicating reversed flow. Ahead of stators two and three the reverse flow values were smaller. Ahead of rotor one the Va/U values were between 0.57 and 0.29 but were always positive. As we can see from Fig. 5, in the rear interrow spaces, the stalled flow occupied approximately 50 percent of the radial span. In the remainder of the span, the throughflow increased in velocity (because of continuity) by 60 percent of the unstalled flow.

Discussion

A major feature observed in these tests was the suppression of rotating stall in heavily stalled stages, which were closely coupled with unstalled stages. To the authors' knowledge, this behavior has only previously been reported by Turner et al. (Turner, 1959; Turner and Hargest, 1959; Turner and Burrows, 1961), although others have suggested these effects (Greitzer, 1981; Freeman and Dawson, 1983). No internal flow details, however, have previously been noted. In this study it was clearly observed that abrupt single-cell stall occurred only when all stages (in each build) reached stall.

Considering the mismatched condition of a conventional multistage compressor when operating near surge, the present tests suggest that stall cell formation in the stalling stages will be considerably influenced by the presence of unstalled stages. This influence will depend on the distance between the first and later stages, the degree of mismatching, and the individual stage characteristics.

In actual multistage compressors, at low speeds, many cases have been reported where several front stages have operated in stall without severely affecting the rear stages. This is usually because the disturbance to the flow, created by the early stages, is attenuated toward the rear, given the number of blade rows, the mismatch, and the distance that separates the inlet from the rear stages.

In the present study (with only three stages available), however, there was simply not enough attenuation for complete suppression of the cells through the compressor. In the case of the third build, there was a situation of four hub rotating cells (in the second and third stages) that were attenuated, permitting the inlet stage to operate free of stall (although the presence of the rotating stall downstream was seen by the first stage as a rotating distortion). A further observation made in this study was that the rotating stall did not develop (or appeared not to depend) on the stalling point of an individual stage or blade row. This suggests that in multistage machines (where stage mismatching is present), a simple blade stall is not the only necessary condition for rotating stall to develop. It is proposed that a situation similar to that described here occurs as high-speed multistage compressors approach stall and is more complicated than that represented by multistage low-speed compressors with geometrically repeating stages.

The present results of the second build suggest that for rotating stall to develop, in addition to individual blade stall, some system instability is required, such as exceeding the peak of the overall pressure rise characteristics. In multistage machines, however, this may be an insufficient criterion (Elder and Gill, 1984) for system stability or surge.

In the third build, part-span rotating stall appeared in the part of the overall performance curve with negative slope as it may do in actual multistage compressors operating at high speeds. In these machines, however, rotating stall is not actually detected because under these conditions the high-speed compressors usually develop surge.

Finally, the results of this study have clearly demonstrated that the structure of the abrupt single-cell rotating stall (also reported by Das and Jiang, 1984, and Day, 1976), which extends axially throughout the machine, is quite different from the part-span multiple-cell rotating stall cell also observed in the present tests, which was restricted to the two rear stages. This multiple-cell flow occupied only two stages, leaving the third almost unaffected. This part-span structure appears to be closer to the actual rotating stall, which occurs in most high-speed multistage machines where the compressor may operate with only a few stages stalled (leaving the rest unaffected), than the single-cell full-span stall more commonly reported from low-speed tests.

Conclusions

Detailed measurements in the rotating stall regime of a three-stage low-speed compressor have been performed. Three builds have been tested, one in which the stages repeated (matched) and two in which either the inlet or the exit stages were arranged to stall prematurely. These studies were performed using a fast response cylindrical yawmeter with a real time data acquisition system. The major observations of this study were as follows:

- The full-span single-cell rotating stall results confirmed, in general, the results published by other investigators, e.g., Das and Jiang (1984) and Day (1976).
- The part-span multicell rotating stall of build 3 (increas-

ing stagger toward the rear stages) show that it is possible for a mismatched compressor to operate with only some stages of the compressor exhibiting rotating stall. This type of operation is thought to be more relevant to high-speed multistage compressor operation.

- Rotating stall operation is also possible with rotating stall restricted to only the hub region of the span. This is not unique but unusual.
- For rotating stall to develop in a multistage machine, a simple blade or stage stall is not necessarily followed by rotating stall as other factors, such as stage interaction and overall compressor stability, influence the point of rotating stall inception.

References

Das, D. A., and Jiang, H. K., 1984, "An Experimental Study of Rotating Stall in a Multistage Axial-Flow Compressor," ASME *Journal of Engineering for Gas Turbines and Power*, Vol. 106, pp. 542–551.

Day, I. J., 1976, "Axial Compressor Stall," PhD Thesis, Christ's College, Cambridge, United Kingdom.

Elder, R. L., and Gill, M. E., 1984, "A Surge Prediction Method for Multistage Axial Flow Compressors," IMechE, Birmingham Conference, Paper No. C74/84.

Freeman, B., and Dawson, R. E., 1983, "Core Compressor Development for Large Civil Jet Engines," ASME Paper No. 83-Tokyo-IGTC-46.

Greitzer, E. M., 1981, "The Stability of Pumping Systems – The 1980 Freeman Scholar Lecture," ASME *Journal of Fluids Engineering*, Vol. 103, pp. 193–242.

Huppert, M. C., and Benser, W. A., 1953, "Some Stall and Surge Phenomena in Axial-Flow Compressors," *Journal of Aeronautical Sciences*, Jan., pp. 835–845.

Turner, R. C., 1959, "The Effect of Axial Spacing on the Surge Characteristics of Two Mismatched Axial Compressor Stages," A.R.C. Technical Report C.P. No. 431.

Turner, R. C., and Burrows, R. A., 1961, "Some Surge Investigations on a Low Speed Compressor," A.R.C., C.P. No. 548.

Turner, R. C., and Hargest, T. J., 1959, "Stall Cell Propagation in Two and Burrows, R. A., Mismatched Compressor Stages," A.R.C. Technical Report C.P. No. 449.

Application of Bifurcation Theory to Axial Flow Compressor Instability

F. E. McCaughan[1]

Cornell University,
Ithaca, NY 14853

When a compression system becomes unstable, the mode of response depends on the operating and system parameters, such as throttle setting and B *parameter. Previous numerical work on the model developed by Moore and Greitzer has provided a limited picture of the parametric effects. Applying bifurcation theory to a single-harmonic version of the model has supplied much more complete information, defining the boundaries of each mode of response in the parameter space. Specifically this is shown in a plot of* B *versus throttle setting, which compares well with the corresponding map produced experimentally. We stress the importance of the shape of the rotating stall characteristic. The analysis shows the qualitative difference between classic surge and deep surge.*

Introduction

When the mass flow in an axial compression system is reduced, the pressure rise increases until a point is reached where steady axisymmetric flow is no longer stable. Clearly one wants to operate the system as close as possible to this critical point, but then a small change in the flow may be enough to cause instability. From the engine designer's point of view it is desirable to be able to predict what type of flow will develop in place of the design flow, if circumstances happen to put one into the unstable region.

The flows that are observed can be basically categorized as steady rotating stall, deep surge, and classic surge. When the machine experiences rotating stall, part of the annulus of the compressor operates in stalled flow, and this so-called "stall cell" rotates around the annulus at about half of the wheel speed. If the angle-averaged mass flow and pressure rise are constant and one moves in a frame of reference with the stall cell, the flow is steady and this type of flow is classified as steady rotating stall. This new steady point has a much lower pressure rise than the design point. Varying the mass flow traces out a line of rotating stall points on the compressor map of pressure rise versus mass flow, called the rotating stall characteristic. Surge is an oscillation of mass flow and pressure rise along the axial length of the compressor, with a frequency that is an order of magnitude lower than that associated with the passage of a stall cell. Rotating stall is usually observed to a greater or lesser extent as a high-frequency disturbance superimposed on the surge, causing two qualitatively different types of surge. When the machine operates in reverse flow over part of the cycle and rotating stall is only observed over a small fraction of the period, the flow is classified as deep surge, and when the oscillation of mass flow is smaller and rotating stall is present over most of the cycle, the flow is known as classic surge.

When the machine goes into rotating stall, severe blade vibrations are set up, which soon have catastrophic consequences, and recovery to the design condition is made difficult by a hysteresis effect; the mass flow has to be increased beyond the point where instability first occurred before the machine recovers to steady axisymmetric flow. However, during surge the compressor comes back close to the design point and recovery of steady axisymmetric flow is somewhat simpler. Experimental work has shown that the relationship between the mode of response and the parameters is not simple. For example, the experimentally produced map in Fig. 12 shows how the compression response is related to the wheel speed and the equilibrium mass flow.

The recent upsurge of computational power and developments in theory by Moore and Greitzer (1986) have renewed interest in this problem. They have developed a complex set of partial differential equations, which model the fluid mechanics of the compression system. These equations can only be solved by a major computational effort, and this line of approach is discussed in the companion paper (McCaughan, 1989a). In the present paper, we look at a simplified version of the equations, which has already been tackled numerically by Greitzer and Moore (1986) and Moore (1985). Herein we use a more analytical approach, i.e., bifurcation theory. The computations of Greitzer and Moore (1986) and Moore (1985) showed that the simple model captures most of the essential physics, but those papers have only a limited discussion of the parametric effects. Such a study is long and tedious when carried out numerically, but with the application of the bifurcation theory we can define the boundaries of the regions

[1]Current address: Case Western Reserve University, University Circle, Cleveland, OH 44106.

Contributed by the International Gas Turbine Institute and presented at the 33rd International Gas Turbine and Aeroengine Congress and Exhibition, Amsterdam, The Netherlands, June 5–9, 1988. Manuscript received by the International Gas Turbine Institute July 8, 1987. Paper No. 88-GT-231.

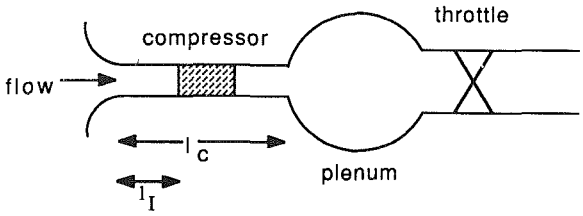

Fig. 1 Schematic of an axial flow compression system

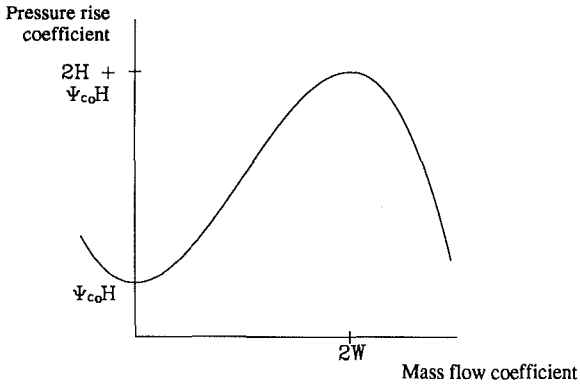

Fig. 2 The cubic axisymmetric function, Ψ_c (Φ). Included are the parameters *W*, *H*, and Ψ_{co}.

in parameter space where each flow can occur. So for a given set of parameters, we learn which modes of response are possible and in the case where more than one solution is possible, a prediction can be made in light of the initial conditions.

The simplified model referred to above results from representing the rotating stall component of a general disturbance by its first Fourier mode. Since it is observed both experimentally and numerically that most of the energy of any rotating stall is contained in this mode, we are justified in studying the three time-dependent ordinary differential equations that result from such a severe truncation. The simplification has the added advantage that the eight parameters of the full model can now be reduced to four.

A schematic of the axial compression system is shown in Fig. 1. The flow enters an inlet region where it is assumed to be incompressible and irrotational. Any disturbance that develops in the inlet is assumed to move straight through the compressor into a plenum chamber where all the angular variation is lost. The flow is then discharged through a throttle duct. The full model is described in detail in the companion paper and in the references and so we move straight to the simplified model.

The ordinary differential equations that result from the one mode truncation are as follows:

$$\Phi'(\xi) = -\Psi + \Psi_c(\Phi) - 3\Phi R \tag{1}$$

$$\Psi'(\xi) = \frac{1}{\beta^2}(\Phi - \Phi_T(\Psi)) \tag{2}$$

$$R'(\xi) = \sigma R(1 - \Phi^2 - R) \tag{3}$$

The variable Φ is nondimensional mass flow coefficient, which has been shifted so that zero mass flow actually occurs at $\Phi = -1$, and rescaled with W. Ψ is the nondimensional pressure rise of the compressor rescaled with H. It can never be less than zero. Both of these variables are averaged over the annulus of the compressor. These rescalings give rise to the parameter S, which is equal to H/W. The third variable, R, is the square of the amplitude of the first mode of the rotating stall disturbance, so it only has physical meaning when it is positive. Equation (1) results from summing the pressure rise through each component and then averaging over the annulus of the compressor. The function Ψ_c represents the response of the compressor in steady axisymmetric flow, and we represent this with the following cubic function:

$$\Psi_c(\Phi) = \Psi_{co} + 1 + \frac{3}{2}\Phi - \frac{1}{2}\Phi^3$$

It is a good representation when such a flow is stable, and a reasonable guess when the flow is unstable. The parameter Ψ_{co} is the shutoff head, and it is proportional to the number of stages in the compressor. Parameters Ψ_{co}, H, and W are shown in Fig. 2.

Equation (2) is the mass conservation equation for the plenum chamber, where Φ_T is the mass flow leaving the plenum and exiting through the throttle duct. The pressure rise through the throttle is modeled by a simple parabolic relationship

$$\Psi = \frac{1}{\gamma}(\Phi_T + 1)^2$$

Nomenclature

a = parameter reflecting stability of periodic orbits
B = Greitzer's B parameter
H = half of the difference between the maximum pressure rise and the shutoff head
l_c = total length of compressor and ducts in wheel radii
norm = norm reflecting the size of periodic orbits and the position of the equilibria
r = a variable used in discussion of Hopf bifurcation, equation (6)
R = square of the amplitude of the first mode of rotating stall disturbance
R_e = equilibrium value of R
S = parameter reflecting rescaling of mass flow and pressure rise = H/W
W = half of the mass flow, which gives the maximum pressure rise
x = a variable used in discussion of bifurcations, equations (4) and (5)
x_{01} = axisymmetric equilibrium point
x_{02} = rotating stall equilibrium point
x_{03} = saddlelike nonaxisymmetric equilibrium point
β = $2BS$
γ = parabolic throttle coefficient
γ_c = parabolic throttle coefficient where throttle passes through peak of cubic
γ_s = parabolic throttle coefficient where throttle first touches the rotating stall characteristic
λ_1 = eigenvalue of the Jacobian derivative = $\sigma(1-\Phi_e^2)$
μ = a parameter used in the discussion of the bifurcation equations (4), (5), and (6)
ξ = time, referred to time for wheel to rotate one radian, rescaled with l_c/S
σ = parameter reflecting l_c
Φ = flow coefficient averaged over angle (axial velocity divided by wheel speed) rescaled with W
Φ_e = equilibrium value of Φ
Ψ = total-to-static pressure rise coefficient (inlet to plenum) rescaled with H
Ψ_c = axisymmetric pressure rise coefficient rescaled with H
Ψ_{co} = shutoff head coefficient rescaled with H
Ψ_e = equilibrium value of Ψ

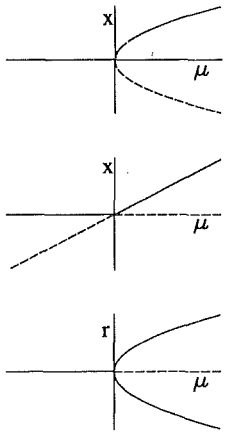

Fig. 3 The static bifurcations observed in equations (1)–(3). The stationary solutions correspond to equations (4)–(6), and the dashed lines indicate instability.

The cross-sectional area of the throttle is directly proportional to the parameter γ. We control the equilibrium mass flow by opening and closing the throttle, i.e., by increasing and decreasing γ.

The remaining parameters of equations (1)–(3) are combinations of the parameters from the full model. β is the combination of Greitzer's B parameter and the parameter S just described:

$$S = \frac{H}{W} \quad \text{and} \quad \beta = 2BS$$

The parameter σ is a complicated combination of physical dimensions and modeling parameters, which mainly reflects the inertial length of the compressor ducting. This parameter has little influence on the solution of equations (1)–(3), so it is fixed at a reasonable physical value of 7.

It is to these equations that we apply the bifurcation theory, the results from which allow the prediction of the compressor response before resorting either to experiment or to large-scale numerical calculation. In this paper we compare these analytical results with the experimental results of Greitzer (1976). In the companion paper (McCaughan, 1989a) a further check is made against the numerical results of the full set of partial differential equations. Before proceeding with the analysis of equations (1)–(3), we give a simple introduction to the ideas involved in the bifurcation theory.

Bifurcation Theory

The first step in the application of bifurcation theory to a system of ordinary differential equations is the classic small perturbation analysis. We locate the stationary solutions of the equations, and then examine the eigenvalues of the Jacobian derivative evaluated at each such point. A "static" bifurcation occurs when one of the eigenvalues has a zero real part. The dynamics of the equations change qualitatively at such points. The static bifurcations that occur in equations (1)–(3) are the saddle node bifurcation, the transcritical bifurcation, and the Hopf bifurcation, and we look at the simplest occurrences of these bifurcations in equations with one parameter, μ. In all of the following cases, the bifurcation occurs at $\mu = 0$.

When the Jacobian derivative associated with a fixed point has a single zero eigenvalue, the qualitative change in behavior can be shown by a single equation. For example, the following equation captures the essence of the saddle node bifurcation:

$$x'(t) = \mu - x^2 \tag{4}$$

Figure 3(a) is called a bifurcation diagram, and it shows how the equilibria vary with a parameter, in this case μ. When $\mu < 0$, there are no equilibria and for any initial condition, $x \to -\infty$, but when μ is positive there are two stationary solutions, $x = \pm\sqrt{\mu}$. A simple linearization around each stationary point shows that the positive solution is stable and the negative one is unstable. Now the solution depends on the initial condition, i.e.,

$$\text{if } x_0 < -\sqrt{\mu} \quad \text{then} \quad x \to -\infty$$

$$\text{if } x_0 > -\sqrt{\mu} \quad \text{then} \quad x \to -\sqrt{\mu}$$

Clearly the qualitative behavior changes at the bifurcation point, $\mu = 0$. Extending this to the two-dimensional situation, one of the fixed points appearing at a saddle node bifurcation is always a saddle, with one positive eigenvalue and one negative eigenvalue. The other fixed point has two eigenvalues with the same sign. If they are negative it is a stable and attracting node, and if they are positive the fixed point is an unstable and repelling node. Hence the name, saddle-node.

The next equation also has a fixed point with a single zero eigenvalue at $\mu = 0$

$$x'(t) = \mu x - x^2 \tag{5}$$

There are two stationary solutions to this equation, $x = 0$ and $x = \mu$, which exist for all μ and are shown in the bifurcation diagram, Fig. 3(b). The bifurcation in this instance causes the stability of these solutions to change. When $\mu < 0$, the $x = 0$ solution is stable and $x = \mu$ is unstable. When μ becomes positive, $x = 0$ loses stability, and $x = \mu$ gains stability. In each case the solution depends on the initial condition x_0. When $\mu < 0$

$$\text{if } x_0 < \mu, \quad \text{then } x \to -\infty$$

$$\text{if } x_0 > \mu, \quad \text{then } x \to 0$$

and when $\mu > 0$

$$\text{if } x_0 < 0, \quad \text{then } x \to -\infty$$

$$\text{if } x_0 > 0, \quad \text{then } x \to \mu$$

This kind of qualitative change is called a transcritical bifurcation.

A Hopf bifurcation is responsible for the change in stability of a fixed point and the birth of a periodic orbit, as is easily seen in the following example given in cylindrical coordinates:

$$r'(t) = r(\mu - ar^2) \tag{6}$$

$$\theta'(t) = f(r, \theta) \tag{7}$$

For all values of μ there is a stationary solution, $r = 0$. When $\mu < 0$, this fixed point is stable and all trajectories nearby spiral into this point. It loses stability when μ becomes positive and nearby trajectories then spiral outward. The existence of another solution depends on the signs of μ and a

$$r^2 = \frac{\mu}{a}$$

When $a > 0$, a stable solution is born at $\mu = 0$ and exists for $\mu > 0$. This case is shown in Fig. 3(c) and is called a supercritical bifurcation. On the other hand, when $a < 0$, an unstable solution exists for $\mu < 0$, and the Hopf bifurcation is called subcritical. Neither of these nonzero equilibrium solutions of r defines a fixed point since $\theta'(t) \neq 0$. Instead they define a periodic solution where $\theta'(t)$ gives the angular velocity. If these equations were rewritten in Cartesian coordinates, it would be obvious that the bifurcation occurs when the eigenvalues associated with the fixed point are purely imaginary.

In general, when analyzing a bifurcation of a given type, we can systematically reduce the dimension of a large problem using the center manifold theorem. On the center manifold, an invariant manifold tangent to the center eigenspace, the

generic bifurcation is qualitatively the same as the relevant case discussed above. For more details on this theory the reader is referred to Guckenheimer and Holmes (1983).

In summary, a saddle-node bifurcation produces two stationary solutions, at least one of which will always be unstable. A transcritical bifurcation leads to the change in stability of two stationary solutions and a Hopf bifurcation causes the change in stability of one stationary solution, and the birth of a periodic orbit. In the next section we apply these ideas to equations (1)–(3), locating the stationary solutions and then discussing their bifurcations.

Axisymmetric Solutions

Equations (1)–(3) always have a steady solution with $R_e = 0$. We label this point x_{01}, where

$$x_{01} = (\Phi_e, \Psi_e, 0)$$

and

$$\Phi_e = \Phi_T(\Psi_e)$$

$$\Psi_e = \Psi_c(\Phi_e)$$

These equilibrium values of mass flow and pressure rise are located at the intersection of the throttle line and the axisymmetric characteristic. It is worthy of note that if $R = 0$ initially, then it will remain zero for all time. The (Φ, Ψ) plane is then called invariant, and trajectories on the plane represent axisymmetric flow. If the perturbations have no asymmetric component, the flow will remain axisymmetric.

The diagram showing the bifurcation points in parameter space is called a bifurcation set. In this case the important parameters are β and γ, and the bifurcation set of x_{01} is shown in Fig. 4.

The Jacobian derivative of the equations is

$$\begin{pmatrix} \Psi_c'(\Phi_e) - 3R_e & -1 & -3\Phi_e \\ \beta^{-2} & -\beta^{-2}\Phi_T'(\Psi_e) & 0 \\ -2\sigma\Phi_e R_e & 0 & \sigma(1-\Phi_e^2-2R_e) \end{pmatrix} \quad (8)$$

Into this we substitute x_{01} and calculate the associated eigenvalues. When the throttle is opened enough, the eigenvalues all have negative real part and the steady axisymmetric flow is stable. The first eigenvalue to become positive is:

$$\lambda_1 = \sigma(1-\Phi_e^2)$$

The associated eigenvector is $(\Phi_e, \Psi_e, 1)$, pointing up out of the $R = 0$ plane. When $\Phi_e = 1$, $\lambda_1 = 0$, and we label this throttle setting γ_c. Closing the throttle further results in the loss of stability of x_{01}. Another fixed point with $R_e = 1 - \Phi_e^2$ is involved in this loss of stability and we recognize this as a transcritical bifurcation. We will discuss the nonaxisymmetric fixed points with $R \neq 0$ in the next section. At the bifurcation point, the throttle line intersects the axisymmetric characteristic at the point where it has zero gradient. After the transcritical bifurcation, x_{01} is unstable to perturbations of rotating stall, but the steady flow is still axisymmetrically stable, so the design flow loses stability first to rotating stall disturbances. The other eigenvalues of x_{01} at the bifurcation point are a complex pair with negative real part, and the eigenspace associated with them is the $R = 0$ plane. Since this plane is invariant, we can drop equation (3) and consider only equations (1) and (2), which describe the purely axisymmetric flow.

If we continue to close the throttle, a point is reached where the real part of the complex pair of eigenvalues is zero—a Hopf bifurcation point. The transcritical bifurcation is fixed at $\gamma = \gamma_c$, but the Hopf bifurcation is a function of β and γ. Location of the Hopf bifurcations in a two-dimensional problem is quite straightforward. The Jacobian derivative reduces to

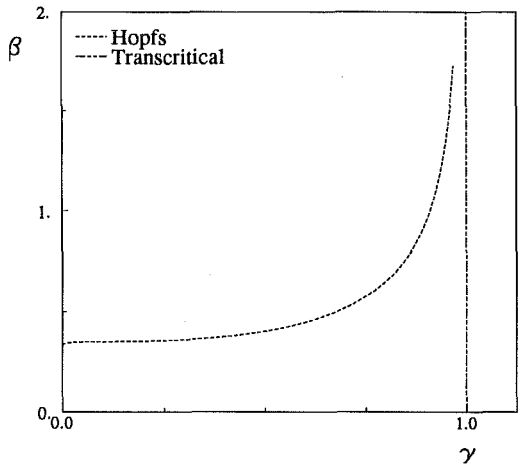

Fig. 4 Bifurcation set for x_{01}. The throttle parameter γ is normalized with γ_c.

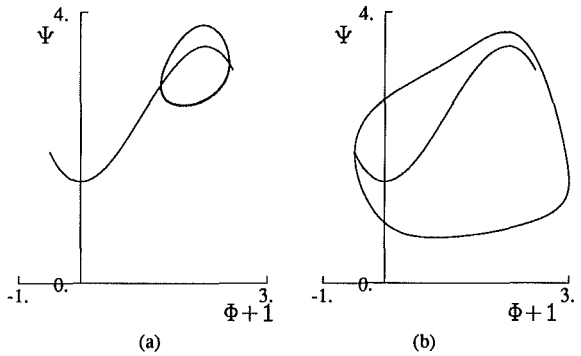

Fig. 5 Axisymmetric periodic orbits: (*a*) unstable to perturbations with nonaxisymmetric component; (*b*) stable to all perturbations, represents deep surge

$$\begin{pmatrix} \Psi_c'(\Phi_e) & -1 \\ \beta^{-2} & -\beta^{-2}\Phi_T'(\Psi_e) \end{pmatrix} \quad (9)$$

and this matrix has a purely imaginary pair of eigenvalues when its trace is zero. In that case it follows that

$$\beta^2 = \frac{\Phi_T'(\Psi_e)}{\Psi_c'(\Phi_e)}$$

and this function is depicted in Fig. 4. When $\gamma > \gamma_c$, the fixed point is stable to all perturbations, and under the curve it is axisymmetrically stable.

A periodic solution is born when we cross the line of Hopf bifurcation points in the parameter space. The stability of the orbit depends on the sign of the coefficient a in equation (6), and once we determine this value we can then say whether the periodic solutions appear above or below the lines of Hopf bifurcation points. By suitable changes of variables we can reduce equations (1) and (2) to the form discussed in the last section for the Hopf bifurcation. First we make the linear transformation that diagonalizes (9) and then, by means of a nonlinear transformation, we remove as many as possible of the higher order terms. Equations (1) and (2) are then in what is called their "normal form." For these calculations it is sufficient to remove terms up to third order. Then a change to cylindrical coordinates reduces these equations to equations (6) and (7). In this case, all the Hopf bifurcations are supercritical, so that the new limit cycle is stable on the axisymmetric plane. However, like x_{01}, this periodic orbit lies in the part of the $R = 0$ plane that is unstable to perturbations off the plane, i.e., nonaxisymmetric perturbations. As these are always pres-

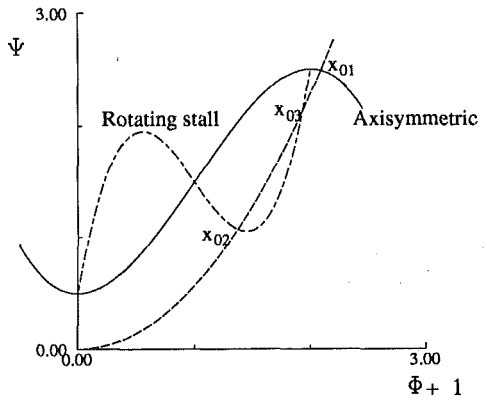

Fig. 6 The rotating stall characteristic resulting from the single harmonic analysis. Included are the cubic axisymmetric and throttle functions.

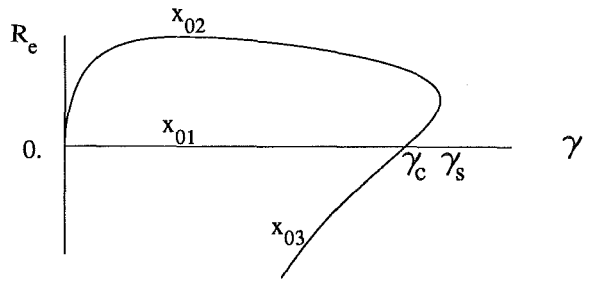

Fig. 7 The bifurcation diagram showing the equilibrium values of R_e versus the throttle setting γ. x_{01} is the axisymmetric fixed point, and x_{02} is the equilibrium amplitude of rotating stall.

ent in an engine, it seems that this is not a useful solution. However, periodic orbits can also undergo bifurcations, and we shall show in section 4 that this periodic orbit gains stability at a transcritical bifurcation point. Before carrying out these algebraic manipulations, we can get useful information about the periodic orbit by examining the type of the equations and carrying out some numerical time integrations.

Numerical work shows that as the parameter β is increased, the periodic orbit grows very rapidly. A closer examination of the two-dimensional equations reveals that they are very similar in structure to the Van der Pol equations with a cubic damping term. When the Van der Pol parameter is large, those equations yield a limit cycle that spends most of its time on the side arms of the cubic damping function, and computations show that this is true also for our axisymmetric limit cycle. On the side arms of the axisymmetric characteristic, $\Phi^2 > 1$ and hence $R' < 0$. During this part of the orbit any angular variations will be heavily damped, but when $\Phi^2 < 1$ the rotating stall component of a disturbance will tend to be amplified. As we first move away from the Hopf bifurcation of x_{01}, the limit cycle lies largely in the latter region and so is unstable (Fig. 5). However, as we move away from the bifurcation point by increasing β, the periodic orbit grows until it spends most of its time in the former region; see Fig. 5(*b*). A nonaxisymmetric disturbance decays more while the trajectory is moving close to the side arms of the cubic characteristic, than it is amplified during the remaining time. This large amplitude axisymmetric orbit has the shape that is associated with deep surge.

The experimentally observed deep surge cycles are not purely axisymmetric; rotating stall is observed over part of the cycle. In an actual compression system there will always be some level of distortion, and if we add nonaxisymmetric noise to the model, this is amplified over the part of the orbit where the axisymmetric characteristic has positive slope and damped over the remainder. This corresponds to the parts of the deep surge cycle where rotating stall is observed. So even though the limit cycle itself is purely axisymmetric, trajectories will exhibit nonaxisymmetric behavior.

We conclude that for parameters that lie above the line of Hopf bifurcation points in Fig. 4, an axisymmetric limit cycle is a solution of the equations, and when this orbit acquires stability to all perturbations at large enough β, it represents deep surge. In the next section we will discuss the bifurcations of the periodic orbits that define the boundary of the region in parameter space where deep surge may be observed. But first we locate the other stationary solutions and discuss their bifurcations.

Nonaxisymmetric Solutions

The analysis in the previous section is restricted to the invariant $R = 0$ plane. We now extend the study to the dynamics off the plane, i.e., the nonaxisymmetric behavior. We discuss both the steady and unsteady solutions of the equations, and find the parameter values where each type of flow is stable. The equations exhibit both periodic and apparently chaotic behavior, and we show how it is possible to locate these solutions in parameter space by following a series of bifurcations starting with the Hopf bifurcation of the stationary point.

$R_e = 1 - \Phi_e^2$ is the second stationary solution of equation (3). By setting equation (1) equal to zero, and substituting this value of R_e, we find the equilibrium solution of the pressure rise coefficient

$$\Psi_e = \Psi_{co} + 1 - \frac{3}{2}\Phi_e + \frac{5}{2}\Phi_e^3 \qquad (10)$$

where the equilibrium value of Φ is fixed by the throttle setting. When such an equilibrium point is stable, it represents steady rotating stall, where the angle-averaged mass flow coefficient, the pressure rise coefficient, and the rotating stall amplitude are steady. Thus the line of equilibrium points, traced out as the throttle setting is varied, represents the rotating stall characteristic (Fig. 6). When the throttle is open wide there will be no intersection of these two curves and so no stationary solution exists other than the steady axisymmetric flow x_{01}. When the throttle setting lies in the range $\gamma_c < \gamma < \gamma_s$, the throttle line cuts the rotating stall characteristic twice. As the throttle is closed, γ_s is the throttle line that first touches the stall characteristic. Both of the points of intersection x_{02} and x_{03} are stationary solutions of equations (1)–(3).

All the equilibria are shown in a bifurcation diagram (Fig. 7), which is a plot of R_e versus γ. For large values of γ, x_{01} ($R_e = 0$) is the only stationary solution. At γ_s, the two solutions, x_{02} and x_{03}, appear in a saddle node bifurcation. Calculation of the eigenvalues associated with x_{03} shows that it is a saddle with two negative eigenvalues and one positive eigenvalue. It retains this character as the throttle is closed until $\gamma = \gamma_c$. At this point it meets x_{01} and goes through a transcritical bifurcation. The positive eigenvalue becomes negative, causing x_{03} to become stable. We recall from the last section that x_{01} lost stability at this bifurcation point. When x_{03} becomes stable at $\gamma = \gamma_c$, it also crosses the invariant $R = 0$ plane and assumes negative values of R, so it has no longer any physical significance. However we continue to keep it in mind as it contributes further to the bifurcation analysis. Despite the fact that this fixed point does not represent any physical flow, it is involved in the bifurcations that result in the appearance of x_{02} and the change of stability x_{01}.

The remaining fixed point, x_{02}, exists for all γ in the range $0 < \gamma < \gamma_s$. As mentioned above, when this solution is stable it represents steady rotating stall. The question we now ask is which parameter values allow it to be stable. After x_{02} appears in the saddle node bifurcation, its Jacobian derivative has one negative real eigenvalue and a complex pair. The real eigen-

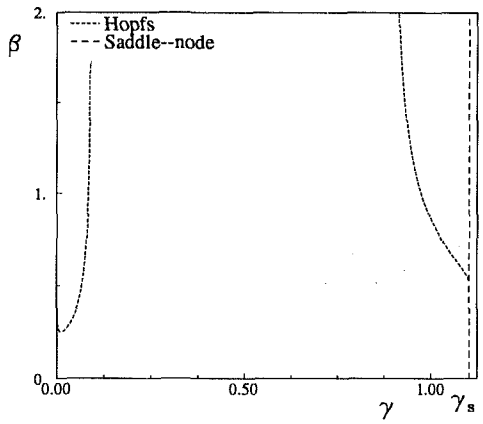

Fig. 8 Bifurcation set for x_{02}. The throttle parameter γ is normalized with γ_c.

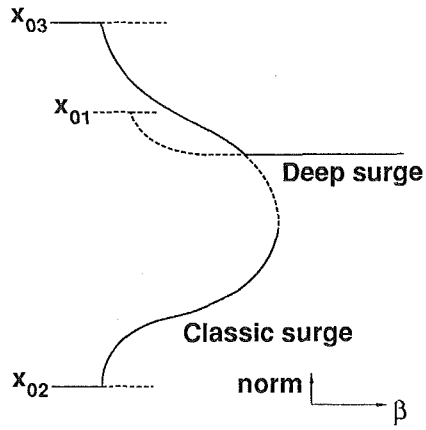

Fig. 9 Bifurcations of the periodic solutions as β is increased

value is negative for all γ and so the stability is dependent only on the sign of the complex pair. For small values of β, this is negative, and x_{02} is stable. But at larger values of β, the real part of the complex pair is positive and hence x_{02} is unstable. The region of parameter space where x_{02} is stable is bounded by the lines of Hopf bifurcation points, where the complex pair of eigenvalues are purely imaginary. With a little manipulation of the characteristic equation of the Jacobian derivative, we determine the function $\beta(\gamma)$, for which x_{02} has a purely imaginary pair of eigenvalues. This function is shown in Fig. 8. Fixed point x_{02} is stable below the lines of Hopf bifurcation points. No bifurcations are possible when $\gamma_1 < \gamma < \gamma_2$, since in this range of throttle settings, x_{02} lies on the negatively sloped part of the rotating stall characteristic, and is stable for all values of β. When the throttle setting lies in the range $\gamma_c < \gamma < \gamma_s$, and β is small, both the rotating stall point and the steady axisymmetric point are stable. This results in a hysteresis effect as the throttle is opened and closed, and this phenomenon is consistent with experimental observations.

The Hopf bifurcations signal the presence of periodic solutions in parameter space and we now proceed to the nonlinear analysis in order to determine the stability of the orbits. In the previous case the analysis was simple since the axisymmetric limit cycle was confined to the invariant $R = 0$ plane. In this case, we need to reduce the dimension of equations (1)–(3) by limiting our attention to the two-dimensional center manifold. We first need to put equations (1)–(3) into Jordan normal form so that they take on the form

$$\dot{x}_1 = \omega x_2 + O(2)$$
$$\dot{x}_2 = -\omega x_1 + O(2)$$
$$\dot{x}_3 = \lambda x_3 + O(2)$$

where the x_i are linear functions of Φ, Ψ, and R. The center eigenspace of the imaginary eigenvalues is the first-order approximation to the center manifold. A nonlinear coordinate change is necessary to make the $x_3 = 0$ plane invariant up to third order—this is the second-order approximation to the center manifold. The two remaining equations are put in normal form, and a final change to cylindrical coordinates produces the desired form, equations (6) and (7). This extension of the linear analysis tells us the stability of the periodic orbit close to the Hopf bifurcation point. In this case, the sign of coefficient a and hence the stability of the limit cycle varies along the line of the Hopf bifurcation points in Fig. 8. For values of γ close to γ_s, the periodic orbit is stable and exists above the line of Hopf bifurcation points. The situation gets a little more complicated for smaller γ, but it is sufficient for our purposes to say that the region where this limit cycle exists has as its lower bound the line of Hopf bifurcation points. Time integrations of equations (1)–(3) show that as we move away from the line of Hopf bifurcation points in the parameter space, this periodic orbit grows rapidly and assumes the character of classic surge. A more complete discussion of the bifurcations involved can be found in McCaughan (1988, 1989b).

We now return to the discussion of the change in stability of the axisymmetric limit cycle. For this we need to look at the bifurcations of periodic orbits and these can only be located using the numerical branch tracking software developed by Doedel (1986). This code locates the bifurcations of the periodic orbits in the parameter space by tracking the Floquet multipliers. A sample of the results of this branch tracking procedure is shown in Fig. 9. For a particular value of γ we increase β and follow the various solutions. In this case $\gamma < \gamma_c$ and x_{01} is unstable for all β. This schematic shows the periodic orbits and the equilibria for a given value of γ, in a plot of the norm versus β, where

$$norm = (\Phi^2 + \Psi^2 + R^2)^{1/2} \tag{11}$$

For the equilibria, *norm* is evaluated using the stationary values and for the periodic orbits, this function is integrated over the period of the orbit. For small values of β, x_{02} is the only meaningful stable solution. x_{03} is also stable but it has a negative value of R. β is increased until the Hopf bifurcation point of x_{02}. After this point the only relevant stable solution is the nonaxisymmetric limit cycle. The fixed point x_{03} has also passed through a Hopf bifurcation leading to the appearance of another stable periodic solution, but these solutions both lie entirely in the negative half space of R. The x_{03} limit cycle eventually moves above the $R = 0$ plane and in doing so, it loses stability in a transcritical bifurcation point. The other limit cycle involved at the bifurcation point is the axisymmetric limit cycle, born at the Hopf bifurcation of x_{01}, and it gains stability.

As γ is varied a line of transcritical bifurcation points is traced out in the parameter space. They lie just above the Hopf bifurcations in Fig. 4, showing that as the axisymmetric limit cycle grows, it rapidly acquires stability to all types of perturbation. The line of transcritical bifurcations is the lower boundary of the deep surge region in the parameter space.

Once above the $R = 0$ plane the unstable x_{03} limit cycle soon collides with the classic surge cycle and they disappear in a saddle-node bifurcation. This saddle-node bifurcation defines the upper boundary of the region in parameter space where classic surge is a possible solution of the equations. The bifurcations of the periodic orbits are reminiscent of the static bifurcations. The saddle-node bifurcation produces two periodic orbits, one stable and one unstable. The unstable one then crosses the invariant $R = 0$ plane at a transcritical bi-

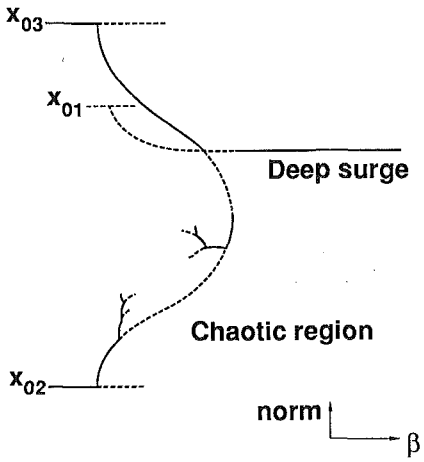

Fig. 10 Bifurcation diagram showing the period doubling bifurcations that lead to aperiodic behavior

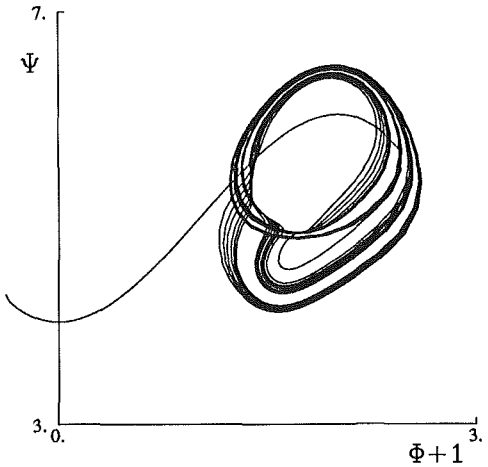

Fig. 11 The aperiodic behavior observed after the limit cycle representing classic surge has gone through the sequence of period doubling bifurcations shown in Fig. 10

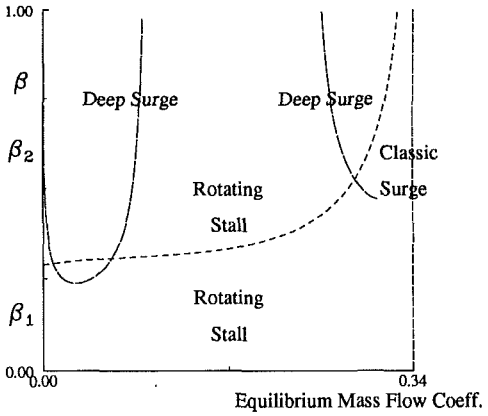

Fig. 12 Bifurcation set showing regions where each mode of compressor response is possible

furcation and causes the change in stability of the axisymmetric solution.

As β is increased further the only stable solution is the large axisymmetric limit cycle, which represents deep surge. This analysis clearly shows that deep and classic surge are two quite different phenomena; one arises from a Hopf bifurcation of the steady axisymmetric flow, and the other is born at a Hopf bifurcation of the rotating stall point.

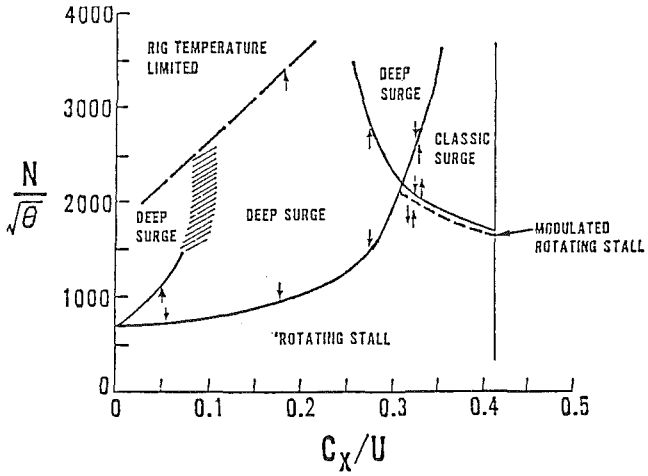

Fig. 13 Experimental bifurcation set determined by Greitzer (1976)

The lines of bifurcation points of periodic orbits define the regions of parameter space where the axisymmetric and nonaxisymmetric limit cycles are stable. On the map of the parameter space we have so far only marked the stable steady solutions. In the next section we look at a more complete map showing the stable steady and periodic solutions.

Before leaving this section, we show an example of the apparently chaotic behavior that the equations exhibit. This is the end result of a series of period-doubling bifurcations starting with the nonaxisymmetric limit cycle. Figure 10 shows another bifurcation diagram resulting from the numerical branch tracking, where a different value of γ was chosen. The value of Ψ_{co} is 4 and the throttle is closed only slightly past the peak of the axisymmetric performance. In the previous case the nonaxisymmetric limit cycle remained stable between the two saddle node bifurcations. The nonaxisymmetric limit cycle here undergoes a series of period-doubling bifurcations leading apparently to a chaotic region. Now the nonaxisymmetric behavior seems to be a strange attractor as in Fig. 11. The system then goes through the reverse sequence of period doublings arriving back at an orbit with period close to the original, which then completes the bifurcation picture with the bifurcations as in Fig. 9. There are windows of periodic behavior in the chaotic region, having various periods, including period three. Theory proves that if there is a period three orbit, then there can be an orbit of any period. This apparently aperiodic behavior is another interesting aspect of the equations.

Discussion

Having located all the bifurcations of the stationary solutions and periodic orbits, we are now able to state which system responses are possible for a given set of parameters. An example is shown in Fig. 12, where we plot β versus the equilibrium flow coefficient, $(\Phi_e + 1)W$, where $W = 0.17$. We chose this abscissa in order to compare with the experimental results of Greitzer (1976), but it reflects the parameter γ.

Steady axisymmetric flow is the only solution possible for parameter values on the right of the diagram. This is the region where the cubic axisymmetric has negative slope. When the mass flow is reduced past the point of zero slope on the characteristic, this flow is no longer stable. The response of the compressor then depends on β. Choosing two representative values of β, we can follow the compression system response as the throttle is closed. For $\beta = \beta_1$ the compressor first goes into rotating stall, and for $\beta = \beta_2$ the system experiences classic surge. As the throttle is progressively closed, the machine with $\beta = \beta_1$ remains in rotating stall, but at $\beta = \beta_2$ classic surge

exists for only a small range of values of flow coefficient. We then pass into a region where only deep surge is possible. Crossing the line of Hopf bifurcation points of the rotating stall point, we reach a region where both rotating stall and deep surge are possible. The compression system will continue to surge, unless given a very large amplitude angular distortion. In that case, the compressor would go into rotating stall. At this point, if we decrease the value of β, eventually we cross the line of bifurcation points where the deep surge loses stability. Then we are back with parameter values that allow only rotating stall. When β is increased again, the compressor remains in rotating stall. Clearly the response of the compressor in this region of multiple solutions depends on the initial condition and the path taken through the parameter space. The value of β is varied with the wheel speed.

These patterns of behavior are qualitatively very similar to those observed experimentally, as can be seen from the results of Greitzer (1976) shown in Fig. 13. The ordinate is the wheel speed, which is directly proportional to β, and so the two maps are comparable. It is clear that the bifurcation analysis provides a good representation of the system response boundaries. Greitzer (1976) observed the hysteresis between deep surge and rotating stall, which occurs in the center region of the parameter space as the wheel speed is varied. This is the behavior that we have just discussed and it is simply explained in terms of bifurcation boundaries.

A quantitative comparison can be made by evaluating β from its constituent parameters and the agreement of the parameter boundaries is found to be within 30 percent.

The parameter boundaries depend strongly on the shapes of the two characteristics, axisymmetric and rotating stall. The deep surge boundary depends on the shape of the axisymmetric characteristic, so we are reassured that the cubic function $\Psi_c(\Phi)$ is a good representation. The effect of different axisymmetric functions was examined by McCaughan (1988).

The classic surge–rotating stall boundary depends on the shape of the rotating stall characteristic and at first glance it is surprising that the one harmonic model gives such good results. The rotating stall characteristic shown in Fig. 6 seems not a very good representation of experimental results. However we make the following observations. When the rotating stall characteristic has negative slope, the rotating stall point is stable regardless of the gradient. It is only for positive slopes that the question of stability arises. In that case the characteristic is quite a good representation and so the bifurcation analysis captures the rotating stall–classic surge boundary well.

The analysis also shows simply the qualitative difference between deep surge and classic surge. The former is a purely axisymmetric periodic orbit with actual trajectories showing some amplitude of rotating stall caused by the background distortion. Classic surge, on the other hand, would disappear if the flow was axisymmetric. It is associated with the Hopf bifurcation of the rotating stall point.

This analysis has value from several points of view. It provides a complete picture of the parametric effects, allowing a good prediction of the compression system response. Since these results compare well with experiment we have confidence in the model and its physical description of each mode of response. It also gives a good basis for a parametric study of a more sophisticated model, such as the full set of partial differential equations examined by McCaughan (1989a).

Acknowledgments

This work was supported under NASA contract NAG-3-349.

References

Doedel, E. J., 1986, "Software for Continuation Problems in Ordinary Differential Equations," Tech. Report, Applied Math Dept., California Institute of Technology.

Greitzer, E. M., 1976, "Surge and Rotating Stall in Axial Flow Compressors: Part II—Experimental Results and Comparison With Theory," ASME *Journal of Engineering for Power*, Vol. 98, pp. 199–217.

Greitzer, E. M., and Moore, F. K., 1986, "A Theory of Post-stall Transients in Axial Compression Systems: Part II—Application," ASME *Journal of Engineering for Gas Turbines and Power*, Vol. 108, pp. 231–239.

Guckenheimer, J., and Holmes, P., 1983, *Nonlinear Oscillations, Dynamical Systems and Bifurcations of Vector Fields*, Applied Mathematical Sciences 42, Springer-Verlag, New York.

McCaughan, F. E., 1988, "An Analytical and Numerical Study of Axial Flow Compression System Instability," Ph.D. Thesis, Cornell University, Ithaca, NY.

McCaughan, F. E., 1989a, "Numerical Results for Axial Flow Compressor Instability," ASME JOURNAL OF TURBOMACHINERY, Vol. 111, this issue.

McCaughan, F. E., 1989b, "Bifurcation Analysis of Compressor Instability," *SIAM Journal of Applied Math*, to appear.

Moore, F. K., 1985, "Stall Transients of Axial Compression Systems With Inlet Distortion," presented at the AIAA/SAE/ASME/ASEE 21st Joint Propulsion Conference, Montery, CA, AIAA Paper No. 85-1348.

Moore, F. K., and Greitzer, E. M., 1986, "A Theory of Post-stall Transients in Axial Compression Systems: Part I—Development of Equations," ASME *Journal of Engineering for Gas Turbines and Power*, Vol. 108, pp. 68–76.

Numerical Results for Axial Flow Compressor Instability

F. E. McCaughan[1]
Cornell University,
Ithaca, NY 14853

Using Cornell's supercomputing facilities, we have carried out an extensive study of the Moore-Greitzer model, which gives accurate and reliable information about compressor instability. The bifurcation analysis in the companion paper shows the dependence of the mode of compressor response on the shape of the rotating stall characteristic. The numerical results verify and extend this with a more accurate representation of the characteristic. The effect of the parameters on the shape of the rotating stall characteristic is investigated, and it is found that the parameters with the strongest effects are the inlet length, and the shape of the compressor pressure rise versus mass flow diagram (i.e., tall diagrams versus shallow diagrams). We also discuss the effects of inlet guide vane loss on the characteristic. An evaluation is made of the h′ = −g *approximation, and a spectral analysis of the rotating stall cell given by the full model suggests why this breaks down.*

Introduction

An axial compression system is designed to operate in steady axisymmetric flow. As the mass flow through the compressor is decreased, the pressure rise increases until a critical point is reached. Beyond this point the flow is no longer stable, and the new flow configuration that develops is dependent upon the parameters of the engine. The choices for the new flow are classic surge, deep surge, and rotating stall. Surge is a periodic motion, with oscillating mass flow and pressure rise. Rotating stall is a new equilibrium condition (steady in the frame of reference of the stall cell) with part of the annulus of the compressor operating in stalled flow, which causes a drop in compressor performance. It is important to the engine designer to know which one of these will occur when conditions render the engine unstable. We would like to have a reliable fluid mechanics model allowing accurate prediction of compressor response. Such a model has been developed recently by the combined efforts of Moore and Greitzer (1986), and Greitzer and Moore (1986).

This model is a complex set of partial differential equations and thus far the only lines of attack have used simplified versions of these. In this paper we give the results for the full set of equations, specifically computing rotating stall performance, providing reliable and accurate results, and we compare these with available experimental data.

The single-harmonic model showed the importance of the rotating stall characteristic in the prediction of compression system response and we use the same ideas to show how the response is affected by more realistic characteristics. These results are verified by numerical integration of the partial differential equations. A simple theory is presented to estimate the rotating stall-classic surge boundary in parameter space. The effects of the relevant parameters on the rotating stall performance are discussed and the trends are compared with available experimental results. A simple model for inlet guide vane loss is presented and we show the effect of this additional loss on the stall performance.

Using a spectral analysis of the rotating stall cells, we suggest why the $h' = -g$ approximation breaks down and also why the previous pure rotating stall calculations of Chue and Joseph gave much shorter characteristics than observed herein.

Equations and Numerical Approach

A key task of this problem is to predict the post-stall mode of compressor response. Greitzer (1976) described the equations governing surge, and Moore (1986) discussed the case of pure rotating stall. It is the combination of these two models that allows us to characterize post-stall transients and solve for the compression system response for a given set of parameters. We will not rederive the combined equations here, but rather refer the reader to the work of Moore and Greitzer (1986) where the underlying assumptions are also discussed. In the idealized compression system, flow enters the compressor from a straight inlet duct and exits into a plenum chamber. It is then discharged to the atmosphere via a throttle. The plenum chamber and the throttle model the combustion chamber and turbine of an actual compression system.

The following equation arises from the pressure balance of the compressor:

$$S\Psi(t) = S\Psi_c(\phi) - l_c\Phi'(t) - \left[m\tilde{\phi}_{,t} + \frac{1}{a}\tilde{\phi}_{,\eta t} \right]\Big|_{\eta=0} - \frac{1}{2a}\tilde{\phi}_{,\eta\theta}\Big|_{\eta=0} \quad (1)$$

[1]Current address: Case Western Reserve University, University Circle, Cleveland, OH 44106.

Contributed by the International Gas Turbine Institute and presented at the 33rd International Gas Turbine and Aeroengine Congress and Exhibition, Amsterdam, The Netherlands, June 5-9, 1988. Manuscript received by the International Gas Turbine Institute July 8, 1987. Paper No. 88-GT-252.

where the prime denotes differentiation with respect to time t. We identify Ψ as the total-to-static pressure rise coefficient rescaled with H, the half-height of the compressor performance diagram, and Φ as the angle-averaged mass flow coefficient rescaled with W, the half-width of the compressor diagram (the flow coefficients are all shifted so that zero throughflow occurs at $\Phi = -1$). These two variables are angle-averaged and hence are functions only of t, time referred to the time for the wheel to rotate one radian. Parameter S is the result of the rescaling of Φ and Ψ; $S = H/W$.

The first term on the right of equation (1), $\Psi_c(\phi)$, is the quasi-steady axisymmetric compressor characteristic, where $\phi + 1$ is the mass flow coefficient rescaled with W. Koff and Greitzer (1984) argue that the axisymmetric characteristic is typically a smooth S-shaped curve, and Moore and Greitzer (1986) postulate that the following simple cubic function would be a physically realistic function:

$$\Psi_c(\phi) = \Psi_{co} + 1 + \frac{3}{2}\phi - \frac{1}{2}\phi^3 \tag{2}$$

The remaining dependent variable in equation (1), $\tilde{\phi}$, is the potential describing any disturbance in the inlet, where η is the axial coordinate in the inlet ($\eta = 0$ at the compressor face) and θ is the angle. Thus, $\tilde{\phi}_{,\eta}|_{\eta=0}$ and $\tilde{\phi}_{,\theta}|_{\eta=0}$ are the axial and circumferential flow coefficient disturbances at the compressor face with

$$\phi = \Phi + \tilde{\phi}_{,\eta}|_{\eta=0}$$

The parameter l_c is the effective flow passage length taking into account the tortuous flow passage through the compressor. It is measured in wheel radii. The remaining parameters arise from the modeling, with m reflecting the length of the exit duct and a being the reciprocal time lag parameter of the blade passage.

Another equation arises from realizing that equation (1) involves terms that are functions only of time. Integrating equation (1), with respect to θ, over 2π results in the following angle-averaged relation:

$$S\Psi(t) = -l_c\Phi'(t) + \frac{S}{2\pi}\int_0^{2\pi}\Psi_c(\phi)d\theta$$

The next equation is the mass conservation of the plenum chamber

$$l_c\Psi'(t) = \frac{1}{(2B)^2 S}[\Phi(t) - \Phi_T(\Psi)]$$

The parameter B is the well-known grouping of system parameters suggested by Greitzer. The variable $\Phi_T(\Psi)$ is the plenum discharge coefficient, which is also the throttle flow coefficient. The pressure drop across the throttle is modeled by the following simple parabolic relationship:

$$\Psi = \frac{1}{\gamma}(\Phi_T + 1)^2 \tag{3}$$

where γ is proportional to the cross-sectional area of the throttle, so that decreasing γ corresponds to closing the throttle and vice versa.

In order to simplify the parameter groupings and make the time scale consistent with that in the companion paper (McCaughan, 1989), we rescale time with l_c/S and call the new time variable ξ. This results in the following set of equations:

$$\Phi'(\xi) = \Psi(\xi) + \frac{1}{2\pi}\int_0^{2\pi}\Psi_c(\phi)d\theta \tag{4}$$

$$\Psi'(\xi) = \frac{1}{(2BS)^2}[\Phi(\xi) - \Phi_T(\Psi)] \tag{5}$$

$$\Phi'(\xi) = -\Psi(\xi) + \Psi_c(\phi) - \frac{1}{2aS}\tilde{\phi}_{,\eta\theta}|_{\eta=0} - \frac{1}{l_c}\left[m\tilde{\phi}_{,\xi} + \frac{1}{a}\tilde{\phi}_{,\eta\xi}\right]|_{\eta=0} \tag{6}$$

Since both $\tilde{\phi}|_{\eta=0}$ and $\tilde{\phi}_{,\eta}|_{\eta=0}$ are unknowns in this last equation, we must also determine the inlet flow field.

For simplicity the inlet is modeled as a straight duct, but this could be replaced by a more realistic configuration. Assuming that the flow is incompressible and irrotational, the potential describing any disturbance in the inlet will satisfy Laplace's equation. Taking the inlet length to be l_I and imposing the boundary conditions of periodicity and uniform flow at the entrance, the following solution is found:

$$\tilde{\phi} = \sum_{n=1}^{\infty} a_n(\xi)e^{in\theta}\{e^{n(\eta+l_I)} + e^{-n(\eta+l_I)}\} + \text{c.c.} \tag{7}$$

where the $a_n(\xi)$ are unknown coefficients, which are solved for using the fourth unsteady mixed boundary condition (equation (6)) at the compressor face. The periodic boundary conditions are satisfied naturally and it is easily verified that the axial

Nomenclature

- a = inverse time lag parameter for the blade passage
- a_n = coefficients in Fourier expansion of $\tilde{\phi}$
- B = Greitzer's B parameter
- g = axial mass flow coefficient disturbance at the compressor face
- h = circumferential mass flow coefficient disturbance at the compressor face
- H = half of the difference between the maximum pressure rise and the minimum one
- l_I = length of compressor inlet duct in wheel radii
- l_c = total length of compressor and ducts in wheel radii
- m = parameter reflecting length of exit duct
- S = parameter reflecting rescaling of mass flow and pressure rise = H/W
- W = half of the mass flow giving maximum pressure rise
- β = $2BS$
- γ = parabolic throttle coefficient
- ζ = time variable ξ rescaled with $1/al_c$
- η = axial variable in inlet
- θ = angle in compressor annulus
- ξ = time, referred to time for wheel to rotate one radian, rescaled with l_c/S
- $\tilde{\phi}$ = potential of disturbance in the inlet
- $\tilde{\phi}_{,\theta}|_{\eta=0}$ = h, circumferential mass flow coefficient disturbance at the compressor face
- $\tilde{\phi}_{,\eta}|_{\eta=0}$ = g, axial mass flow coefficient disturbance at the compressor face
- ϕ = mass flow coefficient (axial velocity divided by wheel speed) rescaled with W
- Φ = flow coefficient averaged over angle (axial velocity divided by wheel speed) rescaled with W
- Ψ = total-to-static pressure rise coefficient (inlet to plenum) rescaled with H
- Ψ_c = axisymmetric pressure rise coefficient rescaled with H
- Ψ_{co} = shutoff head coefficient rescaled with H

velocity of the disturbance at the inlet entrance $\tilde{\phi}_{,n}|_{\eta=-l_I}$ is zero.

The Fourier representation of the potential describing an angular disturbance in the inlet was originally suggested by C. S. Tan. A pseudospectral numerical scheme for this problem was first developed by Chue (1985) and subsequently used by Lavrich (1988) to compare his experimentally obtained rotating stall characteristics with those from the Moore–Greitzer model.

In the ensuing calculations the coefficients $a_n(\xi)$ were evaluated using Fast Fourier Transforms. Equation (6) is discretized with respect to time and the right-hand side is transformed into Fourier space. The $a_n(\xi)$ at the next time level can be determined algebraically. We then solve for variables Ψ and Φ at the next time level by discretizing equations (4) and (5). FFTs run very efficiently on vector machines, and with access to the Cornell National Supercomputing Facility we have improved the turnaround time for the problem by an order of magnitude over the time taken on a serial machine. This numerical scheme enables us to calculate the post-stall transients and trace out the rotating stall characteristics. The latter are discussed in the next section.

Rotating Stall Characteristic

Despite the simplicity of the numerical scheme, the problem is complicated by the large number of parameters. The single-harmonic bifurcation analysis described by McCaughan (1989) gave a useful basis for the parametric study of this more sophisticated model. It showed that the mode of compressor response depends on the shapes of the axisymmetric characteristic and the rotating stall characteristic. The former is given in equation (2) and the latter can be represented more realistically by the partial differential equations. We first extend the parametric study by showing the influence of the relevant parameters on the stall performance.

In the calculations the characteristic is determined in much the same way as it is measured in experiments. The flow is perturbed from the design condition and the parameters are chosen so that the compressor will go into rotating stall, i.e., a small value of BS. When observed experimentally, rotating stall may feature one or more stall cells. The equations also show this feature, where the number of stall cells is dependent on the amplitudes of the various harmonics in the initial perturbation. We restrict our attention to one cell stall by perturbing the axisymmetric flow with a sine wave like disturbance.

Once a new steady position (in an angle-averaged sense) has been reached, the throttle is slightly opened or closed, and the transient is allowed to settle to the new equilibrium point. In a numerical calculation this means that the solution converges within some specified bounds. This is repeated over the whole range of throttle settings from fully closed to recovery to axisymmetric flow, thereby tracing out the characteristic. The convergence limits are chosen small enough so that smaller bounds do not make any significant change in the converged solution.

Before looking at the parameter effects we include some characteristics determined experimentally by Day and Greitzer (1978) (Fig. 1). We observe from this figure that one of the effects of parameter S is to move the point of recovery. For smaller values of S ($\phi^* = 0.55$, $S = 0.8$) the characteristic curves up and recovers before the peak of the axisymmetric behavior. However at larger values of S ($\phi^* = 1.0$, $S = 1.4$) the characteristic is quite different, continuing with negative slope to the right of the maximum point. We will show that this aspect of S dependence is captured by the equations.

A typical characteristic calculated from equations (4)–(6) (with $S = 0.5$) is shown in Fig. 2. As in all the rotating stall characteristics given herein, X marks the point of recovery to axisymmetric flow. It was first noted by Chue (1985) and later by Lavrich (1988) that rotating stall is found as a stable solution at mass flow coefficients past the peak of the axisymmetric performance.

This is in contrast to the results of the pure rotating stall problem studied by Koff (1984), Chue (1985), and Joseph (1985). These studies encountered a problem of lack of convergence at larger values of S and mass flow coefficient. It was not clear whether this implied that no rotating stall solution was possible or merely that the computations were insufficiently accurate. Some rotating stall characteristics, calculated (Joseph, 1985) from the pure rotating stall equations using a finite difference scheme, are illustrated in Fig. 3. We observe that as S is increased, the range of values of mass flow coefficient where a pure rotating stall solution is found becomes narrower, and the characteristic is shorter.

When the throttle was opened past the peak of the axisymmetric curve in the transient calculations, the same convergence problem was encountered. Opening the throttle further did not result in recovery to steady axisymmetric flow, and convergence was obtained when the numerical accuracy was improved by increasing the number of Fourier modes used to represent the rotating stall cell. A breakdown of the energy in the various

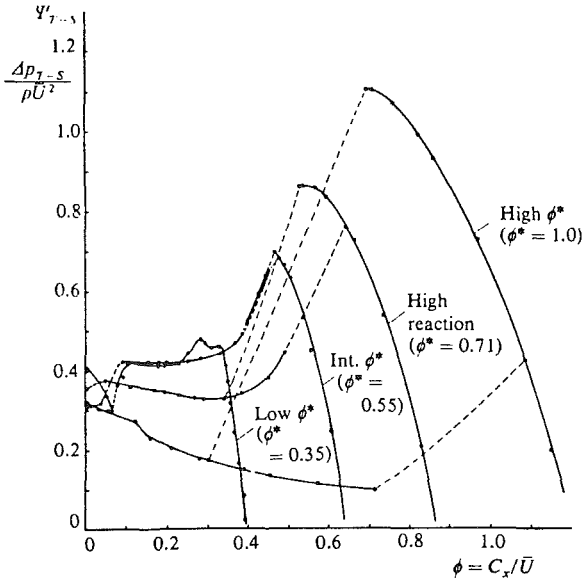

Fig. 1 Rotating stall characteristics determined experimentally by Day and Greitzer (1978)

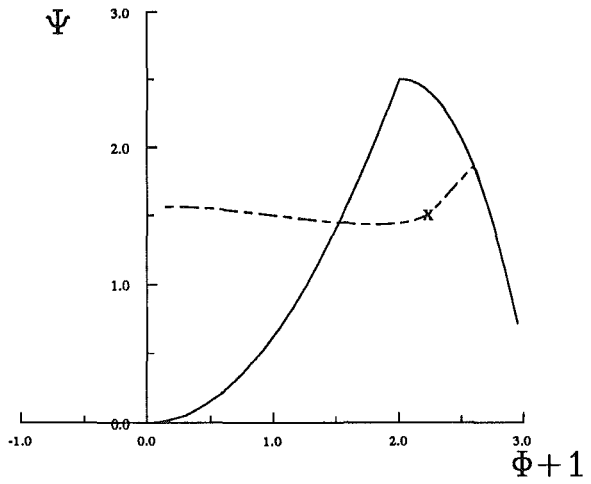

Fig. 2 Typical rotating stall characteristic from transient calculations

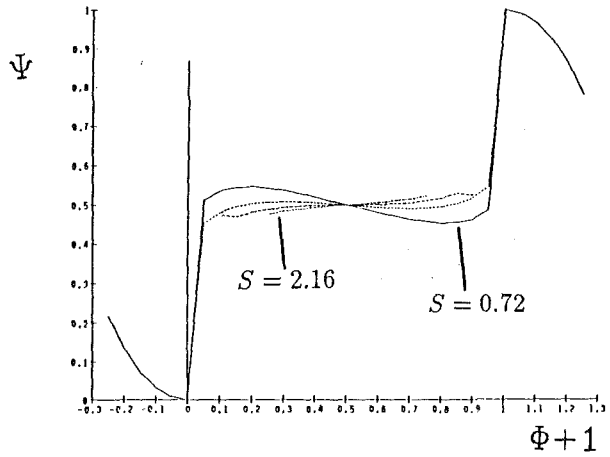

Fig. 3 Rotating stall characteristics calculated by Joseph (1985) using equations for special case of pure rotating stall

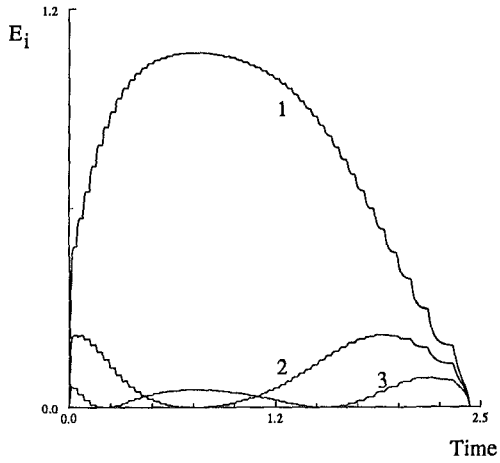

Fig. 4 Distribution of energy in the first three modes as the throttle is closed from the shutoff setting to recovery to axisymmetric flow

Fourier modes suggests a reason for the convergence problem. Figure 4 shows a time history of the energy in the first three modes where the throttle is being opened in discrete steps, tracing out the characteristic in Fig. 2, starting with the throttle almost fully closed. In the middle of the characteristic (halfway through the time history) the first harmonic of the rotating stall contains most of the energy, but as the throttle is opened the energy in the first mode decays, while the energy in the higher modes grows. This occurs because the stall cell becomes narrower and more Fourier modes are needed to resolve the structure.

In the one-harmonic model the rotating stall characteristic was independent of the parameters, but this is not true for the full model. In order to assess which parameters are relevant, we examine the equation resulting from the limiting case of pure rotating stall. The angle-averaged mass flow and pressure rise coefficients are fixed by equations (4) and (5) and in equation (6) $\Phi'(\xi) = 0$. Reorganizing the parameters and rescaling the time to $\zeta = \xi/al_c$, equation (6) can be reduced to

$$[ma\tilde{\phi}_{,\zeta} + \tilde{\phi}_{,\eta\zeta}]|_{\eta=0} = -\Psi + \Psi_c(\phi) - \frac{1}{2aS}\tilde{\phi}_{,\eta\theta}|_{\eta=0} \qquad (8)$$

This equation is in the lab frame of reference, and changing to a frame of reference moving with the stall cell removes the remaining time dependence. We are not going to solve the pure rotating stall problem; we have only restated the equations here to show which parameter groupings are relevant. From equation (8) we can see that the rotating stall solution (and

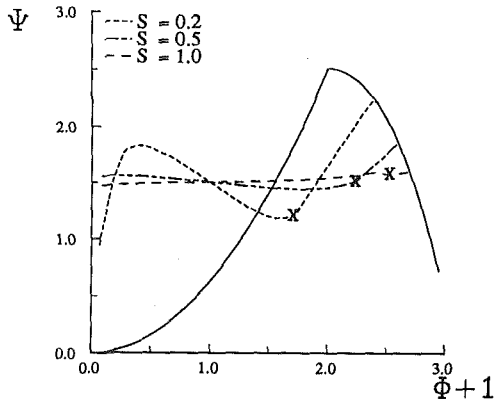

Fig. 5 Effect of parameter S on the rotating stall performance

hence the rotating stall characteristic) is dependent on Sa and ma. We recall from equation (7) that the parameter l_I also affects the solution for $\tilde{\phi}$ and hence $\tilde{\phi}_{,\eta}|_{\eta=0}$, the axial flow coefficient disturbance at the compressor face. The other parameters in equations (4)–(6) affect the transient behavior, but do not affect the rotating stall performance.

Having identified the relevant parameters, we now investigate the effects of each on the characteristic, starting with parameter $S = H/W$, which reflects the shape of the compressor diagram. Large values of S correspond to tall diagrams and small values to shallow diagrams. Increasing the number of stages in the compressor and increasing the stage loading both give large values of S. The characteristics calculated at various values of S are depicted in Fig. 5. When S is small the characteristic tends toward the single harmonic solution. An analysis of the energy content of the Fourier modes for this case shows that in fact more than 90 percent of the energy of the axial mass flow disturbance *is* in the first harmonic. We note that recovery occurs before the peak of the axisymmetric performance. As S is increased to $S = 1$ the characteristic becomes much flatter and recovery is delayed past the peak. Further increase of S has no effect on the shape of the characteristic. Associated with the change in shape of the characteristic is a change in the shape of the stall cell. As S is increased the stall cell becomes more like a square wave than a sine wave.

This result agrees with the observations of Day et al. (1978), i.e., the point at which full span stall ceases moves to larger and larger values of mass flow coefficient as the number of stages increases (i.e., S increases), and this trend was seen in Fig. 1. An examination of the energy in the various modes shows that the fraction of the energy contained in the higher order harmonics increases with S. In the case $S = 2$ it was necessary to increase the number of Fourier modes to 256 in order to resolve the cell structure and achieve convergence at large values of axial mass flow. We also note that numerical calculations had previously shown that the mode of compressor response depends on the product BS rather than B and S individually, except at small values of S. The compressor response is related to the shape of the rotating stall characteristic, which changes shape significantly only when S is small (all other parameters being held constant).

Next we consider the case with S, a, and l_I constant and vary m. The parameter m reflects the length of the exit duct ($m = 1$ implies an abrupt expansion and $m = 2$ implies a very long exit duct). The characteristics for three different values of m are shown in Fig. 6. Parameter m does not have a strong effect, but we observe that recovery is delayed to larger values of Φ as m is decreased, i.e., for shorter exit ducts.

The effects of parameters S and m on the rotating stall performance are opposing, and so it is not clear what the effect

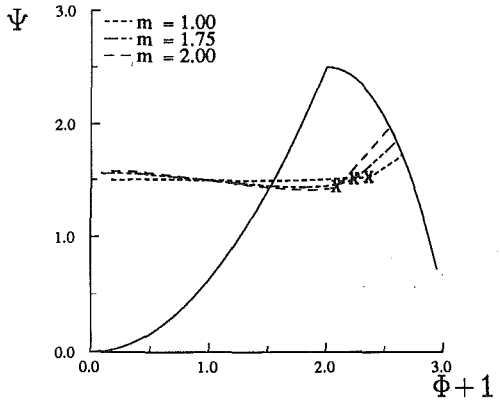

Fig. 6 Effect of parameter m on the rotating stall characteristic when $S = 0.5$

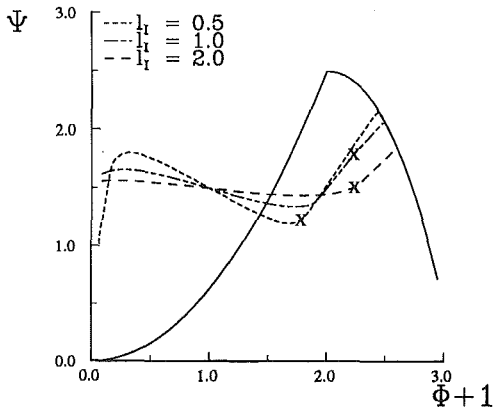

Fig. 7 Effect of the inlet length on the rotating stall performance when $S = 0.5$

will be when a is varied. It is found that a has little effect on the rotating stall solution, which is useful since a is a modeling parameter. As it does not appear elsewhere in equations (4)–(6) one need not be overly concerned about assigning it an accurate value.

The last parameter of importance here is the inlet length l_I. In Fig. 7 we see that this parameter, like S, has a significant effect on the rotating stall performance. As the inlet length is increased the characteristic becomes flatter and recovery occurs later. Choosing values of $l_I > 2$ has no further effect, as thereafter the solution does not differ from the case of an infinitely long inlet.

In summary, recovery to axisymmetric flow occurs at larger values of mass flow coefficient in any of the following cases: large S, small m (short exit duct), or large l_I (long inlet duct). In all these cases the later recovery is associated with a flatter characteristic and a more abrupt rotating stall cell. Only the effect of S has been discussed in the experimental literature.

In the next section we discuss the response of the compression system in light of these numerically calculated rotating stall characteristics.

Compression System Response

We now use the ideas of the analysis in the companion paper (McCaughan, 1989) to predict which modes of compression system response may be possible for a given set of parameter values. First we consider deep surge, a largely axisymmetric periodic solution, which appears when the axisymmetric equilibrium point loses stability to axisymmetric perturbations (McCaughan, 1989). When the resulting limit cycle is small, it is unstable to rotating stall-like disturbances, but it grows rapidly and acquires stability to all perturbations. Bifurcation theory supplies a lower boundary in the (BS, γ) parameter space, below which deep surge is not possible. Any angular disturbances that are observed during deep surge are merely superimposed on the axisymmetric limit cycle and so we postulate that the deep surge boundary will be unchanged by the more accurate rotating stall representation. Numerical integrations show this to be true. The bifurcations that give this boundary are discussed in detail in the companion paper. It is noteworthy that the analysis and results described therein require only the axisymmetric characteristic $\Psi_c(\Phi)$, equation (2) and the throttle function $\Phi_T(\Psi)$, equation (3).

On the other hand, the rotating stall–classic surge parameter boundary depends on the shape of the rotating stall characteristic. Below this boundary, rotating stall is a stable solution of the equations and above the boundary classic surge is a stable solution. The single harmonic analysis showed that rotating stall is possible for all values of the parameters when the equilibrium mass flow coefficient lies on a negatively sloped part of the characteristic. When the characteristic has positive slope, rotating stall is stable for small values of BS, but loses stability as this parameter grouping is increased, bifurcating to a classic surgelike limit cycle. The same trends are observed in the numerical integrations of the partial differential equations and we use the following limiting case to help explain this. When the compressor experiences pure rotating stall, equations (4) and (5) reduce to

$$\Psi_e(\Phi) = \frac{1}{2\pi}\int_0^{2\pi} \Psi_c(\phi)d\theta$$

$$\Phi = \Phi_T(\Psi)$$

We then take small perturbations about this point and assume that the quasi-steady response of the compressor is given by

$$\Psi_{rs}(\Phi) = \Psi_e(\Phi)$$

and then

$$\Phi'(\xi) - \Psi(\xi) + \Psi_{rs}(\Phi),$$

$$\Psi'(\xi) = \frac{1}{\beta^2}(\Phi(\xi) - \Phi_T(\Psi)),$$

where $\beta = (2BS)$. This means that the rotating stall disturbance instantaneously assumes its equilibrium amplitude when the mass flow coefficient is varied. The Jacobian derivative of these two equations is

$$\begin{pmatrix} \Psi'_{rs}(\Phi) & -1 \\ \beta^{-2} & -\beta^{-2}\Phi'_T(\Psi) \end{pmatrix}$$

and the critical value of β (neutral stability) occurs when the trace of this matrix is zero, so that

$$\beta_{cr}^2 = \frac{\Phi'_T(\Psi)}{\Psi'_{rs}(\Phi)}$$

The throttle gradient is always positive, so when the rotating stall characteristic has negative slope there is no solution for β_{cr}. Thus rotating stall is possible for all values of the parameters. However, when the rotating stall characteristic has positive slope, there is a solution for β_{cr} and for all $\beta > \beta_{cr}$ the rotating stall solution is unstable. In such a case, if the throttle setting is such that steady axisymmetric flow is unstable, the compression system will experience surge. At large values of β the solution observed is deep surge, but if β lies below the deep surge boundary, classic surge is the only possible response.

This simple limiting case will not give accurate quantitative boundaries in the parameter space as the one harmonic model did, but it does allow reliable predictions. When the characteristic has negative slope it is found that rotating stall is always a stable solution of the equations. For small values of β rotating

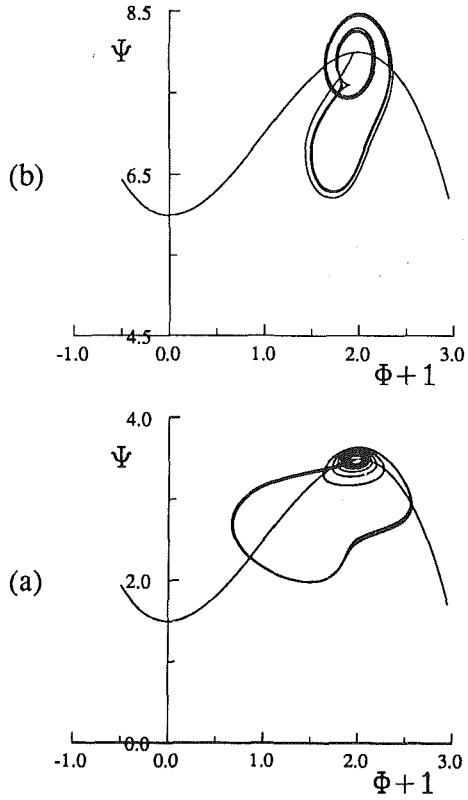

Fig. 8 Examples of classic surgelike solutions of partial differential equations (4)–(6)

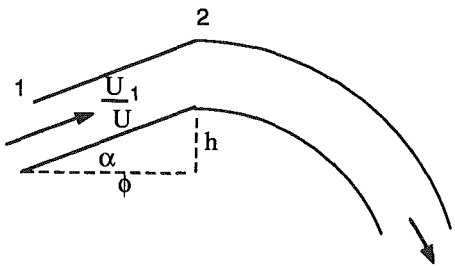

Fig. 9 Schematic for inlet guide vane loss model

stall is the only mode of response, but at large enough β the deep surge limit cycle is also stable and then the compressor response depends on the initial conditions. For large β and initial conditions close to the design point, the compression system is likely to experience deep surge as this solution becomes more and more strongly attractive as β is increased. But for lower values of β, closer to the deep surge parameter boundary, the solution depends on the amount of distortion present. Low levels of distortion encourage deep surge and high levels of distortion encourage rotating stall. When the initial condition is far from the design point, the response can be determined only by numerical integrations.

When the characteristic has positive slope, rotating stall will be stable only when $\beta < \beta_{cr}$. Most of the characteristics shown herein have only a slight positive slope when the throttle is closed past the maximum point (if the throttle is opened beyond this point and the rotating stall point is not stable, the compressor will recover), so that Ψ'_{rs} is very small and β_{cr} is very large. In those instances deep surge is strongly attractive and since classic surge is observed only when neither rotating stall nor deep surge are possible, it is not found. The choice of compression system response is then between deep surge and

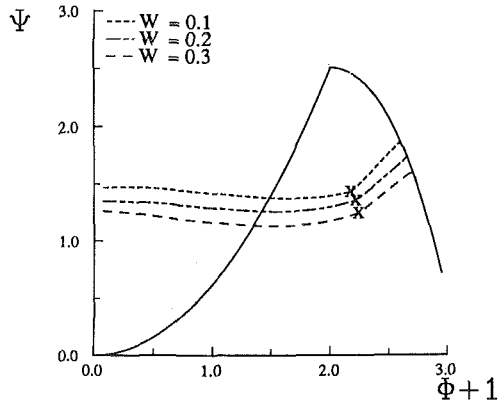

Fig. 10 Rotating stall performances for different level of inlet guide vane loss when $S = 0.5$, $l_l = 2.0$

rotating stall (large values of BS give the former and small values give the latter as observed by Greitzer (1976)) and classic surge is seldom observed. There are two exceptions to this. First, when the shutoff head Ψ_{co} is large, the gradient of the throttle line at the point where it crosses the characteristic is very large and so $\Phi'_T(\Psi)$ is very small. This causes β_{cr} to decrease and so it is possible to find classic surge, if $\Psi'_{rs}(\Phi) > 0$. An example of such a case is depicted in Fig. 8(a). The second exception occurs when S is small. Part of the rotating stall characteristic then has significant positive slope. At the appropriate throttle setting the value of Ψ'_{rs} increases and the corresponding value of β_{cr} decreases, allowing classic surge as shown in Fig. 8(b). Characteristics observed generally have positive slope only when the throttle setting is close to design, and Greitzer (1976) observed both numerically and experimentally that classic surge is found only at throttle settings close to design. This is consistent with the above analysis.

Given any rotating stall characteristic it is possible to estimte the rotating stall-classic surge boundary in (B, γ, Ψ_{co}) parameter space. The procedure can be used with either numerically or experimentally determined characteristics.

In the next section we discuss the effect of the inclusion of inlet guide vane loss on stall performance.

Inlet Guide Vane Losses

When an angular disturbance is present in the inlet, flow does not enter the inlet guide vanes (IGVs) at the correct angle of attack. The loss associated with this has previously been neglected in this model, with the recovery coefficient K_G at the IGV entrance assumed to be 1. We now include this loss in equation (6) such that

$$\Phi'(\xi) = -\Psi(\xi) + \Psi_c(\phi) - \frac{1}{2aS}\tilde{\phi}_{,\eta\theta}|_{\eta=0} - \frac{1}{l_c}\left[m\tilde{\phi}_{,\xi} + \frac{1}{a}\tilde{\phi}_{,\eta\xi}\right]|_{\eta=0} - \frac{W}{2S}(1-K_G)\tilde{\phi}^2_{,\theta} \tag{9}$$

Moore (1988) suggested the following approach in an effort to estimate K_G. A simple schematic of an inlet guide vane channel is shown in Fig. 9. The pressure loss due to the angle of turning α is estimated by

$$\frac{(p_2 - p_1)}{\rho U_1^2} = \frac{A_1}{A_2}\left(1 - \frac{A_1}{A_2}\right) \tag{10}$$

where A_1 and A_2 are the cross-sectional areas at points 1 and 2. The recovery coefficient is defined by the following equation:

$$\frac{(p_2 - p_1)}{\rho U^2} = \frac{1}{2}K_G h^2$$

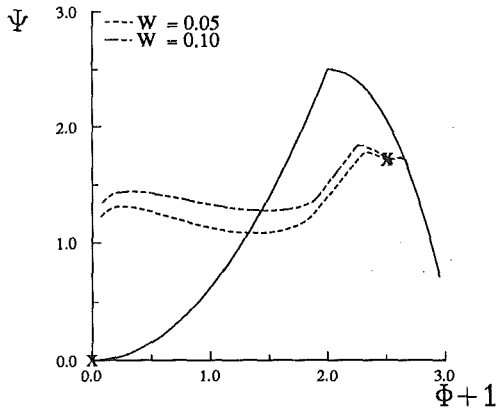

Fig. 11 Rotating stall performances for different inlet guide vane losses when S = 1.0, l_I = 0.5

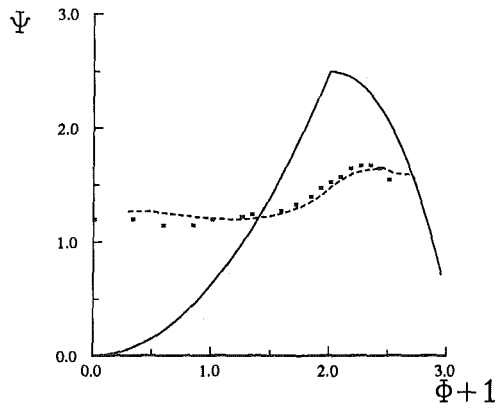

Fig. 12 Comparison of numerical result with the experimental result of Lavrich (1987)

Variable h, the circumferential flow coefficient disturbance at the compressor face, can also be written as $h = \tilde{\phi}_{,\theta}|_{\eta=0}$. Substituting

$$\frac{A_1}{A_2} = \cos\alpha = \frac{\phi}{(\phi^2+h^2)^{1/2}}$$

into equation (10) and carrying out some algebra gives the following expression for the recovery coefficient:

$$\frac{1}{2}K_G h^2 = \phi^2\left(\left(1+\frac{h^2}{\phi^2}\right)^{1/2}-1\right)$$

Note that it is necessary to treat reverse flow as a special case. The extra term in equation (9) is then

$$\frac{1}{2}(1-K_G)h^2 = \left(\frac{h^2}{2}-\phi^2\left(\left(1+\frac{h^2}{\phi^2}\right)^{1/2}-1\right)\right)$$

The coefficient W is used to vary the size of the inlet guide vane loss. Figure 10 shows the effect of the inlet guide vane loss on the rotating stall characteristic for various values of W. We observe that the performance level drops as the inlet guide vane loss increases, but there is only a slight change in *shape* of the characteristic.

Figure 11 shows the same effect at different values of parameters S and l_I. It is again clear that the IGV loss causes a drop in performance but no change in shape of the characteristic.

We finally present in Fig. 12 a comparison of the numerical results with the experimental results of Lavrich (1987). The value of S is given by the experimental data and we vary W and l_I to give the best fit.

The parameters with the strongest effects on the stall performance are size of IGV loss, length of inlet, and shape of compressor map as reflected by S. Varying these parameters gives a range of both shape and level of the characteristics. Figure 12 shows that, by varying these parameters, the model is able to capture this experimental result quite accurately.

$h' = -g$ Approximation

This approximation was proposed by Moore (1986) in order to remove the necessity of solving for the inlet flow. In the terminology of the present paper, this approximation is equivalent to $\tilde{\phi}_{,\theta\theta}|_{\eta=0} = -\tilde{\phi}_{,\eta}|_{\eta=0}$. This is completely true only when all of the energy of the rotating stall is in the first harmonic, but it was hoped that it would be a satisfactory approximation when most of the energy is in the first harmonic, i.e., for one cell stall. For many values of the parameters this is a good approximation, but at the parameter values where the full model had difficulty converging, these calculations failed to converge. We observed in section 4 that the convergence problem was associated with a more abrupt stall cell, which required more Fourier modes to resolve the structure. Unlike the full model, however, the $h' = -g$ transient calculations refused to converge to a single traveling wave even when the number of modes was increased. Instead a two-cell structure developed with the various harmonics moving at different phase speeds.

When most of the energy of the rotating stall is in the first harmonic the higher harmonics play only a very minor role and $h' = -g$ is sufficiently accurate. But as the amplitude of the second and higher harmonics increases, the approximate method fails to apportion the energy correctly among the various modes. It usually overestimates the energy in the second harmonic and then the equations find it impossible to converge to a single traveling wave. Since this approximation gives spurious results for some parameter values we decided to restrict our attention to the full set of equations (4)–(6) and the single-harmonic approximation discussed in the companion paper (McCaughan, 1989).

Discussion

1 The full model developed by Moore and Greitzer (1986) has been tackled numerically, allowing accurate transient calculations.

2 The shape of the rotating stall characteristic is shown to be important in the determination of mode of compression system response and we argue that the same is true for the full model. Classic surge is observed only when the characteristic has a significant positive slope.

3 The parameters that affect the shape of the rotating stall characteristic are investigated:

- Increasing S (reflecting the stage loading and number of stages) delays recovery to axisymmetric flow and causes a flatter characteristic.
- Increasing m (reflecting length of exit duct) encourages earlier recovery to axisymmetric flow.
- Increasing l_I (reflecting length of inlet duct) delays recovery to axisymmetric flow and again this is accompanied by flatter characteristics.
- Varying a (the inverse time lag parameter of the blade passage) has no significant effect.

4 Inclusion of inlet guide vane losses causes a drop in compressor performance, but does not affect the shape of the characteristic much.

5 The $h' = -g$ approximation breaks down when the rotating stall cell becomes more like a square wave than in a sine wave.

Acknowledgments

This research was supported under NASA contract NAG-3-349. It was conducted, in part, using the Cornell National

Supercomputer Facility, a resource of the Center for Theory and Simulation in Science and Engineering (Cornell Theory Center), which receives major funding from the National Science Foundation and IBM Corporation, with additional support from New York State and members of the Corporate Research Institute.

References

Chue, R. S., Greitzer, E. M. and Tan, C. S., 1985, "An Analysis of General Post-stall Transients in Axial Compression Systems," unpublished M.I.T. G.T.L. report.

Day, I. J., and Cumpsty, N. A., 1978, "The Measurement and Interpretation of Flow Within Rotating Stall Cells in Axial Compressors," *IMechE Jour. of Mech. Eng. Science*, Vol. 20, No. 2, pp. 101–114.

Day, I. J., Greitzer, E. M., and Cumpsty, N. A., 1978, "Predictions of Compressor Performance in Rotating Stalls," ASME *Journal of Engineering for Power*, Vol. 100, pp. 1–14.

Greitzer, E. M., 1976, "Surge and Rotating Stall in Axial Compressors: Parts I, II," ASME *Journal of Engineering for Power*, Vol. 96, pp. 190–217.

Greitzer, E. M., and Moore, F. K., 1986, "A Theory of Post-stall Transients in Axial Compression Systems: Part II—Application," ASME *Journal of Engineering for Gas Turbines and Power*, Vol. 108, pp. 231–239.

Koff, S. G., and Greitzer, E. M., 1984, "Stalled Flow Performance for Axial Compressors—I: Axisymmetric Characteristics," ASME Paper No. 84-GT-93.

Lavrich, P., 1988, "Time Resolved Measurements of Rotating Stall in Axial Flow Compressors," Ph.D. Thesis, Massachusetts Institute of Technology, Cambridge, MA.

McCaughan, F. E., 1989, "Application of Bifurcation Theory to Axial Flow Compressor Instability," ASME JOURNAL OF TURBOMACHINERY, Vol. 111, this issue.

Moore, F. K., 1986, "A Theory of Rotating Stall of Multistage Compressors. Parts I, II, III," ASME *Journal of Engineering for Power*, Vol. 106, pp. 313–336.

Moore, F. K., 1988, private communication.

Moore, F. K., and Greitzer, E. M., 1986, "A Theory of Post-stall Transients in Axial Compression Systems: Part I—Development of Equations," ASME *Journal of Engineering for Gas Turbines and Power*, Vol. 108, pp. 68–76.

Joseph, S. T., 1985, "Effect of Compressor Parameters on Rotating Stall," M.S. Thesis, Cornell University, Ithaca, NY.

Weak Rotating Flow Disturbances in a Centrifugal Compressor With a Vaneless Diffuser

F. K. Moore
Cornell University,
Ithaca, NY 14853

A theory is presented to predict the occurrence of weak rotating waves in a centrifugal compression system with a vaneless diffuser. As in a previous study of axial systems, an undisturbed performance characteristic is assumed known. Following an inviscid analysis of the diffuser flow, conditions for a neutral rotating disturbance are found. The solution is shown to have two branches; one with fast rotation, the other with very slow rotation. The slow branch includes a dense set of resonant solutions. The resonance is a feature of the diffuser flow, and therefore such disturbances must be expected at the various resonant flow coefficients regardless of the compressor characteristic. Slow solutions seem limited to flow coefficients less than about 0.3, where third and fourth harmonics appear. Fast waves seem limited to a first harmonic. These fast and slow waves are described, and effects of diffuser-wall convergence, backward blade angles, and partial recovery of exit velocity head are assessed.

Introduction

A previous line of study of rotating stall (Moore, 1984a, 1984b) and later, combined surge and rotating stall (Moore and Greitzer, 1986), of axial compression systems, built successfully on a linearized treatment of the diffuser flow. Specifically, the pressure disturbance at the diffuser entrance provided an important part of the "spring constant" for the flow oscillations of interest.

In that analysis, the diffuser flow was considered inviscid, and boundary conditions were that pressure disturbance vanishes where the diffuser exits to a reservoir; that a given weak, circumferentially varying disturbance of axial velocity exists at the diffuser entrance; and that any disturbance of circumferential velocity must vanish at the diffuser entrance. This last condition states, in effect, that flow leaves the last blade row in the blade direction (assumed axial) whether or not axial velocity is disturbed; it would clearly be correct in a limit of infinite solidity of that blade row. As a consequence of this last condition, the flow in the diffuser must have vorticity.

Under the foregoing assumptions, solution of the diffuser flow-field equations gave a quantity crucial for rotating-stall analysis—pressure disturbance at the diffuser entrance. In Moore's original paper (1984a), the result was easily obtained, and it was found expedient to combine it with a similar pressure disturbance in the entrance-duct flow, which turned out to be in the same phase.

In the present study, the same philosophy is applied to the more complicated centrifugal compression system, and we begin with certain background observations. First, vaneless diffusers are of interest. If the diffusers have parallel walls (this is not necessary in the present analysis), the undisturbed flow would be a potential flow along the familiar logarithmic spiral streamlines from the impeller exit (diffuser entrance) to the diffuser exit (a scroll or constant-pressure reservoir). There is a body of literature on the analysis of fluctuations of this flow, beginning with Jansen (1964) and Abdelhamid (1980). Inviscid analysis did not seem to show clearly the expected features of observed stall patterns, and subsequent studies have adopted the opinion that viscous separation is a vital feature of the fluctutating flow field. In the present paper, it is shown that if more complete disturbance solutions are used, with proper boundary conditions, the observed features are indeed found, without recourse to boundary-layer considerations.

The expected features (see Frigne and Van Den Braembussche, 1984) are that the centrifugal compression system should show two kinds of rotating stall, one in a single lobe having a high rotational speed, typically more than 50 percent of wheel speed at the impeller exit, commonly called "impeller stall"; and the other having a very low rotational speed, typically 10 percent of wheel speed, and commonly called "diffuser stall." Various numbers of lobes are found for this latter type, but two to four lobes are common, according to Frigne and Van Den Braembussche (1984), Kämmer and Rautenburg (1986), and also Abdelhamid et al. (1979). The terms "impeller stall" and "diffuser stall" will not be used here, both because it seems incorrect to specify a special place of origin for the disturbances, and because, as will be shown, blade stall is not necessarily present when a rotating wave occurs. Rather, the terms "fast wave" or "slow wave" will be used.

It might be noted that the stationary disturbance observed by Haupt et al. (1986) should be classed as a slow wave of zero speed. Also, observations show a great variety of wave

Contributed by the International Gas Turbine Institute and presented at the 33rd International Gas Turbine and Aeroengine Congress and Exhibition, Amsterdam, The Netherlands, June 5-9, 1988. Manuscript received by the International Gas Turbine Institute September 1, 1987. Paper No. 88-GT-76.

modes, often with abrupt transitions following changes of flow conditions. In contrast, rotating stalls of axial systems show only one class of disturbances. (It is true, of course, that there are mode-number considerations within that class, but it will be seen that the two centrifugal classes each may have higher modes.)

This discussion will begin by outlining a rotating-wave analysis for the compression system, and then will consider the diffuser flow field in some detail, emphasizing the appearance of certain resonances. The diffuser results will then be related to the wave analysis of the system. Finally, some remarks are made about future research directions.

Rotating-Wave Analysis

The axial analysis of Moore (1984a) is carried over for the centrifugal system sketched in Fig. 1; basically, pressure disturbances are accumulated from the entrance (in this case, approaching the eye of the impeller at ⓪); passing through the impeller, in which only inertial effects of unsteadiness will be considered, just as was done for a single blade row by Moore (1984a); and then radially through the diffuser from ① to Ⓕ, to a large reservoir. The net pressure change must vanish, and that statement provides the rotating-wave equation. The undisturbed net pressure change (total-to-static coefficient Ψ) from entrance to diffuser exit is assumed given. The "axisymmetric characteristic" ψ_c, that is, the pressure-rise coefficient that would be measured in the absence of any disturbance, is assumed known as a function only of flow coefficient. It is convenient to measure all velocities in units of wheel speed at ①; thus, the flow coefficient is the radial velocity at ① itself, as shown in Fig. 1. Also, all lengths are measured in units of impeller outer radius.

The resulting equation, which governs any possible weak disturbance, is

$$\Psi = \psi_c(V+g) + fh(\theta) - \frac{1}{2}\tau(1-f)g'(\theta) - C_{p_1}(\theta) = 0 \quad (1)$$

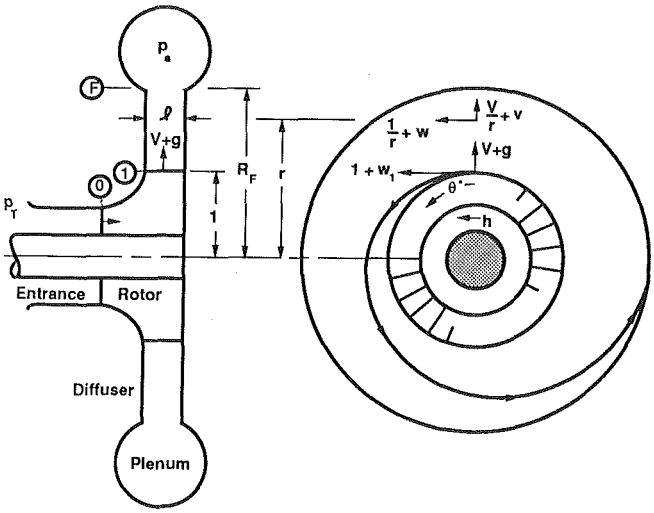

Fig. 1 Sketch of centrifugal compression system, with parallel-wall vaneless diffuser. Rotor blades are radial at exit, and angular velocity is 1.

where g is the postulated disturbance of radial velocity coefficient at the rotor exit. It is assumed steady in a frame rotating with an angular speed, which is a fraction f of that of the rotor. In that frame, g is allowed to be a function of circumferential coordinate θ, but it will vanish on the average. Thus, the flow coefficient will be V when the flow is undisturbed, and $V + g$ when disturbed. Moore (1984a) defined g at the compressor entrance; here, it will be more convenient to locate g at the rotor exit, or diffuser entrance ①. The induced disturbance of circumferential component of velocity coefficient at the impeller entrance is h. The difference between pressure at ① and the undisturbed value there is, in coefficient form, C_{p_1}. The coefficient τ reflects inertia in the impeller

Nomenclature

A = coefficient of radial velocity disturbance, equation (6)
b = circumferential wave number, equation (21)
C_p = coefficient, relative to ρU^2, of difference of pressure at any radius and the undisturbed pressure at ① (Fig. 1)
f = angular speed of rotating wave
g = disturbance of radial velocity coefficient at $r = 1$
h = circumferential velocity disturbance at ⓪
K_1, K_2 = constants, equation (15)
l = width of diffuser
n = exponent in formula for diffuser width, equation (22)
P = pressure disturbance, equation (8)
P_1, P_2 = complementary solutions for pressure, equations (16) and (17)
PP_1, PP_2 = particular solutions for pressure, equations (18) and (19)
PM = imaginary part of P, a function of r
PR = real part of P, a function of r
R = ratio $(r - 1)/(R_F - 1)$, used in Figs. 4 and 7
R_F = ratio of diffuser exit radius to entrance radius
r = radial coordinate (1 at diffuser entrance)
U = wheel speed at rotor exit, taken to be 1
V = average flow coefficient at rotor exit; ratio of average radial velocity to wheel speed there
v = radial velocity coefficient
W = coefficient of circumferential velocity disturbance, equation (7)
w = circumferential velocity coefficient
z = function of r, equation (20)
β = angle of blades at rotor exit (Fig. 9)
ζ = function of ξ, equation (20)
η = coefficient; ratio of flow areas at ⓪ and ①; taken to be 0.5
θ = angular coordinate fixed in rotating wave
θ^* = angular coordinate fixed in laboratory
λ = coefficient of dynamic head recovery at Ⓕ
ξ = variable of integration
ρ = density
τ = coefficient of blade-passage lag (see Moore, 1984a); taken to be 1
Ψ = given coefficient of pressure rise from upstream total to reservoir static, $(p_s - p_T)/\rho U^2$; see Fig. 1
ψ_c = axisymmetric pressure-rise coefficient in the absence of any disturbance, presumed known as a function of V

Subscripts

0 = at rotor entrance
1 = at rotor exit (diffuser entrance)
F = at diffuser exit

blade passage; in the calculations to be presented, the choice was $\tau = 1$. Inertia effect will also be proportional to $1-f$, because the rotor blade-passage flow would be steady if the wave should travel just at rotor speed (i.e., $f = 1$); in that case, the inertia effect would vanish. In the original Moore analysis (1984a), rotor-stator blade combinations were considered, and the corresponding factor was $1-2f$.

Adopting the inlet flow analysis of the latter paper, one writes

$$h'(\theta) = -\eta g(\theta) \tag{2}$$

In the axial problem, η was 1. In the present case, because g is defined at the rotor exit rather than the entrance, a smaller value would probably be appropriate, in proportion to the ratio of rotor inlet and exit flow areas. In the calculations to be presented, η was chosen to be 0.5.

Now, still following Moore (1984a), one assumes weak harmonic disturbances at the impeller exit (diffuser entrance) in the form that follows. For the moment, only the fundamental mode will be considered

$$g = A(1)e^{i\theta}; \qquad C_{p_1} = P(1)e^{i\theta} \tag{3}$$

$A(1)$ will be defined real, and C_{p_1} must be complex, as will be shown later when the diffuser flow field is studied. That is, $P(1) = PR(1) + iPM(1)$. Equation (2) provides a formula for $h(\theta)$. For small disturbances (i.e., $g \ll V$), substituting equations (2) and (3) into equation (1) then gives the following real and imaginary parts:

$$\psi_c'(V) - PR(1) = 0 \tag{4}$$

$$\frac{1}{2}\tau(1-f) - \eta f + PM(1) = 0 \tag{5}$$

These are the requirements for a "permanent" rotating wave. However, they cannot be applied until $P(1)$ is found from an analysis of the flow in the diffuser that connects the rotor exit and the final large reservoir. ψ_c is, of course, given; a typical shape of the characteristic function for a centrifugal system is shown in Fig. 11(*b*).

In the axial case (Moore, 1984a), analysis of the diffuser flow gave, for an infinite straight duct, $PM(1) = -f$, and $PR(1) = 0$, in effect. In other words, $P(1)$ was 90 deg out of phase with g. In consequence, equation (4) gave the familiar result that a weak rotating stall could occur only at a V for which the slope of the characteristic vanishes. Later nonlinear analysis (Moore, 1984b) showed further that positive characteristic slope ($\psi_c'(V) > 0$) implies amplification of rotating stall and negative slope implies damping. In the circumferential problem, with $PR(1)$ not zero, as will be shown, the stable point will no longer be at zero slope of the characteristic; it would in fact be somewhere on the hitherto stable negative slope if $PR(1) < 0$. Further, negative $PR(1)$ would tend toward amplification.

In the previous linear analysis (Moore, 1984a), the second equation (5), determined the rotating-wave speed f; it still does so in the centrifugal case. The question is, for what f is equation (5) satisfied? It may be noted that for higher circumferential harmonics, the first term of equation (5) should be multiplied by, and the second term divided by, wave number.

The foregoing discussion sets the stage for analyzing the diffuser flow. The object of that analysis will be to find the real and imaginary parts of pressure disturbance evaluated at the diffuser entrance, namely $PR(1)$ and $PM(1)$, resulting from a given radial velocity disturbance at the diffuser entrance.

Inviscid Small-Disturbance Flow in a Vaneless Diffuser

A General Solution. The right-hand sketch in Fig. 1 shows the assumed velocity field in a vaneless diffuser, in coordinates r, θ^*, which are fixed in the laboratory. An important parameter will be the diffuser radius ratio R_F. The plates of the diffuser are at first assumed parallel, and later the theory will be modified to allow a different shape. A second important parameter will be V, the average flow coefficient leaving the impeller. Of course, V sets the pitch of the undisturbed potential-flow spiral streamlines, one of which is sketched in Fig. 1.

In coordinates r, θ, fixed in a frame that rotates with an assumed disturbance pattern (angular speed f) so that $\theta = \theta^* - ft$, steady flow is assumed. The flow is split into the basic spiral potential flow, with small disturbances superposed. The later are written in forms consistent with the forms assumed in equation (2) for the disturbance at (1). Radial and circumferential velocity components, and the coefficient of pressure rise above the average value at (1), are

$$v = \frac{V}{r} + A(r)e^{i\theta} \tag{6}$$

$$w = \frac{1}{r} - fr + W(r)e^{i\theta} \tag{7}$$

$$C_p = \frac{1}{2}(V^2+1)\left(1 - \frac{1}{r^2}\right) + P(r)e^{i\theta} \tag{8}$$

These equations describe only a first harmonic; later, higher harmonics will also be considered.

Adopting the foregoing definitions, one may show that the governing inviscid (Euler) differential equations for radial and circumferential momentum and continuity become, respectively,

$$V(rA' - A) + i(1-fr^2)A - 2W + r^2P' = 0 \tag{9}$$

$$V(rW' + W) + i(1-fr^2)W + irP = 0 \tag{10}$$

$$rA' + A + iW = 0 \tag{11}$$

The flow is expected to be rotational. The scheme of solution will be simply to eliminate P between equations (9) and (10), and then use equation (11) to eliminate W. The resulting third-order equation for $A(r)$ can then be solved by successive power-law substitutions.

The three boundary conditions that follow have already been discussed in the Introduction:

$$A(1) = 1 \tag{12}$$

This defines the assumed disturbance: A at the entrance $r = 1$ is pure real, and because the weak-wave problem is linear, may be assigned the magnitude 1 for convenience.

$$W(1) = 0 \tag{13}$$

This is a crucial condition, saying that flow leaves the impeller in a radial direction, no matter how radial velocity may change. This condition implies radial impeller blading with no "slip." Later, this condition will be adjusted to account for backward-facing blades. Finally,

$$P(R_F) = 0 \tag{14}$$

That is, pressure disturbance must vanish at the diffuser exit. There is no apparent basis for a condition sometimes used, that P' also vanishes there. Equation (14) is an ideal condition, which may not be met in many practical arrangements. It states, in effect, that all dynamic head is lost at the diffuser exit (F). Later, this condition will be modified to allow for partial recovery of dynamic head, perhaps by use of exit turning vanes.

So far, equations (6)–(14) are consistent with the analysis of Abdelhamid (1980), who integrated an equivalent set of equations numerically for certain cases, in the context of a compressor stabilty analysis. Here, we achieve a fuller, more revealing description of the flow by first finding an analytical solution of the system of equations. This step is independent of compressor performance; only after the diffuser flow is described does the compressor come into play, through equations (4) and (5). The following solution for pressure P was found for the first circumferential harmonic:

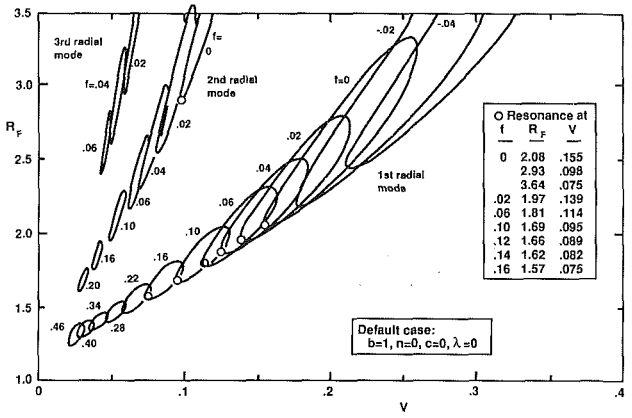

Fig. 2 Contours of diffuser radius ratio R_F versus flow coefficient V upon which equation (5) is satisfied, thus permitting "slow" rotating waves, for various assumed wave speeds f, and for $\tau = 1$ and $\eta = 0.5$. The table gives the resonant points shown by circles on the figure.

$$P = [K_1P_1(r) - K_2P_2(r) - PP_1(r)] + i[K_2P_1 + K_1P_2 - PP_2] \tag{15}$$

where

$$P_1 = V\left[\cos z - \frac{1}{r}\int_1^r \left(\frac{\xi^2}{r^2} - 1\right)\cos \zeta d\xi - (1 - fr^2)\frac{1}{2r}\int_1^r \left(\frac{\xi^2}{r^2} + 1\right)\sin \zeta d\xi\right] \tag{16}$$

$$P_2 = V\left[\sin z - \frac{1}{r}\int_1^r \left(\frac{\xi^2}{r^2} - 1\right)\sin \zeta d\xi + (1 - fr^2)\frac{1}{2r}\int_1^r \left(\frac{\xi^2}{r^2} + 1\right)\cos \zeta d\xi\right] \tag{17}$$

$$PP_1 = \frac{V}{2r}\left(1 + \frac{1}{r^2}\right) \tag{18}$$

$$PP_2 = (1 - fr^2)\frac{1}{2r}\left(1 - \frac{1}{r^2}\right) \tag{19}$$

and where

$$z \equiv \left(-\ln r + \frac{1}{2}fr^2\right)/V; \qquad \zeta \equiv \left(-\ln \xi + \frac{1}{2}f\xi^2\right)/V \tag{20}$$

The constants K_1 and K_2 are adjusted to make pressure disturbance vanish at the exit, as required by equation (14). It is regrettable that the integrals appearing in the foregoing equations must be done numerically. If the ln term were not present in the formula for ζ, the integrals would reduce to Fresnel's Integral, a function that is tabulated in various mathematics references.

The foregoing solution has been computed on a Macintosh, for various combinations of the governing parameters. Recalling equations (4) and (5), which give the necessary conditions for a rotating wave, one wishes to evaluate the real and imaginary parts of equation (15) at the entrance $r = 1$, thus finding $PR(1)$ and $PM(1)$, respectively. Therefore it has seemed best first to find combinations of the three open parameters—radius ratio R_F, flow coefficient V, and wave speed f—that produce values of $PM(1)$ satisfying equation (5). Then, for each such solution, the diffuser's contribution to wave damping, namely $PR(1)$, can be noted. This procedure has the merit that the first step is independent of the compressor (except for the less crucial parameters τ and η).

Slow Waves and Resonance. In accordance with the foregoing scheme, Fig. 2 was prepared to show a series of contours

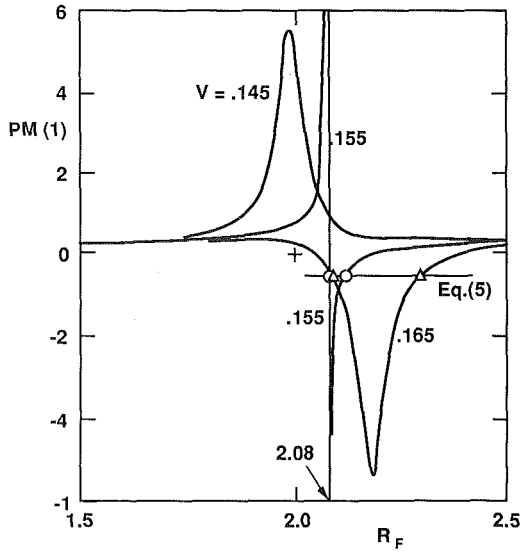

Fig. 3 Graphs of $PM(1)$ near the resonant condition for $f = 0$, for values of V just above, at, and just below the resonant value 0.155. Equation (5) would give the triangle-point intersections when $V = 0.165$ and the circle-point ones when $V = 0.155$ (see Fig. 2).

in R_F, V space for various values of f. Each contour represents a locus of possible rotating wave solutions according to equation (5). These waves are "slow," with f ranging from small negative values to 0.46. Apparently, for a given R_F, slow waves are possible only in a series of rather narrow bands of flow coefficient. These bands are labeled according to "radial mode," which will be explained shortly. First, a surprising and important resonance feature of the solution requires discussion.

For a certain range of small values of f, up to about 0.16 for the first radial mode of the first circumferential harmonic (the right-hand band of Fig. 2), there are points (R_F, V) that are eigenvalues, in that P_1 and P_2 of equation (15) (which are complementary solutions) both vanish at the exit R_F. Thus, even if there were no velocity disturbance (g), there could be a pressure disturbance at the diffuser entrance of arbitrary amplitude. In other words, if R_F were fixed, and V were decreased from some large value, a critical or resonant value of V would be reached, at which pressure disturbance could be arbitrarily large. The table to the right in Fig. 2 shows some of these resonant points. Such points are found for various circumferential harmonics and radial modes.

The importance of this feature of the solution would seem to be that "slow" rotating-wave disturbances would inevitably occur at or near these resonant conditions, regardless of the compressor characteristic, and also regardless of the parameters τ and η. Figure 3 shows why this is so. For the particular choice $f = 0$, the curve of pressure function $PM(1)$ versus R_F for $V = 0.155$ is a typical resonant response curve, going to plus or minus infinity at $R_F = 2.08$. Now, in this case, $PM(1)$ must have the value -0.5 in order to satisfy equation (5); clearly, this equation will be satisfied close to resonance no matter what the values of τ and η might be; that is, because the particular value -0.5 is unimportant near resonance. Quite near resonance, for a somewhat larger value of $V = 0.165$, waves can also occur, but they cannot occur for a lower value such as $V = 0.145$ (compare the $f = 0$ contour on Fig. 2).

A set of profiles of velocity and pressure variation across the diffuser from (1) to (F), in the first radial mode and away from resonance, is shown in Fig. 4(*a*) for $f = 0.1$. Another set of profiles, now at resonance in the first radial mode, still

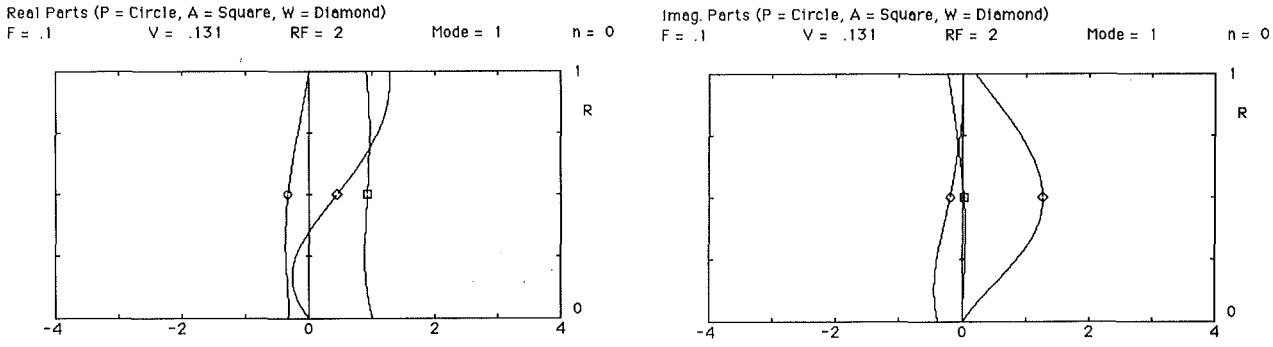

Fig. 4(*a*) On the $f = 0.1$ contour, first radial mode of Fig. 2, but away from the resonant point

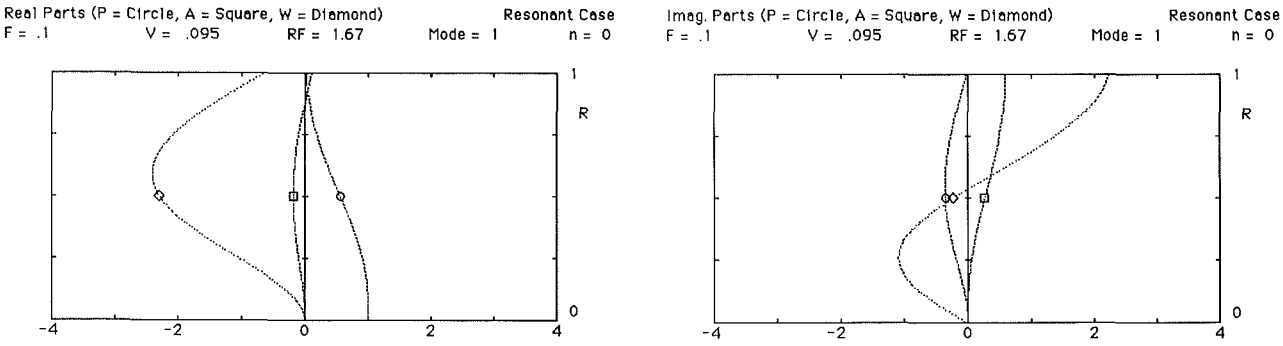

Fig. 4(*b*) On the $f = 0.1$ contour, first radial mode, but at resonance; normalized so that $P = 1$ at the entrance; note large swings of W

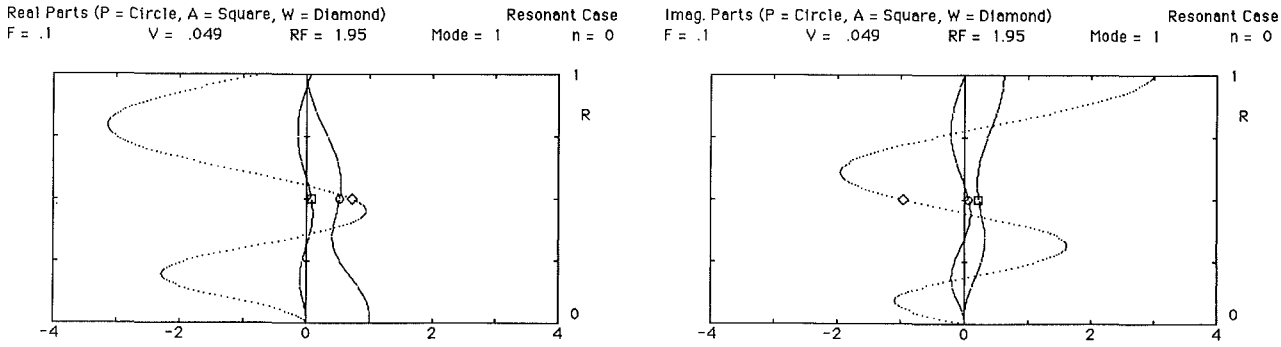

Fig. 4(*c*) On the $f = 0.1$ contour, second radial mode, at resonance

Fig. 4 Profiles of real and imaginary parts of fluctuations of pressure (P), and radial and circumferential velocities (A, W) for $f = 0.1$ and $R_F = 2$. Note that equations (12)–(14) are satisfied. Diffuser entrance and exit are at $R = 0, 1$.

with $f = 0.1$, is shown in Fig. 4(*b*). Owing to the resonance, it is appropriate to normalize these profiles on real pressure at ①, rather than on $A(1)$. Resonance for the same f in a second radial mode is shown in Fig. 4(*c*); that resonant point can be located on the second band of contours on Fig. 2. The banded aspect of Fig. 2 suggests that very abrupt transitions are to be expected between the various slow radial and, as we shall see, slow circumferential modes.

The significance of resonance lies not only in the behavior of $PM(1)$ as part of equation (5), but also in the fact that the associated function $PR(1)$ is also resonant. Through equation (4), it provides damping (if it is positive) or amplification (if it is negative) which will modify the familiar effect of the slope of the compressor characteristic function. Because $PR(1)$, like $PM(1)$, is either plus or minus infinity at resonance, the theory suggests that the diffuser will provide an overwhelmingly amplified slow wave near any point of resonance, regardless of the compressor characteristic. It is for this reason that the term

"wave" is used here instead of "stall"; a resonant wave could occur, owing to the effect of the diffuser, but with neither compressor nor diffuser in a stalled condition.

Figure 5 illustrates the foregoing argument. For various fixed values of R_F, the damping effect $PR(1)$ is shown as a function of flow coefficient V, which one might imagine decreasing as a throttle is closed. The associated wave speed f is also shown. These results are limited to the first radial and circumferential modes. If, for example, $R_F = 2$, infinite amplification (negative $PR(1)$) will arise when V is reduced to about 0.14. As one might guess, smaller radius ratios allow smaller flow rates before resonance is felt.

A physical, qualitative explanation for the resonance effect is elusive. Obviously, the dynamics of a diverging flow with vorticity is difficult to describe in simple terms. It may be noted that the resonance, in the first radial mode, always involves a V, R_F combination for which the undisturbed spiral streamline travels through an angle of nearly $3\pi/2$ between entrance (1) and exit (F); such a case is illustrated in Fig. 1. For higher radial modes, multiples of 2π are to be added.

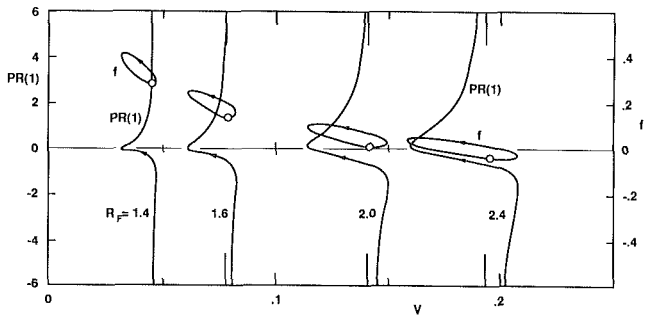

Fig. 5 Traces of amplification $PR(1)$ for "slow" waves as V is changed, for four values of R_F. Corresponding speed f is also shown (right-hand scale), with values at resonance indicated by circles. $PR(1)$ goes to $\pm\infty$ at resonance.

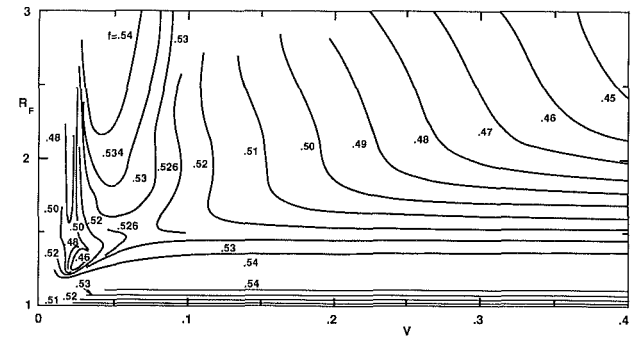

Fig. 6 Contours as in Fig. 2, except that the permitted waves are "fast." The two sets of contours are joined at the common contour for $f = 0.46$.

The "slow wave" possibilities shown on Fig. 2 extend only to $f = 0.46$. Calculations of equation (15) show another sheet of possibilities, on the same map of R_F and V, but with larger values of f. These are shown on Fig. 6. These "fast wave" contours begin with $f = 0.46$, where the two sheets (Figs. 2 and 6) are connected at a common contour. The "fastest" contour in the range of R_F shown is about 0.54. These values of f, representing possible solutions of equation (5), are sensitive to the values assumed for the lag and entrance parameters τ and η.

There are no resonances evidenced by these "fast wave" solutions. Also, there are no such narrow bands of solution as there were for slow waves, and therefore no expectation of abrupt transitions when V changes. In fact, for $R_F < 2$, large changes of V will nearly trace a single control of constant f. Fast-wave profiles do not show as much variation of pressure and velocity as do slow wave profiles. Figure 7, for $f = 0.5$, is typical, and may be contrasted with the slow-wave profiles of Fig. 4(*a*).

Figure 8 shows the damping function $PR(1)$ for fast waves, for various radius ratios R_F. The function is negative, implying amplification. The amplification effect increases without limit as V increases. However, the level of amplification is much smaller than in the slow-wave regime, as may be seen by comparing the vertical scales of Figs. 5 and 8. Also, as V increases, one expects the (unstalled) slope of the characteristic function to make a very negative (stabilizing) contribution in equation (4), overcoming the diffuser's amplifying effect now under discussion.

Extensions of the Analysis

Certain limitations of the foregoing inviscid theory may easily be removed, and the resulting changes in the rotating-wave prediction can be assessed. Four such changes (sketched in Fig. 9) will be considered in the paragraphs to follow.

Circumferential Harmonics. So far, only the fundamental circumferential mode has been considered. If equation (3) is replaced by

$$g = A(1)e^{ib\theta}; \qquad C_{p_1} = P(1)e^{ib\theta} \tag{21}$$

one may choose the wave number b to represent various harmonics above the fundamental, $b = 1$. Consequently, equation (5) and the equations that follow must be modified to include b. When this is done, new results are found.

Some results for slow-wave damping appear in Fig. 10, in the first radial mode. The original result from Fig. 5 is shown dashed for comparison. The resonance effect remains, as do higher radial modes for each b. The chief change is the shift to higher values of V, with largest V (about 0.3) corresponding to $b = 3$ and 4. Resonance occurs at a smaller V for both lower ($b = 2$) and higher ($b = 5$) mode numbers. The implication that modes 3 and 4 should be the first to appear when

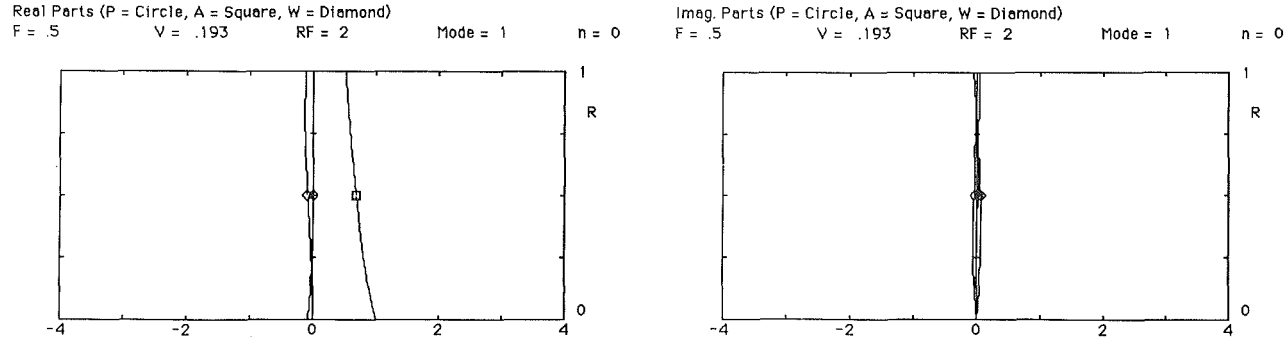

Fig. 7 Profiles at a contour point when $f = 0.5$ (a "fast" wave). Compared with Fig. 4(*a*), all perturbations are quite weak.

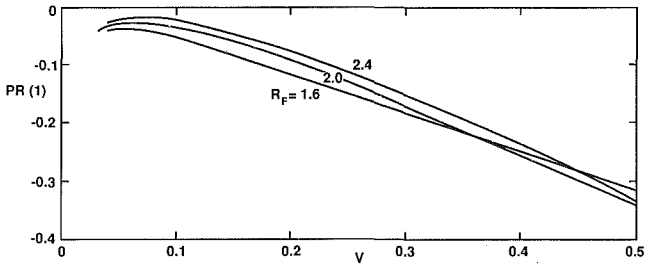

Fig. 8 Traces of amplification *PR*(1) for "fast" waves as *V* is changed, for three values of R_F. When comparing Fig. 5, note that the vertical scale is reduced by a factor of 5.

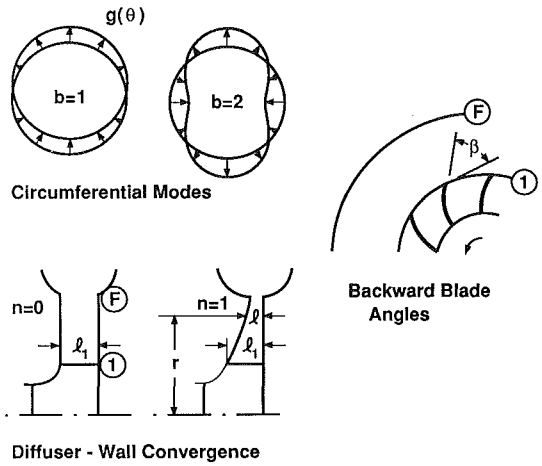

Fig. 9 Sketches related to extensions of the theory

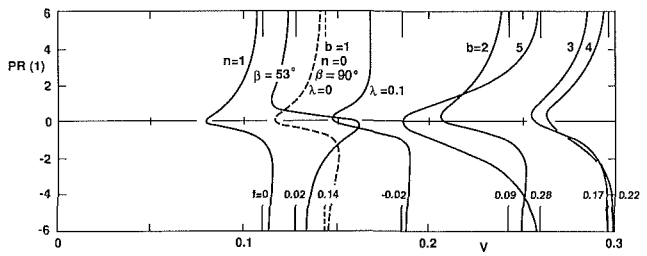

Fig. 10 Traces of amplification for "slow" waves, all for R_F = 2, but after certain extensions of the theory. The comparison case, from Fig. 5, is shown dashed. Values of *f* at resonance are also shown. Mode number (*b*) and the parameters relating to wall shape (*n*), blade angle (β), and exit head recovery (λ) are changed separately.

flow coefficient is progressively reduced to 0.3 and below is borne out by the experiments of Frigne and Van Den Braembussche (1984). For values of V below about 0.15, higher radial modes of higher circumferential modes become possible, and the resonant possibilities become very dense.

For all circumferential modes above the fundamental, the fast-wave damping becomes positive. Generally, then, waves of the fast variety would only be expected in the fundamental mode, again as indicated by the experiments of Frigne and Van Den Braembussche (1984).

Diffuser-Wall Convergence. The diffuser walls of Fig. 1 are parallel; the spacing l has been assumed constant. Of course, the walls might converge, as shown in Fig. 9, providing more gradual diffusion. Choosing a power law form for l, but continuing to neglect any axial velocity component, only the continuity equation (11) needs to change:

$$l = l_1 r^{-n}; \qquad rA' + (1-n)A + iW = 0 \tag{22}$$

It is easy to modify the power-law solution procedure to account for n being different from 0. The result for slow-wave damping is shown on Fig. 10 for $n = 1$. As one might expect, the fundamental-mode possibility appears at a smaller V when $n = 1$ than when $n = 0$. For the fast waves, convergence decreases the amplification effect shown in Fig. 8; when $n = 1$, fast waves are slightly damped.

Backward Blades. So far, radial impeller blades ($\beta = 90$ deg in Fig. 9) have been assumed, but one might expect that backward-induced blades at (1) would affect stability. One change needed in the diffuser-wave analysis is to write a new boundary condition on $W(1)$ to replace that given in equation (13). The new boundary condition is

$$W(1) = -A(1)\cot\beta \tag{23}$$

It is also proves necessary to change the disturbance differential equations (9)–(11) by dividing V, f, and P by the expression $1 - V\cot\beta$, wherever they appear. The new solution is then readily obtained by combining a solution of the previous type (having $W(1) = 0$) and the simple particular solution $W = W(1)$, $A = iW(1)$. The boundary conditions of equations (12) and (14) need to be applied, of course.

The new solution shows a slight shift of the slow-wave singularity to smaller V, depending on the leaving angle β; Fig. 10 shows the effect on damping for the rather large $\beta = 51$ deg. The fast-wave damping is strongly positive for that value of β. The implication is that backward blade angles are stabilizing for the fast variety of rotating waves, but have little effect on slow waves.

Partial Head Recovery at Diffuser Exit. The profiles in Figs. 4(*a–c*) show rather strong velocity disturbances at the diffuser exit. Therefore, one might wonder if stability would be affected by arranging for recovery of a fraction λ of the dynamic head at exit (F). In terms of pressure and velocity perturbations, the boundary condition to replace equation (14) would be

$$P(R_F) + \lambda[VA(R_F) + W(R_F)] = 0 \tag{24}$$

This change is easily accommodated by a new determination of the K_1 and K_2 that appear in equation (15).

Figure 10 shows that a 10 percent recovery shifts the slow-wave singularity to a substantially higher value of V. The fast-wave damping, however, is virtually unaffected by a 10 percent exit head recovery.

Appearance of Waves in a System

The total damping effect of a vaneless diffuser ($PR(1)$) would have the form shown in Fig. 11(*a*); at some values of V a fast wave is favored, while at other values of V a slow wave is indicated. Many slow (but not fast) modes are possible; Fig. 11(*a*) shows only the first three circumferential modes, all in the first radial mode.

According to equation (4), this damping effect combines with the slope of the axisymmetric characteristic, $\psi_c'(V)$, to indicate the possibility of rotating waves in a centrifugal compression system. A possible characteristic function is sketched in Fig. 11(*b*), and its slope is shown as the parabolic curve in Fig. 11(*c*), which cuts the V axis at point C. In the absence of any diffuser effect, limit cycles of a fast-wave type would presumably be expected to the left of point C, wherever the characteristic slope is positive. Equation (4), which includes the effect of $PR(1)$, would give a different stability point, C', in a fast mode for the case sketched. For smaller values of V corresponding to the shaded zone above the V axis, limit cycles would be expected, often of a slow type.

Clearly, the position along the V axis of the maximum of ψ_c relative to the V's for resonance will determine what type of mode would first be expected as V is throttled down from a large value. If the maximum of ψ_c were to occur when $V <$ 0.3, the first wave would be of the slow type, probably of the

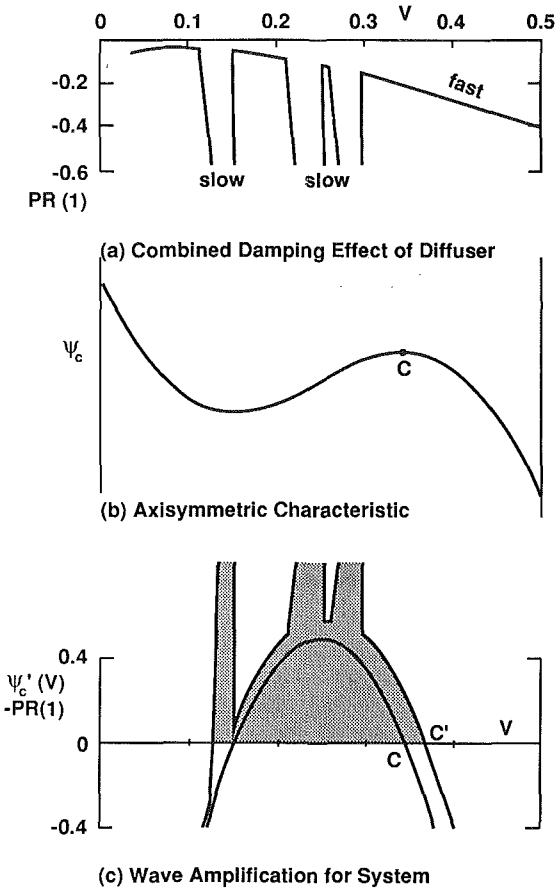

Fig. 11 Sketches showing how results of diffuser analysis and compression characteristic are combined to indicate occurrence of rotating waves

third or fourth harmonic, and it would be found near $V = 0.3$, where the resonant peak penetrates the V axis.

Concluding Remarks

The foregoing analysis corresponds to that of Moore (1984a); it assumes small perturbations of flow coefficient, and therefore explicitly only yields the neutral condition under which a weak rotating wave may exist. When interpreting the neutral condition, equation (4), we have nevertheless adopted the rather obvious idea that, since ψ_c' positive is destabilizing and leads to limit cycles in axial systems (Moore, 1984b), negative $PR(1)$ must be similarly destabilizing. The next step might be to find limit cycles in the manner of that paper, assuming that a linear analysis of the diffuser flow remains applicable. How, or whether, such an analysis could accommodate the resonances present in the diffuser flow is a question for further research.

Probably, the right strategy would be to develop a Galerkin procedure in the manner of Moore and Greitzer (1986). Though nonlinear, that procedure retains harmonic representation of waves. Using such an approach, a theory capable of dealing with combined surge and rotating waves, and with hybrid axial-centrifugal systems, may be feasible.

The inviscid assumption used in the study merits further consideration. However, the fact that experimentally observed phenomena seem well represented gives confidence in that assumption. The prediction of fast and slow rotating waves, the prediction of sudden transitions between many slow-wave modes, and even the prediction of the dominance of third and fourth harmonics among slow waves and of the first mode among fast waves are consistent with reported experiments.

Although analysis of the type described in this paper may prove of engineering importance for exploratory purposes, especially when resonances can appear, one can easily imagine a purely theoretical approach getting out of hand in terms of complexity. Armed with an understanding of the roles of the various system parameters gained from the analysis, one may then find that direct numerical solution of the Euler equations is best for practical studies.

Acknowledgment

The research upon which this paper is based was supported by NASA through the Lewis Research Center.

References

Abdelhamid, A. N., 1980, "Analysis of Rotating Stall in Vaneless Diffusers of Centrifugal Compressors," ASME Paper No. 80-GT-184.

Abdelhamid, A. N., Colwill, W. H., and Barrows, J. F., 1979, "Experimental Investigation of Unsteady Phenomena in Vaneless Radial Diffusers," ASME *Journal of Engineering for Power*, Vol. 101, pp. 52–60.

Frigne, P., and Van Den Braembussche, R., 1984, "Distinction Between Different Types of Impeller and Diffuser Rotating Stall in a Centrifugal Compressor With Vaneless Diffuser," ASME *Journal of Engineering for Gas Turbines and Power*, Vol. 106, pp. 468–474.

Haupt, U., Kaemmer, N., and Rautenberg, M., 1986, "Excitation of Blade Vibration by Flow Instability in Centrifugal Compressors," ASME Paper No. 86-GT-283.

Jansen, W., 1964, "Rotating Stall in a Radial Vaneless Diffuser," ASME *Journal of Basic Engineering*, pp. 750–758.

Kämmer, N., and Rautenberg, M., 1986, "A Distinction Between Different Types of Stall in Centrifugal Compressor Stage," ASME *Journal of Engineering for Gas Turbines and Power*, Vol. 108, pp. 83–92.

Moore, F. K., 1984a, "A Theory of Rotating Stall of Multistage Compressors: Part I—Small Disturbances," ASME *Journal of Engineering for Power*, Vol. 106, pp. 313–320.

Moore, F. K., 1984b, "A Theory of Rotating Stall of Multistage Compressors: Part III—Limit Cycles," ASME *Journal of Engineering for Gas Turbines and Power*, Vol. 106, pp. 328–336.

Moore, F. K., and Greitzer, E. M., 1986, "A Theory of Post-Stall Transients in Axial Compression Systems: Part I—Development of Equations," ASME *Journal of Engineering for Gas Turbines and Power*, Vol. 108, pp. 68–76.

The Vortex-Filament Nature of Reverse Flow on the Verge of Rotating Stall

Y. N. Chen
Sulzer Brothers, Ltd.,
Winterthur, Switzerland

U. Haupt

M. Rautenberg

Institute for Turbomachinery,
University of Hannover,
Hannover, Federal Republic of Germany

On the verge of rotating stall, very orderly reverse flow forms from the outlet of the rotor/impeller along the casing/shroud toward the inlet in axial/centrifugal compressors (Koch, 1970; Haupt, et al., 1987). The experiment on a centrifugal compressor reveals furthermore that the reverse flow is composed of stable spiral vortex filaments. Their vorticity can be transferred to the inlet tip vortex, known as prerotation. The behavior of these vortex filaments is examined based on the fundamental research work on rotating bodies available in the literature. This result shows that the vortex filaments are composed of Taylor's vortex pairs, but with unequal vortex strengths within the pair. They form the transition range from a laminar to a turbulent three-dimensional boundary layer with a very steep tangential velocity profile. This profile is associated with the appearance of a toroidal ring vortex in the rotor/impeller, acting as a recirculatig secondary flow. It can be further shown from the analysis of the extensive literature that the orderly path of the reverse flow is enabled by the cessation of the leakage flow of the rotor tip clearance. The reason for this is that the growing tangential flow field extends beyond the rotor tip up to the close proximity of the endwall, so that the tip clearance is blocked.

Introduction

It is generally suggested that there are at least three candidates for the fluid dynamic mechanism of rotating stall inception (Casey, 1987), namely:

- incidence stall due to separation of the nose bubbles of the blade leading edges at excessive incidence,
- blade stall due to separation of the blade profile boundary layers, and
- wall stall due to separation of the casing or hub boundary layers.

In the present paper, the effort is concentrated on the flow phenomena related to the inception of incidence stall.

On the verge of rotating stall, reverse flow appears from the outlet of the rotor/impeller along the casing/shroud toward the inlet in axial/centrifugal compressors, according to Koch (1970) and Haupt et al. (1987). Then, the reverse flow appears to be common feature for the occurrence of rotating stall, independent of the type of turbocompressor. At the same time the two components of the three-dimensional boundary layer on the endwall surface, the tangential and the meridional, develop into the opposite trends, i.e., steepening of the former and flattening of the latter. This very striking phenomenon can be derived from the experimental results given by L.H. Smith (1970) and Cumpsty (1986).

The present experimental investigation shows, furthermore, that the reverse flow is composed of stable spiral vortex filaments, which are fixed to the impeller, without any movement crossing the clearance of the blade tip.

Contributed by the International Gas Turbine Institute and presented at the 33rd International Gas Turbine and Aeroengine Congress and Exhibition, Amsterdam, The Netherlands, June 5–9, 1988. Manuscript received by the International Gas Turbine Institute September 15, 1987. Paper No. 88-GT-120.

It is known that the three-dimensional boundary layer on the surface of a rotating body, either a disk, a cone, or a cylinder, can be separated into spiral vortices, either simple vortices or Taylor's vortex pairs. It is shown in the paper that close similarity exists between the three-dimensional boundary layer of the rotating body and the reverse flow of the compressor. Then the property of the reverse flow can be clarified to a great extent, using the results obtained on the rotating bodies.

The mechanism of the appearance of the reverse flow is also investigated. It can be shown that the reverse flow is a kind of Stewartson layer (known as the three-dimensional boundary layer formed on the wall of a rotating tank), associated with a toroidal ring vortex in the rotor as a recirculating secondary flow. This can be derived from the experimental investigations given in the literature.

The explanation for the stability of the spiral vortex filaments in the reverse flow is the final goal of the paper. For this purpose a great number of experimental results available in the literature are analyzed. It can be shown that the rotor tip clearance is blocked by the growing tangential flow field, and then the tip leakage jet, which may disturb the spiral vortex filaments, is suppressed.

Experimental Investigations of the Nature of the Reverse Flow

It was shown in the papers of Haupt et al. (1987) and Chen et al. (1987), presenting results of flow characteristics on a centrifugal compressor, that the reverse flow, which occurs

from the outlet of the impeller along the shroud surface, plays a central role for initiating the inception of rotating stall.

The experimental result given by Koch (1970) on the verge of rotating stall in a four-stage axial compressor also showed that the reverse flow occurred from the outlet of the rotor along the casing wall in all of the four stages.

The nature of the reverse flow should be very important as regards the initiation of rotating stall. The method of injection colored dye, used in the papers of the present authors cited above, for the visualization of the path of the reverse flow, cannot reveal its fine structure during the period of rotating stall, because the path of the reverse flow accompanying the stalled region will be swept up by the stall cell itself and by the throughflow in the unstalled region. Therefore, on a centrifugal compressor with radial blading and a vaneless diffuser, three operating points outside of the rotating stall range were selected for the investigation of the impeller unsteady flow characteristics, at which a steady-state reverse flow appears in both—absolute and reference—frames, but without any disturbance of the accompanying flow. These three points are:

1 between the rotating stall and the occurrence of massive surge at $n_{red} = 14{,}000$ rpm
2 normal operative point without fluctuations in static wall pressure at $n_{red} = 14{,}500$ rpm, and
3 on the verge of rotating stall at $n_{red} = 13{,}140$ rpm.

For the first operating point, colored dye was injected through the shroud at the outlet edge of the impeller. As shown in Fig. 1, the reverse flow follows a very sharp spiral path upstream to the suction pipe, with a rotational sense equal to that of the impeller. This indicates that the colored dye is carried out by the impeller upstream. This reverse flow then returns downstream to joint the forward flow. The disturbances on the path, showing a forward-flow nature, appear to be caused by the shutdown procedure of the compressor, in which the flow at the smaller rotating speeds of the impeller recovers to its normal forward condition. These disturbances were explained by Chen et al. (1988).

Vortex-Filament Nature of the Reverse Flow. The reverse flow in Fig. 1 has a very sharp path along the shroud. Since it

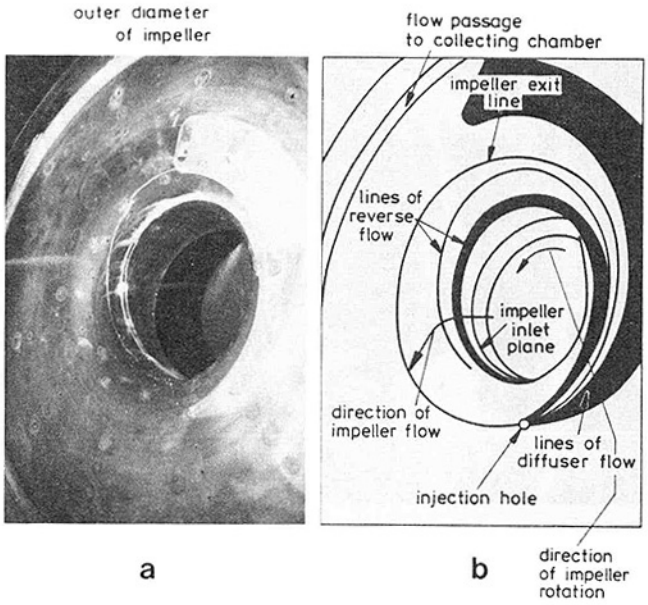

Fig. 1 Trace of the colored dye (injection through the shroud at the outlet of the impeller) along the shroud surface: (*a*) photo after disassembly, (*b*) sketch of the trace

is traveling through the boundary layer of the shroud surface, this shear layer does not diffuse it, but rather stablize it. This indicates that the reverse flow has to behave as a vortex filament in order to conserve its own particles (i.e., its colored dye), and thus to get rid of the outer diffusing effect of the surrounding shear layer. In addition, the vorticity in the vortex filament should be constantly renewed by the shear layer in order to balance its diffusion into the surroundings.

For the examination of this vortex-filament theory the photograph of a part of the reverse flow was 20 times enlarged as given in Fig. 2. The path of the reverse flow $R1$ shows very clearly a spiral pattern as sketched in the figure. This reverse flow then rolls up into the ring vortex formed as prerotation at the leading edge of the rotor/impeller on the side of the casing/shroud at off-design points. The conventional supposition

Nomenclature

c = blade chord
c = absolute velocity
d = width between two concentric circular cylinders
D = diameter
Ek = Ekman number
f = rotor tangential force
F = force
F = forward flow streamlines
h = spiral vortex height
l = chord length
m = number of rotating stall cells
$\dot{m}$ = mass flow
n = rotational speed
p = pressure
PS = blade pressure surface
r = radius
R = radius
R = reverse flow streamlines
Re = Reynolds number
s = blade length at tip
S = ratio between tangential and meridional velocity
SS = blade suction surface
t = tip clearance
Ta = Taylor number
u = velocity
U = tangential velocity
U_e = meridional velocity
v = velocity
V = free-stream velocity
w = relative velocity
x = distance from inducer inlet along blade tip
x = meridional direction
β = relative flow angle
δ = boundary layer thickness
δ^* = displacement thickness
ν = kinematic viscosity
ν = thickness of the tangential force loss
ξ = vorticity
π = pressure ratio
ρ = density
τ = tip clearance
ϕ = mass flow rate
ψ = pressure rise coefficient
ψ = stream function
ω = angular velocity
Ω = angular velocity

Subscripts

c = lid of rotating tank
F = tangential force
i = inner
m = medium plane
max = maximum value
o = outer
p = pressure side of blade
t = tip
tot = stagnation
T = tangential component
u = tangential component
x = meridional/axial component
1 = blade inlet
2 = blade outlet
φ = tangential component
$*$ = design point
$'$ = off design point
$'$ = fluctuating velocity

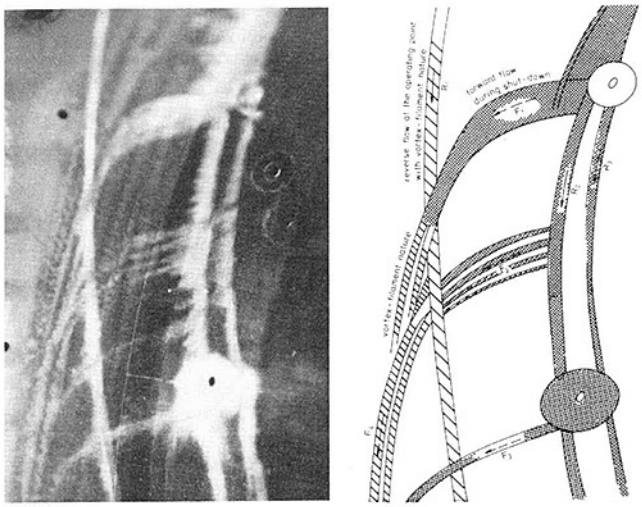

Fig. 2 Reverse flow on the shroud surface and streamlines during shutdown procedure of the compressor

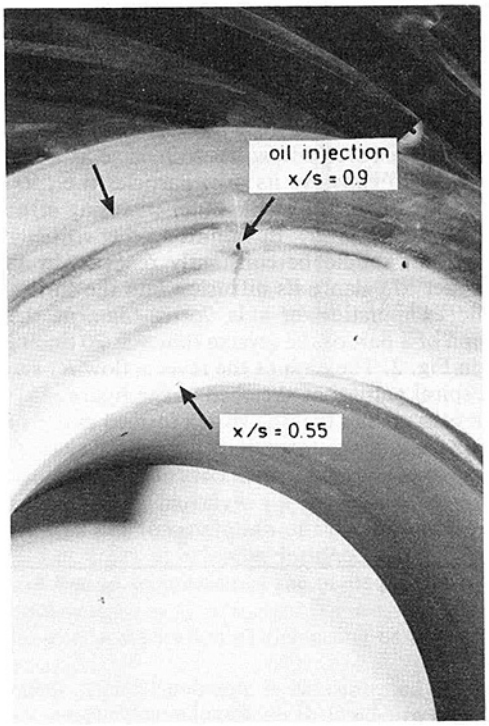

Fig. 3 Trace of the colored dye (injected at $x/s = 0.9$) showing the reverse flow along the shroud surface up to $x/s = 0.55$ for the normal operating point

about the origin of this ring vortex is that the flow after entering the leading edge on the hub side returns back directly to the casing/shroud side, and then generates this ring vortex as a phenomenon of flow separation. The investigations of Haupt et al. (1987), Chen et al. (1987), and Koch (1970) reveal, however, that the reverse flow originates from the outlet annulus of the rotor/impeller, but not from the entrance flow directly at the inlet region.

From the present investigation it is obvious that the ring vortex is fed by the vorticity of the reverse flow, but not a phenomenon of pure flow separation. The sense of the ring vortex always coincides with that of the vorticity mentioned.

Reverse Flow and Rotor Impeller Tip Leakage Flow. The sharp path of the reverse flow reveals furthermore that the leakage flow through the clearance of the impeller tip has ceased to exist in this off-design point. Otherwise, this path would be disturbed by the leakage flow.

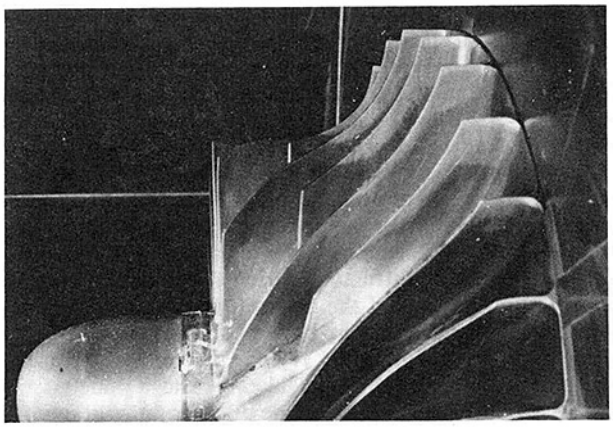

Fig. 4 Deposited colored dye on the pressure surface of blades due to reverse flow near shroud at normal operating point conditions

The inference given is verified by the measurement about the relative velocity fields carried out by Mizuki et al. (1976). At the design point of $\phi = 0.330$, the leakage flow is strong in the impeller outlet region corresponding to a zone centered at $x/s = 0.8$, related blade length.

For a very low flow rate of $\phi = 0.110$, however, no such leakage-flow field can be detected across this section. In addition, the experimental results given by Inoue et al. (1987) clearly shows that the leakage jet weakens, when the flow rate is decreased from the design value of $\phi = 0.5$ to $\phi = 0.45$. The sealing of the clearance between rotor tip and endwall becomes stronger with lower flow rate.

Reverse Flow at Normal Operating Point. For the second experiment at a normal operating point the colored dye was injected at a position of related blade length $x/s = 0.9$. As shown in Fig. 3, this colored dye forms a ring on the surface of the shroud upstream to the station of $x/s = 0.55$. Its rotational sense is opposite to that of the colored dye in Fig. 1, thus opposite to the rotation of the impeller. Therefore, the colored dye is not carried out by the rotating impeller directly, but by the leakage jet through the rotor tip clearance from the pressure to the suction side of the blade, therefore opposite to the impeller rotation. Since the leakage flow is strong in the zone of about 0.8, the colored dye is carried by it from $x/s = 0.9$ upstream. The strong turbulence activity of the jet then causes the dye to spray out to $x/s = 0.55$.

The deposited color on the outlet edge of the pressure surface, in addition to its tip region, as shown in Fig. 4, indicates furthermore that leakage flow does not only have its path through the clearance of the impeller tip, but also over the outlet edge to the suction side of the blade. The deposition of colored dye on the pressure surface near the trailing edge reveals furthermore that a separation of the flow takes place there, before bending to the suction side. This separation zone becomes larger, the lower the flow rate, as shown by the present authors elsewhere (1987). This may explain the strange phenomenon that cavitation occurs on the pressure surface near the trailing edge of pump impellers when operating at low capacity (Fraser, 1982). The fan-shaped streamlines on the suction surface directed from the trailing edge upstream in Fig. 5 attests this kind of leakage flow as a reverse flow.

The further range of the deposited colored dye on the suction surface near the tip along the high-pressure-rise zone shows the restricted region of the leakage flow over the blade tip.

The leakage flow through the tip clearance is thus active in the normal operating range, but ceases to exist at all in the off-design range.

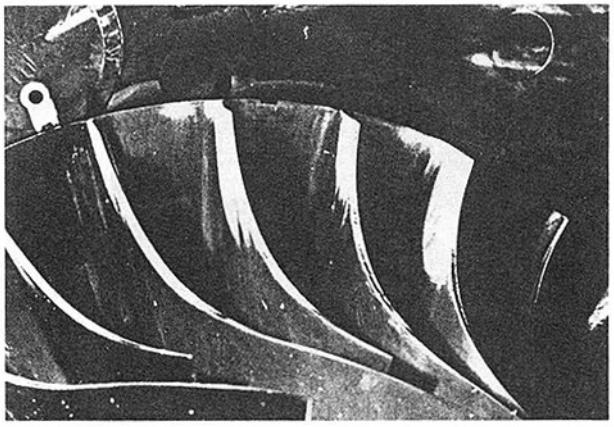

Fig. 5 Deposited colored dye on the suction surfaces of blades due to reverse flow near shroud at normal operating point conditions: (*a*) showing leakage flows over the tip and the trailing edge, with a narrow branch of the reverse flow penetrating further upstream along the tip; (*b*) showing the vortex-filament pattern of this narrow reverse flow

The vortex-filament-natured reverse flow can be discovered in the experimental results obtained by Eckardt (1974) and Mizuki et al. (1976), even at the normal operating point.

These experiments show that the pressure drops steeply from the pressure side to the suction side of the blade. Afterward, the curve rises very slowly up to the pressure side once more. But there is a sharp pressure pulse A embedded within the curve directly on the suction surface, i.e., just at the beginning of the rising curve; see curves for the normal flow rate of $\varphi = 0.330$ in Fig. 6. This sharp pressure pulse can be very well interpreted to represent the core of the vortex-tube-natured reverse flow. The high pressure in the outlet annulus of the impeller then penetrates backward through the core of this vortex tube up to the front of the reverse flow. The width of this pressure pulse represents thus the dimension of the vortex core. The vortex tube can penetrate this deeply because of the conservation nature of its vorticity. In addition, the flow through its core will maintain its strength owing to the effect encountered on the bathtub vortex.

In the experiment of Eckardt (1974) this vortex-tube-natured reverse flow can penetrate upstream beyond $x/s = 0.434$. The intensity of this pressure pulse decreases during traveling upstream, which is obviously due to the diffusion effect of the surrounding flow on the vortex tube.

When the flow rate is lowered to $\phi = 0.220$, 0.165, and 0.110, this sharp pressure pulse gives way to a general rise of the curve above the atmospheric pressure. If the extreme curves in the pressure traces of these four flow rates are redrawn into diagrams, with each of the curves for $\phi = 0.220$, 0.165 and 0.110 over that of $\phi = 0.330$, as shown in Fig. 6, we can detect that the drop of all the four curves from the pressure surface follows nearly the same line. The rising parts of the curves for the three lower flow rates, however, are much higher than the deepest curve of $\phi = 0.330$. This testifies that the vortex tube restricted to the suction-surface/shroud-corner at $\phi = 0.330$ has widened out over the entire surface of the shroud up to the station of $x/s = 0.7$ at least, when ϕ is lowered to $\phi = 0.220$. The distance between the two curves of $\phi = 0.220$ and 0.330 indicates the effect of the high pressure of the outlet annulus via the cores of the vortex tubes of the reverse flow sheet on the shroud surface. The reasoning for this consideration was shown in the Appendix of a previous paper (Chen et al., 1988). That the reverse flow sheet at this stage still possesses the vortex-tube nature will be covered in the third experiment.

The pressure difference, measured on the shroud wall, between the pressure and suction surface of the blade, is also given in Fig. 6. It decreases first steeply down to $\phi = 0.165$ and

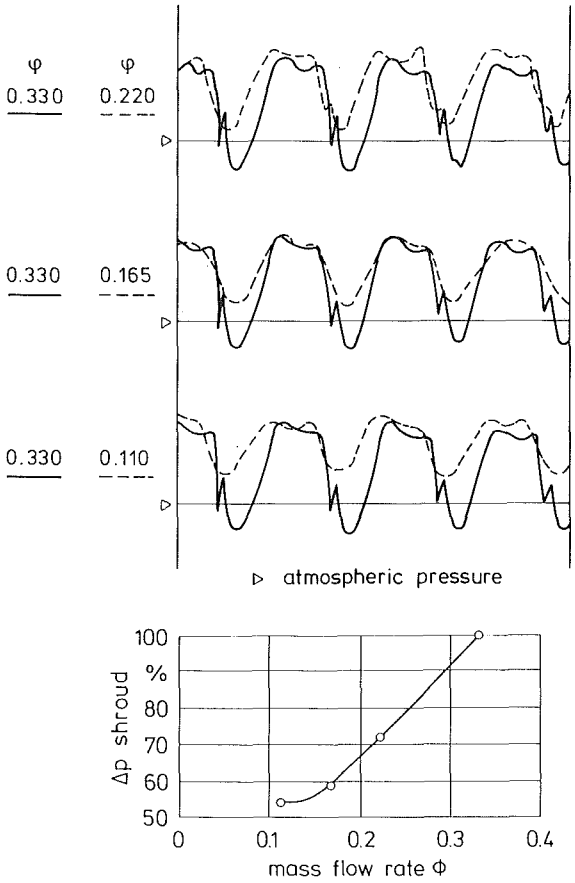

Fig. 6 Comparison of the pressure fluctuation pattern at $\phi = 0.330$ with the others of 0.220, 0.165, and 0.110, based on the experimental data of Mizuki et al. (1976)

then remains flat. It seems that the rotor tip clearance will soon be blocked by the thickening axial velocity boundary layer. We then reach the verge of rotating stall.

Reverse Flow on the Verge of Rotating Stall. The results of the third experiment carried out, just on the verge of rotating stall, are shown in Fig. 7.

Figure 7 reveals that the injected colored dye is especially well deposited in the form of a sharp ring R at about $x/s = 0.7$. The colored dye injected through the hole at $x/s = 0.8$ is carried by the impeller in its rotational sense, similar to the case in Fig. 1. The streamlines formed by the dye on the shroud surface indicate that their rotational sense is also the same as that in Fig. 1, thus equal to the rotational sense of the impeller again. This reveals that this reverse flow has a property similar to that in Fig. 1. Quite regular streamlines are formed up to the sharp ring, as sketched in Fig. 8(*b*). No disturbances from the leakage jet of the rotor tip clearance are present. The ring in Fig. 7 separates the two different flow regions, namely the reverse flow, originating from the outlet of the impeller, and the forward flow, coming directly from its inlet. The ring is sharp on both sides. The colored dye is partly carried into the forward flow, apparently by the narrow branch of the reverse flow along each of the inner corners between the blade suction surface and shroud, as stated in the previous section (cf. Fig. 6). Without these narrow branches of colored dye, the forward flow cannot be colored at all. The paths of these narrow branches penetrate farther into the inlet front of the impeller, as revealed by Fig. 7. While the separated streamlines can be well detected in the reverse flow (see also Fig. 8(*b*)), no such clear structure can be found in the forward flow. The colored dye deposited in the forward flow shows a rather wiped-out pattern.

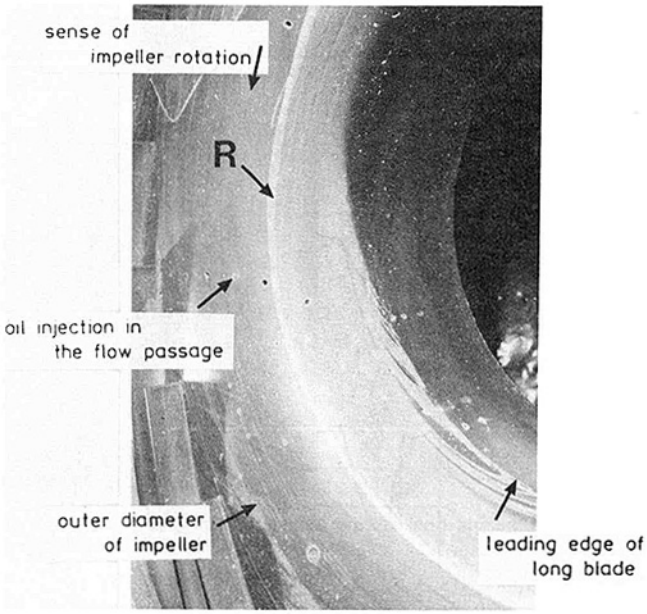

Fig. 7 Heavily deposited colored dye along ring R at about $x/s = 0.7$, separating the reverse flow from the forward flow. Experimental conditions: compressor operating on the verge of rotating stall; $n_{red} = 13100$ rpm; oil injection at $x/s = 0.8$.

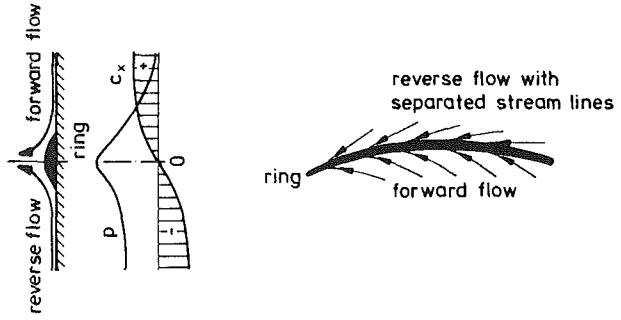

Fig. 8 Ring as a stagnation front between two flows with opposite meridional velocities

The sharp ring is thus a stagnation zone between the two flows in the meridional plane, a forward flow (positive c_x) and a reverse flow (negative c_x). The front between them is stagnated to a meridional velocity of zero (see Fig. 8*a*). The pressure p has a peak there due to stagnation. It is this zero meridional velocity that causes the pile-up of the heavy colored dye carried by the flow. The approaching flow will be deflected by the stagnation to the radial and tangential directions.

If the reverse flow is considered, it has to travel against a pressure rise up to the stagnation point. An instability can be caused in it due to this positive pressure gradient. This approaching boundary layer flow is thus separated into parallel lines in this zone, as it can be detected from the photo (also see Fig. 8*b*). They enter the ring under an angle of about 20 deg. It will be shown in the section about vortex behavior that these parallel streamlines are in reality vortex filaments because of the steep gradient of their tangential velocities on the shroud surface. The colored dye deposited in the forward boundary layer flow shows turbulence. The streamlines enter the ring under a very small angle of about 5 deg.

The separation of the reverse flow into a series of relatively parallel streamlines when approaching the ring can also be detected in the experimental result given by Koch (1970) on a four-stage axial compressor.

The similarity of the reverse flows in both types of compressor, the centrifugal and the axial, is thus quite obvious. The properties of the reverse flow found in the experiments on either type can therefore be applied to both.

Fig. 9 Colored dye pattern deposited on the pressure surface showing a line A separating the leakage flow region near shroud from the trailing edge zone as the origin of reverse flow

The boundary layer on the shroud surface is therefore a rather normal one in the forward-flow region, but is separated into individual vortex-filament-natured streamlines in the reverse flow region.

Figure 9 shows the very clear pattern of the streamlines on the pressure surface of two blades as indicated by A. Line A separates the flow field into two regions. The streamlines in the lower region ($x/s < 0.7$) end at the tip, indicating a leakage flow over the tip into the clearance. The streamlines in the upper region bend tangentially along the contour of the tip into the forward-flow direction. This indicates that the tip clearance flow is blocked there by the reverse flow along the suction surface of the blade, making the flow sound on the pressure side. Here it follows the radial contour of the blade, accompanied by the continuity of the rise of the characteristic curve in the compressor chart up to the inception point of rotating stall, despite the occurrence of the strong reverse flow.

Comparison of the Three Experimental Results. The measurements of the three operating points, namely the normal design point, the point near rotating stall, and the point between rotating stall and surge, reveal quite different behaviors of the reverse flow.

At the normal operating point, the reverse flow is restricted to the corner shroud/suction surface. Very clear leakage flow arises through the rotor tip clearance in a direction opposite to the rotational sense of the impeller.

When the operating point approaches rotating stall, the reverse flow covers the entire shroud surface. No essential leakage flow of the rotor tip clearance exists any longer in the reverse flow zone. The reverse flow is carried by the impeller into its rotational direction. The reverse flow boundary layer is quite smooth along the shroud surface, until the stagnation ring is approached. Owing to the deceleration of the meridional velocity component, the flow becomes unstable and separates into parallel streamlines, which are, in fact, vortex filaments due to a steep tangential velocity gradient.

At the operating point between rotating stall and surge, the reverse flow becomes very intensive and penetrates into the

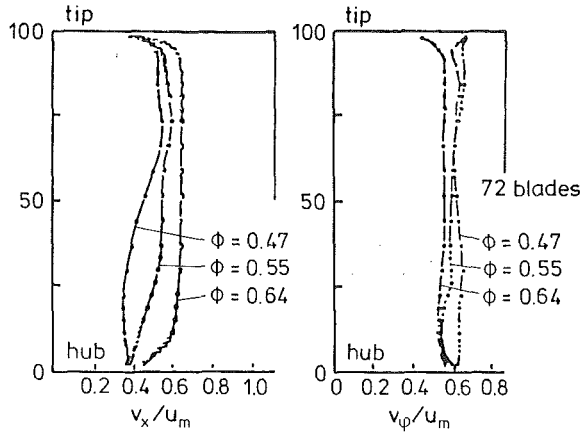

Fig. 10 Axial and tangential velocity profiles downstream of the last rotor (4) at three flow rates of $\phi = 0.64$, 0.55 (design point), and 0.47 (on the verge of rotating stall), according to Cumpsty (1986)

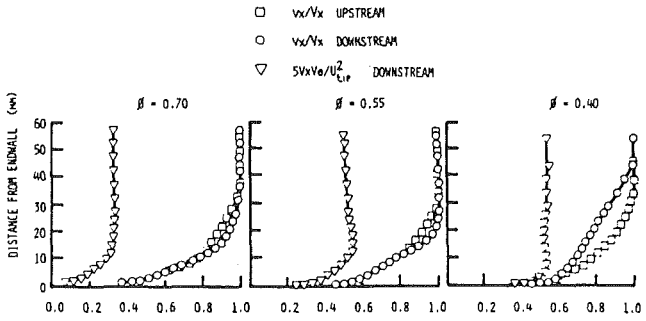

Fig. 11 Axial velocity profiles upstream and downstream of rotor tip, as well as downstream tangential velocity profiles (in an expression of $5v_x v/U_{tip}^2$) at three flow rates of $\phi = 0.70$ (design point), 0.55, and 0.40 (at ψ_{max} or on the verge of rotating stall) according to Hunter and Cumptsy (1982)

suction pipe. This reverse flow, covering again the entire surface of the shroud, is already separated into strong spiral vortices, quite at the starting point from the outlet annulus of the impeller. Once the colored dye is injected into a spiral vortex, all the following dye is caught by the same spiral vortex. A very sharp spiral colored patch is formed, carried by the impeller into its rotational direction. Because of this extreme sharpness of the spiral patch, the dye should remain fixed within the blade channel into which it first enters at the impeller outlet edge. Otherwise it would be strongly disturbed by passing through the blade tip clearance. Absence of phase velocity of the spiral vortices relative to the impeller is thus their peculiar property. This property will be further examined in the theoretical consideration about the vortex behavior.

Theoretical Considerations About the Stewartson Layer

Boundary Layer of Casing on the Verge of Inception of Rotating Stall. The experimental results obtained by Cumpsty (1986) on a four-stage axial compressor (solidity $\sigma = 1.88$) about the axial and tangential velocities are given in Fig. 10, namely for the maximum flow coefficient (0.64), the flow coefficient at design (0.55), and the flow coefficient at the maximum pressure rise (0.47), i.e., on the verge of rotating stall.

The axial velocity v_x/u_m decreases as the flow rate is lowered, whereas the opposite is true for the tangential velocity v_φ/u_m. The outlet velocity triangle then shows the increase in c_{u2} from design point to part flow rate. On the endwall side all the profiles of the axial velocity show a clear boundary layer, the thickness of which increases with the decrease of the flow rate. The tangential velocity profile, however, shows a clear boundary layer only at the maximum flow. As the flow rate is lowered to the verge of rotating stall, the tangential velocity profile remains practically flat over the entire blade span up to the region nearest the endwall. The boundary layer must be extremely thin for this case. There is a very striking detail embedded within this profile, i.e., an increase in the velocity toward the endwall, an overshoot, just outside this thin boundary layer. The generation of the overshoot was shown in Chen et al. (1988).

Similar phenomena can be found in the experimental result obtained by Smith and Cumpsty (1984). We can conclude that the opposite trend of the endwall boundary layers of v_x/u_m and v_φ/u_m, i.e., the broadening for v_x/u_m and the narrowing for v_φ/u_m with a steep rise in the free-stream zone toward the boundary layer outer edge, is a characteristic factor for initiating the inception of rotating stall.

The similarity of the boundary layers of c_x and c_φ at the design point indicates that the condition of the radial equilibrium between c_x and c_φ

$$c_x dc_x/dr + (c_\varphi/r)(d(rc_\varphi)/dr) = 0$$

is satisfied. No essential radial flow takes place.

As the verge of rotating stall is approached, no similarity of the boundary layers of c_x and c_φ exists any longer. The radial equilibrium is injured. Strong radial flows should arise in the form of tangential and axial recirculations within the rotor/impeller. This can be derived from Fig. 11 according to the experimental result obtained by Hunter and Cumpsty (1982) on an axial compressor.

Three diagrams for flow coefficients of $\phi = 0.70$ (design point), 0.55, and 0.40 (at ψ_{max}, i.e., on the verge of rotating stall) are given in the figure. Each diagram consists of three velocity profiles near the casing, namely those for axial velocity v_x/V_x upstream (1) and downstream (2) of the rotor, as well as that for the tangential velocity downstream (3) expressed as $5u_x u_\varphi/U_{tip}^2$. At the design point, the three profiles are quite similar. When ϕ is lowered to 0.55, profile 3 gets steeper near the casing. On the verge of rotating stall ($\phi = 0.40$), the boundary layer of the tangential velocity becomes very thin and both the upstream and downstream axial velocity boundary layers are getting broader with a deficit on the downstream side. This deficit indicates a recirculation along the casing. This reverse flow then turns to the central region of the rotor, before the leading edge of the blade row is reached.

Development of the Boundary Layers on the Casing (Endwall). The opposite trend of the boundary layers between v_x and v_φ mentioned in the previous section can also be derived in another way using the experimental result given by Smith (1970). He defined a tangential force on a blade row per unit span:

$$F_u = 2\pi r_2 \rho c_{x2}(r_2 c_{u2} - r_1 c_{u1})/\bar{r}.$$

Then the thickness of the tangential force loss in the endwall boundary layer δ_F is

$$v_\varphi = (1/r\bar{F}_u)\int_{r-\delta_F}^{r} (\bar{F}_u - F_u) r\, dr$$

where $\bar{F}_u$ is the tangential force in the free-stream flow, i.e., outside the boundary layer δ_F.

v_φ is related to the tangential-force loss in the endwall boundary layer in a manner similar to how the displacement thickness δ_x^* is related to the flow loss. The ratio v_φ/δ_x^* measured by this author at various nondimensional pressure rises ψ/ψ_{max} for a series of blade rows is given in Fig. 12. A very clear trend can be detected in this diagram, as shown by curve 1. The original approach of the author by a horizontal line seems to be too rough. Curve 1 starts with a value of unity

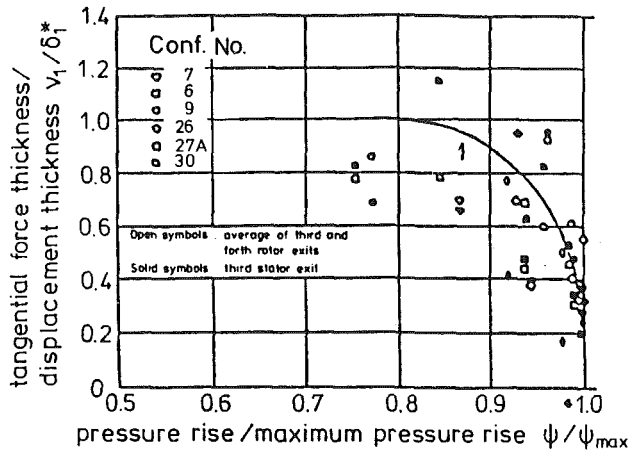

Fig. 12 Tangential force thickness/displacement thickness ratios of casing boundary layers as function of pressure rise/maximum pressure rise ratio for different tip clearances, according to Smith (1970)

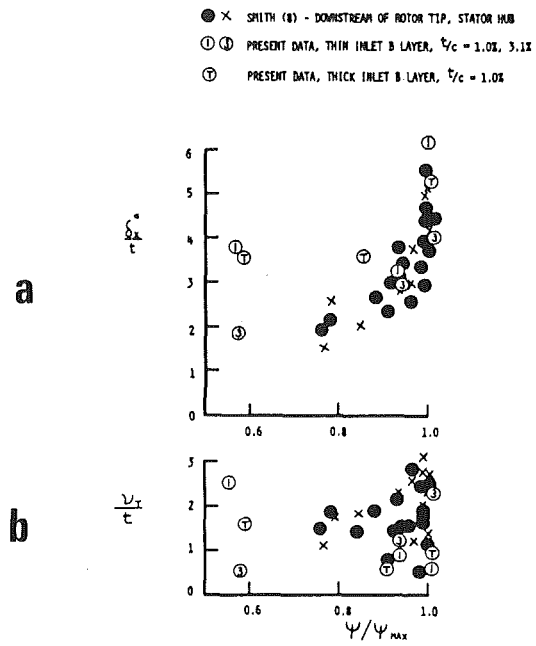

Fig. 13 Downstream displacement and tangential force deficit thickness , normalized by rotor tip clearance, versus pressure rise ratio, acording to Hunter and Cumpsty (1982)

at about $\psi/\psi_{max}=0.8$ and ends very steeply with a zero value at $\psi/\psi_{max}=1$, i.e., on the verge of rotating stall.

A similar diagram was found by Hunter and Cumpsty (1982).

The boundary layer on the hub surface does not show any clear trend like that found for the endwall. The flow along the hub surface has thus a quite different property from that along the endwall.

The correlation curve 1 in Fig. 12 reveals that the boundary layer thickness δ_x^* of the axial velocity and the boundary layer ν_φ of the tangential force loss have opposite trends, when the pressure rise ψ is increasing to its maximum value ψ_{max}. This opposite trend is especially pronounced when ψ is approaching ψ_{max} within the last margin of 1 percent. As the tangential force is proportional to $c_x c_u$, this opposite trend can also be applied to the boundary layers of the axial velocity and the tangential velocity, as already derived using Fig. 10.

In the range of normal operating condition, the flow is forced by the rotor straight from inlet to outlet. The field of the tangential velocities dictates the behavior of the axial velocities. Therefore, the endwall boundary layers of both the tangential and axial velocities show a similar pattern.

When the verge of rotating stall is approached, the profiles of these two boundary layers have developed to completely different patterns. There exists no longer a straightforward flow through the rotor. Secondary flows appear to arise in both the axial and tangential directions. The axial flow does not share the same origin of the tangential flow any longer.

Rotor Tip Clearance and Casing Boundary Layer. According to Fig. 13(a) about the relationship between the axial velocity boundary layer displacement thickness δ_x^*, normalized by rotor tip clearance t, and the pressure rise ratio ψ/ψ_{max} (Hunter and Cumpsty, 1982), a very good correlation exists between these two quantities. This reveals that the axial boundary layer displacement thickness δ_x^* of the endwall increases linearly with the increase of the rotor tip clearance t for a given pressure-rise point ψ/ψ_{max}. The tip clearance determines thus the degree of the growth of the axial boundary layer, when the pressure rise is increased.

If the curve drawn through the points in Fig. 13(a) is extrapolated to the low-pressure region, we have $\delta_x^*/t \approx 1.5$ for the design point. The rotor tip is here practically just touching the outer edge of the axial boundary layer displacement thickness. The rotor is thus rotating nearly entirely within the inviscid free-stream field on the endwall side. Referring to the curve mentioned, δ_x^*/t grows nearly linearly up to a value of 2.2, when the pressure rise ψ/ψ_{max} is raised from the design point to 0.8. Beyond this limit, the boundary layer displacement thickness δ_x^*/t grows steeply first to 3 at $\psi/\psi_{max}=0.92$ and finally to 6 at $\psi/\psi_{max}=1.0$. The rotor tip then penetrates very deeply into the c_x boundary layer. Contrary to this steep increase in the c_x boundary layer in the range of $\psi/\psi_{max}=0.97$ to 1.0, the c_φ boundary layer decreases sharply (Fig. 13b). We have thus a very strongly opposite trend between the c_x and c_φ boundary layers in this narrow range of ψ/ψ_{max}.

Figure 14(a) (Hunter and Cumpsty, 1982) shows the rotor tangential force profiles for four tip clearances of $t/c=1.0$, 3.1, 5.1, and 9.2 percent with characteristics given in Fig. 14(c). At the design point ($\phi=0.70$), the tangential force decreases to very small values in the annular space of the tip clearance for all of the four cases. This reveals that the annular space within the clearance is practically not driven by the rotor into any noticeable rotating movement. The tangential velocity c_φ is very small. At the same time the axial velocity in this annular space is also very small; see Fig. 14(b). At the design point, the boundary layer is thus nearly formed within the tip of the rotor. The fluid in the annular space of the tip clearance is practically not driven by the rotor. The leakage flow through the rotor tip clearance from pressure to suction side of the blade compensates nearly all the driving activity of the blade in this clearance. This inference is supported by the experiment of Inoue et al. (1986). The fluid within the clearance acts as an isolating sheet for the rotor against the casing. The operation in this flow condition shows the best efficiency.

When the flow rate is lowered to $\phi=0.55$, the boundary layer of the axial velocity c_x thickens considerably (see Fig. 14b). However, c_x remains much less changed within the annular space of the clearance, despite that the tangential velocity c_φ, expressed by the tangential force in Fig. 14(a), increases considerably within this space. This evaluation reveals that the rotating motion of the rotor extends to the fluid of the annular space of the clearance at this moderately low flow rate. The leakage flow through the rotor tip clearance then degenerates. We can thus argue, that, when the flow rate is lowered to approach the stall limit, the effect of c_φ in the region next to the endwall will outweigh that of c_x.

This derivation can explain the phenomenon that at the maximum pressure rise point the extension of the rotating mo-

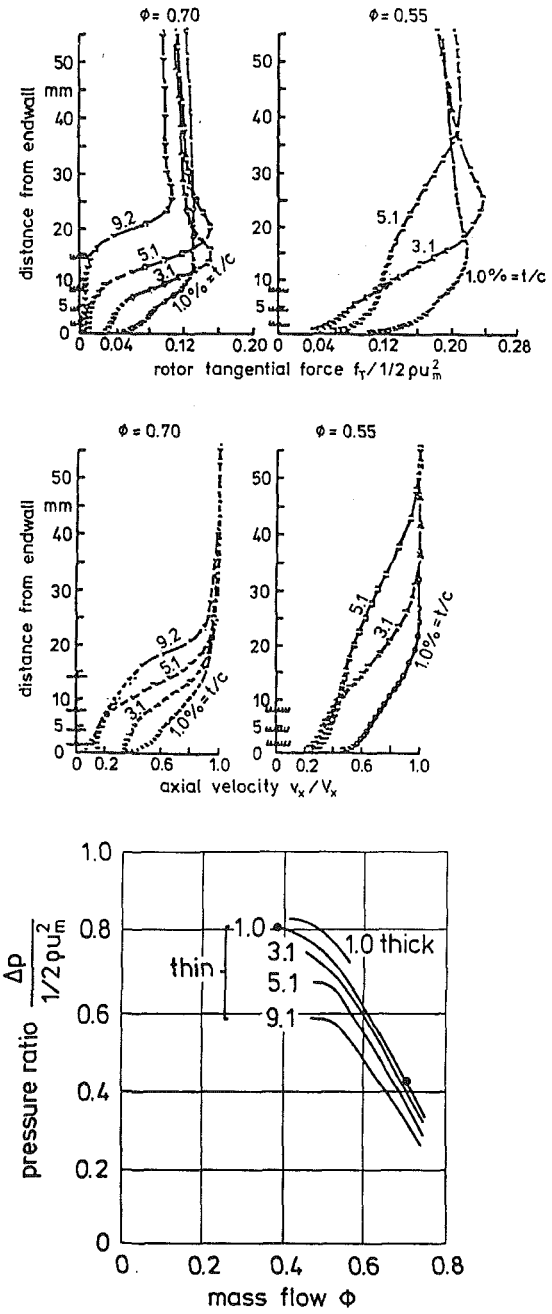

Fig. 14 Variation of tangential velocity (*a*) (in expression of the tangential force f_T) and axial velocity (*b*) downstream of rotor with tip clearance of $t/c = 1.0$, 3.1, 5.1, and 9.2 percent at two flow rates of $\phi = 0.70$ (design point) and 0.55 (*c*), according to Hunter and Cumpsty (1982)

tion into the annular space of the clearance is such as to cause the extremely thin c_φ boundary layer. Then, the radial equilibrium is badly injured and recirculating flows arise.

As soon as the rotor tip penetrates deeper into the c_x boundary layer, the fluid in this layer gets into the compulsion of the rotor rotation as a vortex booster. The fluid will be forced by the rotor into a fast tangential movement. The incidence angle of the inlet flow becomes large, so that the flow on the suction surface begins to be separated in the tip region. The rotor blade can no longer exert its axial force on the fluid as effectively as before, so that F_x decreases and then the c_x boundary layer thickens. The flow becomes free from the suction surface, causing further thinning of the tangential boundary layer.

As the process described above develops very fast in the narrow range from $\psi/\psi_{max} = 0.97$ to 1.0, there must be a feedback effect arising in this range in the following way. The stronger the reverse flow of the meridional recirculation, the more the c_x boundary layer will be lifted. This thickening of the c_x boundary layer causes a still thinner c_φ boundary layer, which leads to a still stronger reverse flow. This feedback effect then causes very steep change in δ_x^*/t, ν_T/t, and ν_T/δ_x^* in the narrow range mentioned. The rapid increase in the c_x boundary layer and the sharp decrease in the c_φ boundary layer then initiate the inception of rotating stall.

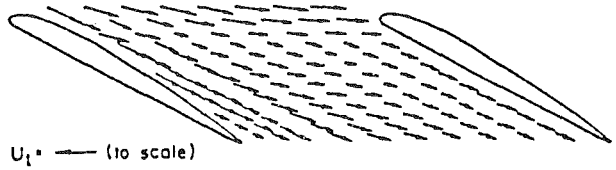

Fig. 15 Relative flow velocities measured in the blade passage 6 mm above the solid wall; $\phi = 0.42$; results according to Smith and Cumpsty (1984)

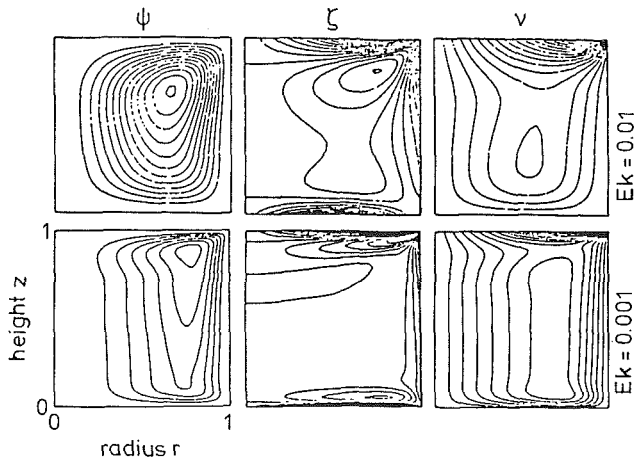

Fig. 16 Relative patterns (lines of constant stream function ψ, vorticity ζ, and tangential velocity v) in a rotating tank with a slowly rotating lid; with rotating axis at $r = 0$, side wall at $r = 1$, bottom at $z = 0$, and lid at $z = 1$. Ro = 1, Ek = 0.01 (upper) and 0.001 (below), according to Lugt and Haussling (1973).

Effect of the Free-Swirl Flow in the Leading Edge Zone of Rotor.

On the verge of the appearance of rotating stall, a strong nose bubble is formed at the leading edge on the suction surface of the rotor blade in the tip region, according to Popovski and Lakshiminarayana (1986). The measurement of Flueckiger and Melling (1981) shows that the nose bubble extends still further into the inner region of the rotor. A free swirl flow field is thus induced in the leading edge region, rotating oppositely relative to the main body of the downstream flow, which is still guided by the blades under the compulsion. These flow characteristics coincide with the results of Smith and Cumpsty (1984) given in Fig. 15.

The flow pattern shown in Fig. 15 can be compared with a rigidly rotating fluid contained in a rotating tank whose lid has slowed down to a smaller rotating speed than that of the tank. The Ekman layer formed on the lid surface can be compared with the free swirl flow field mentioned. The very thick axial velocity boundary layer and the very thin tangential velocity one formed on the endwall behind the outlet edge of the rotor blade row correspond to the two components of the Stewartson layer formed on the tank-wall surface, as shown in Fig. 16 according to the investigation of Lugt and Haussling (1973). A recirculation flow is generated in the fluid (see streamlines ψ),

being composed of a reverse flow along the Stewartson layer, bending over the Ekman layer, turning back to the downward direction and then traveling along the bottom to the starting point again. This is a toroidal ring vortex. The Ekman number, defined as

$$\mathrm{Ek} = \nu/\Omega L^2$$

where L is a characteristic length, e.g., the outer radius, determines the viscous effect in balance with the pressure and acceleration fields. The Ekman number is typically 0.2×10^{-6} for compressors and 10^{-8} for pumps. Figure 16 indicates that, with the decrease of Ek from 0.01 to 0.001, the tangential velocity profile in the Stewartson layer becomes very much steeper and the axial velocity profile becomes much broader. If we still further extrapolate to the range of $\mathrm{Ek}=10^{-6}$-10^{-8}, then the Stewartson layer has a very thin tangential velocity boundary layer and a much broader axial velocity one. This property corresponds well to the situation encountered in turbomachinery concerning the reverse flow.

The flow over the bottom of the rotating tank corresponds to the secondary flow at the outlet of the rotor blade row. The vorticity ξ is generated in the upper Ekman layer, the bottom Ekman layer, and the sidewall Stewartson layer (see Fig. 16). The interior is quite inviscid. A steady-state, geostrophic rotating flow, with a Taylor–Proudman structure, prevails there. This flow pattern is still axisymmetric. Owing to the strong vorticity, the reverse flow along the side wall has therefore a vortex-filament nature.

Experimental axial compressor data during operation on the verge of rotating stall are given by Schlamann et al. (1985). Flow characteristics of the first instability phase before reaching the maximum pressure rise were explained as blade leading edge tip separation, which can be related to the occurrence of strong nose bubbles on the leading edge of the rotor blades. A rather random pressure fluctuation appears in this range previous to the occurrence of the regular rotating stall cycles. Since the interior flow is still in a steady-state stage in this range, the corresponding branch of the characteristic does not deviate much from the ascending trend of its normal operating part. The asymmetric flow pattern accompanying rotating stall has not yet been induced by the reverse flow in this stage. This leading edge tip separation was also found by Haupt (1984) on a centrifugal compressor.

The formation of nose bubble on the leading edge of the rotor blades is thus a precondition for introducing the reverse flow and with it the rotating stall. If the entrance flow to the leading edge is strongly disturbed, e.g., either by the wakes of foregoing stationary blades (Koch, 1970), or by turbulence produced artificially by a full-annulus screen at the inlet (Koff and Greitzer, 1984), the reverse flow can be retarded.

Vorticity of the Reverse Flow. According to the conservation law of vorticity, a secondary flow will be formed in the blade channel of the rotating rotor because of the irrotational nature of the absolute flow (in the absolute frame of reference) entering the rotor. The vorticity vector of this secondary flow must be -2Ω in the axial direction, thus counterclockwise against the clockwise (designated as positive) rotor rotation with angular velocity of Ω. Since the vortex of the leakage jet also has the counterclockwise rotational sense, the secondary flow is therefore augmented by it.

Referring to the experiment carried out by Dring et al. (1982), the secondary flow at $\phi=0.65$ is deficient in the negative vorticity by $0.2\,\Omega$, and the secondary flow at ϕ 0.85 is in surplus by $0.2\,\Omega$ with respect to this neutral condition of -2Ω. This may be interpreted by saying that the reverse flow appears in the form of a sink with a vortex filament nature of a rotational sense equal to the rotational sense of the rotor. This vortex filament will then generate a vorticity of $0.2\,\Omega$ in the blade channel. This vorticity of $0.2\,\Omega$ is thus in a position to explain the deficit in negative vorticity at $\phi=0.65$ mentioned.

The fact that the reverse flow should swirl in the same rotational sense as the rotor corresponds very well to its origin from the region of the high absolute tangential velocity outside the outlet edge of the rotor, i.e., corresponding to the special property of the Stewartson layer there as shown in a previous section.

In this manner, the intensity of the vortex filament of the reverse flow can be evaluated from the experimental result given by Dring et al.

Nature of the Spiral Vortex Filaments. The nature of the sprial vortex filaments in the three-dimensional boundary layer along the casing/shroud, with very steep profile of the tangential velocity and much flatter profile of the reverse flow velocity, can be studied by means of a series of fundamental experiments carried out on simple models.

Our three-dimensional boundary layer can be first compared with the annular flow in the experiment carried out by Ludwieg (1964). The annular flow is contained between two concentric cylinders of which the inner one is rotating and the outer one is at rest. Then we have an unstable stratification within the flow caused by centrifugal force. The fluid particles near the inner wall experience a higher centrifugal force and show a tendency to being propelled outwards. Taylor vortices will be generated by this instability in the annular flow, if the following condition for the Taylor number is fulfilled:

$$\mathrm{Ta} = (U_i d/\nu)\times(d/R_i)^{1/2} \geq 41.3 \quad \text{(viscous instability)},$$

where d denotes the width of the gap, R_i the inner radius, and U_i the tangential velocity of the inner cylinder.

These vortices rotate in alternately opposite directions, with their axes along the circumference. They thus form pairs similar to the convection cells. If, in addition, an axial movement is imposed on the inner cylinder, the annular flow will obtain an axial velocity in addition to the tangential one. The Taylor vortices take the shape of spirals. The spirals do not have the same intensity. Each second one is much stronger than the one in between. This indicates that one member of the Taylor vortex pair is enhanced by the axial flow at the expense of the other member. This phenomenon will be further shown below in the experiment on a rotating cone.

The formation of the orderly spiral vortices, however, is limited to the range of low axial velocity, as shown by Kaye and Elgar (1958). In their experiment, again with the inner cylinder rotating and the outer cylinder being at rest, a uniform axial flow is forced through the annular space. Only in a zone of moderate axial flow velocity, spiral-shaped Taylor's vortices can be maintained. If the axial velocity is too large, the annular flow becomes turbulent. The condition of small axial velocity is fulfilled in the reverse flow along the casing/shroud in compressors.

The spiral vortex is thus the transition form for the annular flow from a laminar to a turbulent state.

The property of the spiral vortex in a three-dimensional boundary layer has been investigated by a great number of authors in some more detail on rotating circular disks. When a disk rotates, a boundary layer in the tangential direction is formed on the surface. Due to centrifugal effect, a radial flow is generated along the surface from the center to the outer edge. An additional boundary layer with a radial velocity profile will thus form at the same time. We then have a three-dimensional boundary layer. This boundary layer has a property of the Ekman layer, so that its displacement thickness δ^* depends only on the kinematic viscosity ν and the angular velocity ω:

$$\delta^* = 1.271(\nu/\omega)^{1/2}$$

(see Kobayashi et al., 1980).

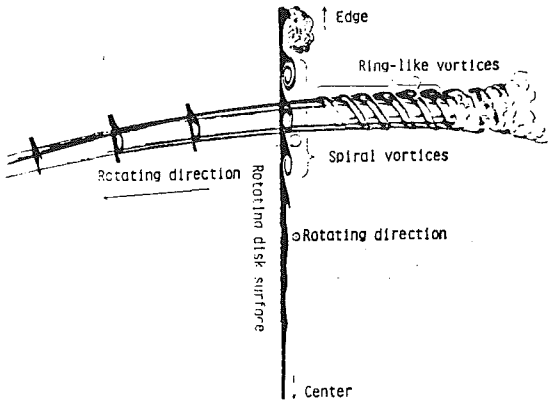

Fig. 17 Schematic structure of the transition regime according to Kohama (1984a)

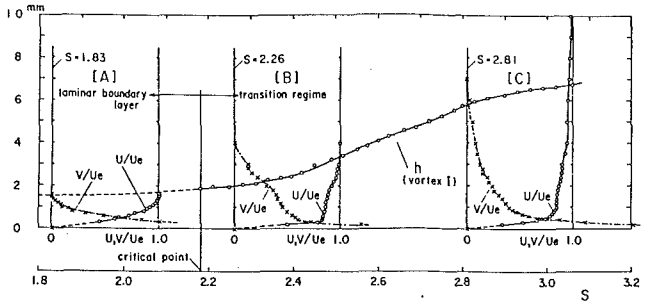

Fig. 18 Comparison of a spiral vortex height h with velocity profiles, according to Kohama (1984b)

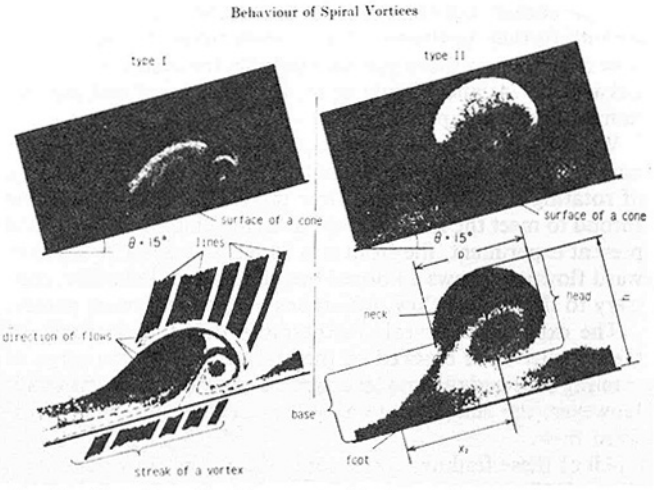

Fig. 19 Formation of vortices, according to results of Kohama (1984b)

Kohama (1984a) showed that the spiral vortices appear in the transition zone between the inner laminar zone and the outer turbulent zone of the rotating disk.

The spiral vortices in the transition zone propagate outward in the opposite rotational sense with respect to the rotation of the disk. When they become turbulent, groupings are formed by them. However, the turbulent packages around the groupings line up into a spiral pattern, which shows the rotational sense of the disk again.

For the case of the centrifugal compressor investigated in the present paper at the operating point near the rotating stall onset, the reverse flow along the shroud surface shows the transition stage from laminar to spiral vortices. At the operating point between rotating stall and surge, however, the reverse flow is separated into strong spiral vortices already not very far from the entrance to the shroud surface.

As further shown in the experiment quoted, the pattern of the spiral vortices stays stationary on the surface of the disk, i.e., with a phase velocity of zero in both tangential and radial directions. In other words, the pattern is fixed to the disk surface. This is a quite prominent property of the spiral vortices. It was already shown previously that the vortex filaments in the reverse flow of the compressor are also fixed to the impeller. The similarity between these two cases is thus obvious. The property of the spiral vortex determined in the experiments on rotating disks is thus similar to that of the vortex filament detected in the reverse flow of compressors.

The structure of the spiral vortex is given in Fig. 17 according to Kohama (1984a), sketched from a measurement on a rotating disk. The spiral vortex shows a property of the vortex tube, which then separates into spirally spaced ringlike vortices, before transition to turbulence. There are 34 spiral vortices on the disk, each of which causes a strong fluctuating velocity field. In the reverse flow for the case of the compressor it will then cause an additional drag force on the impeller.

The three-dimensional property of the spiral vortex was further investigated by Kohama (1984b) on a rotating cone, which was placed in an axial flow directed to its apex. The dimensionless number $S=\omega R/Ue$ is used to characterize the transition behavior of the boundary layer, where R is the local radius and U_e the meridional velocity along the surface of the cone. This number increases from the apex to the base of the cone.

The velocity profiles of the boundary layer for the tangential direction $y(V/U_e)$ and the meridional direction $x(U/U_e)$ are shown in Fig. 18 for three stations corresponding to $S=1.83$ (A), 2.26 (B), and 2.81 (C) according to Kohama. The height h of the spiral vortex is also plotted in this figure.

Below the critical point of $S=2.18$, the boundary layer remains laminar and stable. A very steep tangential velocity boundary layer, compared to the meridional one, prevails there. However, the horseshoe vortices, similar to the Taylor vortices, already start their formation within the boundary layer (see Fig. 19*a*).

Above the critical point, the vortices gain in strength and gradually lift up from the surface. A cross section of those vortices is given in Fig. 19(*b*). The horseshoe vortex is degenerated into an asymmetric one with a pronounced rotational sense on one side. This process is accompanied by the appearance of the inflection points in both the tangential and meridional velocity profiles, which indicates that the instability of the boundary layer causes the growth of the asymmetric vortex. We then have a spiral vortex filament with a pronounced rotational sense similar to the one sketched in Fig. 17.

At $S>2.81$, the two components of the boundary layer become turbulent.

We can summarize that on the surface of the rotating cone, symmetric horseshoe vortices first appear in the laminar boundary layer. In the transition range from laminar to turbulent, they then degenerate to asymmetric ones. We have therefore spiral vortices with a definite rotational sense similar to those on the rotating circular disk The lower limit of $S=2.18$ for the formation of these spiral vortices indicates that the tangential velocity profile of the boundary layer has to be more than twice as steep as the meridional velocity profile in order to promote the formation of the spiral vortices.

The experiment on the rotating cone thus supplies a further theoretical background for the findng in the turbocompressors that the steep profile of the tangential velocity in the boundary layer along the casing/shroud is the cause for the separation of the reverse flow into vortex filaments.

The transition of the spiral vortex filaments to turbulence does not take place in turbocompressors. Rather, the vorticity of the spiral vortex filaments of the reverse flow is transferred

into the swirling flow of the ring vortex formed at the inlet edge of the impeller, known as the prerotation in the operating ranges during rotating stall, and between the rotating stall and the surge.

Conclusions

The present experiment on a centrifugal compressor with radial blading reveals that the reverse flow along the shroud always accompanies the forward flow, even at the design point. The intensity of the reverse flow increases with the lowering of the flow rate. The reverse flow has a nature of vortex filaments.

At the design point, the reverse flow is restricted to the zone of the high pressure-rise. Some branch of it can penetrate the innerst corner between the blade-suction-surface and the shroud further upstream. This vortex-tube-natured reverse flow appears as a sharp pressure pulse in the measurements of Eckardt (1974) and Mizuki et al. (1976), carried out also on radial-blading compressors.

When the flow rate is lowered, the reverse flow extends to a much larger region of the blade-suction-surface. On the verge of rotating stall, the reverse flow travels backward along the shroud to meet the forward flow at a ring-shaped front. In the present experiment, the front was found at $x/s = 0.7$. The forward flow still shows a normal boundary-layer behavior, contrary to the reverse flow, which has a vortex-filament nature.

The experiment reveals furthermore that the clearance of the impeller tip is blocked by the reverse flow on the verge of rotating stall and then no leakage flow over the tip exists at all. However, the leakage flow is still present in part of the forward flow.

All of these findings correspond well to the flow pattern on the casing of a four-stage axial compressor shown by Koch (1970).

A theory is establised that this reverse flow belongs to a recirculation that arises in a rigidly rotating fluid with its inlet region suddenly slowed down. This case is similar to a fluid of a rotating tank with slowly rotating lid.

The nose bubbles that form on the leading edges of the rotor blades on the verge of rotating stall induce a flow field, which rotates slower than the main body of the fluid downstream. This slowly rotating flow field can be compared with the slowly rotating lid mentioned. The reverse flow is then situated within the Stewartson layer, whose axial and tangential velocity distributions show quite different profiles. The present theory can thus explain the corresponding findings of Smith (1970), Hunter and Cumpsty (1982), and Cumpsty (1986).

The result of the present experiment that the rotor tip clearance is blocked by the reverse flow also finds support in the experimental evidence given by the same authors cited previously.

The investigations on the centrifugal compressors reported in this paper were all made with impellers having radial blading. The reverse flow arising along the inner corner of blade suction surface/shroud at the design point may be influenced by this special blading form. It could be expected that impellers with backward blading may have weaker reverse flow at the design point.

Ackowledgments

The authors wish to thank Mr. P. Moser, Mr. F. Majer, and Dr. M. Casey for supporting this investigation and making critical discussions. Dr. M. Casey has been kind enough to supply a series of valuable documents contributing greatly to the completeness of the theoretical considerations.

In addition, the authors wish to thank gratefully the German Research Association (DFG) for funding the described research work. The contribution of Mr. Tanneberg in his assistance in the experiments and of Mrs. Schleifer in her assistance in finishing the paper is also gratefully acknowledged.

References

Casey, M. V., 1987, "A Mean-Line Prediction Method for Estimating the Performance Characteristics of an Axial Compressor Stage," presented at the IMechE International Conference on Turbomachinery, Cambridge, Sept.

Chen, Y. N., Haupt, U., and Rautenberg, M., 1987, "On the Nature of Rotating Stall in Centrifugal Compressors with Vaned Diffuser, Part II. Karman Vortices as the Controlling Mechanism," 1987 Tokyo International Gas Turbine Congress, Paper No. 87-TOKYO-IGTC-23, Proceedings, Vol. II, pp. 169–182.

Chen, Y. N., Haupt, U., and Rautenberg, M., 1988, "The Vortex-Filament Nature of the Reverse Flow on the Verge of Rotating Stall," ASME Paper No. 88-GT-120, 33rd ASME International Gas Turbine and Aeroengine Congress, June 5–9, 1988, Amsterdam.

Cumpsty, N. A., 1986, "Annulus Wall Boundary-Layer Measurements in a Four Stage Compressor," ASME *Journal of Engineering for Gas Turbines and Power*, Vol. 106, pp. 2–6.

Day, I. J., 1976, "Axial Compressor Stall," Ph.D. Dissertation, University of Cambridge, Cambridge, United Kingdom.

Dring, R. P., Joslyn, H. D., and Hardin L. W., 1982, "An Investigation of Axial Compressor Rotor Aerodynamics," ASME *Journal of Engineering for Power*, Vol. 104, pp. 84–98.

Eckardt, D., 1974, "Untersuchung der Laufradströmung in hochbelasteten Radialverdichterstufen, Abschlußbericht Teil I: Versuchsaufbau, Meßtechnik, Strömungsanalyse," Deutsche Forschungs- und Versuchsanstalt für Luft- und Raumfahrt, Porz-Wahn, Forschungs-berichte Verbrennungskraftmaschinen, Vol. 154 (cited by Chen et al., 1988).

Flueckiger, G., and Melling, A., 1981, "Flow Instability at the Inlet of a Centrifugal Compressor," ASME *Journal of Engineering for Power*, Vol. 103, pp. 451–456.

Fraser, W. H., 1982, "Recirculating in Centrifugal Pumps," *World Pumps*, pp. 227–235.

Haupt, U., 1984, "Untersuchung des Schaufelschwingungsverhaltens hochbelasteter Radialverdichterlaufräder," Dissertation, University of Hannover, Hannover, Federal Republic of Germany.

Haupt, U., Chen, Y. N., and Rautenberg, M., 1987, "On the Nature of Rotating Stall in Centrifugal Compressors with Vaned Diffusers, Part 1: Detection of Reverse Flow," 1987 Tokyo International Gas Turbine Congress, Paper No. 87-TOKYO-IGTC-22, Proceedings, Vol. II, pp. 161–168.

Hunter, I. H., and Cumpsty, N. A., 1982, "Casing Wall Boundary-Layer Development Through an Isolated Compressor Rotor," ASME *Journal of Engineering for Power*, Vol. 104, pp. 805–818.

Inoue, M., Kuroumaru, M., and Fukuhara, M., 1986, "Behavior of Tip Leakage Flow Behind an Axial Compressor Rotor," ASME *Journal of Engineering for Gas Turbines and Power*, Vol. 108, pp. 7–14 (cited by Y. Senoo, 1987, and Chen et al., 1988).

Inoue, M., Kuroumaru, M., and Fukuhara, M., 1987, "Development of Casing Wall Boundary Layer Through an Axial Compressor Rotor," 1987 Tokyo International Gas Turbine Congress, Proceedings, Vol. II, pp. 93–100 (cited by Chen et al., 1988).

Kaye, J., and Elgar, E. C., 1958, "Modes of Adiabatic and Diabatic Fluid Flow in an Annulus With Inner Rotating Cylinder," ASME *Transactions*, Vol. 80, pp. 753–765 (see Schlichting, 1979, pp. 525–536, and Chen et al., 1988).

Kobayashi, R., Kohama, Y., and Takamadate, Ch., 1980, "Spiral Vortices in Boundary Layer Regime on a Rotating Disk," *Acta Mechanica*, Vol. 35, pp. 71–82.

Koch, C. C., 1970, Discussion on the paper: "Transonic Compressor Technology Advancements," by W. A. Benser, *Fluid Mechanics, Acoustics and Design of Turbomachinery*, Part II, NASA SP-304, pp. 597–598 (cited by Chen et al., 1988).

Koff, S. G., and Greitzer, E. M., 1984, "Stalled Flow Performance for Axial Compressor-I: Axisymmetric Characteristic," ASME Paper No. 84-GT-93.

Kohama, Y., 1984a, "Study on Boundary Layer Transition of a Rotating Disk," *Acta Mechanica*, Vol. 50, pp. 193–199 (cited by Chen et al., 1988).

Kohama, Y., 1984b, "Behaviour of Spiral Vortices on a Rotating Cone in Axial Flow," *Acta Mechanica*, Vol. 51, pp. 105–117 (cited by Chen et al., 1988).

Ludwieg, H., 1964, "Experimentelle Nachprüfung der Stabilitätstheorien für reibungsfreie Strömungen mit schraubenförmigen Stromlinien," *Zeitschrift Flugwissenschaften*, Vol. 12, pp. 304–309 (cited by Chen et al., 1988).

Lugt, H. J., and Haussling, H. J., 1973, "Development of Flow Circulation in a Rotating Tank," *Acta Mechanica*, Vol. 18, pp. 255–272.

Lugt, H. J., 1983, *Vortex Flow in Nature and Technology*, Wiley, New York, pp. 138–139.

Mizuki, S., Hottori, T., Ariga, I., and Watanabe, I., 1976, "Reverse Flow Phenomena Within Centrifugal Compressor at Lower Flow Rates," ASME Paper No. 76-GT-86 (cited by Chen et al., 1988).

Murthy, K. N. S., and Lakshminarayana, B., 1986, "Laser Doppler Velocimeter Measurement in the Tip Region of a Compressor Rotor," *AIAA Journal*, Vol. 24, pp. 807–814.

Popovski, P., and Lakshiminarayana, B., 1986, "Laser Measurements in a

Compressor Rotor Flowfield of Off-Design Condition," *AIAA Journal*, Vol. 24, pp. 1337–1345.

Schlamann, U., Teipel, I., and Riess, W., 1985, "Experimentelle Untersuchung der Strömungsphänomene des Rotating Stall und des Pumpens bei mehrstufigen, hochbelasteten Axialverdichtern," Fortschritt-Berichte VDI, Reihe 7: Strömungstechnik, No. 91.

Schlichting, H., 1979, *Boundary Layer Theory*, McGraw-Hill, New York.

Senoo, Y., 1987, "Pressure Losses and Flow Field Distortion Induced by Tip Clearance of Centrifugal and Axial Compressors," *JSME International Journal*, Vol. 30, No. 261, pp. 375–385.

Smith, L. H., 1970, "Casing Boundary Layers in Multistage Axial-Flow Compressors," in: *Flow Research on Blading*, L. S. Dzung, ed., Elsevier, New York, pp. 275–299.

Smith, G. D. J., and Cumpsty, N. A., 1984, "Flow Phenomena in Compressor Casing Treatment," ASME *Journal of Engineering for Gas Turbines and Power*, Vol. 106, pp. 532–541 (cited by Chen et al., 1988).

Taylor, G. I., 1923, 1935, 1936, "Stability of a Viscous Liquid Contained Between Two Rotating Cylinders," *Phil. Trans. A*, Vol. 223, pp. 289–293 (1923); *Proc. Roy. Soc. A*, Vol. 151, pp. 494–512 (1935) and Vol. 157, pp. 546–564; 565–578 (1936).

R. E. Kielb

J. K. Ramsey

NASA Lewis Research Center
Cleveland, OH 44135

Flutter of a Fan Blade in Supersonic Axial Flow

An application of a simple aeroelastic model to an advanced supersonic axial flow fan is presented. Lane's cascade theory is used to determine the unsteady aerodynamic loads. Parametric studies are performed to determine the effects of mode coupling, Mach number, damping, pitching axis location, solidity, stagger angle, and mistuning. The results show that supersonic axial flow fan and compressor blades are susceptible to a strong torsional mode flutter having critical reduced velocities that can be less than one.

Introduction

The development of an axial compressor with supersonic axial flow has been the subject of a limited amount of research over the last 30 years (Klapproth, 1961; Savage et al., 1961). During the early 1970s a supersonic axial flow fan was constructed, but encountered a blade failure before reaching the design point (Breugelmans, 1975). As a result of this and other problems, many reached the conclusion that the supersonic axial flow compressor was a very difficult, if not practically impossible, design problem. However, renewed attention to supersonic and hypersonic flight vehicles, and developments in the area of computational fluid mechanics, have rekindled interest in supersonic axial flow fans. For example, a research project to design, build, and conduct experiments on a single-stage supersonic axial flow fan is now underway at the NASA Lewis Research Center (Schmidt et al., 1987; Wood et al., 1988).

In the process of blade design for the NASA Lewis experiment, the question of aeroelastic stability naturally arose. Although our previous background with fan blade flutter considered supersonic relative flow, we did not have experience or a predictive tool for the case of supersonic axial flow. Fortunately, this aeroelastic cascade problem is simpler than that with subsonic axial flow. For unloaded, inviscid, flat plate cascades, this problem has been solved by a number of researchers.

Miles (1956) addressed the problem of an oscillating airfoil subjected to supersonic flow in a wind tunnel. Later Drake (1957) considered the same problem but with porous wind tunnel walls. Lane (1957) extended the Miles model to include cascade effects. Some additional papers that address the problem of a cascade in supersonic axial flow are by Gorelov (1960), Platzer and Chalkley (1972), Chalkley (1972), Nishiyama and Kikuchi (1973), and Nagashima and Whitehead (1977).

The most comprehensive numerical studies were presented by Platzer and Chalkley (1972) and Chalkley (1972). Two methods were employed, an elementary analytical method for low frequency and the method of characteristics for arbitrary frequency. Most of their calculations were for an unstaggered cascade and showed that cascade effects were very strong. That is, the flutter speed of the cascade was more than a factor of two lower than that of an isolated airfoil. As the solidity increased, the flutter speed decreased. Flutter was found at reduced velocities as low as 2.0. Studies of elastic axis position demonstrated that a pitching axis location of approximately 40 percent chord had the lowest flutter speed. Flutter for pure plunging motion was not reported by any researchers. The effects of structural damping were found to be strongly dependent on mass ratio. For low mass ratios (approximately 10) the flutter speed was relatively independent of damping (strong instability). For high mass ratios (approximately 500) the flutter speed was highly dependent on damping (weak instability). For the high mass ratio case the inclusion of 1 percent damping could double the flutter speed. Finally, the authors reported that the critical interblade phase angle was always near 180 deg.

Nishiyama and Kikuchi (1973) showed that the critical interblade phase angle was 180 deg for an unstaggered cascade and increased to approximately 210 deg for a cascade with 60 deg of stagger. They reported flutter at reduced velocities as low as 1.5. Nagashima and Whitehead (1977) presented limited results for an unstaggered cascade. For an interblade phase angle of 180 deg, the cascade was shown to be unstable for reduced velocities greater than 2.2

The results discussed above were not sufficient to predict the stability of the NASA blade. The primary reason is that the results presented were for considerably different design conditions. That is, the NASA blade has higher solidity, lower stagger angle, and higher Mach number. Therefore, a computer code, based on the theory presented by Lane (1957), was developed and applied to the NASA blade. For a detailed description of this computer code see Ramsey and Kielb (1987).

The computer code was used to predict the aeroelastic stability of the blade designed for the NASA experiment. To understand the aeroelastic phenomenon of blades operating in supersonic axial flow better, parametric studies were also conducted to investigate the effects of mode coupling, Mach number, structural damping, pitching axis location, stagger angle, solidity, and mistuning. The objectives of this paper are

Contributed by the International Gas Turbine Institute and presented at the 33rd International Gas Turbine and Aeroengine Congress and Exhibition, Amsterdam, The Netherlands, June 5-9, 1988. Manuscript received by the International Gas Turbine Institute October 1, 1987. Paper No. 88-GT-78.

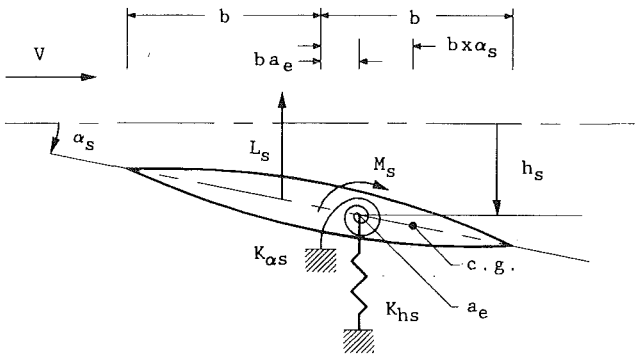

Fig. 1 Typical section model

to describe a flutter analysis of a fan operating in supersonic axial flow and to present the results of the parametric studies.

Theory

Since no new theories are developed, only brief summaries of the structural model, unsteady aerodynamic model, and equations of motion are given herein. See the references for additional details.

Structural Model. The classical "typical section model" is used to model the structure. As shown in Fig. 1, each airfoil is assumed to be a two-degree-of-freedom oscillator suspended by bending and torsional springs. The airfoil is assumed to be rigid in the chordwise direction. The coupling between plunging and pitching motions is modeled through the offset distance between the center of gravity and the "elastic axis." For the analysis of the NASA blade the 73.3 percent span location was chosen as being representative.

Unsteady Aerodynamic Models. The method of Lane (1957) is used to calculate the unsteady aerodynamic loads. This is an extension of a Laplace transform method first proposed by Miles (1956) for a single airfoil with wind tunnel wall interference. Lane's formulation considers a cascade with arbitrary stagger and interblade phase angle. The effects of airfoil thickness, camber, and steady-state angle of attack are neglected. Although the subject of this paper is supersonic axial flow, some comparative results are given for subsonic axial flow. The theory of Rao and Jones (1976) is used for subsonic relative flow and the theory of Adamczyk and Goldstein (1978) is used for supersonic relative (subsonic axial) flow.

As mentioned above, the unsteady aerodynamic theory used herein ignores complicating effects such as actual airfoil geometry and loading effects. However, research is currently in progress to develop improved unsteady aerodynamic models.

Equations of Motion. A simple application of Lagrange's method to the model shown in Fig. 1 leads to the following coupled equations:

$$\begin{bmatrix} m_s & S_{\alpha s} \\ S_{\alpha s} & I_{\alpha s} \end{bmatrix} \begin{Bmatrix} d^2/dt^2(h_s e^{i\omega t}) \\ d^2/dt^2(\alpha_s e^{i\omega t}) \end{Bmatrix} + \begin{bmatrix} (1+2i\zeta_{hs})m_s\omega_{hs}^2 & 0 \\ 0 & (1+2i\zeta_{\alpha s})I_{\alpha s}\omega_{\alpha s}^2 \end{bmatrix} \begin{Bmatrix} h_s e^{i\omega t} \\ \alpha_s e^{i\omega t} \end{Bmatrix} = \begin{Bmatrix} -L_s \\ M_s \end{Bmatrix} \tag{1}$$

As can be seen, structural damping is added to the equations by using the complex stiffness approach. The linearized aerodynamic forces are expressed in terms of the nondimensional coefficients as

$$L_s = -\pi\rho b^3\omega^2 \sum_{r=0}^{N-1} [l_{hh}h_{ar} + l_{h\alpha}\alpha_{ar}]\, e^{i(\omega t+\beta_r s)}$$

$$M_s = \pi\rho b^4\omega^2 \sum_{r=0}^{N-1} [l_{\alpha h}h_{ar} + l_{\alpha\alpha}\alpha_{ar}]\, e^{i(\omega t+\beta_r s)} \tag{2}$$

The coefficients l_{hh}, $l_{h\alpha}$, $l_{\alpha h}$, and $l_{\alpha\alpha}$ are calculated by the unsteady aerodynamic theory for given values of M_r, k, c/g, ξ, β_r, and a_e. Equation (2) shows that the total aerodynamic load is the summation of the loads associated with all possible interblade phase angles. This allows structurally mistuned cascades (for example, each blade having different frequencies) to be considered. To determine stability, an equation (1) is written for each blade and the resulting complex eigenvalue problem is solved. The real part of the eigenvalues represents the damping and the imaginary part represents the frequency. For additional details see Kaza and Kielb (1982) and Kielb and Kaza (1983).

Nomenclature

a = acoustic velocity
a_e = elastic axis position
b = semichord
c = chord
g = circumferential gap between adjacent blade
h_s = plunging amplitude
h_{ar} = plunging amplitude in rth mode of tuned cascade
$I_{\alpha s}$ = polar mass moment of inertia about elastic axis
k = reduced frequency $= \omega b/V$
k_f = flutter reduced frequency
K_{hs} = bending stiffness
$K_{\alpha s}$ = torsion stiffness
l_{hh}, $l_{h\alpha}$ = nondimensional lift due to plunging and pitching motions, respectively
$l_{\alpha h}$, $l_{\alpha\alpha}$ = nondimensional moment due to plunging and pitching motions, respectively
L_s = aerodynamic lift
m_s = mass per unit span of blade
M_a = axial Mach number
M_r = Mach number relative to blade
M_s = aerodynamic moment
N = number of blades
r = integer specifying mode of tuned rotor
$r_{\alpha s}$ = nondimensional radius of gyration
s = blade index
$S_{\alpha s}$ = mass moment about elastic axis
t = time
V = free-stream air velocity relative to blade
V_r = reduced velocity $= V/\omega b$
$x_{\alpha s}$ = dimensionless static imbalance
α_s = pitching amplitude
α_{ar} = pitching amplitude in rth mode of tuned cascade
β_r = interblade phase angle
ζ_{hs} = critical damping ratio for bending mode
$\zeta_{\alpha s}$ = critical damping ratio for torsion mode
μ = mass ratio $= m/\pi\rho b^2$
ξ = stagger angle
ρ = air density
ω = circular frequency
ω_{hs} = bending frequency
$\omega_{\alpha s}$ = torsion frequency

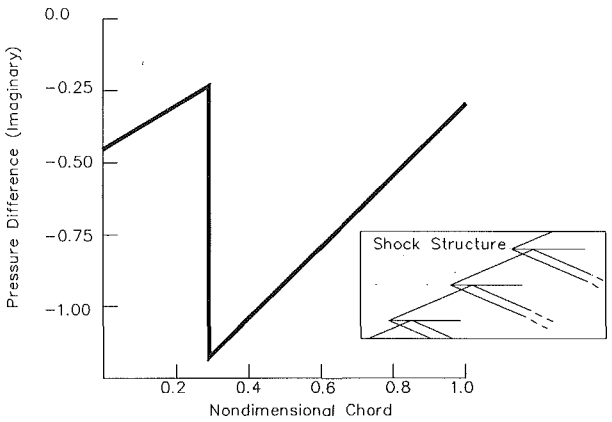

Fig. 2 Pressure distribution along chord (pitching midchord), $c/g = 1$, $\xi = 60$, M = 2.5, $\beta_r = 180$, $k = 0.5$

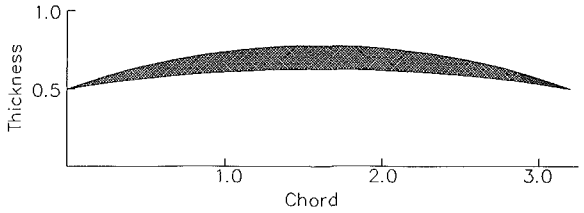

Fig. 3 Airfoil cross section (73.3 percent span)

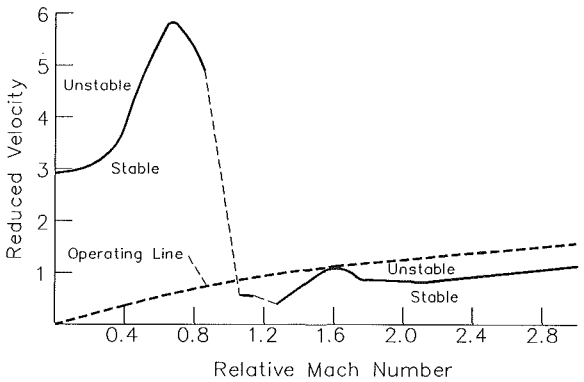

Fig. 4 Critical reduced velocity versus Mach number, undamped, $\xi = 28$, $c/g = 3.215$

Results and Discussion

As mentioned previously, a computer code, based on Lane's equations (1957), was written to calculate the unsteady aerodynamic loads for a cascade in supersonic axial flow. The resulting subroutines were then installed in an existing aeroelastic code with solves the stability problem. This code was used to analyze the blade designed for the NASA experiment. As will be shown, this original blade design is unstable at the design point. Although the blade was subsequently redesigned, the present results will emphasize the original, unstable blade design. This section presents the results of this analysis and additional parametric studies. First, a comparison with previously reported results is given.

Comparison With Previous Results. Before checking the cascade capabilities of the code, a comparison was made with the isolated airfoil results of Runyan et al. (1952) and Jordan (1953). The results of Runyan show a torsional instability in the Mach number range 1.0–1.6. The worst pitching axis location is predicted to be approximately 30 percent chord. Good agreement was found with the results of both Runyan and Jordan.

Table 1 Aeroelastic properties, 73.3 percent span, original design

Number of blades, N	58
Mass ratio, μ	456.2
Radius of gyration (midchord), $r_{\alpha s}$	0.431
Stagger angle, deg, ξ	28
Solidity, c/g	3.215
At design point:	
Axial Mach number, M_a	2.300
Relative Mach number, M_r	2.606
Reduced frequency (bending mode)	0.376
Reduced frequency (torsion mode)	0.663

The cascade capabilities for torsional motion were checked by comparing results with Nagashima and Whitehead (1977). An example is shown in Fig. 2. Here the imaginary part of the pressure difference distribution is plotted versus chord. The agreement between methods is within plotting accuracy. Note that this case has one pressure jump, which is due to the Mach wave from an adjacent blade intersecting at approximately 30 percent chord. Most of the following results are for conditions that result in multiple reflections of the leading edge Mach wave and hence, multiple pressure jumps. Additional detailed comparisons with previous results are given by Ramsey and Kielb (1987).

Blade Design Parameters. Table 1 lists the cascade parameters (73.3 percent span, original design) that are required for the aeroelastic analysis. The design is much higher in solidity and much lower in stagger angle than typical fan stages. However, the airfoil cross section (see Fig. 3) is similar to that of a conventional fan blade. The thickness-to-chord at 73.3 percent span is approximately 0.03.

Although the first natural mode is commonly referred to as first bending, the motion is not pure plunging. In this mode the airfoil motion at 73.3 percent span can be described as having a pitching axis a few chord lengths upstream. The second natural mode is the torsion mode. In this mode the airfoil motion at 73.3 percent span can be described as having a pitching axis at a point slightly forward of midchord. Most of the present results assume the mode shapes to be pure plunging (first mode) and pitching about midchord (second mode). For more details concerning the blade design, see Schmidt et al. (1987) and Wood et al. (1988).

Effects of Mode Coupling. Conventional fan blades normally encounter single-mode flutter. A brief study was conducted to determine the conditions under which the subject blade would encounter multimode flutter. The critical reduced velocity was determined for various values of bending-to-torsion frequency ratio (assumed to be an independent variable). The critical reduced velocity was found to be independent of bending-to-torsion frequency ratio except in the range 0.95 to 1.05. For the blade of interest the bending-to-torsion frequency ratio is well outside this range (0.567).

In addition, the complex eigenvector was examined for a wide variety of flutter conditions. In all cases a single mode was found to be dominant. Considering the high mass ratio of the subject blade, these results are not surprising.

Effects of Mach Number. A study was performed in which the critical reduced velocity was determined for relative Mach numbers ranging from 0.0 to 3.0. The results, assuming pure pitching motion about midchord, are shown in Fig. 4. In the subsonic regime the critical reduced velocity is generally 3.0 or above, and compressibility effects are shown to be stabilizing up to a Mach number of 0.65. As the transonic regime is approached, the critical reduced velocity drops. For supersonic Mach numbers less than 1.6 the critical reduced

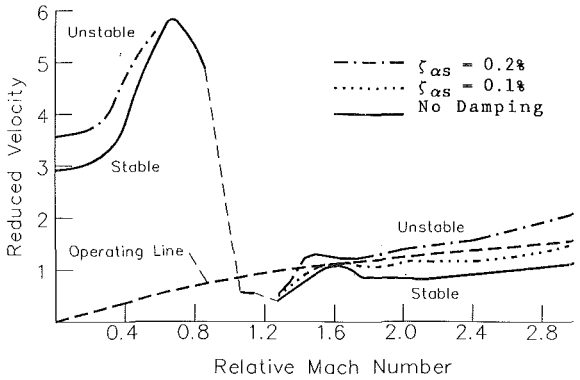

Fig. 5 Comparison of critical reduced velocity with damping, $\xi = 28$, $c/g = 3.215$

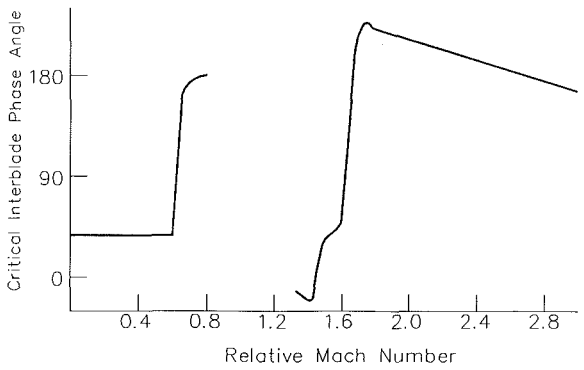

Fig. 6 Critical interblade phase angles, undamped, $\xi = 28$, $c/g = 3.215$

velocity starts at the very low value of approximately 0.5 and increases with Mach number to approximately 1.0. For relative Mach numbers greater than 1.6, the critical value is always near 1.0. These critical values are much smaller than those previously reported (approximately 1.5 reported by Nishiyama and Kikuchi, 1973). The main differences between the previous and present results are stagger angle and solidity. Not that the unsteady aerodynamic theories used herein break down as the relative Mach number approaches one.

Also shown in Fig. 4 is an approximate "operating line" for the first mode. That is, the line representing the relationship between the reduced velocity and Mach number as the fan increases its operational speed. Since the acoustic velocity is a function of Mach number, this line is not straight. As can be seen, the fan is in the stable region during subsonic operation. However, as it accelerates into the supersonic regime, the blade becomes unstable and remains unstable well beyond the design point ($M_r = 2.606$).

Effects of Damping. One method of determining the "strength" of an instability is to calculate the critical velocity for various assumed values of damping. The critical reduced velocities for 0.1 and 0.2 percent structural damping are compared with those of the undamped cascade in Fig. 5. Near the design point the inclusion of damping has a significant effect on the critical velocity. That is, 0.2 percent damping raises the flutter critical reduced velocity from approximately 1.0 to 1.7, which is above the operating line. This is indicative of a relatively weak instability. Platzer and Chalkley (1972) also reported a weak instability for high mass ratios. However, at a relative Mach number of 1.6, damping has little effect on critical velocity. This is indicative of a fairly strong instability. In the subsonic regime the inclusion of damping raises the flutter speed somewhat.

Critical Interblade Phase Angle. Previous researchers have demonstrated that the critical interblade phase angle is

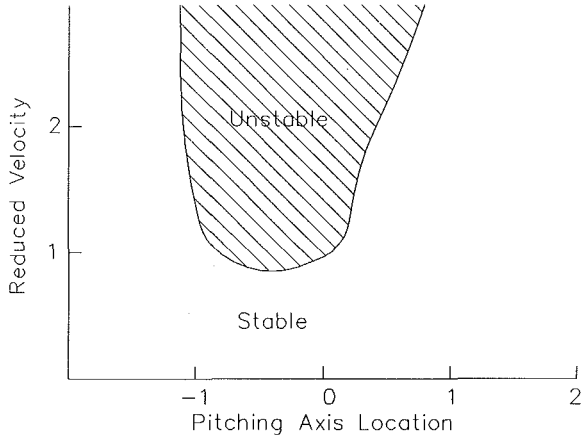

Fig. 7 Effect of pitching axis, $M_r = 2.606$, undamped, $\xi = 28$, $c/g = 3.215$, $\beta_r = 186.6$

between 180 and 200 deg. For relative Mach numbers greater than 1.65 the present results show a similar trend. However, for lower supersonic Mach numbers the critical interblade phase angle was found to vary significantly. Shown in Fig. 6 are the critical interblade phase angles corresponding to the critical points (undamped) in Fig. 4. For supersonic relative Mach numbers less than 1.5, the critical interblade phase angle is near 0.0. As the Mach number increases beyond 1.5, the critical interblade phase angle quickly increases to about 220 deg and then gradually drops to approximately 170 deg. For reference, the critical interblade phase angle for unstalled torsional flutter of a typical fan blade is usually between 45 and 90 deg.

For comparison the critical interblade phase angles for subsonic operation are also shown. For most of the subsonic range the critical interblade phase angle is approximately 40 deg. As the blade approaches the transonic regime the critical interblade phase angle varies widely.

Effects of Pitching Axis. While investigating the effects of pitching axis location, some interesting phenomena were observed. At the design Mach number, stability was determined as a function of pitching axis location. All other cascade parameters were held constant. An exception is the radius of gyration, which is related to pitching axis by the parallel axis theorem. Since the center of gravity is assumed to move with the pitching axis, the pitching axis and the elastic axis position are coincident. The interblade phase angle is fixed at the critical value for pitching about midchord (186.6 deg). Although not shown, the critical interblade phase angle varies somewhat with pitching axis location.

As shown in Fig. 7, the lowest critical velocity is for a pitching axis at approximately 30 percent chord ($a_e = -0.4$). Very high critical velocities are found when the pitching axis was upstream of the leading edge or beyond 70 percent chord. This finding is consistent with the results of previous researchers. They reported the worst location to be approximately 40 percent chord and reported no pure plunging (pitching axis at infinity) flutter.

When the above parametric study was repeated at a lower supersonic Mach number (1.4), very different results were found. Figure 8 shows the unstable regions. In addition to the instability associated with pitching motions near midchord, a band of instability is found for pitching axis locations well ahead of the leading edge and well beyond the trailing edge. A check of stability for pure plunging motion resulted in a similiar band, which is also shown on the figure. To authors' knowledge this is the first instance in which pure plunging flutter has been predicted for an unstalled cascade.

To determine the strength of this pure plunging type in-

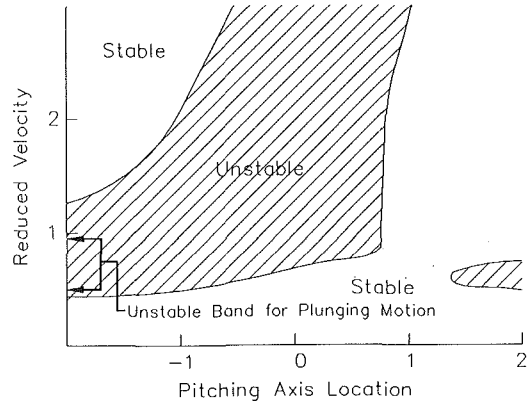

Fig. 8 Effect of pitching axis, $M_r = 1.4$, undamped, $\xi = 28$, $c/g = 3.215$, $\beta_r = 6.2$

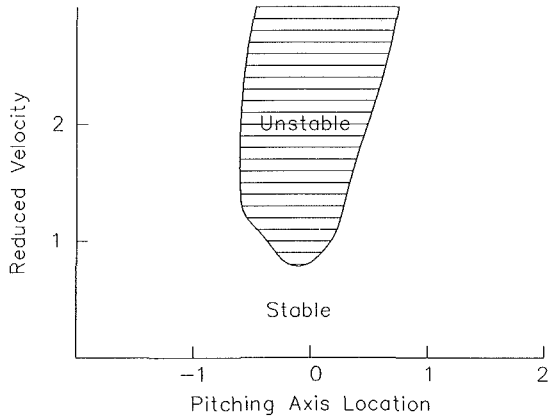

Fig. 9 Effect of pitching axis, $M_r = 1.4$, 0.1 percent damping, $\xi = 28$, $c/g = 3.215$, $\beta_r = 6.2$

stability, the study was repeated with 0.1 percent damping (Fig. 9). A comparison of Figs. 8 and 9 shows that a small amount of damping eliminates the pure plunging type instability. Also, the pure plunging instability is eliminated by removing the cascade effects. Hence, this is a weak instability of little practical interest. However, the instability associated with pitching motions near midchord is shown to be strong and must be avoided.

Effects of Solidity and Stagger Angle. Platzer and Chalkley (1972) found that stability was strongly dependent on solidity. They analyzed a cascade with a stagger angle very close to that of the NASA blade, but at lower Mach number (1.414) and with large damping (1.0 percent). As the solidity was increased from 1.47 to 3.58 the critical reduced velocity was almost cut in half. In studying the NASA blade at the design point a similar effect was found (Fig. 10). Decreasing the solidity from the design value of 3.22 to 2.00 nearly doubles the critical reduced velocity.

Another geometric effect to consider is that of stagger angle. The effect of stagger on the stability was studied at the design point. Increasing the stagger angle from 28 to 45 deg resulted in a decrease in critical reduced velocity of approximately 10 percent. Thus, stagger angle has a weak effect on stability.

Effects of Mistuning. For the results presented thus far it has been assumed that all blades are identical (tuned). When the individual blades on a disk differ in some property, the system is said to be mistuned. The type of mistuning in which the bladed disk consists of one set of high-frequency blades and one set of low-frequency blades, which are alternated in adjacent disk slots, is known as alternate mistuning. Crawley and Hall (1983) have shown that alternate frequency (torsion mode) mistuning is nearly optimal for stabilizing unstalled torsional flutter. Therefore, a limited study of the effect of alterntae frequency mistuning was conducted at the design point. The inclusion of 1 percent alternate mistuning (plus or minus 0.05 percent) stabilizes the cascade and is roughly equivalent to adding 0.3 percent damping to the tuned cascade.

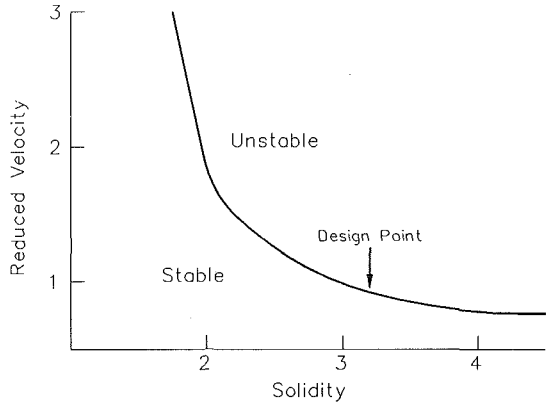

Fig. 10 Effect of solidity, $M_r = 2.606$, $\xi = 28$, $\beta_r = 186.2$

Summary and Conclusions

An application of a simple aeroelastic model to an advanced supersonic axial flow fan blade has been presented. The cascade theory of Lane (1957) is used to determine the unsteady aerodynamic loads. In addition, results were presented that show the effects of mode coupling, Mach number, structural damping, pitching axis location, solidity, stagger angle, and mistuning. The major conclusions from this investigation are:

1 Supersonic axial flow fan and compressors blades are susceptible to a strong torsional mode flutter having critical reduced velocities that can be less than 1.0.

2 The practically important instabilities involve a single mode, which has a pitching axis location between the leading edge and 70 percent chord. The worst pitching axis location is slightly upstream of midchord.

3 The critical interblade phase angle for high supersonic operation ($M_r > 1.65$) is between 165 and 225 degrees. No general statement can be made for the entire supersonic operating regime.

4 For low supersonic operation a band of very weak instability was found for pure plunging motion.

5 Stability is strongly dependent on solidity and weakly dependent on stagger angle.

6 Improved unsteady aerodynamic models that consider actual geometry and loading effects are needed for supersonic axial flow cascades.

References

Adamczyk, J. J., and Goldstein, M. E., 1978, "Unsteady Flow in a Supersonic Cascade With Subsonic Leading-Edge Locus," *AIAA Journal*, Vol. 16, No. 12, pp. 1248–1254.

Breugelmans, F. A. E., 1975, "The Supersonic Axial Inlet Component in a Compressor," presented at the Gas Turbine Conference & Products Show, Houston, TX, Mar. 2–6.

Chalkley, H. G., 1972, "A Study of Supersonic Cascade Flutter," Aeronautical Engineers Thesis, Naval Postgraduate School, Monterey, CA.

Crawley, E. F., and Hall, K. C., 1983, "Optimization and Mechanisms of Mistuning in Cascades," ASME *Journal of Engineering for Gas Turbines and Power*, Vol. 107, No. 2, pp. 418–426.

Drake, D. G., 1957, "The Oscillating Two-Dimensional Aerofoil Between Porous Walls," *Aeronautical Quarterly*, Vol. 8, pp. 226–239.

Gorelov, D. N., 1960, "Lattice of Plates in an Unsteady Supersonic Flow," *Trans. Fluid Dynamics*, Vol. 1, No. 4.

Jordan, P. F., 1953, "Aerodynamic Flutter Coefficients for Subsonic, Sonic, and Supersonic Flow (Linear Two-Dimensional Theory)," Aeronautical Research Council R&M 2932.

Kaza, K. R. V., and Kielb, R. E., 1982, "Effects of Mistuning on Bending-Torsion Flutter and Response of a Cascade in Incompressible Flow," *AIAA Journal*, Vol. 20, No. 8, pp. 1120–1127.

Kielb, R. E., and Kaza, K. R. V., 1983, "Aeroelastic Characteristics of a Cascade of Mistuned Blades in Subsonic and Supersonic Flows," ASME *Journal of Vibration, Acoustics, Stress, and Reliability in Design*, Vol. 105, pp. 425–433.

Klapproth, J. F., 1961, "A Review of Supersonic Compressor Development," ASME *Journal of Engineering for Power*, Vol. 83.

Lane, F., 1957, "Supersonic Flow Past an Oscillating Cascade With Supersonic Leading-Edge Locus," *Journal of the Aeronautical Sciences*, Vol. 24, pp. 65–66.

Miles, J. W., 1956, "The Compressible Flow Past an Oscillating Airfoil in a Wind Tunnel," *Journal of the Aeronautical Sciences*, Vol. 23, No. 7.

Nagashima, T., and Whitehead, D. S., 1977, "Linearized Supersonic Unsteady Flow in Cascades," Aeronautical Research Council R&M 3811.

Nishiyama, T., and Kikuchi, M., 1973, "Theoretical Analysis for Unsteady Characteristics of Oscillating Cascade Aerofoils in Supersonic Flows," *The Technology Reports of the Tohoku University*, Vol. 38, No. 2, pp. 565–597.

Platzer, M. F., and Chalkley, H. G., 1972, "Theoretical Investigations of Supersonic Cascade Flutter and Related Interference Problems," AIAA Paper No. 72-377.

Ramsey, J. K., and Kielb, R. E., 1987, "A Computer Program for Calculating Unsteady Aerodynamic Coefficients for Cascades in Supersonic Axial Flow," NASA TM 100204.

Rao, B. M., and Jones, W. F., 1976, "Unsteady Airloads for a Cascade of Staggered Blades in Subsonic Flow," *Unsteady Phenomena in Turbomachinery*, AGARD-CP-177.

Runyan, H. L., Cunningham, H. J., and Watkins, C. E., 1952, "Theoretical Investigation of Several Types of Single-Degree-of-Freedom Flutter," *Journal of the Aeronautical Sciences*, Vol. 19, No. 2.

Savage, M., Boxer, E., and Erwin, J. R., 1961, "Resume of Compressor Research at the NACA Langley Laboratory," ASME *Journal of Engineering for Power*, Vol. 83.

Schmidt, J. F., Moore, D., Wood, J. R., and Steinke, R. J., 1987, "Supersonic Through-Flow Fan Design," NASA TM-88908.

Wood, J. R., Schmidt, J. F., Steinke, R. J., Chima, R. V., and Kunik, W. G., 1988, "Application of Advanced Computational Codes in the Design of an Experiment for a Supersonic Throughflow Fan Rotor," ASME JOURNAL OF TURBOMACHINERY, Vol. 110, pp 270–279.

Turbomachinery Blade Vibration and Dynamic Stress Measurements Utilizing Nonintrusive Techniques

J. R. Kadambi
Associate Professor.

R. D. Quinn
Assistant Professor.

M. L. Adams
Professor.

Department of Mechanical and Aerospace Engineering,
Case Western Reserve University,
Cleveland, OH 44106

The vibration of large turbomachinery blading is well known to be one of the most important design factors in modern turbomachinery. Typically, blade vibration is dominated by the unsteady flow phenomena and the interaction effects set up by vibration of blades within a high-velocity compressible fluid medium. This paper addresses the feasibility of developing an in-service noninterference measuring/monitoring system for steam turbine and gas turbine jet engine blade vibrations and stresses. The major purpose of such a measurement system is to provide a technically feasible, cost-effective means to isolate potential turbine and fan blade failures before they occur; thus minimizing costly machinery failure and risk of injury. The techniques that are examined include magnetic, inductive, optical, and laser and acoustic Doppler measurement methods. It appears likely that the most feasible and promising approach would include use of a few properly chosen measurement points on the blading in combination with use of advanced finite-element computational techniques and vibration modal methods. The modal analysis, performed experimentally and/or computationally, is especially useful in converting vibration measurements to the desired dynamic stresses.

1 Introduction

In the power generation and propulsion industries, the continuing trend in the last 20 or 30 years is to generate more power or thrust-per-pound of equipment. A particular example of this trend is the building of larger steam turbines and gas turbine jet engines that operate with closer tolerances and at higher speeds. However, the reliability and service life of such equipment is of equal economic importance. A consequence of these criteria is more stringent requirements for operational safety and reliability of these machines.

The design of turbomachinery generally involves the approximation that the flow is steady, despite the fact that the flow actually experiences several types of unsteady behavior. This neglect of unsteadiness may lead to reduced reliability in the turbine, especially in the heavily loaded latter stages of turbomachinery. Instances of asynchronous response of turbine blading have been observed during field testing of steam turbines, and it is thought that this response is due to inherent flow instability in the flow passages (Kadambi et al., 1986). The unsteady flowblade interactions are not limited to steam turbines, but also apply to the general area of rotating turbomachinery, including gas turbines, compressors, centrifugal pumps, etc.

The measurement of blade vibrations during operation is an important guide to preventive maintenance, which can be a major contributor to increased reliability and service life. For the operational safety of these machines, it is essential that the turbine blades not be subjected to any potentially harmful vibrations. For example, the problem is particularly severe in the later stages of the large steam turbines and, therefore, attention must be given to dynamic stresses developed in the rotor blades due to these vibrations. A noninterference blade stress and vibration measurement system would be a very useful tool in obtaining this information during turbine operation.

This paper contains an examination of the state of the art of measurement systems that would potentially be used for blade vibrations. The techniques that are investigated include strain gage, magnetic, inductive, optical, acoustic Doppler, and laser Doppler measurement methods. The most promising techniques for obtaining blade stress information are termed "momentary" processes. The term momentary process refers to those methods for measuring blade vibrations that utilize the transit time of the blade underneath one or more detection devices mounted on the periphery of the casing. This type of technique permits the observation of all rotating blades of a row from the casing with a single set of sensors. In this class of technique, optical methods (optical sensors and laser Doppler techniques) probably hold the most promise. In addition, the laser Doppler method is unique in that it is the only momentary method capable of observing the blade at various points along its height.

Contributed by the Power Division for publication in the JOURNAL OF TURBOMACHINERY. Manuscript received by the Power Division July 26, 1988.

2 Survey and Evaluation of Published Techniques and Approaches

A literature survey in the area of nonintrusive blade vibration measurement techniques was performed. The survey revealed techniques ranging from the established strain gage methods utilizing slip rings and modern telemetry techniques to the recently applied optical techniques. The following techniques and their relative merits and short comings are discussed:

- Strain gage-telemetry methods
- Laser Doppler anemometry method
- Meander (magnetic)/inductive/capacitive methods
- Optical methods
- Acoustic Doppler methods

2.1 Strain Gage-Telemetry Methods. The strain gage-telemetry method is the long-established and field-proven system for obtaining direct information on the alternating strains arising in certain critical parts of the blade (Donato et al., 1981; Rajgopalan et al., 1983; Shimoda et al., 1983; We-Shung et al., 1981). However, there are significant problems associated with the strain gage systems. In practice, the number of measuring points (blades) is limited; significant problems are associated with the installation and operational life expectancy; and the transmission of signals via a slip ring assembly or telemetry system is quite expensive. Additionally, the wire paths can affect both the structural stiffness and damping and the local flow field. The strain gages are, therefore, part of a random test method that produces extremely valuable information on certain parts of the blades but that is statistically unreliable due to the irregularity of the blade tolerances. The limited life of the gages and their supply lines due to environmental influences such as unsteady flow and centrifugal forces is also a disadvantage.

2.2 Laser Doppler Anemometry Method (LDA). The advent of laser light with its coherent wave structure has opened a new door to the measurement of velocity. The motion of a surface normal to the coherent wave front adds a Doppler shift to the frequency of the scattered light, which can be related to the velocity of the surface. The problem has been detecting this frequency shift and converting it to a reliable velocity reading. This is accomplished in most cases by heterodyning two signals to obtain the difference or beat frequency and then relating this to velocity. The signal processing equipment used to do this is commerically available. It was developed for the measurement of fluid velocity where the Doppler signal comes from particles in the fluid. The manufacturers of such equipment, DANTEC and Thermosystems, Inc. (TSI) have now developed vibration-measuring devices using laser Doppler anemometry. We shall now briefly describe the principle of the technique.

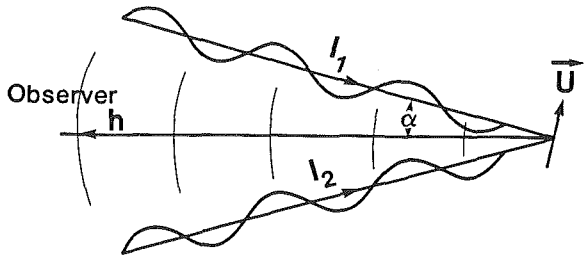

Fig. 1 Measurement of lateral vibration from surface moving with a velocity U using light scattered from the laser beams

The frequency ν of light and its wavelength λ, are related by the equation

$$\lambda = \frac{c}{\nu} \tag{1}$$

where c is the velocity of light in the medium of transmission. When light with a coherent, planar wave structure is transmitted with a unit vector $\mathbf{l}_1$ to a moving surface with velocity $\mathbf{U}$, the wavelength λ' of the light seen by the moving surface is Doppler shifted, and is given by the following equation:

$$\lambda' = \frac{c - \mathbf{U} \cdot \mathbf{l}_1}{\nu} \tag{2}$$

When light is radiated by a surface moving with velocity $\mathbf{U}$ to a stationary observer in the direction of unit vector $\mathbf{k}$ away from the surface, the frequency of the light ν' seen by the observer is Doppler shifted and is given by the equation

$$\nu' = \frac{c - \mathbf{U} \cdot k}{\lambda} \tag{3}$$

Combining equations (2) and (3), one gets the equation for the Doppler-shifted frequency ν' of light transmitted by a laser with frequency ν in the direction l_1 to a moving surface with velocity $\mathbf{U}$ and reradiated by the moving surface in the direction $\mathbf{k}$ to the stationary observer.

$$\nu' = \frac{c - \mathbf{U} \cdot \mathbf{k}}{\lambda'} = \frac{c - \mathbf{U} \cdot \mathbf{k}}{c - \mathbf{U} \cdot \mathbf{l}_1} \nu \tag{4}$$

These equations will be used in the following discussion.

(a) Lateral Vibration Measurement. The dual beam backscatter mode of operation of the laser anemometer is used to detect lateral vibrations. As shown in Fig. 1, light from two laser beams is reradiated from the moving surface to a detector located on the bisector of the angle made by the two beams. The detector cannot respond rapidly enough to detect the laser frequency but can detect the ratio of the difference frequency to the undisturbed frequency of the heterodyned signals. Considering equation (4), this ratio is given by the equation

Nomenclature

a = tip amplitude
B = matrix
Δb = probe separation distance
c = velocity of light
f = frequency
$\bar{k}$ = direction vector
$\mathbf{l}_1, \mathbf{l}_2$ = unit vectors
n = number of degrees of freedom
q = modal coordinate, ratio
t = time
t_s = time interval between a reference signal and blade signal
t_u = full revolution time
u = displacement
$\mathbf{U}$ = velocity
U_x = lateral velocity of the plane
U_y = on-axis velocity
x = abscissa
y = ordinate
α = half-angle between beams
λ = light wavelength
λ' = Doppler-shifted light wavelength
ν = light frequency
ν' = Doppler-shifted light frequency
ϕ = eigenfunction
ω = $2\pi f$ = natural angular frequency of a blade

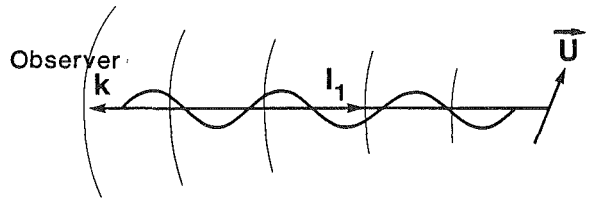

Fig. 2 Measurement of on-axis vibration from a surface moving with velocity U using light scattered from a laser beam and a reference laser beam

$$\frac{\nu_1' - \nu_2'}{\nu} = \frac{c - \mathbf{U}\cdot\mathbf{k}}{c - \mathbf{U}\cdot\mathbf{l}_1} - \frac{c - \mathbf{U}\cdot\mathbf{k}}{c - \mathbf{U}\cdot\mathbf{l}_2} \tag{5}$$

Assuming that the velocity of light c is much greater than the velocity of the surface **U**, this equation can be approximately expressed as

$$\frac{\nu_1' - \nu_2'}{\nu} = \frac{2U_x \sin\alpha}{c} \tag{6}$$

where u_x is the lateral velocity in the plane defined by the two beams and in the direction normal to the bisector. The angle α is half of the angle between the beams (see Fig. 2).

(b) On-Axis Vibration Measurement. The reference beam mode of operation of the laser anemometer is used to detect on-axis vibration. As shown in Fig. 2, light from only one laser beam is reradiated from the moving surface to a detector located with the laser. The Doppler-shifted light transmitted to the detector is heterodyned with the unshifted light. Again, the difference frequency ratio is the measurable quantity. This ratio is given by

$$\frac{\nu_1' - \nu}{\nu} = \frac{c - \mathbf{U}\cdot\mathbf{k}}{c - \mathbf{U}\cdot\mathbf{l}_1} - 1 \tag{7}$$

Assuming that the velocity of light c is much greater than the velocity of the surface **U**, this equation can be approximately expressed as

$$\frac{\nu_1' - \nu}{\nu} = \frac{2U_y}{c} \tag{8}$$

where U_y is the on-axis velocity of the surface in the direction of the detector that is located with the laser.

The use of the laser Doppler technique to obtain measurements of vibration of moving objects and, in particular, rotating turbine blades, was reported as early as 1973 (Kulczyk et al., 1973). The authors met with only limited success, but the difficulty at that time was due to unavailability of equipment, not the technique itself. LDA was also used for measuring the torsional vibration of rotating shafts (Simpson et al., 1977). Now, with the LDA-based vibration-measuring devices being available commercially, this method seems to be a promising one. Laser Doppler Anemometry has been used successfully in making velocity measurements in superheated steam (Decuypere et al., 1985) as well as in high-temperature (2500°F) combustion gases (Wilson et al., 1977). Therefore, the high-temperature steam and combustion gases, encountered in steam and gas turbines, respectively, should not have detrimental effects on LDA usage for vibration measurements. With judicious selection of the location of the optical window on the casing between the rotating and stationary rows, it would be possible to obtain vibration measurements along the blade height as well as near or on the tip

2.3 Meander Methods. In the meander method, the vibration amplitudes of the blade tips are measured (Staeheli, 1975). A small permanent magnet at the tip of the blade induces an electric voltage in a meander-shaped winding installed in the casing. The oscillating vibrational motion can be isolated from the voltage curve by filtering or frequency analysis. Only one blade can be measured at a time, or a small number with partial winding. Considerable modifications are necessary for installation of the winding support, and the small permanent magnet installed at the tip has to withstand large centrifugal forces.

2.4 Inductive/Capacitive Methods. In these methods, capacitive transmitters are used instead of the magnet in the meander technique (Zablotky et al., 1969; Raby, 1970). The detectors must be placed in close proximity to the blade tip passage for maximum sensitivity. For safety reasons, a greater clearance is generally required, which results in greatly reduced sensor sensitivity. The measuring signals received then show only slight edge steepness and, therefore, cannot be used for determining the transit time accurately. The following example serves to illustrate the demands made on timing accuracy.

Assuming a blade tip speed of 300 m/s and an amplitude of vibration in the peripheral direction of 0.3 mm results in a time amplitude of

$$\Delta t = \frac{(3)\ (10)^{-4}}{300} = 1\ \mu s$$

This implies that the time lag must be measured at least one order of magnitude more accurately, i.e., to 100 ns. For the capacitive or inductive probes, safety requires a clearance between probes and blade tips about 5 to 7 mm. The signals these probes can put out are, therefore, very weak and have to be strongly amplified, introducing a high noise level. More important, these probes will produce broad bell-shaped signals with long rise and fall times. Such pulses are not suitable for derivation of accurate and well-defined start and stop times. In spite of these difficulties, some investigators claim to have successfully measured rotating blade tip vibrations in steam turbines using inductive sensors.

2.5 Optical Sensor Methods. As discussed above, since the vibration measurement from the casing using proximity detectors is basically a time measurement, the problem is reduced to obtaining suitable proximity detectors. From the experience of researchers at NASA-Lewis Research Center, Cleveland, OH (Kurkov, 1984) and Brown-Boveri, Ltd., Baden Switzerland (Roth, 1977, 1980), it appears that optical probes are suitable proximity detectors. The basic principle of the probe consists of focusing a narrow laser light beam on the enveloping surface of the blade tips, intercepting the light reflected back from the blade ends, and conveying it to an optoelectric transducer. The focus diameter must be of the same magnitude as the smallest measurement amplitude because the edge steepness of the signal is provided by their ratio (peripheral speed/focus diameter). As compared to conventional probes, the effects of the fluctuations in radial play on the edge steepness in this case are insignificant due to the small diameter of the incident ray. In the Brown-Boveri method (Roth, 1980), an optical detector mounted in the stator is activated when a blade tip passes. Another detector located near the shaft of the machine produces the reference signal.

If the time interval t_s, between a reference signal and a blade signal is divided by t_u, the full revolution time of the machine, then the ratio $q = t_s/t_u$ is a constant as long as the blade does not vibrate and the change in rotational speed (rpm) is negligible during a revolution. If a stochastically excited vibration occurs, q will show a jitter. Also, if the vibration frequency is not equal to an even multiple of the revolution frequency $[f_u = 1/t_u]$ in each revolution, a slightly changed time interval t_s and, consequently, a different value of q will be obtained.

In the case of integral vibration (resonance excitation by a

distinct machine order), the tip of a particular vibrating blade will repetitively pass the detectors in an unchanged phase position and the ratio q remains constant. As long as the rpm is constant, resonance vibrations remain unidentified. Usually, the rpm is allowed to change within a few percent, or measurements could be made during run-up or run-down regime of the machine. In Roth (1980), the authors felt that resonance passages could be detected with only small changes in rpm due to strong phase changes within the resonance region of a lightly damped system. Also, it was noted that a single-probe method has some advantages. The reference probe at the shaft is far away in the axial direction from blade zero and, therefore, torsional and radial vibrations of the shaft could reduce the accuracy of measurements. For higher vibration modes, the tip amplitudes could be unmeasurably small for the single-probe method while blade vibrations, and stresses, at other locations would reach noticeably higher levels. A two-probe method was recommended for avoiding these problems. The time measurement would be started at the instant a blade passes the first probe and stopped when the blade passed the second probe. There would be a jitter in the travel time t_s along the probe separation; along the probe separation, Δb, if there were vibrations. Roth (1980) derived equations for the circumferential component of the tip amplitude (a). These equations were

$$a = t' U$$

for the single-probe method and

$$a\omega = \frac{U^2 t''}{\Delta b}$$

for the two-probe method, where $t' =$ variations in t_s; $U =$ blade tip circumferential velocity; $a\omega =$ vibrational velocity; $\Delta b =$ probe separation distance; $t'' =$ variation in blade travel time between the two probes.

In a later paper (McCarty et al., 1982), trials with prototype noninterference stress-measuring systems for nonintegral vibrations were made based on utilizing blade tip deflection measurements. Special data processing algorithms to infer local stresses in a turbine engine compressor blade were discussed. The objectives were:

1 To verify the ability of the system of extract both amplitude and spectral information from blade tip vibrations nonintegral to engine speed using a single-periphery blade tip measuring station.

2 To display this information in a manner identical to strain gage system displays for the benefit of stress analysis to monitor the compressor health and analysis of blade vibration characteristics.

The details of the technique and a description of the prototype system are contained in McCarty and Thompson (1980). As is the case for strain gage systems, prior knowledge of blade characteristics is required to correlate blade-tip deflections with the maximum stress on the blade. Blade tip deflection versus stress must be obtained from bench tests of representative blades in the same manner as is currently done for strain gage measurements. The authors claim to have satisfactorily extracted amplitude and spectral information using a single tip measurement station on the compressor periphery. Some problems were associated with the lens of the sensor getting coated with opaque material requiring it to be wiped clean. The prototype system requires variation of rotor speed for determining blade vibration frequency, but the inherent variations in the engine speed of approximate by 0.5 percent were insufficient, necessitating intentional speed changes. The comparison with strain gage systems on the same engine was satisfactory. However, further development is required in this system to achieve the capability for measuring blade variations that are integral with respect to engine speed.

In a later paper, Kurkov (1984) reported measurements of self-excited rotor blade vibrations in a turbofan engine using casing-mounted optical displacement sensors. Three sensors were located at ports corresponding to the passing of the leading edge and trailing edge locations. As the blades passed the optical ports, a light beam was reflected from the blade tips and conducted to a photomultiplier tube by a fiber optics bundle. Essentially, the basic principle is similar to earlier descriptions. McCarty and Thompson (1980) provide a detailed description of the optical method. The blade tip relative Mach number was 0.94. Several vibratory modes were excited simultaneously and flutter occurred in the second mode, which involved both bending and torsional blade displacements. In concluding remarks, it was stated that a complex stall flutter mode can be reasonably resolved into its principal bending and torsional contributions using the casing-mounted optical displacement sensors. Detection of nonintegral engine order excitation in the blade displacement spectra for higher modes was difficult. It was also noted that implementation of on-line spectral analysis is essential when using optical sensors for vibration monitoring. In steam turbine applications, one must also be careful to take into consideration the effects of two-phase steam flow encountered in the later stages of the turbine.

2.6 Acoustic Doppler Methods. As a blade or blade group passes through a resonant condition, there is a corresponding marked increase in vibration. Noninterfering acoustic sensors fixed to the casing downstream of the blade row can, in theory, detect the sound radiated by the vibrating blades (Leon and Scheibel, 1986). Through spectral analysis, the resonating blade can then be identified along with the particular mode and amplitude of vibration. Only two sensors are required for each monitored blade row.

As a blade weakens because of crack propagation, its natural frequency decreases. In this way, a blade can traverse a resonance while the turbine is operating at constant speed. With the acoustic Doppler method, these occurrences can be monitored and recorded and a history of the blade row can be produced. Hence, this method differs from the other methods in that its purpose is to provide a warning when a dangerous situation occurs, while the other methods are meant to provide instantaneous stress information not just during resonant conditions. The danger of a warning system is that it may malfunction at an inconvenient time and a hazardous condition can be overlooked. For this reason, methods that provide instantaneous stress data are much more desirable.

The major difficulty in applying the acoustic Doppler method is filtering the signal from the pressure sensors to remove the background noise without diminishing the comparatively weak blade vibration signal. In fact, the background noise in an operating steam turbine is of much higher amplitude and of broad frequency band. Also, the desired signal is characteristically Doppler shifted. Leon and Scheibel (1986) provide several algorithms for filtering and enhancing the blade vibration signal during resonance. Since only resonant conditions are considered, the only frequencies of interest are multiples of turbine rotational frequency. Time averaging and a transfer function averaging technique are shown to be useful for removing the other "asynchronous" components.

The high sensitivity of the vibration phase to changes in excitation frequency during resonance provides a mechanism for extracting the desired signal from extraneous data of the same frequency. The turbine speed is not actually constant but varies by approximately 0.03 percent. During resonance, this small change in excitation frequency can cause significant fluctuations in vibration phase in a lightly damped system. Components of the signal that do not exhibit these fluctuations can be neglected.

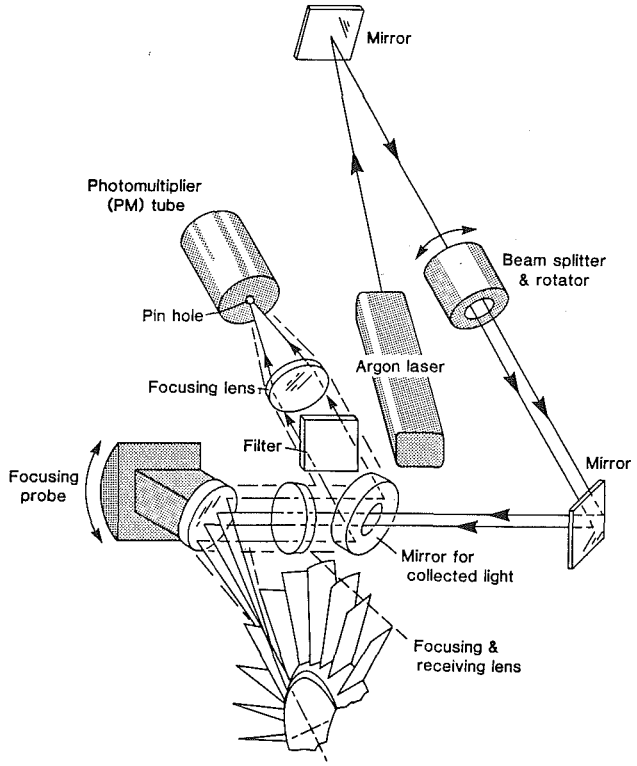

Fig. 3 Optical layout of a Laser Doppler Anemometer for turbine rotor blades (turbine casing not shown in this figure)

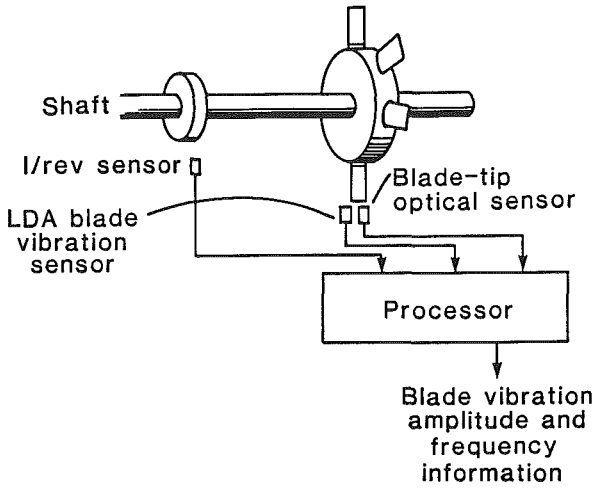

Fig. 4 A conceptual configuration of a noninterference vibration and stress measurement system showing the locations of the vibration sensors

Overall, even if the stringent signal conditioning requirements are adequately satisfied, the acoustic Doppler method, at its best, can only provide blade vibration information at resonance, not at any chosen time as is desirable. However, the acoustic process may produce a transient indication of damage and the acoustic sensor might be useful as a "damage detector"

3 Promising Approaches That Warrant Further Study and Development

From the preceding section, one can observe that problems might be encountered using strain gage telemetry methods, acoustic Doppler methods, meander methods, and the capacitive/inductive methods for on-line turbomachinery blade vibration/stress analysis. However, the laser Doppler

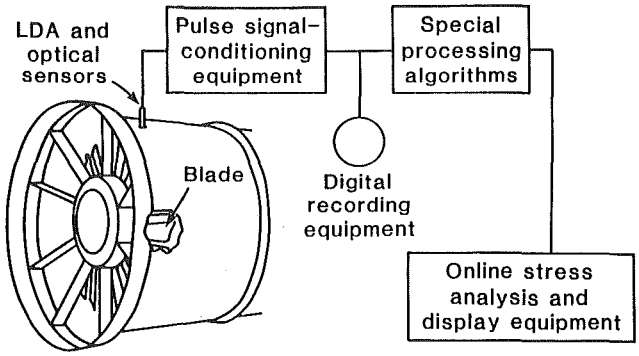

Fig. 5 A schematic of noninterference vibration and stress measurement system for a turbomachine

and the optical sensor method hold a lot of promise. As indicated earlier, laser Doppler anemometry vibration measurement systems are now commercially available. The laser Doppler technique, even during its infancy when equipment was not commercially available, was somewhat successful for obtaining such measurements (Kulczyk et al., 1973). At the present time, the challenge seems to be the integration of the LDA vibration measuring system and its data acquisition system with the signal processing and special data processing algorithms that infer local blade stresses. As compared to the optical sensor probes, this method offers if not better than at least equally good possibilities of obtaining nonintegral and integral blade tip vibration measurements. A unique advantage it might have would be the ability to measure vibrations at more than one location along the blade height. A schematic optical layout of LDA looking into the blade and blade passage is shown in Fig. 3. The focusing probe will include the beam positioning mirrors. Use of fiber optics would allow the probe to be positioned in such a way as to be able to reach different blade evaluations. The potential use of two-color backscatter mode LDA would allow simultaneous measurements in two mutually perpendicular directions. The LDA blade vibration sensor locations are shown in a conceptual configuration in Fig. 4 and a simplified schematic in Fig. 5. The LDA vibration sensor signals would then be further processed in the processing system shown in the functional block diagram in Fig. 6 for obtaining stress information.

The optical sensors also hold promise, as they have been tried with limited success in turbomachinery, as indicated earlier. The disadvantages of the optical sensors is that they are limited to the blade tip and some difficulties might be encountered with shrouded blades. The optical sensor technique has to be extended to measure integral blade vibrations. A schematic of an optical blade tip sensor is shown in Fig. 7. The conceptual configuration, the simplified schematic, and the block diagram shown in Figs. 4, 5, and 6 also include the optical sensors.

From this survey and evaluation, it appears that at present, both LDA and optical sensor methods may prove successful for on-line noninterference blade vibration and stress measurements and, therefore, warrant further study and development. Techniques for the conversion of blade vibration measurements into meaningful stress information are discussed next.

4 Techniques for Conversion of Vibration Measurements Into Dynamic Stresses

In order to determine stress at a point, strain must be found in some manner. It is important to distinguish between the measurement of vibration and that of strain in terms of stress analysis. Strain gages directly measure local strain (both static and dynamic) from which local stresses can be obtained given

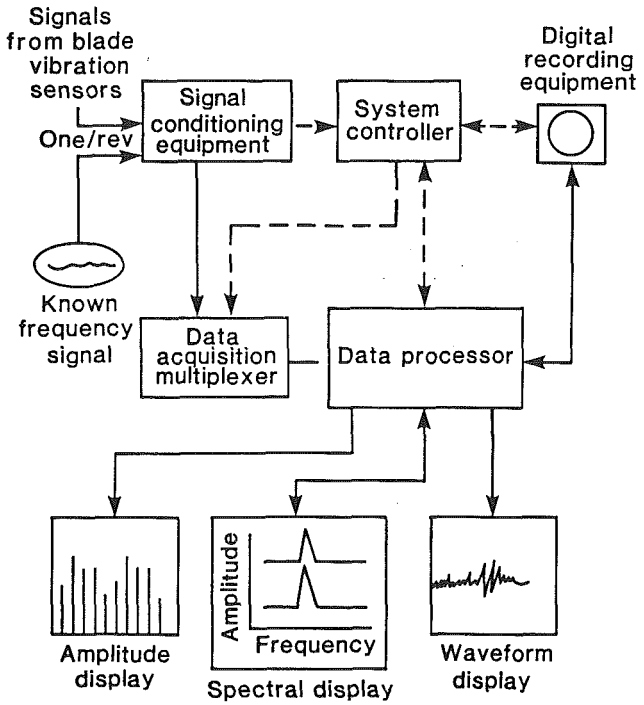

Fig. 6 Block diagram for processing the vibration sensor signals for a noninterference stress measuring system

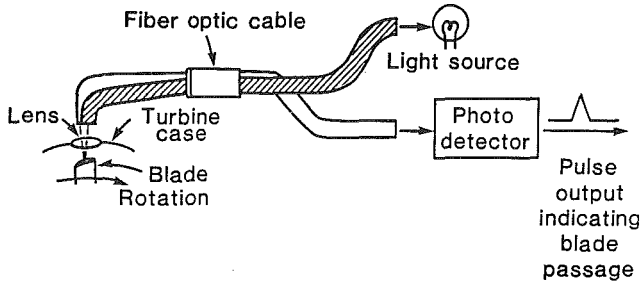

Fig. 7 Schematic of an optical sensor probe (the light source could be a laser)

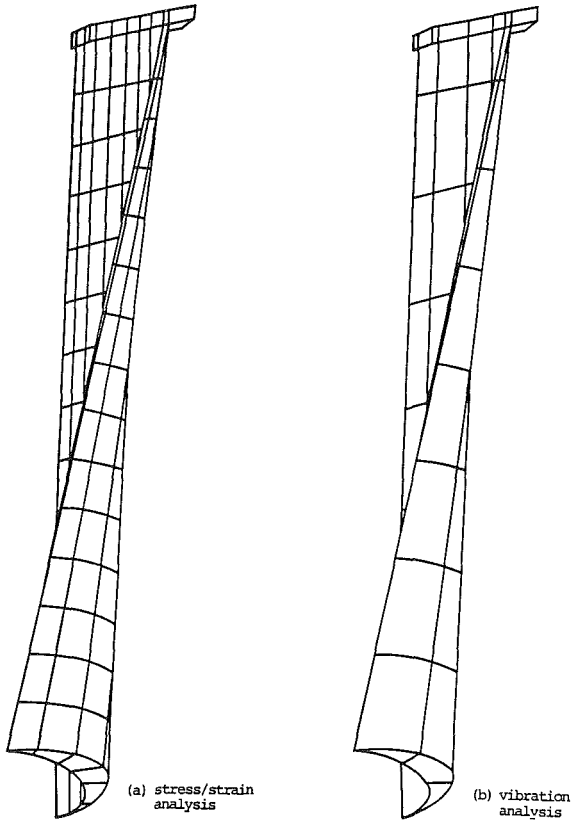

Fig. 8 Comparison of mesh size for a turbine blade

a knowledge of the material properties. However, in vibration measurement, dynamic displacements are measured and dynamic strains must be derived from this information, which, in the most straightforward approach, requires spatial differentiation of the displacement. This brings to mind two major differences between these measurement approaches:

(*a*) Strain gages measure total strain, both static and dynamic, whereas in vibration measurement, only dynamic strain can be determined. However, the static strain can be modeled (or measured by other means) and added to the dynamic strain to yield total strain or

$$\text{total strain} = \text{static strain} + \text{dynamic strain}$$

where static (or slowly varying) strain is caused by centrifugal forces and temperature gradients across the blade thickness and dynamic strain is caused by outside forces such as the fluid interacting with the blade. Also, a method that measures dynamic strains alone can be advantageous since the measured signal will not be contaminated with d-c offsets, which require compensation as with strain gages.

(*b*) Accurate strain information requires the measured blade deformation data to be accurate to at least the next highest order. For instance, in finite element analysis, stress/strain data require a much finer mesh than does deflection or vibration analysis, as illustrated by a comparison of Figs. 8(*a*) and 8(*b*). One might conclude that for stress/strain analysis, the vibration of many points on each blade must be monitored simultaneously, which is not possible. Fortunately, the use of modal analysis greatly reduces the number of measurements that are required.

For simplicity, consider the lateral vibration of a beam. Let the displacement at a point x at a time t be expressed as $u(x, t)$. With an LDA approach we would measure velocities of points on a blade. Therefore let us consider the velocity of this point $\dot{u}(x, t)$. The expansion theorem (Meirovitch, 1980) permits the velocity to be expressed as a linear combination of the eigenfunction (mode shapes) of the beam, or

$$\dot{u}(x, t) = \sum_{r=1}^{n} \phi_r(x)\dot{q}_r(t) \tag{9}$$

where $\phi_r(x)$ is the eigenfunction of the rth mode and $\dot{q}_r(t)$ is the time derivitive of the rth modal coordinate. In theory, the number of degrees of freedom n of a beam is infinite. However, for practical cases, the motion can be approximated by a finite number of modes. Evaluation of dynamic strain due to bending requires the $\dot{u}(x, t)$ to be differentiated with respect to the position x, or

$$\frac{\partial \dot{u}^2(x, t)}{\partial x^2} = \sum_{r=1}^{n} \frac{\partial^2 \phi_r(x)}{\partial x^2}\, \dot{q}_r(t) \tag{10}$$

Hence, if the mode shapes are well known (either experimentally or computationally), then the differentiation of each mode can be computed off line yielding *modal-strain shapes*. Knowledge of the modal speeds $\dot{q}_r(t)$, $r = 1, 2, \ldots, n$, provides the required strain information.

Finite element computer codes can predict the mode shapes and corresponding frequencies of each blade. By comparing bench test information with the computer analysis, the shapes of the modes can be known very accurately and spatially differentiated to obtain modal-strain shapes. Selected vibration

measurements are used to scale or "calibrate" the modal-strain shapes determined a priori by bench test measurements and/or finite element modeling. The stress associated with strain caused by varying amplitudes of each mode can then be determined also with the aid of a finite element computer code. The problem then is to convert vibration measurements at discrete points to modal amplitudes. This can be thought of as a filtering or transformation process where the output signals from the vibration detectors are filtered to obtain modal information.

There are two types of filter that are useful to determine modal information from real-time signals. A spectral filter is a device such as a spectrum analyzer that determines the frequency content of a signal. This device can show approximately to what extent each mode is excited. This is particularly useful in determining the number n of participating modes in the motion. However, if two modes have closely spaced natural frequencies, this method cannot differentiate between them. The second type of filter is a modal filter, which can be implemented digitally, and the outputs are the modal amplitudes. However, the number of measured signals must, at least, equal the number of modes that are actively participating in the motion. Modal filters have recently been developed and employed in the area of active structural control (Meirovitch and Baruh, 1984). Essentially, modal filters involve an inversion of equation (9) so that the $\dot{q}_r(t)$, $r=1, 2, \ldots, n$, can be found from vibration measurements.

If measurements are taken at m points on the blade, equation (9) can be expressed in discrete form as

$$\dot{u}(x_i, t) = \sum_{r=1}^{n} \phi_r(x_i)\dot{q}_r(t) \qquad i=1, 2, \ldots, m \tag{11}$$

or

$$\dot{u}(t) = B\dot{q}(t) \tag{12}$$

where

$$\dot{u}^T(t) = [\dot{u}(x_1, t) \quad \dot{u}(x_2, t). \ldots \dot{u}(x_m, t)] \tag{12a}$$

$$\dot{q}^T(t) = [\dot{q}_1(t) \quad \dot{q}_2(t). \ldots \dot{q}_n(t)] \tag{12b}$$

$$B = \begin{bmatrix} \phi_1(x_1) & \phi_2(x_1). \ldots \phi_n(x_1) \\ \phi_1(x_2) & \phi_2(x_2). \ldots \phi_n(x_2) \\ \cdot & \\ \cdot & \\ \cdot & \\ \phi_1(x_m) & \phi_2(x_m). \ldots \phi_n(x_m) \end{bmatrix} \tag{12c}$$

The modal amplitudes can be found given the blades' displacement by inverting equation (12) as follows:

$$\dot{q}(t) = B^{-1}\dot{u}(t) \tag{13}$$

If the number m of measurements does not equal the number n of modes of interest, then the matrix B^{-1} is not true inverse of B, but a least-square approximation known as a pseudo-inverse.

With spectral filtering, one displacement measurement on each blade is adequate to approximate modal participation. However, the best filtering system, especially during transient conditions, would involve a combination of both spectral and modal filters and, thus, would require multiple sensors for each blade.

Actually, the mode shapes and natural frequencies are speed and temperature dependent. This does not create a serious obstacle since these functional relationships can be computed off-line in the finite element code and incorporated into the on-line digital signal processing.

5 Summary

Based upon an evaluation of the currently available methods, it appears that the following methods hold the greatest promise in noninterference turbomachinery blade stress and vibration measurements:

1 Laser Doppler vibration probes
2 Optical sensor probes
3 Combination laser Doppler–optical sensor probes

The other problem that has to be addressed is the conversion of the blade vibration measurements into meaningful blade stresses. As discussed in Section 4, finite element computational techniques and modal analysis can be used for obtaining this conversion of vibration measurements into stresses.

References

Decuypere, R., and Bosschaerts, W., 1985, "Utilization of Laser Doppler and Laser Transit Velocimeters in Superheated, Saturated and Wet Steam Flows," presented at the International Symposium on Laser Anemometry, ASME Winter Annual Meeting, Miami Beach, FL, Nov.

Donato, V., Bannister, R.L., and DeMartini, J. F., 1981, "Measuring Blade Vibration of Large Low Pressure Steam Turbines," *Power Engineering*, Mar.

Kadambi, J. R., Whirlow, D. K., et al., 1986, "Effect of Flow Induced Unsteady Forces on Steam Turbine Blade Design," ASME Paper No. 86-JPGC-PWR-40.

Kulczyk, W. K., and Davis, Q. V., 1973, "Laser Doppler Instrument for Measurement of Vibration of Moving Turbine Blades," *Proceedings of the Institution of Electrical Engineers (London)*, Vol. 120, No. 9.

Kurkov, A. P., 1984, "Measurements of Self-Excited Rotor Blade Vibrations Using Optical Displacements," ASME *Journal of Engineering for Gas Turbines and Power*, Vol. 106, No. 1.

Leon, R. L., and Scheibel, J. R., 1986, "Current Status of the EPRI Acoustic Doppler Blade Monitor," presented at EPRI Steam Turbine Blade Reliability Workshop, Los Angeles, CA, Mar. 18-20.

McCarty, P. E., Thompson, J. W., Jr., and Ballard, R. S., 1982, "Noninterference Technique for Measurement of Turbine Engine Compressor Blade Stress," *Journal of Aircraft*, Vol. 19, No. 1.

McCarty, P. E., Thompson, J. W., 1980, "Development of a Noninterference Technique for Measurement of Turbine Engine Compressor Blade Stress," AEDC TR-79-78, June.

Meirovitch, L., 1980, *Computational Methods in Structural Dynamics*, Sijthoff-Noordhoff Company, The Netherlands, 1980.

Meirovitch, L., and Baruh, H., 1984, "On the Implementation of Modal Filters for Control of Structures," presented at the AIAA Guidance and Control Conference, Seattle, WA, Aug. 20-22.

Nieberding, W. C., and Pollock, J. L., 1977, "Optical Detection of Blade Flutter," ASME Paper No. 77-GT-66.

Raby, H., 1970, "Rotor Blade Vibrations Observed From the Casing," presented at the Conference on Methods of Transmitting Signals From Rotating Machinery, Central Electricity Research Laboratories, Leatherhead, United Kingdom, June.

Rajopalan, P., Srinivasan, R., and Narsimhan, G. S. L., 1983, "Telemetry Systems for Measurements in Rotating Machines," *Journal of Institution of Electronics and Telecommunication Engineers*, Vol. 29, No. 8.

Roth, H., 1977, "Measuring Vibration on Turbine Blades by Optical Means," *Brown-Boveri Review*, Vol. 64, No. 1.

Roth, H., 1980, "Vibration Measurements on Turbomachine Rotor Blades With Optical Probes," *Measurement Methods in Rotating Components of Turbomachines*, presented at Joint Fluids Engineering Gas Turbine Conference and Product Show, New Orleans, LA, Mar.

Shimoda, H., et al., 1983, "Measurement of Blade Vibration Stress in a Blast Furnace Top Pressure Recovery Turbine," *Hitachi Zosen Tech. Review*, Vol. 44, No. 4.

Simpson, D. G., and Lamb, D. G. S., 1977, "A Laser Doppler System for the Measurement of Torsional Vibration," NEL Report No. 639, Department of Industry, United Kingdom, July.

Staeheli, W., 1975, "Inductive Method for Measuring Rotor Blade Vibrations on Turbomachines," *Sulzer Tech. Rev.*, Vol. 57, No. 3.

We-Shung, W., Wen-Hu, Y., and Wen-Fwou, L., 1981, "Use of Multichannel Radio Telemetering Techniques for Stress and Temperature Measurements in Gas Turbine Rotating Components." ASME Paper No. 81-GT-116.

Wilson, W. W., and Srikantarah, D. V., 1987, "Particle Velocity Measurements in the Diffuser Section of a Coal Fixed MHD Channel," Third International Symposium of Laser Anemometry, ASME Winter Annual Meeting, Boston, MA, Dec.

Zablotsky, I.E., et al., 1986, "Vibration Indicator for Turboengine Rotor Blading," U. S. Patent No. 3,467,356.

Two-Component Phase-Averaged Turbulence Statistics Downstream of a Rotating Spoked-Wheel Wake Generator

J. E. O'Brien
NASA Lewis Research Center,
Cleveland, OH 44135

S. P. Capp
University of Pittsburgh at Johnstown,
Johnstown, PA 15904

Measurements of the axial and tangential components of the unsteady turbulent flow downstream of a rotating spoked-wheel wake generator have been obtained. The results of this study have implications for the use of this type of wake generator to produce simulated turbine guide vane wakes. Instantaneous velocity information was phase averaged based on a signal synchronized with the bar-passing frequency. Mean velocity profiles and phase-averaged Reynolds stress results were found to be consistent with measurements obtained behind a stationary cylinder. Reynolds stresses were significantly higher than corresponding measurements obtained in large-scale research turbomachines, however. Phase-averaged triple velocity correlations, also calculated from the digital velocity records, reveal the sign and magnitude of skewness in the velocity probability density distributions for the two components. Large crossflow gradients observed in the triple correlations in the wake indicate the importance of the tangential-component fluctuations in the net turbulent transport of turbulent energy across the wake. Streamwise-component wake velocity spectra for low values of reduced bar-passing frequency include a peak associated with vortex shedding from the cylindrical wake-generating bars at a shedding Strouhal number of 0.2. For higher bar-passing frequencies, the energy associated with vortex shedding is shifted to lower frequencies and becomes broadband from the stationary reference frame viewpoint.

Introduction

There has been a great deal of interest in recent years on the unsteady effects of wake passing in turbomachinery. The high levels of unsteadiness present in the wakes give rise to increased stagnation-region heat transfer and early boundary layer transition on downstream blades. Unsteady and time-averaged heat transfer effects have been documented by Dunn et al. (e.g., 1989) in a shock-tunnel facility that accommodates a full-scale rotating turbine stage. Full-scale rotating-stage experiments aimed at documenting both time-resolved and time-averaged heat transfer have also been performed by Guenette et al. (1989) in a short-duration blowdown facility. Heat transfer results of these experiments compared favorably to results obtained by Ashworth et al. (1985) on the same blade profiles in a linear cascade behind a rotating spoked wheel wake generator. The wake generator, which was developed by Doorly and Oldfield (1985), was used to produce simulated inlet-guide-vane (IGV) wakes in the cascade. This type of simulation, which is relatively easy to implement, has been shown to reproduce very closely the correct relative velocity vector diagram and mean wake velocity profiles associated with the IGV/rotor combination found in an actual turbine stage (Doorly, 1984). A similar rotating spoked-wheel wake generator was consequently adopted for experiments on the effects of wake passing on stagnation region heat transfer (Morehouse and Simoneau, 1986; O'Brien et al., 1986; O'Brien, 1988).

The experiments described by Doorly and Oldfield were performed in a short-duration light-piston tunnel, which is quite convenient for heat transfer measurements since the air is heated by isentropic compression before passing through the test section. Detailed flowfield documentation is difficult to obtain in short-duration facilities, however. The objective of the present study was to document more fully the unsteady and phase-averaged turbulence characteristics of the flowfield behind a spoked-wheel wake generator and to compare the results to typical turbomachinery flowfield results. This objective was quite feasible in the steady-flow tunnel of the present work. The flowfield measurements obtained by Sharma et al. (1983) and Raj and Lakshminarayana (1976) in large-scale research turbomachines provide a useful database for comparison with the present results.

Results will also be compared to flowfield results obtained in the near wake of a stationary cylinder. Of particular interest are the detailed measurements obtained by Cantwell and Coles (1983) for flow in the near wake (first eight diameters) behind a stationary circular cylinder. In that study, measurements

Contributed by the International Gas Turbine Institute for publication in the JOURNAL OF TURBOMACHINERY. Manuscript received by the International Gas Turbine Institute March 9, 1988.

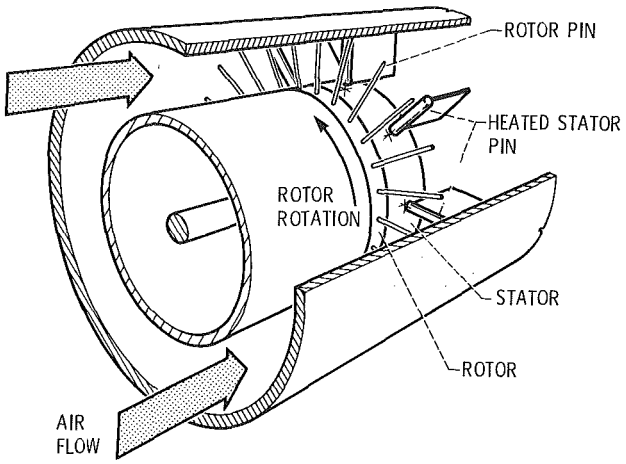

Fig. 1 Schematic of rotor-wake heat transfer facility test section

were phase averaged based on a surface pressure signal synchronized with the vortex-shedding process. It was therefore possible to resolve the velocity information into contributions from periodic (related to vortex shedding) and random (turbulent) contributions. The wake-passing-based phase-locking procedure utilized in the present study and in previous turbomachinery flowfield studies does not resolve the random and vortex-related unsteadiness.

Wake decay downstream of a cylinder moving transverse to the main flow has been studied previously by Pheil and Schroder (1981) using a squirrel-cage arrangement. Only one set of representative turbulence results were presented, however, and the axial measurement station at which these results were obtained was not reported. The wake decay process was the main focus of the paper. Comparison will be made with the wake decay observed in the present study.

Facility and Instrumentation

Test Facility. The experiments were carried out in an annular-flow open-circuit wind tunnel, which has been described in detail previously (Simoneau et al., 1984). Air flow drawn from the test cell passes through a flow-conditioning section and an 8.3 to 1 contraction before entering the test section, which is shown schematically in Fig. 1. The test-section annulus (40.64 cm o.d., 27.05 cm i.d.) was fitted with a turbulence grid, which produced a background free-stream turbulence intensity of about 1.2 percent at the measurement station.

A special feature of this tunnel was the incorporation of a wake-generating rotor for the production of simulated turbine inlet-guide-vane (IGV) wakes. Previous work in this facility was aimed at determining the effects of these wakes on heat transfer in the stagnation region of a downstream circular cylinder (Morehouse and Simoneau, 1986; O'Brien et al., 1986; O'Brien, 1988). For this purpose, there were a total of eight stationary cylinders (two of which were instrumented), located 45 deg apart, mounted downstream of the spoked-wheel rotor. Four of these stators can be seen in Fig. 1. Flowfield measurements of the present study were obtained in midpassage at a circumferential location halfway between these cylinders and at an axial station in the plane of the cylinder leading edges. This measurement phane was eight bar diameters downstream of the rotor.

The wake simulation was accomplished by means of the rotating spoked wheel shown in Fig. 1. The rotor was fitted with 24 equally spaced cylindrical spokes (or bars), which were 3.175 mm in diameter. Bar-passing frequencies f_b could be set from 200 to 2800 Hz, and were nondimensionalized in terms of the bar-passing Strouhal number S_b, defined as

$$S_b = \frac{2\pi f_b d_b}{\bar{U}}$$

where d_b is the bar diameter and $\bar{U}$ is the overall-average velocity at the measurement plane. An additional relevant parameter is the rotor flow coefficient, $\bar{U}/V_b$, which can be obtained directly from the Strouhal number as follows:

$$\frac{\bar{U}}{V_b} = \frac{\bar{U}}{r_b(2\pi f_b/24)} = \frac{24 d_b}{r_b S_b} = 0.4502/S_b$$

where r_b is the midspan radius of the wake-generating bars measured from the rotor centerline (16.92 cm). The factor of 24 arises from the fact that there are 24 bars and therefore 24 blade passings per revolution. The bar-passing Strouhal number and rotor flow coefficient could be varied independently by changing the number of wake-generating bars on the rotor. This was not done in the present study, however.

In order to enable the calculation of phase-averaged data, a fiber-optic sensor was mounted on the outside annulus of the tunnel. This sensor detected the passage of one of the wake-generating bars whose tip had been coated with a silver reflecting paint. The resulting once/rev signal was input to an electronic shaft-angle encoder, which generated a corresponding once/wake signal updated each rotor revolution.

Downstream of the stator row, the air encounters a set of flow straighteners designed to minimize large-scale swirl. Flow velocities in the test section could be set from 10 to 120 m/s, yielding Reynolds numbers based on axial flow velocity and wake-generating bar diameter up to 24,000. An ASME standard sharp-edged orifice located downstream of the test section exit was used to establish and monitor tunnel flow rates.

Nomenclature

d_b = cylinder (or bar) diameter, m
f = frequency, Hz
k = correction factor for deviation from cosine law
N = total number of samples
PDF = velocity probability density function
r_b = midspan bar radius from rotor centerline, m
Re = Reynolds number
s = general quantity to be phase averaged
S = Strouhal number
u = fluctuating axial velocity, m/s
$u(f)$ = power spectral density of axial velocity, $m^2/s^2/Hz$
U = axial velocity, m/s
U_o = actual velocity magnitude, m/s
U_{eff} = effective cooling velocity, m/s
v = fluctuating tangential velocity, m/s
V = tangential velocity, m/s
V_b = midspan bar velocity, m/s
x = axial coordinate, m
α = rotor phase angle, deg
θ = flow angle with respect to wire normal, deg
ξ = angle between wire bisector and the normal to wire 1, deg
ψ = angle between wire bisector and the flow direction, deg

Subscripts

b = bar or bar-passing
1 = wire 1
2 = wire 2

Superscripts

$\bar{}$ = overall (time) average quantity
$\tilde{}$ = phase-averaged quantity

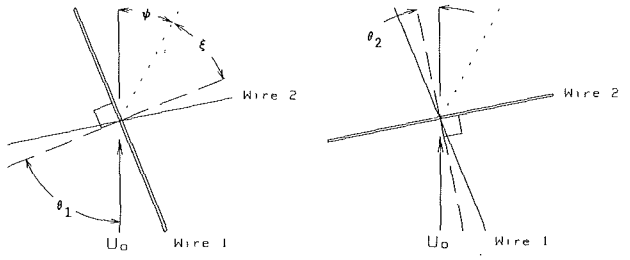

Fig. 2 X-wire angle schematic

Instrumentation and Probes. Steady-state rig operating conditions (temperatures, pressures, flow rates, etc.) were sampled and displayed on a control-room CRT by means of a 256-channel multiplexing digitizer and remote minicomputer, which provided data updates in engineering units approximately every 2 s. High-speed multichannel data acquisition was achieved using an eight-channel system, which provided simultaneous 12-bit digitization with sampling rates up to 1 MHz and 128k of digital memory per channel. The high-speed data acquisition system was controlled by a dedicated desktop computer system, which was also used for data analysis and graphics. Frequency domain data were acquired using a separate hardware-based FFT analyzer, which was also interfaced to the cell desktop computer.

Instantaneous velocity information was obtained using a commercial two-channel hot-wire anemometer system (DISA 55M10). A single wire (TSI model 1211) was used in conjunction with a signal linearizer (DISA 55M25) in obtaining velocity spectra. A standard crossflow X-wire (TSI model 1240) was used for the two-component measurements. Use of an end-flow X-wire was not possible due to limited probe access. Bridge voltage signals from each of these wires were recorded directly using the high-speed data acquisition system. The conversion from voltage to velocity was done in software.

Experimental Procedure

X-Wire Calibration. Hot-wire probe calibration was performed in a free jet. An overheat ratio of 1.6 was used for the calibration and operation of the wires. The crossflow X-wire was calibrated for velocity and angle in the following manner. First, the outer wire was oriented perpendicular to the flow and bridge output voltages were recorded for 20 velocities ranging from 10 to 130 m/s. Angle calibrations were then performed on the outer wire at three different velocities for 20 angular orientations from 0 to 180 deg. Finally, the probe was oriented with both wires at 45 deg to the flow and an additional velocity calibration was performed. An independent angle calibration of the inner wire is not possible with this type of probe due to interference from the outer-wire support prongs.

The calibration analysis consisted of first fitting the velocity calibration data for the outer wire in the normal orientation to a fourth-order polynomial using a least-squares procedure. The two-wire calibration data from the 45-deg orientation was then used to obtain a fourth-order polynomial relating the effective cooling velocity of the inner wire to its voltage output. The effective cooling velocity used in this case was obtained by applying the normal-orientation outer-wire calibration result to the 45-deg outer-wire bridge voltage. The relationship between the actual velocity and the effective cooling velocity was then obtained from a decomposition using Champagne's law (Champagne et al., 1967):

$$U_{\text{eff}}^2 = U_o^2(\cos^2\theta + k^2\sin^2\theta)$$

where U_o is the actual velocity magnitude, θ is the flow angle with respect to the wire normal (see Fig. 2), and k is the correction factor to account for deviation from the Cosine Law. A least-squares procedure was then used to evaluate k from the outer-wire effective-cooling-velocity polynomial in conjunction with the angle calibration data. The k value for the inner wire was assumed to be the same as the outer-wire value (typically 0.22).

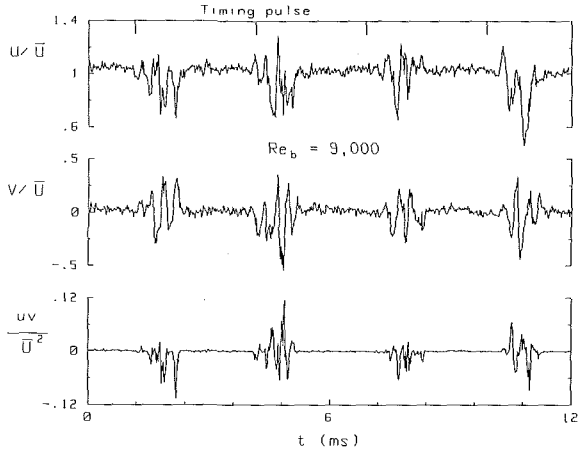

Fig. 3 Instantaneous *U*, *V*, and *uv* velocity records

This calibration procedure resulted in average deviations between predicted and actual jet velocities of 0.5 percent for flow angles between 15 and 75 deg. A pitot-static probe located in the tunnel test section at the same axial station as the X-wire provided an additional in-situ check on the accuracy of the wire calibration. Free-stream velocities indicated by the wire and the pressure probe agreed to within 3 percent for all the cases reported herein.

Two instantaneous components of velocity were obtained from the calibrated X-wire using

$$U_{\text{eff1}}^2 = U_o^2[\cos^2(\xi+\psi) + k_1^2\sin^2(\xi+\psi)] \quad (1)$$

and

$$U_{\text{eff2}}^2 = U_o^2[\cos^2(\xi-\psi) + k_2^2\sin^2(\xi-\psi)] \quad (2)$$

Referring to Fig. 2, ψ is the angle between the wire bisector (depicted by the short-dashed line) and the flow direction. The nominal steady-flow value for this angle is 0 deg since the X-wire is normally oriented with the wire bisector in the flow direction. The angle ξ depends only on the wire geometry and is the angle between the wire bisector and the normal to wire 1. For a standard X-wire, such as the one used in this study, the two wires are mounted perpendicular to each other, and consequently ξ is 45 deg. During operation of the X-wire in the unsteady flow, ψ represents the instantaneous flow angle and U_o the instantaneous velocity magnitude. Instantaneous values for ψ and U_o were obtained from the digital record of bridge voltages by simultaneous solution of equations (1) and (2). The values for U_{eff} were obtained from the polynomial results of the velocity calibrations.

Data Reduction. The primary objective of this study was to obtain measurements of phase-averaged turbulence quantities in the stationary frame behind the wake-generating rotor. The method used to calculate the phase-averaged results can best be explained by referring to Fig. 3. This figure shows a small portion of an instantaneous record of axial and circumferential velocities and uv product normalized with respect to the overall mean axial velocity. In addition, the timing signal used for calculating phase-averaged turbulence statistics is shown at the top of the figure. The time between timing pulses represents one bar-passing cycle, which was approximately 3 ms for the data of Fig. 3. In the figure, the large-scale fluctuations associated with each wake-passing event are evident. In addition, fluctuations associated with the background free-stream turbulence can be seen between the wake-passing events.

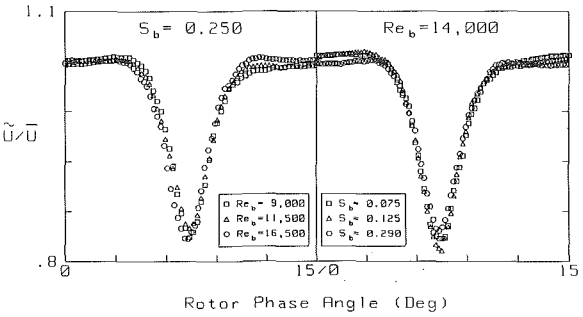

Fig. 4 Phase-averaged axial velocity profiles: (*a*) Reynolds number dependence; (*b*) Strouhal number dependence

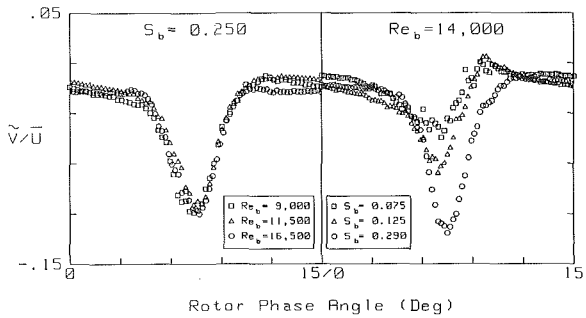

Fig. 5 Phase-averaged tangential velocity profiles: (*a*) Reynolds number dependence; (*b*) Strouhal number dependence

Phase-averaged quantities were formed by dividing each bar-passing cycle into an arbitrary number of bins (typically 50) and entering data from the appropriate portion of the cycle into each bin. The phase-averaged quantity for each bin is then simply the sum of all the entries for that bin divided by the number of entries:

$$\tilde{s}=\frac{1}{N}\sum_{i=1}^{N} s_i(\alpha)$$

where $\tilde{s}$ represents any phase-averaged quantity and (α) indicates at constant phase. For the present study, digital sampling rates were selected in a range from 50 to 200 kHz, depending on bar-passing frequency, such that approximately 900 bar-passing cycles and 140 samples per cycle were included in each digital record.

Velocities were decomposed into an overall mean component, a periodic phase-averaged component, and a random component as follows:

$$U=\bar{U}+\tilde{u}+u=\tilde{U}+u$$

and

$$V=\bar{V}+\tilde{v}+v=\tilde{V}+v$$

This definition for fluctuating velocities distinguishes the periodic "rotor-wake-generated" unsteadiness ($\tilde{u}$, $\tilde{v}$) caused by the wake velocity defect from the unsteadiness arising from all other sources such as turbulence, vortex shedding, mass-flow fluctuations, etc. Fluctuations arising from these other sources (u, v) may be referred to as "unresolved unsteadiness" (Suder et al., 1987; Adamczyk, 1985) since no distinction has been made between contributions from purely random fluctuations and contributions from nonrandom sources such as vortex shedding.

Results

Mean Profiles. Representative normalized phase-averaged axial velocity profiles are presented in Fig. 4(*a*) and 4(*b*). The abscissa in these figures is the rotor-position phase angle α, which for one bar-passing cycle includes 15 deg of rotor circumferential motion.

In Fig. 4(*a*), profiles are shown for several bar Reynolds numbers ranging from 9000 to 16,500 at a fixed bar-passing Strouhal number of 0.25. Recall that the X-wire measurement station is located (8) diameters downstream of the wake-generating bars. The profiles, which are nearly symmetric about the wake centerline, indicate a minimum axial wake velocity of about $0.83\bar{U}$. This value is very close to the normalized mean centerline velocity reported by Cantwell and Coles (1983), Fig. 11) at $x/d=8$ for flow behind a stationary cylinder at a Reynolds number of 140,000. The wake decay correlation of Pfeil and Schroder (1981, equation (24)), however, predicts a wake depth of 0.77 for $x/d=8$. This correlation was based on data acquired in the range $10<x/d<535$ and consequently may not be applicable at $x/d=8$. At this Strouhal number, the circumferential motion of the wake-generating bars appears to have very little effect on the depth of the mean axial profiles.

An independent measurement of wake depth was provided by a small, permanently mounted pitot probe whose nose was located behind the wake-generating bars at $x/d=3$. In this case the bars were stationary and the minimum wake velocity was obtained by positioning one of the bars directly in front of the probe. The minimum axial wake velocity at $x/d=3$ obtained from this measurement was $0.69\bar{U}$, which is also in excellent agreement with the data of Cantwell and Coles.

The depths of the mean axial profiles observed in the present study are similar to the midspan wake depth measured by Sharma et al. (1983) at a measurement station (station 1) located 3.2 trailing-edge diameters (18 mm) downstream of the inlet guide vane of a large-scale axial turbine. The IGV axial chord for this machine was 15.1 cm. The wake depths are also similar to those measured by Raj and Lakshminarayana (1976) for flow in the stationary frame behind the rotor of a large-scale research fan at a measurement station located 6.2 mm downstream of the rotor trailing edge. The rotor chord in this case was 15.2 cm. Comparisons of turbulence quantities obtained in these studies will be made to the present turbulence results.

Wake widths in Fig. 4 measure approximately 3.5 bar diameters, which is slightly larger than is indicated by the intermittency data of Cantwell and Coles at $x/d=8$, but is in excellent agreement with flowfield data obtained by Davies (1976) for flow behind a **D**-shaped cylinder at a Reynolds number of approximately 25,000. Not surprisingly, the far-field cylinder wake-width correlation of Schlichting (1979) significantly underpedicts the wake width at $x/d=8$.

A cross-plot of mean axial velocity profiles at several bar-passing Strouhal numbers ranging from 0.075 to 0.290 at a fixed Reynolds number of 14,000 is shown in Fig. 4(*b*). The figure indicates that over this Strouhal number range, there is no significant dependence of the normalized axial mean profiles on bar-passing frequency.

Tangential mean velocity profiles are presented in Figs. 5(*a*) and 5(*b*) for the same conditions as for the axial profiles of Figs. 4(*a*) and 4(*b*). Positive tangential velocities are opposite to the direction of rotor rotation. In contrast to the axial-profile results, the tangential profiles are very different from their stationary-cylinder counterparts. For a stationary cylinder, mean crossflow velocity profiles are antisymmetric about the cylinder centerline, with a value of zero on the centerline. The present results exhibit a relatively large negative mean tangential velocity in the early and midwake followed by a slightly positive mean tangential velocity near the end of wake-passing. Tangential velocities outside the wake are very close to zero, indicating the near absence of swirl between wakes.

The normalized tangential profiles are nearly independent of Reynolds number, as were the axial profiles. However, there is a strong dependence on bar-passing Strouhal number,

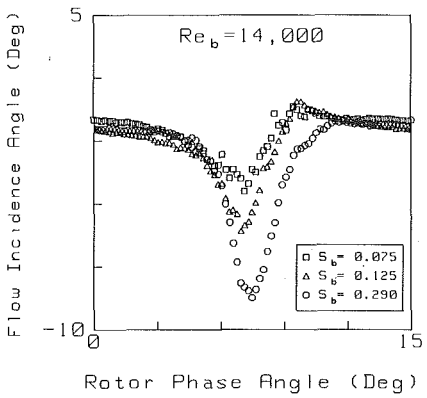

Fig. 6 Phase-averaged flow incidence angles—Strouhal number dependence

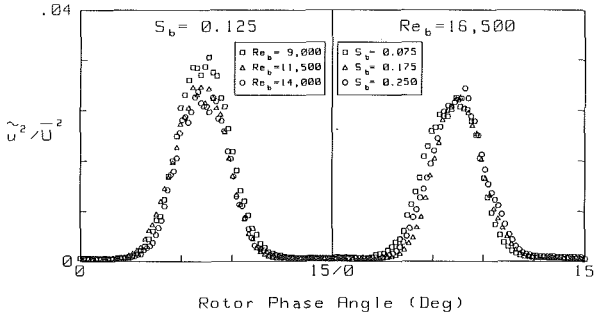

Fig. 7 Phase-averaged axial component of Reynolds normal stress: (*a*) Reynolds number dependence; (*b*) Strouhal number dependence

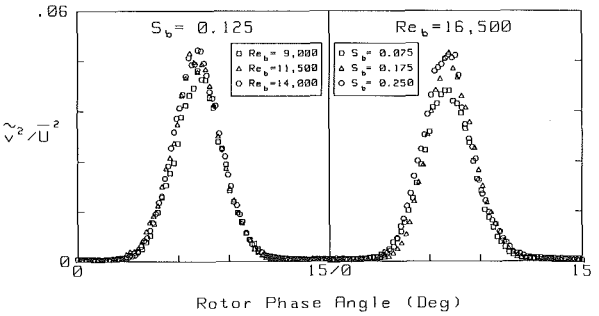

Fig. 8 Phase-averaged tangential component of Reynolds normal stress: (*a*) Reynolds number dependence; (*b*) Strouhal number dependence

as seen in Fig. 5(*b*). Profiles obtained with larger Strouhal numbers are deeper, due to the higher relative tangential bar velocities associated with the high Strouhal numbers. The high-Strouhal-number profiles ($S_b \gtrsim 0.25$) also do not include any positive mean tangential velocities.

Phase-averaged flow incidence angles calculated from the mean profile data of Figs. 4(*b*) and 5(*b*) are presented in Fig. 6. These flow-angle profiles are qualitatively similar to the tangential velocity profiles. The maximum mean flow-angle magnitude of approximately -9 deg occurs in the midwake for the highest Strouhal number case shown.

Reynolds Stresses. Phase-averaged axial Reynolds normal stresses are shown in Figs. 7(*a*) and 7(*b*) for several cases. The values shown are normalized with respect to the square of the overall mean velocity. The profiles are symmetric about the wake centerline with peak values of about 0.035 in midwake, in excellent agreement with the peak *random* contribution to the streamwise global mean Reynolds normal stress reported by Cantwell and Coles (1983, Fig. 27*b*) at $x/d=8$ and also in good agreement with the results of Owen and Johnson (1980, Fig. 20). The measurements of Cantwell and Coles also indicate that the *periodic* contribution to the total streamwise

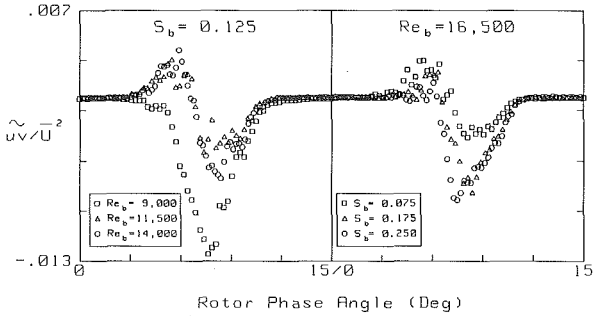

Fig. 9 Phase-averaged Reynolds shear stress: (*a*) Reynolds number dependence; (*b*) Strouhal number dependence

normal Reynolds stress due to vortex shedding is very small across the entire wake width at $x/d=8$ and virtually zero on the centerline. A nearly direct comparison between their random-component results with the "unresolved-component" results of the present study is therefore possible for this quantity.

The normalized axial Reynolds normal stress results shown in Figs. 7(*a*) and 7(*b*) indicate very weak Reynolds- and Strouhal-number dependence, with peak values decreasing slightly with Reynolds number and increasing slightly with Strouhal number.

Phase-averaged tangential Reynolds normal stresses, also normalized with respect to $\bar{U}^2$, are shown in Figs. 8(*a*) and 8(*b*) for the same cases as were presented in Figs. 7(*a*) and 7(*b*). These profiles are also nearly symmetric about the wake centerline, but have peak values close to 0.05. The corresponding random-component peak value from Cantwell and Coles (1983, Fig. 28*b*) is only about 0.044. However, the periodic-component contribution to the crossflow Reynolds normal stress is quite high ($\simeq 0.05$ at $x/d=8$, Cantwell and Coles, 1983, Fig. 28*a*) for a stationary cylinder. For the moving cylinder of the present study, any periodic contribution, such as due to vortex shedding, will be added to the random contributions since the present phase-locking process is based on a bar-passing signal, which is independent of the vortex shedding frequency. Nevertheless, the peak tangential Reynolds normal stress values of Fig. 8 are significantly lower than the sum (at $x/d=8$) of the random and periodic contributions from Cantwell and Coles. This apparent discrepancy is partly due to the difference in reference frames (with respect to the cylinder) between the two cases. There could also be a Reynolds-number effect since the measurements of Cantwell and Coles were obtained at a Reynolds number an order of magnitude higher.

With respect to measurements obtained in large-scale research turbomachines, the Reynolds normal stresses behind the rotating spoked wheel are higher than the corresponding (i.e., at stations of equal mean wake depth) components of the Reynolds normal stress obtained in those studies. Peak values obtained by Sharma et al. (1983) at the first vane exit, when normalized with respect to the absolute-frame local interwake velocity magnitude (see also Butler and Wagner, 1983), were about 0.004 and 0.01 for the streamwise and normal components, respectively, compared to 0.035 and 0.05 in the present study. In the rotor-relative reference frame (Joslyn et al., 1983), however, the streamwise and normal components of Sharma et al. would be about 0.012 and 0.03, still lower than, but much closer to the present results. Peak Reynolds normal stress values obtained by Raj and Lakshminarayana (1976) were 0.01 and 0.008, also significantly lower than the cylinder results.

Reynolds shear stress results (normalized axial-tangential component) are presented in Figs. 9(*a*) and 9(*b*) for the same conditions as in Figs. 7 and 8. For high Reynolds numbers and low bar-passing Strouhal numbers, these profiles exhibit some

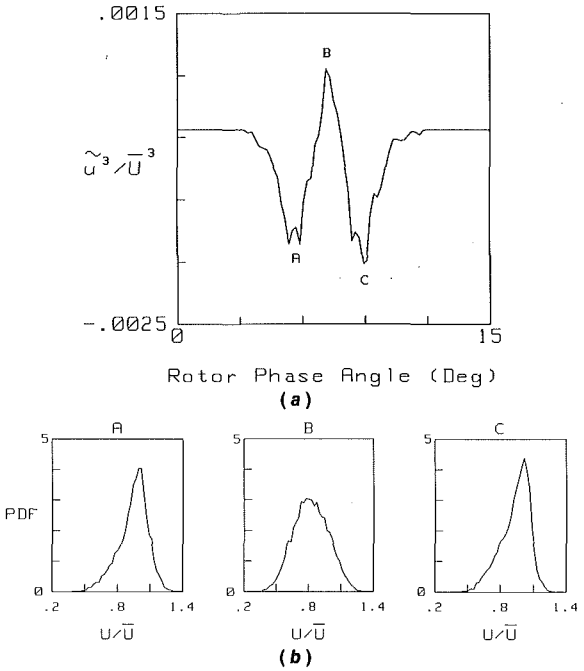

Fig. 10 (*a*) Phase-averaged u triple product: $Re_b = 14{,}000$; $S_b = 0.125$; (*b*) corresponding phase-resolved u probability density functions

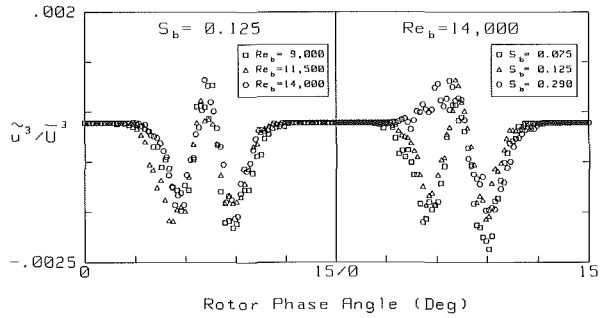

Fig. 11 Phase-averaged u triple product: (*a*) Reynolds number dependence; (*b*) Strouhal number dependence

degree of the antisymmetry (oddness) that would be expected for Reynolds shear stresses in the wake of a stationary cylinder. However, for other cases, the profiles include only negative values. For the cases that do exhibit antisymmetry, the magnitudes of the extreme values compare well with the stationary-cylinder random-component results of Cantwell and Coles ($\simeq 0.004$ at $x/d = 8$). For low Reynolds and/or high Strouhal numbers, however, the peak Reynolds shear stress magnitude is much higher, typically 0.015. Peak values obtained by Sharma et al. for this quantity, in the rotor-relative reference frame, were close to 0.0075. Raj and Lakshminarayana report a similar peak value of 0.007.

The higher levels of turbulent stresses produced by a spoked-wheel wake generator as compared to those measured behind an actual IGV could be responsible for the higher stagnation-line heat transfer obtained by Ashworth et al. (1985) in cascade as compared to the results of Guenette et al. (1989) in an actual rotating turbine stage using the same blade profile.

Higher-Order Moments. Third and fourth-order phase-averaged turbulent correlations were also calculated from the instantaneous velocity records. Gradients of the third-order correlations appear as turbulent transport terms in the conservation equations for turbulent kinetic energy and Reynolds stress. Selected results will be discussed.

A representative low-Strouhal-number triple-product profile for the axial velocity fluctuations, $\tilde{u}^3$, is shown in Fig. 10(*a*). The profile is nearly symmetric (even) about the wake centerline and exhibits two minima in the shear layer ($\alpha \simeq 6$ deg and $\alpha \simeq 9$ deg) and a central peak in the midwake region. The shape of the profile is similar to the $\tilde{u}^3$ profile measured by Fabris (1983) for flow in the far wake of a stationary circular cylinder.

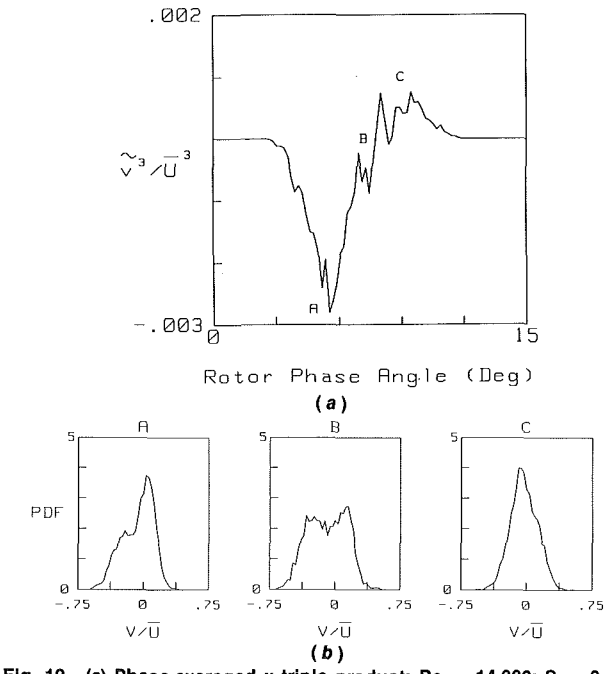

Fig. 12 (*a*) Phase-averaged v triple product: $Re_b = 14{,}000$; $S_b = 0.125$; (*b*) corresponding phase-resolved v probability density functions

Nonzero values of the $\tilde{u}^3$ triple correlation indicate asymmetry in the probability density distributions (PDFs) of u. Three of these probability distributions are shown in Fig. 10(*b*). Each PDF contains u velocity data from a window 0.75 deg of rotor rotation in width, collected over approximately 900 rotor revolutions. The three PDFs shown correspond to the two local minima and the midwake local maximum observed in the $\tilde{u}^3$ profile. Negative skewness is obvious in the PDFs for $\alpha \simeq 6$ deg (corresponding to point A in Fig. 10(*a*)) and $\alpha \simeq 9$ deg (point C), consistent with the relatively large negative values of the u triple correlation at those rotor positions. The PDF for $\alpha \simeq 0$ deg (point B) is nearly unskewed (slight positive skewness), consistent with the relatively small positive value of the $\tilde{u}^3$ triple correlation at this point.

The Reynolds- and Strouhal-number dependence of $\tilde{u}^3$ is depicted in Fig. 11. Over the range covered, dependence on Reynolds number is minimal. There is, however, a fairly strong dependence on Strouhal number, which is characterized by an elimination of the first local minimum ($\alpha \simeq 6$ deg) in the profile.

A profile of $\tilde{v}^3$ triple correlation is shown in Fig. 12(*a*) for the same conditions as for Fig. (10*a*). This profile indicates a relatively large negative value at $\alpha \simeq 6$ deg (point A), near zero at midwake (point B), and slightly positive at $\alpha \simeq 9$ deg (point C). The corresponding PDFs are shown in Fig. 12(*b*). Negative skewness is again observed in the v PDF for $\alpha \simeq 6$ deg (point A). However, a second low-speed peak in the PDF is beginning to emerge. The midwake v PDF (point B) is unskewed but highly bimodal due to vortex-induced periodicity. Similarly biomodal PDFs were observed by Hathaway et al. (1986) in the wake of a transonic axial flow fan. Positive skewness is observed in the $\alpha \simeq 9$ deg (point C) PDF.

As shown in Fig. 13(*a*), the normalized $\tilde{v}^3$ profiles are also nearly independent of Reynolds number. With increasing Strouhal number (Fig. 13(*b*), however, the magnitudes of both the negative and positive extremes increase.

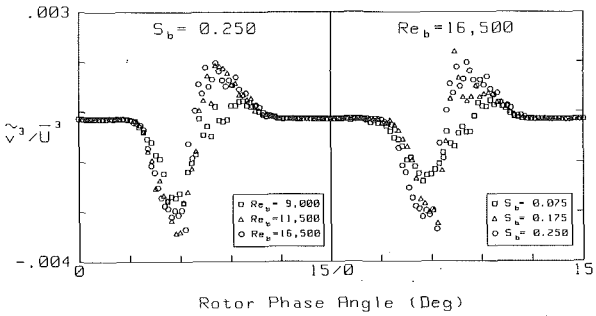

Fig. 13 Phase-averaged v triple product: (*a*) Reynolds number dependence; (*b*) Strouhal number dependence

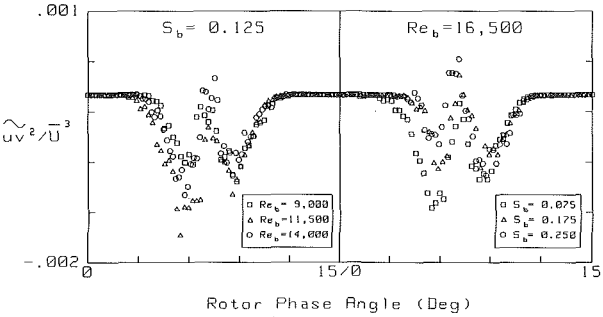

Fig. 14 Phase-averaged uv^2 product: (*a*) Reynolds number dependence; (*b*) Strouhal number dependence

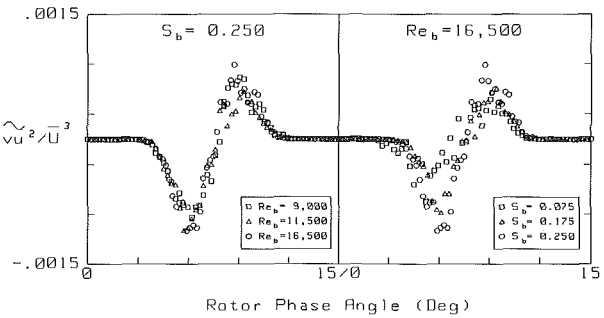

Fig. 15 Phase-averaged vu^2 product: (*a*) Reynolds number dependence; (*b*) Strouhal number dependence

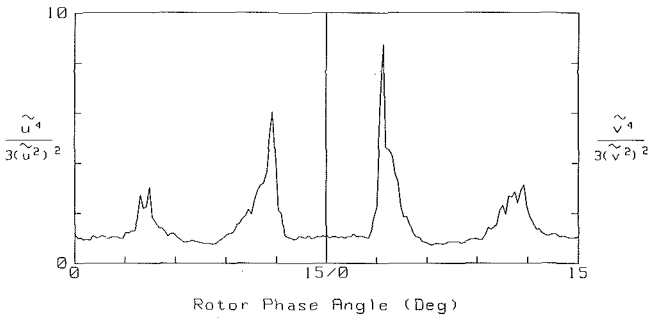

Fig. 16 Phase-averaged flatness factors: $Re_b = 14{,}000$; $S_b = 0.290$; (*a*) axial component; (*b*) tangential component

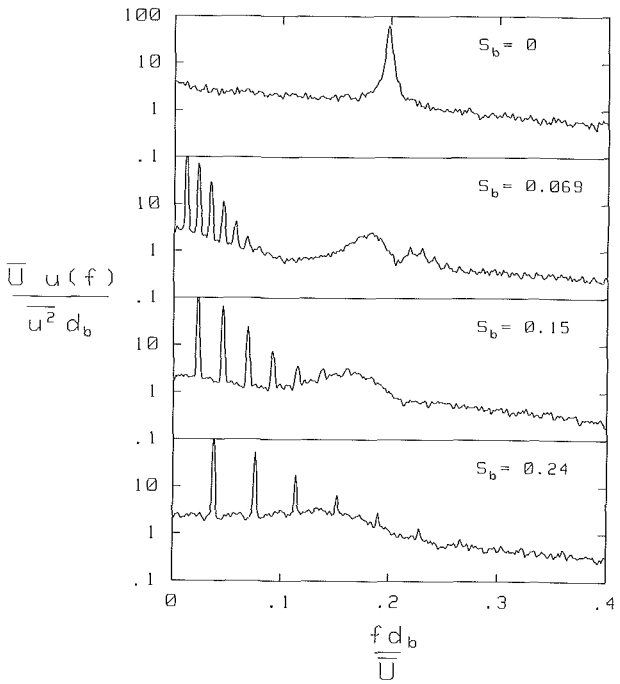

Fig. 17 Wake axial velocity spectra—effect of Strouhal number ($Re_b = 14{,}000$)

Representative profiles of $u\tilde{v}^2$ correlation are presented in Fig. 14. This quantity is also an even function of y for a stationary cylinder. It represents the streamwise turbulent transport of v^2 or the crossflow turbulent tranport of uv. These profiles are similar to the $\tilde{u}^3$ profiles, but lower in magnitude. The Strouhal-number dependence indicated in Fig. 14(*b*) is also similar to the Strouhal-number dependence of the $\tilde{u}^3$ profiles.

Profiles of $v\tilde{u}^2$ correlation are presented in Fig. 15. The shape and Strouhal-number dependence of this correlation is similar to those observed for the $\tilde{v}^3$ correlation, but the magnitudes are smaller. The large crossflow gradients of the $\tilde{v}^3$ and $v\tilde{u}^2$ correlation in the wake indicate the importance of the v fluctuations in the net transport of turbulent energy across the wake.

Representative fourth-order correlations $\tilde{u}^4$ and $\tilde{v}^4$ are shown in Fig. 16. These correlations are normalized with respect to $3(\tilde{u}^2)^2$ and $3(\tilde{v}^2)^2$, respectively. For a normal distribution, the value of this ratio, referred to as the flatness factor, is unity. Values in excess of one are indicative of inhomogeneity in the turbulence intensity field. Large peaks in this quantity occur at rotor phase angles of $\alpha \simeq 4$ deg and $\alpha \simeq 11$ deg near the edge of the shear layer produced by the wake-generating bars. The large peaks are due to the intermittent nature of the flow at these rotor positions. Corresponding average turbulence intensities are actually quite low at these rotor positions as shown in Figs. 7 and 8. Outside of the peaks, the flatness factors are essentially equal to 1.0, indicating a normal distributions of u and v in the undisturbed free stream. In the midwake region, the flatness factors are slightly under 1.0.

Spectra. A series of nondimensionalized power spectra obtained with a single hot wire is presented in Fig. 17. The sensing length of the wire was oriented in the radial direction in this case. The wire is therefore sensitive to fluctuations in the instantaneous streamwise direction. No conditional sampling has been applied to the spectra.

The topmost spectrum was acquired with no rotor motion and one of the wake-shedding cylinders located directly upstream of the wire. A very large (note the logarithmic vertical scale) peak in the spectrum occurs at $fd_b/\bar{U} \simeq 0.2$, the standard subcritical vortex-shedding Strouhal number for a cylinder. Subsequent spectra were obtained with the wake-generating rotor spinning. The numerous peaks at the left of each spectrum represent the primary bar-passing frequency and harmonics.

For low values of bar-passing Strouhal number (e.g., $S_b = 0.069$), there is a bifurcation in the vortex-shedding peak. The higher-frequency peak ($S \simeq 0.22$) in this case is probably due to the higher relative velocity of the cylinder with respect

to the fluid, generating a correspondingly higher vortex-shedding frequency. This results in a vortex-shedding Strouhal number apparently in excess of 0.2 since the abscissa for the spectra is $fd_b/\bar{U}$, where $\bar{U}$ is the overall mean *axial* velocity, which is the same for all the spectra shown. For higher bar-passing Strouhal numbers, the energy associated with vortex shedding is shifted to lower frequencies and becomes broadband from the stationary reference frame viewpoint. This behavior is due to the fact that as the bar-passing Strouhal number is increased, vortices encounter the wire more and more randomly due to the steeper angle at which the wake is convected past the sensing location.

Concluding Remarks

Unsteady flowfield measurements have been obtained in the stationary reference frame behind a rotating spoked-wheel wake generator. Mean axial velocities were found to agree well with those obtained from measurements behind a stationary cylinder and were independent of both Reynolds and bar-passing Strouhal numbers. Tangential-component mean velocity profiles were indicative of the circumferential motion of the wake-generating bars, with increasing magnitudes for higher bar-passing Strouhal numbers. Phase-averaged Reynolds stresses were found to be consistent with related cylinder-wake measurements, but were significantly higher than corresponding (i.e., at stations of equal mean wake depth) measurements of Reynolds stresses obtained in large-scale research turbomachines. The higher levels of turbulent stresses produced by a spoked-wheel wake generator as compared to those measured behind an actual IGV could be responsible for the higher stagnation-line heat transfer obtained by Ashworth et al. (1985) in cascade as compared to the results of Guenette et al. (1989) in an actual rotating turbine stage using the same blade profile. Phase-averaged triple velocity correlations were also calculated from the velocity records. The results for $\tilde{u}^3$ and $\tilde{v}^3$ were shown to be consistent with phase-resolved probability density distributions, revealing the sign and magnitude of skewness in the PDFs. Large crossflow gradients observed in the $\tilde{v}^3$ and $v\tilde{u}^2$ correlations in the wake indicate the importance of the v fluctuations in the net turbulent transport of turbulent energy across the wake. Wake velocity spectra for low bar-passing Strouhal numbers included a peak associated with vortex shedding from the cylindrical wake-generating bars at a shedding Strouhal number of 0.2. For higher bar-passing Strouhal numbers, the energy associated with vortex shedding is shifted to lower frequencies and becomes broadband from the stationary reference frame viewpoint.

References

Adamczyk, J. J., 1985, "Model Equations for Simulating Flows in Multistage Turbomachinery," ASME Paper No. 85-GT-226.

Ashworth, D. A., Lagraff, J. E., Schultz, D. L., and Grindrod, K. J., 1985, "Unsteady Aerodynamic and Heat Transfer Processes in a Transonic Turbine Stage," ASME *Journal of Engineering for Gas Turbines and Power*, Vol. 107, pp. 1022–1030.

Butler, T. L., and Wagner, J. W., 1983, "Application of a Three-Sensor Hot-Wire Probe for Incompressible Flow," *AIAA Journal*, Vol. 21, No. 5, pp. 726–732.

Cantwell, B., and Coles, D., 1983, "An Experimental Study of Entrainment and Transport in the Turbulent Near Wake of a Circular Cylinder," *Journal of Fluid Mechanics*, Vol. 136, pp. 321–374.

Champagne, F. H., Sleicher, C. A. and Wehrmann, O.H., 1967, "Turbulence Measurements With Inclined Hot Wires," *Journal of Fluid Mechanics*, Vol. 28, Part I.

Davies, M. E., 1976, "A Comparison of the Wake Structure of a Stationary and Oscillating Bluff Body, Using a Conditional Averaging Technique," *Journal of Fluid Mechanics*, Vol. 75, pp. 209–231.

Doorly, D. J., 1984, "A Study of the Effect of Wake-Passing on Turbine Blades," OEUL Report No. 1515/84, Oxford Univ., Oxford, United Kingdom.

Doorly, J. J., and Oldfield, M. L. G., 1985, "Simulation of Wake-Passing in a Stationary Turbine Rotor Cascade," AIAA *Journal of Propulsion and Power*, Vol. 1, No. 4, pp. 316–318.

Dunn, M. G., Seymour, P. J., Woodward, S. H., George, W. K., and Chupp, R. E., 1989, "Phase-Resolved Heat-Flux Measurements on the Blade of a Full-Scale Rotating Turbine," ASME JOURNAL OF TURBOMACHINERY, Vol. 111, pp. 8–19.

Fabris, G., 1983, "Third-Order Conditional Transport Correlations in the Two-Dimensional Turbulent Wake," *Physics of Fluids*, Vol. 26, No. 2, pp. 422–427.

Guenette, G. R., Epstein, A. H., Giles, M. B., Haimes, R., and Norton, R. J. G., 1989, "Fully Scaled Transonic Turbine Rotor Heat Transfer Measurements," ASME JOURNAL OF TURBOMACHINERY, Vol. 111, pp. 1–7.

Hathaway, M. D., Gertz, J., Epstein, A., and Strazisar, A. J., 1986, "Rotor Wake Characteristics of a Transonic Axial Flow Fan," *AIAA Journal*, Vol. 24, No. 11, pp. 1802–1810.

Joslyn, H. D., Dring, R. P., and Sharma, O. P., 1983, "Unsteady Three-Dimensional Turbine Aerodynamics," ASME *Journal of Engineering for Power*, Vol. 105, pp. 322–331.

Morehouse, K. A., and Simoneau, R. J., 1986, "Effect of a Rotor Wake on the Local Heat Transfer on the Forward Half of a Circular Cylinder," *Proceedings, 8th International Heat Transfer Conference*, C. L. Tien et al., eds., Hemisphere Publishing Corp., Washington, DC, Vol. 3, pp. 1249–1256.

O'Brien, J. E., 1988, "Effects of Wake Passing on Stagnation Region Heat Transfer," ASME HTD-Vol. 103, pp. 17–28.

O'Brien, J. E., Simoneau, R. J., LaGraff, J. E., and Morehouse, K. A., 1986, "Unsteady Heat Transfer and Direct Comparison to Steady-State Measurements in a Rotor-Wake Experiment," *Proceedings, 8th International Heat Transfer Conference*, C. L. Tien et al., eds., Hemisphere Publishing Corp., Washington, DC, Vol. 3, pp. 1243–1248.

Owens, F. K., and Johnson, D. A., 1980, "Measurements of Unsteady Vortex Flowfields," *AIAA Journal*, Vol. 18, No. 10, pp. 1173–1179.

Pfeil, H., and Schroder, T., 1981, "Decay of the Wake Behind a Cylinder Crossing Rapidly the Flow," AIAA Paper No. AIAA-81-0209.

Raj, R., and Lakshminarayana, B., 1976, "Three Dimensional Characteristics of Turbulent Wakes Behind Rotors of Axial Flow Turbomachinery," ASME *Journal of Engineering for Power*, Vol. 98, pp. 218–228.

Schlichting, H., 1979, *Boundary-Layer Theory*, 7th ed., McGraw-Hill, New York, p. 741.

Sharma, O.P., Butler, T. L., Joslyn, H. D., and Dring, R. P., 1983, "An Experimental Investigation of the Three-Dimensional Unsteady Flow in an Axial Flow Turbine," AIAA Paper No. AIAA-83-1170.

Simoneau, R. J., Morehouse, K. A., VanFossen, G. J., and Behning, F. P., 1984, "Effect of a Rotor Wake on Heat Transfer From a Circular Cylinder," NASA TM-83613.

Suder, K. L., Hathaway, M.D., Okiishi, T. H., Strazisar, T. J., and Adamczyk, J. J., 1987, "Measurements of the Unsteady Flowfield Within the Stator Row of a Transonic Axial-Flow Fan," ASME Paper No. 87-GT-226.

A Quasi-Steady Approach of Wake Effects on Leading Edge Transfer Rates

N. T. Van Dresar

R. E. Mayle

Department of Mechanical Engineering,
Rensselaer Polytechnic Institute,
Troy, NY 12130-3590

Mass transfer experiments are described for a circular cylinder with a steady incident wake flow. Measurements of the velocity, turbulence intensity, intermittency, and integral length scale within the wake are presented together with measurements of the stagnation mass transfer as a function of the cylinder's position in the wake. Comparison of the results indicates that although the increase in mass transfer occurring along the wake centerline depends on the turbulence intensity, length scale, and possibly other factors, the functional relation with respect to the cylinder's lateral position in the wake depends on the intermittency and not turbulence level. In addition, a simple quasi-steady theory is developed to account for the unsteady effects caused by the passing of wakes in the incident flow on the stagnation transfer rate at the leading edge of a gas turbine airfoil.

Introduction

Although the flow through a gas turbine engine is highly unsteady, only recently has its effect on heat transfer captured the interest of those trying to predict turbine component heat loads. In the past, designers always circumferentially mass-averaged the flow and thermal energy leaving a turbine row, which provided, in turn, a "time-averaged" steady flow entering the next row. This, of course, considerably simplified the heat load analysis, and led to the development of rather sophisticated two and quasi-two-dimensional boundary layer calculation programs. Difficulties that may arise from these steady-state analyses were first pointed out by Kerrebrock and Mikolajczak [1] who showed that the gas in the wakes from the airfoils in the preceding row migrates toward the suction side of the airfoils (turbine) in the following row as they pass through the row. This is easy to see by considering the velocity triangles of the leaving flow both within and out of the wake relative to the following row as shown in Figs. 1 and 2. If the wake is relatively cold, as from cooled airfoils, then cool gas drifts toward the suction side and hot gas is "ingested" in the moving wake near the pressure side of the airfoil. Hence, near the suction surface of an airfoil, the unsteady effect of upstream wakes passing through a row is not only one of imposing an unsteady "freestream" temperature on the surface, but also one of producing a convective flow of cool gas toward the surface. This has been sometimes referred to as "phantom cooling" and can result in as much as a 30°C reduction in the time-averaged freestream temperature on the airfoil's suction surface. On the pressure side of an airfoil, the effect of the wake is opposite and at the leading edge, the wake appears to be "cut" as shown in Fig. 3. In addition to the effects just mentioned, wakes produce turbulence of a different intensity and scale than that which generally exists outside them. Hence, the surfaces affected by the wakes also experience a "washing" with flow having different turbulent structures. The effect of this can be substantial, as will be discussed and shown shortly. On the whole, the effect of flow and thermal unsteadiness, a characteristic of all turbines, is quite complex, which until recently is a partial reason for its neglect. The actual reason is more likely, however, that turbine designers are only now beginning to find that even the more sophisticated

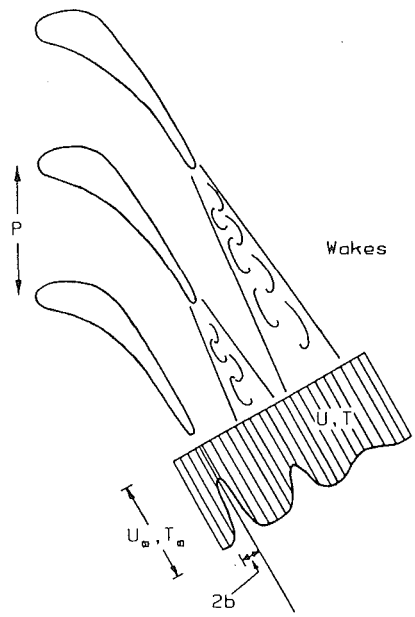

Fig. 1 Airfoil wakes

Contributed by the International Gas Turbine Institute and presented at the ASME Winter Annual Meeting, Boston, Massachusetts, December 13-18, 1987. Manuscript received by the International Gas Turbine Institute December 1987.

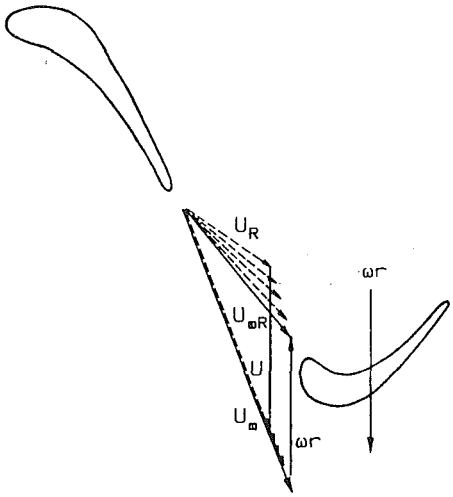

Fig. 2 Velocity triangles at an interrow position

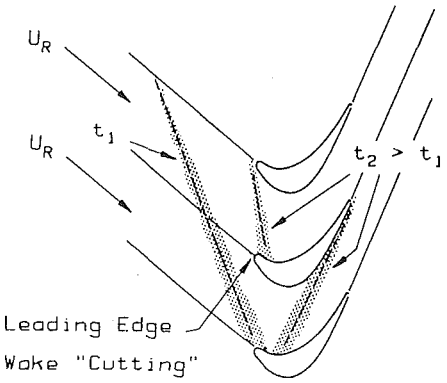

Fig. 3 Schematic of wake movement in airfoil row

computational programs still fail to predict the time-averaged heat loads accurately.

Recently, a number of unsteady heat transfer experiments have been conducted using actual turbine components and facilities that model most of the engine operating conditions. These include the work described by Dunn and his co-workers [2–4] and Guenette et al. [5]. In general, their results contain either time-averaged or time-resolved heat flux measurements on airfoil, endwall, and blade tip surfaces. Dunn et al. [3] have found that variations in time-resolved surface heat flux are large compared to time-averaged values and occur at the fundamental wake-cutting frequency and its harmonics. Guenette et al. also observed a highly unsteady heat flux near the rotor tip where fluctuations of 80 percent across the blade spacing were found. Comparisons of measured time-averaged results with a current calculation program are also presented by Dunn [2] and Dunn et al. [4], and show that the program is unable reliably to predict the heat load over the surface. In particular, the program was found to underestimate the heat load on the suction surface by as much as 30 percent and that on the forward portion of the pressure surface by as much as 100 percent.

Similar experiments have been conducted in a large-scale, low-speed rotating facility by Dring et al. [6]. Although this facility does not model as many of the engine conditions as those described above, they do have the potential to provide the detailed flow information required to understand the complex physics associated with these flows (e.g., see Joslyn et al., [7] and Hodson [8]). Dring et al. report unsteady leading edge pressures as high as +80 percent of the incident relative dynamic pressure. They were also able to distinguish laminar, transitional, and turbulent levels of heat transfer, and determine the location of transition.

The unsteady effects of passing wakes in an airfoil row have been investigated by Doorly et al. [9], Ashworth et al. [10], and Doorly and Oldfield [11]. In each, a rotating wheel of cylinders was used to produce the moving wakes, and again large increases in the surface heat flux were measured at the wake cutting frequency. The increases in the time-averaged heat transfer were attributed to the passing wakes, leading edge separation bubbles, and shock-boundary layer interactions. As suggested by all, further work is required to separate the various effects.

Experiments to evaluate the effect of wake-generated turbulence on turbine cascade heat loads have been conducted by Bayley and Priddy [12] and Wittig et al. [13]. While the first used a rapidly rotating squirrel cage of bars to produce incident turbulence levels up to 30 percent, the second used an upstream airfoil to produce a steady incident flow with an imbedded wake having turbulence levels up to 15 percent. In each case, the increased turbulence was found to have a significant effect on the heat transfer rate. This was most notable in Bayley and Priddy's work on the leading edge, pressure side, and forward suction side where increases by fac-

Nomenclature

b = wake one-half velocity width (from centerline)
$\mathfrak{D}$ = diffusion coefficient
D = diameter of test cylinder
d = diameter of upstream rod
I = intermittency function
L = length scale of turbulence
Nu = Nusselt number
P = pitch of airfoil row
r = radius of turbine wheel
Re = Reynolds number
Sc = Schmidt number
Sh = Sherwood number
T = temperature
TH = threshold for intermittency scheme
Tu = turbulence level
t = test duration
U = mean velocity
u = instantaneous streamwise turbulent velocity
u' = streamwise turbulence component (rms)
v' = lateral turbulence component (rms)
w' = spanwise turbulence component (rms)
x = distance downstream of upstream rod centerline
y = lateral distance from wake centerline (also coordinate in blade-to-blade direction)
$\bar{y}$ = mean value of intermittency distribution
γ = wake intermittency factor
Δ = measured sublimation depth
δ = correction to sublimation depth
θ = wake momentum thickness
ν = kinematic viscosity
ρ = naphthalene density
σ = standard deviation of intermittency distribution
τ = wake passing period
ϕ = angle from stagnation
ω = rotation speed of turbine

Subscripts

R = relative to following row
s = solid
v = vapor
0 = wake centerline
1 = first
2 = second
∞ = mainstream

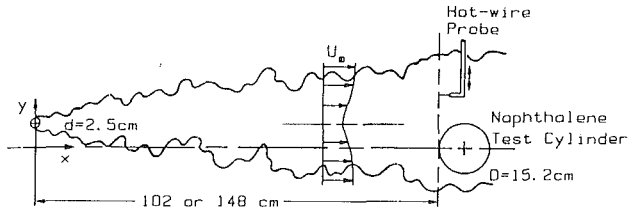

Fig. 4 Experiment

tors of 4–5 were found. Wittig et al., on the other hand, found a large effect on laminar-to-turbulent transition. Along these lines, the interested reader may want to refer to the work by Pfeil et al. [14].

The effect of wake-generated turbulence on the leading edge has been examined by Simoneau et al. [15], O'Brien et al. [16], and Morehouse and Simoneau [17]. This series of experiments was conducted using a rotating spoked wheel followed by a cylindrical test cylinder. In general, they measured time-averaged, wake-induced enhancements in stagnation heat transfer levels of about 10 percent, which were nearly independent of the wake passing frequency and directly related to the integrated time-resolved heat transfer spikes observed at the wake passing frequency. The spikes had peak magnitudes 30–40 percent above the interwake transfer level, and increasing the interwake turbulence level was found to raise both the no-rotor and rotor wake heat transfer data uniformly. In addition, the data suggest that random turbulence and periodic unsteadiness are separate effects.

Interestingly, the effect of oscillating uniform flow on heat transfer to either a flat plate or circular cylinder has been found to be less than 10 percent unless the pulsation amplitude is much greater than the dynamic head of the mean incident flow or unless it affects a laminar to turbulent transition. Work in this area was conducted by Miller [18] and Bayley [19] on flat plates and on cylinders by Andraka and Diller [20] and Gundappa and Diller [21]. In addition, an experiment conducted by Marziale and Mayle [22], which examined the effect of a fluctuating incident angle on the leading edge stagnation transfer rate, also showed a small effect. All of these results are more or less in agreement with existing theory, e.g., compare Marziale and Mayle [22] and Childs and Mayle [23].

The current effort examined the effect of lateral position within the wake, rather than that caused by oscillations in either the magnitude or direction of the flow, on the leading edge transfer rate. In particular, the effect of a wake-generated, variable, incident turbulent structure on the stagnation transfer rate was examined. To investigate this problem, the set of simple, steady-state experiments in Fig. 4 was performed using a circular cylinder to model a turbine blade's leading edge. Measurements of the transfer rates were obtained using a mass transfer technique. A smaller diameter rod was placed upstream of the test cylinder at various lateral positions to produce a two-dimensional, turbulent wake flow closely scaled to that found in present-day turbines.

If the characteristic eddy residence time is much less than the leading edge wake "cutting" time, which it is for most turbine situations, then the unsteady turbine wake flow near stagnation at the leading edge can be modeled using the present quasi-steady approach. Care must be exercised, however, not to extend this type of modeling too far around the leading edge of an actual turbine airfoil where separation bubbles (Doorly and Oldfield [11] and Bellows and Mayle [24]) can form and collapse unsteadily as a result of an oscillating incident flow.

In light of the fact that the present work involves two-dimensional wake flow, the reader should be aware that it by itself is a classical example of free turbulent shear flow which has been extensively studied. The relaxed, equilibrium flow far downstream from the cylinder, $x/d > 400$, is self-preserving and is usually specified by similarity solutions (Townsend [25]). In the near-wake region, $x/d < 400$, the flow is not in equilibrium and is dependent on the wake generating object used. A summary of experimental studies of wake flow is given by Patel [26]. Commonly used quantities for a characteristic velocity are the incident velocity U_∞, and the maximum velocity defect $U_\infty - U_0$. The cylinder diameter and/or wake momentum thickness θ are often used to scale x, the distance downstream from the wake generator and y, the distance from the wake centerline.

Experimental Apparatus and Procedure

The tests were conducted in a low-speed, open-circuit wind tunnel consisting of a centrifugal fan, plenum chamber, and a nozzle followed by the test section. The plenum contained a series of flow management devices to provide a uniform, straight, parallel flow entering the test section. This flow was found uniform to within ± 1 percent except at the walls, and was measured by a pitot-static tube in the test section. Air leaving the tunnel entered the room, mixed with the surrounding air, and circulated back to the fan's inlet. An air conditioner in the room with its sensor placed in the tunnel automatically controlled the air temperature to within ±1°C.

The test section was a 46 cm high by 76 wide rectangular duct, which contained the vertically positioned naphthalene test cylinder. A turbulent wake was created upstream of the naphthalene cylinder by a vertically mounted rod. The rod had a diameter of 2.5 cm and was positioned at either 102 or 148 cm upstream (x/d = 40 and 58) from the leading edge of the test cylinder. Lateral positioning of the upstream rod relative to the naphthalene cylinder was variable, which made it possible to obtain mass transfer data at various positions within the wake. The test cylinder had a 15.2 cm diameter and was centered in the test section. Although the length-to-diameter ratio of the test cylinder is rather small, the flow around the central portion is two dimensional. In a previous investigation by the present authors [27], the extent of the horseshoe vortex flow was found to be about 1/5 of a diameter from the ends of the test cylinder. The cylinder was constructed with a removable central test section. This section was 10 cm long and had a 6.4 mm thick, 7.6 cm wide naphthalene band cast into its circumference.

Profile measurements of the napthalene surface were made using a rotary milling head and four displacement transducers. The central test section of the cylinder was positioned onto an alignment plate attached to the rotary head. The transducers were a lever type, which could measure to within 1 μm using approximately 2.5 gms of gaging pressure. Two of the gages were mounted directly to the same table as the rotary head and contacted the outer steel rims of the test section. The other two contacted the naphthalene surface and were mounted to a vertical cross slide mounted to the table. Initial adjustments of the transducers were made to position all of the transducers' contact points along a common line parallel to the axis of the test section. With this arrangement, the position of the naphthalene surface relative to the rims could be obtained by combining the outputs of the transducers on the naphthalene with those on the two rims. Depth measurements before each test run were subtracted from those after to obtain the local mass loss. The reader is referred to Marziale [28] for further details concerning casting and measurement of the naphthalene test surface.

Both the mass transfer tests and surface measurements were conducted at a nominal temperature of 19°C. During the test, temperatures were measured at 1 min intervals by a ther-

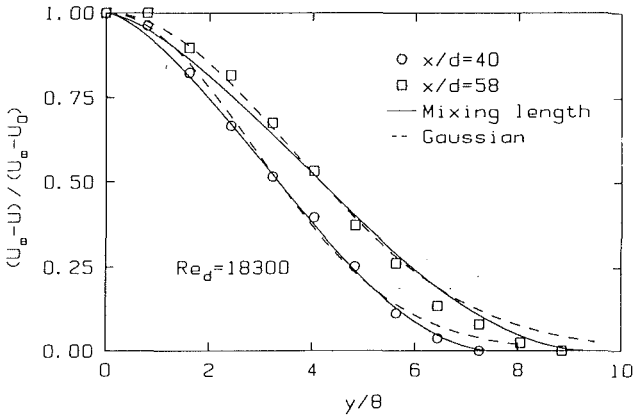

Fig. 5 Mean velocity profiles

mocouple placed in the flow. The density of the naphthalene vapor at the surface was determined for each measured temperature using Sogin's [29] vapor pressure–temperature relation and the ideal gas law. These were then averaged for the entire test interval to obtain the average density of naphthalene vapor at the surface, ρ_v. Calculations of the naphthalene concentration of the incident flow indicated that the maximum during the test were less than 1.5 percent of that at the surface and could be neglected.

The Sherwood number was calculated from

$$\mathrm{Sh} = \frac{\rho_s(\Delta - \delta)D}{\rho_v t \mathfrak{D}}$$

where ρ_s is the density of the solid naphthalene, Δ is the measured sublimation depth, t is the test duration time, and D is the naphthalene cylinder diameter. The quantity δ is a correction for the mass lost during the measurement time by an experimentally determined sublimation rate. Typical values for δ and t were 0.2 mm and 6–8 h, respectively. The diffusion coefficient of naphthalene in air $\mathfrak{D}$ was determined using the Schmidt number Sc and the kinematic viscosity of air ν, i.e., $\mathfrak{D} = \nu/\mathrm{Sc}$. Consistent with Sogin and others, a Schmidt number of 2.5 was used. Sherwood numbers at the wake centerline were repeatable to within ± 3 percent. Repeatability was not as good at offset positions near the wake half-width, where variations as high as ± 8 percent occurred.

All tests were run at a Reynolds number Re_d = 18,300 based on the incident flow velocity and upstream rod diameter and with a freestream turbulence level of about 0.3 percent. The corresponding Reynolds number Re_D for the test cylinder was 110,000. Mean velocity measurements were made using a pitot-static probe, while a Thermo-Systems 1051 hot-wire anemometer system was utilized for turbulence measurements. The streamwise turbulence component was measured with a TSI Model 1210 straight probe. A Model 1213 45 deg angled probe was used to measure the vertical and lateral turbulence components. A traversing device was used for accurate positioning of the hot-wire probes. All velocity measurements were made with the naphthalene test cylinder removed from the wind tunnel in a plane corresponding to the leading edge of the cylinder and perpendicular to the mean flow direction.

A microcomputer equipped with a 12-bit analog-to-digital converter was utilized for data acquisition from the anemometer. The microcomputer was capable of storing a sample size of 23.5 kilobytes. A spectrum analysis of the hot-wire response indicated a maximum turbulence frequency of approximately 5 kHz. The data were sampled at a rate equal to twice this maximum frequency such that the Nyquist criterion was satisfied.

The intermittency distributions were obtained via digital analysis of the stored hot-wire data. At each data point, first and second derivatives of the u velocity component with respect to time were compared to threshold values and the corresponding value for the intermittency function I was specified as follows:

$$I = 1, \quad \begin{cases} \text{if } |\partial u/\partial t| \geq TH_1 \\ \text{or } |\partial u^2/\partial t^2| \geq TH_2 \end{cases}$$
$$I = 0, \quad \text{otherwise.}$$

The intermittency is then a simple time average of the intermittency function. This technique is similar to the "retail" algorithm used by Murlis, et al. [30] in a turbulent boundary layer except that their algorithm was applied to vorticity fluctuations instead of velocity as is done in the present work. The chosen threshold values, TH_1 and TH_2, were slightly less than the maximum levels that still allowed an intermittency of zero in the irrotational flow outside of the wake boundary.

The two-threshold discrimination scheme underestimates the true intermittency factor due to the behavior of high-frequency velocity fluctuations, which are intermittent even in fully turbulent flows (see Sandborn [31]). It was necessary to correct the measured intermittency distributions at x/d = 40 and 58 by factors of 0.9 and 2.5 percent, respectively, in order to obtain intermittency factors of unity at the wake centerline. This value at the centerline was verified by visual observation of the hot-wire response on an oscilloscope.

Integral length scales were obtained by sampling the hot-wire response to turbulent fluctuations and autocorrelating the sampled data. Due to the limited computer storage capabilities, the resulting sampling time is shorter than desired for highly repeatable results. Under these conditions, accurate autocorrelations were obtained by using a large number of samples, as suggested by Frenkiel and Klebanoff [32].

Results

The mean velocity profiles, in the wake of the 2.5 cm rod, as measured in the plane corresponding to the leading edge of the test cylinder, are shown in Fig. 5 for x/d = 40 and 58. The wake momentum thickness θ, determined by numerical integration of the mean velocity profile, the maximum velocity deficit $(U_\infty - U_0)/U_\infty$, and the ratio of wake width to test cylinder diameter $4b/D$, are tabulated below:

x/d	θ/d	$(U_\infty - U_0)/U_\infty$	$4b/D$
40	0.62	0.16	1.38
58	0.62	0.13	1.72

The moment thicknesses are in good agreement with a value calculated using a drag coefficient for a circular cylinder [33]. The mean velocity profiles have been fitted with Gaussian distributions, which fit Townsend's self-preserving far-wake measurements and with the theory based on Prandtl's mixing length [33]. While the measurements at x/d = 40 fit the mixing length theory surprisingly well, the results at x/d = 58, especially at the outer region of the wake, do not fit either theory as well. This is believed to be the result of blockage effects in the test section.

Distributions of single-component turbulence levels (u'/U, v'/U, and w'/U), where the turbulence components are root-mean-square values and U is the local mean velocity, are shown in Fig. 6. At both x/d = 40 and 58, the components are of approximately the same magnitude, indicating that the turbulence is nearly isotropic in the wake at these positions. Careful observation of the u' and w' distributions, along with the mean velocity distribution from Fig. 5, reveals that the maximum turbulent velocity fluctuations occur away from the

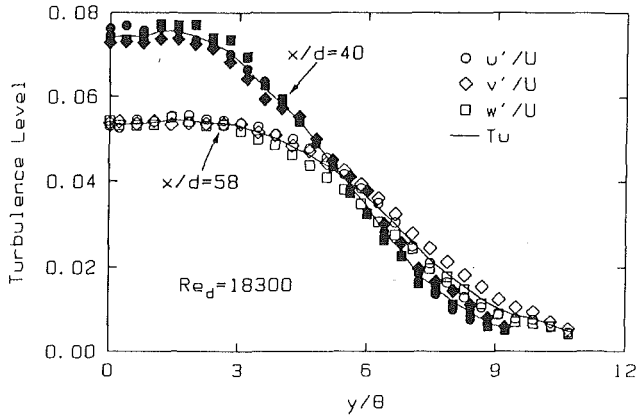

Fig. 6 Turbulence profiles

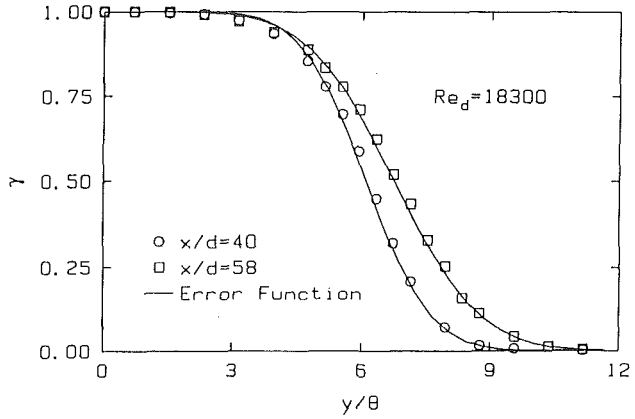

Fig. 7 Intermittency profiles

centerline of the wake. Similar trends, although at differing intensity levels, have been observed by Townsend [25] and Narasimha and Prabhu [34]. Also shown in Fig. 6 are lines indicating the turbulence level Tu for both locations. This turbulence level is defined by the three fluctuating velocity components and the local mean velocity

$$Tu = \frac{1}{U}\sqrt{\frac{1}{3}\left[u'^2 + v'^2 + w'^2\right]}$$

The measured distribution of intermittency γ (the fraction of time that the incident flow consists of wake generated turbulence) is shown in Fig. 7. The data symbols represent the results from the two-threshold intermittency scheme corrected to $\gamma = 1$ at the wake centerline. The lines indicate an error function fit of the corrected data having the form used by Gartshore [35]

$$\gamma = \frac{1}{2}\left[1 - \text{erf}\left(\frac{y-\bar{y}}{\sqrt{2}\sigma}\right)\right]$$

where $\bar{y}$ and σ are the mean value and standard deviation, respectively, and are tabulated below. Results of intermittency measurements in wake flows by Thomas [36] and Townsend [37] are included for comparison.

x/d	$\bar{y}$ (cm)	σ (cm)	$\bar{y}/b$	$\sigma/\bar{y}$
40	3.80	0.76	1.8	0.20
58	4.20	1.00	1.6	0.24
160	Thomas [36]		1.7	0.21
160	Townsend [37]			0.38

An experimental and theoretical study by Corrsin and Kistler [38] suggests that a unique value of $\sigma/\bar{y}$ exists for wake flows (and also for boundary layers and jets). The present results are in good agreement with Thomas' results, which is quite different from Townsend's.

The integral length scale measurements were restricted to the wake centerline where the intermittency is unity. The length scale L and length scale-to-diameter ratios at the two downstream locations are provided below:

x/d	L (cm)	L/d	L/D
40	2.5	1.0	0.16
58	3.5	1.4	0.23

The average eddy size in the wake was approximately equal to the upstream rod diameter at the upstream position and increased by 40 percent at the downstream location. Low turbulence intensities, coupled with low frequency transients in the mainstream flow, prevented accurate measurement of the mainstream length scale.

Initial mass transfer tests were conducted without the upstream rod in position. The resulting mass transfer rate in the form of a Sherwood number is plotted in Fig. 8 against the angular position ϕ around the test cylinder. The results of Kestin and Wood [39], corrected to the present work's Reynolds number, and Frössling's [40] theory with Sc = 2.5 (see Marziale and Mayle [22]) are also shown in the figure. The theory, which is good only for the forward portion of the cylinder, is in excellent agreement with the present results. Kestin and Wood's data is also in good agreement at stagnation, differing by about 2 percent. Beyond separation, the present results are substantially higher than Kestin and Wood's. This is due to the small height of the naphthalene band on the test cylinder combined with large-scale spanwise transport of mass in the separated flow, an effect substantiated by Marziale [28]. The measured Sherwood number at stagnation, $\phi = 0$ deg, is 534 and will be considered the value one would obtain far away from the wake, i.e., $Sh_\infty = 534$. Spanwise variations in the mass transfer along a 5 cm portion of the stagnation line were less than ± 3 percent and were not considered significant. Besides being symmetric about stagnation, the data also indicates that the leading edge boundary layer separates from the cylinder at an angle of about 80 deg.

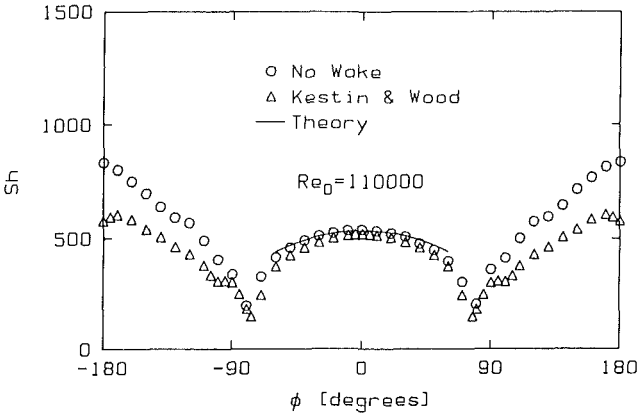

Fig. 8 Freestream mass transfer distribution

The circumferential mass transfer distributions around the cylinder for two lateral positions in the wake at $x/d = 40$ are shown in Figs. 9 and 10. Figure 9 presents the results obtained for the cylinder positioned on the wake centerline, and shows high rates of mass transfer, symmetry about stagnation, and a delayed separation as a result of the higher incident turbulence. For this situation, the measured Sherwood number at stagnation is $Sh_0 = 699$, which is 31 percent higher than that obtained without the rod. Also shown are data from Kestin and Wood for a uniform incident flow having a similar tur-

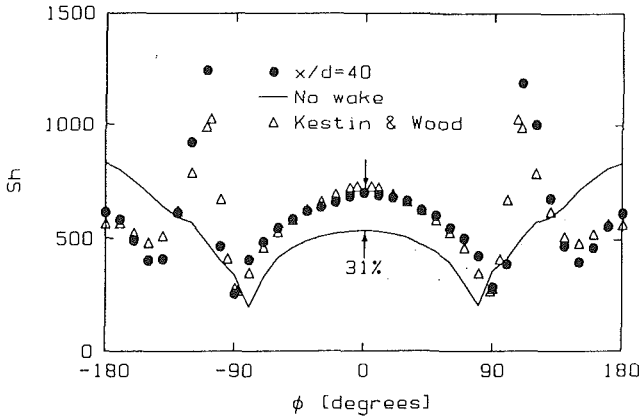

Fig. 9 Mass transfer at wake centerline

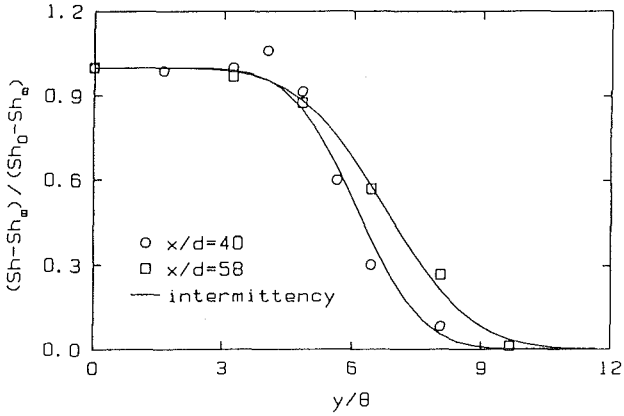

Fig. 11 Stagnation mass transfer distribution

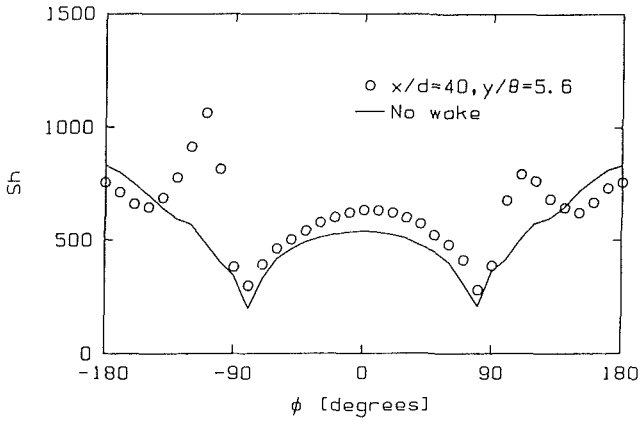

Fig. 10 Offset wake mass transfer

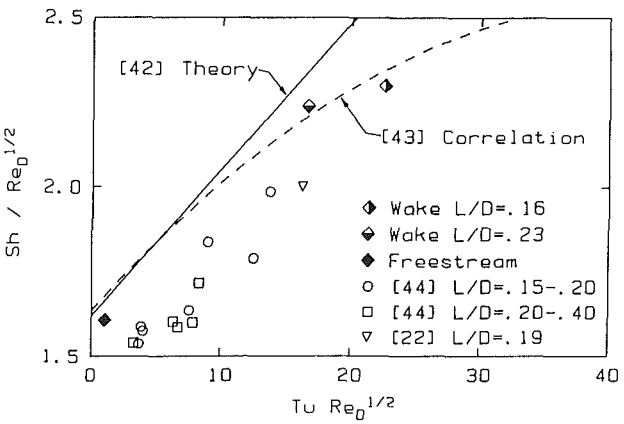

Fig. 12 Mass transfer versus turbulence level

bulence level (7 percent). Their data have been adjusted to the present wake centerline Reynolds number. It is seen that this distribution is very similar to the present results. Figure 10 presents the Sherwood number distribution with the cylinder off the centerline of the wake at a position of $y/\theta = 5.6$. In this position, the incident shear flow causes an asymmetric mass transfer distribution. The maximum value on the forward portion of the cylinder, however, is still near $\phi = 0$ deg. Using the theory presented by Tsien [41], the calculated shift in the stagnation position as a result of the incident shear flow was found to be only 2 deg. Similarly shaped distributions were obtained for various lateral positions at $x/d = 58$. The centerline stagnation Sherwood number at $x/d = 58$ was $Sh_0 = 694$, which is nearly the same as at $x/d = 40$.

The distribution of Sherwood number at stagnation is plotted in Fig. 11 versus lateral position in the wake. In this plot, the difference between the Sherwood number at the various positions, Sh, and that without the wake, Sh_∞ has been normalized by the difference using the centerline value, $Sh_0 - Sh_\infty$. The data points represent the average of 3–5 tests at each location. Most important, however, is that the lines drawn in the figure are the error function curve fits to the intermittency data as shown in Fig. 7. From this, it appears that the mass transfer distribution is related to the fraction of time that the incident flow consists of wake generated turbulence. This result can be shown theoretically, if the time-averaged mass transfer (Sherwood number) is assumed to be the time-averaged sum of two components: (1) that associated with the mass transfer in the turbulent core of the wake, and (2) that associated with the mass transfer outside the wake. Then, the time-averaged Sherwood number can be easily shown to be given by

$$Sh = \gamma Sh_0 + (1-\gamma)Sh_\infty$$

This can be rearranged as

$$\gamma = (Sh\text{-}Sh_\infty)/(Sh_0 - Sh_\infty)$$

which is exactly the result shown experimentally in Fig. 11.

The stagnation mass transfer rates on the wake centerline and in the mainstream are plotted in Fig. 12 as functions of the incident turbulence level (as defined above) and Reynolds number Re_D, based on the local incident velocity. Also shown are the theory of Smith and Kuethe [42], an empirical correlation by Lowery and Vachon [43], and the experimental results from Yardi and Sukhatme [44] and Marziale and Mayle [22] for grid-generated turbulence with similar values of the turbulence length scale-to-diameter ratios L/D.

It should be noted that [42–44] and [22] use the streamwise component only to define Tu, i.e., $Tu = u'/U$. The heat-mass transfer analogy was used to convert the heat transfer results of [42–44] into the present format. The theoretical result, which does not account for an effect of length scale, is shown only to reflect the trend and average value for most of the available data on stagnation heat and mass transfer with incident turbulence, e.g., see Lowery and Vachon. Typical data scatter about this line is about ±10 percent for $TuRe_D^{1/2} < 12$. At higher values of $TuRe_D^{1/2}$, experimental data tend to fall below the theory, as is indicated by Lowery and Vachon's correlation. The results on the wake centerline for $x/d = 40$ and 58 agree very well with the correlation. The experimental results of others for grid-generated turbulence with the same length scale-to-diameter ratio as the present results are seen to fall well below Smith and Kuethe's theory. As shown by Yardi and Sukhatme, the augmentation of heat or mass transfer is less than optimum for length scales greater than about ten

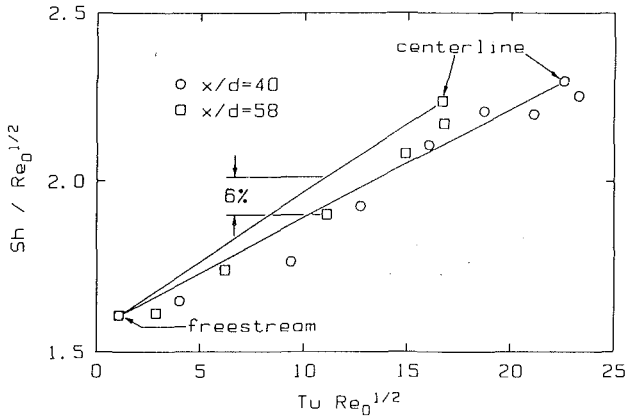

Fig. 13 Wake mass transfer versus turbulence level

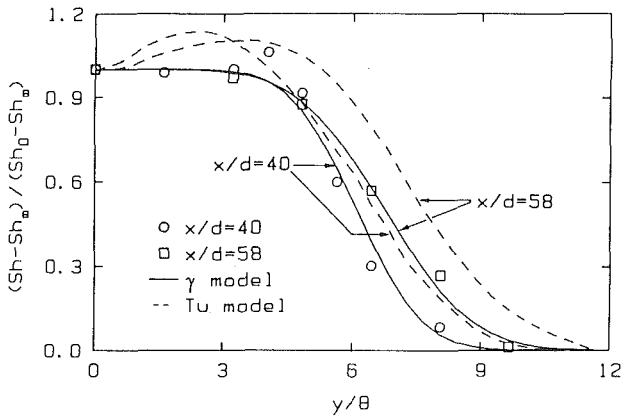

Fig. 14 Turbulence model predictions

boundary layer thicknesses, which is certainly the case for the present results. The centerline result at $x/d = 58$, while falling below the theory on Fig. 12, is high compared to the rest of the data. The cause of this is not presently understood. Traci and Wilcox [45] have also examined the effect of length scale on stagnation transfer rates and suggest that there is little effect for large-scale turbulence, which may be the case for the result at $x/d = 58$.

In Fig. 13, the mass transfer rates at the various lateral wake positions are plotted as functions of the local turbulence levels using the grid-turbulence format of the previous figure. The lines drawn in the figure connect the data points from the wake centerline with the freestream data point. Although the relation between mass transfer and turbulence is approximately linear for each downstream location, predictions of the mass transfer distributions using the measured turbulence levels and the linear approximation are not as good as those using the intermittency results. These comparisons are shown in Fig. 14. Although not shown, it should be noted that these conclusions will also be reached if the freestream velocity instead of the local velocity is used to define Tu and Re. This result does not imply, however, that the turbulence level is not important. Indeed, the turbulence structure, of which the turbulence level is one characterizing parameter, determines the mass transfer in both the core of the wake and outside, i.e., Sh_0 and Sh_∞.

The present results suggests a rather simple, quasi-steady model for determining the time-averaged stagnation heat load on turbine airfoil leading edges. If τ is the wake passing period, then the time-averaged Nusselt number is

$$\overline{Nu} = \frac{1}{\tau}\int_t^{t+\tau} Nu\, dt = Nu_\infty + (Nu_0 - Nu_\infty)\int_0^1 \gamma d(y/P)$$

where $P = \omega r \tau$ is the pitch of the upstream row of air-foils and y is the coordinate in the direction of the measured pitch. If the wake cutting angle is not too acute, and if it is assumed that the intermittency distribution does not change rapidly in the mainflow direction, which is true for most gas turbine applications, then it does not matter whether y is measured normal to the wake or in the blade-to-blade direction. The last equality in the above expression also implies that adjacent wakes have not merged. This model, of course, requires that the intermittency distribution in the wake, $\gamma = \gamma(x, y)$ such as shown in Fig. 7, is known.

In addition, the functional dependence of Nusselt number on Reynolds number and turbulence structure must be known, e.g., Nu = Nu (Re, *Tu*, *L/D*) analogous to Fig. 12, so that Nu_0 and Nu_∞ can be obtained, e.g., $Nu_0 = Nu_0$ [Re_0, Tu_0, $(L/D)_0$] and $Nu_\infty = Nu_\infty[Re_\infty, Tu_\infty, (L/D)_\infty]$. Using Nu, Nu_0, and Nu_∞ as measured by O'Brien et al. [16] together with the above expression for the time-averaged Nusselt number, one calculates that the wake width in their experiments was about 0.3 times their pitch, i.e., $4b/P = 0.3$, which is in good agreement with the time-resolved data shown in their Fig. 4(*b*). In addition, as found in [16], this simple model provides a time-averaged stagnation heat load, which is independent of the wake passing frequency for a given wake pitch.

Conclusions

Mass transfer measurements on a cylinder positioned at various locations within the wake indicate that the mass transfer at stagnation is intimately connected to the turbulence level, length scale, and intermittency. In particular, it was found that although the level of mass transfer with the cylinder placed in the turbulent core of the wake depends, at the very least, on the turbulence level and length scale, the distribution of mass transfer relative to the lateral position in the wake depends on the intermittency. That is, the mass transfer distribution depends on the fraction of time that the incident flow contains wake-generated turbulence.

Combining this result with the concept that wakes from the upstream row of airfoils are "cut" by the following airfoil's leading edge, a simple quasi-steady model has been proposed for the time-averaged stagnation heat load caused by wake-generated turbulence.

References

1 Kerrebrock, J. L., and Mikolajczak, A. A., "Intra-stator Transport of Rotor Wakes and Its Effect on Compressor Performance," ASME *Journal of Engineering for Power*, Vol. 92, No. 4, 1970, pp. 359–368.

2 Dunn, M. G., "Heat-Flux Measurements for the Rotor of a Full-Stage Turbine: Part 1 – Time-Averaged Results," ASME JOURNAL OF TURBOMACHINERY, Vol. 108, No. 1, July 1986, pp. 90–97.

3 Dunn, M. G., George, W. K., Rae, W. J., Woodward, S. H., Moller, J. C., and Seymour, P. J., "Heat-Flux Measurements for the Rotor of a Full-Stage Turbine: Part 2 – Description of Analysis Technique and Typical Time-Resolved Measurements," ASME JOURNAL OF TURBOMACHINERY, Vol. 108, No. 1, July 1986, pp. 98–107.

4 Dunn, M. G., Martin, H. L., and Stanek, M. J., "Heat Flux and Pressure Measurements and Comparison With Prediction for a Low-Aspect-Ratio Turbine Stage," ASME JOURNAL OF TURBOMACHINERY, Vol. 108, No. 1, July 1986, pp. 108–115.

5 Guenette, G. R., Epstein, A. H., Norton, R. J. G., and Yuzhang, Cao, "Time Resolved Measurements of a Turbine Rotor Stationary Tip Casing Pressure and Heat Transfer Field," AIAA Paper No. AIAA-85-1220, 1985.

6 Dring, R. P., Joslyn, H. D., Hardin, L. W., and Wagner, J. H., "Turbine Rotor–Stator Interaction," ASME *Journal of Engineering for Power*, Vol. 104, No. 4, 1982, pp. 729–742.

7 Joslyn, H. D., Dring, R. P., and Sharma, O.P., "Unsteady Three-Dimensional Turbine Aerodynamics," ASME JOURNAL OF ENGINEERING FOR POWER, Vol. 105, No. 2, 1983, pp. 322–331.

8 Hodson, H. P., "Measurements of Wake-Generated Unsteadiness in the Rotor Passages of Axial Flow Turbines," ASME *Journal of Engineering for Gas Turbines and Power*, Vol. 107, No. 2, 1985, pp. 467–476.

9 Doorly, D. J., Oldfield, M. L. G., and Scrivener, C. T. J., "Wake-Passing in a Turbine Rotor Cascade," *Heat Transfer and Cooling in Gas Turbines*, AGARD Conf. Preprint No. 390, Bergen, Norway, May 6–10, 1985.

10 Ashworth, D. A., LaGraff, J. E., Schultz, D.L., and Grindrof, K. J., "Unsteady Aerodynamic and Heat Transfer Processes in a Transonic Turbine Stage," ASME *Journal of Engineering for Gas Turbines and Power*, Vol. 107, No. 4, 1985, pp. 1011–1030.

11 Doorly, D. J., and Oldfield, M. L. G., "Simulation of the Effects of Shock Wave Passing on a Turbine Rotor Blade," ASME *Journal of Engineering for Gas Turbines and Power*, Vol. 107, No. 4., 1985, pp. 998–1006.

12 Bayley, F. J., and Priddy, W. J., "Effects of Freestream Turbulence Intensity and Frequency on Heat Transfer to Turbine Blading," ASME *Journal of Engineering for Power*, Vol. 103, No. 1, 1981, pp. 60–64.

13 Wittig, S., Dullenkopf, Schulz, A., and Hestermann, R., "Laser-Doppler Studies of the Wake-Effected Flow Field in a Turbine Cascade," ASME JOURNAL OF TURBOMACHINERY, Vol. 109, No. 2, 1987, pp. 170–176.

14 Pfeil, H., Herbst, R., and Schröder, T., "Investigation of the Turbulent Transition of Boundary Layers Distuned by Wakes," ASME *Journal of Engineering for Power*, Vol. 105, No. 1, 1983, pp. 130–137.

15 Simoneau, R.J., Morehouse, K. A., VanFossen, G. J., and Behning, F. P., "Effect of a Rotor Wake on Heat Transfer From a Circular Cylinder," NASA TM 83613, Aug. 1984.

16 O'Brien, J. E., Simoneau, R. J., LaGraff, J. E., and Morehouse, K. A., "Unsteady Heat Transfer and Direct Comparison to Steady-State Measurements in a Rotor-Wake Experiment," *Proceedings of the Eighth International Heat Transfer Conference*, San Francisco, CA 1986, pp. 1243–1248.

17 Morehouse, K. A., and Simoneau, R. J., "Effect of a Rotor Wake on the Local Heat Transfer on the Forward Half of a Circular Cylinder," *Proceedings of the Eighth International Heat Transfer Conference*, San Francisco, CA, 1986, pp. 1249–1255.

18 Miller, J. A., "Heat Transfer in the Oscillating Turbulent Boundary Layer," ASME *Journal of Engineering for Power*, Vol. 91, No. 4, 1969, pp. 239–244.

19 Bayley, F. J., Edwards, P. A., and Singh, P. P., "The Effect of Flow Pulsations on Heat Transfer by Forced Convection From a Flat Plate," International Heat Transfer Conference, Boulder, CO, Aug. 1961.

20 Andraka, C. E., and Diller, T. E., "Heat Transfer Distribution Around a Cylinder in Pulsating Crossflow," ASME *Journal of Engineering for Gas Turbines and Power*, Vol. 107, 1985, pp. 976–982.

21 Gundappa, M., and Diller, T.E., "The Effects of Freestream Turbulence and Flow Pulsation on Heat Transfer From a Cylinder in Crossflow," ASME WAM, Miami Beach, Nov. 1985.

22 Marziale, M. L., and Mayle, R. E., "Effect of an Oscillating Flow Direction on Leading Edge Heat Transfer," ASME *Journal of Engineering for Gas Turbines and Power*, Vol. 106, No. 1, 1984, pp. 222–228.

23 Childs, E. P., and Mayle, R. E., "Heat Transfer on a Rotationally Oscillating Cylinder in Crossflow," *International Journal of Heat and Mass Transfer*, Vol. 27, No. 1, 1984, pp. 85–94.

24 Bellows, W. J., and Mayle, R. E., "Heat Transfer Measurements Downstream of a Leading Edge Separation Bubble," ASME JOURNAL OF TURBOMACHINERY, Vol. 108, No. 1, July 1986, pp. 131–136.

25 Townsend, A. A., *The Structure of Turbulent Shear Flow*, Cambridge University Press, Cambridge, UK, 1956.

26 Patel, V. C., "Two-Dimensional Wakes," Data Evaluation Report, 1980–81 AFOSR-HTTM-Stanford Conference on Complex Turbulent Flows, 1980.

27 Van Dresar, N., and Mayle, R. E., "Convection at the Base of a Cylinder With a Horsehoe Vortex," *Proceedings of the Eighth International Heat Transfer Conference*, San Francisco, CA, Vol. 3, 1986, pp. 1121–1126.

28 Marziale, M. L., "Mass Transfer From a Circular Cylinder – Effects of Flow Unsteadiness and Slight Nonuniformities," Ph.D. Thesis, Rensselaer Polytechnic Institute, Troy, NY, 1982.

29 Sogin, H., "Sublimation From Disks to Air Stream Flowing Normal to Their Surface," *Transactions of the ASME*, Vol. 80, 1958, pp. 61–71.

30 Murlis, J., Tsai, H. M., and Gradshaw, P., "The Structure of Turbulent Boundary Layers at Low Reynolds Numbers," *Journal of Fluid Mechanics*, Vol. 122, 1982, pp. 13–56.

31 Sandborn, V. A., "Measurements of Intermittency of Turbulent Motion in a Boundary Layer," *Journal of Fluid Mechanics*, Vol. 6, 1959, pp. 221.

32 Frenkel, F. N., and Klebanoff, P. S., "Higher-Order Correlations in a Turbulent Field," *Physics of Fluids*, Vol. 10, No. 3, 1967, pp. 507–519.

33 Schlichting, H., *Boundary Layer Theory*, McGraw-Hill, New York, 1979.

34 Narasimha, R., and Prabhu, A., "Equilibrium and Relaxation in Turbulent Wakes," *Journal of Fluid Mechanics*, Vol. 54, Part 1, 1972, pp. 1–17.

35 Gartshore, I. S., "An Experimental Examination of the Large-Eddy Equilibrium Hypothesis," *Journal of Fluid Mechanics*, Vol. 24, Part 1, 1966, pp. 89–98.

36 Thomas, R. M., "Conditional Sampling and Other Measurements in a Plane Wake," *Journal of Fluid Mechanics*, Vol. 57, Part 3, 1973, pp. 549–582.

37 Townsend, A. A., "The Mechanism of Entrainment in Free Turbulent Flows," *Journal of Fluid Mechanics*, Vol. 6, Part 4, 1966, pp. 689–715.

38 Corrsin, S., and Kistler, A. L., "Freestream Boundaries of Turbulent Flows," NACA Report 1244, 1955, pp. 1033–1064.

39 Kestin, J., and Wood, R., "The Influence of Turbulence on the Mass Transfer from Cylinders," ASME *Journal of Heat Transfer*, Vol. 93, 1971, pp. 321–327.

40 Frössling, N., "Verdunstung Wärmeübertragung und Gershwindigkeitsverteilung bei Zweidimensionaler und Rotationssymmetrischer laminar Grenzschictströmung," *Acta Univ. Jund*, Vol. 2, No. 4, 1940, p. 36, see also NACA TM 1432.

41 Tsien, H., "Symmetrical Joukowsky Airfoils in Shear Flow," *Quarterly of Applied Mathematics*, Vol. 1, No. 2, 1943, pp. 130–148.

42 Smith, M., and Kuethe, A., "Effects of Turbulence on Laminar Skin Friction and Heat Transfer," *Physics of Fluids*, Vol. 9, 1966, pp. 2337–2344.

43 Lowery, G. W., and Vachon, R. I., "The Effect of Turbulence on Heat Transfer From Heated Cylinders," *International Journal of Heat and Mass Transfer*, Vol. 18, 1975, pp. 1229–1242.

44 Yardo, N. R., and Sukhatme, S. P., "Effect of Turbulence Intensity and Integral Length Scale of a Turbulent Freestream on Forced Convection Heat Transfer From a Circular Cylinder in Cross Flow," *Proceedings of the Sixth International Heat Transfer Conference*, Toronto, Canada, Vol. 5 FC (b)-29, 1978, pp. 347–352.

45 Traci, R. M., and Wilcox, D. C., "Freestream Turbulence Effects on Stagnation Point Heat Transfer," *AIAA Journal*, Vol. 13, No. 7, 1965, pp. 890–896.

The Influence of a Mainstream Thermal Boundary Layer on Film Effectiveness

D. E. Paxson

R. E. Mayle

Department of Mechanical Engineering,
Rensselaer Polytechnic Institute,
Troy, NY 12181

A theoretical and experimental investigation on the effect of a mainstream thermal boundary layer on adiabatic film effectiveness is presented. The theory is based on a simple model which accounts for mixing between the injected flow and a mainstream flow with a viscous and thermal boundary layer. In order to apply this theory, the adiabatic film effectiveness in a flow with uniform temperature must be known either from experiments or from another theory. Experiments are described for an injection geometry having a simple two-dimensional slot. These tests were conducted with an insulated lip having a lip-diameter to slot-height ratio of 0.6. The mainstream thermal boundary layer was produced by heating the surface in contact with the mainstream flow upstream of the slot. Velocity and temperature distributions were measured at various distances downstream of the slot, along with measurements of the adiabatic wall temperatures. All tests were performed at a secondary to mainstream mass flux ratio of 0.7, but with different amounts of mainstream heating. While a comparison between theoretical and experimental results shows a discrepancy near injection, the trend is correct, and the agreement downstream is good.

Introduction

Within the last twenty years, film cooling has become a common method of protecting mechanical components from hot gaseous environments. Examples abound in modern gas turbine engines, as described by Metzger and Mayle (1983), where combustor linings and components in the first two stages of the turbine are usually film cooled. In many cases, film cooling is combined with conventional convective cooling methods so that the air, after passing through the cooling channels, is used for film cooling.

Usually, heat transfer with film cooling is determined by using a film heat transfer coefficient h_f and an adiabatic wall or film temperature T_{aw} as described by Goldstein (1971), i.e.,

$$q_f = h_f(T_{aw} - T_w)$$

where T_w is the component wall temperature. Introducing the adiabatic wall or film effectiveness η defined as

$$\eta = \frac{T_\infty - T_{aw}}{T_\infty - T_s}$$

where T_∞ and T_s are the mainstream and secondary or injected air temperatures, respectively, the surface heat flux with film cooling is obtained from

$$q_f = h_f(T_\infty - T_w)\left[1 - \eta\left[\frac{T_\infty - T_s}{T_\infty - T_w}\right]\right]$$

Both h_f and η must be known before the heat flux can be obtained and both depend, at least, on the injection geometry, coolant-to-mainstream mass and momentum flux ratios, and the distance measured from injection. They are usually obtained experimentally and, in the past, most effort has been spent in measuring the film effectiveness η. Effectiveness experiments are conducted under nearly adiabatic conditions where the mainstream air temperature is uniform.

Difficulties do not usually arise in using the adiabatic effectiveness determined in this manner unless coolant is used to cool the surface preceding injection, injection is preceded by another film injection, or simply stated, the mainstream thermal boundary layer is thick compared to the "equivalent slot height" of the injection scheme. In this case, the mainstream temperature profile at injection does not resemble that under which the effectiveness measurements were obtained, namely, constant and equal to T_∞. As a result, when the measured effectiveness distribution is used together with the perceived mainstream temperature, the heat flux is overestimated.

Sellers (1963) was first to make this point and proposed a method to account for the case of multiple film injections. The method is simple in that the mainstream temperature is replaced by the local adiabatic wall temperature, which results from all preceding injections. In order to predict the correct result, the method requires that the temperature profiles should be relatively flat near the wall and up to the height of injection. Its simplicity however, has made it a mainstay in design systems for multiple film injections.

Contributed by the International Gas Turbine Division and presented at the 33rd International Gas Turbine and Aeroengine Congress and Exhibition, Amsterdam, The Netherlands, June 5-9, 1988. Manuscript received by the International Gas Turbine Division September 15, 1987. Paper No. 88-GT-17.

Situations without previous film injections, but with a significant thermal deficit in the mainstream boundary layer, remain to be analyzed. It is this problem that the present paper addresses.

Theory

Consider the control volume shown in Fig. 1. Consider the upper boundary of the control volume to be a streamline and assume that, for any such control volume that can be drawn downstream of the slot, the fluid from the slot has completely mixed with the mainstream fluid up to the height y as shown. If the specific heats of the fluids are considered identical and constant, an energy balance can be written in the following form:

$$\int_0^y \rho_\infty u_\infty T dy + \rho_s U_s T_s s = T_{aw}\left[\int_0^y \rho_\infty u_\infty dy + \rho_s U_s s\right]$$

where the subscripts ∞ and s refer to the mainstream and secondary fluid, respectively, $u_\infty = u_\infty(y)$ is the streamwise velocity, U_s is the average velocity in the slot, T is the temperature, s is the slot height, and T_{aw} is the adiabatic wall temperature. In addition to the above assumptions, it has also been assumed that the conduction of heat across the upper streamline boundary of the control volume can be neglected compared to the slot energy deficit $\rho_s U_s c(T_\infty - T_s)s$, where c is the specific heat. Thus, the theoretical model simply considers the downstream increase in the adiabatic wall temperature to be the result of a progressively upward mixing of the slot fluid with a hotter mainstream fluid. As such, y, the distance up to which mixing has occurred, and T_{aw} are intimately connected, as will be shown later. Although a flat, completely mixed-out temperature profile has been assumed at the downstream boundary of the control volume, it is only necessary to assume that the profiles for every such control volume are similar (such as done by Wieghardt, 1964) and that the mixing occurs as previously described. For these more realistic conditions, the results will be identical to those presented below. The above expression may be rearranged to yield

$$\eta = \frac{T_\infty - T_{aw}}{T_\infty - T_s} = \frac{\int_0^y \frac{u_\infty}{U_\infty}\left[\frac{T_\infty - T}{T_\infty - T_s}\right]dy + Ms}{\int_0^y \frac{u_\infty}{U_\infty}dy + Ms}$$

where the mainstream velocity U_∞ and the coolant mass flux ratio $M = \rho_s U_s / \rho_\infty U_\infty$ have been introduced.

For the case where no thermal deficit in the mainstream exists, one has $T = T_\infty$ everywhere in the mainstream, and the integral in the numerator is zero. Therefore, the adiabatic film effectiveness, η_a is given as

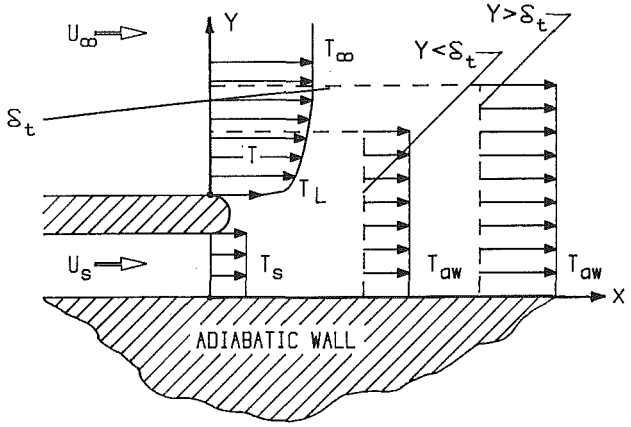

Fig. 1 Control volumes for energy balance with $y \le \delta_t$ and $y \ge \delta_t$

$$\eta_a = Ms\left[\int_0^y \frac{u_\infty}{U_\infty}dy + Ms\right]^{-1} \quad (1)$$

This expression is identical to that obtained by Goldstein (1971). Substituting this into the original effectiveness equation provides

$$\eta = \eta_a\left\{\frac{1}{Ms}\int_0^y \frac{u_\infty}{U_\infty}\left[\frac{T_\infty - T}{T_\infty - T_s}\right]dy + 1\right\}$$

A lip effectiveness ϕ may be defined as

$$\phi = \frac{T_\infty - T_L}{T_\infty - T_s}$$

where T_L is the lip temperature on the surface adjacent to the mainstream. The above expression then becomes

$$\eta = \eta_a\left\{\frac{\phi}{Ms}\int_0^y \frac{u_\infty}{U_\infty}\left[1 - \frac{T - T_L}{T_\infty - T_L}\right]dy + 1\right\} \quad (2)$$

This expression can only be evaluated if the mainstream velocity and temperature distributions at the slot, i.e., $x = 0$, and the streamwise distribution of the adiabatic film effectiveness, η_a, are known. In what follows, it will be presumed that η_a is known from either experiment or another theory. In order to assess the effect of a mainstream thermal boundary layer, it will be assumed that both the mainstream velocity and temperature profiles at the lip obey a simple power law approximation, i.e.,

$$\frac{u_\infty}{U_\infty} = \left[\frac{y}{\delta}\right]^{\frac{1}{n}} \equiv \gamma^{\frac{1}{n}} \text{ and } \frac{T - T_L}{T_\infty - T_L} = \left[\frac{y}{\delta_t}\right]^{\frac{1}{n}} = (\gamma/r)^{\frac{1}{n}}$$

where r is the ratio of the thermal to viscous bounday layer thickness, $r = \delta_t/\delta$.

Substituting the above expression for the velocity profile into equation (1), integrating, and rearranging, one obtains

Nomenclature

c = specific heat
h_f = heat transfer coefficient with film cooling
M = secondary-to-mainstream mass flux ratio
q_f = surface heat flux with film cooling
r = Thermal to viscous boundary layer thickness
s = slot height
T = temperature
u = local streamwise velocity = $u(y)$
U = free-stream or average velocity
x = streamwise distance measured from slot exit
y = distance measured normal from upper lip surface
y_1 = distance measured normal from adiabatic surface
γ = dimensionless distance normal to upper lip surface
δ_1 = displacement thickness
δ_2 = momentum thickness
Δ_2 = enthalpy thickness
η = adiabatic film effectiveness
η_a = adiabatic film effectiveness without heated lip surface
ρ = density
ϕ = dimensionless lip temperature

Subscripts

aw = adiabatic wall
L = Lip
s = secondary air
w = wall
∞ = mainstream air

$$\gamma = \left\{ \left[\frac{\delta}{Ms} \right]^{-1} \left[\frac{n+1}{n} \right] \left[\frac{1-\eta_a}{\eta_a} \right] \right\}^{\frac{n}{n+1}} \tag{3}$$

This may now be regarded as the height in the mainstream flow above the lip to which mixing occurs for a control volume that extends to $x = x(\eta_a)$, i.e., this expression relates the height of any one control volume to its length. Note that in the following any single control volume is not changing, but that numerous control volumes are being considered.

There are now at least two cases to evaluate: that for $\gamma \le r$ and that for $\gamma \ge r$. The first is for all control volumes where the mixing height y is less than the thermal boundary layer thickness δ_t. This generally corresponds to small distances from injection, say $0 \le x \le x_r$. The second case is that where mixing has occurred beyond the thermal boundary layer, into the region where the mainstream temperature is constant. It corresponds to large distances from injection, $x \ge x_r$. In addition, one may have either $r \le 1$ or $r \ge 1$. Substituting the assumed form for the velocity and temperatures profiles into equation (2) and integrating yields

$$\frac{\eta}{\eta_a} = 1 + \phi \left(\frac{\delta}{Ms} \right) \left[\frac{n}{n+1} \gamma^{\frac{n+1}{n}} - \frac{n}{n+2} r^{-\frac{1}{n}} \gamma^{\frac{n+2}{n}} \right]$$

which upon substituting into equation (3) provides

$$\frac{\eta}{\eta_a} = 1 + \phi \frac{1-\eta_a}{\eta_a} \left\{ 1 - \frac{n+1}{n+2} r^{-\frac{1}{n}} \left[\frac{n+1}{n} \frac{Ms}{\delta} \frac{1-\eta_a}{\eta a} \right]^{\frac{1}{n+1}} \right\} \tag{4}$$

This expression implicitly relates the film effectiveness with a mainstream thermal deficit, η, to the streamwise distance x through the functional $\eta_a = \eta_a(x)$, which in turn has been assumed known. The restriction $\gamma \le r \le 1$ requires (see equation (1))

$$\eta_a \ge \left[1 + \frac{n}{n+1} \frac{\delta}{Ms} r^{\frac{n+1}{n}} \right]^{-1} \ge \left[1 + \frac{n}{n+1} \frac{\delta}{Ms} \right]^{-1}$$

In other words, equation (4) is valid for the region between the slot ($x = 0$) and the distance $x = x_r$, which corresponds to the position where η_a equals the first expression in the above restriction. Beyond this point η continues to decrease as mixing continues. In this region, however, mixing occurs with air at the free-stream temperature T_∞. Thus, the integrand in equation (2) is zero for $y \ge \delta_t$ or $x \le x_r$. The upper limit to the integral becomes $\gamma = r$ and one obtains

$$\frac{\eta}{\eta_a} = 1 + \frac{n}{(n+1)(n+2)} \phi \left(\frac{\delta}{Ms} \right) r^{\frac{n+1}{n}}; \quad (x \ge x_r) \tag{5}$$

This result is valid for $\gamma \ge r$ ($y \ge \delta_t$) provided that $r \le 1$ ($\delta_t \le \delta$) and implies that beyond $x = x_r$, the film effectiveness with a thermal boundary layer is a simple multiple of that without. This completes the necessary analysis for all of the cases corresponding to $r \le 1$.

The cases corresponding to $r \ge 1$ are as easily determined as those above, but result in somewhat more complicated expressions. Integration of equation (2) with the assumed velocity and temperature profiles, noting that $u_\infty = U_\infty$ for $y \ge \delta$ yields

$$\frac{\eta}{\eta_a} = 1 + \phi \frac{1-\eta_a}{\eta_a} \left\{ 1 - \frac{n+1}{n+2} r^{-\frac{1}{n}} \left[\frac{n+1}{n} \frac{Ms}{\delta} \frac{1-\eta_a}{\eta_a} \right]^{\frac{1}{n+1}} \right\}$$

for

$$\eta_a \ge \left[1 + \frac{n}{n+1} \frac{\delta}{Ms} \right]^{-1}$$

which is identical to equation (4) and corresponds to $y \le \delta$.

$$\frac{\eta}{\eta_a} = 1 + \phi \left\{ \frac{1-\eta_a}{\eta_a} - \frac{n}{n+1} \frac{\delta}{Ms} r^{-\frac{1}{n}} \left[\left[\frac{1}{n+1} + \frac{Ms}{\delta} \frac{1-\eta_a}{\eta_a} \right]^{\frac{n+1}{n}} - \frac{1}{n+2} \right] \right\} \tag{6}$$

for

$$\left[1 + \frac{\delta}{Ms} \left[r - \frac{1}{n+1} \right] \right]^{-1} \le \eta_a \le \left[1 + \frac{n}{n+1} \frac{\delta}{Ms} \right]^{-1}$$

which corresponds to $\delta \le y \le \delta_t$, and finally

$$\frac{\eta}{\eta_a} = 1 + \phi \frac{\delta}{Ms} \left[\frac{r-1}{n+1} + \frac{n}{(n+1)(n+2)} r^{-\frac{1}{n}} \right] \tag{7}$$

which corresponds to $y \ge \delta_t$.

All of the above equations show that there are four parameters on which the actual, or corrected, effectiveness depends. The first is the ratio of thermal to viscous boundary layer thicknesses, $r = \delta_t/\delta$; the second is the mainstream boundary layer to secondary mass flow ratio, δ/Ms; the third is the dimensionless lip temperature ϕ; and the last is the power of the assumed velocity and temperature profiles, $1/n$. From either equation (4) or (5) it is obvious that $(\eta/\eta_a) - 1$ is directly proportional to the dimensionless lip temperature ϕ, which suggests plotting the theory in the form $1/\phi\ (\eta/\eta_a - 1)$ versus η_a. Such a plot is shown in Fig. 2, where the values for r, δ/Ms, and n are 0.9, 2, and 7, respectively. These values are similar to those for the present experiment. A decrease in the abscissa (decreasing η_a) corresponds to an increase in the distance from the slot. The regions corresponding to $x \ge x_r$ and $x \le x_r$ are marked in the figure. For typical gas turbine conditions $\phi \cong 0.75$. Thus the maximum gain in film effectiveness resulting from a mainstream thermal boundary layer having the conditions used in Fig. 2 would be about 12 percent. Maximum gains for other conditions can be readily obtained from either equation (5) or (7). A maximum gain of about 20 percent is predicted from the more realistic ratio of thermal to viscous boundary layer thicknesses, $r = 1.4$.

Experimental Facility

The tests were performed using a low-speed test facility with separate mainstream and secondary air supply systems. The mainstream air supply system was an open-circuit wind tunnel powered by a centrifugal fan. A plenum containing baffles and screens followed by a nozzle insured a uniform mainstream flow in the test section. Thermocouples located upstream of the nozzle were used to measure the mainstream air temperature. The mainstream flow velocity was measured

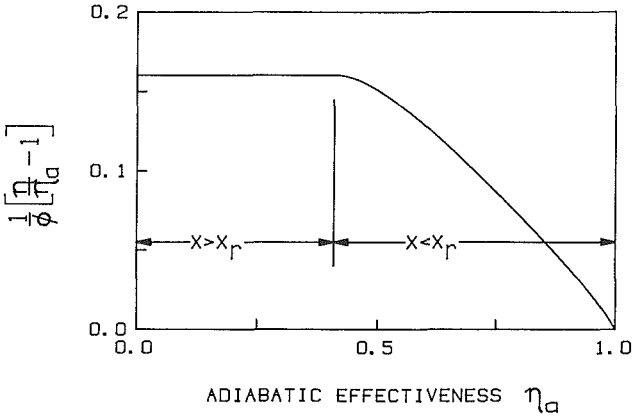

Fig. 2 Theoretical result for $r = 0.9$, $\delta/Ms = 2$, and $n = 7$

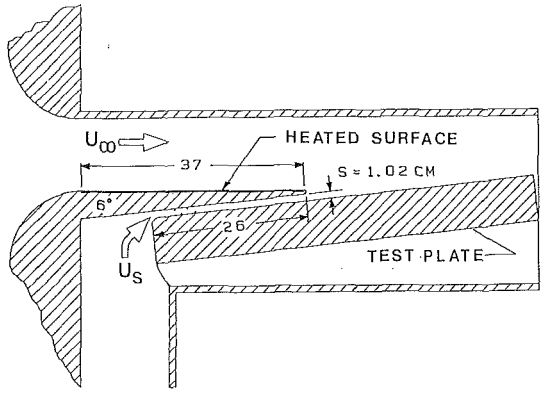

Fig. 3 Test section with slot injection and a lip with a heated surface

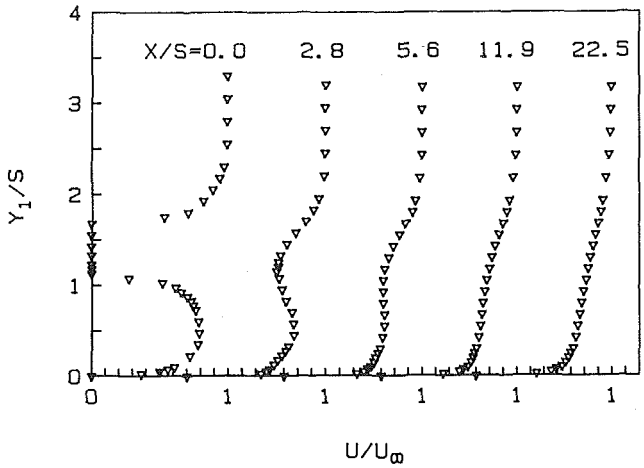

Fig. 4 Velocity profiles at different downstream positions, $M = 0.7$

using a Kiel probe, and a static pressure tap located within the test section. The secondary air supply consisted of a centrifugal fan, a heating chamber, and a secondary air plenum chamber. The latter was directly attached to the test section. The heating chamber contained four individually regulated heating units of stranded nichrome wire sandwiched between sets of filtering screens. The plenum contained a series of screens and baffles, which provided a uniform injection flow. The secondary mass flow rate was obtained using a calibrated nozzle positioned between the heating and plenum chambers. The secondary air temperature was measured directly at the slot exit.

The test section is shown in Fig. 3. It was composed of a top wall, a heated-lip model, and an "adiabatic" test plate attached to plexiglass sidewalls. The width of the test section was 30.5 cm and its height before the slot was 12.7 cm. Four trip wires were mounted at the slot entrance to insure turbulent flow within the channel. The heated-lip model is 37 cm long and had a lip diameter of 0.64 cm. The model was designed to provide an injection angle of 6 deg and was positioned to provide a slot height of $s = 1.02$ cm. The model was made primarily from plywood and balsa wood. The upper surface of the model (that in contact with the mainstream flow) was covered with a heating unit, which consisted of a continuous 2.54-cm steel foil strip folded back and forth to create a "heating sheet". The foil was sandwiched between two layers of fiberglass, bonded to the upper surface of the model, and connected to an a-c power supply. Thermocouples positioned at various locations throughout the model were used to measure the upper and lower lip surface temperatures. The entire model was painted with a flat black enamel finish that had an emissivity of 0.985.

The test plate was 30.5 cm wide and 64 cm long. It was constructed from a 1.27-cm-thick plywood support plate covered with a 2.54-cm-thick balsa wood layer. This arrangement provided a nearly adiabatic wall for measuring film effectiveness. Seventeen thermocouples, mounted in the surface from $x/s = -3.75$ to 36.25 along the center of the plate, were used to obtain the adiabatic surface temperatures. Thermocouples located to either side of center were used to check the two dimensionality of the flow. In addition, thermocouples located on the back of the test plate were used to evaluate the conduction losses through the test plate. In order to further reduce back loss, the space behind the test plate was filled with fiberglass insulation. All of the thermocouples were connected to junction blocks located within the test plate. As with the model, the entire test plate was coated with flat black enamel.

All tests were conducted with the mainstream air velocity and temperature nominally maintained at 18.3 m/s and 19°C, respectively. The mass flux ratio was maintained at a constant nominal value of $M = 0.7$. The secondary air and lip temperatures depended on the value of ϕ and varied between $30 \le T_S \le 50$°C and $25 \le T_L \le 50$°C, respectively. It should be noted that with a heated secondary flow, $T_S \ge T_\infty$, and no surface heating, the lip temperature was always somewhat greater than the mainstream air temperature, i.e., $\phi \ge 0$, because of conduction through the lip.

The velocity and temperature profile measurements were obtained using a vertical traversing mechanism, which could be moved in the streamwise direction to various x/s positions. Velocity traverses were performed using a miniature boundary layer total pressure probe. These traverses were taken with the mainstream and secondary air at the same temperature. For each x/s position traversed, a static pressure tap was mounted in the sidewall at the same x/s location. Temperature traverses were made using a small thermocouple probe with flow conditions matching the effectiveness tests. The temperature traverses performed with the lip surface heated were conducted with the lip temperature equal to the secondary air temperature, i.e., $\phi = 1.0$.

The effectiveness tests were performed with the lip surface heated and unheated. The secondary air and lip surface temperatures (ϕ) were selected and the plenum and model heaters set appropriately. When all the mainstream and secondary flow rates and temperatures were set, the facility was run for a minimum of six hours in order to achieve a steady-state condition. At the end of this period, temperature readings from all of the thermocouples were recorded and the flow rates checked.

The effectiveness measurements were corrected for heat transfer losses by conduction through the test plate and radiation to the surroundings. A one-dimensional model of each surface element was used and a heat balance performed to obtain the "adiabatic" wall temperature. Radiation corrections were particularly difficult to ascertain exactly because the test surface radiates to the inside of the slot, as well as to the surrounding surfaces. However, corrections to the measured adiabatic film effectiveness due to radiation were always less than 7 percent and those due to conduction were less than 4 percent.

Results

Velocity and Temperature Profiles. The measured velocity profiles at several x/s positions are shown in Fig. 4, where the origin of each profile is shifted by 0.7 along the abscissa. In order to avoid confusion, the vertical distance y_1 is measured from the test surface, and not from the top of the lip as in the theory, i.e., $y_1 = y + s +$ lip thickness. The profile at the slot exit is seen to have a region directly behind the lip where the velocity is zero. The actual data gathered in this vicinity,

Table 1

x/s	δ_1/s	δ_2/s	H
0	1.07	0.30	3.57
2.8	0.53	0.37	1.43
5.6	0.49	0.36	1.36
11.9	0.45	0.34	1.32
22.5	0.43	0.33	1.30

however, registered a small negative pressure difference between total and static pressures. Because it was not certain whether this was caused by a slight difference between the mainstream and secondary static pressure, and because the readings were very small (within the error range of the manometer), the values were simply taken to be zero. The remaining profiles illustrate the mixing trend as the flow moves downstream. The final profile at $x/s=22.5$ looks very much like a typical flat plate turbulent profile. Values of the displacement thickness, momentum thickness, and shape factor are provided in Table 1. The shape factor for $x/s=22.5$ agrees well with the generally accepted value for a fully turbulent profile.

The temperature profiles for an unheated and a heated lip surface, $\phi=0.34$ and 1.07, respectively, are shown in Fig. 5. As with the velocity, these profiles are plotted as functions of y_1/s, but each profile is shifted along the abscissa by 0.8. The triangular symbol for each profile at $y_1/s=0$ represents the wall temperature measured by the thermocouples embedded in the wall, as opposed to the probe thermocouple. (Actually, the traverses were done at x/s positions that fell between wall thermocouples; thus an interpolation was performed.) In all traverses, this value was lower than the temperature measured by the probe. The discrepancy illustrates the effects of back loss through, and radiation from, the test surface. It is also due, in part, to conduction along the probe stem. Both sets of profiles exhibit behavior that is intuitively expected. At $x/s=0$ the profiles appear reasonably uniform up to the slot height. Above this there is a region that seems nearly linear. Here, in the wake of the lip, conduction appears to be the important heat transfer mechanism. Finally, a typical heated boundary layer profile is seen above the lip. Comparison of the profiles at $x/s=0$ shows for the heated case that a substantial amont of heat is contained both in the flow above the lip and in the wake. The latter is presumably a result of the downstream mixing and reverse flow in the wake. Moving downstream, mixing occurs and the additional thermal energy introduced by the heated surface becomes more and more diffuse.

The enthalpy thickness was evaluated for each traverse position for both the heated and unheated cases. The average value of Δ_2/s for the unheated case is 0.72, with a deviation from the mean of less than 10 percent. For the heated case, the value is $\Delta_2/s=0.79$, also with a deviation of less than 10 percent. Thus it appears as if the test facility represents a reasonably closed control volume. If the lip were truly adiabatic, it should be observed that the value of Δ_2/s would be equal to the mass flux ratio M. Recalling that a nominal value for M of 0.7 was used for the traverses, the above experimental result for the unheated surface, $\Delta_2/s=0.72$, is further reassurance for the accuracy of the data.

Effectiveness Results. The measured film effectiveness distributions for four different values of $\phi>0$ are plotted in Fig. 6 as functions of x/s. Here, as in the theory, η denotes the adiabatic film effectiveness with a mainstream thermal boundary layer. The data for $\phi=0.34$ were actually obtained without applying current to the heater strip on the lip surface and is simply a result of heat transferred from the secondary air by conduction through the lip.

Figure 6 indicates a rather significant effect caused by the presence of a mainstream thermal boundary layer. All of the

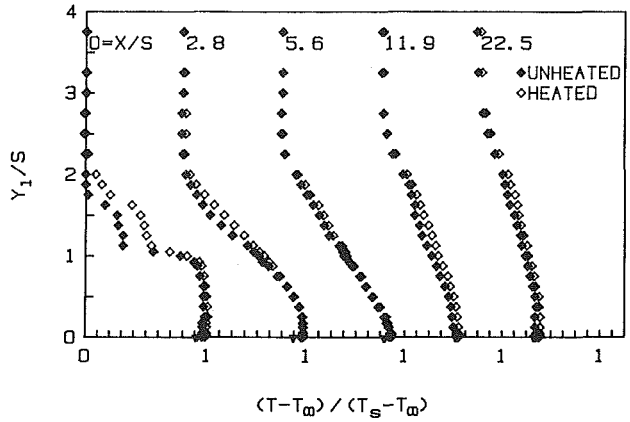

Fig. 5 Temperature profiles with and without lip surface heating

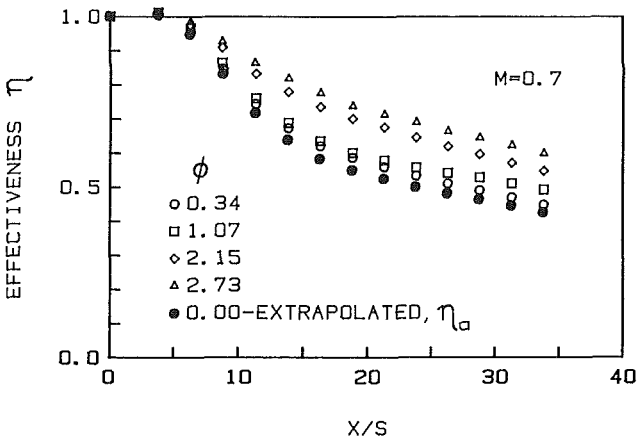

Fig. 6 Effectiveness results for different lip surface temperatures

effectiveness distributions follow the same trend, for a given value of ϕ. Each begins at the exit with $\eta=1$, and maintains nearly this value to about $x/s=6$. The effectiveness then drops off rapidly as mixing near the wall begins. Farther downstream the decay becomes more gradual. The effect of the lip boundary layer is seen as soon as the mixing near the wall begins. However, it is much more noticeable downstream after most of the mixing has occurred. Furthermore, it is seen that for a given x/s position, the effectiveness value increases with ϕ. A plot of η against ϕ for each streamwise position produces a linear correlation. This should be expected since the energy equation is linear and the heated case can be considered as the superposition of two thermal profiles, one of which has a constant mainstream temperature. In heat transfer tests, a constant mainstream temperature profile is impossible to achieve. Nevertheless, the truly adiabatic film effectiveness η_a can be obtained from these tests by a linear extrapolation of η versus ϕ to $\phi=0$ for each x/s position. This result is also presented in Fig. 6 and is denoted by the closed symbols as $\phi=0$-extrapolated, or simply η_a.

In Fig. 7, the film effectiveness η for two test conditions are plotted. In this figure, however, the results are plotted in the format suggested by the theory (Fig. 2). The solid symbols represent the average of the data previously plotted in Fig. 6 for the two highest values of ϕ. For this case, $\delta/Ms=1.96$. The second set of data was obtained for a thickened mainstream boundary layer having $\delta/Ms=2.65$ with $\phi=2.04$ and 2.78. In both cases, $\delta_t/\delta=0.76$. In addition, the theoretical results obtained from equations (4) and (5) are also shown.

In general, the overall trend at lower values of η_a (larger x/s), and the effects of boundary layer thickness, are reasonably well predicted. A major discrepancy between

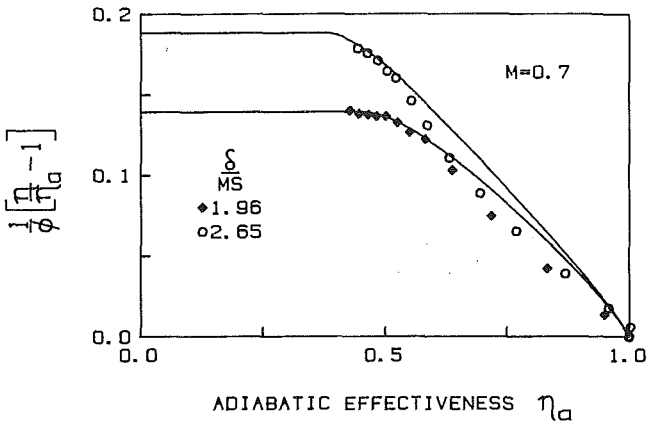

Fig. 7 Comparison of experimental results with theory, $M = 0.7$

theory and experiment, however, is noted at the higher values of η_a (smaller x/s). Theory consistently predicts a higher corrected effectiveness η than actually exists. The reason for this is presently attributed to the mixing process immediately downstream of injection. While the theory assumes mixing across the whole profile, the profile results indicate that the mixing occurs away from the lip until the wall is encountered. One may question why, contrary to the conventional notion, a higher degree of mixing would yield a higher effectiveness. The answer lies in the failure of conventional thinking to consider the effects of a mainstream boundary layer with an energy deficit. In this case, mixing more fluid with less energy improves the effectiveness. In light of the present results, then, it appears that the beneficial effect of the mainstream thermal boundary layer is not immediately realized to the extent predicted by the theory. As the mixing becomes more complete, however, the effect is more fully realized and the experimental and theoretical results compare quite favorably.

Conclusions

It is apparent that the adiabatic wall effectiveness is significantly altered by the presence of a thermal boundary layer in the mainstream flow. Since, in an actual turbine blade, this boundary layer always exists, one might question the accuracy of previous analyses, which assume the conventional adiabatic condition. In this respect, the effect studied here helps the designer.

It also appears that the simple theoretical model presented herein is quite adequate for estimating the effect of a mainstream thermal boundary layer on the film effectiveness. The model does, however require that the adiabatic wall effectiveness without a thermal boundary layer, η_a, be known a priori. In addition, one must also know the ratio of the mainstream thermal to viscous boundary layer thicknesses, δ_t/δ, and the ratio of the mass flow in the mainstream boundary layer to that injected, δ/Ms. Since η_a itself is used as a measure of the mixing that actually takes place, it appears that the model may be applied to injection geometries other than the slot.

Acknowledgments

The theory was developed while the second author was visiting the Institut für Thermische Strömungsmaschinen, Universität Karlsruhe, Karlsruhe, Federal Republic of Germany, under the Sonderforschungsbereich 167, Jan. 1985.

References

Goldstein, R. J., 1971, "Film Cooling," *Advances in Heat Transfer*, Academic Press, Vol. 7, pp. 321–379.

Metzger, D. E., and Mayle, R. E., 1983, "Gas Turbine Heat Transfer," *Mechanical Engineering Magazine*, Vol. 105, 6, pp. 44–52.

Seller, J. P., 1963, "Gaseous Film Cooling With Multiple Injection Stations," *AIAA Jour.*, Vol. 1, 9, pp. 2154–2156.

Wieghardt, K., 1946, "Hot-Air Discharge for De-Icing," AAF Translation No. F-TS919-RE, Air Material Command.

The Effect of Free-Stream Turbulence on Gas Turbine Blade Heat Transfer

V. Krishnamoorthy
Propulsion Division,
National Aeronautical Laboratory,
Bangalore—560017 India

S. P. Sukhatme
Professor,
Department of Mechanical Engineering,
Indian Institute of Technology,
Bombay—400076 India

This paper describes the results of systematic investigations undertaken to study the effect of free-stream turbulence on the heat transfer coefficient distribution around gas turbine rotor blades and nozzle guide vanes. The heat transfer coefficient distribution around the blade surface was obtained under a uniform heat flux boundary condition. Experiments were conducted in the Reynolds number range 2.0–8.1 × 10^5 (exit Mach number range 0.182 to 0.600) with the free-stream turbulence level in the range 1.0–21.3 percent. A new type of active turbulence generator was used for generating high turbulence levels. Correlations were obtained for the effect of free-stream turbulence on the local heat transfer coefficient in the laminar, transitional, and turbulent boundary layer regions.

Introduction

A knowledge of the variation of the heat transfer coefficient around a gas turbine blade surface is required for optimum design of the cooling configuration. The variation depends on the development of the thermal and hydrodynamic boundary layers over the blade surface, which in turn is influenced by a large number of interacting flow parameters such as Reynolds number, pressure gradient over the blade surface, blade radius of curvature, free-stream turbulence, etc. (Nealy et al., 1983). Of these, the turbulence in the free stream is an important parameter (Junkhan and Serovy, 1967; Yardi, 1978; Lowery and Vachon, 1975). The high turbulence levels in the gas stream (> 10 percent) at the combustor exit (Kurosh and Epik, 1970) suggest that for a satisfactory estimate of the heat transfer coefficient distribution around a gas turbine blade in engine flow conditions, a knowledge of the effect of free-stream turbulence on the extent of the different boundary layer regimes and on the transport of fluxes within the boundary layer would be required.

A number of systematic investigations had been carried out to measure the effect of free-stream turbulence on the local heat transfer coefficient distribution around turbine blade surfaces (Turner, 1969; Dunham and Edwards, 1973; Martin et al., 1978; Ligrani and Breugelmans, 1981; Bayley and Priddy, 1981; Zysina Molozhen et al., 1977; Priddy and Bayley, 1985; Consigny and Richards, 1982). However, most of these experiments were carried out at turbulence levels below 6 percent and conventional rod grids and perforated plates were used as turbulence generators with the distance between the turbulence generator and the cascade less than twice the chord. The data generated by Martin et al. (1978), as mentioned in their paper, were not corrected for the step change in surface temperature while Bayley and Priddy (1981) were mainly concerned with the evaluation of the effect of turbulence frequency. Considerable differences exist in the results of different investigators, in particular on the effect of free-stream turbulence on the heat transfer coefficient distributions in the favorable pressure gradient region on the blade suction surface. For the same turbulence level range, Priddy and Bayley (1985) and Dunham and Edwards (1973) observed a small and systematic change in the local heat transfer coefficient, whereas Turner (1969) observed a significant change in the heat transfer coefficient distribution. The differences in the blade profile, cascade parameters, and test condition do not permit the identification of factors responsible for the difference in the test results. The observations of Priddy and Bayley (1985) that the wake produced by turbulence generator might modify the flow over the blade surface suggest that sufficient distance must be provided between the turbulence generator and the cascade.

The object of the present investigation is to study systematically the effect of free-stream turbulence on the local heat transfer coefficient distribution over gas turbine blades at high turbulence levels representative of those observed in modern gas turbine engines. Experiments were conducted using a rotor blade and two nozzle guide vane profiles (Vane I and Vane II). The heat transfer coefficient distribution was obtained under the uniform heat flux boundary condition in the Reynolds number range 2.0 × 10^5 to 8.1 × 10^5 with the free-stream turbulence level in the range 1.0 to 21.3 percent. A detailed description of the investigation is given by Krishnamoorthy (1986).

Experimental Setup

Wind Tunnels. The experiments were conducted in two subsonic wind tunnels, one providing relatively low turbulence conditions and the other providing high turbulence. Both were

Contributed by the International Gas Turbine Institute for publication in the JOURNAL OF TURBOMACHINERY. Manuscript received at ASME Headquarters February 8, 1989.

Table 1 Cascade data and range of flow parameters

(A) Cascade Data

	Rotor	N.G.V. I	N.G.V. II
Span	140	140	140
Pitch	42.9	45.5	52.4
Chord	50.4	69.5	70.7
Stagger angle	22	41	38

All dimensions are in mm

(B) Range of Parameters

	Re_c	M_e	ϵ_i, percent
Rotor blade	$2.0\text{–}4.5\times10^5$	0.18–0.4	1.8–21.3
N.G.V. I	$4.15\text{–}8.1\times10^5$	0.28–0.55	1.6–12.7
N.G.V. II	$2.5\text{–}8.1\times10^5$	0.18–0.55	3.7–16.2

blowdown tunnels supplied with air at room temperature from a central storage facility, and the flow was controlled by means of a gate valve at the inlet. The cascade was fixed at the end so that the exit was to the atmosphere. The width of the test section was 140 mm. The height of the test section was fixed depending on the blade pitch and the number of blades.

Cascade. One rotor blade and two nozzle guide vane profiles were selected for the investigation. The airfoil profile data are available in Krishnamoorthy (1986) and the cascade data are given in Table 1. A five-blade cascade was used with the blades set at nominally zero incidence. The test blade, instrumented for heat transfer coefficient distribution measurement, was located at the center. It was fabricated by fixing a thin stainless steel sheet over a blade model made by casting "Araldite." The thicknesses of the stainless steel sheets used in the fabrication of the rotor blade and nozzle guide vane model were 0.25 mm and 0.1 mm, respectively. Before fixing the stainless steel sheet to the blade model, thermocouples (copper-constantan, 32 SWG) were soldered to the sheet. In the case of the rotor blade, 22 thermocouples were used, 12 on the suction surface and 10 on the pressure surface. In the case of the nozzle guide vanes, 35 thermocouples were used, 19 on the suction surface and 16 on the pressure surface. The uniform heat flux boundary condition was generated by heating the stainless steel sheet by means of a low-voltage high-current a-c source. The axial heat conduction through the sheet in the flow direction due to surface temperature variation was calculated. The local heat transfer coefficient was obtained by dividing the measured heat flux (suitably corrected for axial heat conduction) by the difference between the blade surface temperature and the free-stream total temperature. The error in the measured value of the heat transfer coefficient was estimated to be always less than ±11 percent (Krishnamoorthy, 1986).

Separate blades made by casting Araldite were used for making surface pressure measurements. A total of 19 pressure tappings 0.5 mm in diameter were provided, 10 on the suction surface and 9 on the pressure surface. The output from the pressure tappings was connected to a manometer bank for the static pressure measurement and the local free-stream Mach number was calculated using the one-dimensional isentropic relation.

Turbulence Generator. A new type of active turbulence generator was used for generating high turbulence levels. It consisted of a cylindrical tube in which two rows of holes of 1 mm diameter and 2 mm pitch were drilled along the axial direction 180 deg apart. The turbulence generator was located at a distance of 625 mm upstream of the cascade inlet with its axis in the blade spanwise direction. It was supplied with air under pressure from both ends. The interaction between the mainstream and the jets of air issuing perpendicular to it from the turbulence generator produced a high turbulence level. The turbulence level at the cascade inlet was varied by varying the injection pressure. Detailed measurements were made to characterize the turbulence generated by this turbulence generator. The decay of $\langle u'^2\rangle$ was measured in the region of the test section, with the cascade removed, and the exponent in the general decay relation was estimated. The values of the exponent varied with the injection pressure but were within that observed for the decay of homogeneous and isotropic turbulence generated by screens (Krishnamoorthy, 1986; Hinze, 1959). The mean velocity and turbulence level distribution across the tunnel cross section was fairly uniform and was independent of the turbulence level. The integral length scale of turbulence was found to be small ($\approx$2.6 mm) and did not vary significantly with free-stream turbulence level.

The turbulence level in the flow direction was measured by means of a thin film wedge type hot-film probe (TSI Model No. 1233, USA) in conjunction with a DISA 55 M10 anemometer system. The accuracy of the measured turbulence level was restricted by the single component measurement and was around ±10 percent (Hinze, 1959).

Results and Discussion

The temperature distribution around the blade surface was recorded after reaching steady state. The difference between the free-stream total temperature and the surface temperature was measured directly. In a specific test, the required Mach number at the exit of the cascade was obtained by setting the total pressure at the cascade inlet. A variation in flow Reynolds number was obtained by varying the exit Mach number. The Reynolds number of the flow was calculated based on the exit flow conditions. Table 1 also shows the range of parameters used in the experiment.

Local Free-Stream Mach Number Distribution. Detailed surface pressure measurements were first made to obtain the local free-stream Mach number distribution over the rotor blade and the vanes. Figure 1 shows the distribution for one exit Mach number. Similar trends were observed at other exit Mach numbers also. The pressure gradients on the suction surface were similar in the case of the rotor blade and the nozzle guide vanes. The stagnation flow region was followed by a favorable pressure gradient region and then an adverse pressure gradient region. However, the pressure gradients on the pressure surface were slightly different. In the case of the rotor blade, the stagnation region was followed by an essentially zero pressure gradient region and then a strong favorable pressure gradient region. In the case of the vanes, a favorable pressure gradient region was observed over the entire pressure surface. The Mach number distribution around the vanes used in the present experiments was similar to that observed by Turner (1969) for the vane used in his experiments. The profiles

Nomenclature

C = chord length, mm
h = local heat transfer coefficient, W/m²K
M_e = exit Mach number
M_L = local free-stream Mach number
Re_c = flow Reynolds number (based on blade chord and exit flow condition)
U_i = free-stream velocity at cascade inlet, m/s
U_L = local free-stream velocity, m/s
$\langle u'^2\rangle$ = rms of fluctuating component of velocity in mean flow direction, m/s
ϵ_i = free-stream turbulence level at cascade inlet, percent
ϵ = local turbulence intensity = $\langle u'^2\rangle * 100/U_L$, percent

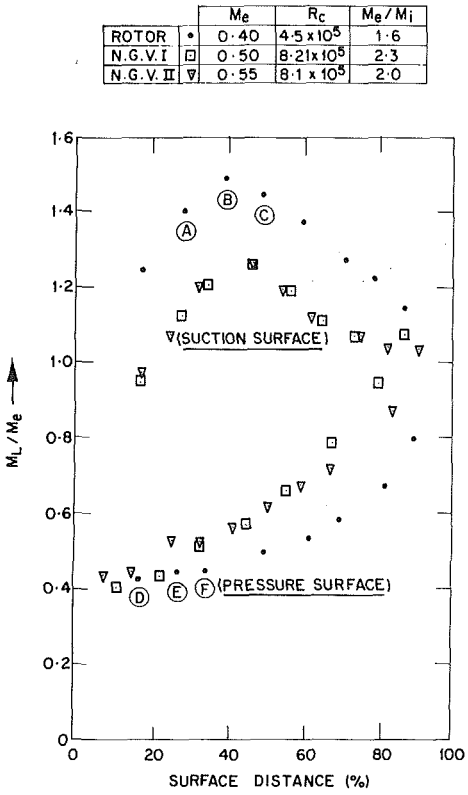

Fig. 1 Experimental free-stream Mach number distribution

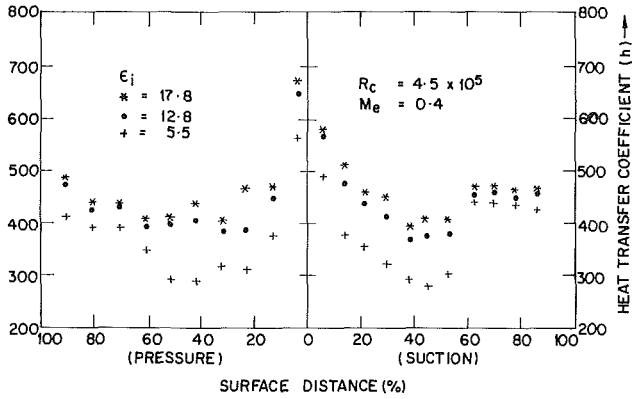

Fig. 2 Effect of turbulence on the heat transfer coefficient distribution: rotor blade

used were similar. Local free-stream Mach number distributions were also obtained at higher inlet free-stream turbulence levels and it was ascertained that the distributions were not influenced by the turbulence level.

Effect of Free Stream Turbulence on Transition and the Heat Transfer Coefficient Distribution. The effect of free-stream turbulence on the heat transfer coefficient distribution around the rotor blade is shown in Fig. 2 for $Re_c = 4.5 \times 10^5$. A similar trend was observed at other Reynolds numbers. Figures 3 and 4 show the effect of free-stream turbulence on the heat transfer coefficient distribution around the nozzle guide vanes at two Reynolds numbers, which also shows the effect of Reynolds number on the heat transfer coefficient distribution.

The different boundary layer regions were identified from the analysis of the heat transfer data obtained at low turbulence levels in conjunction with the predictions obtained using a boundary layer analysis. The heat transfer coefficient distribution in the laminar and turbulent boundary layer region was

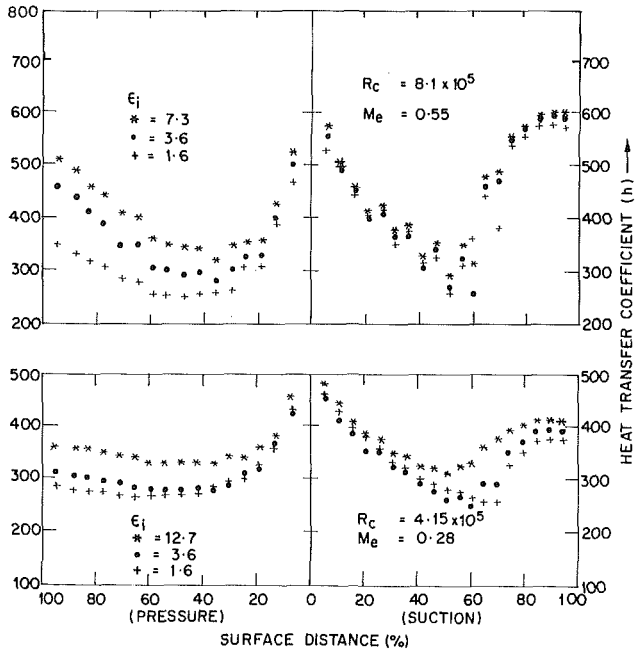

Fig. 3 Effect of turbulence on the heat transfer coefficient distribution: N.G.V. I

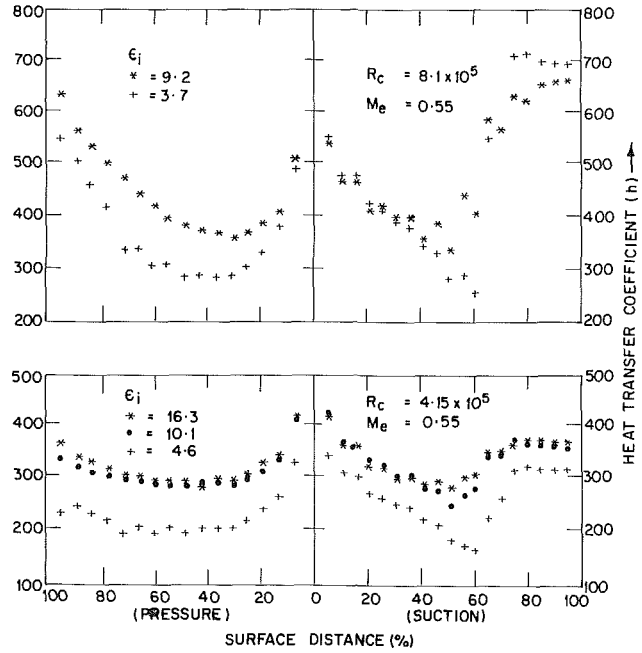

Fig. 4 Effect of turbulence on the heat transfer coefficient distribution: N.G.V. II

estimated using a boundary layer program based the GENMIX program developed by Patankar and Spalding (1970). The calculations in the turbulent boundary layer regime were carried out using the Prandtl mixing length hypothesis with Van Driest damping coefficient (Krishnamoorthy, 1986).

Suction Surface. The boundary layer analysis predicted laminar separation on the suction surface of the rotor blade and nozzle guide vanes at 53 and 58 percent surface distance, respectively. In the case of the rotor blade, on the suction surface, the boundary layer was laminar up to 53 percent of surface distance. In the case of nozzle guide vanes at $Re_c < 4.15 \times 10^5$ the boundary layer was laminar up to the predicted laminar separation point. At a higher Reynolds number, the initial laminar boundary layer region was followed by a gradual

transition region up to the predicted separation point. The gradual transition could be due to the high favorable pressure gradient (K) on the surface and was similar to that observed by Rued and Wittig (1986) and Blair (1982) in a favorable pressure gradient flow.

Pressure Surface. The boundary layer on the pressure surface of the rotor blade was found to be turbulent. In the case of guide vanes, the boundary layer was laminar in the initial region and was undergoing gradual transition over the remaining distance. The heat transfer coefficient distribution in the transition region suggested a natural transition in a strong favorable pressure gradient region (Blair, 1982; Rued and Wittig, 1986). Due to the gradual transition, it was not possible to locate a point of transition. However, the similarity in the heat transfer coefficient distribution obtained at different Reynolds numbers and turbulence level seems to suggest that the effect of both the parameters on the location of the transition point is small. A comparison of the heat transfer coefficient variation in the transitional region obtained at different Reynolds numbers suggests a reduction in the transition length with increase in Reynolds number. A similar trend was observed, at each Reynolds number, with increase in the turbulence level from 1.6 to 3.6 percent. The reduction in the transition region at higher Reynolds numbers could be due to the reduction in the pressure gradient parameter, $K = (\nu/U^2)dU/dx$ (Blair, 1982).

A systematic change in local heat transfer coefficient was observed with a change in free-stream turbulence, in the laminar, transitional, and turbulent boundary layer region. The change observed in the turbulent boundary layer on the suction surface was small and was in agreement with the observations of Dunham and Edwards (1973) and Ligrani and Breugelmans (1981). However, for the same turbulence level, the change observed in the turbulent boundary layer on the pressure surface of the rotor blade was significant. Similarly, in the case of the vanes, the change in heat transfer coefficient in the laminar boundary layer region on the pressure surface was more than that observed on the suction surface for the same inlet turbulence level.

The heat transfer coefficient distribution obtained for vanes I and II can be compared with those obtained by Turner (1969) as the blade profile and velocity distribution are similar. Significant differences were observed on the effect of turbulence on the transition region as well as on the magnitude of local heat transfer coefficient. The large change in the transition region observed on the suction surface with change in turbulence level in the range 2.2 to 5.9 percent was not observed in the present investigations. The magnitude of change in the local heat transfer coefficient with turbulence level was smaller in the present study. However, the heat transfer data obtained for all three blade profiles investigated in this study exhibited the same trend with change in turbulence level. The magnitude of change in local heat transfer coefficient with free-stream turbulence was of the same order as that observed for a cylinder in crossflow and the transition behavior observed was consistent with the natural transition observed in a favorable pressure gradient region (Blair, 1982; Narasimha et al., 1984).

Correlations for the Effect of Free-Stream Turbulence on Local Heat Transfer. An attempt was made to estimate the effect of free-stream turbulence on the heat transfer in different

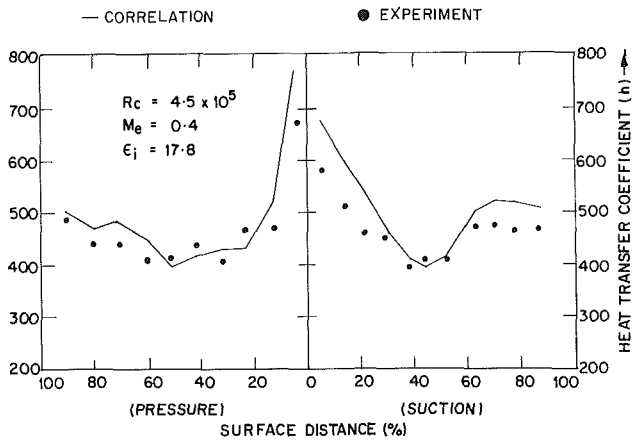

Fig. 5 Comparison between heat transfer data obtained from experiment and correlation: rotor blade

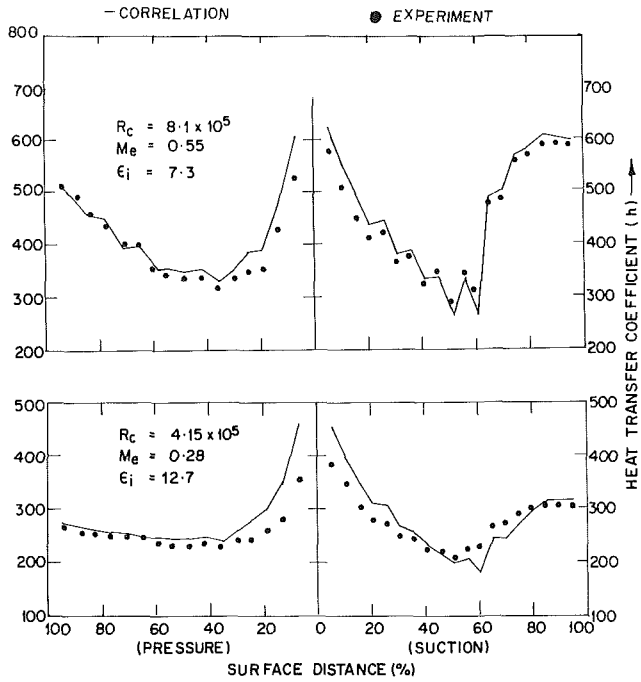

Fig. 6 Comparison between heat transfer data obtained from experiment and correlation: N.G.V. I

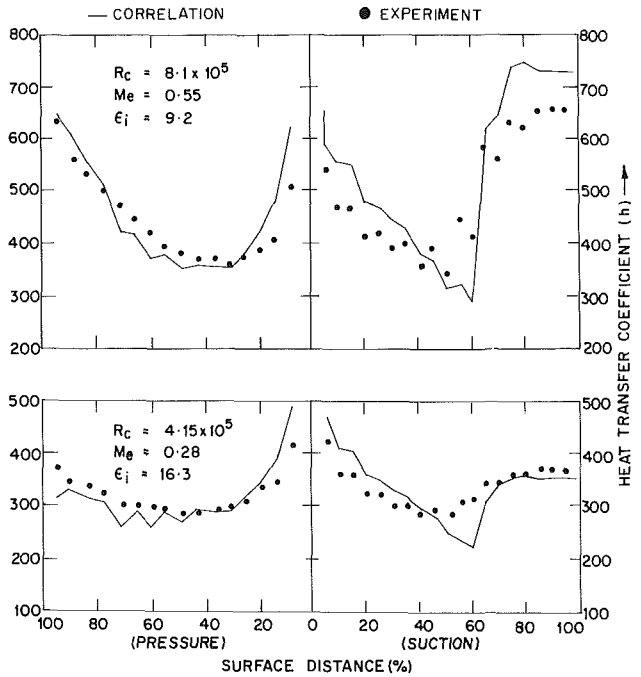

Fig. 7 Comparison between heat transfer data obtained from experiment and correlation: N.G.V. II

boundary layer regions using the correlations of Brown and Martin (1979) and Zysina Molozhen et al. (1977). These correlations employed the turbulence level at the cascade inlet as the correlating parameter and indicated that the effect of turbulence on the heat transfer would be the same on both the suction and pressure surfaces. However, the present experimental data indicated that in the same type of boundary layer the effect of free-stream turbulence on the heat transfer on the pressure surface was much higher than that on the suction surface. Hence, based on turbulence decay measurement within a scaled-up blade passage, correlations were developed for the effect of free-stream turbulence level on the local heat transfer coefficient with the local turbulence level as the correlating parameter. In this case, the variation in the $\langle u'^2 \rangle$ component of velocity in the blade passage was assumed to be negligible (frozen turbulence) and the local turbulence level was estimated by dividing it by the local free-stream velocity around the blade surface. The data obtained for the rotor blade at different Reynolds numbers and turbulence levels were used for generating the correlation. The data from the points where the local turbulence was the same were used for the correlation. The correlation for the laminar boundary layer was obtained using the data at points A, B, and C located on the suction surface and that for the turbulent boundary layer was obtained using the data at points D, E, and F on the pressure surface of the rotor blade (Fig. 1). From the analysis of the data, the following correlations were obtained:

1 Laminar boundary layer

$$h = h_{\epsilon=0} * (1 + 0.04\epsilon) \quad \text{for } \epsilon \lesssim 2$$
$$= h_{\epsilon=0} * (1.0 + 0.44\epsilon^{0.55})/1.502 \quad \text{for } 2 < \epsilon \leq 12$$

2 Turbulent boundary layer

$$h = h_{\epsilon=0} * (1 + 0.0235\epsilon) \quad \text{for } \epsilon < 36 \text{ percent}$$

The above correlations, obtained by processing the data from a small portion in the laminar and turbulent boundary layer region on the rotor blade, were applied to the entire suction and pressure surface of the rotor blade and the vanes in order to establish their accuracy. A comparison of the experimental heat transfer coefficient distributions obtained at high free-stream turbulence levels with those obtained from the correlations is shown in Figs. 5, 6, and 7. As the development of the transition region, in particular on the pressure surface of the vanes, was influenced by free-stream turbulence levels <3 percent, the heat transfer coefficient distribution obtained at $\epsilon_i = 5.5$, 3.6, and 4.6 percent were used as the baseline data in the above estimate, for the rotor blade and the guide vanes. For the transitional boundary layer region on the pressure surface of the vanes, the laminar correlations were used as they provided good agreement with the experimental data. It can be observed that the agreement between the values obtained from the correlations and the experimental data is very satisfactory. A similar comparison, carried out using the proposed laminar correlation for the variation in the local heat transfer coefficient in the laminar boundary layer region over the forward region of the cylinder kept in crossflow, also exhibited good agreement (Krishnamoorthy, 1986).

Conclusions

Systematic investigations were carried out to study the effect of free-stream turbulence on the development of the hydrodynamic and thermal boundary layer over a rotor blade and two nozzle guide vanes. The results indicated that:

1 The transition to the turbulent boundary layer on the suction surface appears to be through a separation bubble. The effect of free-stream turbulence and the Reynolds number on the location of this separation bubble was negligible.

2 The effect of flow Reynolds number and free-stream turbulence appears to be small on the location of the transition point on the pressure surface where the gradual transition begins. However, the length of the transition region decreased with increase in Reynolds number. A similar effect was observed with the variation in the free-stream turbulence in the range 1.6 to 3.6 percent.

3 A systematic change in local heat transfer coefficient was observed with a change in free-stream turbulence level, in the laminar, transitional, and turbulent boundary layer regions.

4 Correlations developed for estimating the effect of free-stream turbulence on the local heat transfer coefficient using the local turbulence intensity as the correlating parameter predict with satisfactory accuracy the variation in heat transfer coefficient distribution observed over the entire suction and pressure surfaces.

Acknowledgments

The authors wish to thank the reviewers for their suggestions. The financial support provided by the Aeronautical Research and Development Board, India is gratefully acknowledged.

References

Baines, W. D., and Peterson, L. G., 1951, "An Investigation of Flow Through Screens," *Trans. ASME*, Vol. 73, pp. 467–480.

Bayley, F. J., and Priddy, W. J., 1981, "Effects of Free Stream Turbulence Intensity and Frequency on Heat Transfer to Turbine Blading," ASME *Journal of Engineering for Power*, Vol. 103, pp. 60–64.

Blair, M. F., 1982, "Influence of Free Stream Turbulence on the Boundary Layer Transition in Favorable Pressure Gradients," ASME *Journal of Engineering for Power*, Vol. 104, pp. 743–750.

Brown, A., and Martin, B. W., 1979, "Heat Transfer to Turbine Blades, With Special Reference to the Effects of Mainstream Turbulence," ASME Paper No. 79-GT-26.

Consigny, H., and Richards, B. E., 1982, "Short Duration Measurements of Heat Transfer to a Gas Turbine Rotor Blade," ASME *Journal of Engineering for Power*, Vol. 104, pp. 542–551.

Dunham, J., and Edwards, J. P., 1973, "Heat Transfer Calculation for Turbine Blade Design," AGARD-CP-73-71.

Hinze, J. O., 1959, *Turbulence*, 2nd ed., McGraw-Hill, New York.

Junkhan, G. H., and Serovy, G. K., 1967, "Effects of Free Stream Turbulence and Pressure Gradient on Flat Plate Boundary Layer Velocity Profile and on Heat Transfer," ASME *Journal of Heat Transfer*, Vol. 89, pp. 169–176.

Krishnamoorthy, V., 1986, "Effect of Free Stream Turbulence on the Convective Heat Transfer to Gas Turbine Blades," Ph.D. Thesis, Mechanical Engineering Department, India Institute of Technology, Bombay.

Kurosh, V. D., and Epik, E. Ya., 1970, "The Effect of Turbulence on Heat Transfer in Turbomachinery Flow Passages," *Heat Transfer—Soviet Research*, Vol. 2, No. 1.

Ligrani, M., and Breugelmans, A. E., 1981, "Turbine Blade Cooling Research at Von Kármán Institute for Fluid Dynamics," presented at 5th ISABE, Bangalore, India.

Lowery, G. W., and Vachon, R. I., 1975, "The Effect of Turbulence on Heat Transfer From Heated Cylinders," *International Journal of Heat and Mass Transfer*, Vol. 18, pp. 1229–1242.

Martin, B. W., Brown, A., and Garrent, S. E., 1978, "Heat Transfer to a PVD Rotor Blade at High Subsonic Passage Throat Mach Numbers," *Proc. Instn. Mech. Engrs.*, Vol. 192, pp. 225–235.

Narasimha, R., Devasia, K. J., Gururani, G., and Badrinarayanan, M. A., 1984, "Transitional Intermittency in Boundary Layers Subject to Pressure Gradient," *Experiments in Fluids*, Vol. 2, pp. 171–176.

Nealey, D. A., Mihelc, M. S., Hylton, L. D., and Gladden, H. J., 1984, "Measurements of Heat Transfer Distribution Over Surfaces of Highly Loaded Turbine Nozzle Guide Vanes," ASME *Journal of Engineering for Gas Turbines and Power*, Vol. 106, pp. 149–158.

Priddy, W. J., and Bayley, F. J., 1985, "Effects of Free Stream Turbulence on the Distribution of Heat Transfer Around Turbine Blade Sections," *Int. J. Heat and Fluid Flow*, Vol. 6, No. 3, pp. 181–192.

Rued, K., and Wittig, S., 1986, "Laminar and Transitional Boundary Layer Structures in Accelerating Flow With Heat Transfer," ASME JOURNAL OF TURBOMACHINERY, Vol. 108, pp. 116–123.

Turner, A. B., 1969, "Local Heat Transfer Measurement on a Gas Turbine Blade," University of Sussex, 69/ME/15.

Zysina-Molozhen, L. M., Dergach, A. A., Medvedeva, M. A., and Roost, E. G., 1977, "The Development of Thermal Boundary Layer in Turbine Cascades," *Heat Transfer—Soviet Research*, Vol. 9, No. 4, pp. 88–95.

Correlation and Prediction of Film Cooling From Two Rows of Holes

B. A. Jubran
Department of Mechanical Engineering,
University of Jordan,
Amman, Jordan

This paper reports the correlation and prediction of film cooling effectiveness and the velocity field from two rows of holes inclined in the streamwise and spanwise directions. The correlation of film cooling from two rows of holes can be achieved by using a two-dimensional correlating group provided that account is taken of the momentum ratio I. *The effectiveness and velocity field were predicted using the PHOENICS package. Two versions of* k–ϵ *turbulence model were explored for the film cooling predictions, which were successful at the centerlines and for low blowing rates. A nonisotropic* k–ϵ *model improved the prediction by allowing the jet to spread laterally.*

1 Introduction

Better thermal efficiency of gas turbines implies a higher gas temperature at the turbine inlet and consequently a much harsher working environment for "hot end" components. Acceptable working lives of these components can be achieved only by sophisticated design, better material, and more efficient cooling methods. One cooling method is that of film cooling in which injection of coolant through multiple rows of holes is used to protect surfaces.

For many years researchers have been involved in developing correlations to represent film cooling effectiveness measurements and computational procedures for predicting the film cooling field. Most of the correlations are based on the de-icing work of Wieghardt (1946) or the two-dimensional injection flow model of Hatch and Papell (1959) and Papell (1960) extended by Brown (1967) to allow for exchange between the two-dimensional jet and the free stream via an energy balance. The correlations have been developed for continuous slot, single hole, and a row-of-holes injection configurations but to the knowledge of the author, not to a two-rows-of-holes configuration. Heat sink models for a discrete hole injection started from the work of Ramsey et al. (1970) and was developed by Eriksen et al. (1971) through a point sink model. Saluja (1977) considered the use of a line sink model to improve the prediction of off-centerline effectiveness for a discrete hole injection and developed it further to cover a row of holes.

Ramette and Louis (1984) carried out an analytical study of cooling film injected from a single line of the inclined round holes. The path of the jets, the growth of the layer, the trajectory of the vortices, the velocity, and temperature profiles were determined using a self-contained analytical formulation. A very satisfactory comparison was found with the experimental data. Tillman et al. (1985) predicted the cooling air flow from blades with angled holes that are oriented so the internal flow must turn more than 90 deg to enter the holes, together with study of blades in which the cooling air is distributed along the spanwise length of the blade by an insert.

In recent years many investigators have developed numerical procedures for film cooling based on the Patankar and Spalding (1967) procedure for the calculation of heat, mass, and momentum transfer for three-dimensional parabolic flows. This procedure can simulate regions of recirculation flow in the cross-stream plane but not in a plane parallel to the direction of the free stream. However, it has been revealed by Bergeles et al. (1976) that a recirculation region exists near the injection holes, hence elliptic equations must be solved to represent the true situation. The procedure of Patankar and Spalding was used by Patankar et al. (1973) to predict the film cooling from three-dimensional slots. Bergeles (1976) developed a semi-elliptic procedure for the film cooling from two rows of holes. In these predictions the most serious problem affecting the solution is the selection of turbulence mode. Also most of the published work on film cooling predictions consider the solution as either parabolic or semi-elliptic; none have considered the problem as elliptic, which is the true situation due to the recirculation involved.

This paper explores the application of correlation groups developed for two-dimensional film cooling by Brown (1967), extended to a single row of holes by Brown and Saluja (1979), to film cooling from two rows of holes with streamwise and spanwise direction of inclination. Also the application of isotropic and nonisotropic k–ϵ turbulence models together with that of the function model of Rodi (1972) using an elliptic procedure embodied in the PHOENICS package developed by CHAM is presented.

2 Experimental Details

2.1 Experimental Rig. The experimental investigation was carried out in a low-speed recirculatory wind tunnel (Fig. 1), which provided a uniform free stream at a controlled velocity up to 15 m/s and temperature up to 60°C. Cold air was injected through the base of the working section. Temperature measurements were made on the base of the working section downstream of the cold air injection tubes in the streamwise and lateral directions (Fig. 2). The injection

Contributed by the International Gas Turbine Institute for publication in the JOURNAL OF TURBOMACHINERY. Manuscript received at ASME Headquarters June 14, 1988.

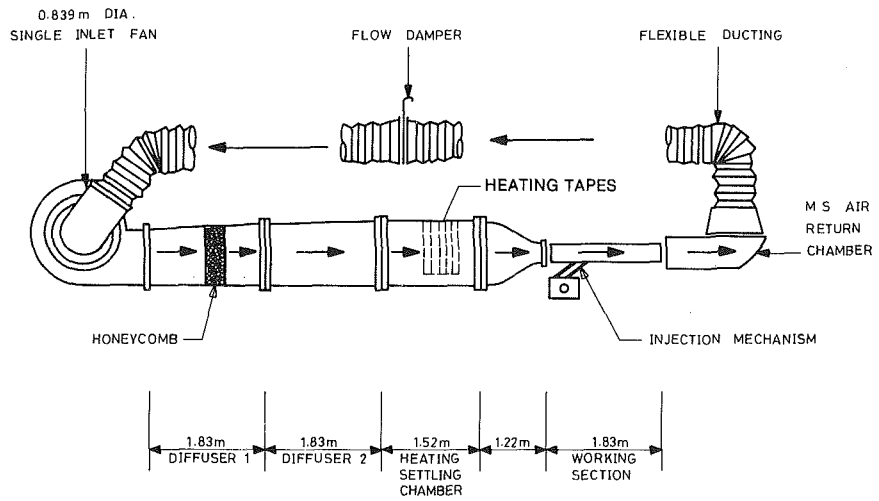

Fig. 1 Schematic diagram of low-speed wind tunnel

configurations investigated were two symmetric staggered rows of holes of constant hole diameter (equal to 19.4 mm) spaced 10 hole diameters in the streamwise direction, the pitch to diameter ratio was 3, and the angles of injection were either 30 or 90 deg to the streamwise direction and 90 or 45 deg to the lateral direction. A summary of the injection configurations is given in Table 1. A detailed description of the experimental work used in this study is reported in Jubran and Brown (1985).

2.2 Measurement Techniques. The surface temperature of the test section was measured before and after the coolant was introduced, by chromel/alumel thermocouples embedded in the surface. The output of the thermocouples was fed to a Solatron data logger.

A DISA constant-temperature hot-wire anemometer with a single hot-wire probe type 55P11 was used to investigate the flow at the exit of the injection hole. In the absence of a transverse stream, the measurements with the above system using a single-wire probe would, according to the analysis of Ribeiro and Whitelaw (1972), be expected to yield injection

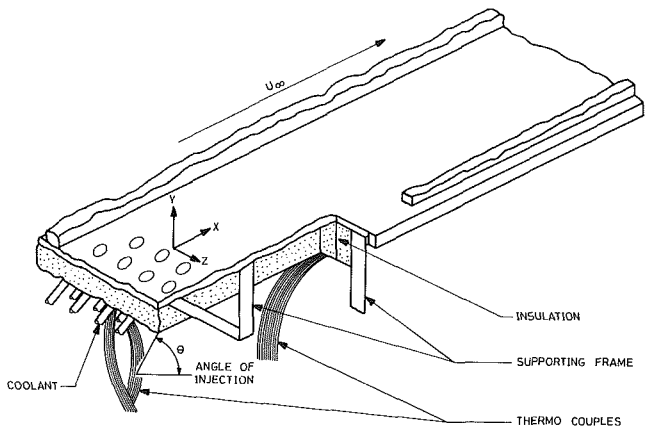

Fig. 2 Schematic diagram of test section

Nomenclature

A = nondimensional correlating group
C_m = coefficient
C_μ, C_τ, C_D = coefficients in the turbulence model
D = diameter of the injection tube
f = function (see equations (2), (3) and (4))
I = momentum ratio
k = turbulent energy
l = mixing length
M = blowing rate
P = pitch distance between the holes
Re = Reynolds number
s = equivalent slot opening
u_1 = x, (x_1) direction velocity
u_2 = y, (x_2) direction velocity
u_3 = z, (x_3) direction velocity
u_i' = fluctuating velocity, with $i = 1, 2, 3$
x = streamwise direction
X_1 = distance from the center of the first row of holes
X_2 = distance from the center of the second row of holes
y = distance normal to the surface direction
z = lateral direction
γ = exponent, see equations (3) and (4)
Γ = fluctuating energy function
δ = boundary layer thickness
ϵ = dissipation rate of k
η = local film cooling effectiveness
$\bar{\eta}$ = average film cooling effectiveness $= \dfrac{1}{\int_0^{P/2D} \eta d(Z/D)}$
μ = laminar dynamic viscosity
μ_t = eddy (or turbulent) viscosity
ν = kinematic molecular viscosity
ρ = density of the fluid

Subscripts

c = coolant
i = injection
m = mainstream
t = turbulent

Table 1

Model	Angle to streamwise direction		Angle to lateral direction		S/D	P/D
	Row 1	Row 2	Row 1	Row 2		
A	30	30	90	90	10	3
B	30	90	90	90	10	3
C	30	90	90	45	10	3

velocities and turbulence intensities accurate to within 1 and 8 percent, respectively. However, the presence of transverse flow, with the attendant distortion of the streamlines and generation of high turbulence levels, introduces problems of signal interpretation that make it difficult to estimate the accuracy attained near the surface of the test plate. The errors in the readings of the turbulence signals were minimized by taking five readings and averaging them. No problems with the signal readings of the hot-wire anemometer were experienced when the measurements were taken away from the injection holes and at the free stream. The free-stream velocity and the free-stream turbulence errors were within 5 percent. The accuracy of the film cooling effectiveness measurements is estimated to be at least 2 percent (for effectiveness >0.7) and at worst 15 percent (for effectiveness <0.05).

2.3 Conditions of the Experiment. In the absence of cold air injection the free-stream velocity at the first row of holes was 10 m/s throughout the measurements described in this article, giving a value of $\mathrm{Re}_x = 3.54 \times 10^5$ at the point of injection at the first row of holes. The ratio of free-stream displacement thickness to hole diameter for the first row of holes was 0.077 and the length of the hole of diameter ratio of air injection was 15 for the cases of 30 deg streamwise inclination. During film cooling measurements the temperature of the free stream was maintained at about 30°C above the temperature of the injected coolant and the ratio of coolant to free-stream density was about 1.1. The velocity ratio U_c/U_m was variable up to 1.2; the blowing rate, $M = \rho_c U_c/\rho_m U_m$, varied to 1.35. The corresponding upper limit for the momentum flux ratio, $I = \rho_c U_c^2/\rho_m U_m^2$ was about 1.6. The free-stream turbulence intensity was 0.03.

3 Correlation of Film Cooling

The correlation of the local film cooling effectiveness downstream of the second row of holes and the average film cooling effectiveness are examined for three injection models having inclinations of 30 or 90 deg in the stream direction and 90 or 45 deg in the lateral direction. Brown (1967) developed correlation groups based on a heat balance model for a two-dimensional flow model and suggested that the following group is most useful:

$$A = (Ms/x)(\mathrm{Re}_x)^{0.2}/(1 - x_i/x) \tag{1}$$

where x is the distance from the leading edge of the test plate and x_i is the distance up to the injection point. Brown further found that introducing the momentum ratio I into the correlation groups caused the effectiveness measurements to collapse into a single curve for a given injection angle in the streamwise direction. This led to the following correlation:

$$\eta = f_1(I) f_2(A) \tag{2}$$

where

$$f_2(A, I) = A^{\gamma} \tag{3}$$

and

$$\gamma = f_3(I) \tag{4}$$

The value of s used in the present investigation for group A is the equivalent slit width of area equal to the area of the holes through which the coolant was injected, that is, $s = (\pi D^2/4p)$. Equations (1), (2), (3), and (4) have been applied

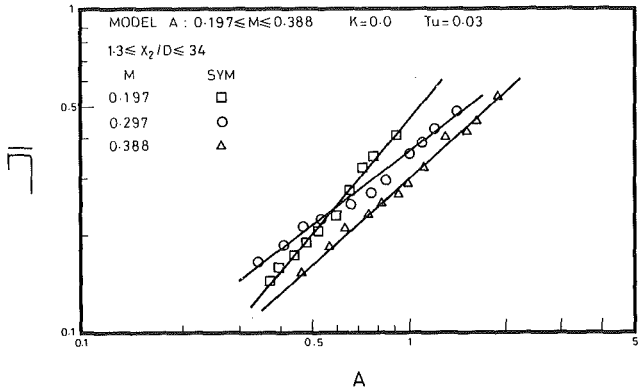

Fig. 3(a) $\bar{\eta}$ versus correlation group A

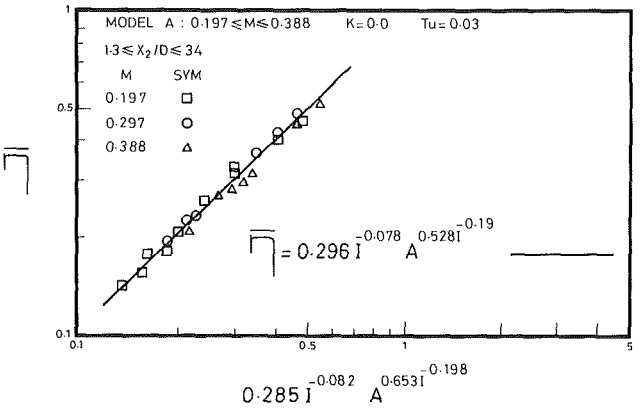

Fig. 3(b) Correlation of $\bar{\eta}$ for model A at low blowing rates

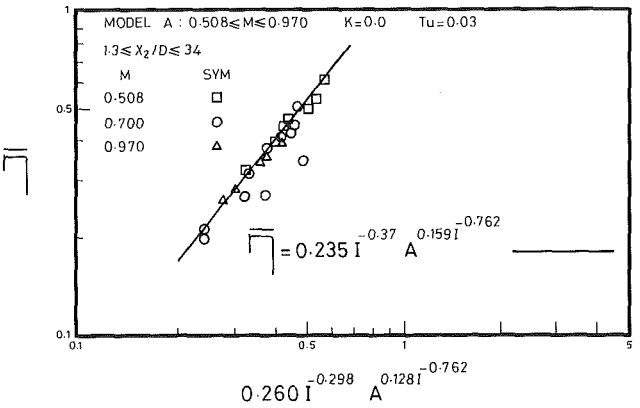

Fig. 4 Correlation of $\bar{\eta}$ for model A at high blowing rates

with some success to effectiveness measurements for a single row of holes (see Brown and Saluja, 1979).

Film cooling performance based on the blowing rate tends to divide into two distinct regions: low blowing rates $M<0.5$ and high blowing rates $M>0.5$. For high blowing rates the jet tends to lift off the cooled surface and, therefore, one would expect the correlation for these blowing rates to be different from those when the jets are attached to the surface.

Figure 3(*a*) shows plots of averaged film cooling effectiveness for model A for three blowing rates $M = 0.197$, 0.297, and 0.388 in the surface region $1.3 < X_2/D < 34$. For each blowing rate the points collapsed into individual straight lines; applying equations (2), (3), and (4) collapsed the measurements onto a single line, as can be seen in Fig. 3(*b*), described by the following correlation:

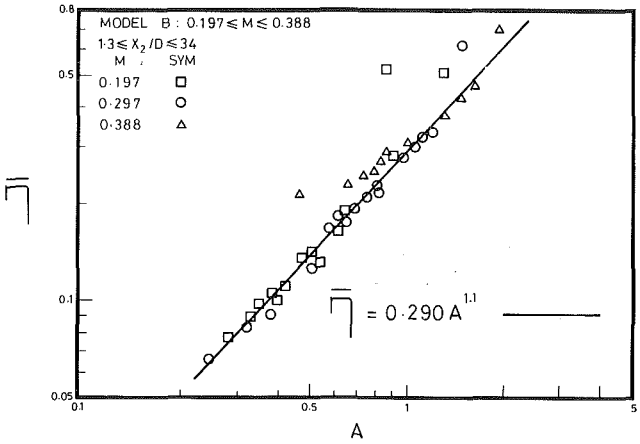

Fig. 5(*a*) Correlation of $\bar{\eta}$ for model B at low blowing rates

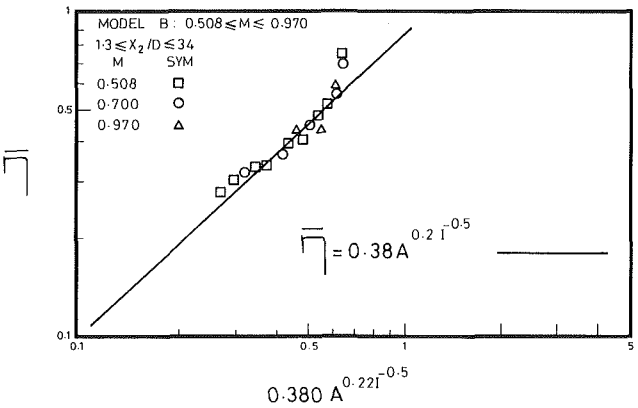

Fig. 5(*b*) Correlation of $\bar{\eta}$ for model B at high blowing rates

$$\bar{\eta} = 0.296 I^{-0.078} \quad A^{0.528 I^{-0.198}} \tag{5}$$

Using the same approach as above, the correlation of the averaged effectiveness for model A for high blowing rates $0.508 < M < 0.970$ and the same surface region as far as the low blowing rate case, is shown in Fig. 4 and is given by

$$\bar{\eta} = 0.235 I^{-0.37} \quad A^{0.159 I^{-0.762}} \tag{6}$$

From Figs. 3 and 4 it can be seen that the correlation group can be used to correlate $\bar{\eta}$ results from two rows of holes when the momentum ratio I is incorporated. A similar approach has been applied to the average film cooling effectiveness for models B and C illustrated in Figs. 5 and 6 and centerline effectiveness for models A, B, and C illustrated in Figs. 7, 8, and 9, respectively. Clearly the film cooling measurements downstream of two rows of holes can be sensibly correlated.

4 Prediction of Film Cooling

The PHOENICS package developed by CHAM has been used to predict film cooling temperature and velocity fields for model A. Solutions are obtained by solving three-dimensional continuity, momentum, and energy equations for turbulent flow in which the Reynolds stress $\overline{u_i' u_j'}$ was modeled using modified isotropic and nonisotropic k-ϵ models developed by Bergeles (1976); the heat transfer counterpart was that developed by Launder et al. (1975).

For both momentum and heat the diffusive transport properties are proportional to that of the normal stresses in the respective direction. Bergeles suggested that in order to explain the near-wall temperature profiles, Γ_3 must be greater than Γ_2 where

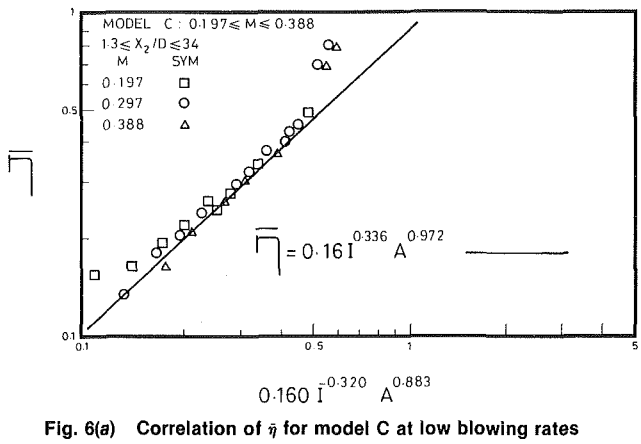

Fig. 6(*a*) Correlation of $\bar{\eta}$ for model C at low blowing rates

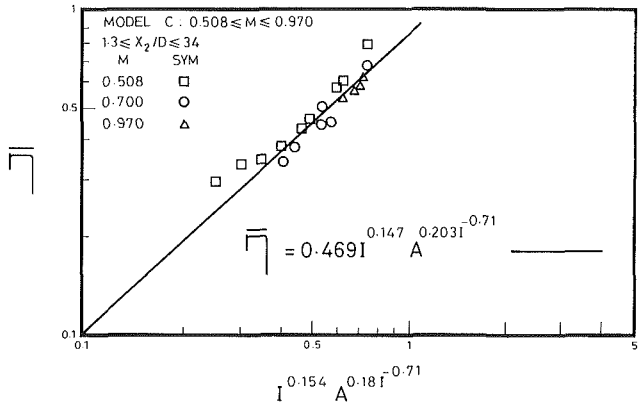

Fig. 6(*b*) Correlation of $\bar{\eta}$ for model C at high blowing rates

$$\Gamma_i = 0.31 \frac{k}{\epsilon} \overline{u_i'^2}$$

and suggested the following relation:

$$\frac{\Gamma_3}{\Gamma_2} = \frac{\mu_{t_3}}{\mu_{t_2}} = 1 + C_m(1 + y/\delta) \text{ for } y < \delta \tag{7}$$

i.e., assuming nonisotropic viscosity, and

$$\frac{\Gamma_3}{\Gamma_2} = \frac{\mu_{t_3}}{\mu_{t_2}} = 1 \text{ for } y > \delta \tag{8}$$

i.e., assuming isotropic viscosity. The constant C_m in the present investigation was found to be 3.5 and $\overline{u_2'^2}$ was assumed to be $k/3$, which leads to the following expressions for the effective turbulent viscosity and diffusivity, respectively:

$$\mu_{t_2} = C_\mu \frac{k^2}{\epsilon} \tag{9}$$

$$\Gamma_2 = C_\tau \frac{k^2}{\epsilon} \tag{10}$$

and where C_μ and C_τ are 0.09 and 0.1, respectively. However during the course of the present investigation it was found that $C_\mu = 0.09$ cannot be used for high blowing rates over the region of the holes, so the function model $C_\mu = f(\overline{E/\epsilon})$ of Rodi (1972) was used. Figure 10 shows the variation of C_μ with $\overline{E/\epsilon}$, the ratio of production to dissipation, from Rodi, and $C_\mu = 0.09$ is only correct for the flow in equilibrium, which is not the case at high blowing rates.

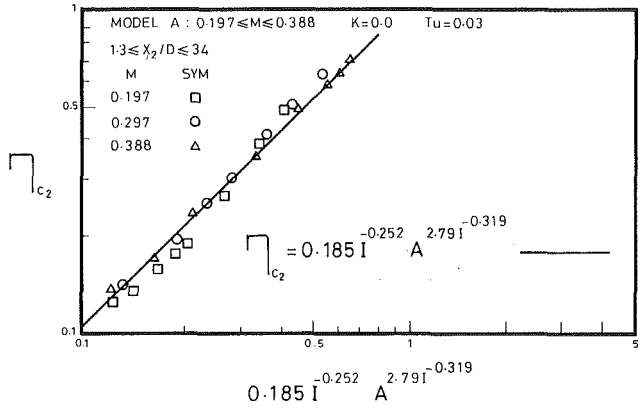

$$0.185\, I^{-0.252}\, A^{2.79 I^{-0.319}}$$

Fig. 7(*a*) Correlation of η_{C_2} for model A at low blowing rates

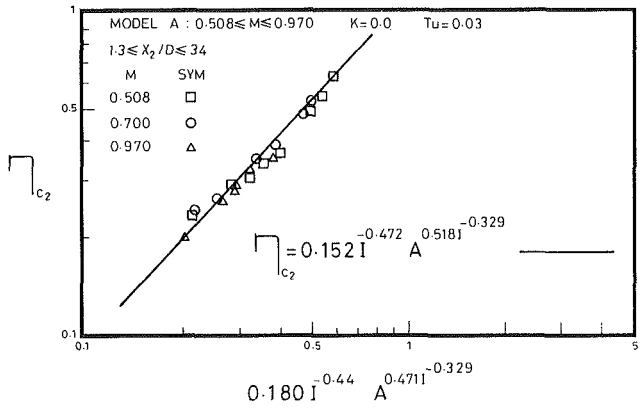

$$0.180\, I^{-0.44}\, A^{0.471 I^{-0.329}}$$

Fig. 7(*b*) Correlation of η_{C_2} for model A at high blowing rates

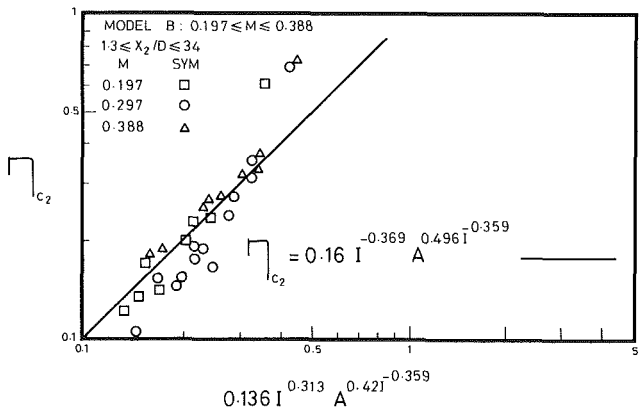

$$0.136\, I^{0.313}\, A^{0.42 I^{-0.359}}$$

Fig. 8(*a*) Correlation of η_{C_2} for model B at low blowing rates

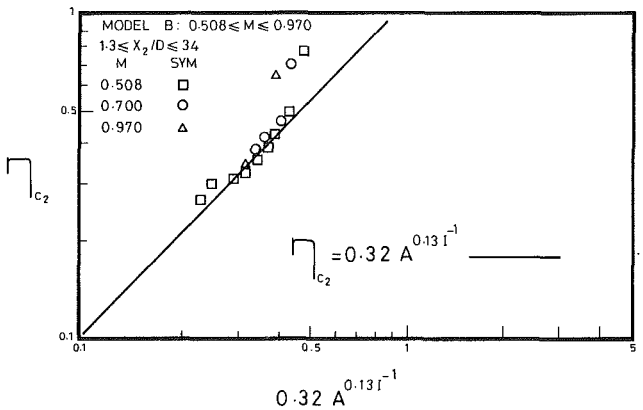

$$0.32\, A^{0.13 I^{-1}}$$

Fig. 8(*b*) Correlation of η_{C_2} for model B at high blowing rates

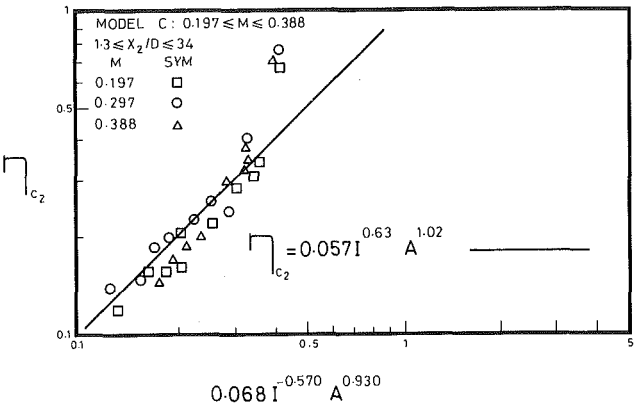

$$0.068\, I^{-0.570}\, A^{0.930}$$

Fig. 9(*a*) Correlation of η_{C_2} for model C at low blowing rates

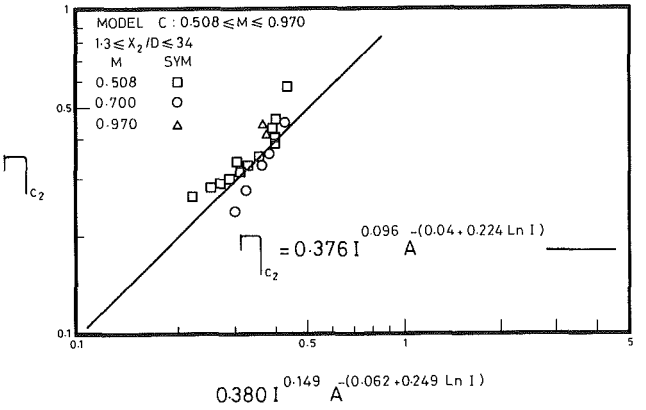

$$0.380\, I^{0.149}\, A^{-(0.062\, +0.249\, \mathrm{Ln}\, I)}$$

Fig. 9(*b*) Correlation of η_{C_2} for model C at high blowing rates

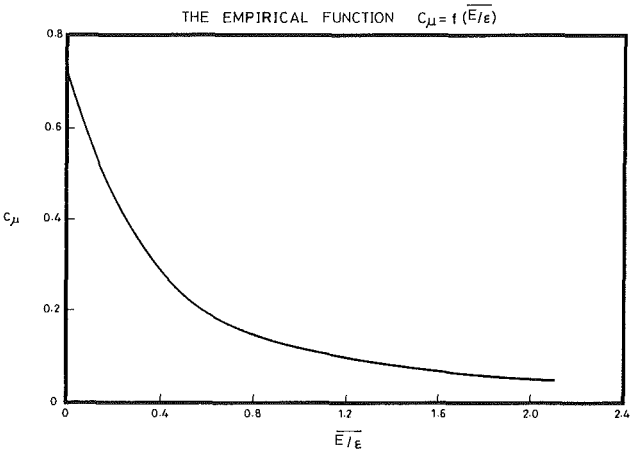

Fig. 10 The empirical function $C_\mu = f(\overline{E/\epsilon})$

The policy used for assigning the boundary conditions was as follows:

(*i*) The inlet boundary was taken far away from the injection so it can be assumed uniform, and the lateral velocity u_3 was set equal to zero.

(*ii*) The free-stream velocity was put equal to 10 m/s and k and ϵ were prescribed according to Launder and Spalding (1972), given by

$$k = l^2 \left(\frac{\partial u}{\partial y}\right)^2 / \sqrt{C_D} \tag{11}$$

and

$$\epsilon = C_D^{0.75} k^{1.5} / l \tag{12}$$

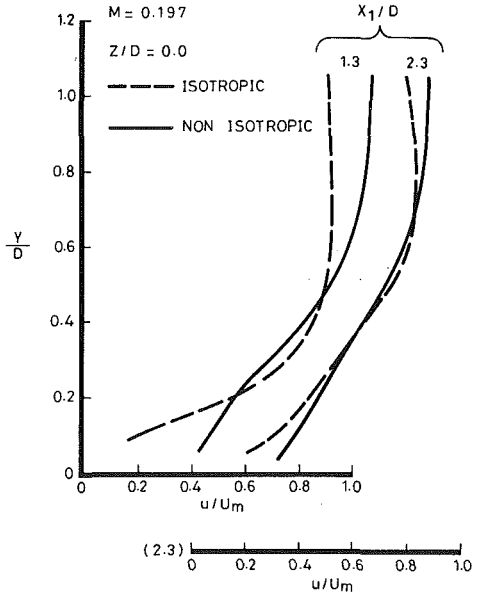

Fig. 11(a) Prediction of velocity profiles at $Z/D = 0.0$ and $M = 0.197$

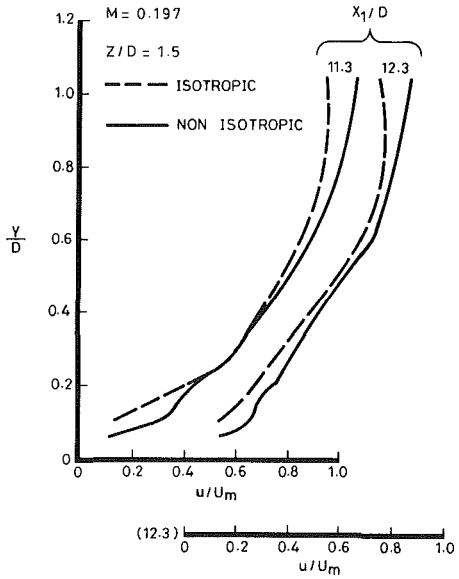

Fig. 11(b) Prediction of velocity profiles at $Z/D = 1.5$ and $M = 0.197$

where l is the Prandtl mixing length and $C_D = 0.8$.

(*iii*) The inlet velocity was assumed either uniform or to have a power law profile over the hole. k and ϵ were evaluated using equations (11) and (12).

(*iv*) The wall boundary was that embodied in the PHOENICS package for velocities and k and ϵ.

Grid-dependence test runs were done to explore the grid dependence and the number of iterations of the predicted solutions for flow conditions corresponding to the experiment carried out on model A. The three grid distributions tested were 12×10, 24×25, and 30×25 nodes in the vertical and the lateral directions (Y, Z), respectively. The forward steps were such that very close to the holes, they were very small, as small as $0.2D$ and away from the hole the distance increased. The runs made indicated that a 12×10 grid have an almost grid-independent solution for the streamwise direction at the centerline of the first row of holes, a 24×25 grid was required for the solution at the centerline of the second row of holes, and at the lateral position $Z/D = 0.9$. The effects of forward steps and the number of iterations were obtained by a few runs and found to be 30 steps and 40 iterations.

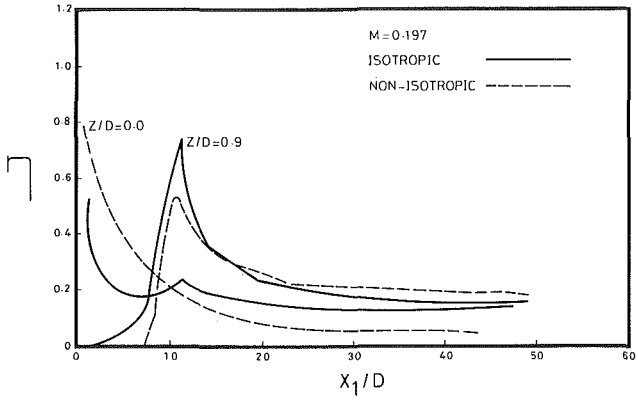

Fig. 12 Prediction of η using isentropic and nonisentropic k-ϵ model

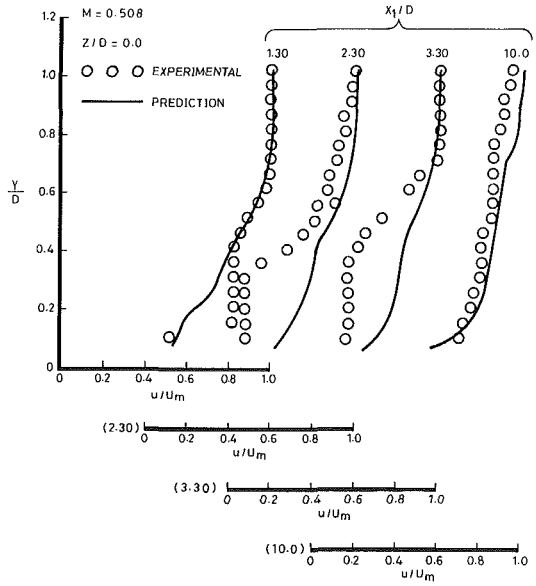

Fig. 13 Prediction of the velocity profiles at $Z/D = 0.0$ and $M = 0.197$

The effect of the nonisotropic k-ϵ model on the prediction of velocity profile is shown in Fig. 11 for the positions just behind the first and second rows of holes. At $X_1/D < 2.3$, just behind the first row of holes, using an isotropic viscosity model tends to slow the flow, especially at $X_1/D = 1.3$. At the centerline of the second row of holes the effect is the same, but not as severe as at the first row of holes. The corresponding effect of the nonisotropic viscosity on film cooling effectiveness is shown in Fig. 12. At the centerline of the first row of holes employing a nonisotropic viscosity model reduced the film cooling effectiveness for $X_1/D < 10$. This may be due to the fact that at the centerline of the first row of holes as was shown in Fig. 11, the nonisotropic viscosity model tends to accelerate the flow, hence increasing the mixing between free stream and jet and so reducing the film cooling effectiveness. At $X_1/D > 10$ the nonisotropic viscosity model increased the film cooling, which implies that the nonisotropic model helps spreading of the jets, bearing in mind that the row spacing is 10 hole diameters. This also can be seen at the lateral location $Z/D = 0.9$, where for $X_1/D < 10$ the nonisotropic model increased the spreading of the jets and hence increased the film cooling effectiveness.

Figure 13 shows the prediction of the velocity profiles on centerlines for $M = 0.197$ at different distances downstream of the first row of holes. The predicted results compare well with the experimental results for $X_1/D < 10$, after which the prediction underestimated the experimental results due to the effect of the second row of holes; its spreading may not be accounted

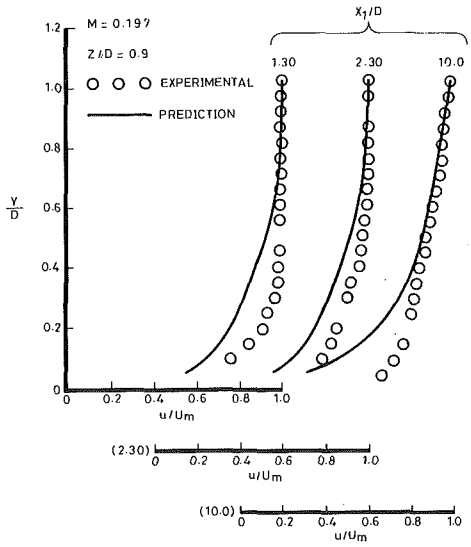

Fig. 14 Prediction of the velocity profiles at $Z/D = 0.9$ and $M = 0.197$

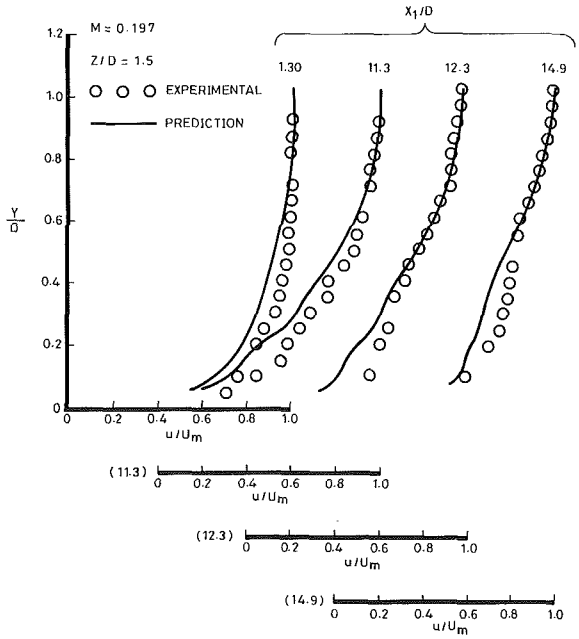

Fig. 15 Prediction of the velocity profiles at $Z/D = 1.5$ and $M = 0.197$

for by the turbulence modeling. The prediction at the lateral position $Z/D = 0.9$ (see Fig. 14) is less satisfactory than that for $Z/D = 0$, again implying that the turbulence modeling fails to account for the spreading of jets. The prediction downstream of the second row of holes is shown in Fig. 15, and again there is a tendency to underestimate the velocity profile. This is true in particular close to the surface where the experimental measurements show jetting to occur. The corresponding prediction and measurements of film cooling effectiveness are shown in Fig. 16.

At the centerline of the first row of holes the predictions are good up to $X_1/D = 11$, after which the prediction tends to underestimate. The prediction uses the nonisotropic viscosity model and takes into account both the convective and the diffusive transport in the solution. At the lateral position $Z/D = 0.9$ the prediction tends to underestimate the measurements considerably for $X_1/D < 10$. However, just downstream of the second row of holes at this lateral position the experimental results were predicted very well up to $X_1/D = 30$. At the centerline of the second row of holes and at

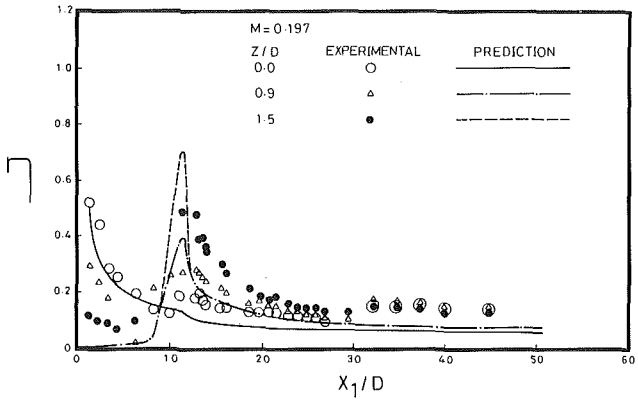

Fig. 16 Prediction of η at low blowing rate

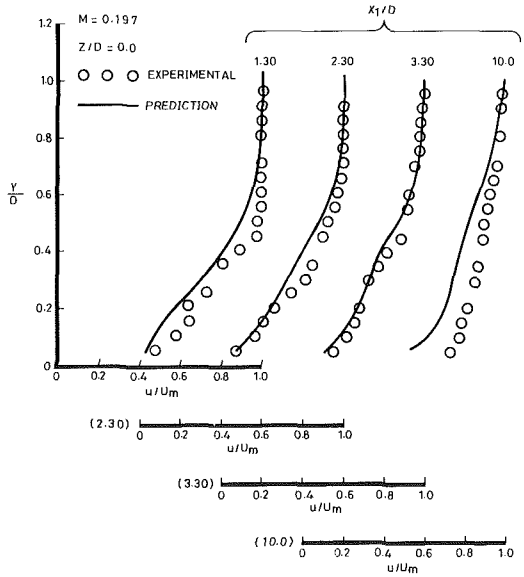

Fig. 17 Prediction of the velocity profiles at $Z/D = 0.0$ and high blowing rate

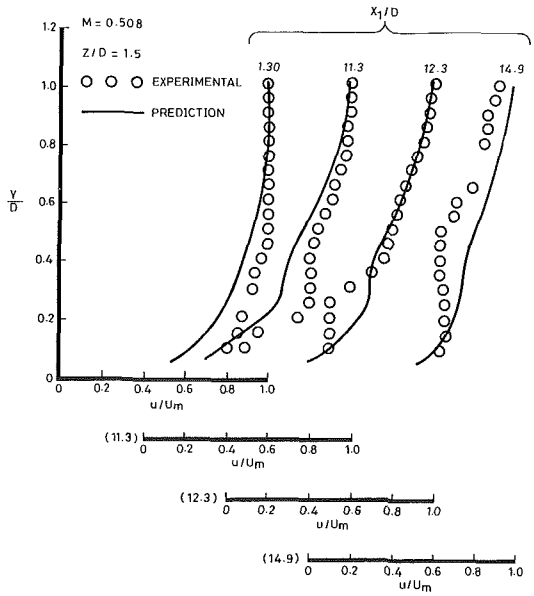

Fig. 18 Prediction of the velocity profiles at $Z/D = 1.5$ and high blowing rate

all distances downstream, except over the holes, the prediction underestimated film cooling effectiveness.

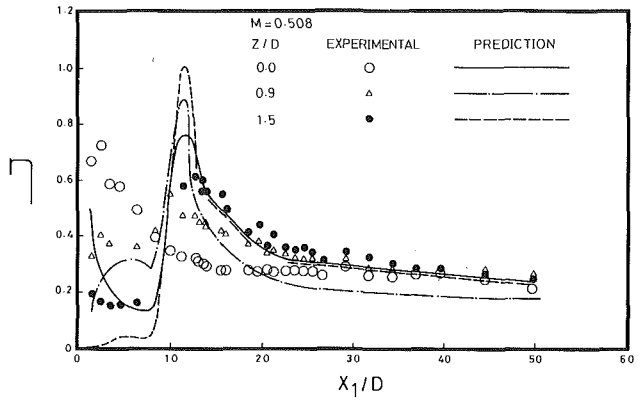

Fig 19 Prediction of η at high blowing rate

As the blowing rates were increased to $M = 0.508$ the prediction of velocity and effectiveness got worse (see Figs. 17–19). The reason for this is that as the blowing rates increased the assumptions made during the modeling, in particular that the flow is in equilibrium and that only two components of Reynolds stresses are important, become less satisfactory.

5 Conclusions

The following points emerged from the present investigation:

(*i*) The centerline and the average film cooling effectiveness results from two rows of holes can be correlated by using a two-dimensional film cooling correlation provided that the momentum ratio I is incorporated in the correlation.

(*ii*) As the injection angle increased to 90 deg in the streamwise direction or to 45 deg in the spanwise direction the correlation become less satisfactory. In the region close to the holes this is most apparent for centerline film cooling when injection is in the lateral direction. The average film cooling correlation is less affected by the injection angle.

(*iii*) The application of a nonisotropic viscosity model to the prediction of velocity and film cooling effectiveness is fairly satisfactory for low blowing rates and the prediction is improved by using the function model of Rodi (1972) to evaluate turbulence viscosity.

(*iv*) The prediction of film cooling effectiveness using an elliptic procedure did not show significant improvement over the semi-elliptic procedure of Bergeles et al. (1976), hence it seems that the main problem for poor predictions, especially at high blowing rates $M > 0.197$, is due to the assumption of equilibrium flow and only accounting for two components of Reynolds shear stresses.

Acknowledgments

The author would like to thank CHAM for allowing him to use the PHOENICS package in this investigation.

References

Bergeles, G., 1976, "Three Dimensional Discrete Hole Cooling Processes. An Experimental and Theoretical Study," PhD Thesis, Imperial College of Science, London.

Bergeles, G., Gosman, A. D., and Launder, B. E., 1976, "The Near-Field Character of a Jet Discharged Normal to a Mainstream," ASME *Journal of Heat Transfer*, Vol. 98, pp. 373–378.

Brown, A., 1967, "A Theoretical and Experimental Investigation Into Film Cooling," JSME Semi-Int Symp., Paper No. 224.

Brown, A., and Saluja, C. L., 1979, "Film Cooling From a Single Hole and a Row of Holes of Variable Pitch to Diameter Ratio," *Int. J. Heat Mass Transfer*, Vol. 22, pp. 525–533.

Eriksen, V. L., Eckert, E. R. G., and Goldstein, R. J., 1971, "A Model for Analysis of the Temperature Field Downstream of a Heated Jet Injected Into an Isothermal Cross Flow at an Angle of 90 degree," NASA CR 72990.

Hatch, J. E., and Papell, S. S., 1959, "Use of a Theoretical Flow Model to Correlate Data for Film Cooling or Heating an Adiabatic Wall by Tangential Injection of Gases of Different Fluid Properties," NASA TN-130.

Jubran, B., and Brown, A., 1985, "Film Cooling From Two Rows of Holes Inclined in the Streamwise and Spanwise Directions," ASME *Journal of Engineering for Gas Turbines and Power*, Vol. 107, No. 1, pp. 84–91.

Launder, B. E., Reece, G. J., and Rodi, W., 1975, "Progress in the Development of a Reynold-Stress Turbulence Closure," *J. Fluid Mechanics*, Vol. 68, No. 3, pp. 537–566.

Launder, B. E., and Spalding, D. B., 1972, *Lectures in Mathematical Models of Turbulence*, Academic Press, New York.

Papell, S. S., 1960, "Effect on Gaseous Film Cooling of Coolant Injection Through Angled Slots and Normal Holes," NASA TN D-299.

Patankar, S. V., and Spalding, D. B., 1967, "Heat and Mass Transfer in Boundary Layers," *Morgan-Grampian*.

Patankar, S. V., Rastogi, A. K., and Whitelaw, J. H., 1973, "The Effectiveness of Three Dimensional Film Cooling Slots—Part 2, Prediction," *Int. J. Heat Mass Transfer*, Vol. 16, pp. 1673–1681.

Ramette, P. H., and Louis, J. F., 1984, "Analytical Study of the Thermal and Fluid Mechanical Evaluation of a Cooling Film Injected From a Single Line of Inclined Round Holes," *Turbo and Jet-Engines*, Vol. 1, No. 1.

Ramsey, J. W., Goldstein, R. J., and Eckert, E. R. G., 1970, "A Model for Analysis of Temperature Distribution With Injection of a Heated Jet Into an Isothermal Flow," Fourth International Heat Transfer Conference, Paper No. FC 8.5, Elsevier, Amsterdam.

Riberio, M. M., and Whitelaw, J. H., 1972, "Verification of Turbulence Models With Hot Wire Anemometry," HTS/72/20, Imperial College, Mechanical Engineering Dept.

Rodi, W., 1972, "The Prediction of Free Turbulent Boundary Layers by Use of a Two Equations Model of Turbulence," PhD Thesis, University of London, London.

Saluja, C. L., 1977, "Film Cooling From Rows of Discrete Holes," PhD Thesis, University of Wales Institute of Science and Technology, Cardiff.

Tillman, E. S., Hartel, E. O., and Jen, H. F., 1985, "The Prediction of Flow Through Leading Edge Holes in a Film Cooled Airfoil With and Without Insert," ASME *Journal of Engineering for Gas Turbines and Power*, Vol. 107, No. 1.

Wieghardt, K., 1946, "Hot-Air Discharge for De-icing," AAF translation, Report No. F-Ts-919-Re, Wright Field, OH.

Optimum Trailing Edge Ejection for Cooled Gas Turbine Blades

T. Schobeiri
Associate Professor,
Department of Mechanical Engineering,
Turbomachinery Laboratory,
Texas A&M University,
College Station, TX 77843-3123
Mem. ASME

The effect of trailing edge ejection on the flow downstream of a cooled gas turbine blade is investigated. Parameters that affect the mixing losses and therefore the efficiency of cooled blades are the ejection velocity ratio, the cooling mass flow ratio, the slot-width ratio, and the ejection angle. For ejection velocity ratio $\mu = 1$, the trailing edge ejection reduces the mixing losses downstream to the cooled blade. For given cooling mass flow ratios, optimum slot-width/trailing edge ratios are found, which correspond to the minimum mixing loss coefficients.

1 Introduction

Increasing the thermal efficiency of power generation gas turbines requires high turbine inlet temperatures. For conventional turbine blade materials, cooling of the front stages allows an increase of the turbine inlet temperature. The required cooling mass flow is injected partially or entirely through the trailing edge slots into the downstream axial gap, where the cooling and main mass flows are mixed. The trailing edge ejection affects the flow regime downstream to the cooled blade, especially the losses associated with the mixing of the cooling mass flow and the main mass flow. The ejection velocity ratio, the cooling mass flow ratio, the slot-width ratio, and the ejection angle affect the mixing losses and therefore the efficiency of cooled blades. Improper selection of these parameters results in higher mixing losses that reduce drastically the efficiency of the cooled turbine stage.

Analytical investigations made by Schobeiri (1985) of significant design parameters for trailing edge ejection have practical applications in the power generation gas turbine industry. Experimental research work by Prust (1974, 1975) on a two-dimensional turbine stator cascade shows that the trailing edge ejection significantly affects the blade efficiency.

This extension of Schobeiri's (1985) analytical method investigates the influence of the above parameters and determines the optimum criterion for the aerodynamic design of trailing edge ejection.

2 Theoretical Background

Starting from the conservation laws of fluid mechanics, relations are derived that describe precisely the influence of the above parameters on the flow field downstream of the cooled turbine blade. Figure 1 shows the flow stations upstream of the blade, immediately at the trailing edge plane and at the mixing plane. The continuity equation can be written as

$$\int_0^{t-d} \rho_2 V_2 \sin\alpha_2 dy + \rho_c \bar{V}_c \sin\alpha_c f d = \rho_3 V_3 \sin\alpha_3 t \qquad (1)$$

The momentum equation in the y direction is

$$\int_0^{t-d} \rho_2 V_2^2 \sin\alpha_2 \cos\alpha_2 dy + \rho_c \bar{V}_c^2 \sin\alpha_c \cos\alpha_c f d = \rho_3 V_3^2 \sin\alpha_3 \cos\alpha_3 t \qquad (2)$$

The momentum equation in the x direction is

$$\int_0^{t-d} \rho_2 V_2^2 \sin\alpha_2^2 dy + \rho_c \bar{V}_c^2 \sin\alpha_c^2 f d + \int_0^t p_2(y) dy = \rho_3 V_3^2 \sin\alpha_3^2 t + p_3 t \qquad (3)$$

In equations (1)–(3) the parameter $f = s/b$ represents the ratio of slotwidth s and the trailing edge thickness b; α_2 and α_c are the exit flow angle and ejection angle, respectively, of the cooling mass flow; V_2 and $\bar{V}_c$ are the blade exit velocity and the mean ejection velocity; $p_2(y)$ is the static pressure distribution along the spacing t. The angles α_2 and α_c are assumed to be constant.

Outside the trailing edge region, the static pressure $p_2(y) = p_{20}$ can be assumed as constant. As shown by Sieverding (1982), inside the trailing edge region, p_2 has a nonlinear distribution whose average might differ from p_{20}. Since this pressure difference occurs only in a relatively small trailing edge region, its contribution compared with the other terms in

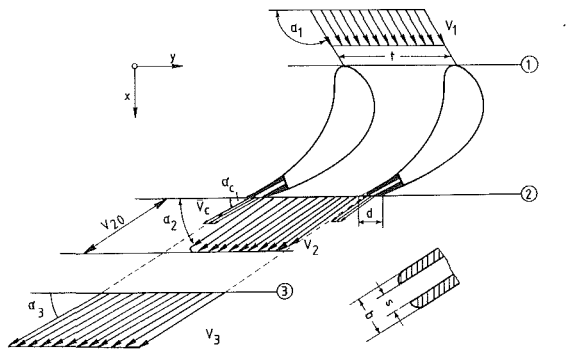

Fig. 1 Trailing edge ejection downstream of a cooled gas turbine blade

Contributed by the International Gas Turbine Institute for publication in the JOURNAL OF TURBOMACHINERY. Manuscript received at ASME Headquarters March 1989.

equation (3) can be neglected. At the exit of the slot, the pressure $p_2(y)$ is determined by the static pressure p_c of the cooling mass flow. By presuming $p_c = p_{20}$ and considering the above facts, the static pressure can be approximated over the entire spacing by $p_2 = p_{20}$.

For further treatment of equations (1)–(3), the boundary layer parameters, namely displaced thickness, momentum thickness, and the shape parameter, are introduced:

$$\delta^* = \int_0^{t-d} \left(1 - \frac{V_2}{V_{20}}\right) dy,$$

$$\delta^{**} = \int_0^{t-d} \frac{V_2}{V_{20}}\left(1 - \frac{V_2}{V_{20}}\right) dy, \quad H = \frac{\delta^*}{\delta^{**}}$$

The dimensionless thicknesses are found by dividing

$$\Delta^* = \frac{\delta^*}{t} \text{ by } \delta^* = \frac{\delta_S^* + \delta_P^*}{\sin\alpha_2}, \; D = \frac{b}{\sin\alpha_2 t} = \frac{b}{t}$$

$$\Delta^{**} = \frac{\delta^*}{t} \text{ by } \delta^{**} = \frac{\delta_S^{**} + \delta_P^{**}}{\sin\alpha_2} \tag{4}$$

where the indices S and P refer to the suction and pressure surfaces. Introducing the dimensionless parameters (4) into the dimensionless versions of equation (1)–(3), the continuity relation yields

$$\frac{\rho_3}{\rho_2}\frac{V_3}{V_2} = \frac{\sin\alpha_2}{\sin\alpha_3}\left[1 - \Delta^* - D\left(1 - \frac{\sin\alpha_c}{\sin\alpha_2}\mu\tau f\right)\right] \tag{5}$$

With equation (5), the momentum equation in the y direction is:

$$\cot\alpha_3 = \frac{\rho_3}{\rho_2}\cot\alpha_2 \times \left\{\frac{1 - \Delta^* - \Delta^{**} - D\left(1 - \frac{\sin 2\alpha_c}{\sin 2\alpha_2}\mu\tau f\right)}{\left[1 - \Delta^* - D\left(1 - \frac{\sin\alpha_c}{\sin\alpha_2}\mu\tau f\right)\right]^2}\right\} \tag{6}$$

The momentum equation in the x direction determines the static pressure difference

$$\frac{p_{20} - p_3}{\frac{1}{2}\rho_3 V_3^2} = 2\sin^2\alpha_3 \times \left\{1 - \frac{\rho_3}{\rho_2}\frac{1 - \Delta^* - \Delta^{**} - D\left(1 - \frac{\sin^2\alpha_c}{\sin^2\alpha_2}\mu^2\tau f\right)}{\left[1 - \Delta^* - D\left(1 - \frac{\sin\alpha_c}{\sin\alpha_2}\mu\tau f\right)\right]^2}\right\} \tag{7}$$

with

$$\mu = \frac{\bar{V}_c}{V_{20}}, \quad \tau = \frac{T_2}{T_c}, \quad R = \frac{\rho_3}{\rho_2}$$

as velocity, temperature, and density ratio.

To define the energy dissipation due to the mixing process, it is necessary to consider not only the contribution of the main flow but also the cooling mass flow. For the calculation of unsteady total pressure changes within the gas turbine components, the author combined the mechanical and thermal energy balances and arrived at a general relation. As a result, equation (3) by Schobeiri (1986) represents the time change of total pressure within a system, where an exchange of thermal and mechanical energy with the surroundings takes place. For an adiabatic steady flow with no mechanical energy exchange, this equation is reduced to

$$\nabla \cdot (\mathbf{V}P) = \frac{\kappa - 1}{\kappa} \nabla \cdot (\mathbf{V} \cdot T) \tag{8}$$

where $P = p + \rho V^2/2$ is the total pressure, T the shear stress tensor, and κ the ratio of the specific heats. Equation (8) states that the rate of work done on fluid per unit volume by viscous forces causes a defect of total pressure work per unit volume. For an inviscid flow, equation (8) reduces to the Bernoulli equation.

Integrating equation (8) over the control volume and converting the volume integrals into the surface integrals by means of Gauss' divergence theorem results in

$$\int_S (\mathbf{n} \cdot \mathbf{V}P) dS = \int_{S_{in}} (\mathbf{n} \cdot \mathbf{V}P) dS + \int_{S_{out}} (\mathbf{n} \cdot \mathbf{V}P) dS = \Delta\dot{E} \tag{9}$$

The second and third integrals are carried out over the entire surface under consideration. Introducing the individual mass flows $\dot{m}_c$ and $\dot{m}_2$, and substituting the inlet total pressure by the total pressure of the potential core at station 2, the total energy dissipation is obtained from

$$\Delta\dot{E} = \dot{m}_2\left(\frac{p_{20}}{\rho_2} + \frac{1}{2}V_{20}^2\right) + \dot{m}_c\left(\frac{p_c}{\rho_c} + \frac{1}{2}V_c^2\right) - \dot{m}_3\left(\frac{p_3}{\rho_3} + \frac{1}{2}V_3^2\right) \tag{10}$$

With respect to the exit kinetic energy, the loss coefficient is defined as

$$\zeta = \frac{\Delta\dot{E}}{\frac{1}{2}\dot{m}_3 V_3^2} \tag{11}$$

Nomenclature

b = trailing edge thickness (Fig. 1)
d = $a/\sin\alpha_2$ = trailing edge thickness in cascade front (Fig. 1)
D = dimensionless trailing edge thickness
f = s/b = slot-width/trailing edge thickness ratio
G_i = auxiliary functions
H = shape parameter
$\dot{m}$ = mass flow
M = Mach number
$\mathbf{n}$ = normal unit vector
p = static pressure
P = $p + \rho V^2/2$ = total pressure
R = ρ_3/ρ_2 = density ratio
s = slot width
S = surface
t = spacing
T = $e_i e_j T_{ij}$ = shear stress tensor
$\mathbf{V}$ = velocity vector
$\bar{V}$ = averaged velocity
α = flow angle
δ^*, δ^{**} = displacement, momentum thickness
Δ^*, Δ^{**} = dimensionless displacement and momentum thickness
ζ = loss coefficient
μ = $\bar{V}_c/V_2$ = velocity ratio
ρ = density
τ = T_2/T_c = temperature ratio

Subscripts

c = coolant
P = pressure side
S = suction side
o = with respect to zero trailing edge thickness (ζ_o)
2 = with respect to plane 2 (Fig. 1)
20 = with respect to the potential core
3 = with respect to mixing plane 3 (Fig. 1)
in = inflow
out = outflow

We incorporate the mass flow ratios

$$\frac{\dot{m}_2}{\dot{m}_3} = \frac{1-\Delta^*-D}{1-\Delta^*-D\left(1-\dfrac{\sin\alpha_c}{\sin\alpha_2}\mu\tau f\right)}$$

$$\frac{\dot{m}_c}{\dot{m}_3} = \frac{\sin\alpha_c\mu\tau f D}{\sin\alpha_2\left[1-\Delta^*-D\left(1-\dfrac{\sin\alpha_c}{\sin\alpha_2}\mu\tau f\right)\right]}$$

into equation (11) and use equations (5)–(7) and introduce the following auxiliary functions:

$$G_1 = 1-\Delta^*-D\left(1-\frac{\sin\alpha_c}{\sin\alpha_2}\mu\tau f\right)$$

$$G_2 = 1-\Delta^*-\Delta^{**}-D\left[1-\frac{\sin^2\alpha_c}{\sin^2\alpha_2}\mu^2\tau f\right)\Big]$$

$$G_3 = 1-\Delta^*-D\left[1-\frac{\sin\alpha_c}{\sin\alpha_2}\mu^3\tau f\right)\Big]$$

$$G_4 = \frac{\sin\alpha_c\sin(\alpha_c-\alpha_2)}{\sin^2\alpha_2\cos\alpha_2}\mu^2\tau f D$$

The loss coefficient ζ is completely described by

$$\zeta = \frac{G_1^3-2RG_1^2G_2+R^2G_3}{G_1^3} - \cos^2\alpha_3\left[\frac{2G_1^3-2RG_2G_1^2+R^2G_3}{G_1^3}-\frac{G_1G_3}{(G_2-G_4)^2}\right] \tag{12}$$

where all the significant parameters determining the influence of trailing edge ejection are present. With this relation, it is possible to predict the energy dissipation due to the trailing edge thickness, the boundary layer thickness at the trailing edge, and the trailing edge ejection. In this connection, the contribution of the trailing edge ejection to the energy dissipation is of particular interest. For this purpose, a typical gas turbine cascade is considered, where its geometry, exit flow angle α_2, and the boundary layer parameters are known. To show the effect of trailing edge ejection, the loss coefficient ζ is calculated from equation (12) as a function of cooling mass flow ratio $\dot{m}_c/\dot{m}_2$.

The loss coefficient ζ includes the profile losses that are caused by viscosity effects. To eliminate this contribution, a cascade with the same flow conditions and boundary layer parameters but with an infinitesimally thin trailing edge and no ejection is considered. This cascade has almost the same pressure distribution on the suction and pressure sides and also the same profile loss coefficient. The difference $(\zeta-\zeta_o)$ in this case illustrates for a given trailing edge thickness the effect of trailing edge ejection.

3 Results

Equation (12) includes three major parameter groups. The first group represents the cascade geometry; the second one pertains to the boundary layer development at the trailing edge plane; the third group consists of all trailing edge ejection parameters such as temperature, velocity of the cooling mass flow exiting from the slot, and the slot-width/trailing edge thickness ratio.

Influence of Cooling Mass Flow Ratio. Figure 2 reveals the influence of temperature ratio. For a constant trailing edge thickness ratio $b/t=0.031$, an exit flow angle $\alpha_2=20$ deg, and a slot ratio $f=0.4$, the difference $(\zeta-\zeta_o)$ is plotted against the cooling mass flow ratio $\dot{m}_c/\dot{m}_2$ with temperature ratio τ as parameter. Starting from a zero cooling mass flow ratio $\dot{m}_c/\dot{m}_2=0$, the loss coefficient difference $(\zeta-\zeta_o)$ originates from the trailing edge thickness. For an arbitrary temperature ratio $\tau=1.5$, the difference $(\zeta-\zeta_o)$ increases with increasing mass flow ratio $\dot{m}_c/\dot{m}$ until its maximum $(\zeta-\zeta_o)_{max}$ is reached. With further increase of the mass flow ratio, $(\zeta-\zeta_o)$ decreases, reaches a minimum, and increases again. As shown in Fig. 2, for each slot-width and temperature ratio there is a cooling mass flow ratio that corresponds to an optimum loss coefficient. This phenomenon can be explained by Fig. 3.

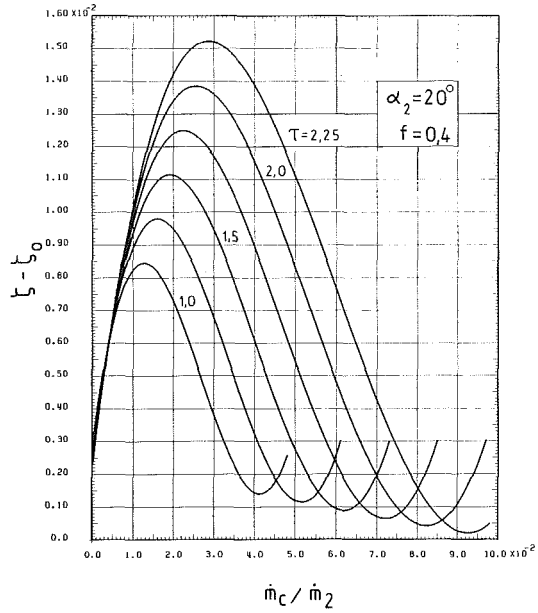

Fig. 2 Loss coefficient difference $(\zeta-\zeta_o)$ as a function of cooling mass flow ratio $\dot{m}_c/\dot{m}_2$ with temperature ratio $\tau=T_2/T_c$ as a parameter and a constant slot ratio $f=0.4$

Influence of Ejection Velocity Ratio. In Fig. 3, the loss coefficient difference $(\zeta-\zeta_o)$ is plotted against the ejection velocity ratio μ. For lower velocity ratios $\mu<1$, the momentum contribution of the cooling mass flow is not sufficient to influence favorably the strong dissipative character of the wake flow downstream of the blade. The cooling mass flow is entrained by the main flow and its total energy is completely dissipated. Thus the process is associated with a higher entropy increase, which results in higher total pressure losses. Increasing the velocity ratio intensifies the dissipation process until its maximum is reached. This occurs for all temperature ratios τ at $\mu\simeq 0.3$. Further increasing the velocity ratio μ decreases the loss coefficient difference $(\zeta-\zeta_o)$. This is the first indication that the momentum contribution of the cooling mass flow gradually becomes capable of overcoming the wake flow without being dissipated completely. A significant reduction of losses compared to the case without mass flow injection is then possible, when the ejection does not cause additional dissipation. This occurs for velocity ratios $\mu>0.85$. For $\mu=1$, the loss coefficient reaches its minimum for all τ. Further increasing of $\mu>1$ increases the loss coefficient again. The mechanism is similar to that explained above.

For a higher temperature ratio range τ and $\mu<0.3$, as shown in Fig. 3, there is a steep increase of loss coefficient; it decreases rapidly for $\mu>0.85$.

Influence of Slot-Width/Trailing Edge Thickness Ratio. The effect of slot-width/trailing edge thickness ratio (slot ratio) $f=s/b$ is shown in Figs. 4 and 5 for a temperature ratio $\tau=1.5$. In Fig. 4, the loss coefficient difference $(\zeta-\zeta_o)$ is plotted against the cooling mass flow ratio with f as parameter. The course of $(\zeta-\zeta_o)$ reveals for each given slot

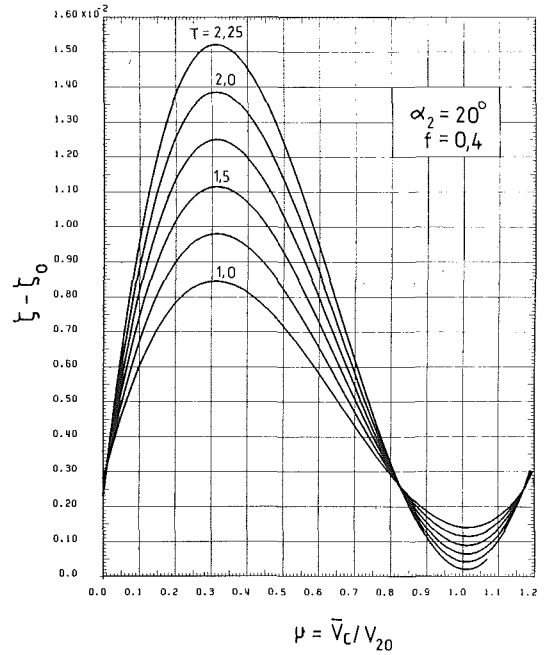

Fig. 3 Loss coefficient difference ($\zeta - \zeta_o$) as a function of velocity ratio $\mu = \bar{V}_c/V_2$ with temperature ratio $\tau = T_2/T_c$ as a parameter and a constant slot ratio $f = s/b = 0.4$

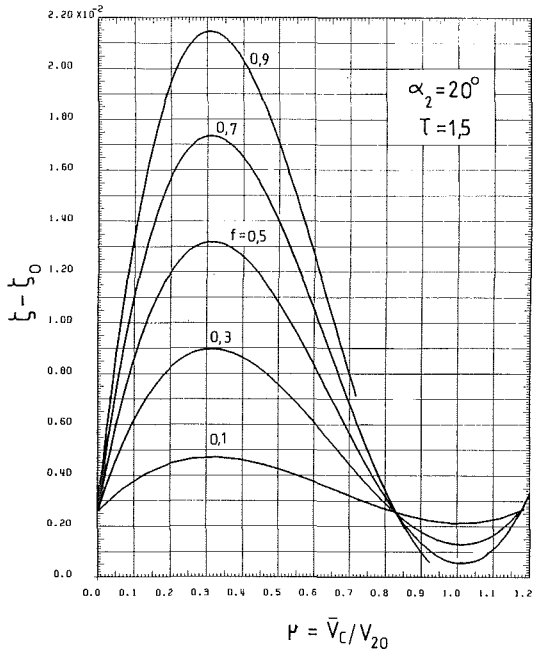

Fig. 5 Loss coefficient difference ($\zeta - \zeta_o$) as a function of velocity ratio $\mu = \bar{V}_c/V_2$ with slot ratio f as a parameter and a constant temperature ratio $\tau = T_2/T_c = 1.5$

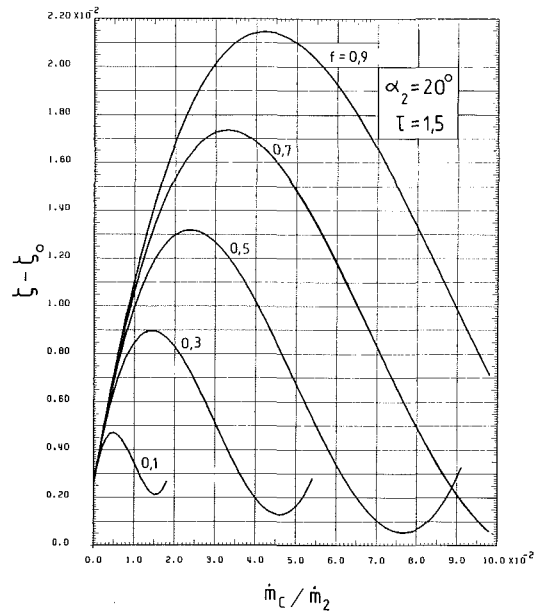

Fig. 4 Loss coefficient difference ($\zeta - \zeta_o$) as a function of cooling mass flow ratio $\dot{m}_c/\dot{m}_2$ with slot ratio $f = s/b$ as a parameter and a constant temperature ratio $\tau = T_2/T_c = 1.5$

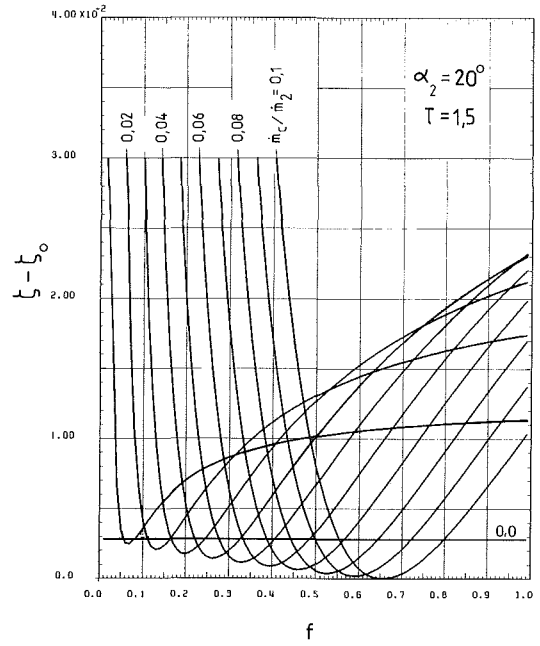

Fig. 6 Loss coefficient difference ($\zeta - \zeta_o$) as a function of slot ratio $f = s/b$ with the cooling mass flow ratio $\dot{m}_c/\dot{m}_2$ as a parameter and a constant temperature ratio $\tau = T_2/T_c = 1.5$

ratio f a pronounced optimum because there is a cooling mass flow ratio with an optimum velocity ratio $\mu = 1$ for each slot ratio (Fig. 5). For the existing cooled blades, the slot ratio f varies between 0.3 and 0.5.

Influence of the Ejection Angle. For small positive differences $\delta = \alpha_c - \alpha_2 = 1$ deg -2 deg, the ejection angle α_c has little influence on the loss coefficient difference ($\zeta - \zeta_o$). For a cascade with $\alpha_2 = \alpha_c = 20$ deg, and optimum ejection parameters, $f = 0.4$, and $\dot{m}_c/\dot{m}_2 = 0.06$, the following values are obtained:

$\alpha_c(o)$	$\alpha_2(o)$	$\delta(o)$	$f(-)$	$m_c/m(-)$	$(\zeta - \zeta_o)$
18.0	20.0	−2.0	0.40	0.06	0.10163E−2
19.0	20.0	−1.0	0.40	0.06	0.92952E−3
20.0	20.0	−0.0	0.40	0.06	0.87540E−3
21.0	20.0	+1.0	0.40	0.06	0.85803E−3
22.0	20.0	+2.0	0.40	0.06	0.88191E−3

As shown in this table, the optimum ($\zeta - \zeta_o$) lies at $\alpha_c = 21$ deg, where $\delta = 1$ deg. For a practical slot ratio range $f > 0.3$, a positive $\delta = 1$ deg can be chosen.

Optimum Ejection. Of particular interest to the turbine

blade aerodynamicist and designer is how small the slot ratio f should be to meet the optimum conditions for $(\zeta - \zeta_o)$ with a given mass flow, which is dictated by the heat transfer requirements. In this connection, Fig. 6 gives the required design information. The loss coefficient difference $(\zeta - \zeta_o)$ is plotted against the slot ratio f, with mass flow ratio $\dot{m}_c/\dot{m}_2$ as parameter for a temperature ratio $\tau = 1.5$. For each given $\dot{m}_c/\dot{m}_2$, the corresponding optimum f can be found easily at which $\mu = 1$. The trailing edge thickness loss with no injection is represented by the curve $\dot{m}_c/\dot{m}_2 = 0.0$. Comparison of this curve with the other curves in Fig. 6 shows that improper selection of the slot ratio f can cause losses more than ten times as high as losses due to the trailing edge thickness. This is one of the reasons the cooled gas turbine blades with the trailing edge ejection do not have adequately high efficiency. For a high subsonic blade Mach number M_2, the slot ratio is chosen to exclude eventual choking of the cooling mass flow. Therefore the maximum cooling flow Mach number M_c, which can be estimated from $M_c = M_2\sqrt{\tau} < 1$, should not exceed unity. In this connection, it should be pointed out that the design of the cooling system, under some circumstances, might place a restriction on optimization of trailing edge ejection.

The above investigation focused entirely on the parameters relevant to the trailing edge ejection. Equation (12) enables calculation of the trailing edge mixing losses also.

4 Conclusions

The effect of trailing edge ejection on the flow downstream of a cooled gas turbine blade was determined. The significant parameters determining the mixing losses and therefore the efficiency of cooled blades are the ejection velocity ratio, the cooling mass flow ratio, the slot ratio, and the ejection angle. The results show that for ejection velocity ratio $\mu = 1$, the trailing edge ejection reduces the mixing losses downstream to the cooled blade. For given cooling mass flow ratios, optimum slot-width/trailing edge ratios are found, which correspond to the minimum mixing loss coefficients. For small positive angle differences δ, the ejection angle α_c has little influence on the loss coefficient difference $(\zeta - \zeta_o)$. In this connection, a positive $\delta = 1$ deg is recommended.

References

Prust, H., 1974, "Cold-Air Study of the Effect of Turbine Stator Blade Aerodynamic Performance of Coolant Ejection From Various Trailing-Edge Slot Geometries," NASA Reports I: TMX 3000.

Prust, H., 1975, "Cold-Air Study of the Effect on Turbine Stator Blade Aerodynamic Performance of Coolant Ejection From Various Trailing-Edge Slot Geometries," NASA Reports II: TMX 3190.

Schobeiri, T., 1985, "Einfluss der Hinterkantenausblasung auf die hinter den gekuehlten Schaufeln entstehenden Mischungsverluste," *Forschung im Ingenieurwesen*, Vol. 51, No. 1, pp. 25–28.

Schobeiri, T., 1986, "A General Computational Method for Simulation and Prediction of Transient Behavior of Gas Turbines," ASME Paper No. 86-GT-180.

Sieverding, C. H., 1983, "The Influence of Trailing Edge Ejection on the Base Pressure in Transonic Turbine Cascades," ASME *Journal of Engineering for Power*, Vol. 105, pp. 215–222.

Pressure Loss Distribution in Three-Pass Rectangular Channels With Rib Turbulators

J. C. Han
Professor.

P. Zhang
Research Assistant.

Turbomachinery Laboratory,
Department of Mechanical Engineering,
Texas A&M University,
College Station, TX 77843

The present study investigated the combined effects of the flow channel aspect ratio, the rib turbulator configuration, and the sharp 180-deg turn on the distributions of the local pressure drop in three-pass rectangular channels for a Reynolds number range of 15,000 to 60,000. The channel aspect ratios (the channel width-to-height ratios W/H*; ribs on the channel width,* W, *side) were 1, 1/2, and 1/4. The rib height-to-hydraulic diameter ratios* (E/D) *were 0.063, 0.047, and 0.039; the rib pitch-to-height ratios* (P/E) *were 5, 7.5, 10, and 15; the rib angles of attack* (α) *were 90, 60, and 45 deg. The results showed that the rib turbulators dominated the pressure drops in the first pass of the three-pass channel. The pressure drops in the two-pass and the three-pass channels were caused by both the rib turbulators and the sharp 180-deg turns. The differences of the pressure drops caused by the different rib configurations (rib angle, spacing, and height) were significant in the first pass. The differences, however, were diluted by the sharp 180-deg turns in the two-pass and the three-pass channels, and by the smaller channel aspect ratio* (W/H *changed from 1 to 1/4). The friction factor correlations for the first pass, the first two-pass, and the three-pass were obtained to account for the rib configuration, the channel aspect ratio, and the Reynolds number. The correlations can be used in the design of the turbine airfoil cooling passages.*

Introduction

In advanced gas turbine blades and vanes, rib turbulators are often cast on two opposites walls of internal cooling passages to enhance the heat transfer to the cooling air. A typical cooling passage can be modeled as a straight or a multipass rectangular channel with two opposite rib-roughened walls. In a straight rib-roughened channel, the effects of the turbulator configuration (such as rib height, spacing, and angle), the flow channel aspect ratio, and the flow Reynolds number on the distributions of the local heat transfer and pressure drop have been reported (Han et al., 1985; Han and Park, 1988).

In a multipass rib-roughened channel, in addition to the rib turbulators and the flow channel aspect ratios, the effects of the sharp 180-deg turns on the distributions of the local heat transfer and pressure drop are important. Boyle (1984) studied the effect of the sharp 180-deg turn on the local heat transfer coefficient and the pressure drop in a two-pass square channel ($W/H = 1$) roughened by the transverse ribs. Both the heat transfer and the pressure drop in a two-pass square channel were higher than those in a straight square channel. With the naphthalene sublimation technique, the effect of the sharp 180-deg turn on the distributions of the local mass transfer coefficient in a two-pass square channel ($W/H = 1$) roughened by the transverse ribs and by the angled ribs was presented by Han et al. (1988) and by Chandra et al. (1988), respectively. The effect of the sharp 180-deg turn on the local and average pressure drops in a two-pass square channel roughened by the transverse ribs and by the angled ribs was reported by Han and Chandra (1987). The results, in general, agree with those reported by Boyle (1984) for the case of transverse ribs. In two-pass smooth rectangular channels, Metzger et al. (1984), Metzger and Sahm (1986), and Fan and Metzger (1987) studied the effects of the channel geometry (such as the before-turn and after-turn channel aspects ratios, and the turn clearance) and the flow Reynolds number on the heat transfer and the pressure drop. Both the channel aspect ratio and the turn clearance had important effects on the heat transfer and the pressure drop of two-pass smooth rectangular channels ($W/H = 0.83$, 1.25, and 2.5).

The distributions of the local heat transfer coefficient in a multipass rig-roughened channel are important in designing effectively cooled airfoils that are not susceptible to structural failure from uneven thermal stresses. It is well known that the local heat transfer coefficient depends strongly on the local mass flow rate (i.e., Reynolds number). In a multipass rib-roughened channel, the local coolant flow rate distribution is determined by the local pressure drop distribution in the channel for a given supply pressure. Therefore, it is essential to determine accurately the local pressure drop distribution in a multipass rib-roughened channel to design effectively cooled airfoils. In the air-cooled turbine blades and vanes, however, the coolant passages often have more than one sharp 180-deg

Contributed by the International Gas Turbine Institute for publication in the JOURNAL OF TURBOMACHINERY. Manuscript received by the International Gas Turbine Institute May 1988.

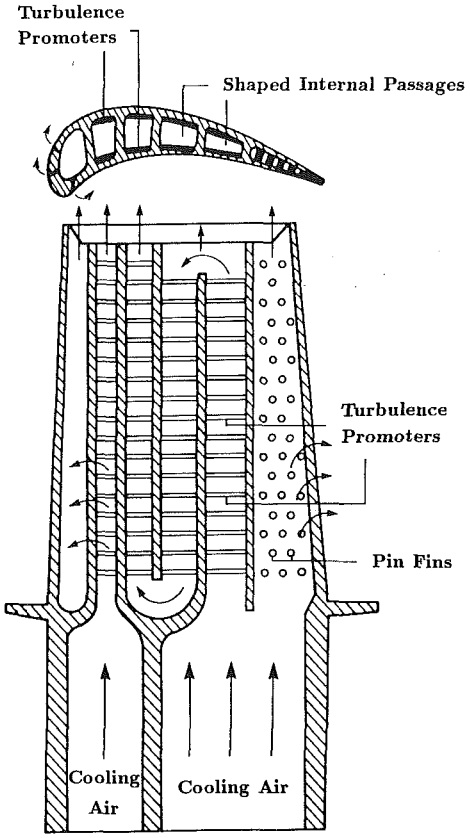

Fig. 1 Cooling concepts of a modern multipass turbine blade

turn, as shown in Fig. 1. The open literature contains no information on the distributions of the local pressure drop in such three-pass rectangular channels with rib turbulators.

The objective of the present study was to investigate the combined effects of the rib turbulator configuration, the sharp 180-deg turn, and the flow channel aspect ratio on the distributions of the local pressure drop in three-pass rectangular channels for Reynolds numbers from 15,000 to 60,000, which are typical values in turbine cooling passages. The present investigation was aimed at determining the effect of these parameters on the average friction factors and obtaining the average friction factor correlations to account for these parameters. First, the distributions of the local pressure drop in each of three three-pass rib-roughened channels (W/H = 1/4, 1/2, and 1) are presented and discussed. Then the average friction factors in each of three-pass rectangular channels are obtained, and the friction factor correlations are developed.

Additional information on the present investigation is given by Zhang (1988).

Experimental Program

Pressure Drop Test Channels. Figure 2(*a*) is a schematic of the test channel for pressure drop experiments. The test section, which consisted of three straight, rectangular channels joined by two sharp 180-deg turns, fabricated of plexiglass, was used for measuring the distributions of the local pressure drop in the channel. The channel aspect ratios (the channel width-to-height ratios W/H; ribs on the channel width, W, side) were 1/4, 1/2, and 1, respectively, for the corresponding three three-pass rectangular channels. The first test section was a three-pass channel with a 2.54-cm (1-in.) square cross section. The first test section (square channel, W/H = 1) served as the second test section (rectangular channel, W/H = 1/2) by changing the channel height from 2.54 cm (1 in.) to 5.08 cm (2 in.). Similarly, the second test section was modified to be the third test section (rectangular channel, W/H = 1/4) by changing the channel height from 5.08 cm (2 in.) to 10.16 cm (4 in.). To simulate actual turbine cooling passages in each of the three test channels, the length (L) of each of the three straight sections was 13 times the channel width (W = 2.54 cm); the thickness of each of the two divider walls was 0.25 times the channel width; and the turn clearance of each of the two sharp 180-deg turns was equivalent to the channel width. A smooth channel (the length was also 13 times the width) was attached to the entrance of each of three test channels. This smooth entrance channel was used to provide a fully developed flow before entering the test section. The test channels were oriented in the horizontal direction. In each test section, brass ribs with a 0.159-cm (0.063-in.) square cross section were glued periodically on the top and bottom surfaces (the channel width, W, side) of the three straight sections of the test channel. The ribs on the top surfaces were parallel to those on the bottom surfaces of the test channel. The rib

Nomenclature

D = channel hydraulic diameter = $2WH/(W+H)$
E = rib height
$\bar{F}$ = average friction factor
$\bar{F}1$ = average friction factor in the first pass of the three-pass channel
$\bar{F}2$ = average friction factor in the first two passes of the three-pass channel
$\bar{F}3$ = average friction factor in the entire three-pass channel
$F(FD)$ = fully developed friction factor in smooth tube flow
g_c = conversion factor
G = mass flux = ρV
H = channel height
L = channel length in each of the three passes
P = rib pitch
P_i = static pressure at channel entrance
P_x = static pressure at axial distance from channel entrance
$\Delta P1$ = static pressure drop across the first pass of the three-pass channel
$\Delta P2$ = static pressure drop across the first two passes of the three-pass channel
$\Delta P3$ = static pressure drop across the entire three-pass channel
Re = Reynolds number based on channel hydraulic diameter = GD/μ
V = average air velocity in flow channel
W = channel width
X = axial distance from channel entrance
$X1$ = channel length for frictional pressure drop measurements in the first pass of the three-pass channel
$X2$ = channel length for frictional pressure drop measurements in the first two passes of the three-pass channel
$X3$ = channel length for frictional pressure drop measurements in the entire three-pass channel
α = alpha; rib angle of attack
μ = air dynamic viscosity
ρ = air density

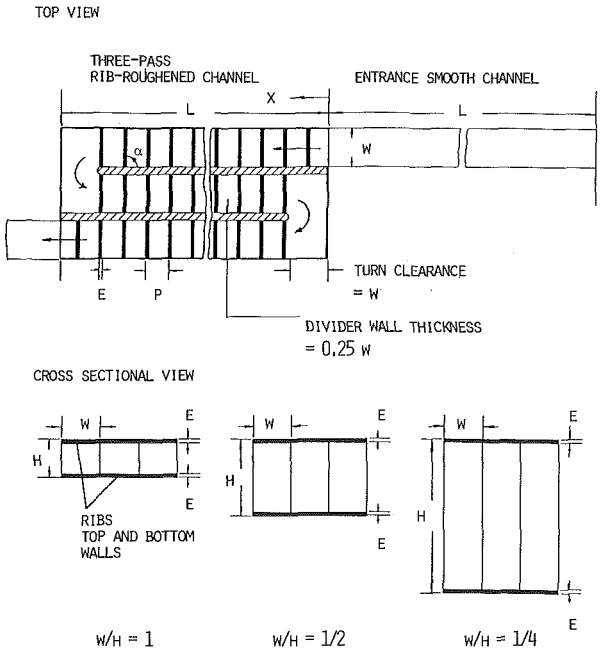

Fig. 2(a) Sketch of the test channels

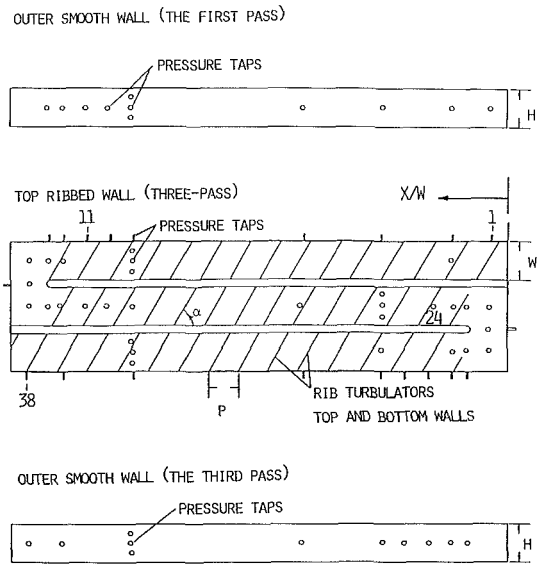

Fig. 2(b) Detailed pressure tap locations

height-to-hydraulic diameter ratios corresponding to the three test sections were 0.063, 0.047, and 0.039, respectively. The rib pitch-to-height ratio was 5, 7.5, 10, or 15. The rib angle of attack was 90, 60, or 45 deg. No rib was placed in the turn clearance regions. Dimensions of the test channels and rib geometries are given in Table 1.

Data Reduction. In each of the three test sections, 25 pressure taps along the smooth wall (the channel height, H, side) and 30 along the top rib-roughened wall (the channel width, W, side) were used for the static pressure drop measurements, as shown in Fig. 2(b). The pressure drop across the test section was measured by a Dywer microtector with an accuracy up to 0.025 mm (0.001 in.) of water.

The pressure drop of the present study was based on the adiabatic conditions (tests without heating). The distributions of the local pressure drop in each of the three three-pass test channels were normalized by the fluid dynamic pressure as

$$(P_x - P_i)/((1/2)\rho V^2) \tag{1}$$

Table 1 Dimensions of the test channels and rib geometries (cm)

	SQUARE	RECTANGULAR	RECTANGULAR
W/H	1	1/2	1/4
W	2.54	2.54	2.54
H	2.54	5.08	10.16
D	2.54	3.39	4.06
L/W	13	13	13
E	0.159	0.159	0.159
	0.119		
E/D	0.063	0.047	0.039
	0.047		
P/E	10	10	10
	15		
	5		
	7.5		
α	90°	90°	90°
	60°	60°	60°
	45°	45°	45°

In each of the three test channels, the average friction factor in the first pass (the first straight section), the first two passes (the first and the second straight sections plus the first sharp 180-deg turn), and all three passes (the three straight sections plus the two sharp 180-deg turns) of the test channel were calculated as

$$\bar{F}1 = (\Delta P1)/[4(X1/D)\ (G^2/2\rho g_c)] \tag{2}$$

$$\bar{F}2 = (\Delta P2)/[4(X2/D)\ (G^2/2\rho g_c)] \tag{3}$$

$$\bar{F}3 = (\Delta P3)/[4(X3/D)\ (G^2/2\rho g_c)] \tag{4}$$

The effect of rib turbulators in the first straight section on the average friction factors for the first pass of the three-pass rectangular channels ($\bar{F}1$) was calculated by equation (2); the combined effects of rib turbulators in the first two straight sections and of the first sharp 180-deg turn on the average friction factors for the first two passes of the three-pass rectangular channels ($\bar{F}2$) were determined by equation (3); the combined effects of rib turbulators in the three straight sections and of the two sharp 180-deg turns on the average friction factors for the entire three-pass rectangular channels ($\bar{F}3$) were obtained by equation (4).

The maximum uncertainty in the average friction factor was estimated to be less than 8 percent by the uncertainty estimation method of Kline and McClintock (1953). The average friction factor was normalized by the friction factor for fully developed turbulent flow in smooth circular tubes (10,000 < Re < 100,000) proposed by Blasius as

$$\bar{F}(\bar{F}1,\ \bar{F}2,\ \text{or}\ \bar{F}3)/F(FD) = \bar{F}(\bar{F}1,\ \bar{F}2,\ \text{or}\ \bar{F}3)/(0.046\ \text{Re}^{-0.2}) \tag{5}$$

Experimental Results and Discussion

Local Pressure Drop. The detailed raw data for all test runs are given by Zhang (1988). Only the most representative results are presented here. The local pressure drop results are presented as the axial distributions of a dimensionless pressure drop as shown in equation (1).

Effect of Reynolds Number. Typical results to demonstrate the effect of Reynolds number on the dimensionless local pressure drop in a three-pass square channel are shown in Fig. 3(a) for $E/D = 0.063$, $P/E = 10$, and $\alpha = 90$

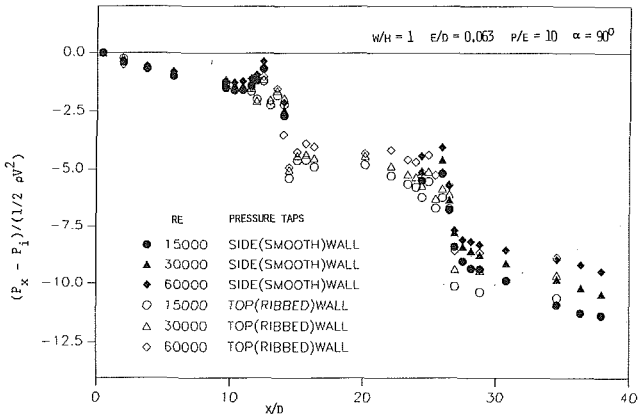

Fig. 3(*a*) Effect of Reynolds number for rough square channel

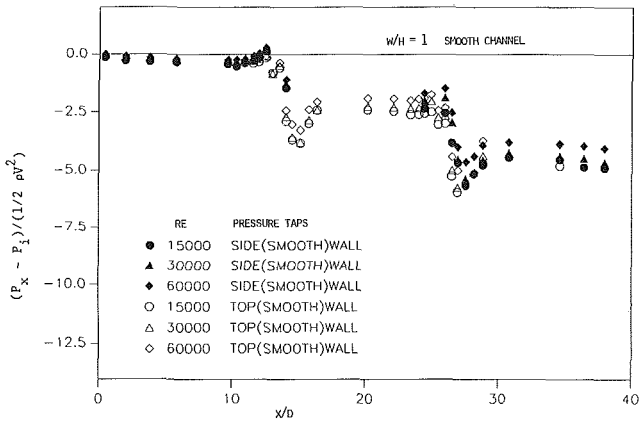

Fig. 3(*b*) Effect of Reynolds number for smooth square channel

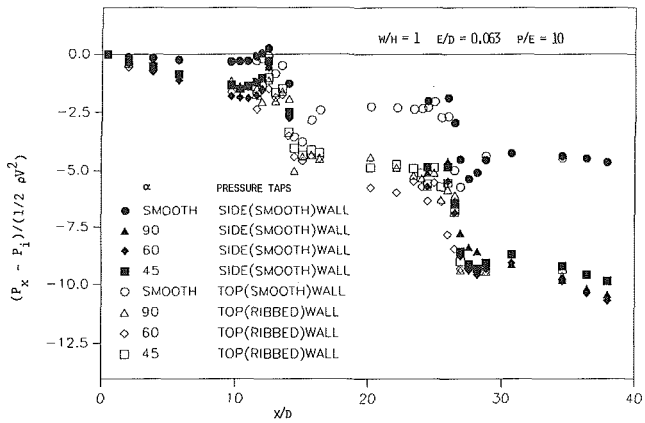

Fig. 4 Effect of rib angle for *W/H* = 1 at Re = 30,000

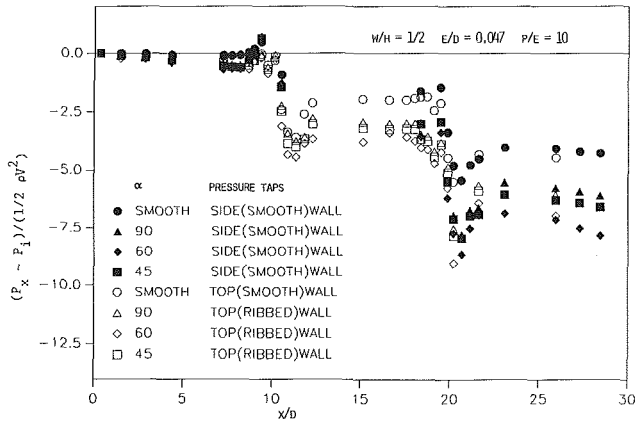

Fig. 5 Effect of rib angle for *W/H* = 1/2 at Re = 30,000

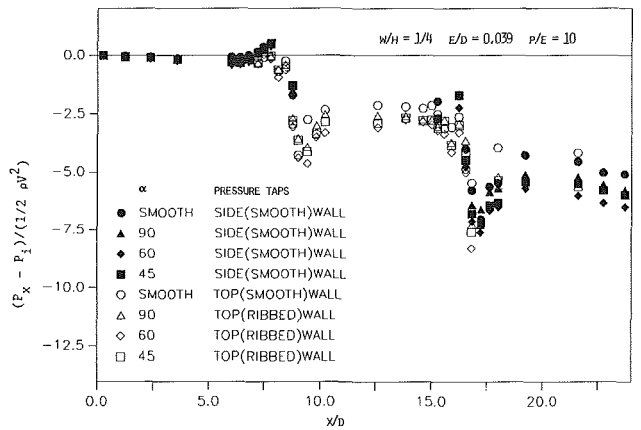

Fig. 6 Effect of rib angle for *W/H* = 1/4 at Re = 30,000

deg. The results in the same channel with smooth surfaces are included for comparison (Fig. 3(*b*)). Pressure drops calculated from pressure taps on both the smooth and rib-roughened walls are presented. The dimensionless pressure drop has similar trends for all three Reynolds numbers and decreases with increasing Reynolds number. The pressure drops almost linearly from the channel entrance until before the first sharp 180-deg turn ($X/D = 11$). The pressure then rises slightly in the vicinity of the upstream corner of the turn ($X/D = 11.5$). There is a rapid drop in pressure in and just after the turn region ($X/D = 11.5$ to 15). The pressure is recovered at X/D around 16 because of flow recirculation after the sharp turn. There is a decrease in pressure toward the end of the second straight section of the channel ($X/D = 16$ to 24). The effect of the second sharp 18-deg turn on the local pressure drop is similar to that of the first sharp turn. After the second sharp turn, the local pressure decreases continuously until the end of the third straight section of the channel. In the smooth channel, the pressure drop is primarily caused by the two sharp 180-deg turns. In the rib-roughened channel, the pressure drop is caused by both the two sharp turns and the ribs on the three straight sections of the channel. Note that the distributions of the dimensionless local pressure drop in three-pass rectangular channels ($W/H = 1/2$ and 1/4) show trends similar to those in the three-pass square channel (Zhang, 1988).

Effect of Rib Angle. Typical results to illustrate the effect of rib angle on the dimensionless pressure drop in three three-pass rectangular channels ($W/H = 1$, 1/2, and 1/4) are shown in Figs. 4, 5 and 6 for $P/E = 10$ and Re = 30,000. The smooth channel results are included for comparison. In each of the three channels, the distributions of the dimensionless local pressure drop show the same trends for all three rib angles. The local pressure drops for $\alpha = 90$ and 45 deg are about equal and are lower than that for $\alpha = 60$ deg. Again, the pressure drop is caused by both the two sharp turns and ribs on the three straight sections of the channel. The contribution of rib turbulators on the pressure drop (with the same rib height in each of the three channels) decreases as the channel aspect ratio (W/H, ribs on the channel width, W, side) is decreased from 1 to 1/4.

Average Friction Data. To develop the friction correlations in three-pass rectangular channels with rib turbulators, the average friction factors are required. The average friction

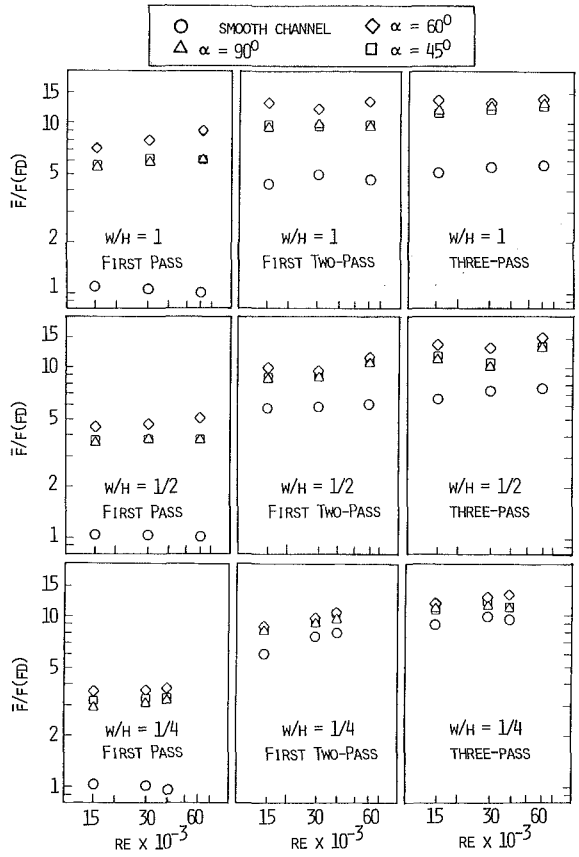

Fig. 7 Average friction factor ratio in each channel with $P/E = 10$

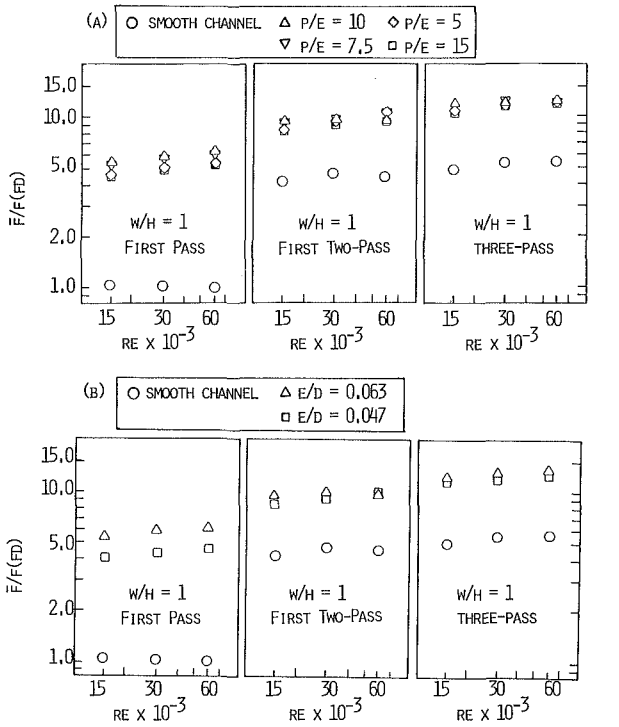

Fig. 8 *(a)*Effect of rib pitch with $E/D = 0.063$ and $\alpha = 90$ deg; *(b)* effect of rib height with $P/E = 10$ and $\alpha = 90$ deg

factors were based on the data averaged from $X/W = 1$ to 11 for the first pass of the three-pass channel (the first straight section of the channel), the data averaged from $X/W = 1$ to 24 for the first two passes of the three-pass channel (the first and the second straight sections plus the first sharp turn), and the data averaged from $X/W = 1$ to 38 for the whole three-pass channel (three straight sections plus two sharp turns), respectively, as shown in Fig. 2(*b*). These friction factors for the first pass ($\bar{F}1$), the first two passes ($\bar{F}2$), and all three passes ($\bar{F}3$) were used for developing correlations in a later section.

Combined Effects of Sharp Turns and Rib Turbulators. Typical results showing the effects of the sharp 180-deg turns and the rib turbulators on the normalized friction factors $\bar{F}(\bar{F}1, \bar{F}2, \text{and } \bar{F}3)/F(FD)$ are plotted in Fig. 7 for three three-pass rectangular channels ($W/H = 1$, 1/2, and 1/4) with $P/E = 10$. The results in the corresponding smooth channels are included for comparison. In all three channels, the averaged friction factor ratios show the same trend and increase slightly with increasing Reynolds number. In the square channel, the rib turbulators cause 5.5 to 8 times as much pressure drop as there is in the first pass without rib turbulators. They caused only 2 to 2.5 times as much pressure drop as there is in the first two passes or three passes without them. In other words, both the rib turbulators and the sharp turns cause pressure drop in the two-pass or three-pass channels. Similarly, in the rectangular channels ($W/H = 1/2$ or 1/4), the rib turbulators cause 4 or 3 times as much pressure drop as there is in the first pass without turbulators; they cause only about 60 or 30 percent as much pressure drop as there is in the first two passes or three passes without them. Thus the rib turbulators have the greatest effect on the pressure drop in the first pass; this effect is diluted gradually in the two-pass or three-pass channels because of the important effect of the sharp turn. Using the same rib height in each of three channels gradually decreases the role of the turbulators when the channel aspect ratio (W/H) is changed from 1 to 1/4 (corresponding to the E/D ratio from 0.063 to 0.039).

Figure 7 also shows the effect of the rib angle on the normalized friction factor ratios in each of the channels. In each of the channels, the friction factor ratios with $\alpha = 90$ and 45 deg are about equal and are 30 percent lower than that with $\alpha = 60$ deg. The difference of the friction factor ratios between $\alpha = 60$ deg and $\alpha = 90$ deg (or 45 deg) is the greatest in the first pass. The difference is gradually reduced in the two-pass and three-pass channels because the rib angle effect is diluted by the strong effect of the sharp turn. The difference of the friction factor ratios between the angled ribs and the transverse ribs is gradually diminished when the channel aspect ratio (W/H) is changed from 1 to 1/4 by keeping the same rib pitch and height in each of the channels. Note that the friction factor ratios in the three-pass rib-roughened channels are between 10 and 13 regardless of the channel aspect ratios ($W/H = 1$, 1/2, or 1/4).

Effect of Rib Height and Rib Pitch. The effect of the rib height and the rib pitch on the normalized friction factor is shown in Fig. 8 for the square channel with $\alpha = 90$ deg and for the smooth channel. The friction factor ratios with $E/D = 0.063$ are 40 percent higher than those with $E/D = 0.047$ in the first pass. The effect of the rib height on the friction factor ratios is dramatically reduced in the two-pass and three-pass channels because of the strong effect of the sharp 180-deg turns. The friction factor ratios for $P/E = 10$ are slightly (3 percent) higher than those for $P/E = 7.5$, and the friction factor ratios for $P/E = 5$ are slightly (5 percent) higher than those for $P/E = 15$. The friction factor ratios for $P/E = 10$ (or 7.5) in the first pass are 20 percent higher than those for $P/E = 5$ (or 15). Again, the difference of the friction factor ratios between $P/E = 10$ (or 7.5) and $P/E = 15$ (or 5) is diminished in the two-pass and three-pass channels because of the strong effect of the sharp 180-deg turns.

Checking the accuracy of the present frictional data requires comparison of this study and the available data. Figure 9 com-

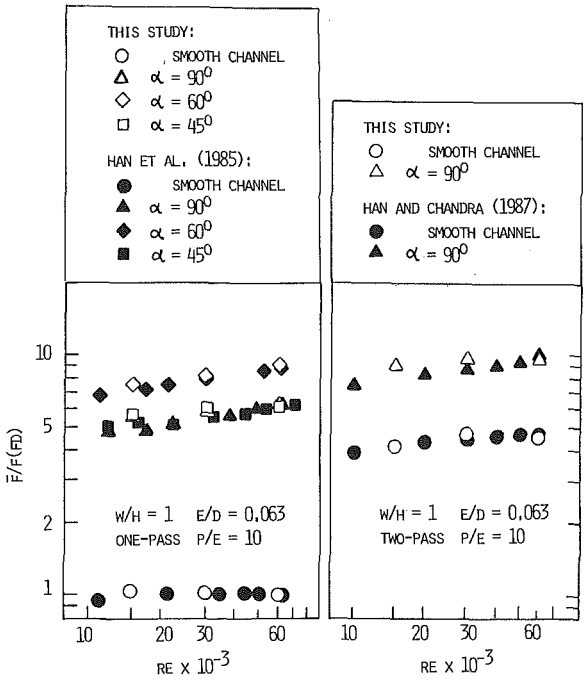

Fig. 9 Comparison between present results and published data

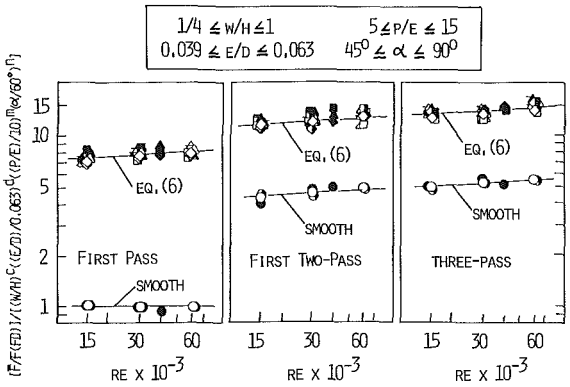

Fig. 10 Friction factor correlation

pares the present data to those reported by Han et al. (1985) for the one-pass straight square channel, and those reported by Han and Chandra (1987) for the two-pass square channel ($W/H=1$) with the same rib configurations (E/D, P/E, and α). The present friction factor ratios agree well with the previous data for the one-pass and two-pass square channels.

Friction Factor Correlations. The average friction factor ratios were used to develop the friction factor ratio correlations to account for the rib angle, pitch, and height, and the channel aspect ratio and the Reynolds number. The friction factor correlations in the first pass, the first two passes, and the entire three-pass channel were obtained empirically; they are shown in Fig. 10. The correlations can be expressed in the general form

$$[\bar{F}/F(FD)]/\{(W/H)^c[(E/D)/0.063]^d[(P/E)/10]^m(\alpha/60°)^n\} = a\,\mathrm{Re}^b \quad (6)$$

For rib-roughened channels, the empirically determined constants a, b, c, d, m, and n are given in Table 2. Note that the absolute constants d, m, and n in the first two passes and the entire three passes are much smaller than those in the first pass. This implies that the effect of the rib configuration (rib height, spacing, and angle) on the friction factors in the two-pass or three-pass channels is diluted by the effect of the sharp 180-deg turns, as discussed earlier. In smooth channels, the empirically determined constants a, b, and c are also shown in Table 2 with d, m, and $n=0$. The deviations in equation (6) from the test data are about ±10 percent. The correlations are valid for $0.039 \le E/D \le 0.063$, $5 \le P/E \le 15$, $45\text{deg} \le \alpha \le 90\text{deg}$, $1/4 \le W/H \le 1$, and $15{,}000 \le \mathrm{Re} \le 60{,}000$.

Table 2 Numerical values of the coefficients *a*, *b*, *c*, *d*, *m*, and *n*, in equation (6)

SMOOTH CHANNEL

	First Pass	First Two-Pass	Three-Pass
a	1	2.02	2.32
b	0	0.08	0.08
c	0	-0.31	-0.41

RIB-ROUGHENED CHANNEL

	First Pass	First Two-Pass	Three-Pass
a	3.38	5.48	5.92
b	0.08	0.08	0.08
c	0.15	0.05	0.09
d	1.05	0.35	0.05
m	-0.45; P/E ≥ 10	-0.27	-0.20
m	0.21; P/E < 10	0.12	0.12
n	-0.70; α ≥ 60°	-0.50	-0.35
n	0.80; α < 60°	0.65	0.30

Concluding Remarks. The combined effects of the sharp 180-deg turns and of the rib turbulator configuration on the distributions of the local pressure drop in the three-pass rectangular channels have been investigated. The main findings of the study are:

1 In the smooth rectangular channels, the pressure drops are caused primarily by the sharp 180-deg turns. In the rib-roughened rectangular channels, the pressure drops are caused by the sharp turns and the rib turbulators.

2 With the same rib height (E) in each of the channels, the pressure drop caused by the rib turbulators decreases with decreasing channel aspect ratio (W/H from 1 to 1/4; ribs on the channel width, W, side).

3 The angled ribs with $\alpha=60$ deg produce the highest pressure drops in the first pass of the three-pass channel. The differences between $\alpha=60$ deg and $\alpha=90$ (or 45 deg) are reduced in the two-pass and three-pass channels.

4 The pressure drops with $P/E=10$ are higher than those with other P/E ratios studied (such as $P/E=5$, 7.5, and 15). The pressures drops decrease with decreasing or increasing the P/E ratio from 10. The effects of the P/E and E/D ratios are reduced in the two-pass and three-pass channels.

5 The empirical correlations for the friction factors obtained for the first pass and for the first two passes and the entire three passes are valid for $0.039 \le E/D \le 0.063$, $1/4 \le W/H \le 1$, $5 \le P/E \le 15$, $45\text{ deg} \le \alpha \le 90\text{ deg}$, and $15{,}000 \le \mathrm{Re} \le 60{,}000$. The correlations can be used in the design of turbine airfoil cooling passages.

Acknowledgments

This investigation was supported in part by the NSF through Grant No. CBT-8713833.

References

Boyle, R. J., 1984, "Heat Transfer in Serpentine Passages With Turbulence Promoters," ASME Paper No. 84-HT-24.

Chandra, P. R., Han, J. C., and Lau, S. C., 1988, "Effect of Rib Angle on Local Heat/Mass Transfer Distribution in a Two-Pass Rib-Roughened Channel," ASME JOURNAL OF TURBOMACHINERY, Vol. 110, pp. 233–241.

Fan, C. S., and Metzger, D. E., 1987, "Effects of Channel Aspect Ratio on Heat Transfer in Rectangular Passage Sharp 180-deg Turns," ASME Paper No. 87-GT-113; ASME JOURNAL OF TURBOMACHINERY, in press.

Han, J. C., Park, J. S., and Lei, C. K., 1985, "Heat Transfer Enhancement in Channels With Turbulence Promoters," ASME *Journal of Engineering for Gas Turbines and Power*, Vol. 107, pp. 628–635.

Han, J. C., and Park, J. S., 1988, "Developing Heat Transfer in Rectangular Channels With Rib Turbulators," *International Journal of Heat and Mass Transfer*, Vol. 31, No. 1, pp. 183–195.

Han, J. C., Chandra, P. R., and Lau, S. C., 1988, "Local Heat/Mass Transfer Distributions Around Sharp 180 deg Turns in Two-Pass Smooth and Rib-Roughened Channels," ASME *Journal of Heat Transfer*, Vol. 110, pp. 91–98.

Han, J. C., and Chandra, P. R., 1987, "Local Heat/Mass Transfer and Pressure Drop in a Two-Pass Rib-Roughened Channel for Turbine Airfoil Cooling," NASA CR-179635; AVSCOM TR-87-C-14.

Metzger, D. E., Plevich, C. W., and Fan, C. S., 1984, "Pressure Loss Through Sharp 180 Deg Turns in Smooth Rectangular Channels," ASME *Journal of Engineering for Gas Turbines and Power*, Vol. 106, pp. 677–681.

Metzger, D. E., and Sahm, M. K., 1986, "Heat Transfer Around Sharp 180-deg Turns in Smooth Rectangular Channels," ASME *Journal of Heat Transfer*, Vol. 108, pp. 500–506.

Kline, S. J., and McClintock, F. A., 1953, "Describing Uncertainties in Single-Sample Experiments," *Mechanical Engineering*, Vol. 75, pp. 3–8.

Zhang, P., 1988, "Pressure Drop and Heat Transfer Distributions in Three-Pass Rectangular Channels With Rib Turbulators," M.S. Thesis, Texas A&M University, College Station, TX.

Preswirl Blade-Cooling Effectiveness in an Adiabatic Rotor-Stator System

Z. B. El-Oun[1]

J. M. Owen

Thermo-Fluid Mechanics Research Centre,
School of Engineering and Applied Sciences,
University of Sussex,
Falmer, Brighton, BN1 9QT, United Kingdom

Blade-cooling air for a high-pressure turbine is often supplied from preswirl nozzles attached to a stationary casing. By swirling the cooling air in the direction of rotation of the turbine disk, the temperature of the air relative to the blades can be reduced. The question addressed in this paper is: Knowing the temperatures of the preswirl and disk-cooling flows, what is the temperature of the blade-cooling air? A simple theoretical model, based on the Reynolds analogy applied to an adiabatic rotor-stator system, is used to calculate the preswirl effectiveness (that is, the reduction in the temperature of the blade-cooling air as a result of preswirling the flow). A mixing model is used to account for the "contamination" of the blade coolant with disk-cooling air, and an approximate solution is used to estimate the effect of frictional heating on the disk-cooling air. Experiments were conducted in a rotor-stator rig that had preswirl nozzles in the stator and blade-cooling passages in the rotating disk. A radial outflow or inflow of disk-cooling air was also supplied, and measurements of the temperature difference between the preswirl and blade-cooling air were made for a range of flow rates and for rotational Reynolds numbers up to $Re_\theta = 1.8 \times 10^6$. Considering the experimental errors in measuring the small temperature differences, good agreement between theory and experiment was achieved.

1 Introduction

The problems associated with the cooling of turbine blades and disks become more severe as the pressure ratios and turbine entry temperatures increase. One method of introducing blade-cooling air into the rotor-stator wheel space is by accelerating it through preswirl nozzles at an acute angle to the rotating blade-feed holes in the rotor, as illustrated in Fig 1. While the stagnation temperature of the air is unchanged relative to the stator, its temperature relative to the rotor is reduced with consequent benefit to the blade-cooling system. If disk-cooling air is also used, with either radial outflow or inflow, then unless the two flows are physically separated mixing can occur. The nature of the mixing process affects the temperature of the cooling air in the system, and the problem is further complicated if hot mainstream gas is ingested into the wheel space.

There is very little published literature describing the effect of preswirling the cooling air on the temperature of the flow in rotor-stator systems in gas turbines. Meierhofer and Franklin (1981) were the first to report the performance of a preswirled cooling-air supply by measuring the cooling-air temperature in the rotating channels that feed air to the blades in a real engine. A correlation was obtained for the test data as a whole, in which the system effectiveness E was given as a function of the ratio of the disk rotational speed (ωr) to the effective velocity, $V_{p,e}$, of the preswirl flow arriving at the rotor. The effectiveness E was defined by Meierhofer and Franklin as follows:

$$E \equiv V_{p,e}/V_{p,is} \tag{1.1}$$

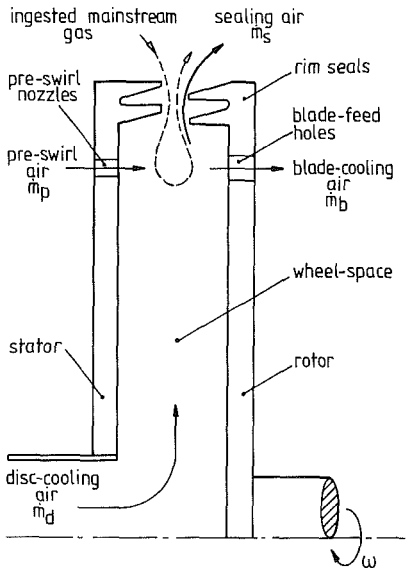

Fig. 1 Simplified diagram of a gas turbine cooling system (with a radial outflow of disk-cooling air)

[1]Current address: BHRA, Fluid Engineering Centre, Cranfield, Bedford MK430AJ, United Kingdom.

Contributed by the International Gas Turbine Institute and presented at the 33rd International Gas Turbine and Aeroengine Congress and Exhibition, Amsterdam, The Netherlands, June 5-9, 1988. Manuscript received by the International Gas Turbine Institute September 15, 1987. Paper No. 88-GT-276.

where $V_{p,is}$ is the velocity that the preswirl coolant flow would have at entry to the cavity if the nozzles were isentropic. The effective preswirl velocity $V_{p,e}$ was calculated using the temperature measurements in the preswirl nozzles and blade-feed holes. The form of the correlated curve showed that as the velocity ratio ($\omega r/V_{p,e}$) increased E decreased; for a velocity ratio of 1.0 the effectiveness was around 70 percent.

The ingress of mainstream gas into the wheel space depends on the system geometry, the coolant flow rate, the rotational speed of the rotor, and the asymmetry of the external flow. A discussion of the so-called "ingress problem" is given by Phadke and Owen (1988) and by El-Oun et al. (1988). El-Oun et al., using a rig similar to that employed in the tests described below, determined the effect of preswirl "cooling air" on the sealing performance. The dimensionless minimum flow rate of air necessary to prevent ingress, $C_{w,\min}$, was determined using both preswirl "blade-cooling" air, injected near the outer radius, and nonswirled "disk-cooling" air, injected near the center of the wheel space. When no air was extracted through the blade-cooling holes in the outer part of the rotor, $C_{w,\min}$ was found to be independent of the entry location of the sealing air. However, when air was extracted through the blade-cooling holes, $C_{w,\min}$ was increased, and gas-concentration measurements showed that most or all of the disk-cooling flow could be entrained into the holes in the rotor. Thus, for most practical cases, the blade coolant will be "contaminated" with disk-cooling air.

In this paper, the question addressed is: Knowing the temperatures of the preswirl and disk-cooling flows at inlet to the system, what is the temperature of the blade-cooling air in a sealed adiabatic system? In Section 2, a simple theoretical model is developed, the experimental apparatus is described in Section 3, and a comparison between the theoretical and experimental results is discussed in Section 4. Finally, in Section 5 the conclusions drawn are presented.

2 Calculation of the Temperature of the Blade-Cooling Air

2.1 Outline of Problem. In the absence of superimposed flows, and at sufficiently large rotational speeds, separate boundary layers form on the rotor and stator, and the core of fluid between rotates at an intermediate speed. A radial outflow of disk-cooling air reduces the speed of the core rotation and, at large flow rates, the rotation stops and radially inward flow in the stator boundary layer is suppressed. The preswirl air must cross the boundary layers and the core region if it is to penetrate the holes in the rotor. However, in practice, the blade-cooling air is supplied from both the preswirl flow (either directly across the rotor–stator gap or down the stator and into the boundary layer on the rotor) and the disk-cooling flow. There is no simple means of determining the proportions of disk-cooling and preswirl air that is drawn into the blade-feed holes.

The resulting flow is three-dimensional, but it is assumed below that the average effects can be described by two-dimensional axisymmetric equations. It is also assumed that the flow rate is sufficient to prevent ingress and that the boundary layer on the shroud does not significantly influence the flow near the blade-cooling holes. Heat transfer is not considered, and the rotor and stator are regarded as adiabatic surfaces; frictional work from the rotor is, however, taken into account as described below.

In order to calculate temperatures on an adiabatic disk, it is useful to consider the Reynolds analogy. The results can then be applied separately to the cases where either the disk-cooling flow or the preswirl flow occurs. When both flows are present, some assumptions must be made about how they mix to form the blade-cooling flow.

2.2 Reynolds Analogy. Owen (1971) applied the Reynolds analogy to calculate the adiabatic-disk temperature

Nomenclature

$C_{mo} \equiv M_o/\frac{1}{2}\rho\omega^2 r_o^5$ = moment coefficient on the stator side of the rotor
C_p = specific heat capacity at constant pressure
$C_w \equiv \dot{m}/\mu r_o$ = dimensionless mass flow rate
$C_{w,\min}$ = minimum dimensionless mass flow required to prevent ingress
$E \equiv V_{p,e}/V_{p,is}$ = effectiveness of preswirl process
$G = s/r_o$ = rotor/stator axial gap ratio
$G_{cm} = s_{cm}/r_o$ = clearance ratio for the 15 deg mitered shrouds
$G_{cr} = s_{cr}/r_o$ = clearance ratio for the radial shroud
h = total enthalpy of fluid
Δh = increase in total enthalpy
k = thermal conductivity
$\dot{m}$ = coolant mass flow rate
M_o = moment on the stator side of the rotor
$\mathrm{Pr} \equiv \mu C_p/k$ = Prandtl number
q = heat flux
Q = volumetric flow rate
r = radial distance from rotor–stator central line
r_a = inlet radius from the center of the stator
r_b = radius of central axis of "blade" feed holes and of preswirl nozzles
r_o = outer radius of the rotor
R = recovery factor
$\mathrm{Re}_b \equiv \rho\omega r_b^2/\mu$ = rotational Reynolds number based on the radius (r_b) of central axis of blade holes
$\mathrm{Re}_\theta \equiv \rho\omega r_o^2/\mu$ = rotational Reynolds number based on the outer radius (r_o) of the disk
s = axial gap between rotor and stator
s_{cm} = mitered clearance in rotor–stator rim seal
s_{cr} = radial clearance in rotor–stator rim seal
$S_r \equiv V_{\phi,p}/\omega r_b$ = swirl ratio of preswirl flow
T = temperature
T_b = total temperature of blade-cooling air (with respect to the rotor)
T_c = total temperature of coolant (preswirl or disk flow) at inlet
$T_{o,ad}$ = adiabatic-surface temperature on the stator side of the rotor

for the cases where the core rotation outside the boundary layer is zero, and Chew (1985) used the analogy for the case where the core rotation is nonzero. A more complete discussion of the Reynolds analogy is given by Owen and Rogers (1989).

It is useful to define the total enthalpy h as

$$h = C_p T + \tfrac{1}{2} V_r^2 + \tfrac{1}{2} V_\phi^2 \tag{2.1}$$

where T is the static temperature of the fluid, and V_r and V_ϕ are the radial and tangential components of velocity, respectively, in a stationary frame of reference. An effective viscosity model is assumed where $\mu_{\text{eff}} = \mu + \mu_t$, and the laminar and turbulent Prandtl numbers are assumed to be unity. The boundary layer equations can be expressed in terms of streamline coordinates, where $\xi = r$ and ψ is the streamfunction, as

$$\frac{\partial h}{\partial \xi} = r \frac{\partial}{\partial \psi} \left(\rho r V_r \mu_{\text{eff}} \frac{\partial h}{\partial \psi} \right) \tag{2.2}$$

and

$$\frac{\partial (r V_\phi)}{\partial \xi} = r \frac{\partial}{\partial \psi} \left(\rho r V_r \mu_{\text{eff}} \frac{\partial}{\partial \psi} (r V_\phi) \right) \tag{2.3}$$

The solutions of equations (2.2) and (2.3) will be similar if the initial and boundary conditions are similar, that is

$$r V_\phi = \omega r^2, \quad h = A + B\omega r^2 \text{ for } \psi = \psi_o \, (z = 0) \tag{2.4a}$$

$$\frac{\partial}{\partial \psi} (r V_\phi) = \frac{\partial h}{\partial \psi} = 0 \text{ as } \psi \to \psi_\infty \, (z \to \infty) \tag{2.4b}$$

where A and B are constants. If at $r = r_a$, say, rV_ϕ and h have similar profiles, then

$$\frac{h - h_\infty}{h_o - h_\infty} = \frac{V_\phi - V_{\phi\infty}}{\omega r - V_{\phi\infty}} \tag{2.5}$$

for all values of r and z for $r \geq r_a$. In particular, the heat flux q is given by

$$q = -\mu_{\text{eff}} C_p \frac{\partial T}{\partial z}$$

$$= -\mu_{\text{eff}} \frac{\partial h}{\partial z} + V_r \tau_r + V_\phi \tau_\phi$$

and, using equation (2.5),

$$q = V_r \tau_r + V_\phi \tau_\phi - \frac{h_o - h_\infty}{\omega r - V_{\phi\infty}} \tau_\phi \tag{2.6}$$

where τ_r and τ_ϕ are the radial and tangential components of shear stress, respectively. On the surface of the disk, $z = 0$, $V_r = 0$, $V_\phi = \omega r$, and $q = q_o$, where

$$q_o = -\frac{\tau_{\phi o}}{\omega r - V_{\phi\infty}} \left[(h_o - h_\infty) - \omega^2 r^2 (1 - \beta) \right] \tag{2.7}$$

and $\beta \simeq V_{\phi\infty} / \omega r$.

For an adiabatic disk, $q_o = 0$, hence

$$h_{o,ad} = h_\infty + \omega^2 r^2 (1 - \beta) \tag{2.8}$$

Thus, knowing h_∞, $h_{o,ad}$ can be calculated from equation (2.8) and the adiabatic-disk temperature, $T_{o,ad}$, is given by

$$T_{o,ad} = T_\infty + \tfrac{1}{2} \omega^2 r^2 (1 - \beta)^2 / C_p \tag{2.9}$$

For $\text{Pr} \neq 1$, a recovery factor R is often used such that

$$T_{o,ad} = T_\infty + \tfrac{1}{2} R \omega^2 r^2 (1 - \beta)^2 / C_p \tag{2.10}$$

By analogy with high-speed flow over an adiabatic flat plate (Schlichting, 1979), it is assumed that for Pr of order unity, $R \simeq \text{Pr}^{1/3}$. For air, where $\text{Pr} = 0.71$, this gives a value of approximately 0.89 for R. Although this value may not be completely correct for rotating flows, there is no available evidence to support an alternative hypothesis.

2.3 Application to Preswirl Flows. Consider the case where flow leaves a series of nozzles in the stator and enters a

Nomenclature (cont.)

$\Delta T^* \equiv 2C_p (T_c - T_b)/(\omega r_b)^2$ = dimensionless temperature drop or rise in rotor-stator system
V_p = actual velocity of preswirl flow (calculated from continuity)
$V_{p,e}$ = effective velocity of preswirl flow (calculated from temperature measurements)
$V_{p,is}$ = velocity of preswirl flow assuming an isentropic process across the preswirl nozzles
V_r, V_ϕ, V_z = radial, tangential and axial velocity components in a stationary cylindrical coordinate system (r, ϕ, z)
z = axial distance from the surface of the rotor
$\beta = V_{\phi\infty}/\omega r$ = swirl ratio of fluid in the core of the rotor-stator wheel space
δ = boundary layer thickness
θ = angle of preswirl nozzle to axial direction = 70 deg
$\lambda \equiv C_{w,d} \, \text{Re}_b^{-0.8}$ = flow coefficient
μ = fluid dynamic viscosity
$\nu = \mu/\rho$ = fluid kinematic viscosity
ρ = fluid density
τ = shear stress
ψ = stream function
ω = angular velocity of rotor

Subscripts

a = refers to conditions at $r = r_a$
ad = refers to adiabatic condition
b = refers to blade-cooling flow
d = refers to disk-cooling flow
eff = effective (for turbulent flow)
m = refers to conditions after mixing
o = refers to conditions at $z = 0$ (rotor surface)
p = refers to preswirl flow
s = refers to sealing flow
t = refers to turbulent conditions
∞ = refers to conditions at $z \to \infty$

series of "blade-cooling" holes in the rotor, as shown in Fig. 2. It is assumed that the holes are sufficiently small in size and plentiful in number for the flow to be treated as axisymmetric. It is also assumed that the axial components of velocity are small enough not to contribute significantly to the viscous dissipation in the boundary layer on the rotor (that is, $V_z/\omega r_b << 1$).

If the blade-cooling holes are normal to the surface of the rotor, then the no-slip condition still applies for V_ϕ and V_r, and equation (2.10) is still valid for an adiabatic disk. However, it is necessary to know both T_∞ and β in order to determine $T_{o,ad}$.

The simplest assumption to make for β is that $\beta = S_r = V_{\phi,p}/\omega r_b$. In practice, the preswirl flow has to penetrate the boundary layer on the stator and interact with a "core" of fluid, which is probably rotating, before reaching the boundary layer on the rotor. At low preswirl flow rates, where the flow entrained by the boundary layer on the rotor is of the order of that of the preswirl flow, the effect of the core rotation generated by the rotor would be expected to affect β. At large preswirl flow rates, the effect of the entrained flow in the boundary layer on the rotor would be expected to have less influence. A model to account for this effect is discussed in Section 2.5.

If the total enthalpy of the flow leaving the preswirl nozzles is known, T_∞ can be calculated. If $V_{r,p}$ and $V_{z,p}$ are small compared with $V_{\phi,p}$, then

$$C_p T_p = h_p - \tfrac{1}{2} V_{\phi,p}^2 \tag{2.11}$$

Assuming that $\beta = S_r$ and $T_p = T_\infty$, equation (2.10) can be written as

$$C_p T_{o,ad} = h_p + \tfrac{1}{2}\phi\omega^2 r_b^2 \tag{2.12}$$

where

$$\phi = R(1 - S_r^2) - S_r^2$$

Thus knowing the total enthalpy and the swirl ratio of the preswirl air, the adiabatic-disk temperature can be calculated from equation (2.12).

The total temperature (relative to the rotor) of the blade-cooling air, T_b, is found from

$$T_b = T_{o,ad} + V_{z,b}^2/2C_p \tag{2.12a}$$

where $V_{z,b}$ is the average axial velocity of the blade-cooling flow in the blade-feed holes.

It should be noted that, for $R = 1$,

$$(h_p - C_p T_{o,ad})/\tfrac{1}{2}\omega^2 r_b^2 = -1 \text{ if } S_r = 0$$
$$= 0 \text{ if } S_r = \tfrac{1}{2}$$
$$\geq 1 \text{ if } S_r \geq 1$$

2.4 Application to Disk-Cooling Flows. Consider the case where the cooling air is supplied at some radius $r = r_a$, say, and flows outward in the boundary layer on the rotor. In the absence of heat transfer from the rotor, equation (2.10) is still valid but it is necessary to calculate T_∞.

Referring to Section 2.2, if (for $\mathrm{Pr} = 1$) the distributions of h and rV_ϕ are similar, this implies that at the edge of the boundary layer

$$rV_{\phi\infty} = \beta\omega r^2 \text{ and } h_\infty = A + B\beta\omega r^2 \tag{2.13}$$

where A and B are constants. In order for equation (2.8) to be satisfied, $B = \omega$ and A can be chosen to suit the known conditions at $r = r_a$, such that

$$h_\infty = h_{\infty,a} + \omega^2(\beta r^2 - \beta_a r_a^2) \tag{2.14}$$

where the subscript a refers to conditions at $r = r_a$. It therefore follows that

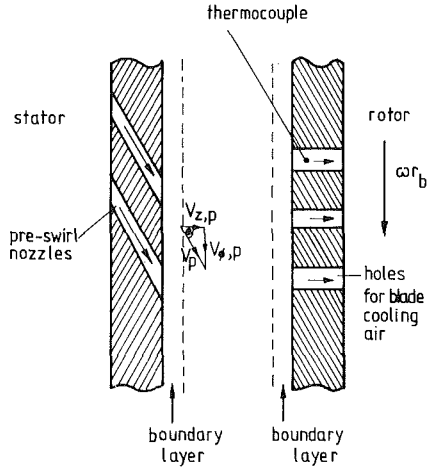

Fig. 2 Section through the rotor-stator system at $r = r_b$

$$h_{o,ad} = h_{\infty,a} - \beta_a\omega^2 r_a^2 + \omega^2 r^2 \tag{2.15}$$

which implies that the enthalpy distribution on the surface of the adiabatic disk is independent of β, the rotational speed of the core.

Introducing a recovery factor for $\mathrm{Pr} \neq 1$, the result analogous to equation (2.10) is

$$T_{o,ad} = (T_{\infty,a} - \tfrac{1}{2}\beta_a\omega^2 r_a^2/C_p) + \tfrac{1}{2}R\omega^2 r^2/C_p \tag{2.16}$$

In a separate study, Owen (1989) solved the momentum-integral equations to provide an approximate solution for the flow between a rotating and a stationary disk. Despite the fact that the equations took no account of the presence of the peripheral shrouds, the approximate solutions for the moment coefficients were in reasonable agreement with the available experimental data of Daily et al. (1964). At $r = r_b$, Owen's solutions for the flow rate in the boundary layer on the rotor, Q_o, for the relative core rotation β, and for the moment coefficient, C_{mo}, can be summarized as follows:

$$C_{w,o} = 0.219\,\mathrm{Re}_b^{4/5}(1-\beta)^{8/5}(1 - 0.51\beta) \tag{2.17}$$

where $C_{w,o} = Q_o/\nu r_o$ and β was calculated from the equation

$$(1-\beta)^{8/5}(1 - 0.51\beta) - 0.638\beta^{4/5} = 4.57\lambda \tag{2.18}$$

where $\lambda = C_{w,d}\,\mathrm{Re}_b^{-4/5}$ and for $\lambda \leq 0.219$

$$C_{mo}\mathrm{Re}_b^{1/5} = 0.0729x_c^{23/5} + 0.0398[(1 - x_c^{23/5}) + 14.7\lambda(1 - x_c^2) + 90.4\lambda^2(1 - x_c^{-3/5})] \tag{2.19a}$$

where $x_c = 1.79\,\lambda^{5/13}$. For $\lambda > 0.219$, $\beta = 0$ and

$$C_{mo} = 0.0729\,\mathrm{Re}_b^{-1/5} \tag{2.19b}$$

The increase in total enthalpy Δh of the fluid entering and leaving the system can be calculated, using the steady-flow energy equation, from

$$\frac{\Delta h}{\tfrac{1}{2}\omega^2 r_b^2} = \frac{C_{mo}\mathrm{Re}_b}{C_w} \tag{2.20}$$

where C_w is the total dimensionless superimposed flow rate.

2.5 Mixing Model. When the preswirl and disk-cooling flows mix, the simplest model to use, assuming perfect mixing and no mainstream ingress, is that the angular momentum is conserved and the steady-flow energy equation is valid. Hence,

$$C_{w,p}V_{\phi,p} + C_{w,d}V_{\phi,d} = (C_{w,p} + C_{w,d})V_{\phi,m} \tag{2.21}$$

where the subscripts p, d, and m refer to the preswirl, disk-

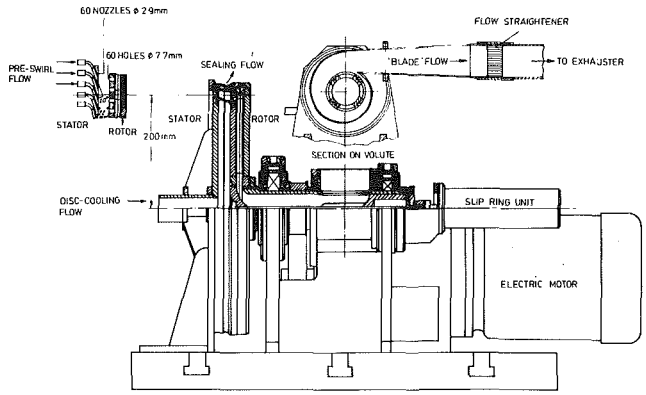

Fig. 3 General arrangement of the preswirl rotor-stator rig

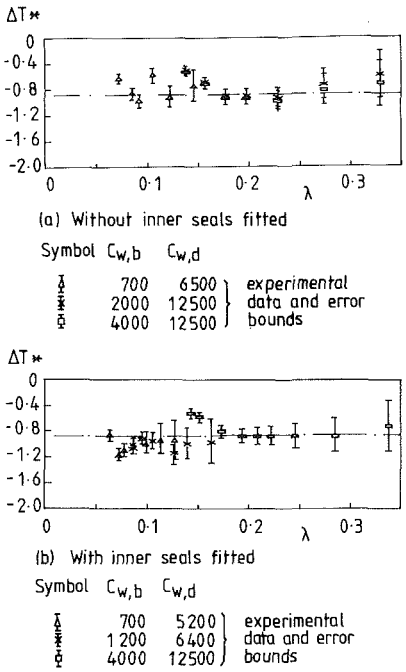

Fig. 4 The variation of ΔT^* with λ for the case where $C_{w,p}=0$: — · — equation (2.16), $R=0.89$

cooling, and mixed flow, respectively. The tangential component of velocity for the disk-cooling air is calculated by

$$V_{\phi,d}=\int_0^{\delta_o} V_r V_\phi dz \Big/ \int_0^{\delta_o} V_r dz \qquad (2.22)$$

and, using the results of Owen (1989), which were based on 1/7th power-law velocity profiles,

$$V_{\phi,d}=\omega r\left(\frac{1}{6}+\frac{5}{6}\beta\right) \qquad (2.23)$$

where β is calculated from equation (2.18).

Using equation (2.20), the enthalpy after mixing h_m can be calculated from

$$C_{w,p}h_p + C_{w,d}h_d + \tfrac{1}{2}\omega^2 r_b^2 \,\mathrm{Re}_b C_{mo} = (C_{w,p}+C_{w,d})h_m \qquad (2.24)$$

where C_{mo} is calculated from equation (2.19).

For the "mixed-flow theory" used below, h_p is replaced by h_m in equation (2.12) and S_r is calculated using $V_{\phi,m}$ instead of $V_{\phi,p}$.

3 Experimental Apparatus

Details of the apparatus are given by El-Oun et al. (1987) but for completeness the more important features are described below. The apparatus, which is shown in Fig. 3, essentially consists of a plane stationary disk (stator) with preswirl nozzles adjacent to a plane rotating disk (rotor) containing blade-feed holes at the same radius as the preswirl nozzles.

The stator was made from perspex (transparent acrylic plastic), 10 mm thick to allow flow visualization and laser-Doppler anemometry, and contained 60 preswirl nozzles, 2.9 mm in diameter, inclined at 20 deg to the face at a radius of 200 mm. The rotor was made from two aluminum alloy disks with two layers of Rohacell insulation sandwiched between. The insulation contained radial passages connected at the outer edge of the cavity to 60 blade-feed holes, each 7.7 mm in diameter, to allow the blade-coolant flow to be drawn radially down through the rotor and then out via the rotating shaft and flow volute (see Fig. 3) through a flow meter and the exhauster.

The rotor and stator both had outer radii of $r_o=221$ mm, and although the rotor-stator gap and the rim-seal clearance were adjustable, they were kept constant for the tests reported below. The gap ratio was maintained at $G=0.10$, and the rim shroud clearance ratio was $G_{cm}=0.0072$. In some tests, inner seals of radial clearance ratio $G_{cr}=0.0033$ were fitted at $r/r_o=0.87$. The rotor was driven by a Tasc electric-motor system affording precise speed control up to 5400 rpm ($\mathrm{Re}_\theta=1.8\times10^6$).

Air, at flow rates up to $C_{w,p}=2\times10^4$, was supplied to the preswirl nozzles via a manifold system at pressures up to 1.28 bar upstream of the nozzles. For rotational Reynolds number $\mathrm{Re}_\theta=10^6$ and preswirl flows over the range $4000<C_{w,p}<18{,}000$, the swirl ratio S_r varied in the range $0.46<S_r<2.07$. The disk-cooling flow, up to $C_{w,d}=1.3\times10^4$, was supplied at essentially atmospheric pressure to the center of the stator via a pipe of 38-mm diameter. For tests where disk-cooling radial inflow was required, the same pipework was used to draw the coolant out from the wheel space through the central hole. Air, at flow rates up to $C_{w,b}=1.45\times10^4$, could also be extracted through the blade-cooling holes in the rotor. All mass flow rates were measured with an accuracy of ±3 percent, by Annubar (differential-pressure) flow meters. The flow through the seals was not measured directly but determined from the other flow rates. Thus the nondimensional seal flow was found from

$$C_{w,s}=C_{w,p}+C_{w,d}-C_{w,b}$$

The stator was instrumented with static-pressure taps on three orthogonal radii. The outer pressure tap, located above the preswirl nozzles and below the stationary rim seal, was used for measuring the pressure difference across the seal for one of the ingress criteria (see El-Oun et al.).

The total entry temperature of the preswirl flow, which was at ambient conditions, was measured upstream of the wheel space using identical stagnation thermocouple probes secured in six separate insulated preswirl nozzles. The average value of the six temperature readings (a maximum temperature difference of ±0.15°C between the probes was recorded) was taken to be the entry temperature of the preswirl flow. The entry temperature of the disk-cooling flow was meaured, using a similar stagnation probe to those used for the preswirl flow, in the insulated central pipe upstream of the wheel space. For tests with both preswirl and disk-cooling flow present, the two flows were maintained at the same temperature. In practice, this was accomplished by heating the colder disk-cooling flow, using an electric heater mounted in the central pipe. The temperature of the air flow entering the blade-feed holes was measured using five identical stagnation thermocouple probes secured in five equiphased holes. The average value of the five readings was taken to be the mean temperature of the blade-cooling air. A maximum temperature difference of less than

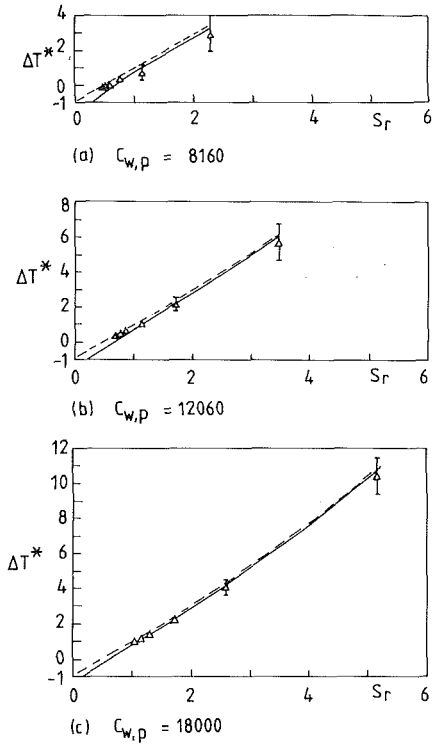

Fig. 5 The variation of ΔT^* with S_r for the case where $C_{w,d}=0$ and $C_{w,b}=4050$, without inner seals fitted: ⊼ experimental data and error bounds; - - - theory for unmixed flow; _____ theory for mixed flow

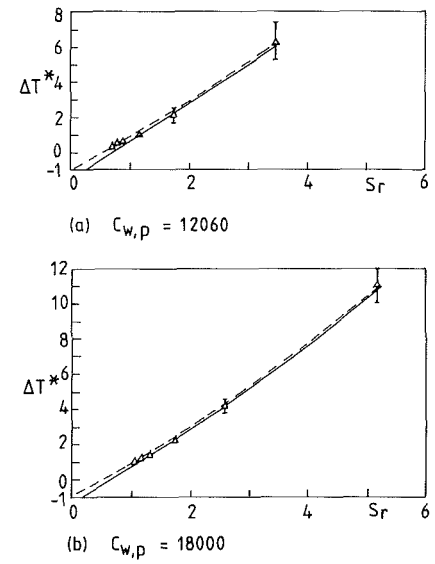

Fig. 6 The variation of ΔT^* with S_r for the case where $C_{w,d}=0$ and $C_{w,b}=4050$, with inner seals fitted: ⊼ experimental data and error bounds; - - - theory for unmixed flow; _____ theory for mixed flow

± 0.1°C between the probes in the blade-feed holes was recorded.

The rotating thermcouples in the blade-feed holes were connected to a slip-ring assembly mounted on the far end of the rotating shaft. The slip-ring unit was air-cooled to reduce brush wear and to minimize the temperature difference inside the unit. The temperature of the junctions between the thermocouples and slip-ring silver wires (i.e., the "cold-junction" temperature) was measured by a Radio Spares RS 590 temperature sensor. The signals from the thermocouples and temperature sensor were fed to a Solartron IMS 3512 data logger, which was controlled by a PDP 11/44 minicomputer. In addition, the surface temperature of the rotor rim seal was monitored using a radiation thermometer giving a direct readout to an accuracy of better than 1 percent of full-scale value (200°C).

All experimental tests were conducted at "near-adiabatic" conditions, whereby the surface temperature of the rotor rim seal was about equal to the blade-cooling air temperature. In some tests, it was necessary to use hot-air blowers to increase the temperature of the rim seal to that of the blade-cooling air. Temperature measurements on the experimental rig could often take several hours to reach the steady-state near-adiabatic conditions.

Tests were conducted to estimate the error between the measured rotating and stationary temperature differences. To avoid dynamic-temperature effects, the temperature differences between a rotating probe located at the center of the disk and a stationary probe located in close proximity were measured for a range of rotational speeds. The differences were found to depend on rotational speed, and a maximum error of 0.3°C was found to occur at the highest speed tested.

The experimental results reported below were obtained with various flow configurations, with and without the inner seals. The sealing air was sufficient to ensure that ingress did not occur for all conditions tested. The tests were conducted over a range of dimensionless flow rates $0 \le C_{w,d} < 1.3 \times 10^4$, $7 \times 10^2 \le C_{w,b} < 10^4$, $0 \le C_{w,p} < 2.0 \times 10^4$, and rotational Reynolds numbers $0.4 \times 10^6 < \mathrm{Re} < 1.8 \times 10^6$.

4 Comparison Between Theory and Experiment

4.1 Temperature Measurements With $C_{w,p}=0$. Figure 4 shows the measured variation of ΔT^* with λ together with the theoretical curve corresponding to equation (2.16) with a recovery factor of $R=0.89$. According to equation (2.16), if $\beta_a=0$, $T_{\infty,a}=T_c$, and $T_{o,ad}=T_b$, then

$$\Delta T^* = \frac{2C_p(T_c - T_b)}{\omega^2 r_b^2} = -R \tag{4.1}$$

The recovery factor R probably depends on the core rotation β, which according to equation (2.18) varies with λ. For $\lambda \ge 0.219$, $\beta=0$, and the recovery factor should be constant. Bearing in mind that the maximum measured temperature difference was 5°C and the estimated maximum error was ± 0.3°C, a value of $R=0.89$ lies within the error bounds of the experimental data for the larger values of λ ($\lambda \gtrsim 0.15$). For the smaller values of λ, where core rotation is expected to be significant, a value of $R=0.89$ may not be appropriate. It should be remembered, however, that the rotor was made from aluminum: hardly an insulating material!

4.2 Temperature Measurements With $C_{w,d}=0$. Figures 5 and 6 show the variation of ΔT^* with S_r for the case where the disk-cooling flow rate was zero and $C_{w,b}=4050$, without and with the inner seals fitted. It should be noted that ΔT^* was based on the temperature of the preswirl air and that the swirl fraction was varied by altering the rotational speed. As well as the experimental data, two theoretical curves are shown: the curve for "unmixed flows" is based on equation (2.12) with $T_{o,ad}=T_b$; the curve for "mixed flows" uses equations (2.21) and (2.24) to modify equation (2.12)

It can be seen that ΔT^* increases with S_r as predicted. The difference between the two theoretical curves is relatively small, but most of the experimental data appear to be closer to the mixed-flow curves. The inner seals do not appear to have a significant effect on the measurements.

4.3 Temperature Measurements With $C_{w,p} \ne 0$ and $C_{w,d} \ne 0$. Tests were conducted with preswirl and disk-

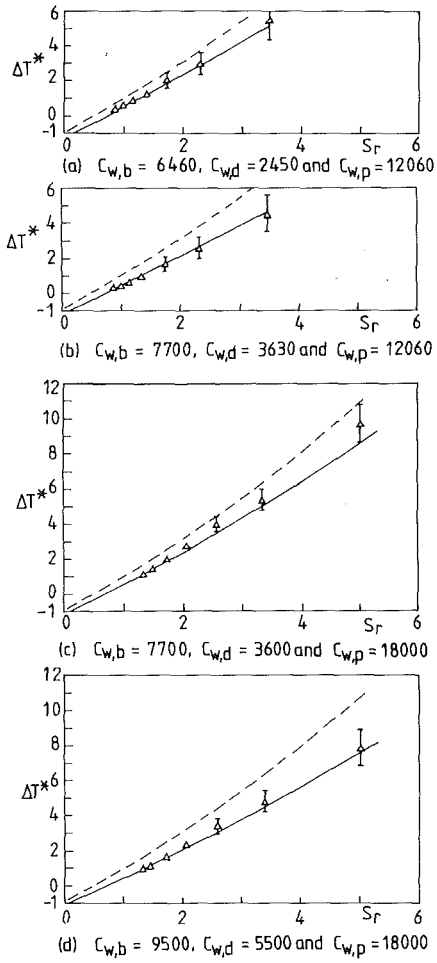

Fig. 7 The variation of ΔT^* with S_r for the case where $C_{w,p}>0$ and $C_{w,d}>0$, without inner seals fitted: ⊥ experimental data and error bounds; - - - theory for unmixed flow; _____ theory for mixed flow

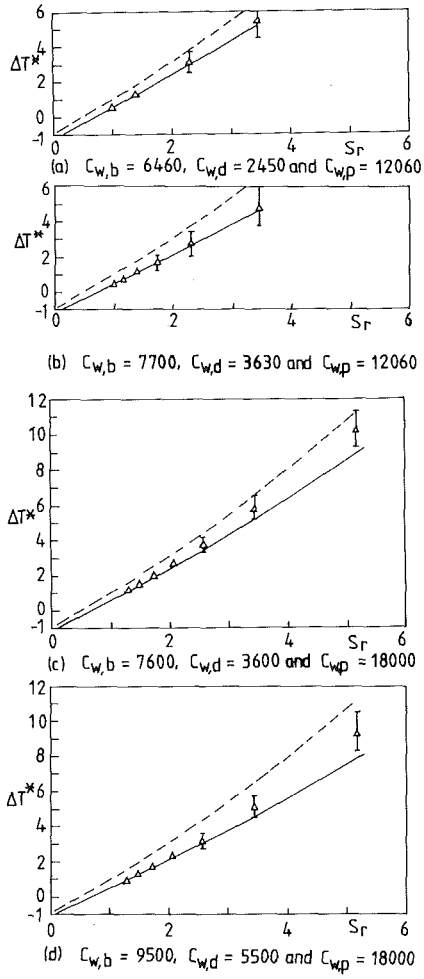

Fig. 8 The variation of ΔT^* with S_r for the case where $C_{w,p}>0$ and $C_{w,d}>0$, with inner seals fitted: ⊥ experimental data and error bounds; - - - theory for unmixed flow; _____ theory for mixed flow

cooling flows, both flows having virtually the same temperature.

Figures 7 and 8 show the variation of ΔT^* with S_r for the case of a radial outflow of disk-cooling air ($C_{w,d}>0$) for various values of $C_{w,d}$, $C_{w,p}$, and $C_{w,b}$, without and with the inner seals fitted. The experimental data are, in the main, in good agreement with the mixed-flow curves and, somewhat surprisingly, the inner seal still appears to have no significant effect.

Figures 9 and 10 show the variation of ΔT^* with S_r for the case of radial inflow ($C_{w,d}<0$) where most of the data can be seen to be in good agreement with the unmixed-flow curve. It should be noted that for $S_r>1$ radial inflow can occur on both the stator and the rotor. Under these conditions, there should be no contamination of blade-coolant with disk-cooling air. Another advantage of radial inflow is that the disk windage is reduced, and for $S_r>1$ it can be reversed (that is, work is put into the disk by the cooling air).

5 Conclusions

A combined theoretical and experimental study has been conducted in a rotor–stator system in which preswirl air was supplied through nozzles in the stator, disk-cooling air flowed either radially outward or radially inward, and blade-cooling air was extracted through a series of holes in the rotor. A simple theoretical model, based on the Reynolds analogy, has been developed to calculate the temperature of the blade-cooling air in an adiabatic rotor–stator system. Using the conservation of angular momentum and the steady-flow energy equation, corrections were introduced to account for mixing between the preswirl and disk-cooling flows.

Experiments were conducted in an adiabatic rotor–stator rig for a wide range of cooling flows and for rotational Reynolds numbers up to 1.8×10^6; the superimposed flows were always sufficient to ensure that the system was sealed (that is, no ingress occurred). Despite the errors in measuring the relatively small temperature differences between the preswirl and blade-cooling flows, most of the measurements were in good agreement with the theoretical results. It was shown that the temperature differences increased with increasing swirl ratio (the ratio of the tangential component of velocity of the preswirl flow to the speed of the rotor) and that mixing between the preswirl and disk-cooling flows could attenuate the temperature differences. For a radial outflow of disk-cooling air, this attenuation was significant; for a radial inflow there was no significant effect. It was also shown that the presence of a radial-clearance seal, located radially inward of the blade-cooling holes, had no measurable effect on the results.

Acknowledgments

We are grateful to Dr. A. B. Turner for his valuable advice and interest throughout the course of the work. We would also

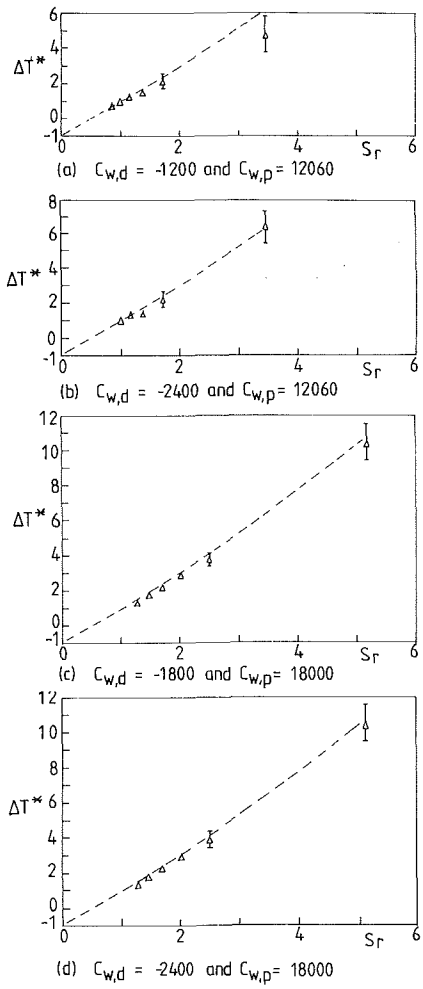

Fig. 9 The variation of ΔT^* with S_r for the case where $C_{w,b} = 4050$, $C_{w,p} > 0$, and $C_{w,d} < 0$, without inner seals fitted: ⊼ experimental data and error bounds; - - - theory for unmixed flow

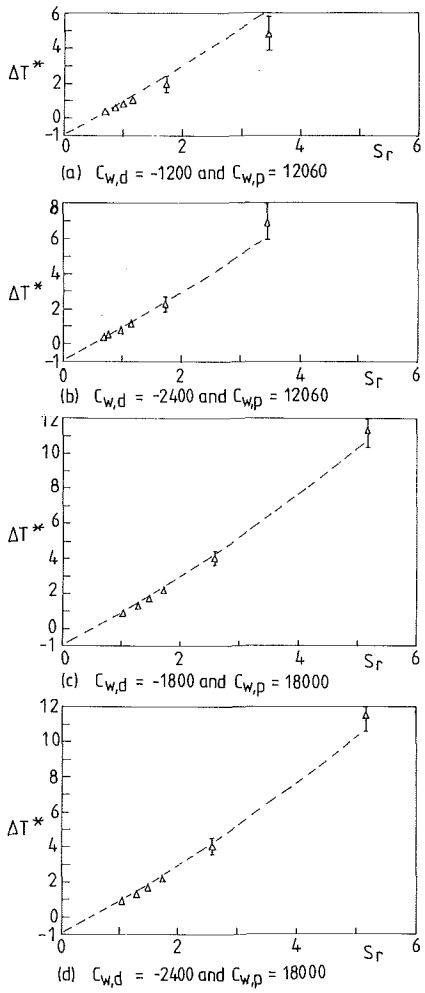

Fig. 10 The variation of ΔT^* with S_r for the case where $C_{w,b} = 4050$, $C_{w,p} > 0$, and $C_{w,d} < 0$, with inner seals fitted: ⊼ experimental data and error bounds; - - - theory for unmixed flow

like to thank SERC, Rolls-Royce plc, and Ruston Gas Turbines plc for supporting the work described in this paper.

References

Chew, J. W., 1985, "Effect of Frictional Heating and Compressive Work in Rotating Axisymmetric Flow," ASME *Journal of Heat Transfer*, Vol. 107, pp. 984–986.

Daily, J. W., Ernst, W. D., and Asbedian, V. V., 1964, "Enclosed Rotating Disks With Superimposed Throughflow: Mean Steady and Periodic Unsteady Characteristics of the Induced Flow," Report No. 64, M.I.T. Hydrodynamic Lab.

El-Oun, Z. B., Neller, P. H., and Turner, A. B., 1988, "Sealing of a Shrouded Rotor-Stator System With Preswirl Coolant," ASME JOURNAL OF TURBOMACHINERY, Vol. 110, pp. 218–225.

Meierhofer, B., and Franklin, C. J., 1981, "An Investigation of a Preswirled Cooling Airflow to a Turbine Disc by Measuring the Air Temperature in the Rotating Channels," ASME Paper No. 81-GT-132.

Owen, J. M., 1971, "The Reynolds Analogy Applied to Flow Between a Rotating and a Stationary Disc," *Int. J. Heat Mass Transfer*, Vol. 14, p. 451.

Owen, J. M., 1989, "An Approximate Solution for the Flow Between a Rotating and a Stationary Disk," ASME JOURNAL OF TURBOMACHINERY, Vol. 111, pp. 323–332.

Owen, J. M., and Rogers, R. H., 1989, *Fluid Flow and Heat Transfer in Rotating-Disc Systems. Vol. I: Rotor–Stator Systems*, Research Studies Press, Taunton, United Kingdom.

Phadke, U. P., and Owen, J. M., 1988, "Aerodynamic Aspects of the Sealing of Gas Turbine Rotor-Stator Systems. Part I: The Behaviour of Simple Shrouded Rotating-Disc Systems in a Quiescent Environment. Part II: The Performance of Simple Seals in a Quasi-Axisymmetric External Flow. Part III: The Effect of Non-Axisymmetric External Flow on Seal Performance," *Int. J. Heat Fluid Flow*. Vol. 9, pp. 98–117.

Schlichting, H., 1979, *Boundary-Layer Theory*, McGraw-Hill, New York.

A Comparison of Secondary Flow in a Vane Cascade and a Curved Duct

M. T. Boyle

M. Simonds

University of Maine,
Orono, ME 04469

K. Poon

Textron Lycoming,
Stratford, CT 06497

This paper describes an experiment performed to measure the aerodynamic characteristics of the three-dimensional flow through a linear cascade of turbine vanes. The three-dimensional cascade flow is compared to the three-dimensional flow through a duct with a shape similar to the cascade passage shape. The measurements provide a description of the cascade flow and of the duct flow. By comparing the viscous flows for these two geometries, the usefulness of the duct shape for simulating cascade aerodynamics is evaluated. Except in the leading edge region, the qualities of the two flows are very similar. However the secondary flow is stronger in the duct passage than in the vane cascade passage. The effect on the cascade passage flow of the horseshoe vortex generated around the leading edge of each vane is shown to be limited to the region near the leading edge/endwall junction.

Introduction

Three-dimensional aerodynamics measurements have been performed in order to describe the flow through a vane cascade and a curved duct. The passage endwalls are flat for both geometries. Flow visualization and a five-hole probe were used to measure flow direction, velocity, total pressure, and static pressure throughout each flow field. The Reynolds number for the cascade experiment is 5.4×10^5 based on chord. For the duct experiment the inlet velocity is adjusted in order to match the Reynolds number based on the pitch or gap dimension. An evaluation of the periodicity of the four-vane cascade is made by investigation of the total and static pressure distribution across the exit of all three passages.

For the cascade and duct geometries, the flow through the passage is primarily two-dimensional. However, the near-surface flow and the passage viscous loss are strongly affected by secondary flow. The secondary flow in both geometries is dominated by a passage vortex. The vortex moves fluid down the pressure side of the passage, across the endwall toward the suction side, and up the suction surface toward midspan. High-loss fluid is moved into the suction side corner and onto the suction surface. The endwall boundary layer on the pressure side of the passage is thinned.

The clockwise passage vortex drives a counterclockwise vortex in the suction side corner for both geometries. In the cascade, the interaction between the passage vortex and the CCW vortex causes separation from the endwall and has a significant effect on the passage loss distribution. In the duct the CCW vortex is swept away by the passage vortex before it has a significant effect on the near endwall flow.

Except in the immediate vicinity of the vane leading edge, where the horseshoe vortex dominates the near endwall flow, the qualities of the duct passage flow are the same as those for the cascade passage flow. However, the effect of the duct geometry extends farther upstream than the effect of the cascade shape. This results in stronger secondary flow and higher viscous loss in the duct passage.

Background

The characteristics of the three-dimensional flow through a cascade of turbine blades are carefully described by Langston et al. (1977). Yamamoto (1987) recently presented a clear description of flow past a cascade of turbine vanes. Primarily, the flow through a gas turbine cascade passage is two-dimensional and the velocity vectors measured over the span are similar to that measured at midspan. Secondary flow has a strong effect on fluid velocity near the endwall and airfoil surfaces. The two-dimensional pressure field set up by the primary flow drives the secondary flow in the low-momentum fluid near the endwall. A horseshoe vortex is formed around the leading edge of the airfoil, near the airfoil/endwall junction. The legs of the vortex wrap around the airfoil. The leg that moves around the pressure side of the leading edge is referred to as the pressure side leg and the leg that wraps around the suction side is referred to as the suction side leg. The legs of the vortex have a storng effect on the flow in the leading edge region and have some effect as they move through the passage. Throughout the passage, the endwall boundary layer experiences crossflow toward the suction side of the passage. This crossflow is driven by the pressure-to-suction pressure gradient set up at midspan. The crossflow of the endwall boundary layer results in the formation of a passage vortex. The passage vortex has a strong effect on overall viscous loss and on component surface heat transfer.

Contributed by the Heat Transfer Division and presented at the ASME Winter Annual Meeting, Chicago, Illinois, November 27–December 2, 1988. Manuscript received by the Heat Transfer Division October 25, 1988.

Moore and Adhye (1985) show increased loss in the cascade exit region to be equal to the decreasing kinetic energy associated with the secondary velocity vectors. The data presented in the results of this paper and the data in Langston (1977) and Yamamoto (1987) show the secondary flow causing high-loss fluid to move out into the high velocity stream. Blair (1974), Graziani (1980), York (1984), and Goldstein (1987) show the secondary flow strongly affecting the heat transfer from the endwall and the suction surface of the airfoil.

The secondary flow in curved ducts is similar in quality to that found in cascades. Figure 1 shows the distribution of total pressure contours measured in the exit plane of a 90-deg bent duct with flat endwalls and coverging sidewalls (Stanitz, 1953). Figure 2 shows the exit plane total pressure contours measured by Langston (1977) for a blade cascade. The clear features shown in both of these figures are thin endwall boundary layers on the pressure side and high-loss fluid in the suction side corner. High-loss fluid is convected up the curved suction surface of the airfoil and from the suction surface out into the high velocity stream. The secondary velocity vectors measured in duct flows by Sanz and Flack (1986) and Taylor et al. (1982) and the secondary velocity vectors shown in Langston et al. (1977) and Yamamoto (1977) all show strong endwall crossflow and spanwise flow on the curved suction surface. A careful comparison of the secondary flow for a vane cascade and a duct is reported herein.

Experimental Geometry

Cascade. A linear cascade consisting of four vanes was installed in the test section of an open circuit wind tunnel. The wind tunnel was designed and built for the purpose of this study (Boyle, 1986). The test section entrance is 0.305 m tall by 1.22 m wide. Figure 3 provides a test section coordinate system and shows important dimensions. The x direction is the axial direction, the y direction is normally out of the plane of the figure toward the reader, and the z-coordinate direction is taken to be consistent with the right-hand rule. The vane shape is taken from the first vane in a Textron Lycoming ALF502 gas turbine and is scaled up to have a chord dimension of 0.463 m. Each vane is 0.305 m long in the spanwise direction and is made in seven sections of machined mahogany. The cascade pitch is 0.305 m. Vanes 2 and 3 have static pressure taps installed around the leading and trailing edge regions at midspan. Vane 2 has static pressure taps installed along the suction side contour at midspan and vane 3 has taps along the pressure side contour. The outer sides of the test section are fitted with flexible sidewall bleeds and the outer vanes have tailboards fixed to their trailing edges. The tailboards and sidewall bleeds are used to adjust the test section flow so that the midspan static pressure distribution for the center of the three passages closely matches the potential flow pressure distribution calculated for an infinite cascade of vanes. This is discussed further in the periodicity section.

Aerodynamics measurements were taken in the six axial planes shown in Fig. 3. The most upstream plane is located one third of the axial chord upstream of the cascade leading edge. The remaining five planes are located at the nondimensional axial locations shown in the figure. Traverses of the five-hole probe were taken in the y direction and cover the lower half of the cascade span with data taken at 26 y loca-

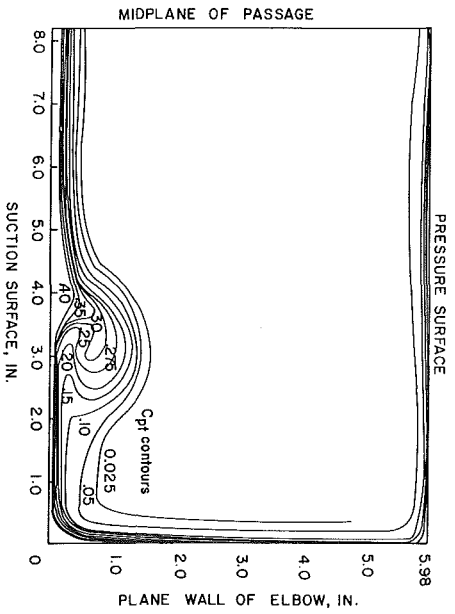

Fig. 1 Total pressure contours at exit of 90 deg deg bent duct (Stanitz, 1953)

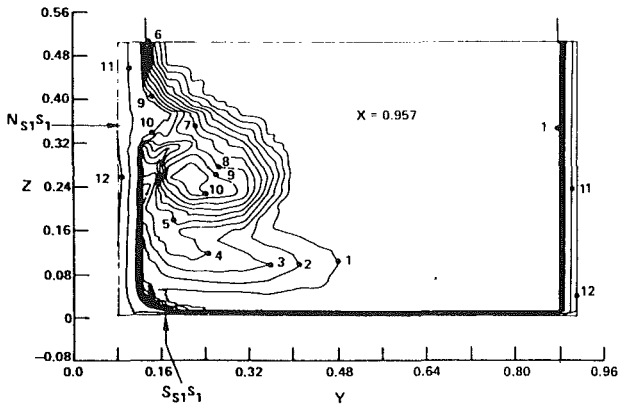

Fig. 2 Total pressure contours at exit of Langston (1977) cascade

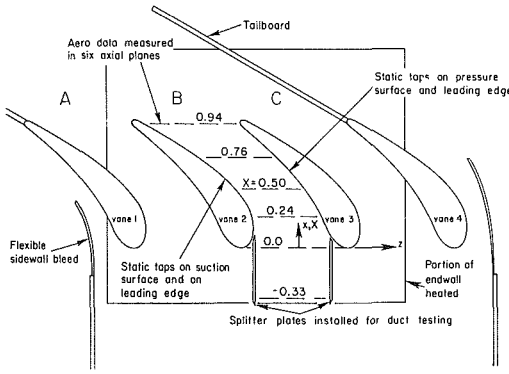

Fig. 3 Top view of test section

Nomenclature

$C_{ps} = (P_s - P_{sr})/1/2\ \rho V_r^2$
$C_{pt} = (P_{tr} - P_t)/1/2\ \rho V_r^2$
H = shape factor
P_s = static pressure
P_{sr} = reference static pressure
P_t = total pressure
P_{tr} = reference total pressure
$q = 1/2\ \rho V^2$ = dynamic head
$s = (x^2 + z^2)^{1/2}$ = horizontal plane
V = velocity
V_r = upstream reference velocity
u, v, w = secondary velocity components
x, y, z = coordinates
W_i = uncertainty in i variable
X = nondimensional axial chord
δ = boundary layer thickness
θ = yaw angle
ρ = mass density
ϕ = pitch angle

tions. In each plane traverses were taken at 9 or 10 z locations across the passage gap.

Duct. The duct geometry is obtained by installing two splitter plates upstream in the center passage. This is shown schematically in Fig. 3. The splitter plate on the suction side of the duct is located so that the curvature of the duct wall is continuous at the junction of the splitter and the curved suction surface. The pressure side splitter plate is installed in the same x location as the suction side plate. The distance between the two plates is 0.229 m. Each plate is 0.22 m in length. The leading edge of each plate is located 0.17 m upstream of the cascade leading edge. The length of the splitters is the minimum required to reach uniform flow upstream, as determined by the use of endwall flow visualization. The minimum length of splitter plate is used in order to keep the boundary layer growth on the plates to a minimum.

Instrumentation

A five-hole probe is used to measure flow direction, velocity magnitude, total pressure, and static pressure throughout the three-dimensional flow field. The probe is calibrated for measurement while nulled in yaw. A probe positioner moves the probe throughout the three-dimensional flow space. The x–z position of the probe is set by push button control. A spanwise traverse over one half of the cascade span is performed automatically by computer control.

All pressure measurements are referenced to a kiel probe installed through the test section side wall. Pressure measurements are made with either a Datametrics Barocel 590 differential pressure transducer or a Setra differential transducer. The Setra transducer is used to null the five-hole probe in yaw and is switched in or out by a two-port pressure switch. All other pressure measurements are switched to the Datametrics transducer with a 24-port Scanivalve fluid wafer switch.

The spatial location of the tip of the five-hole probe and the angular orientation of the probe are followed by four potentiometers used as voltage dividers. The outputs of these displacement transducers and the pressure transducers are measured with a 12 bit QUA TECH A/D board, which is controlled by an IBM personal computer. During a traverse, the probe position and the pressure switches are controlled via the personal computer and the D/A ports of the QUA TECH board.

The uncertainty in each measurement is summarized as follows:

W_θ	= 0.794 deg	$W_{C_{ps}}$	= 0.0123
W_ϕ	= 0.53 deg	W_v	= 0.109 m/s
W_q	= 0.0208 cm water	W_s	= 0.05 cm
$W_{C_{pt}}$	= 0.00729	W_y	= 0.0112 cm

for V = 15.24 m/s, ϕ = 15 deg, and 20 to 1 odds.

The details of the five-hole probe calibration, the operation of the three-space probe positioner, and the uncertainty analysis are provided by Boyle (1987a).

Test Conditions

The vane cascade measurements were made with a free-stream inlet velocity of 19.5 m/s and a corresponding Reynolds number based on a chord of 5.4 × 10^5. The free-stream velocity for the duct experiment was increased to 26.2 m/s. The duct experiment is conducted at a higher free-stream velocity than the cascade experiment in order to match the Reynolds number based on pitch or gap dimension for the two geometries. The pitch of the cascade, or the distance between the stagnation streamlines for vanes 2 and 3, is 0.305 m. The distance between the two splitter plates for the duct geometry is 0.229 m. If the free-stream velocity were the same for the two experimental configurations, then the average velocity in a downstream plane would be higher for the cascade than the duct by 4/3. In the duct configuration the free-stream velocity is set 4/3 larger than the cascade free-stream velocity in order to achieve the same average velocity in planes downstream of the splitter plate location for the two configurations.

The total pressure across the test section entrance was mapped with a kiel head probe prior to installing the vane models in the test section. The dynamic head in the core flow is uniform to better than 0.5 percent of the free-stream dynamic head. The boundary layer is approximately 0.23 cm thicker on the outer portions of the endwall than on the inner portions. This is attributed to secondary flow in the low-speed region of the wind tunnel nozzle and is discussed by Boyle (1986). The characteristics of the boundary layer on the wind tunnel centerline are δ = 2.92 cm and H = 1.37.

Periodicity of Cascade

In order to simulate the flow through a cascade passage accurately and also maximize spatial resolution (large vanes compared to probe size), a four-vane cascade is used to model an infinite cascade. Periodicity in the four-vane cascade is adjusted for by moving the two tailboards and the two sidewall bleeds. Feedback for these adjustments is obtained by comparing the midspan static pressure distribution in the center passage, passage B, to the static pressure distribution calculated for potential flow through an infinite array of vanes. The position of the pressure side tailboard strongly affects the level of static pressure throughout the center passage. The positions of the sidewall bleeds affect the level of static pressure in the center passage to a small extent and strongly affect the position of the leading edge stagnation points. The position of the stagnation points on the leading edges of vanes 2 and 3 agree well with potential flow. Over the pressure surface and most of the suction surface the measured pressures compare well with potential flow. The pressure distribution measured on the downstream portion of the suction surface is higher than that calculated by potential flow. The deviation of the measured pressure distribution from that obtained by a two-dimensional potential flow calculation is caused by strong secondary flow near the passage exit region.

In order to evaluate the periodicity of the four-vane cascade more completely, the total and static pressure distributions in the plane just downstream of the exit of the three passages was measured. Figure 4 shows the static and total pressure contours. Qualitatively, the static and total pressure distributions at the exits of passages A and B compare well. The total pressure distribution in passage C differs from A and B by the absence of high-loss fluid near the endwall on the pressure side. Inspection of the static pressure contours reveals a lower pressure-to-suction pressure gradient on the pressure side of passage C than for the pressure sides of A and B. The orientation of the straight tailboard on the pressure side is appropriate for achieving the required level of pressure in the center passage. However, at the junction of the trailing edge of vane 4 and the tailboard the local streamline direction does not match that found in the same location in the other two passages.

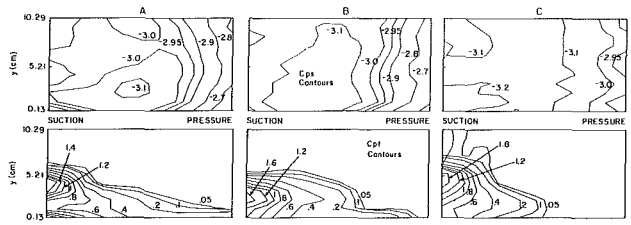

Fig. 4 Static pressure coefficient and total pressure coefficient across exit of all three passages, 1.9 cm downstream of exit plane

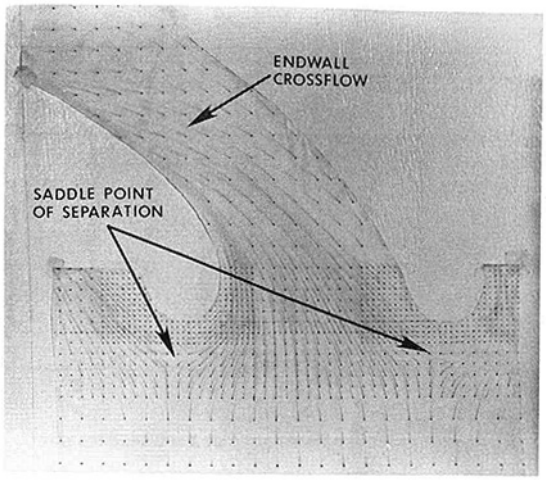

Fig. 5 Cascade endwall flow visualization

The total pressure contours for all three passages show a region of maximum total pressure loss on the curved suction surface. This has been shown by Langston et al. (1977) to be associated with separation from the suction surface. Sharma and Butler (1987) point out that the distance between the endwall and the position of the suction surface separation line is roughly equal to the height of the passage vortex at the exit plane. These authors further hypothesize that this height can be used as a measure of the intensity of secondary flow. The height of the maximum loss region on the suction surface is approximately twice as high in passages A and C as it is in the center passage. Based on this it could be hypothesized that the secondary flow is stronger in the two outside passages than in the center passage. This can only be further evaluated by performing detailed measurements in passages A and C.

Cascade Results

Flow Visualization. Figure 5 is a photograph of the endwall flow visualization for the center passage of the cascade. Flow visualization was performed by the ink-dot method described by Langston and Boyle (1982). The streamline topology associated with the formation of a horseshoe vortex is clearly evident on the endwall around the leading edges of both vanes. The location of the saddle point of separation for each vortex is pointed out in the figure. Crossflow of the endwall boundary layer fluid can be seen throughout the passage. Flow visualization was also performed on the vane surfaces. On the suction surface streamlines converge toward midspan and on the pressure surface streamlines are directed parallel to the endwall.

Five-Hole Probe Data. For each of the six axial planes shown in Fig. 3, measurements are made so that total pressure, static pressure, actual velocity vectors, and secondary velocity vectors can be presented. Actual velocity vectors (AVEL) are presented by projecting the measured velocity vectors into the measurement plane. Secondary velocity vectors are obtained by vectorially subtracting the midspan velocity vector from each velocity vector measured at the same x–z traverse location. The resulting vector is projected into the axial measurement plane for presentation.

Figure 6(*a*) shows the secondary velocity vectors measured at the cascade leading edge plane, $X=0$. Most of the flow in this plane is similar to the two-dimensional midspan flow. Therefore, most of the secondary velocities have magnitude near zero. Secondary velocities are significant near the endwall. A counterclockwise vortex is shown clearly in the suction side/endwall corner. Limited evidence of a clockwise vortex can be seen in the pressure side/endwall corner. The clockwise

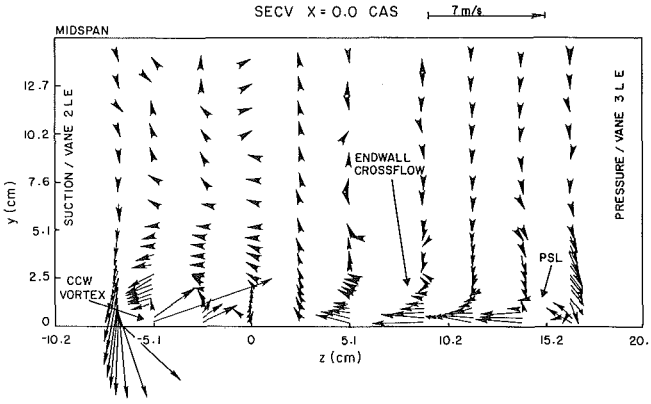

Fig. 6(*a*) Secondary velocity in cascade entrance plane

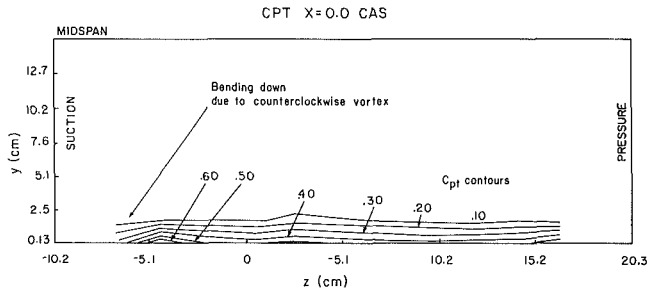

Fig. 6(*b*) Total pressure coefficient in cascade entrance plane

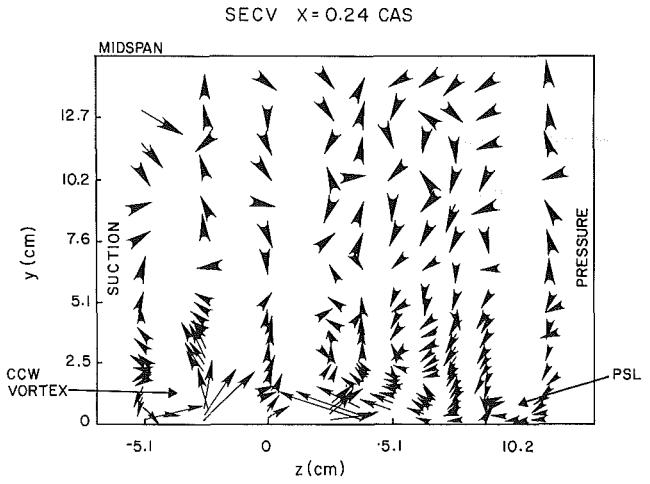

Fig. 7 Secondary velocity at $X=0.24$, cascade

vortex is caused by the pressure side leg (PSL) of the horseshoe vortex associated with vane 3. The counterclockwise vortex is initiated by the suction side leg (SSL) of the horseshoe vortex associated with vane 2. Note that the SSL is significantly stronger than the PSL. Between the SSL and the PSL, endwall fluid moves across the passage toward the suction side. This crossflow drives and strengthens the SSL. Figure 6(*b*) shows the total pressure contours for the leading edge plane. The effect of the SSL can be seen in the suction side corner where the loss contours bend down. The secondary flow is not strong enough at $X=0$ to have a significant effect on the two-dimensional boundary layer loss distribution.

Figure 7 shows the secondary velocity vectors at $X=0.24$. A strong counterclockwise (CCW) vortex is located in the suction side corner. Although there are not many data points showing its effect, the PSL can be seen in the pressure side corner. Strong crossflow of the endwall fluid toward the suction side is evident between the two vortices. The CCW vortex con-

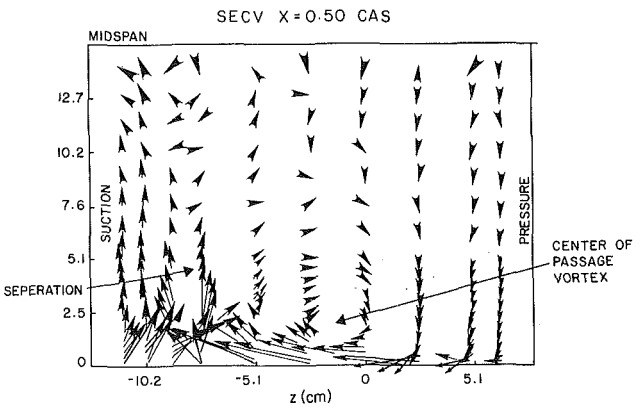

Fig. 8 Secondary velocity at $X = 0.5$, cascade

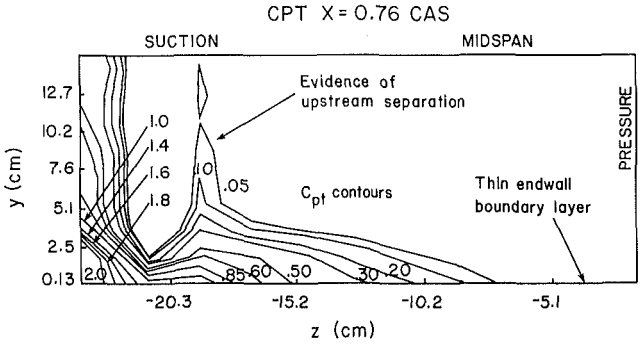

Fig. 9 Total pressure coefficient at $X = 0.76$, cascade

tinues to be strengthened by the endwall crossflow so that it is stronger than the PSL in this plane.

Halfway through the passage (Fig. 8), the secondary velocity vectors show the formation of a passage vortex. This vortex is driven by the endwall crossflow. In this plane the secondary flow is dominated by the passage vortex as the effects of the CCW vortex and the PSL are not evident. The secondary velocity vectors show a separation from the endwall at $X = 0.50$. Evidence of this separation and of the passage secondary flow in general is clear in the total pressure contours at $X = 0.76$ (Fig. 9). The interaction between the CCW vortex and the passage vortex causes high-loss fluid to separate from the endwall and to be mixed into the high-velocity core flow. The passage vortex moves high-loss fluid across the passage and up along the suction surface. The endwall boundary layer gets very thin on the pressure side of the passage.

Figures 10(*a*) through 10(*d*) show the secondary velocity vectors, total pressure contours, static pressure contours, and actual velocity vectors at the cascade exit plane. The exit plane secondary velocity shows the passage vortex dominating the secondary flow. The total pressure contours show that the passage vortex has moved high-loss fluid across to the suction side of the passage, up off the endwall into the high-velocity core flow, and up the suction surface. The total pressure contours taken together with the static pressure distribution show a very thin boundary layer on the pressure side half of the passage. Through most of the passage flow, the secondary flow is not strong enough to affect the static pressure distribution significantly. In the exit plane the secondary flow is strong enough that closed static pressure contours occur with a minimum near the core of the passage vortex. The actual velocity vectors (Fig. 10*d*) show that even in the exit plane, where the secondary flow is the strongest, the velocity field is primarily two-dimensional and similar to that measured at midspan. The passage vortex tends to enhance or impede somewhat the pressure-to-suction motion of the fluid in the endwall region.

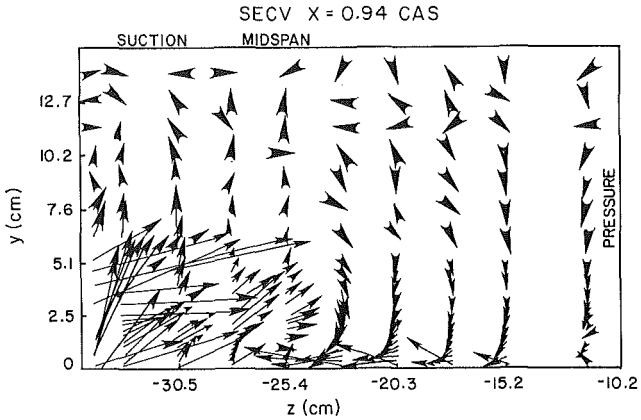

Fig. 10(*a*) Secondary velocity at $X = 0.94$, cascade

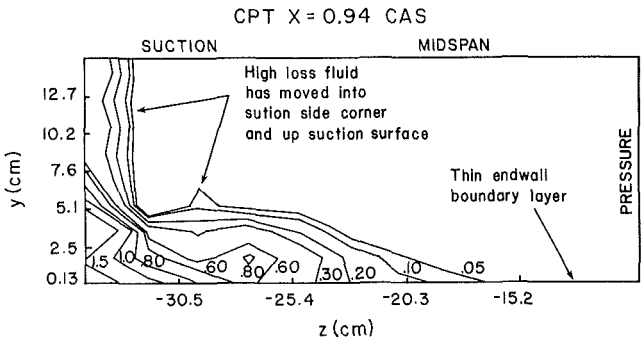

Fig. 10(*b*) Total pressure coefficient at $X = 0.94$, cascade

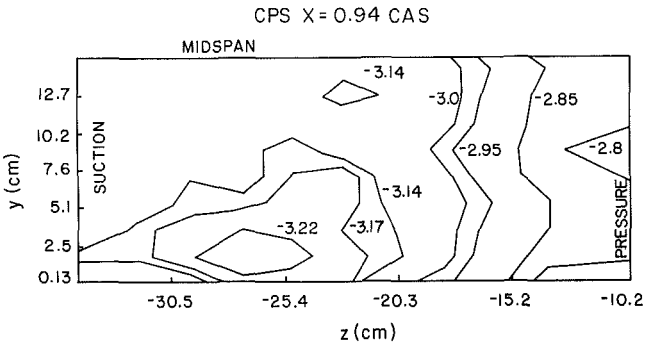

Fig. 10(*c*) Static pressure coefficient at $X = 0.94$, cascade

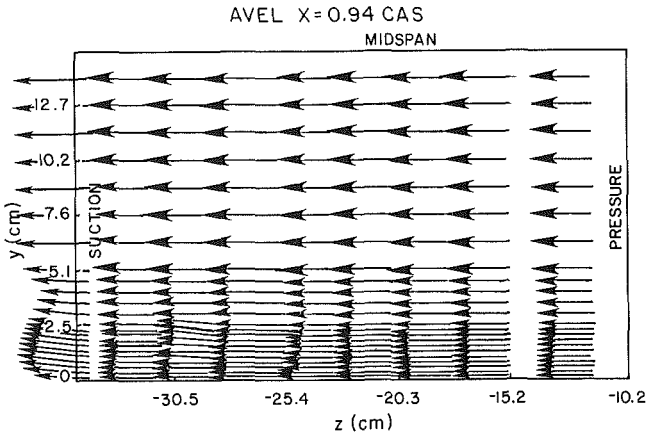

Fig. 10(*d*) Actual velocity at $X = 0.94$, cascade

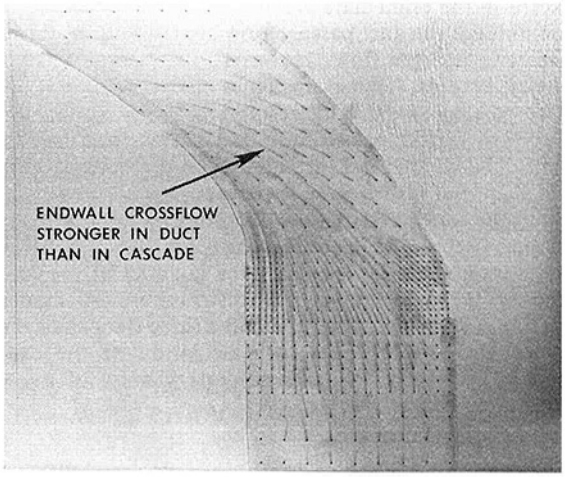

Fig. 11 Duct endwall flow visualization

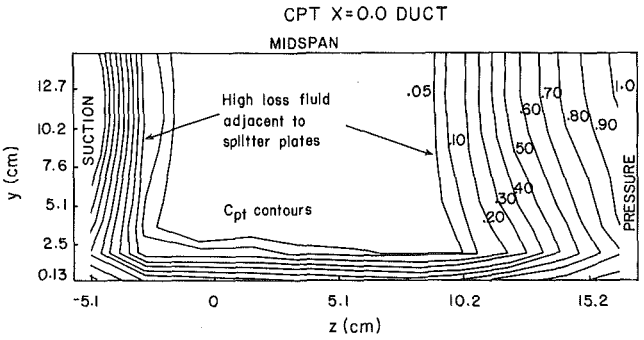

Fig. 12(*a*) Total pressure coefficient in duct entrance plane

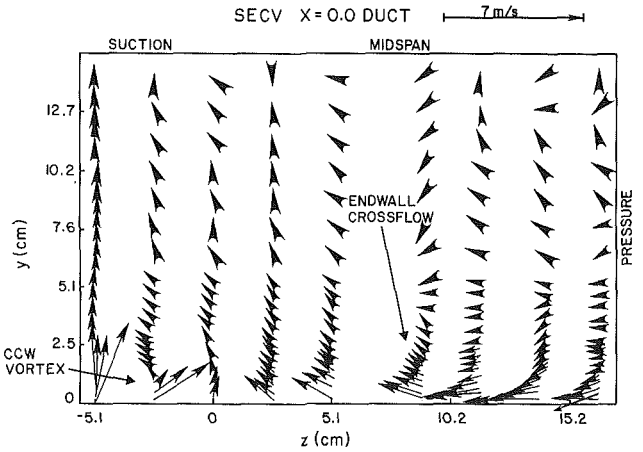

Fig. 12(*b*) Secondary velocity in duct entrance

Although the velocity and static pressure fields are not strongly affected by secondary flow, the total pressure distribution and overall passage loss are strongly affected by the passage vortex flow. It is also clear from these aerodynamics measurements that the endwall surface heat transfer will be strongly enhanced on the pressure side of the passage.

The qualities of the ALF502 vane cascade flow are similar to those reported by other researchers working on vane and blade cascades. Specific to the vane geometry however is the effect of the CCW vortex over 75 percent of the axial chord. The interaction of the CCW vortex with the passage vortex causes the endwall boundary layer to separate and mix high-loss endwall fluid into the core flow. To the authors' best knowledge, the vortex was first reported in the flow visualization performed by Sonoda (1985) at lower Reynolds numbers. The presentation of the duct data in the next section shows how the endwall crossflow associated with the passage vortex strengthens the CCW vortex while the PSL is small in its effect.

Sieverding (1983) used colored smoke flow visualization to show the evolution of horseshoe and passage vortices through a blade cascade passage. These data show the PSL does not evolve to become the passage vortex but rather the PSL and the SSL evolve together with the passage vortex. This is consistent with the cascade data presented in this section.

Duct Results and Comparison with Cascade

Flow Visualization. Figure 11 shows the endwall flow visualization for the duct geometry. The flow moving into the curved duct passage at $X = 0$ is not affected by the legs of a horseshoe vortex. Crossflow of the endwall boundary layer from the pressure toward the suction side is clearly shown throughout the passage. Comparison with the cascade endwall flow visualization reveals stronger crossflow in the duct passage. This is evident by the number of endwall streamlines that intersect the suction surface.

Five-Hole Probe Data. Complete three-dimensional aerodynamics measurements were made for the duct geometry in the six axial planes shown in Fig. 3. A small portion of these data is presented in this section in order to describe the qualities of the duct flow. The duct passage flow is compared to the vane cascade passage flow.

Figure 12(*a*) shows the total pressure contours at $X = 0$ and Fig. 12(*b*) shows the secondary velocity vectors. The viscous loss associated with the duct passage flow is much higher than that associated with the cascade. The total pressure contours at $X = 0$ in the duct show high-loss fluid adjacent to each sidewall as well as in the endwall region. The core flow entering the duct turns toward the suction side farther upstream than the cascade flow. A strong pressure to suction pressure gradient starts secondary endwall crossflow farther upstream in the duct than in the cascade passage. The motion of the core fluid from the pressure side to the suction side moves high loss fluid from near the surface of the passage side splitter plate out into the passage. High-loss fluid moves across the endwall and up the surface of the suction side splitter plate.

Although the effect in the duct is small, a counterclockwise rotating vortex is evident in the suction side/endwall corner of Fig. 12(*b*). The vortex is also shown in the actual velocity vector data. This small vortex is driven by the crossflow of the passage endwall fluid. The existence of the counterclockwise vortex in the duct provides an explanation for the fact that in the cascade the counterclockwise vortex is stronger than the pressure side leg.

The total pressure contours and secondary velocity vectors for the duct exit plane are shown in Figs. 13(*a*) and 13(*b*). The secondary flow in the duct exit plane is dominated by the passage vortex. The core of the passage vortex in the duct exit is closer to the suction side of the passage than for the cascade passage vortex. This is consistent with the stronger endwall crossflow in the duct. The secondary flow and total pressure loss distribution at the duct exit have the same qualities as the flow at the cascade exit. High total pressure fluid moves down the pressure side of the passage to cause a thinning of the pressure side endwall boundary layer. High-loss fluid moves across the endwall into the suction side corner and up the suction surface.

From the qualities of the actual and secondary velocity information, it is difficult to differentiate between the duct passage flow and cascade passage flow. Since the high-loss fluid enters the duct passage from the surface of the splitter plates, and there is stronger crossflow in the duct passage, the

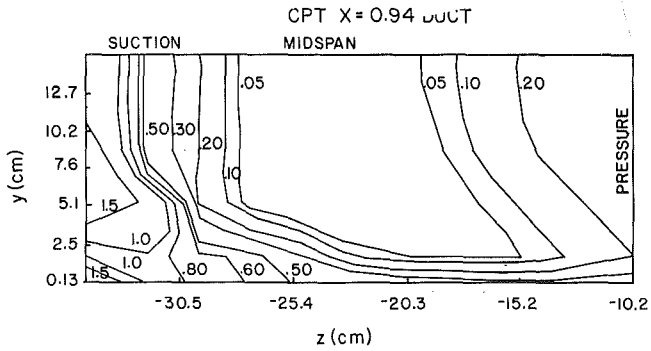

Fig. 13(a) Total pressure coefficient at X = 0.94, duct

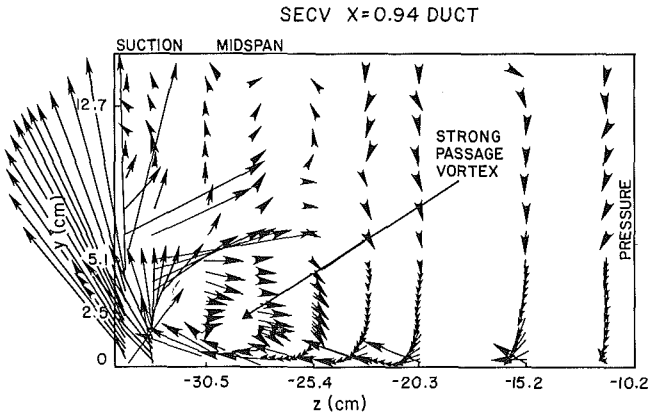

Fig. 13(b) Secondary velocity at X = 0.94, duct

viscous loss that occurs in the duct flow is much higher than that in the cascade.

The complete set of three-dimensional aerodynamic data for both the cascade and the duct is presented graphically and in tabular form by Boyle and Simonds (1987).

Conclusions

Three-dimensional aerodynamics measurements have been performed in order to describe the flow through a vane cascade passage and a similarly shaped duct. The Reynolds number is in the range of application of gas turbine cascades.

The flow through each of the passages is primarily two-dimensional and similar to the midspan flow. However, the fluid near the endwall and suction surfaces is strongly affected by secondary flow. The passage loss is strongly affected by secondary flow. For both geometries, a passage vortex sweeps fluid down the pressure side of the passage, across the endwall toward the suction side, and up the suction surface toward midspan. High-loss fluid is moved into the suction side corner and onto the suction surface. The endwall boundary layer on the pressure side of the passage is thinned.

The passage vortex drives a counterclockwise vortex in the suction side corner, for both geometries. In the cascade, the interaction between the CCW vortex and the passage vortex causes separation from the endwall and has a significant effect on the passage loss distribution. In the cascade, the counterclockwise vortex can be thought of as the suction side leg of the horseshoe vortex, enhanced by the endwall crossflow. The pressure side leg of the horseshoe vortex has a significant effect on aerodynamics in the immediate vicinity of the vane leading/endwall junction. It has almost no effect on the remainder of the passage flow.

Except in the immediate vicinity of the vane leading edge, the qualities of the duct passage flow are the same as those for the cascade passage flow. However, the effect of the duct geometry extends farther upstream than the effect of the cascade passage shape. This results in the generation of secondary flow farther upstream in the duct passage than in the cascade. The viscous loss throughout the duct passage flow is higher than that in the cascade passage.

It must be concluded that the duct shape is not adequate for predicting viscous loss in a turbine cascade passage. However, the duct is valuable for modeling the qualities of the cascade secondary flow, including loss distribution. A numerical prediction scheme tuned to predict the three-dimensional duct flow would be well suited for calculation of the cascade passage flow, except in the immediate vicinity of the vane leading edge.

Acknowledgments

The wind tunnel was built in a timely fashion by G. Wark and T. Pierce. The data acquisition/experiment control system was built by J. Vansandt and D. Reed. Recognition is due to M. Simonds for the performance of a high quality experiment as part of his thesis work. The authors gratefully acknowledge Textron Lycoming Corp. for their support of this work and for their permission to publish the results.

References

Blair, M. F., 1974, "An Experimental Study of Heat Transfer and Film Cooling on Large Scale Turbine Endwalls," ASME *Journal of Heat Transfer*, Vol. 96, Nov.

Boyle, M. T., 1986, "Heat Transfer and Crossflow on Turbine Endwalls," Report No. 3, submitted to Textron Lycoming, available from author.

Boyle, M. T., 1987, "Heat Transfer and Crossflow on Turbine Endwalls," Report No. 4, submitted to Textron Lycoming, available from author.

Boyle, M. T., and Simonds, M., 1987, "Heat Transfer and Crossflow on Turbine Endwalls," Phase II Final Report, submitted to Textron Lycoming, available from author.

Goldstein, R. J., 1987, "Turbulent Transport on the Endwall in the Region Between Adjacent Turbine Blades," ASME HTD-Vol. 87.

Graziani, R. A., Blair, M. F., Taylor, J. R., and Mayle, R. E., 1980, "An Experimental Study of Endwall and Airfoil Surface Heat Transfer in a Large Scale Turbine Blade Cascade," ASME *Journal of Engineering for Power*, Vol. 102.

Langston, L. S., Nice, M. L., and Hooper, R. M., 1977, "Three-Dimensional Flow Within a Turbine Cascade Passage," ASME *Journal of Engineering for Power*, Vol. 99.

Langston, L. S., and Boyle, M. T., 1982, "A New Surface Streamline Flow-Visualization Technique," *Journal of Fluid Mechanics*, Vol. 125.

Moore, J., and Adhye, R. Y., 1985, "Secondary Flows and Losses Downstream of a Turbine Cascade," ASME *Journal of Engineering for Gas Turbines and Power*, Vol. 107.

Sanz, G. M., and Flack, R. D., 1986, "Flow Visualization of Secondary Flows in Three Curved Ducts," ASME Paper No. 86-GT-166.

Sharma, O. P., and Butler, T. L., 1987, "Predictions of Endwall Losses and Secondary Flows in Axial Flow Turbine Cascades," ASME JOURNAL OF TURBOMACHINERY, Vol. 109.

Sieverding, C. H., and Van Den Bosche, P., 1983, "The Use of Coloured Smoke to Visualize Secondary Flows in a Turbine Blade Cascade," *Journal of Fluid Mechanics*, Vol. 134.

Sonoda, T., 1985, "Experimental Investigation on Spatial Development of Streamwise Vortices in a Turbine Inlet Guide Vane Cascade," ASME Paper No. 85-GT-20.

Stanitz, J. D., Osborn, W. M., and Mizisiu, J., 1953, "An Experimental Investigation of Secondary Flow in an Accelerating, Rectangular Elbow With 90° of Turning," NACA TN 3015.

Taylor, A. M. K. P., Whitelaw, J. H., and Yianneskis, M., 1982, "Curved Ducts With Strong Secondary Motion: Velocity Measurements of Developing Laminar and Turbulent Flow," ASME *Journal of Fluids Engineering*, Vol. 104.

Yamamoto, A., 1987, "Production and Development of Secondary Flows and Losses Within Two Types of Straight Turbine Cascades," ASME JOURNAL OF TURBOMACHINERY, Vol. 109.

York, R. E., Hylton, L. D., and Mihelc, M. S., 1984, "An Experimental Investigation of Endwall Heat Transfer and Aerodynamics in a Linear Vane Cascade," ASME *Journal of Engineering for Gas Turbines and Power*, Vol. 106.